
An Investigation of Coupled Processes in Coal in Response to High Pressure Gas Injection

Renato Zagorščak

Geoenvironmental Research Centre
Cardiff School of Engineering
Cardiff University

*Thesis submitted in candidature for the degree of Doctor of Philosophy at
Cardiff University*

February 2017



Acknowledgements

I would first like to express my sincere gratitude to my supervisor, Professor Hywel Thomas for his invaluable guidance, support and encouragement. I am extremely grateful for the opportunity he has provided me with, allowing me to realise this milestone. I would also like to express my deepest thanks and appreciation to Dr Majid Sedighi for his technical guidance and support in the early stages of this work. The work undertaken would not be possible without the financial support of the SEREN Project at the early stage of this research as well as the SEREN2020 (FLEXIS) Project at the later stage of this research, both funded by the Welsh European Funding Office (WEFO) and Cardiff University.

I would also like to thank the past and present members of the Geoenvironmental Research Centre (GRC) at Cardiff University for their support and friendship; Aleksandra, Alejandro, Irfan, Jack, James, Jamie, Hishiv, Manhui, Manju, Mojgan, Richard, Rob, Sanjana and Sivachidambaram among many others. Very special thanks to my dear friends and colleagues Lee and Shakil for their help and support to better understand the aspects of numerical modelling.

Walter Energy Inc., Energy Build Ltd. and Celtic Energy Ltd. are also gratefully acknowledged for providing coal blocks to conduct this research.

Outside the GRC, I am very grateful to many of the technical staff in the School of Engineering: Carl, Gareth, Harry, Jack, Malcolm, Marco, Richard and Steve. Special thanks also to Tony in the Earth Sciences department for his continuous help, friendship and support throughout this work. I would also like to thank Professor Biljana Kovačević-Zelić and Dr Boris Kavur for their support and encouragement to pursue this research.

The greatest thanks are reserved for my family. Words cannot truly express gratitude and appreciation to my mother and brother who have given me exceptional love, support and encouragement. To my dear and beloved father whose memory lives in my heart, I would not be where I am today without you.

A very special mention to my close family members and friends for believing in me: Alen, Dejan, Diana, Dijana, Ivan, Janja, Kristijan, Lana, Ljiljana, Marko, Matea, Mateja, Matija, Mladen, Rade, Ruza, Sanja, Stefica and Vlado.

Most importantly, my wife Marinela deserves a special recognition for her continuing patience, friendship and guidance. Her endless love has afforded me the opportunity to feel fortunate at any given moment.

Summary

This thesis presents a comprehensive investigation into the underlying coupled processes in coal in response to high pressure gas injection. This is achieved by i) developing a new high pressure gas experimental facility and conducting a series of experimental tests, and ii) developing and applying a theoretical and numerical model.

A novel experimental facility was designed, which offers stable and continuous high-pressure injection of gases in fractured rocks, for detailed study of the reactive transport processes. It consists of the gas supply and backpressure control system. Using the newly developed experimental facility, the response of coal subject to subcritical and supercritical gas injection under stable and variable temperature conditions was studied. The experimental investigation consisted of a series of tests: i) sorption capacity and kinetics tests, ii) uniaxial compressive tests, iii) sieve analysis tests, iv) flow and deformation tests. Thirty anthracite coal samples from different depths (i.e. 150 m and 550 m) and locations from the South Wales coalfield were characterised and tested.

The capabilities of the theoretical and numerical modelling platform of thermal, hydraulic, chemical and mechanical processes were advanced. A new theoretical approach was adopted which successfully incorporates reactive gas transport coupled with coal deformation. The development of constitutive relationships describing the sorption induced elastic isotropic swelling of coal and changes in permeability was considered in detail. Numerical solutions of the governing flow and deformation equations were achieved by employing the finite element method for spatial discretisation and the finite difference method for temporal discretisation. The new model was verified for its accuracy via a series of benchmark tests and validated using high-resolution experimental data.

The results of the experimental study showed that the sorption capacity and kinetics are sample-size dependent, particularly for deeper coal. Higher and faster sorption of CO₂ obtained on powdered samples compared to intact samples indicated that sorption processes are governed by fracture interconnectivity and accessibility of pores. Sorption of CO₂ was found to significantly reduce the brittleness, uniaxial compressive strength and elastic modulus of anthracite coals. The results of the post-failure sieve analysis showed that CO₂ saturated samples disintegrated on smaller particles than non-saturated samples indicating that sorption induced swelling weakens the coal structure by enhancing the existing and inducing new fractures. During CO₂ flow through coal under constant stress, samples experienced swelling resulting in initial reduction followed by recovery of measured flow rates. CO₂ sorption induced changes were found to be non-reversible. The results of high CO₂ flow through coal showed that CO₂ reduced the temperature of the system, associated with Joule-Thomson cooling, enhancing the coal swelling and opposite to expected, increasing the flow rates. Overall, the high-resolution data-set obtained is a significant contribution to the scientific community and is able to provide a means of validation for future models.

The results of the verification and validation exercises demonstrated the capability of the developed model to simulate coupled processes involved in gas transport in coal. A series of numerical simulations were conducted to investigate the permeability evolution and CO₂ breakthrough in coal subject to supercritical CO₂ injection using the developed model. Different scenarios were considered, involving a range of values of the elastic modulus and the parameter defining the coal swelling. The results of the advanced numerical simulations showed that the effect of CO₂ sorption induced swelling on permeability reduces with a decrease in coal stiffness suggesting that CO₂ sorption induced reduction of elastic modulus would have a positive effect on the ability of coal to conduct CO₂.

In this work, confidence in the feasibility of CO₂ storage in anthracite coals was improved by enhancing the knowledge of high pressure gas-coal interactions through both experimental and numerical investigations. Moreover, it is claimed that newly developed model enables predictions of coupled processes involved in carbon sequestration in coal.

Nomenclature

A	Cross-sectional area of the sample
A_p	Defined in equation (3.47)
A_{sw}	Defined in equation (3.50)
\mathbf{A}	Defined in equation (3.86)
b_x, b_y, b_z	Body forces in Cartesian coordinate system
\mathbf{b}	Vector of body forces
\mathbf{B}	Defined in equation (3.86)
c_{ads}	Molar density of the adsorbed gas
c_g	Gas concentration
\hat{c}_g	Approximate gas concentration
c_{gs}	Vector of the gas concentration defined in equation (3.68)
\dot{c}_{gs}	Vector of time differentials of gas concentration
c_{g0}	Initial gas concentration
C	Defined in equation (3.91)
$C_{c_g c_g}$	Defined in equation (3.28)
$C_{c_g \mathbf{u}}$	Defined in equation (3.29)
C_f	Fracture compressibility
$C_{\mathbf{u} c_g}$	Defined in equation (3.56)
$C_{\mathbf{u} \mathbf{u}}$	Defined in equation (3.57)
\mathbf{C}	Defined in equation (3.86)
$\mathbf{C}_{c_g c_g}$	Defined in equation (3.70)
$\mathbf{C}_{c_g \mathbf{u}}$	Defined in equation (3.71)
$\mathbf{C}_{\mathbf{u} c_g}$	Defined in equation (3.82)
$\mathbf{C}_{\mathbf{u} \mathbf{u}}$	Defined in equation (3.83)
d	Fracture aperture
D_g	Gas diffusion coefficient
D_g^0	Reference gas diffusion coefficient
D_{ge}	Effective gas diffusion coefficient

D	Elasticity matrix
e	Void ratio
E	Elastic (Young's) modulus
E_{CO_2}	Elastic modulus of CO ₂ saturated coal
$E_{natural}$	Elastic modulus of natural (non-saturated) coal
f_m	Interaction function
f_{c_g}	Approximate pore gas flux normal to the boundary surface
\mathbf{f}_{c_g}	Defined in equation (3.73)
\mathbf{f}_u	Defined in equation (3.84)
F	Applied force
F_T	Target function defined in equation (5.3)
g	Gravitational acceleration
i	Iteration level
J_{c_g}	Defined in equation (3.31)
J_g	Total gas flux
J_{gAdv}	Advective flux of bulk gas
J_{gDif}	Diffusive flux of bulk gas
k	First-order reaction rate defined in equation (5.5)
k'	Seconds-order reaction rate defined in equation (5.6)
k'', k'''	Two first-order reaction rates defined in equation (5.7)
k_g	Gas conductivity
K	Intrinsic permeability
$K_{c_g c_g}$	Defined in equation (3.30)
K_g	Measured permeability to gas
K_R	Compressibility ratio defined in equation (8.11)
K_M	Macrostructural bulk modulus
K_0	Reference intrinsic permeability
$\mathbf{K}_{c_g c_g}$	Defined in equation (3.72)
L	Sample length
L_x	Length of the domain defined in equation (8.3)
m	Unit vector

M_g	Molecular mass
n	Porosity
n^{abs}	Absolute adsorbed amount
n_{ads}^{ex}	Excess amount of adsorbed gas
$n_{ads}^{ex(total)}$	Total excess adsorption
n_{eq}	Total gas adsorption at equilibrium
n_{inj}	Amount of injected gas
n_L	Langmuir capacity
n_L^{abs}	Langmuir absolute sorption
n_t	Gas adsorption amount at time t
$n_{t(0)}$	Initial gas adsorption at the beginning of each pressure step
n_{unads}^{ex}	Amount of unadsorbed gas
n_0	Reference porosity
\underline{n}	Direction cosine normal to surface
N	Number of pressure steps defined in equation (4.6)
N_s, N_r	Shape functions
\mathbf{N}	Shape function matrix
p	Net-mean stress
P	Gas pressure
P_{eq}	Pressure of free gas at equilibrium
P_E	Langmuir pressure of elastic modulus reduction
P_L	Langmuir pressure
P_{UCS}	Langmuir pressure of unconfined compressive strength reduction
P_1	Inlet gas pressure
P_2	Outlet gas pressure
P_0	Reference gas pressure
\mathbf{P}	Strain matrix
q	Deviatoric stress
Q_g	Volumetric flow rate
$Q_{residual}(t)$	Residual (unoccupied) sorption capacity at time t
$Q_{residual}(0)$	Residual (unoccupied) sorption capacity at time zero

Q_1, Q_2	Residual sorption capacities defined in equation (5.7)
R	Universal gas constant
R_g	Sink/source term for geochemical reactions
R_Ω	Residual error introduced due to approximation
s_g	Adsorbed amount in the solid phase
s_{max}	Langmuir constant for the maximum sorption capacity
S_g	Degree of gas saturation
t	Time
T	Temperature
T_c	Critical temperature
$\hat{\underline{T}}_r$	Approximate traction defined in equation (3.79)
\mathbf{TL}_{abs}	Matrix of absolute tolerances
\mathbf{TL}_{rel}	Matrix of relative tolerances
u_g	Gas pressure
u_{gc}	Critical pressure
UCS	Unconfined compressive strength
UCS_{CO_2}	Unconfined compressive strength of CO ₂ saturated coal
$UCS_{natural}$	Unconfined compressive strength of natural (non-saturated) coal
\mathbf{u}	Vector of displacement
$\hat{\mathbf{u}}$	Approximate vector of displacement
\mathbf{u}_s	Vector of displacement defined in equation (3.68)
$\dot{\mathbf{u}}_s$	Vector of time differentials of displacement
v	Specific volume
V	Volume
V_{ads}	Volume taken up by the adsorbed phase
V_c	Critical volume
V_C	Volume of the calibration cylinder
V_{gas}	Volume taken up by the bulk gas phase
V_R	Volume of the reference cell
V_S	Volume of the sample cell
\mathbf{v}_g	Bulk gas velocity

x, y, z	Global Cartesian coordinates
z	Elevation
Z	Compressibility factor
Z_{He}	Compressibility factor for helium
δV	Incremental volume
δV_s	Incremental volume of the solids
ΔE	Elastic modulus reduction
ΔE_{max}	Langmuir constant of maximum elastic modulus reduction
ΔUCS	Unconfined compressive strength reduction
ΔUCS_{max}	Langmuir constant of maximum unconfined compressive strength reduction
ε	Strain vector
ε^e	Elastic component of strain
ε_A	Axial strain
ε_{max}	Langmuir constant for the maximum volumetric strain
$\varepsilon_{p,M}^e$	Elastic component of strain due to change in mean stress
ε_R	Radial strain
ε_{sw}	Volumetric swelling strain
$\varepsilon_{sw,m}^e$	Elastic component of strain due to swelling
ε_v	Volumetric strain
Γ^e	Element boundary surface
θ_g	Volumetric gas content
Θ	Integration constant defined in equation (3.87)
μ_g	Absolute gas viscosity
μ_g^D	Factor for dense gas viscosity
μ_g^0	Reference gas viscosity
ρ	Coal density
ρ_g	Gas density
ρ_g^0	Reference gas density
ρ_s	Density of the solid phase
σ	Total stress

σ_c	Collision diameter
σ''	Effective stress
$\sigma_x'', \sigma_y'', \sigma_z''$	Normal stresses
σ_0''	Initial effective stress
τ_g	Gas tortuosity factor
$\tau_{xy}, \tau_{zy}, \tau_{xz}$	Shear stresses
\emptyset	Variable vector
\emptyset_l	Defined in equation (3.88)
ν	Poisson's ratio
ω	Defined in equation (3.58)
ω_A	Acentricity factor
ω_s	Defined in equation (3.58)
$\hat{\omega}$	Defined in equation (3.58)
Ω	Collision integral
Ω^e	Element area/domain
∇	Gradient operator
ζ	Residual force defined in equation (3.93)
ϑ	Constant defined in equation (3.88)

Contents

Chapter 1 – Introduction

1.1. Introduction	1-1
1.2. Carbon Dioxide Sequestration in Coal	1-2
1.2.1. Field Scale Applications	1-7
1.3. Study Objectives.....	1-8
1.4. Research Background	1-9
1.5. Scope and Assumptions.....	1-12
1.6. Overview of the Thesis.....	1-13
1.7. References	1-15

Chapter 2 – Literature Review

2.1. Introduction	2-1
2.2. Overview of the Experimental Facilities and Measurement Methods	2-2
2.2.1. Gas Sorption Measurements.....	2-2
2.2.2. Gas Flow and Permeability Measurements	2-3
2.2.3. Swelling and Shrinkage Measurements	2-5
2.2.4. Measurement of Strength and Deformation Parameters	2-5
2.3. Physical and Chemical Aspects of CO ₂ Sequestration in Coal – Experimental Findings	2-6
2.3.1. Sorption Capacity	2-7
2.3.2. Sorption Kinetics	2-9
2.3.3. Gas Sorption Induced Swelling	2-9
2.3.4. Gas Flow and Permeability	2-11
2.3.4.1. Klinkenberg effect.....	2-13
2.3.5. CO ₂ Sequestration Associated Effects	2-14
2.3.5.1. Effects of Pressure and Temperature	2-14
2.3.5.2. Effects of Stress State	2-15
2.3.6. Effects of CO ₂ Sorption on Coal Structure	2-16
2.3.7. Effects of CO ₂ sorption on Coal Elastic Deformation and Failure	2-18

2.4. Theoretical and Computational Studies on Gas Transport and Reactions in Coal.....	2-21
2.4.1. Sorption Capacity Models	2-21
2.4.2. Sorption Kinetics Models	2-23
2.4.3. Sorption Induced Swelling Models	2-24
2.4.4. Gas Flow and Permeability Models – An Analytical and Empirical Approach.....	2-25
2.4.5. Numerical Models	2-27
2.5. Conclusions	2-31
2.6. References	2-33

Chapter 3 – Theoretical and Numerical Formulation

3.1. Introduction	3-1
3.2. Theoretical Formulation – General Aspects.....	3-2
3.3. Reactive Transport of Single-component Gas.....	3-3
3.3.1. Gas Properties at High Pressure	3-4
3.3.2. Mechanisms of Gas Transport.....	3-5
3.3.2.1. Advection.....	3-6
3.3.2.2. Diffusion	3-7
3.3.3. Sink/source Term for Adsorption/desorption.....	3-8
3.3.4. Governing Equations for Gas Transport	3-9
3.4. Deformation Behaviour	3-11
3.4.1. Background and Assumptions of the Deformation Model.....	3-11
3.4.2. Stress Equilibrium Equation.....	3-13
3.4.3. Constitutive Elastic Relationship	3-15
3.4.4. Swelling Behaviour	3-18
3.4.5. Permeability-porosity Relationship	3-19
3.4.6. Governing Equation for Deformation	3-19
3.5. Numerical Formulation – General Aspects	3-20
3.6. Spatial Discretisation.....	3-20
3.6.1. Spatial Discretisation of the Governing Equations for Flow Variables	3-21
3.6.2. Spatial Discretisation of the Governing Equations for Displacement Variables	3-24

3.7. Temporal Discretisation	3-25
3.8. Conclusions	3-28
3.9. References	3-28

Chapter 4 – Materials and Methods

4.1. Introduction	4-1
4.2. Coal Description and Sample Preparation Methodology	4-1
4.2.1. Preparation of Powdered Samples for the Gas Sorption Measurements and Characterisation Tests	4-3
4.2.2. Preparation of Core Samples	4-4
4.2.2.1. Cores for the Gas Sorption Measurements	4-5
4.2.2.2. Cores for the Uniaxial Compressive Tests.....	4-5
4.2.2.3. Cores for the Triaxial Flooding Tests	4-7
4.3. Characterisation Tests	4-8
4.3.1. Proximate, Ultimate, Petrographic and Calorimetric Analyses	4-9
4.3.2. The Porosity of Coal.....	4-11
4.4. Experimental Setup and Measurement Methods	4-12
4.4.1. Experimental Temperature and Pressure.....	4-14
4.4.2. Manometric Sorption Apparatus	4-15
4.4.2.1. The Helium Pycnometry Method.....	4-16
4.4.2.2. Sorption Measurements.....	4-18
4.4.3. Uniaxial Compressive Tests	4-22
4.4.3.1. Sieve Analysis.....	4-24
4.4.4. Triaxial Core Flooding System	4-25
4.4.4.1. Gas Flow and Permeability Measurements.....	4-26
4.4.4.2. Deformation Measurements	4-29
4.4.4.3. Temperature Measurements	4-31
4.4.5. Gas Supply System.....	4-31
4.4.5.1. High Pressure Gas Supply Units	4-33
4.4.5.2. Backpressure Units	4-35
4.4.6. Auxiliary Units	4-35
4.5. Conclusions	4-36
4.6. References	4-37

Chapter 5 – CO₂ Sorption and Kinetics Behaviour

5.1. Introduction	5-1
5.2. Experimental Pressure Decay Results	5-2
5.3. The Excess Sorption Isotherms	5-11
5.4. The Absolute Sorption Isotherms	5-15
5.5. Adsorption Kinetics	5-23
5.6. Conclusions	5-31
5.7. References	5-33

Chapter 6 – Effects of CO₂ Sorption on the Deformation Properties

6.1. Introduction	6-1
6.2. CO ₂ Saturation Effect on Deformation Parameters	6-2
6.2.1. Parametrisation of Changes in Unconfined Compressive Strength and Elastic Modulus	6-14
6.3. Failure Patterns	6-17
6.4. Post-failure Sieve Analysis	6-23
6.5. Conclusions	6-29
6.6. References	6-31

Chapter 7 – Gas Transport and Reaction Behaviour

7.1. Introduction	7-1
7.2. Injection of He and CO ₂ in Coal under Confined Conditions	7-2
7.2.1. Low Pressure He Injection	7-3
7.2.2. High Pressure He Injection	7-7
7.2.3. Permeability to He	7-10
7.2.4. Subcritical CO ₂ injection	7-13
7.2.5. Supercritical CO ₂ injection	7-16
7.2.6. Permeability to CO ₂	7-19
7.3. Temperature Changes due to Gas Injection	7-21
7.4. Flow of CO ₂ and the Induced Volumetric Swelling of Coal	7-29
7.5. Reversibility of CO ₂ Sorption and the Effect on Gas Flow	7-35
7.6. Conclusions	7-39
7.7 References	7-41

Chapter 8 – Model Verification and Validation

8.1. Introduction	8-1
8.2. Verification Exercises.....	8-2
8.2.1. Steady State Advection-diffusion of Single-component Gas (Test I)	8-3
8.2.1.1. Analytical Solution	8-3
8.2.1.2. Simulation Conditions	8-4
8.2.1.3. Results.....	8-5
8.2.2. Elastic Deformation Behaviour under the Applied Load (Test II).....	8-6
8.2.2.1. Analytical Solution	8-6
8.2.2.2. Simulation Conditions	8-6
8.2.2.3. Results.....	8-7
8.2.3. Elastic Deformation Behaviour with Permeability-porosity Relationship under the Non-sorbing Gas Injection (Test III)	8-8
8.2.3.1. Simulation Conditions	8-9
8.2.3.2. Results.....	8-10
8.2.4. Elastic Deformation Behaviour with Permeability-porosity Relationship under the Sorbing Gas injection (Test IV).....	8-11
8.2.4.1. Simulation Conditions	8-12
8.2.4.2. Results.....	8-13
8.2.5. Conclusion to Verification Exercises	8-14
8.3. Validation Exercises	8-14
8.3.1. Experimental Data.....	8-15
8.3.2. Simulation Conditions	8-17
8.3.3. Results	8-23
8.3.4. Conclusion to Validation Exercises	8-30
8.4. Conclusions	8-30
8.5. References	8-31

Chapter 9 – Numerical Simulations - Coal Response and Gas Transport During Supercritical CO₂ Injection

9.1. Introduction	9-1
9.2. Simulation Conditions and Material Parameters	9-2
9.3. Simulation Results.....	9-7

9.3.1. Permeability Evolution.....	9-7
9.3.2. Porosity Determination.....	9-10
9.3.3. Gas Breakthrough.....	9-12
9.4. Conclusions	9-16
9.5. References	9-17

Chapter 10 – Conclusions and Suggestions for Further Research

10.1. Introduction	10-1
10.2. Summary of the Laboratory-scale Experimental Study	10-2
10.3. Summary of the Numerical Study	10-6
10.4. Conclusions of the Experimental and Numerical Studies	10-9
10.5. Overall Conclusions of the Thesis.....	10-11
10.6. Suggestions for Further Research.....	10-13

1

Introduction

1.1. Introduction

Warming of the climate system is unequivocal, and since the 1950s, many of the observed changes are unprecedented over decades to millennia (IPCC, 2014). The recent anthropogenic emissions of greenhouse gases (GHG) are the highest in history (IPCC, 2014). Between the pre-industrial time in 1750 and 2011, cumulative anthropogenic carbon dioxide (CO₂) emissions to the atmosphere were 2040±310 Gt whereas about half of the anthropogenic emissions have occurred in the last 40 years (IPCC, 2014).

With more than half of global population, cities in 2013 accounted for about two-thirds of primary energy demand and 70% of total energy related CO₂ emissions (IEA, 2016a). Continuing current energy trends will increase the urban energy demand and the resulting carbon emissions by 70% and 50% from 2013 levels by 2050, respectively (IEA, 2016a).

Adaptation and mitigation are complementary strategies for reducing and managing the risks of climate change (IPCC, 2014). In order to focus on climate mitigation actions after 2020, the Paris Agreement, allowing for greater national level determination of future climate actions, was developed and agreed by the Parties at the 21st Conference of Parties (COP21). A short-term goal is to reach peak emissions as soon as possible, while the longer term goal is to limit average global warming to well below 2°C above pre-industrial times and an aspiration to limit warming to 1.5°C (Global CCS Institute, 2016).

There are multiple mitigation pathways that are likely to limit warming to below 2°C relative to pre-industrial levels. Energy efficiency, fuel switching, renewables, nuclear power and Carbon Capture and Storage (CCS) have been identified as the five main forms of technology that will help to mitigate the climate change (StatoilHydro, 2009; IEA, 2015). According to IEA (2016a), the planned reductions by 2050 would come from end-use fuel and electricity efficiency (38%), renewables (32%), CCS (12%) and nuclear power (7%).

Carbon Capture and Storage is a cost-effective solution able to deliver significant emissions reductions from the use of fossil fuels (IEA, 2015; WCA, 2015). There are three major components of CCS: i) capture of CO₂ released during the burning of a

fossil fuel, ii) transportation through pressurised pipelines and iii) geological storage in carefully selected geological rock formations (WCA, 2015). The level of global emissions that must be delivered to meet the goals of the COP21 positions CCS as a critically important mitigation technology (Global CCS Institute, 2016; IEA, 2016b).

Suitable geologic formations include saline aquifers, depleted oil and gas fields, and coal seams that cannot be mined, as shown in Figure 1.1 (IEA, 2013; WCA, 2017). In addition, oil fields and coal seams have potential for CO₂ induced enhanced oil recovery (CO₂-EOR) and enhanced coalbed methane recovery (CO₂-ECBM), respectively (IEA, 2013).

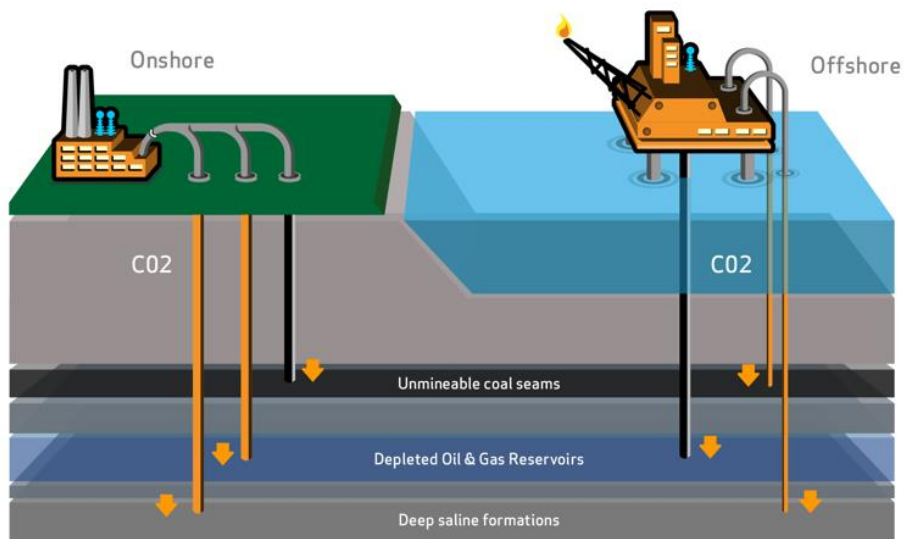


Fig. 1.1. Schematic of the suggested geological storage options, both onshore and offshore carbon dioxide (CO₂) storage (WCA, 2017).

1.2. Carbon Dioxide Sequestration in Coal

Coal is an organic sedimentary rock resulted from the accumulation of vegetable debris in a specialized environment of deposition that contains varying amounts of carbon, hydrogen, nitrogen, oxygen and sulphur as well as trace amounts of other elements, including mineral matter (Speight, 2005; Thomas, 2013).

The degree of coalification that a coal has undergone by burial and tectonic effects determines the coal rank. During the coalification process, there is an increase in the carbon content and a decrease in the hydrogen and oxygen content, resulting in a loss of

volatiles (Thomas, 2013). As a result of the coalification process, substantial amounts of methane (CH_4) are generated (Pini et al., 2010). In addition, water loss and compaction lead to the reduction of the coal volume (Thomas, 2013). Low rank or brown coals are lignite and subbituminous coals while black or hard coals can be classified as higher rank coals including the bituminous, semi-anthracite and anthracite coals (Thomas, 2013). Coal mass consists of organic units (macerals) and inorganic portion (minerals). Macerals are commonly divided into three main groups; vitrinites, liptinites and inertinites (White et al., 2005; Thomas, 2013).

Coals are considered as dual porosity systems consisting of a porous matrix and a network of natural fractures known as cleats, as shown in Figure 1.2 (Laubach et al., 1998). According to Katyal et al. (2007) and Rodrigues and Lemos de Sousa (2002), pore sizes within the coal system can generally be classified as micropores (<2 nm), mesopores (2-50 nm) and macropores (>50 nm). In situ cleat widths can be up to 20 mm (Laubach et al., 1998). Although small amounts of free gas may exist in the coal fracture system, gas is mainly adsorbed on the internal surface area of the coal matrix accounting for 95%-98% of the gas in the coal seam (Laubach et al., 1998; White et al., 2005). As the coal possesses pores of various sizes which can exhibit different type of connectivity, they have a great influence in migration and adsorption of gases (Katyal et al., 2007; Baisheng et al., 2015).

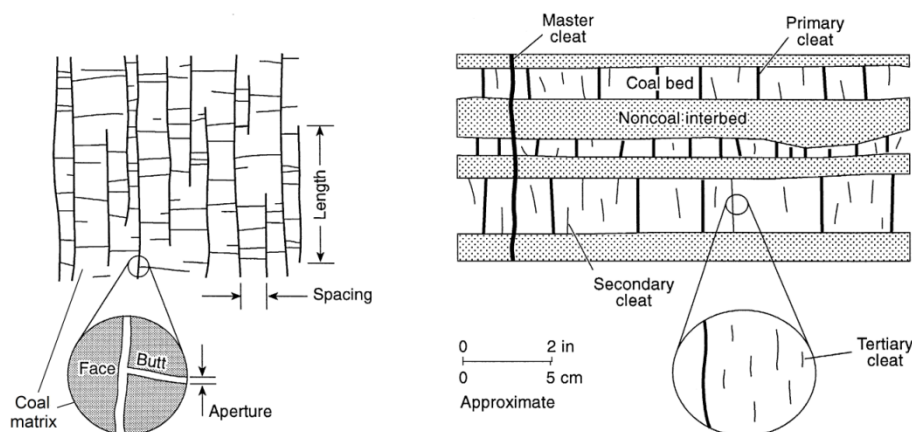


Fig. 1.2. Schematic illustration of coal cleat geometries (modified after Laubach et al., 1998); a) Cleat-trace patterns in plan view, b) coal seam in cross-section view.

The porosity distribution is coal rank-dependent with low rank coals mainly containing macropores, while high rank coals contain predominantly micropores, as shown in Figure 1.3 (Clarkson and Bustin, 1999; Moore, 2012; Thomas, 2013; Baisheng et al.,

2015). Total porosity generally decreases with an increase in coal rank (White et al., 2005). In addition, the system of cleats is present in all coals ranging from low to high rank, however, with low volatile bituminous coals exhibiting the best developed cleat system (Rodrigues et al., 2014). Porosity can be also associated with maceral groups whereas vitrinites are mainly composed of micropores, while liptinites and intertinites are predominantly formed of mesopores and macropores (White et al., 2005).

As pressure and temperature during the coalification process increase, plastic deformations destroy the original cleat structure (Rodrigues et al., 2014). In other words, coal bulk compaction leads to a significant reduction in mesopore size and increase in the number of micropores within higher rank coals (Baisheng et al., 2015). Hence, cleat spacing varies with coal rank where maximum distance between parallel cleats in low rank coals and high rank coals is reported to be 22 cm and 0.2 cm, respectively (Thomas, 2013).

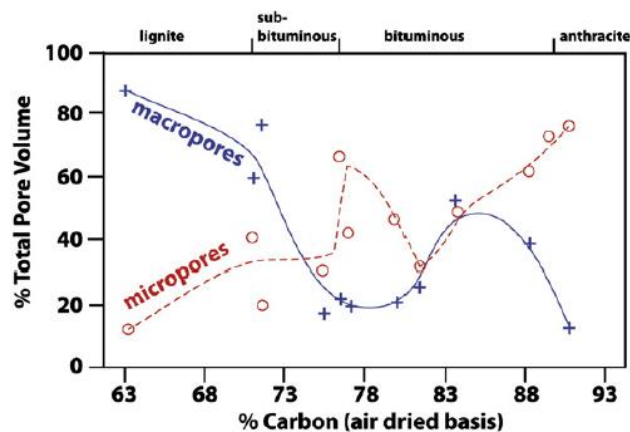


Fig. 1.3. Relationship between the percentage of the total pore volume associated with macropores and micropores versus rank as presented by Moore (2012).

Coal seams can range from fractions of an inch to hundreds of feet in thickness (Speight, 2005). In coal seams, fractures usually occur in two sets mutually perpendicular and also perpendicular to the bedding. These fractures are called face cleats and butt cleats (Laubach et al., 1998).

Network geometry and connectivity of fractures in a system are important to the permeability of the coal seam whereas the coalbed permeability may be 3 to 10 times greater in the face cleat direction than in other directions (Laubach et al., 1998). However, on a local scale, cleat connectivity results from cross cutting and abutting

relations. Although regions hundreds of square kilometres in area can have uniform cleat orientations, the cleat network can shift abruptly from one coal seam to the next within an area as small as a single colliery (Laubach et al., 1998).

Deeper coal seams may be more affected by the tectonism which might obliterate previously formed cleats (Laubach et al., 1998). In addition, butt cleats which connect one face cleat to another may be in some cases only restricted to near-surface locations which will clearly impact interpretation of fracture connectivity in coal beds at depth (Laubach et al., 1998). In particular, at shallower depths uplift and erosion increase driving stress for fracture propagation where pre-existing face cleats tend to relieve induced stresses perpendicular to them and inhibit growth of additional parallel fractures (Laubach et al., 1998).

Among the geological sequestration options, coal seams that cannot be mined are attractive because the storage of CO₂ in the coal beds allows the production of a value-added product such as methane (White et al., 2005). The depth interval for CO₂ storage in coal is expected to be between 300 and 1500 m of depth (White et al., 2005). Most target coal seams in Europe are within that range, i.e. at depths greater than 500 m with correspondingly high temperatures and pressures (Battistutta et al., 2012; Siemons et al., 2007). In general, numerous studies have shown that coal can hold approximately twice the volume of CO₂ as CH₄, however, some studies suggested that it may adsorb from 6 to 18 times as much CO₂ as CH₄ (Jones et al., 2004; White et al., 2005). It was estimated that the worldwide coalbed CO₂ sequestration capacity is large with potential of storing 300-964 Gt of CO₂ (Kuuskraa et al., 1992; White et al., 2005).

A three-stage process characterises the transport and sorption of gas in a coal seam. This includes the flow of gas along the cleat system and migration through a network of interconnected micropores in the coal matrix where it is adsorbed on the micropore walls (White et al., 2005). The gas sorption with respect to gas pressure is generally represented with the Langmuir (1918) isotherm displaying a steep increase in adsorption in the low pressure region followed by a levelling off at higher pressures.

There are general benefits of the CO₂ storage in coal seams, as pointed out above. However, coal is a mixture of inorganic minerals and organic material in a complex, three-dimensional network that may be affected during the injection of gas and the

adsorption process (White et al., 2005; Thomas, 2013). Hence, there is still a need for an improved understanding of the coal-CO₂ interactions. For instance, of particular interest is to investigate the changes in the structure as well as physical and chemical properties of coal induced by CO₂ sorption. In addition, physical and chemical behaviour of coal also depends on the properties of the system being considered. As the CO₂ is known to be a real gas that cools down upon expansion, further work is needed to address the changes within the system as a result of CO₂ flow.

To address and provide a further understanding of the outstanding issues, experimental investigations are an effective way of studying the complex physical and chemical mechanisms involved in the process of carbon dioxide sequestration in coal. Determining the sorption amount and kinetics of CO₂ that can be stored in a particular coal seam is a crucial step to assess the potential of the coal seam for the sequestration purpose. As most of the experimental investigations were focused on gas sorption capacity of powdered coal samples, an improved understanding on the sorption processes in intact coal samples of larger size is required.

In addition, adsorption capacity of coal is a direct function of both the temperature and pressure of coal, with most favourable coal seams for sequestration occurring at depths where pressure and temperature may exceed the critical values of CO₂, i.e. 750 m (White et al., 2005; Perera et al., 2013). Limited publications were found discussing experimental results of supercritical CO₂ injection in coal. Hence, studying the coal response subject to supercritical CO₂ is of importance for obtaining relevant data sets.

Recent theoretical and computational developments have improved the understanding of the coal-gas interactions. However, there is a need for further research to address the complex behaviour of coals under high gas pressure. For instance, studying the coupled chemo-mechanical response of coal caused by interactions with high pressure CO₂ is of particular interest as it enhances the understanding of the effect of adsorption phenomena on the engineering properties of coals and its effect on the CO₂ injectivity. An improved understanding in the areas mentioned above will allow more rigorous and comprehensive development of numerical models. This will ensure the reliability of the numerical simulations conducted to predict both the short-term and long-term behaviour of coals during CO₂ sequestration process.

1.2.1. Field Scale Applications

CCS is the only technology capable of delivering significant emissions reductions from the use of fossil fuels (IEA, 2016b). The number of the large-scale CCS projects in operation is 15, with six more expected to come online before 2018 (IEA, 2016b). However, the number of previous, in operation and under construction pilot and demonstration-scale projects can be counted in hundreds (Global CCS Institute, 2016).

In relation to the CO₂ sequestration in coal seams, Allison Unit field in United States is the world's first experimental pure CO₂-ECBM recovery pilot project commenced in 1995 (White et al., 2005). The Allison Unit is located within the northern portion of the San Juan Basin. Over the 6 years of the project, 1.33×10^8 m³ of CO₂ was injected at a depth of 900 m and at the same time, 4.5×10^7 m³ of CH₄ produced (Bustin et al., 2016).

The field operation of the first micro-pilot test was conducted in China in April 2004 where a total of 192 metric tonnes of CO₂ were injected into an anthracite formation at a depth of 472 m (Wong et al., 2007). Although the absolute permeability of the coal seam prior to CO₂ injection was relatively high at 12.6 milli-Darcy (md), analysis showed that the injectivity to CO₂ decreased during the initial injection. Wong et al. (2007) concluded that the enhancement of CBM production with simultaneous storage of CO₂ is a feasible process, however, further investigations into the coal-gas interactions were recommended.

As a part of the RECOPOL project set-up in the Upper Silesian Coal Basin in Poland, about 760 tons of CO₂ were injected into the coal reservoir from August 2004 to June 2005 (van Bergen et al., 2009). Targeted coal seams were between 1.3 m and 3.3 m thick in the depth interval between 900 m and 1200 m (van Bergen et al., 2006). The results of the gas production showed that the production of CH₄ increased significantly compared to the baseline production. In addition, results indicated that the CO₂ was adsorbed by the coal, but a substantial permeability reduction was observed as a result of coal swelling. In order to improve the injection of CO₂, stimulation of the reservoir by a hydraulic fracture treatment was performed.

The feasibility of extracting methane from coal seam while storing CO₂ and N₂ between May 2004 and October 2007 was evaluated in Japan, near the town of Yubari on the island of Hokkaido (Fujioka et al., 2010). It was estimated that low injectivity of CO₂

was induced by the permeability reduction caused by coal swelling which did not recover to its original value even after nitrogen (N_2) injection. In addition, findings suggested that matrix swelling might have created a high stress zone near the injection well.

Overall, it was recognized by the projects that coal has a great potential to store CO_2 and simultaneously enhance the production of CH_4 which can offset the costs involved in CO_2 capture, transportation and storage. In particular, the Allisson Unit was deemed as a successful full scale CO_2 sequestration pilot project proving that CO_2 storage in coal seams is a feasible process. However, the reduction of permeability is one of the main technical issues that should be solved in order to put economical and large-scale CO_2 -ECBM into practice. This indicates the need for continued experimental and computational research and development. Laboratory experiments can play an important role in improving the understanding of coal response during the gas sorption processes and provide valuable data for validation of developed numerical models by ensuring their reliability for predicting the behaviour of coal-gas-water system.

1.3. Study Objectives

The overall objective of this study is to provide an improved understanding of the underlying coupled processes involved in carbon sequestration in coal. This is to be achieved via an integrated comprehensive programme of research involving experimental work, theoretical consideration, model development and numerical simulations.

To meet this objective, the main tasks of this study are to:

- Study the sorption behaviour of both subcritical and supercritical carbon dioxide in unconfined coal samples of different sizes including powdered and intact coal specimens.
- Investigate the effect of subcritical and supercritical carbon dioxide sorption on the deformation behaviour and failure of coals using uniaxial compressive tests.
- Study the coal response under isotropic confining conditions to continuous injection of subcritical and supercritical gases.

- Analyse the effect of carbon dioxide sorption induced swelling on the ability of coal to allow gas flow.
- Assess the effect of nitrogen injection on the reversibility of CO₂ sorption induced changes.
- Advance a coupled thermo-hydro-chemo-mechanical (THCM) model to include the appropriate constitutive relationship for single porosity coal deformation induced by physical and chemical coal-gas interactions.
- Apply and validate the numerical model using experimental results.
- Perform numerical investigations under a series of conditions of practical importance for carbon dioxide sequestration in coal.

1.4. Research Background

The work presented in this thesis has been undertaken at the Geoenvironmental Research Centre (GRC) at Cardiff University. Significant previous research has been undertaken within the GRC both on the experimental and computational aspects of geoenvironmental engineering. This section provides the context to this work and is not intended to replace more detailed reviews of literature in Chapter 2, nor the theoretical formulations in Chapter 3.

Considerable previous work into the development of the numerical computer code COMPASS (COde for Modelling Partially Saturated Soils), has been performed prior to the study.

A theoretical model of coupled transient heat and moisture (TH) transfer in unsaturated soil was developed by Thomas (1985). The principle of mass conservation was employed for moisture flow and the conservation of energy was used for heat transfer. In this solution moisture vapour flow was modelled by incorporating the diffusive flow proposed by Philip and de Vries (1957) and de Vries (1958), and the latent heat of vapourisation was also introduced following Luikov (1966). The non-linearity of material parameters was included by Thomas (1987), Thomas (1988a) and Thomas (1988b).

Revised time-stepping schemes were investigated under the mentioned coupled TH model by Thomas and Rees (1988) and Thomas and Rees (1990).

Ewen and Thomas (1989) formulated numerical model in terms of moisture content and temperature to simulate the experimental work previously undertaken by Ewen and Thomas (1987). Thomas and King (1991) presented a theoretical heat and moisture formulation cast in terms of capillary potential and temperature and found good agreement with the Ewen and Thomas (1987) experiments. Thomas and Sansom (1995) extended this formulation to include elevated pore-air pressures and validated via comparison to experimental works on sand and clay. This formulation was presented in three-dimensions including work on pre and post-processing, visualisation and parallel computation by Sloper (1997) and Thomas et al. (1998).

Deformation was introduced examining seasonal ground movements by Thomas and Rees (1990) and Thomas and Rees (1993), with an isothermal coupled hydro-mechanical numerical model presented by Thomas et al. (1992) utilising the non-linear elastic state-surface approach proposed by Lloret and Alonso (1985). This model was applied to seasonal ground movements in the work presented by Thomas and Zhou (1995). An elasto-plastic coupled Thermo-Hydro-Mechanical (THM) model was presented by Thomas and He (1994) and Thomas and He (1995) using the elasto-plastic model of Alonso et al. (1990).

Ramesh (1996) applied the THM model to simulate temperature, moisture and void ratio distributions of montmorillonite subjected to heating/hydration. The work also involved investigation of isothermal volume change behaviour of compacted kaolinite in suction controlled tests. Thomas and Cleall (1999) extended the THM model to include highly expansive behaviour. Using the developed model, numerical simulations of large scale experiments were presented by Mitchell (2002), Thomas et al. (2003), Melhuish (2004) and Cleall et al. (2006) which included investigation into the microstructure behaviour of bentonite and the effects on re-saturation of the buffer.

Chemical processes were first introduced as non-reactive chemical solute transport for a single species (Thomas and Cleall, 1997). Hashm (1999) developed the model to two-dimensional coupled moisture and reactive multiple chemical solute transport by linking the non-reactive transport code with the geochemical model, MINTEQA2 (Allison et

al., 1991). The model was applied to simulate a series of leaching cell experiments to study the migration/sorption behaviour of some of the heavy metals. Seetharam (2003) developed the multicomponent chemicals reactive transport module of the coupled THCM model. The geochemical reactions were calculated by the geochemical model, MINTEQA2 using two different coupling schemes to solve transport and reaction equations. The coupled THCM model was used to simulate the reactive transport of chemicals in a small scale laboratory on compacted bentonite under heating and hydration (Seetharam et al., 2006; Cleall et al., 2007).

A number of theoretical and computational developments have recently been made in the model focusing mainly on the behaviour of compacted bentonite as the buffer in a geological nuclear waste repository, in addition to the modelling of the large scale THM behaviour of the repository. Singh (2007) presented a numerical investigation on the heat and moisture transfer in compacted bentonite where the modifications to the existing vapour theory were suggested and introduced in existing THM model. Siddiqua (2008) presented an investigation into the elevated temperature effects (273 to 473 K) on the THM processes in the model. A pore gas transfer equation and thermo-osmotic effect was developed to account for elevated temperature.

Vardon (2009) extended the THM model to accommodate three-dimensional THM behaviour in geological repository, including the development of a high-performance computing algorithm using both multi-threaded and message-passing programming paradigms to enable simulations to be completed in significantly reduced time. The model was utilised for simulation of the THM behaviour of a large-scale experiment, carried out at an underground research laboratory in Sweden.

Thomas et al. (2011) presented the inclusion of biological aspects to the coupled THCM model. The early developments in this area include some biological impacts on coupled transport behaviour in unsaturated porous media. The THCM model incorporates the biodegradation kinetics of organic substrates.

To include both equilibrium and kinetically controlled chemical reactions, Sedighi (2011) linked the transport module in the COMPASS code with an advanced geochemical model, PHREEQC, version 2.0. The extended THCM model was applied to simulate the transport and fate of multicomponent chemicals in the liquid phase in

clays. Subsequently, the combined effects of electrochemical and thermal diffusion potentials on the reactive transport were investigated by Thomas et al. (2012). Masum (2012) developed the geochemical model for multicomponent gas transport, including an extension of the coupling with PHREEQC for gas reactivity. The multicomponent gas formulation was developed under the assumption of an ideal gas.

More recently, Hosking (2014) developed a theoretical framework for the reactive transport of high pressure gas mixtures in fractured rock under coupled hydraulic, gas/chemical and deformation behaviour, based on a dual porosity approach. The existing THCM model was advanced to include high pressure real gas behaviour and dual porosity simulation capabilities.

Laboratory investigations of flow and reaction processes during gas storage and displacement in coal have been recently conducted by Hadi Mosleh (2014). Experimental program aimed to investigate the interactions between coal and various gas species and to provide further insights into the processes and mechanisms involved in coal-gas system.

1.5. Scope and Assumptions

The scope of the work undertaken in this thesis and in particular the assumptions with regards to experimental investigation and numerical model developments are listed below:

Experimental investigation scope and assumptions:

- The experimental study investigates the coal response only to storage of subcritical and supercritical CO₂ (i.e. CH₄ displacement and desorption is not studied).
- The experiments are conducted on dry samples. It is assumed that low content of moisture in high-rank coals does not affect the coal response during CO₂ injection.
- The experiments studying the sorption processes in coal are conducted under constant temperature and unconfined conditions.

- The research related to flow of gases in intact coal samples was conducted under isotropic stress conditions.
- The experiments studying the flow behaviour of gases in coal are conducted under variable temperature conditions to study the effect of gas expansion and related temperature effects on the coal behaviour.

Numerical modelling scope and assumptions:

- Numerical approximation is used to find a solution to the system of coupled differential equations. The finite-element method is used to provide a spatial solution and the finite difference method is used to provide a temporal solution.
- A single porosity technique is employed to model fractured rock which is assumed to be a homogeneous and isotropic continuum.
- Constitutive relationships for coal deformation by physical and chemical mechanisms are developed for linear elastic behaviour.
- The sorption processes are sufficiently fast compared to the transport speed. Local chemical equilibrium is considered to exist.
- The applications of the developed model in this work consider a fully dry system.
- Numerical simulations are conducted under constant temperature.

1.6. Overview of the Thesis

A brief description of the chapters in this thesis is presented below:

Chapter 2 contains a literature review associated with the work presented in the remainder of the thesis. A review of the experimental methods and recent findings related to gas sorption and flow measurements as well as investigations of coal deformation parameters is presented. In addition, a review of the modelling techniques for gas transport and interactions in coal is provided.

The theoretical and numerical formulations for coupled gas/chemical and deformation behaviour of fractured rock are described in Chapter 3. Specific attention is given to the development of a deformation model describing the swelling of the coal mass as a result of coal-gas interactions.

Chapter 4 describes the materials and methods as well as the experimental facilities used in the experimental study. In particular, sample preparation techniques and the characterisation of the coal samples used in this study are presented. Following this, a description of the equipment and procedures related to gas sorption behaviour, uniaxial compressive tests, gas flow measurements, volumetric deformation and temperature measurements is provided. Details with regards to upgrades of the existing equipment are discussed.

Experimental results of the carbon dioxide sorption measurements on powdered and intact coal samples from two different locations and depths using the manometric sorption apparatus are presented in Chapter 5. The excess and absolute sorption isotherms as well as the sorption kinetics described by a number of rate functions are shown.

Chapter 6 presents the experimental results of the uniaxial compressive tests. The influence of carbon dioxide on the deformation parameters, i.e. uniaxial compressive strength and elastic modulus, is presented. In addition, failure patterns of both non-saturated and CO₂ saturated specimens are analysed followed by a post-failure sieve analysis.

In Chapter 7, experimental results obtained during injection of various gas species in intact coal samples under confined conditions using the high pressure triaxial system are presented and discussed. Deformation behaviour of coal and the effect of this behaviour on the coal's ability to conduct gas is investigated both for subcritical and supercritical CO₂ injection. In addition, temperature changes in the system during high pressure gas injection are assessed.

A series of verification tests are presented in Chapter 8 to increase confidence that the solution algorithm of the model is correct. Following this, the validity of the model is explored via comparison against the experimental data obtained as a part of this study.

In Chapter 9, the developed model is applied to investigate the importance of different material parameters on the coal response and gas transport with regards to the injection of supercritical CO₂.

Concluding remarks and suggestions for further work are presented in Chapter 10.

1.7. References

- Allison, J.D., Brown, D.S. and Novo-Gradac, K.J. 1991. *MINTEQA2 user manual version 3.0*. Environmental Research Laboratory, US EPA.
- Alonso, E.E., Gens, A. and Josa, A. 1990. A constitutive model for partially saturated soils. *Géotechnique*, 40(3), pp. 405-430.
- Baisheng, N., Xianfeng, L., Longlong, Y., Junqing, M. and Xiangchun, L. 2015. Pore structure characterization of different rank coals using gas adsorption and scanning electron microscopy. *Fuel*, 158, pp. 908-917.
- Battistutta, E., van Hemert, P., Lutynski, M., Bruining, H. and Wolf, K.H. 2010. Swelling and sorption experiments on methane, nitrogen and carbon dioxide on dry Selar Cornish coal. *International Journal of Coal Geology*, 84(1), pp. 39-48.
- Bustin, A.M.M., Bustin, R.M., Chikatamarla, L., Downey, R. and Mansoori, J. 2016. Learnings from a failed nitrogen enhanced coalbed methane pilot: Piceance Basin, Colorado. *International Journal of Coal Geology*, 165, pp. 64-75.
- Clarkson, C.R. and Bustin, R.M. 1999. The effect of pore structure and gas pressure upon the transport properties of coal: a laboratory and modeling study. 1. Isotherms and pore volume distributions. *Fuel*, 78(11), pp. 1333-1344.
- Cleall, P.J., Melhuish, T.A. and Thomas, H.R. 2006. Modelling the three-dimensional behaviour of a prototype nuclear waste repository. *Engineering Geology*, 85(2), pp. 212-220.
- Cleall, P.J., Seetharam, S.C. and Thomas, H.R. 2007. On the inclusion of some aspects of chemical behaviour of an unsaturated soil in thermo-hydro-chemical-mechanical models, II: Application and transport of soluble salts in compacted bentonite. *Journal of Engineering Mechanics*, ASCE, 133, pp. 348-356.
- de Vries, D.A. 1958. Simultaneous transfer of heat and moisture in porous media. *Transaction American Geophysical Union*, 39(5), pp. 909-916.
- Ewen, J. and Thomas, H.R. 1987. The thermal probe – a new method and its use on unsaturated sand. *Géotechnique*, 37, pp. 91-105.
- Ewen, J. and Thomas, H.R. 1989. Heating unsaturated medium sand. *Géotechnique* 39(3), pp. 455-470.
- Fujioka, M., Yamaguchi, S. and Nako, M. 2010. CO₂-ECBM field tests in the Ishikari Coal Basin of Japan. *International Journal of Coal Geology*, 82(3-4), pp. 287-298.

Global CCS Institute, 2016. *The Global Status of CCS: 2016. Summary report*. Global CCS Institute, Australia.

Hadi Mosleh, M. 2014. *An experimental Investigation of Flow and Reaction Processes during Gas Storage and Displacement in Coal*. Ph.D. Thesis, Cardiff University, Wales, UK.

Hashm, A.A. 1999. *A study of the transport of a selection of heavy metals in unsaturated soils*. PhD Thesis, University of Wales, Cardiff, UK.

Hosking, L.J. 2014. *Reactive transport modelling of high pressure gas flow in coal*. Ph.D. Thesis, Cardiff University, Wales, UK.

IEA, 2013. *Technology Roadmap. Carbon Capture and Storage – 2013 Edition*. International Energy Agency, Paris, France.

IEA, 2015. *Carbon Capture and Storage: The solution for deep emissions reductions*. International Energy Agency, Paris, France.

IEA, 2016a. *Energy Technology Perspectives 2016. Towards Sustainable Urban Energy Systems*. Executive Summary. International Energy Agency, Paris, France.

IEA, 2016b. *20 Years of Carbon Capture and Storage. Accelerating Future Deployment*. International Energy Agency, Paris, France.

IPCC, 2014. *Climate Change 2014: Synthesis Report*. Intergovernmental Panel on Climate Change.

Jones, N.S., Holloway, S., Smith, N.J.P., Browne, M.A.E., Creedy, D.P., Garner, K. and Durucan, S. 2004. *UK Coal Resource for New Exploitation Technologies*. DTI Report No. COAL R271, DTI/Pub URN 04/1879. DTI Cleaner Coal Technology Transfer Programme, Harwell.

Katyal, S., Valix, M. and Thambimuthu, K. 2007. Study of Parameters Affecting Enhanced Coal Bed Methane Recovery. *Energy Sources, Part A*, 29(3), pp. 193-205.

Kuuskraa, V.A., Boyer, C.M. and Kelafant, J.A. 1992. Coalbed gas: Hunt for quality basins goes abroad. *Oil and Gas Journal; (United States)*, 90(40), pp. 49-54.

Langmuir, I. 1918. The adsorption of gases on plane surfaces of glass, mica and platinum. *Journal of the American Chemical Society*, 40(9), pp. 1361-1403.

Laubach, S.E., Marrett, R.A., Olson, J.E. and Scott, A.R. 1998. Characteristics and origins of coal cleat: A review. *International Journal of Coal Geology*, 35(1-4), pp. 175-207.

Lloret, A and Alonso, E.E. 1985. State surfaces for partially saturated soils. *In Proceedings of the 11th International Conference of Soil Mechanics and Foundation Engineering*, San Francisco, 2, pp. 557-562.

Luikov, A.V. 1966. *Heat and Mass Transfer in Capillary Porous Bodies*, Pergamon Press, Oxford.

Masum, S.A. 2012. *Modelling of reactive gas transport in unsaturated soil – a coupled thermo-hydro-chemical-mechanical approach*. Ph.D. Thesis, Cardiff University, Wales, UK.

Melhuish, T.A. 2004. *An investigation of the three-dimensional thermo/hydro/mechanical behaviour of large scale in-situ experiments*. PhD Thesis, Cardiff University, Cardiff, UK.

Mitchell, H.P. 2002. *An investigation into the thermo/hydro/mechanical interactions involved in high level nuclear waste disposal*. PhD Thesis, University of Wales, Cardiff, UK.

Moore, T.A. 2012. Coalbed methane: A review. *International Journal of Coal Geology*, 101, pp. 36-81.

Perera, M.S.A., Ranjith, P.G. and Viete, D.R. 2013. Effects of gaseous and super-critical carbon dioxide saturation on the mechanical properties of bituminous coal from the Southern Sydney Basin. *Applied Energy*, 110, pp. 73-81.

Philip, J.R. and de Vries, D.A. 1957. Moisture movement in porous materials under temperature gradients. *Transaction American Geophysical Union*, 38(2), pp. 222-232.

Pini, R., Ottiger, S., Burlini, L., Storti, G. and Mazzotti, M. 2010. Sorption of carbon dioxide, methane and nitrogen in dry coals at high pressure and moderate temperature. *International Journal of Greenhouse Gas Control*. 4(1), pp. 90-101.

Ramesh, A.D. 1996. *Modelling the thermo/hydraulic/mechanical behaviour of unsaturated soil using an elasto-plastic constitutive relationship*. PhD Thesis, University of Wales, Cardiff, UK.

Rodrigues, C.F. and Lemos de Sousa, M.J. 2002. The measurement of coal porosity with different gases. *International Journal of Coal Geology*, 48(3-4), pp. 245-251.

Rodrigues, C.F., Laiginhas, C., Fernandes, M., Lemos de Sousa, M.J. and Dinis, M.A.P. 2014. The coal cleat system: A new approach to its study. *Journal of Rock Mechanics and Geotechnical Engineering*, 6(3), pp. 208-218.

Sedighi, M. 2011. *An investigation of hydro-geochemical processes in coupled thermal, hydraulic, chemical and mechanical behaviour of unsaturated soils*. Ph.D. Thesis, Cardiff University, Wales, UK.

Seetharam, S.C. 2003. *An investigation of the thermo/hydraulic/chemical/mechanical behaviour of unsaturated soils*. PhD Thesis, Cardiff University, Cardiff, UK.

Seetharam, S.C., Cleall, P.J. and Thomas, H.R. 2006. Modelling some aspects of ion migration in a compacted bentonitic clay. *Engineering Geology*, 85, pp. 221-228.

Siddiqua, S. 2008. *An investigation of the influence of elevated temperatures on the thermal-hydraulic-mechanical response of unsaturated soils*. PhD Thesis, Cardiff University, Cardiff, UK.

Siemons, N., Wolf, K.H.A.A. and Bruining, J. 2007. Interpretation of carbon dioxide diffusion behaviour in coals. *International Journal of Coal Geology*, 72(3-4), pp. 315-324.

Singh, R.M. 2007. *An experimental and numerical investigation of heat and mass movement in unsaturated clays*. PhD Thesis, Cardiff University, Cardiff, UK.

Sloper, N.J. 1997. *The development of a new three dimensional numerical model for fully coupled heat, moisture and air flow in unsaturated soil incorporating scientific visualisation and parallel computing techniques*. PhD Thesis, University of Wales, Cardiff, UK.

- Speight, J.G. 2005. *Handbook of coal analysis*. Hoboken, New Jersey: John Wiley & Sons, Inc.
- StatoilHydro, 2009. *Carbon Dioxide. Capture, Transport and Storage (CCS)*. R&D project CO₂ Value Chain.
- Thomas, H.R. 1985. Modelling two-dimensional heat and moisture transfer in unsaturated soils, including gravity effects. *International Journal of Analytical Methods in Geomechanics*, 9, pp. 573-588.
- Thomas, H.R. 1988a. A non-linear analysis of two-dimensional heat and moisture transfer in partly saturated soil. *International Journal of Analytical Methods in Geomechanics*, 2, pp. 31-44.
- Thomas, H.R. 1988b. The influence of non-linear thermal parameters on moisture content distributions in unsaturated soil. *International Journal of Analytical Methods in Engineering*, 26, pp. 263-279.
- Thomas, H.R. 1997. Non-linear analysis of heat and moisture transfer in partly saturated soil. *Journal of Engineering Mechanics, American Society of Civil Engineering*, 113, pp. 1163-1180.
- Thomas, L. 2013. *Coal Geology*, 2nd Edition, John Wiley & Sons, Ltd.
- Thomas, H.R. and Rees, S.W. 1988. The use of Lee's algorithm in the analysis of some ground heat and mass transfer problems. *In Proceedings of the 6th International Conference on Numerical Methods in Geomechanics*, Innsbruck, Austria.
- Thomas, H.R. and Rees, S.W. 1990. An examination of the performance of a 3-level time stepping algorithm – coupled heat and mass transfer computing. *In Proceedings of the 1st International Conference, Advances in Computer Methods in Heat Transfer*, Southampton, UK.
- Thomas, H.R. and King, S.D. 1991. Coupled temperature/capillary potential variations in unsaturated soil. *Journal of Engineering Mechanics, American Society of Civil Engineers*, 117, pp. 2475-2491.
- Thomas, H.R., Zhou, Z. and He, Y. 1992. Analysis of consolidation of unsaturated soils. *In Proceedings of the 2nd Czechoslovak Conference on Numerical Methods in Geomechanics*, Prague, Dolezalova, M., eds., vol. 1, pp. 242-247.
- Thomas, H.R. and Rees, S.W. 1993. The numerical simulation of seasonal soil drying in an unsaturated clay soil. *International Journal of Numerical and Analytical Methods in Geomechanics*, 17(1), pp. 119-132.
- Thomas, H.R. and He, Y. 1994. An elasto-plastic analysis of the thermo/hydraulic/mechanical behaviour of unsaturated soil. *In Proceedings of the 8th International Conference on Computer Methods and Advances in Geomechanics*, Morgantown, Siriwardane, H.J. and Zaman, M.M. eds., Balkema, Rotterdam, pp. 1171-1176.
- Thomas, H.R. and Rees, S.W. 1994. Seasonal ground movement in unsaturated clay: an examination of field behaviour. *Géotechnique*, 44(2), pp. 353-358.
- Thomas, H.R. and He, Y. 1995. Analysis of coupled heat, moisture and air transfer in a deformable unsaturated soil. *Géotechnique*, 45(4), pp. 677-689.

Thomas, H.R. and Sansom, M.R. 1995. Fully coupled analysis of heat, moisture and air transfer in unsaturated soil. *Journal of Engineering Mechanics, American Society of Civil Engineers*, 121(3), pp. 392-405.

Thomas, H.R. and Zhou, Z. 1995. A comparison of field measured and numerically simulated seasonal ground movement in unsaturated clay. *International Journal for Numerical and Analytical Methods in Geomechanics*, 19, pp. 249-265.

Thomas, H.R. and Cleall, P.J. 1997. Chemico-osmotic effects on the behaviour of unsaturated expansive clays. *Geoenvironmental Engineering, Contaminated Ground; Fate of Pollutants and Remediation*, Yong, R.N. and Thomas, H.R. eds., Thomas Telford, London, pp. 272-277.

Thomas, H.R. and Rees, S.W. 1998. The thermal performance of ground floor slabs – A full scale in-situ experiment. *Building and Environment*, 34, pp. 139-164.

Thomas, H.R., Rees, S.W. and Sloper, N.J. 1998. Three-dimensional heat, moisture and air transfer in unsaturated soils. *International Journal of Numerical and Analytical Methods in Geomechanics*, 22(2), pp. 75-95.

Thomas, H.R. and Cleall, P.J. 1999. Inclusion of expansive clay behaviour in coupled thermo hydraulic mechanical models. *Engineering Geology*, 54, pp. 93-108.

Thomas, H.R., Cleall, P.J., Chandler, N., Dixon, D. and Mitchell, H.P. 2003. Water infiltration into a large-scale in-situ experiment in an underground research laboratory. *Géotechnique*, 53(2), pp. 207-224.

Thomas, H.R., Seetharam, S.C. and Vardon, P.J. 2011. On the inclusion of some biological impacts and influences in coupled transport phenomena in unsaturated soil. *Geotechnical and Geological Engineering*, 29, pp. 181-191.

Thomas, H.R., Sedighi, M. and Vardon, P.J. 2012. Diffusive reactive transport of multicomponent chemical under coupled thermal, hydraulic, chemical and mechanical conditions. *Geotechnical and Geological Engineering*, 30(4), pp. 841-857.

Van Bergen, F., Pagnier, H. and Krzystalik, P. 2006. Field experiment of enhanced coalbed methane-CO₂ in the upper Silesian basin of Poland. *Environmental Geosciences*, 13(3), pp. 201-224.

Van Bergen, F., Krzystalik, P., van Wageningen, N., Pagnier, H., Jura, B., Skiba, J., Winthagen, P. and Kobiela, Z. 2009. Production of gas from coal seams in the Upper Silesian Coal Basin in Poland in the post-injection period of an ECBM pilot site. *International Journal of Coal Geology*, 77(1-2), pp. 175-187.

Vardon, P.J. 2009. *A three-dimensional numerical investigation of the thermo-hydro-mechanical behaviour of a large-scale prototype repository*. Ph.D. Thesis, Cardiff University, Wales, UK.

WCA, 2015. *Carbon Capture and Storage – The vital role of CCS in an Effective COP21 Agreement*. World Coal Association, UK.

WCA, 2017. *Carbon capture, use & storage*. Available at: <https://www.worldcoal.org/reducing-co2-emissions/carbon-capture-use-storage>, (retrieved: January 9, 2017).

White, C.M., Smith, D.H., Jones, K.L., Goodman, A.L., Jikich, S.A., Lacount, R.B., Dubose, S.B., Ozdemir, E., Morsi, B., Schroeder, K.T. 2005. Sequestration of Carbon Dioxide in Coal with Enhanced Coalbed Methane Recovery – A Review. *Energy&Fuels*, 19 (3), 659-724.

Wong, S., Law, D., Deng, X., Robinson, J., Kadatz, B., Gunter, W.D., Jianping, Y., Sanli, F. and Zhiqiang, F. 2007. Enhanced coalbed methane and CO₂ storage in anhracitic coals – Micro-pilot test at Sout Qinshui, Shanxi, China. *International Journal of Greenhouse Gas Control*, 1, pp. 215-222.

2

Literature Review

2.1. Introduction

In this chapter, a literature review will be provided summarising the salient elements of previous work in relation to carbon sequestration in coal and concentrating on the recent findings and developments within this field. A review will be focused on the developments and results of a number of research programmes, including experimental, theoretical and computational studies.

A review of the measurement methods and experimental facilities commonly employed to study coal-gas interactions is given in Section 2.2. In particular, details related to gas sorption and swelling experiments, gas flow and permeability experiments as well as the determination of the coal strength and deformation properties are provided.

Section 2.3 provides a review of physical and chemical aspects of CO₂ sequestration in coal. Recent experimental findings, based on the measurement methods presented in Section 2.2, are discussed in detail. In particular, a review of the results of the gas sorption and induced coal swelling measurements is given. In addition, results of the gas flow and permeability measurements conducted under different conditions are shown. The dependency of such results on temperature, gas pressure and stress state of coal is discussed. Furthermore, a review of the effects of CO₂ sorption on the coal structure and related changes in elastic deformation and failure is provided.

A review of the developments related to theoretical and computational studies on gas transport in fractured rocks is presented in Section 2.4. Models employed to deal with the sorption capacity of coals to gases, the kinetics of sorption and sorption induced swelling are presented. Gas flow and permeability models developed under certain conditions using analytical solutions and empirical approaches are also reviewed. This is followed by a review of the numerical modelling techniques developed to study the behaviour of fractured rocks subject to gas injection under various conditions. Outcomes and conclusions of numerical simulations dealing with a gas flow in porous medium are also reviewed in this section.

Finally, Section 2.5 gives the concluding remarks of the current state of the research field.

2.2. Overview of the Experimental Facilities and Measurement Methods

This section covers a review of the most commonly used measurement methods related to investigate the coal-gas interactions. In particular, experimental apparatuses and related methodologies will be presented with regards to: i) gas sorption measurements (Section 2.2.1), ii) gas flow and permeability measurements (Section 2.2.2), iii) coal swelling measurements (Section 2.2.3), iv) measurements of coal's strength and deformation parameters (Section 2.2.4).

2.2.1. Gas Sorption Measurements

Determination of the adsorption capacity of coal samples can be conducted using two commonly used techniques, i.e. manometric/volumetric method or gravimetric method (Busch and Gensterblum, 2011). In addition, Hol et al. (2013) have recently reported a new method, i.e. the capsule method. The main difference between the methods lies in the choice of the physical parameters used to determine the sorption isotherm. Among all the above mentioned, the manometric sorption method is the most widely used technique to determine sorption capacity of coals (e.g. Krooss et al., 2002; Busch et al., 2003a; Siemons and Busch, 2007; Li et al., 2010; Battistutta et al., 2012; Merkel et al., 2015).

Calculation of the sorption isotherms using the manometric method is based on the pressure changes within the manometric system induced by the sorption of gases. The equation of state is used to determine the density of the non-adsorbed gas in order to calculate the excess or Gibbs sorption amount (Busch and Gensterblum, 2011).

There are number of equations of state available to be used. While Peng and Robinson (1976) equation of state is commonly used for carbon dioxide property calculation, the newer equation of state by Span and Wagner (1996) in the technically most important region up to 30 MPa and temperatures up to 523K offers accuracy of ± 0.03 to 0.05%.

Ozdemir (2005) and Lutynski et al. (2011) have compared the compressibility factors obtained by both equations of state mentioned above and concluded that any literature data on the adsorption and desorption isotherms of CO₂ calculated using the Peng and Robinson (1976) equation is not accurate because the obtained compressibility factors

obtained deviate from the factors calculated using the newly developed equations of state. The main problem associated with using the Peng and Robinson (1976) equation of state would be underestimation of the absolute sorption amount around supercritical point yielding unreliable results and parameters of the fitting models (Lutynski et al., 2011).

Busch and Gensterblum (2011) have provided an extensive overview of the experimental methodology related to sorption measurements.

2.2.2. Gas Flow and Permeability Measurements

Laboratory studies focusing on the multiphase flow properties of gas/water systems in permeable rocks suitable for carbon sequestration purposes are commonly conducted via core flooding experiments. For that purpose, triaxial apparatuses can be employed (e.g. Chen et al., 2011; Connell et al., 2011; Hol et al., 2011; Ranjith and Perera, 2011; Espinoza et al., 2014; Gensterblum et al., 2014). In addition, core holders are also used (e.g. Mazumder and Wolf, 2008; Alexis et al., 2015). A common experimental setup for gas flow and permeability measurements can be seen in Figure 2.1 (Gensterblum et al., 2014).

The majority of the existing setups are designed to allow continuous measurement of the lateral and axial stresses, displacements, gas inlet and outlet flow rates as well as gas pressures both at the inlet and the outlet of the system. However, while the setups mentioned above are designed to maintain constant temperature of the confining cell using the temperature controller, temperature changes within the rock samples induced by gas flow are not usually monitored.

Due to the fact that supplying the gas to the triaxial cell or the core holder directly from the gas cylinders limits the gas injection pressures to the pressures within the cylinders, gas boosters or syringe pumps can be used to increase the pressure from the cylinder level to the desired value (Connell et al., 2011; Ranjith and Perera, 2011; Espinoza et al., 2014).

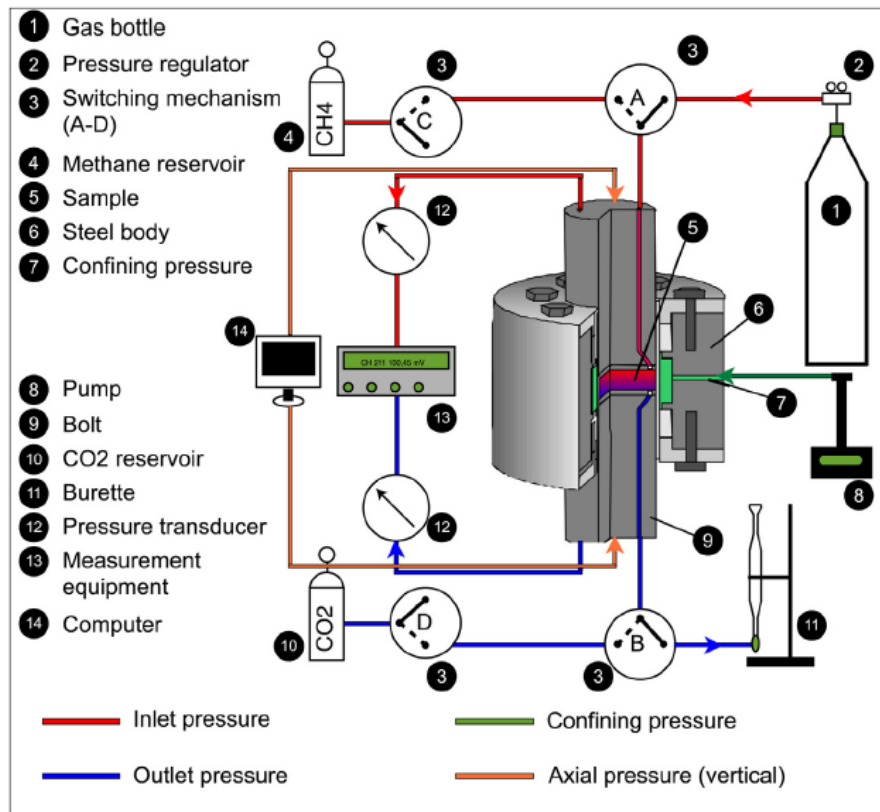


Fig. 2.1. Schematic setup of the fluid flow testing system as presented by Gensterblum et al. (2014).

For the calculation of permeability of a compressible fluid permeating through a porous medium, Darcy's law for compressible fluids is applied (Gensterblum et al., 2014). Using the abovementioned equipment and Darcy's law, the most widely used methods to calculate permeability are the steady-state method and the transient method.

The steady-state method is the simplest method to measure permeability. Using such a method, pressures at the inlet is increased to the desired value, while the volumetric flow rate of the fluid is monitored at the outlet side of the sample (Durucan and Edwards, 1986). The outlet pressure is commonly set to atmospheric pressure which restricts the maximum gas pressure that can be injected into the sample. Hence, in order to more comprehensively replicate the in situ conditions and increase the gas pressure that can be injected into the sample, backpressure regulation is required. However, there is a lack of existing experimental facilities with such ability.

Using the transient pulse-decay method, the decay of the differential pressure between the gas cylinders at the inlet and the outlet of the sample is observed (Brace et al.,

1968). In other words, the progress of pressure loss in the cylinder near the inlet of the sample and the consequent pressure gain in the cylinder near the outlet enables permeability of the sample to be determined using the decay parameter which represents the slope of the pressure change on a semi-log plot (Brace et al., 1968; Chen et al., 2011). Although the transient method is less time-consuming than the steady-state method, it does not reflect the real permeability evolution under the effect of coal matrix swelling caused by pressure and temperature changes during gas flow (Qu et al., 2012).

2.2.3. Swelling and Shrinkage Measurements

As a part of the core flooding and the gas sorption measurements, swelling/shrinkage of the coal samples induced by gas is commonly monitored. Unconfined coal sample deformations are measured by two different methods. Placing the strain gauges directly on the sample surface allows monitoring the microstrains induced by gas injection (e.g. Majewska et al., 2009; Battistutta et al., 2010; Wang et al., 2014a). An optical method, where digital cameras are employed to monitor the change in the lengths between the points on the sample, has also previously been used to determine the coal volumetric deformation under unconfined conditions (e.g. Day et al., 2008a; van Bergen et al., 2009; He et al., 2010; Day et al., 2012).

Under confined conditions, where coal is tested via a core flooding measurement system, the volumetric response of coals to gas injection is monitored using two common methods. It can be measured by placing the radial and axial strain transducers directly onto the rubber sleeve surrounding the sample (Hol et al., 2011; Espinoza et al., 2014). Additionally, the dimension change of the sample within the core holder can be monitored by using the change of the volume of the confining fluid (Masoudian et al., 2014).

2.2.4. Measurement of Strength and Deformation Parameters

Determination of the deformation properties in terms of the behaviour of coal samples subject to stresses and their maximum strength before failure is conducted using common methods reported in the rock mechanics (Speight, 2005). However, such

properties are scarce within the scientific literature for coals which is considered to be a disadvantage as predicting the coal behaviour during different activities, which might induce changes within the stress state of the coal seams, is of importance (Speight, 2005).

The most common way to determine the compressive strength and the elastic modulus of a coal sample is by using the uniaxial compressive test through which the displacement of the coal sample under a compressive load is being observed (Bieniawski, 1968; Viete and Ranjith, 2006; Viete and Ranjith, 2007; Perera et al., 2011; Perera et al., 2013). Using the triaxial testing apparatus, by imposing a deviatoric loading through changes in axial strain under constant confining stress, the bulk elastic response of coal samples is monitored (Medhurst and Brown, 1998; Hol and Spiers, 2012; Masoudian et al., 2014).

2.3. Physical and Chemical Aspects of CO₂ Sequestration in Coal – Experimental Findings

This section provides a review of the current findings and understandings of the physical and chemical interactions of the coal-gas system obtained through experimental investigations. Recent experimental findings in relation to the sorption capacity, sorption kinetics and sorption induced swelling of coals are presented in Sections 2.3.1 to 2.3.3, respectively. Section 2.3.4 deals with the findings related to the gas flow and permeability measurements.

In Section 2.3.5, various effects related to CO₂ sequestration are pointed out. In particular, effects of the gas pressure and temperature, and stress state of the coal studied on measured parameters are described. Moreover, effects of CO₂ sorption on the coal structure and related reductions in both the peak strength and elastic deformation are presented in Sections 2.3.6 and 2.3.7, respectively.

2.3.1. Sorption Capacity

The adsorption phenomenon can be divided in two different processes, namely physical and chemical adsorption (White et al., 2005). In physisorption, there is no chemical bond between the adsorbent and the adsorbate due to the existence of mainly van der Waals and electrostatic forces and hence, it is a reversible process (White et al., 2005). Conversely, a direct chemical bond between the solid surface and the adsorbate exists in chemisorption (White et al., 2005). Adsorption depends on the type of the adsorbent and the adsorbate investigated, however, it is assumed that it occurs as a monolayer at low pressures and as multilayers at higher pressures (White et al., 2005).

Gas mixtures and selective adsorption as well as the transport of individual gases have been explored in several cases (Busch et al., 2003b; Cui et al., 2004; Fitzgerald et al., 2005; Gruszkiewicz et al., 2009; Majewska et al., 2009; Sakurovs et al., 2012). There is an overall agreement that CO₂ sorption capacity is larger than CH₄ and N₂ sorption capacities (Busch and Gensterblum, 2011; White et al., 2005).

Preferential sorption of CO₂ over CH₄ is the highest for low rank coals (Busch et al., 2003b; Gensterblum et al., 2014). A concept has been introduced which states that this is caused by larger amount of functional groups, namely carboxylic and hydroxylic groups present in coals which are preferentially occupied by CO₂ (Gensterblum et al., 2014). These functional groups are also preferential adsorption sites for water molecules due to its polarity leading to the reduced sorption capacity in moisture-equilibrated coals (Gensterblum et al., 2014). In addition, clusters of water molecules formed around polar sites occupy space that would otherwise be available to other sorbates (Day et al., 2008b). Thus, due to the decreasing amount of functional groups (oxygen content) with coal rank, the influence of water on the individual sorption capacities decreases with increasing rank, as well (Day et al., 2008b; Gensterblum et al., 2013).

For dry coals, there is an obvious trend of decreasing the sorption capacity of both methane and carbon dioxide with coal rank, reaching a minimum capacity around 1.0 to 1.2% of vitrinite reflectance and again increasing with increasing the rank, as shown in Figure 2.2 (Busch and Gensterblum, 2011; Li et al., 2010). Reason for that lies in the fact that micropores provide most of the surface area where gas can adsorb.

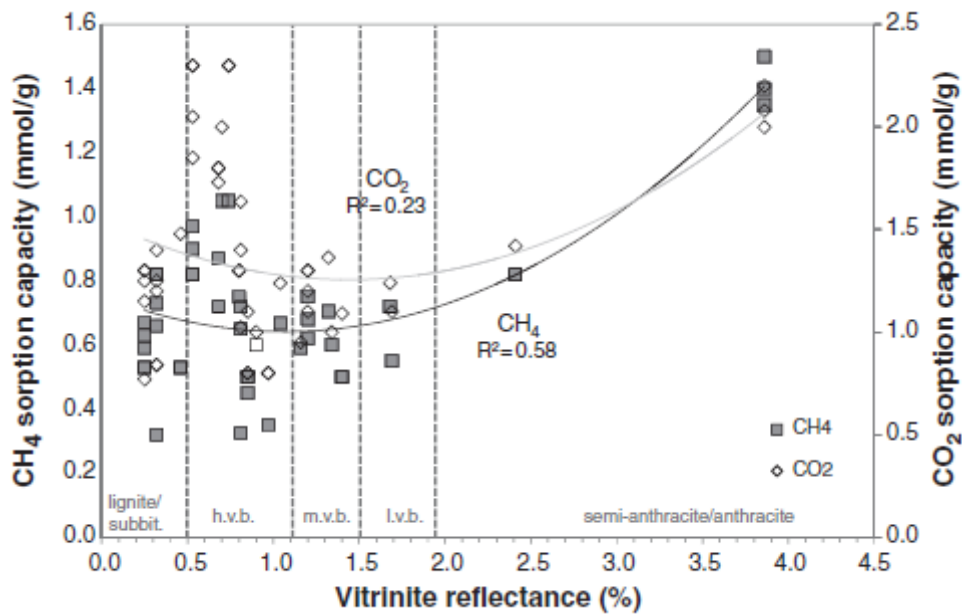


Fig. 2.2. The influence of coal rank on CH_4 and CO_2 sorption capacity of dry coals as presented by Busch and Gensterblum (2011).

From the data presented in Figure 2.2, it can be concluded that there is a lack of sorption data for semi-anthracite and anthracite coals. Hence, this area needs further investigation in order to confirm the reliability of figures and trends presented.

The majority of the previous studies investigating the sorption capacity of coal have been conducted on powdered coal samples as the sorption process in smaller particles is expected to be faster (e.g. Krooss et al., 2002; Busch et al., 2003b; Ozdemir et al., 2004; Bae and Bhatia, 2006; Goodman et al., 2007; Sakurovs et al., 2007; Siemons and Busch, 2007; Gensterblum et al., 2010; Li et al., 2010; Massarotto et al., 2010; Merkel et al., 2015). Only a smaller portion of researchers has dealt with larger coal samples (Pone et al., 2009; Espinoza et al., 2014).

For instance, Pone et al. (2009) have found that CO_2 sorption capacities of powdered and intact low rank coals are different and the conclusion was made that the sorption capacity values obtained on powdered samples do not represent the values obtained on intact coal samples. However, to the author's knowledge, there are no experimental results published for high rank coals describing the differences in sorption capacity between powdered and intact samples.

2.3.2. Sorption Kinetics

Gas transport in coal is commonly considered to occur at two different scales, laminar flow through the cleat system and diffusion through the coal matrix (Clarkson and Bustin, 1999a; Cui et al., 2004). For CO₂-ECBM purposes, both CH₄ diffusing out of the coal matrix and CO₂ diffusing into the coal matrix are of importance (Busch and Gensterblum, 2011). In general, gas transport is influenced by many factors, such as characteristics of sorption, adsorbate molecular geometry and pore structure (Cui et al., 2004).

In order to assess the importance of pore distribution within a coal sample on gas diffusion, several authors have reported adsorption kinetics experiments with CO₂, CH₄ and N₂ on powdered coals of a single size (e.g. Clarkson and Bustin, 1999b; Majewska et al., 2009; Battistuta et al., 2010; Li et al., 2010; Staib et al., 2013). Additionally, some research groups have compared the behaviour of powdered coals of different sizes (e.g. Marecka and Mianowski, 1998; Busch et al., 2004; Siemons et al., 2007; Gruszkiewicz et al., 2009). The conclusion was made that there is a decrease both in sorption rates and capacity with an increase in size of powdered samples, however, no particular relationship could be established. Pone et al. (2009) have compared the sorption rates in the low rank coal blocks and powdered samples, and found a significant reduction in CO₂ and CH₄ sorption rates in coal blocks compared to powdered samples. However, further research is required in that area for high rank coals.

2.3.3. Gas Sorption Induced Swelling

Swelling of the coal during carbon dioxide injection was found to affect the adsorption process. Similarly with the difference in sorption capacity and sorption kinetics between CO₂ and CH₄, swelling in carbon dioxide has been found to be more pronounced than swelling in CH₄ (e.g. van Bergen, 2009). This has been related to the fact that CO₂ has the same effect on coals' behaviour as do liquids known to dissolve in coals and swell them (Larsen, 2004). In other words, besides the adsorption, CO₂ also dissolves in coals and acts as a plasticizer enabling rearrangements in the coal physical structure (Larsen, 2004).

Day et al. (2008a) have found that the volumetric swelling of Australian bituminous coals was fully reversible and that the further pressure increase beyond 8-10 MPa had little or no effect on swelling (Fig. 2.3). Up to that pressure, swelling has been observed to be roughly linearly proportional to the amount of CO₂ adsorbed. However, significant differences have been found for swelling between the perpendicular and parallel direction with respect to the bedding plane, i.e. expansion was 30-70% larger in the perpendicular direction than in the parallel direction.

Measurements in pure CO₂ and CH₄, as well as their mixtures with different compositions have been conducted by Day et al. (2012) on sub-bituminous and bituminous coals at 55°C and up to 20 MPa. Swelling induced by CO₂ was more than 4% at 15 MPa and approximately twice as much produced by CH₄. By completely displacing CO₂ from a coal sample by adding helium (He), Day et al. (2012) have shown that the swelling is reversible. The same observation for reversibility has been made by Battistutta et al. (2010) for semi-anthracite.

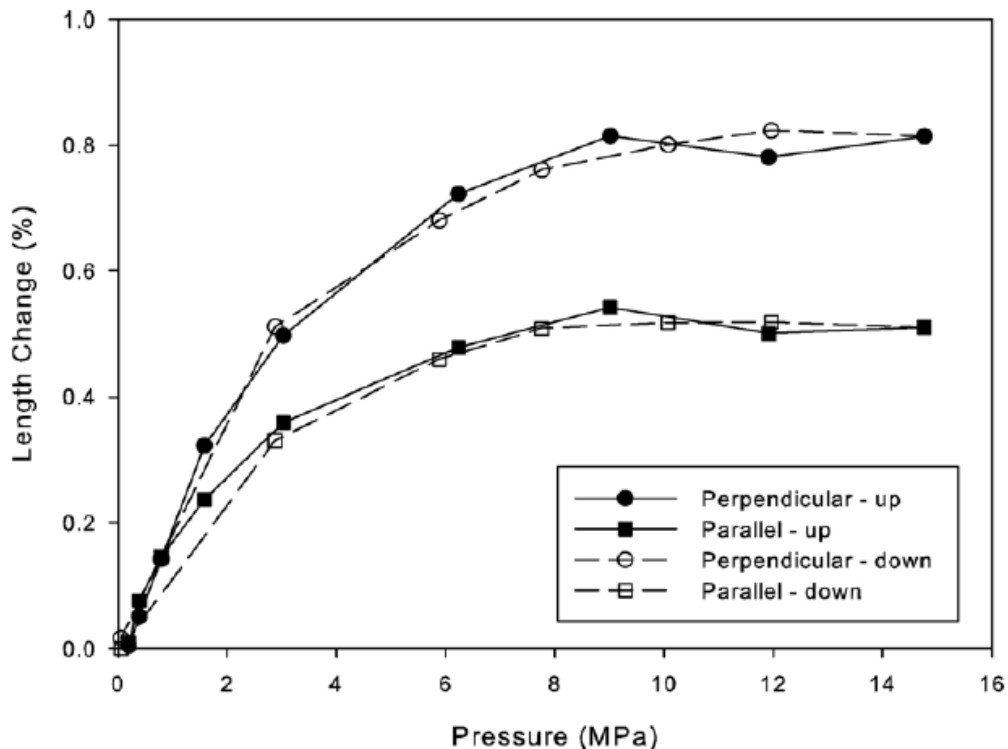


Fig. 2.3. Linear expansion of coal sample at 40°C as a function of CO₂ pressure (Day et al. 2008a). The solid markers represent results obtained during gas adsorption and the open markers during gas desorption.

Conversely, work presented by Majewska et al. (2009; 2010) for bituminous coals and He et al. (2010) for anthracites has shown that coal swelling was not fully reversible. This specific change was associated with structural rearrangements in the coal samples.

van Bergen et al. (2009) have studied the swelling behaviour of small cubical fragments of bituminous and subbituminous coals where the pressure and temperature were maintained at 8 MPa and 40°C, respectively. The swelling of coal increased with an increase in pressure and for CO₂ it was 1.5 to 2.8 times higher than for CH₄ in air-dried samples. The drying effect of CO₂ on the moisturized coal sample was observed suggesting that CO₂ removes the surface moisture added during the specimen preparation. Moreover, by removing some of the moisture additional adsorption sites became available, which was indicated by a larger volumetric strain.

2.3.4. Gas Flow and Permeability

Gas transport in porous media consists of advective and diffusive components (Ho and Webb, 2006). Gas advection is generally analysed using Darcy's law, whereas the Fick's law is the most popular approach to calculate gas diffusion (Ho and Webb, 2006). As described earlier, coal is a naturally fractured porous medium consisting of a microporous matrix and a network of natural fractures. Despite the large porosity of the coal matrix, the flow in micropores is usually neglected as the matrix permeability is up to 8-9 orders of magnitude less than the fracture permeability (Seidle, 2011).

Using the transient method over the steady state method in order to reduce experimental time, Pan et al. (2010) have determined the permeability of bituminous coals to He, CH₄ and CO₂. The behaviour of permeability with respect to effective stress was described using the exponential relationship (Fig. 2.4). Among the three gases used, the permeability to CO₂ was found to be the lowest, which was attributed to the differential swelling behaviour of the coal matrix during CO₂ sorption. In addition, it was found that fracture compressibility is pore pressure and gas type dependent and it should not be regarded as constant.

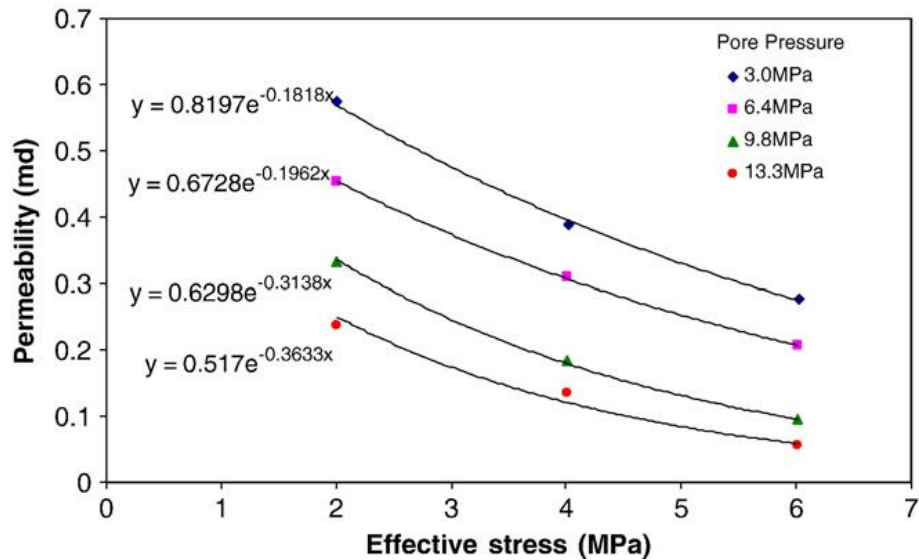


Fig. 2.4. Relationship between permeability using CO_2 and effective stress (Pan et al., 2010).

The same exponential approach for establishing a relationship between the effective stress and gas permeability has been used by numerous authors (e.g. Durucan and Edwards, 1986; Harpalani and Chen, 1997; Gensterblum et al., 2014)

Wang et al. (2011) have used the transient method to determine the permeability of anthracite samples with different fracture geometry (i.e. samples with multiple small embedded fractures, a single longitudinal through-going fracture, and a single radial through-going fracture) under constant confining stress conditions and injection pressures up to 6 MPa. It was found that fracture geometry changes the magnitude of permeability by several orders of magnitude and controls the evolution of permeability, sorption and swelling strain.

Espinoza et al. (2014) have injected CO_2 up to 10 MPa in subbituminous coal subject to near constant volume conditions. It was recognised that effective stress increases significantly during adsorption which was found to be the main driver for changes in core permeability and that swelling strains, swelling stresses and total gas uptake are controlled by the response of the macroporous and microporous systems. This is in agreement with Larsen (2004) who has concluded that dissolution of carbon dioxide and induced swelling should decrease the permeability of the coal as cleats and pores are squeezed. By observing the change in macroscopic strain with an increase in gas pressure under constant confining stress conditions, it was found that the response of the

microporous matrix is dominant over the response of fractures during injection of CO₂ (Espinoza et al., 2014).

From the review presented above, it can be observed that the focus in the majority of the published works has been to determine the permeability as a function of effective stress under isothermal conditions using transient method. Moreover, swelling of coal has been predominantly measured on unconfined coal samples and results on the reversibility of swelling appear to be controversial. Hence, there is a lack of knowledge on coal's dynamic response subject to a continuous flow of supercritical gas under confined conditions, before and after achieving the steady state condition. Overall, such information for high rank anthracitic samples is scarce.

2.3.4.1. Klinkenberg Effect

The transport of gases through the porous medium can be enhanced by a gas slippage which yields an overestimation of the measured gas permeability compared to the permeability measured by liquid (Florence et al., 2007). Klinkenberg (1941) has observed that the mean free path of the gas molecules is inversely proportional to the mean pressure in the pore system where at lower gas pressures the mean path increases and consequently, increases the gas permeability (McPhee and Arthur, 1991).

The Klinkenberg effect in coals has been proven in samples with large number of micro-cleats both for non-sorbing gas, i.e. helium and sorbing gases such as carbon dioxide, methane and nitrogen (Harpalani and Chen, 1997; Gensterblum et al., 2014). For sorbing gases, slip factors appear to be higher than for the non-sorbing gases which has been related to the effect of matrix swelling on the reduction of the pore diameters (Gensterblum et al., 2014; Wang et al., 2014b).

Li et al. (2009) have shown that if the outlet gas pressure is set to atmospheric, the gas slip flow for low permeability cores always exists near the outlet of the sample affecting the measured permeability regardless of the inlet pressure applied. Hence, by applying a backpressure at the outlet of the sample, the gas slippage can be effectively reduced (McPhee and Arthur, 1991; Li et al., 2009). Nevertheless, based on the present findings, gas slippage effect is significant only for mean gas pressures of less than 1.7 MPa both

for carbon dioxide and helium injection in coal (Harpalani and Chen, 1997; Li et al., 2013).

2.3.5. CO₂ Sequestration Associated Effects

This section presents the impact of different effects associated with CO₂ sequestration on the abovementioned experimental findings. In particular, Sections 2.3.5.1 and 2.3.5.2 present the effects of pressure and temperature, and the effect of stress state, respectively.

2.3.5.1. Effects of Pressure and Temperature

The CO₂ and CH₄ adsorption capacity of coal is a direct function of both the temperature and pressure, hence increasing pressure results in increased storage, whereas increasing the temperature results in decreased gas storage (Krooss et al., 2002; Li et al., 2010; Gensterblum et al., 2013). With an increase in sorption capacity at lower temperatures, swelling of the coal increases, as shown in Figure 2.5 (Baran et al., 2015).

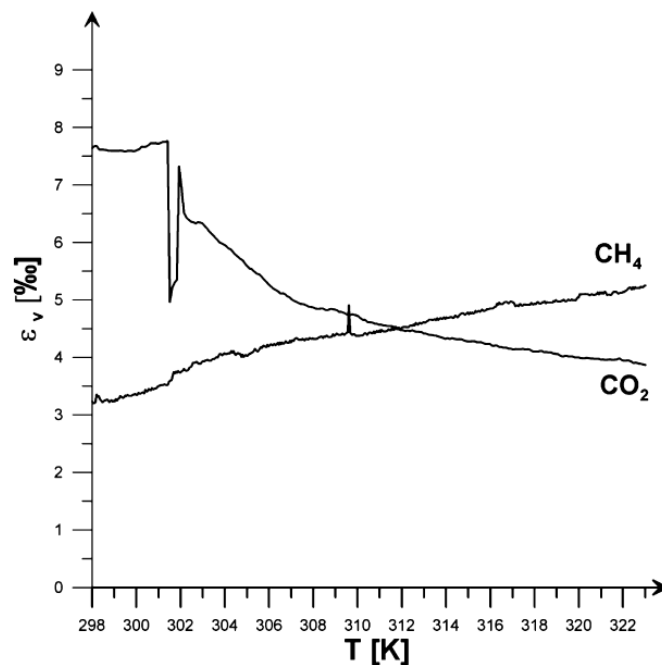


Fig. 2.5. Volumetric strains during the temperature increase (Baran et al., 2015).

The influence of temperature on the sorption kinetics of CO₂ has been investigated by Busch et al. (2004) and Charrière et al. (2010) for high volatile bituminous coals. Equilibration times for measurements at 32°C were significantly longer than those at 45°C, i.e. decrease in sorption rates by a factor of about 2 has been observed upon temperature reduction by 13°C both for CH₄ and CO₂ (Busch et al., 2004). Charrière et al. (2010) have reported an equilibration time decrease by a factor of 4 when increasing the temperature from 10°C to 60°C.

As most gases exhibit non-ideal behaviour, their expansion and related effects are also recognized in the engineering practice (Oldenburg, 2007). At room temperature, gases such as carbon dioxide and nitrogen cool upon expansion while helium warms upon expansion (Oldenburg, 2007). This effect is known as an adiabatic, i.e. Joule-Thomson cooling or heating that accompanies the expansion of a real gas (Burshtein, 1996; Oldenburg, 2007). Kazemifar and Kyritsis (2014) have conducted an experimental investigation to study the Joule-Thomson throttling at the elevated pressures relevant for CCS through a 60 cm long stainless steel pipe with 2.1 mm internal diameter. It was shown that near-critical CO₂ underwent a cooling on the order of 0.5 °C/bar across the steel pipe. Moreover, Joule-Thomson coefficient up to 1 °C/bar has been reported by National Institute of Standards and Technology (Linstrom and Mallard, 2016). Opposite to CO₂, helium experiences slight warming effect on the order of 0.06 °C/bar (Roebuck and Osterberg, 1933).

Although both the cooling effect of CO₂ upon expansion and the increase in sorption induced coal swelling with a decrease in temperature are widely recognised, there has been no attempt so far to assess the effect of CO₂ cooling during continuous CO₂ injection on coal behaviour.

2.3.5.2. Effects of Stress State

Besides the effects of stress on measured permeability presented in Section 2.3.4, in situ stress present in the coal seams or changes in the stress state due to swelling are expected to possibly affect the adsorption process in the coal seam. Pone et al. (2009) have applied different confining pressures to the core sample and observed significant reductions in sorption capacity both for CO₂ and CH₄, in comparison to powdered coal.

In addition, gas transport behaviour in powdered and non-powdered confined coal sample was quantified for CO₂ gas uptake capacity where it was found that the overall gas movement, specifically diffusion, was hindered by confining stresses and takes place at rates significantly less than in unconfined powder coal (Pone et al., 2009).

Hol et al. (2011) have investigated the effect of stress on the physical adsorption of carbon dioxide on pre-compacted coal matrix material. The adsorption capacity under positive effective stress was lower up to 50%, depending on the pressure and temperature conditions used, than the sorption capacity of a crushed coal under hydrostatic CO₂ pressure (Hol et al., 2011).

Similarly, Wang et al. (2011) have shown that sorption isotherms determined under low confining pressure both for methane and carbon dioxide are higher than the sorption isotherms at high confining stress indicating that the higher applied stress reduces the sorption capacity (Fig. 2.6).

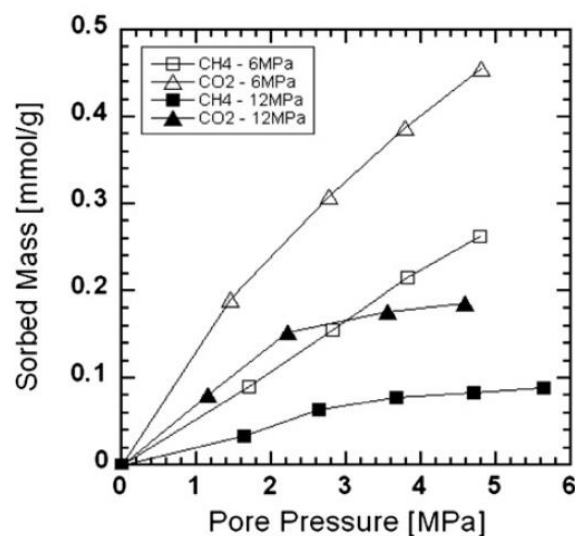


Fig. 2.6. Sorbed mass as a function of applied pore pressure for constant applied confining stresses of 6 and 12 MPa (Wang et al., 2011).

2.3.6. Effects of CO₂ Sorption on Coal Structure

Sorption of CO₂ can have an effect on the coal physical structure (Gathitu et al., 2009). During the dissolution of CO₂ in the coal structure, vitrinite have shown the highest degree of swelling by compressing the inertinite region in response (Karacan, 2007). In addition to that, it has been shown that macropore volume decreases and micropore

volume increases in high rank coals with CO₂ injection (Liu et al., 2010; Liu et al., 2015a).

Masoudian et al. (2014) have presented a series of SEM images taken from the surface of CO₂ saturated coals which suggested much smoother surface with a more visible granular structure compared to wet coals. Such effect was related to the observed decrease in angle of internal friction in the Mohr-Coulomb failure criterion that was used to fit the experimental data (Masoudian et al., 2014). Similarly, Kumar et al. (2015) have found rougher fracture surface in anthracite coal sample due to irreversible structural rearrangement within the coal with carbon dioxide uptake and loss.

Liu et al. (2010) have treated anthracite coal with supercritical CO₂-H₂O mixture and observed a general increase in the total pore volume, porosity and meso- and micro-pores with bulk density decreasing in turn. Vishal et al. (2015) have shown through acoustic emission that the CO₂ induced swelling causes crack initiation and possible enhancement of the fracture lines along the coal which has a direct impact on reduction of coal's mechanical parameters. Such an observation is also consistent with the work of Gathitu et al. (2009), Hol et al. (2012) and Hol et al. (2014) who have reported a creation of micro-fractures as a result of heterogeneous matrix swelling. Through experimental and molecular numerical studies, Liu et al. (2015a) have concluded that such micro-crack growth is an irreversible process.

Similarly, four different coal rank samples have been treated with supercritical CO₂-H₂O mixture focusing on the changes of the pore structure by Liu et al. (2015b). Investigation has suggested that higher rank untreated coals are more difficult to compress than the lower rank coals due to the hardness of the intact coals which usually increases with an increase in maturity. However, after the supercritical CO₂-H₂O treatment, an opposite behaviour has been reported where anthracite coal was easily compressed compared to the low volatile bituminous coal.

Moreover, it has been demonstrated that by introducing supercritical CO₂ and water in high volatile bituminous coals, the mineral matter occurring in the coal matrix and the cleat system can be dissolved and mobilised creating new porosity and increasing the coal permeability and sorption capacity, as shown in Figure 2.7 (Massarotto et al., 2010).

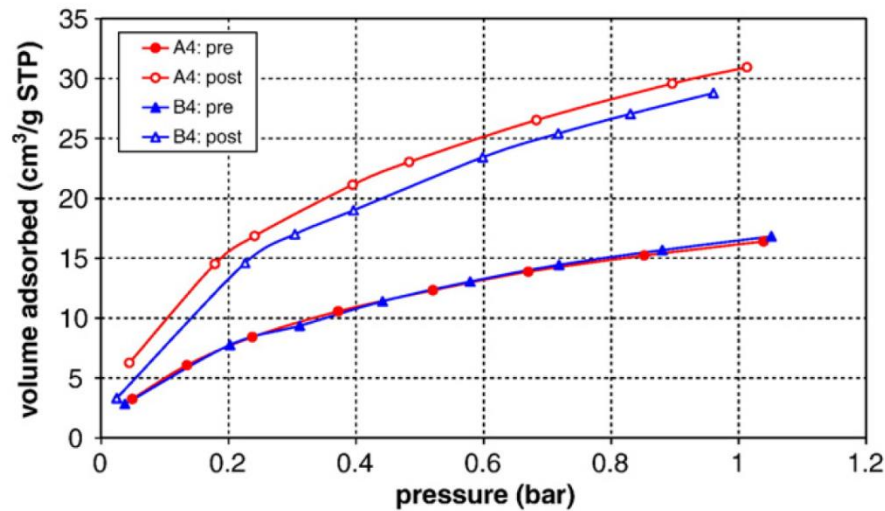


Fig. 2.7. Carbon dioxide adsorption at 0°C on coals A4 and B4 before and after the treatment with supercritical CO₂-H₂O mixture for 60 hours (Massarotto et al., 2010).

2.3.7. Effects of CO₂ sorption on Coal Elastic Deformation and Failure

Elastic deformation of coal under applied stress is of importance for the integrity and the safety of the coal seams targeted for CO₂ sequestration and the overlaying strata. Natural unsaturated coals respond in a highly brittle manner to increasing deformation (Thomas, 2013). In unconfined compressive tests, irregular longitudinal splitting is the most common failure mechanism observed leading to an abrupt failure (Jaeger et al. 2007). Where the rock is fully ductile, a network of shear fractures will develop accompanied by plastic deformation of individual grains, as shown in Figure 2.8 (Jaeger et al. 2007). A detailed review of multiphysics of CO₂ sequestration in coals with a focus on geomechanical characteristics of coal were provided in Masoudian (2016).

Several authors have reported the results of uniaxial compressive tests on non-saturated (natural) coals (Bieniawski, 1968; Medhurst and Brown, 1998; Speight, 2005). In general, the response of coals to applied stress has been shown to be size dependent where smaller specimens show greater strength and elastic modulus than larger specimens which has been attributed to the presence of fracture planes and cleats in the larger specimens.

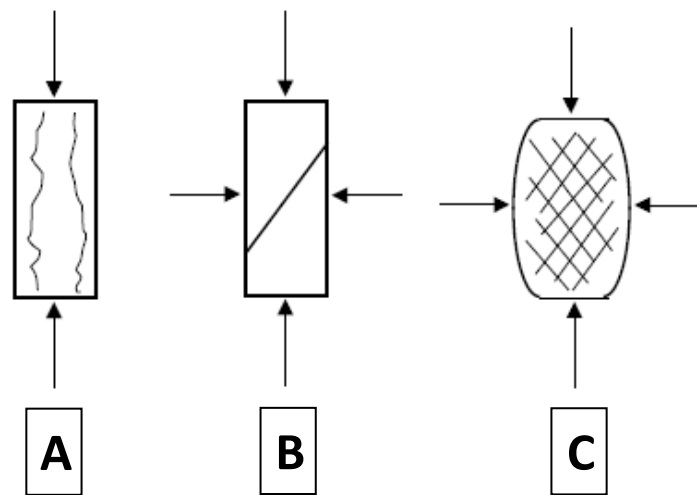


Fig. 2.8. Rock failure types (Jaeger et al., 2007); A) Longitudinal splitting under uniaxial tension, B) Shear Fracture, C) Multiple Shear Fractures.

Viete and Ranjith (2007) have saturated brown coal with CO₂ at 1.5 MPa pressure and found a reduction in the compressive strength and elastic modulus of about 13% and 26%, respectively. Similarly, Perera et al. (2011) have conducted a strength analysis of brown coal at 2 MPa saturation pressure finding a reduction in unconfined compressive strength and elastic modulus of 7% and 19%, respectively. For comparison reasons, Ranjith and Perera (2012) have performed uniaxial compressive tests at same saturation pressures for bituminous coal as Perera et al. (2011) in order to assess the effect of coal rank on reduction of strength parameters. Ranjith and Perera (2012) have concluded that the reduction percentage in coal's strength shows a linearly increasing trend with CO₂ pressure from 1 MPa to 3 MPa, where the slope for bituminous coal was significantly higher compared to lignite.

For bituminous coal saturated at a supercritical pressure of 8 MPa, Perera et al. (2013) have shown 79% and 74% reduction in unconfined compressive strength and elastic modulus, respectively (Fig. 2.9). However, when the saturation pressure increased to 16 MPa, there was a slight recovery of both parameters. Perera et al. (2013) have attributed such behaviour to the reduced sorption potential at pressures above 15 MPa and consequently less swelling where in turn such high pressure induced matrix compression.

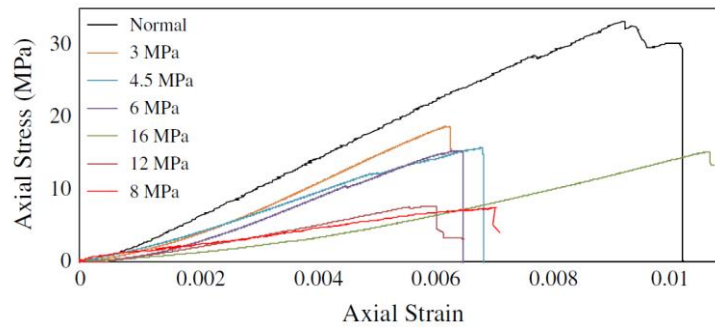


Fig. 2.9. Stress-strain relationship for normal (unsaturated) and CO_2 saturated coal samples (Perera et al., 2013).

Performing triaxial compression tests on over 80 coal specimens of high volatile bituminous coal with CO_2 saturation pressures up to 5.5 MPa, Masoudian et al. (2014) have observed 19% and 20% reduction of elastic modulus and unconfined compressive strength, respectively. However, there was an increase in both parameters with an increase in confining pressure attributed to the gradual closure of pores and fractures. Similar observation has been reported by Espinoza et al. (2014) who observed a non-linear increase in Young's elastic modulus from 2-6 GPa in the range of confining stresses from 0.5-30 MPa.

Hol et al. (2014) have exposed bituminous coal samples to different sorbing gases at 3 MPa CO_2 pressure and subsequently subjected to isotropic loading and unloading at room temperature. Due to the CO_2 adsorption induced swelling of the coal sample, the apparent bulk modulus was approximately 25% lower compared to the initial state.

Petrography of the coal sample has also been related to the mechanical parameter reduction (Bae and Bhatia, 2006; Karacan, 2007). Karacan (2007) has shown that swelling of the coal was mostly attributed to the swelling of vitrinites which yielded 12.5% - 18% of volumetric strain at about 4.5 MPa as a consequence of CO_2 dissolving in their cross-linked macromolecular structure causing its rearrangement. As the amount of CO_2 that can be accommodated by vitrinites decreases with an increase in pressure, reduction in mechanical parameters is less significant with further increase in pressure (Ranjith and Perera, 2012).

Wang et al. (2011; 2013a; 2013b) have also observed the elastic modulus and strength reductions with the decrease in the confining stress. In addition, Wang et al. (2011) have

compared two anthracite coals exposed to CO₂ saturation of 1 MPa for different times and found that coal sample exposed one hundred times longer to CO₂ showed lower strength with post-failure average particle size 3 times smaller than the other coal.

According to the author's knowledge, results related to post-failure size analysis reported by Wang et al. (2011) are the only one reported in the literature with regards to particle size distribution after the failure of CO₂ saturated coals. However, there are no experimental results on the post-failure sieve analysis of coals saturated at different gas pressures, i.e. with both subcritical and supercritical CO₂. In other words, there is no data that could relate the effect of CO₂ saturation pressure on the elastic response of anthracites and the resulting particle size distribution after failure. Overall, based on the abovementioned, it can be observed that there is a lack of understanding of the effects of both subcritical and supercritical CO₂ sorption on the compressive strength, elastic modulus and structure of high-rank coals.

2.4. Theoretical and Computational Studies on Gas Transport and Reactions in Coal

A review of different techniques developed to study gas sorption and induced processes as well as gas transport and permeability evolution is presented in this section. Techniques developed to model the sorption capacity of coal to gases, the kinetics of sorption and sorption induced swelling are discussed in Sections 2.4.1 to 2.4.3, respectively. Models derived to study gas flow and permeability in coals using analytical solutions and empirical relationships are reviewed in Section 2.4.4. In Section 2.4.5, models developed using different numerical techniques and related numerical investigations are described.

2.4.1. Sorption Capacity Models

A range of sorption isotherms exists in the literature to model the experimentally determined sorption capacity, such as Langmuir, Brunauer-Emmett-Teller (BET), Dubinin-Astakhov and Dubinin-Radushkovich (Ozdemir, 2005).

Langmuir (1918) isotherm is the simplest and the most widely used sorption model which assumes that the adsorption of molecules occurs on a fixed number of sorption sites and it occurs as a monolayer. All sites are energetically equivalent and the interaction between the molecules on the adjacent sites is neglected (White et al., 2005). The Langmuir model has been extended to BET multilayer adsorption model by Brunauer et al. (1938) assuming that adsorption occurs in multilayers (White et al., 2005).

Dubinin-Astakhov (1966) isotherm is a pore-filling model without taking into account the monolayer surface coverage (Sakurovs et al., 2007). It is defined by several parameters, such as the pore volume of the adsorbent, the Dubinin constant and the structural heterogeneity parameter (White et al., 2005). Dubinin-Radushkovich is a special form of the Dubinin-Astakhov isotherm with the structural heterogeneity parameter equal to two.

It has been shown that Langmuir curve offers good approximation for high-rank coals since such coals contain mainly micropores of nano-size (Clarkson and Bustin, 1999b; Katyal et al., 2007; White et al., 2005). Such pores are so small that they welcome only a couple of fluid molecules explaining why Langmuir adsorption model provides good fit to the experimental data (Vandamme et al., 2010).

According to some researchers (e.g. Ozdemir et al., 2003; Sakurovs et al., 2007; Siemons and Busch, 2007) swelling of the coal structure may affect the measured sorption capacity. Hence, different modifications of the originally developed sorption isotherms have been suggested to model the absolute sorption on the coal. While no correction procedure has been applied for the swelling by majority of researchers (e.g. Arri et al., 1992; Busch et al., 2003b; Bae and Bhatia, 2006; Goodman et al., 2007; Gensterblum et al., 2010; Pan et al., 2010; Merkel et al., 2015), several authors have used different approaches to account for the swelling effect on absolute sorption capacity (e.g. Ozdemir et al., 2004; Sakurovs et al., 2007; Siemons and Busch, 2007).

A common approach for the correction procedure has been to introduce an additional term when calculating the excess sorption proportional to the density of the gas phase. However, more recent findings from the literature have suggested that the relationship between the swelling and sorption is not straightforward and it is not reasonable to

assume that a swollen coal takes up more gas-impermeable space (Sakurovs et al., 2007). In fact, swelling may increase the internal accessibility to the gas by increasing microporosity (Sakurovs et al., 2007; Gathitu et al., 2009; Liu et al., 2010; Liu et al., 2015b). In addition, recent works have indicated that CO₂ injection might cause micro-fracturing of the coal affecting its sorption behaviour, as previously mentioned.

Battistutta et al. (2010) have calculated the absolute sorption of CO₂, both with and without the correction for swelling, and concluded that both isotherms were almost the same. However, the extrapolated density for the swelling-corrected case was unrealistically high leading to the possible issues related to the correction procedure since the similarity in sorption values was a result of the mathematical procedure.

2.4.2. Sorption Kinetics Models

Methods for determining diffusion coefficients from high-pressure gas adsorption and desorption isotherm data have been developed by different authors based on unimodal or bimodal pore size distribution in the coal samples.

Based upon the solution of the Fick's second law for spherically symmetric flow, the unipore diffusion model is a conventional approach for modelling matrix gas transport with an assumption of isothermal conditions and homogenous pore structure (Clarkson and Bustin, 1999a; Busch et al., 2004; Pone et al., 2009). Potential problems regarding the use of the unipore model have been investigated and explained by Clarkson and Bustin (1999a) where a conclusion was drawn that the unipore model is inadequate for coals with heterogeneous pore structure.

For coals consisting of a bimodal pore size distribution, a bidisperse diffusion model is commonly adopted (Clarkson and Bustin, 1999a; Cui et al., 2004). The model initially developed by Ruckenstein et al. (1971) is a solution for spheres of two distinct sizes, where macrosphere contains an assemblage of microspheres of uniform sizes, which contains one diffusion coefficient for each pore size. The model assumes linear isotherms and a step change in concentration of the adsorptive external to the particle. Restriction of the model lays in the fact that it may be inadequate for application to high-pressure volumetric adsorption/desorption experiments due to the assumption of a

step change in external concentration of the diffusing species at time zero which then remains unchanged with time (Clarkson and Bustin, 1999a). This assumption is not true for variable pressure, constant volume adsorption rate experiments (Clarkson and Bustin, 1999a). In addition, gas sorption isotherms for coal are known to be nonlinear.

Recognizing the deficiencies of the unipore models and complex bidisperse Ruckenstein's model, Busch et al. (2004) have described the gas sorption process through a combination of two first-order rate functions with different rate constants and achieved a perfect fit of the data. Similarly, Siemons et al. (2007) and Staib et al. (2013) have used two-stage models to describe the diffusion process. Such models do not require an assumption of the coal structure, opposite to the abovementioned unipore and bidisperse models, allowing more general link to distinct stages in the adsorption process (Busch et al., 2004; Hosking, 2014).

2.4.3. Sorption Induced Swelling Models

As it is commonly observed that swelling increases linearly with the amount of gas adsorbed and reaches a plateau after a certain pressure step, Langmuir isotherm is used to model the adsorption-induced swelling strain. While Durucan et al. (2009) have used gas pressure as a variable in the Langmuir model, Battistutta et al. (2010) recognised that free swelling is proportional to the gas density and have used this parameter in the model instead. Modified Dubinin-Radushkevich model with additional "k" term has been used by Day et al. (2008a) in relation to swelling where the "k" constant was related to the solubility of CO₂ into the coal.

Pan and Connell (2007) have presented a theoretical model for gas adsorption induced swelling in coal. The model has been derived using an energy balance approach which assumes that the surface energy change caused by the sorption is equal to the elastic energy change of the coal solid. Despite the fact that it has been shown that the model is able to describe the differences in swelling behaviour with respect to gas species, the Langmuir model is the most widely used due to its simplicity and good agreement with the experimental data.

2.4.4. Gas Flow and Permeability Models – An Analytical and Empirical Approach

A broad variety of models has been developed to represent the effect of sorption, swelling and changes in effective stress on the dynamic evolution of coal permeability to gases.

Wu et al. (1998) have presented a set of analytical solutions derived from the gas flow equation. Solutions for analysing steady-state and transient gas flow through porous media including Klinkenberg effects have been developed. These analytical solutions can be applied to analyse gas flow and determine the flow properties of porous media in unsaturated zone or in laboratory tests (Wu et al., 1998). However, the solutions are only restricted to gas flow predictions, neglecting the deformation of the porous material and its effect on gas flow.

In order to study the permeability evolution of coal during gas storage under different conditions, various models have been developed. While some models have been developed based on the porosity change (e.g. Seidle and Huitt, 1995; Palmer and Mansoori, 1996; 1998), others considered changes of the stress state of the system (Shi and Durucan, 2004; Robertson and Christiansen, 2006). In order to link the porosity to changes in permeability, a cubic relationship is commonly used (Somerton et al., 1975):

$$\frac{K}{K_0} = \left(\frac{n}{n_0}\right)^3 \quad (2.1)$$

where K and n are permeability and porosity, respectively. Subscript “0” represents initial value of the respective parameter.

An exponential relationship between the permeability and the effective stress is also used (Seidle et al., 1992):

$$\frac{K}{K_0} = \exp[-3C_f(\sigma'' - \sigma_0'')] \quad (2.2)$$

where C_f and σ'' are fracture compressibility and effective stress, respectively. This model is commonly used to fit the experimental data, as discussed in Section 2.3.4. Such relationships have been derived based on the assumption that coal can be

represented using the matchstick or cubic geometries (Liu et al., 2011; Pan and Connell, 2012).

Based on the experimental measurements of coal matrix shrinkage due to gas desorption, Seidle and Huitt (1995) have found a close relation between the matrix shrinkage and gas content. Following the experimental observations, where the swelling of the coal was fitted using a Langmuir isotherm, and using a matchstick geometry model to relate porosity to permeability, Seidle and Huitt (1995) have derived a model based on porosity change considering coal swelling/shrinkage. The model can be used to predict permeability evolution in coals where the swelling strain dwarfs the mechanical response of coal subject to gas injection. However, it ignores the impact of coal compressibility limiting its applicability to specific conditions.

Palmer and Mansoori (1996; 1998) have developed an analytical model as a function of effective stress following the equation of linear elasticity for strain changes in porous rock. Matrix swelling/shrinkage has been predicted using the Langmuir isotherm and implemented in the model assuming an analogy with the thermal expansion of the porous medium. In order to derive the model, uniaxial strain condition with no change in overburden stress has been assumed.

Shi and Durucan (2004; 2005) have developed a permeability model from the constitutive equations for isotropic linear poroelasticity relating the permeability to effective stress. Uniaxial strain and constant vertical stress conditions, commonly experienced in producing reservoirs, were assumed. Similarly to Palmer and Mansoori model (1998), an analogy between thermal contraction and matrix shrinkage associated with gas desorption in coalbeds has been made. Changes in the permeability were controlled by the variations in the effective horizontal stress normal to the fractures.

Robertson and Christiansen (2006) have developed a permeability model under variable stress conditions which was derived for cubic geometry under triaxial or hydrostatic confining pressures considering the effect of swelling/shrinkage on permeability. In this model, deformation of coal grains has been neglected and equal axial and radial stresses have been assumed.

Recognising the limitation of previous models to uniaxial strain condition, a permeability model based on linear poroelasticity, that includes the effects of triaxial

strain and stress for coal experiencing sorption induced swelling, has been developed by Connell et al. (2010). In this model, the effects of sorption strain of the coal matrix, the pores and the bulk coal on cleat porosity and permeability have been distinguished.

Detailed reviews of the existing permeability models and processes involved during gas flow in coals have been also provided elsewhere (Palmer, 2009; Liu et al., 2011; Pan and Connell, 2012).

Although the models described above are easy to use, their applicability is limited due to the assumptions and boundary conditions used. In order to conduct more detailed and comprehensive analysis of the coupled processes involved in CO₂ storage in coals as well as to study the long term behaviour and stability of CO₂ in coal seams, development and application of numerical models is important.

2.4.5. Numerical Models

In this section, recent developments in terms of numerical modelling techniques are presented. This includes a discussion on the numerical investigations related to some of the experimental work described in previous sections.

Oldenburg (2007) has evaluated the importance of Joule-Thomson cooling during CO₂ injection into depleted natural gas reservoirs using TOUGH2/EOS7C module (e.g. Pruess et al., 1999; Oldenburg et al., 2004). EOS7C is a module for multicomponent gas mixtures with or without an aqueous phase, using a multiphase Darcy's law to model flow and transport of gas and aqueous mixtures over a range of pressure and temperatures. By conducting a numerical simulation, it was concluded that during low injection rates Joule-Thomson cooling is a minor effect in depleted natural gas reservoirs. However, for high CO₂ flow, it could induce temperature reductions up to 20°C. Such temperature drop was shown to be a function of porosity (Fig. 2.10). Moreover, Oldenburg (2007) have suggested that strong Joule-Thomson effect might cause the formation of CO₂ and CH₄ hydrates, freezing of residual water and generation of thermal stresses and therefore, should be considered during high-flow CO₂ injection in porous medium.

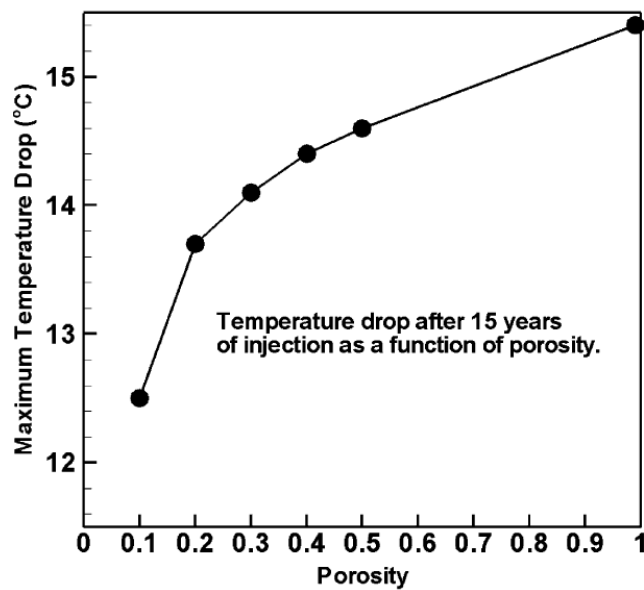


Fig. 2.10. Temperature drop after 15 years of injection into gas reservoir as a function of porosity (Oldenburg, 2007).

Shi et al. (2008a) have presented and applied the METSIM2 simulator to study the two-phase multicomponent transport in coalbeds. The quasi-steady-state diffusion equation, together with the extended Langmuir equation has been implemented to model mixed gas mass transfer between the cleat network and the coal matrix during supercritical flooding test studied. In addition, the dynamic permeability model presented by Shi and Durucan (2004) has been implemented in the simulator (Shi et al., 2008b).

A single porosity-based model considering the volume occupied by the free gas and adsorbed gas, and the pore volume changes induced by gas injection and sorption has been presented by Zhang et al. (2008). Coal was assumed to be homogeneous, isotropic and elastic continuum. Swelling strain was modelled using the analogy between thermal contraction and matrix shrinkage. The set of equations have been implemented into, and solved by commercial software COMSOL Multiphysics. Wu et al. (2010) have modified the single porosity and permeability model presented by Zhang et al. (2008) by considering both the primary medium (coal matrix) and the secondary medium (fractures).

A dynamic multicomponent transport (DMCT) one-dimensional model was developed by Wei et al. (2010) to deal with multi-component gas counter-diffusion and flow in the coal matrix. The assumption was made that the coal matrix consists of a cylindrical cell

surrounded by main fractures. In addition, the coal matrix contains particles with uniform radius following the assumptions of the Ruckenstein model (1971), surrounded by open micro-fractures. The presented model has utilized the Shi and Durucan (2005) analytical solution to simulate the stress-dependent permeability.

A modified version of the commercial reservoir simulator SIMED II has been presented by Connell et al. (2011). Although SIMED II originally includes various two-phase flow processes operating in coal seam reservoirs including porosity gas exchange and storage from adsorption, it uses various models to describe permeability behaviour such as Shi and Durucan (2005) model. Connell et al. (2011) have further modified the SIMED II by implementing the model presented by Connell et al. (2010) to allow history matching of core flooding tests under triaxial strain conditions while the confining stress is uniform around the sample.

Using empirical relationships, Chen et al. (2012) have quantified the moisture effect on the gas sorption capacity, the gas effective diffusivity and the coal swelling strain. Original Shi and Durucan (2005) model and the mass conservation equation for gas have been modified to include the moisture effect. The commercial software COMSOL Multiphysics has been employed to solve the set of equations developed.

Qu et al. (2012) have presented a coupled non-isothermal model incorporating coal deformation, gas flow and thermal transport to evaluate the evolution of coal permeability under the combined effect of gas pressure and temperatures. The equations were solved by COMSOL Multiphysics. Taking into account the effect of Joule-Thomson cooling, the sorption induced strain was defined as a function of temperature. Through set of numerical simulations, it was concluded that the evolution of coal matrix swelling is the primary process that controls the evolution of coal permeability under variable pressure and temperature conditions.

Following the work of Qu et al. (2012), Qu et al. (2014) have recognised the lack of accuracy of the previous models to simulate the laboratory observations commonly conducted under the constant confining pressure conditions. A Critical Swelling Area concept has been introduced which is the area of the coal matrix swelling at the permeability switching point, from reduction to rebound, when the external boundary starts to move outwards as the matrix swelling propagates to it (Fig. 2.11). Such concept

was based on the assumption that fractures do not create a full separation between the matrix blocks, but solid coal bridges exist. In order to introduce such concept, the Thin Elastic Layer feature in the commercial numerical software COMSOL Multiphysics has been utilised.

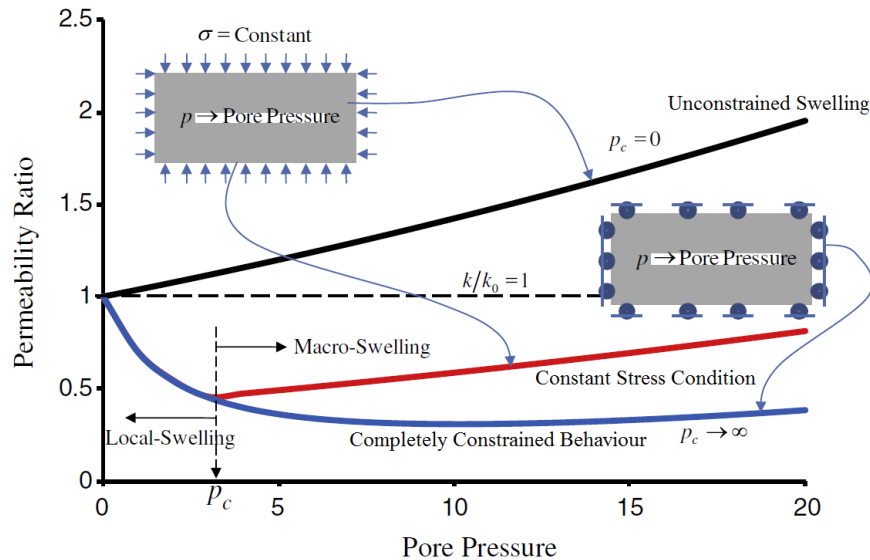


Fig. 2.11. Comparisons of permeability switching models for constrained swelling, unconstrained swelling and constant stress condition (adopted and modified after Qu et al., 2012).

Masoudian (2013) and Masoudian et al. (2013) have presented a dual-porosity chemo-hydro-mechanical model using a quasi-steady state approach to approximate the matrix-fracture transfer function. In addition, the damaging effect of CO_2 sorption on the elastic modulus of coal has been considered. A simple elastic constitutive model has been used to study the mechanical response of coals. To model the damaging effect of CO_2 sorption, a linear relationship between the reduction in elastic modulus and the amount of gas adsorbed has been employed. The gas flow equation was coupled with the mechanical deformation through the volumetric strain rate. However, the stress-strain state was calculated by two different analytical solutions. Once the flow equation has been solved numerically, the mechanical subroutine was called making mechanical calculations always one step behind the flow calculations (Masoudian, 2013). Results of the numerical analysis have revealed that permeability predictions and estimated storage can be affected by changes in elastic modulus. However, further investigations have been suggested in that area to confirm the reliability and relevance of this study.

The importance of elastic modulus on the permeability evolution has been previously studied and confirmed by Balan and Gumrah (2009) who used the commercial compositional simulator CMG (Computer Modeling Group) which utilises the Palmer and Mansoori model to evaluate the permeability change. Based on the results of the analysis, it was concluded that elastic modulus is the most important parameter, besides initial porosity of the system and swelling strain, in controlling the permeability evolution.

Based on the models presented above, it can be observed that commercial softwares combined with theoretical models developed under certain conditions are commonly used to study the processes involved in gas transport and storage in coals. Hence, to the author's knowledge, there appears to be a need to continue to develop numerical models. In particular, further development in the area of coupled modelling to describe chemical and physical phenomena that occur upon CO₂ injection in coal is required.

2.5. Conclusions

In this chapter, a literature review on various aspects of gas-coal interactions has been provided. Existing experimental facilities employed and common measurement methods used to determine gas sorption and its effect on coal response have been described. Recent experimental findings as well as theoretical and computational developments have been highlighted.

The review on the experimental apparatuses and measurement methods showed that despite an increasing number of experimental facilities with ability to produce a comprehensive set of data related to various aspects of coal-gas interactions, temperature changes within the coal induced by gas flow are commonly not measured. Consequently, no experimental data related to non-isothermal flow and the impact of thermal changes on the coal behaviour has been provided up to date for gas flow through coals, according to the author's knowledge.

Based on the literature review presented with regards to experimental studies on gas sorption and kinetics, experimental studies on intact coal samples have received less attention. In other words, gas sorption and its effect on coal behaviour have been

predominantly conducted on powdered coal samples, which might not reflect the behaviour of a coal within the seam. Furthermore, there is a lack of experimental data obtained on high rank (anthracite) coals as well as the coals from South Wales Coalfield which is necessary to provide further confidence in trends and relationships established between the measured parameters and coal rank. In particular, effects of CO₂ sorption on structure and deformation behaviour of high rank coals are yet to be understood. According to the author's knowledge, there is no information on the effects of subcritical and supercritical CO₂ sorption on elastic properties and failure mode of anthracites.

There are two common techniques to assess the ability of coal to conduct gases, i.e. steady-state and transient methods. As the latter one is preferred due to the reduced experimental time and possibility to inject higher mean gas pressures compared to the former one, most experimental studies have focused on determination of permeability values with respect to stress state of coal when the sorption process has finished without presenting and investigating the behaviour of the coal during gas injection. Hence, there is a lack of high-resolution experimental data both under subcritical and supercritical CO₂ injections which would give further insights into the coal's dynamic response to continuous gas injection and provide information on the kinetics of sorption and swelling. Moreover, as the steady-state measurements are commonly conducted by allowing the gas to flow directly to the atmosphere which is the condition difficult to expect in the field, backpressure control would allow injection of gases at higher pressures and replicating more realistic conditions.

A number of models have been developed to study the reactive gas transport in coal. As shown, current models provide a good level of understanding of the underlying processes involved in CO₂ storage in coals, however, commonly under specific conditions only. Hence, further development of a fully coupled model is required to capture the complexity of the gas-coal interaction under various conditions. Moreover, further development and validation of the developed models based on the high-resolution experimental data is crucial to build confidence into their performance and predictive abilities.

2.6. References

- Alexis, D.A., Karpyn, Z.T., Ertekin, T. and Crandall, D. 2015. Fracture permeability and relative permeability of coal and their dependence on stress conditions. *Journal of Unconventional Oil and Gas Resources*, 10, pp. 1-10.
- Arri, L.E. , Yee, D., Morgan, W.D. and Jeansonne, M.W. 1992. Modeling coalbed methane production with binary gas sorption. In *SPE Rocky Mountain Regional Meeting*, Society of Petroleum Engineers.
- Bae, J.-S. and Bhatia, S.K. 2006. High-pressure Adsorption of Methane and Carbon Dioxide on Coal. *Energy & Fuels*, 20, pp. 2599-2607.
- Balan, H.O. and Gumrah, F. 2009. Assessment of shrinkage-swelling influences in coal seams using rank-dependent physical properties. *International Journal of Coal Geology*, 77(1-2), pp. 203-213.
- Baran, P., Zarębska, K. and Bukowska, M. 2015. Expansion of Hard Coal Accompanying the Sorption of Methane and Carbon Dioxide in Isothermal and Non-isothermal Processes. *Energy & Fuels*, 29(3), pp. 1899-1904.
- Battistutta, E., van Hemert, P., Lutynski, M., Bruining, H. and Wolf, K.H. 2010. Swelling and sorption experiments on methane, nitrogen and carbon dioxide on dry Selar Cornish coal. *International Journal of Coal Geology*, 84(1), pp. 39-48.
- Battistutta, E., Eftekhari, A.A., Bruining, H. and Wolf, K.-H. 2012. Manometric Sorption Measurements of CO₂ on Moisture-Equilibrated Bituminous Coal. *Energy & Fuels*, 26(1), pp. 746-752.
- Bieniawski, Z.T., 1968. The effect of specimen size on compressive strength of coal. *International Journal of Rock Mechanics and Mining Sciences*, 5, pp. 325-335.
- Brace, W., Walsh, J.B. and Frangos, W.T. 1968. Permeability of granite under high pressure. *Journal of Geophysical research*, 73(6), pp. 2225-2236.
- Brunauer, S., Emmett, P.H. and Teller, E. 1938. Adsorption of gases in multimolecular layers. *Journal of the American chemical society*, 60(2), pp. 309-319.
- Burshtein, A.I. 1996. *Introduction to thermodynamics and kinetic theory of matter*. John Wiley & Sons, Inc. USA.
- Busch, A., Krooss, B.M., Gensterblum, Y., van Bergen, F. and Pagnier, H.J.M. 2003a. High-pressure adsorption of methane, carbon dioxide and their mixtures on coals with a special focus on the preferential sorption behaviour. *Journal of Geochemical Exploration*, 78-79, pp. 671-674.
- Busch, A., Gensterblum, Y. and Krooss, B.M. 2003b. Methane and CO₂ sorption and desorption measurements on dry Argonne premium coals: pure components and mixtures. *International Journal of Coal Geology*, 55(2), pp. 205-224.
- Busch, A., Gensterblum, Y., Krooss, B.M. and Littke, R. 2004. Methane and carbon dioxide adsorption-diffusion experiments on coal: upscaling and modeling. *International Journal of Coal Geology*, 60(2-4), pp. 151-168.

- Busch, A. and Gensterblum, Y. 2011. CBM and CO₂-ECBM related sorption processes in coal: A review. *International Journal of Coal Geology*, 87(2), pp. 49-71.
- Charrière, D., Pokryszka, Z. and Behra, P. 2010. Effect of pressure and temperature on diffusion of CO₂ and CH₄ into coal from the Lorraine basin (France). *International Journal of Coal Geology*, 81(4), pp. 373-380.
- Chen, Z., Pan, Z., Liu, J., Connell, L.D. and Elsworth, D. 2011. Effect of the effective stress coefficient and sorption-induced strain on the evolution of coal permeability: Experimental observations. *International Journal of Greenhouse Gas Control*, 5(5), pp. 1284-1293.
- Chen, D., Pan, Z., Liu, J. and Connell, L.D. 2012. Modeling and simulation of moisture effect on gas storage and transport in coal seams. *Energy & Fuels*, 26(3), pp. 1695-1706.
- Clarkson, C.R. and Bustin, R.M. 1999a. The effect of pore structure and gas pressure upon the transport properties of coal: a laboratory and modeling study. 2. Adsorption rate modeling. *Fuel*, 78(11), pp. 1345-1362.
- Clarkson, C.R. and Bustin, R.M. 1999b. The effect of pore structure and gas pressure upon the transport properties of coal: a laboratory and modeling study. 1. Isotherms and pore volume distributions. *Fuel*, 78(11), pp. 1333-1344.
- Connell, L.D., Lu, M. and Pan, Z. 2010. An analytical coal permeability model for tri-axial strain and stress conditions. *International Journal of Coal Geology*, 84(2), pp. 103-114.
- Connell, L.D., Sander, R., Pan, Z., Camilleri, M. and Heryanto, D. 2011. History matching of enhanced coal bed methane laboratory core flood tests. *International Journal of Coal Geology*, 87(2), pp. 128-138.
- Cui, X., Bustin, R.M. and Dipple, G. 2004. Selective transport of CO₂, CH₄ and N₂ in coals: insights from modeling of experimental gas adsorption data. *Fuel*, 83(3), pp. 293-303.
- Day, S., Fry, R. and Sakurovs, R., 2008a. Swelling of Australian coals in supercritical CO₂. *International Journal of Coal Geology*, 74(1), pp. 41-52.
- Day, S., Sakurovs, R. and Weir, S. 2008b. Supercritical gas sorption on moist coals. *International Journal of Coal Geology*, 74(3-4), pp. 203-214.
- Day, S., Fry, R. and Sakurovs, R. 2012. Swelling of coal in carbon dioxide, methane and their mixtures. *International Journal of Coal Geology*, 93, pp. 40-48.
- Dubinina, M.M. 1966. Porous structure and adsorption properties of active carbons. *Chemistry and physics of carbon*, 2, pp. 51-120.
- Durucan, S. and Edwards, J.S. 1986. The effects of stress and fracturing on permeability of coal. *Mining Science and Technology*, 3, pp. 205-216.
- Durucan, S., Ahsan, M. and Shi, J.Q. 2009. Matrix shrinkage and swelling characteristics of European coals. *Energy Procedia*, 1(1), pp. 3055-3062.
- Espinoza, D.N., Vandamme, M., Pereira, J.M., Dangla, P. and Vidal-Gilbert, S. 2014. Measurement and modeling of adsorptive–poromechanical properties of bituminous coal cores

exposed to CO₂: Adsorption, swelling strains, swelling stresses and impact on fracture permeability. *International Journal of Coal Geology*, 134, pp. 80-95.

Fitzgerald, J.E., Pan, Z., Sudibandriyo, M., Robinson, J.R.L., Gasem, K.A.M. and Reeves, S. 2005. Adsorption of methane, nitrogen, carbon dioxide and their mixtures on wet Tiffany coal. *Fuel*, 84(18), pp. 2351-2363.

Florence, F.A., Rushing, J., Newsham, K.E. and Blasingame, T.A. 2007, January. Improved permeability prediction relations for low permeability sands. In *Rocky mountain oil & gas technology symposium*. Society of Petroleum Engineers.

Gathitu, B.B., Chen, W.Y. and McClure, M. 2009. Effects of Coal Interaction with Supercritical CO₂: Physical Structure. *Industrial & Engineering Chemistry Research*, 48(10), pp. 5024-5034.

Gensterblum, Y., van Hemert, P., Billemont, P., Battistutta, E., Busch, A., Krooss, B.M., De Weireld, G. and Wolf, K.H.A.A. 2010. European inter-laboratory comparison of high pressure CO₂ sorption isotherms II: Natural coals. *International Journal of Coal Geology*. 84(2), pp. 115-124.

Gensterblum, Y., Merkel, A., Busch, A. and Krooss, B.M. 2013. High-pressure CH₄ and CO₂ sorption isotherms as a function of coal maturity and the influence of moisture. *International Journal of Coal Geology*, 118, pp. 45-57.

Gensterblum, Y., Ghanizadeh, A. and Krooss, B.M. 2014. Gas permeability measurements on Australian subbituminous coals: fluid dynamic and poroelastic aspects. *Journal of Natural Gas Science and Engineering*, 19, pp. 202-214.

Goodman, A.L., Busch, A., Bustin, R.M., Chikatamarla, L., Day, S., Duffy, G.J., Fitzgerald, J.E., Gasem, K.A.M., Gensterblum, Y., Hartman, C., Jing, C., Krooss, B.M., Mohammed, S., Pratt, T., Robinson Jr., R.L., Romanov, V., Sakurovs, R., Schroeder, K. and White, C.M. 2007. Inter-laboratory comparison II: CO₂ isotherms measured on moisture-equilibrated Argonne premium coals at 55°C and up to 15 MPa. *International Journal of Coal Geology*, 72(3-4), pp. 153-164.

Gruszkiewicz, M.S., Naney, M.T., Blencoe, J.G., Cole, D.R., Pashin, J.C. and Carroll, R.E. 2009. Adsorption kinetics of CO₂, CH₄ and their equimolar mixture on coal from the Black Warrior Basin, West-Central Alabama. *International Journal of Coal Geology*, 77(1-2), pp. 23-33.

Harpalani, S. and Chen, G. 1997. Influence of gas production induced volumetric strain on permeability of coal. *Geotechnical and Geological Engineering*, 15, 303-325.

He, J., Shi, Y., Ahn, S., Kang, J.W. and Lee, C. 2010. Adsorption and desorption of CO₂ on Korean coal under subcritical to supercritical conditions. *The Journal of Physical Chemistry*, 114(14), pp. 4854-4861.

Ho, C.K. and Webb, S.W. eds., 2006. *Gas transport in porous media* (Vol. 20). Dordrecht: Springer.

Hol, S., Peach, C.J. and Spiers, C.J. 2011. Applied stress reduces the CO₂ sorption capacity of coal. *International Journal of Coal Geology*, 85(1), pp.128-142.

Hol, S. and Spiers, C.J. 2012. Competition between adsorption-induced swelling and elastic compression of coal at CO₂ pressures up to 100 MPa. *Journal of the Mechanics and Physics of Solids*, 60(11), pp. 1862-1882.

Hol, S., Spiers, C.J. and Peach, C.J. 2012. Microfracturing of coal due to interaction with CO₂ under unconfined conditions. *Fuel*, 97, pp. 569-584.

Hol, S., Gensterblum, Y. and Massarotto, P. 2014. Sorption and changes in bulk modulus of coal – experimental evidence and governing mechanisms for CBM and ECBM applications. *International Journal of Coal Geology*, 128-129, pp. 119-133.

Hosking, L.J. 2014. *Reactive transport modelling of high pressure gas flow in coal*. Ph.D. Thesis, Cardiff University, Wales, UK.

Jaeger, J.C., Cook, N.G.W. and Zimmerman, R.W. 2007. *Fundamentals of Rock Mechanics*, 4th Edition, Blackwell Publishing.

Karacan, C.Ö. 2007. Swelling-induced volumetric strains internal to a stressed coal associated with CO₂ sorption. *International Journal of Coal Geology*, 72(3), pp. 209-220.

Katyal, S., Valix, M. and Thambimuthu, K. 2007. Study of Parameters Affecting Enhanced Coal Bed Methane Recovery. *Energy Sources, Part A*, 29(3), pp. 193-205.

Kazemifar, F. and Kyritsis, D. 2014. Experimental investigation of near-critical CO₂ tube-flow and Joule-Thomson throttling for carbon capture and sequestration. *Experimental Thermal and Fluid Science*, 53, pp. 161-170.

Klinkenberg, L.J., 1941, January. The permeability of porous media to liquids and gases. In *Drilling and production practice*. American Petroleum Institute.

Krooss, B.M., van Bergen, F., Gensterblum, Y., Siemons, N., Pagnier, H.J.M. and David, P. 2002. High-pressure methane and carbon dioxide adsorption on dry and moisture-equilibrated Pennsylvanian coals. *International Journal of Coal Geology*, 51 (2), pp. 69-92.

Kumar, H., Elsworth, D., Liu, J., Pone, D. and Mathews, J.P. 2015. Permeability evolution of propped artificial fractures in coal on injection of CO₂. *Journal of Petroleum Science and Engineering*, 133, pp. 695-704.

Langmuir, I. 1918. The adsorption of gases on plane surfaces of glass, mica and platinum. *Journal of the American Chemical Society*, 40(9), pp. 1361-1403.

Larsen, J.W. 2004. The effects of dissolved CO₂ on coal structure and properties. *International Journal of Coal Geology*, 57(1), pp. 63-70.

Li, S., Dong, M. and Li, Z. 2009. Measurement and revised interpretation of gas flow behavior in tight reservoir cores. *Journal of Petroleum Science and Engineering*, 65(1), pp. 81-88.

Li, D., Liu, Q., Weniger, P., Gensterblum, Y., Busch, A. and Krooss, B.M. 2010. High-pressure sorption isotherms and sorption kinetics of CH₄ and CO₂ on coals. *Fuel*, 89(3), pp. 569-580.

Li, J., Liu, D., Yao, Y., Cai, Y. and Chen, Y. 2013. Evaluation and modeling of gas permeability changes in anthracite coals. *Fuel*, 111, pp. 606-612.

- Linstrom, P.J. and Mallard, W.G., Eds. NIST Chemistry WebBook, NIST Standard Reference Database Number 69, National Institute of Standards and Technology, Gaithersburg MD, 20899, <http://webbook.nist.gov>, (retrieved October 20, 2016).
- Liu, C.J., Wang, G.X., Sang, S.X. and Rudolph, V. 2010. Changes in pore structure of anthracite coal associated with CO₂ sequestration process. *Fuel*, 89(10), pp. 2665-2672.
- Liu, J., Chen, Z., Elsworth, D., Qu, H. and Chen, D. 2011. Interactions of multiple processes during CBM extraction: a critical review. *International Journal of Coal Geology*, 87(3), pp. 175-189.
- Liu, Z., Feng, Z., Zhang, Q., Zhao, D. and Guo, H. 2015a. Heat and deformation effects on coal during adsorption and desorption of carbon dioxide. *Journal of Natural Gas Science and Engineering*, 25, pp. 242-252.
- Liu, C.J., Wang, G.X., Sang, S.X., Gilani, W. and Rudolph, V. 2015b. Fractal analysis in pore structure of coal under conditions of CO₂ sequestration process. *Fuel*, 139, pp. 125-132.
- Lutynski, M.A., Battistutta, E., Bruining, H. and Wolf, K.H.A.A. 2011. Discrepancies in the assessment of CO₂ storage capacity and methane recovery from coal with selected equations of state. Part I. Experimental isotherm calculation. *Physicochemical Problems of Mineral Processing*, 47, pp. 159-168.
- Majewska, Z., Ceglarska-Stefańska, G., Majewski, S. and Ziętek, J., 2009. Binary gas sorption/desorption experiments on a bituminous coal: Simultaneous measurements on sorption kinetics, volumetric strain and acoustic emission. *International Journal of Coal Geology*, 77(1), pp. 90-102.
- Majewska, Z., Majewski, S. and Ziętek, J., 2010. Swelling of coal induced by cyclic sorption/desorption of gas: experimental observations indicating changes in coal structure due to sorption of CO₂ and CH₄. *International Journal of Coal Geology*, 83(4), pp.475-483.
- Marecka, A. and Mianowski, A. 1998. Kinetics of CO₂ and CH₄ sorption on high rank coal at ambient temperatures. *Fuel*, 77(14), pp. 1691-1696.
- Masoudian, M.S. 2013. *Chemo-hydro-mechanical aspects of CO₂ sequestration in deep coal seams*. PhD Thesis, University of Sydney, Sydney, Australia.
- Masoudian, M.S., Airey, D.W. and El-Zein, A. 2013. A chemo-poro-mechanical model for sequestration of carbon dioxide in coalbeds. *Geotechnique*, 63(3), pp. 235-243.
- Masoudian, M.S., Airey, D.W. and El-Zein, A. 2014. Experimental investigations on the effect of CO₂ on mechanics of coal. *International Journal of Coal Geology*, 128-129, pp. 12-23.
- Masoudian, M.S. 2016. Multiphysics of carbon dioxide sequestration in coalbeds: A review with a focus on geomechanical characteristics of coal. *Journal of Rock Mechanics and Geotechnical Engineering*, 8(1), pp. 93-112.
- Massarotto, P., Golding, S.D., Bae, J.S., Iyer, R. and Rudolph, V. 2010. Changes in reservoir properties from injection of supercritical CO₂ into coal seams - A laboratory study. *International Journal of Coal Geology*, 82(3), pp. 269-279.

- Mazumder, S. and Wolf, K. H. 2008. Differential swelling and permeability changes of coal in response to CO₂ injection for ECBM. *International Journal of Coal Geology*, 74(2), pp. 123-138.
- McPhee, C.A. and Arthur, K.G., 1991. Klinkenberg permeability measurements: problems and practical solutions. In *Advances in Core Evaluation II Reservoir Appraisal. Proceedings of the 2nd Society of Core Analysts European Core Analysis Symposium*. Gordon and Breach Science Publishers, Philadelphia, pp. 371-391.
- Medhurst, T.P. and Brown, E.T. 1998. A study of the Mechanical Behaviour of Coal for Pillar Design. *International Journal of Rock Mechanics and Mining Sciences*. 35(8), pp. 1087-1105.
- Merkel, A., Gensterblum, Y., Krooss, B.M. and Amann, A. 2015. Competitive sorption of CH₄, CO₂ and H₂O on natural coals of different rank. *International Journal of Coal Geology*, 150-151, pp. 181-192.
- Oldenburg, C.M., Moridis, G.J., Spycher, N. and Pruess, K. 2004. EOS7C version 1.0: TOUGH2 module for carbon dioxide or nitrogen in natural gas (methane) reservoirs. *Lawrence Berkeley National Laboratory*.
- Oldenburg, C.M. 2007. Joule-Thomson cooling due to CO₂ injection into natural gas reservoirs. *Energy Conversion and Management*, 48(6), pp. 1808-1815.
- Ozdemir, E., Morsi, B.I. and Schroeder, K. 2003. Importance of Volume Effects to Adsorption Isotherms of Carbon Dioxide on Coals. *Langmuir*, 19, pp. 9764-9773.
- Ozdemir, E., Morsi, B.I. and Schroeder, K. 2004. CO₂ adsorption capacity of Argonne premium coals. *Fuel*, 83(7), pp. 1085-1094.
- Ozdemir, E. 2005. *Chemistry of the adsorption of carbon dioxide by Argonne premium coals and a model to simulate CO₂ sequestration in coal seams*. PhD Thesis, University of Pittsburgh.
- Palmer, I. 2009. Permeability changes in coal: analytical modeling. *International Journal of Coal Geology*, 77(1), pp. 119-126.
- Palmer, I. and Mansoori, J. 1996. How permeability depends on stress and pore pressure in coalbeds: a new model. In *SPE Annual Technical Conference and Exhibition*. Society of Petroleum Engineers.
- Palmer, I. and Mansoori, J. 1998. How Permeability Depends on Stress and Pore Pressure in Coalbeds: A New Model. *Society of Petroleum Engineers Reservoir Evaluation and Engineering*, 1(6), pp. 539-544.
- Pan, Z. and Connell, L.D. 2007. A theoretical model for gas adsorption-induced coal swelling. *International Journal of Coal Geology*, 69(4), pp. 243-252.
- Pan, Z., Connell, L.D. and Camilleri, M. 2010. Laboratory characteristics of coal reservoir permeability for primary and enhanced coalbed methane recovery. *International Journal of Coal Geology*, 82(3), pp. 252-261.
- Pan, Z. and Connell, L.D. 2012. Modelling permeability for coal reservoirs: a review of analytical models and testing data. *International Journal of Coal Geology*, 92, pp. 1-44.

- Peng, D.Y. and Robinson, D.B. 1976. A new two-constant equation of state. *Industrial and Engineering Chemistry Fundamentals*, 15(1), pp. 59-64.
- Perera, M.S.A., Ranjith, P.G. and Peter, M. 2011. Effects of saturation medium and pressure on strength parameters of Latrobe Valley brown coal: Carbon dioxide, water and nitrogen saturations. *Energy*, 36(12), pp. 6941-6947.
- Perera, M.S.A., Ranjith, P.G. and Viète, D.R. 2013. Effects of gaseous and super-critical carbon dioxide saturation on the mechanical properties of bituminous coal from the Southern Sydney Basin. *Applied Energy*, 110, pp. 73-81.
- Pone, J.D.N., Halleck, P.M. and Mathews, J.P. 2009. Sorption Capacity and Sorption Kinetic Measurements of CO₂ and CH₄ in Confined and Unconfined Bituminous Coal. *Energy&Fuels*, 23, pp. 4688-4695.
- Pruess, K., Oldenburg, C.M. and Moridis, G.J. 1999. TOUGH2 user's guide version 2. *Lawrence Berkeley National Laboratory*.
- Qu, H., Liu, J., Chen, Z., Wang, J., Pan, Z., Connell, L. and Elsworth, D. 2012. Complex evolution of coal permeability during CO₂ injection under variable temperatures. *International Journal of Greenhouse Gas Control*, 9, pp. 281-293.
- Qu, H., Liu, J., Pan, Z. and Connell, L. 2014. Impact of matrix swelling area propagation on the evolution of coal permeability under coupled multiple processes. *Journal of Natural Gas Science and Engineering*, 18, pp. 451-466.
- Ranjith, P.G. and Perera, M.S.A. 2011. A new triaxial apparatus to study the mechanical and fluid flow aspects of carbon dioxide sequestration in geological formations. *Fuel*, 90(8), pp. 2751-2759.
- Ranjith, P.G. and Perera, M.S.A. 2012. Effects of cleat performance on strength reduction of coal in CO₂ sequestration. *Energy*, 45(1), pp. 1069-1075.
- Robertson, E.P. and Christiansen, R.L. 2006. *A permeability model for coal and other fractured, sorptive-elastic media*. Idaho National Laboratory. INL/EXT-06-11830.
- Roebuck, J.R. and Osterberg, H. 1933. The Joule-Thomson effect in helium. *Physical Review*, 43(1), pp. 60-69.
- Ruckenstein, E., Vaidyanathan, A.S. and Youngquist, G.R. 1971. Sorption by solids with bidisperse pore structures. *Chemical Engineering Science*, 26(9), pp. 1305-1318.
- Sakurovs, R., Day, S., Weir, S. and Duffy, G. 2007. Application of a modified Dubinin–Radushkevich equation to adsorption of gases by coals under supercritical conditions. *Energy & fuels*, 21(2), pp. 992-997.
- Sakurovs, R., Day, S. and Weir, S. 2012. Relationships between the sorption behaviour of methane, carbon dioxide, nitrogen and ethane on coals. *Fuel*, 97, pp. 725-729.
- Seidle, J. 2011. *Fundamentals of coalbed methane reservoir engineering*. PennWell Corporation, Tulsa, Oklahoma, USA.

Seidle, J.P., Jeansonne, M.W. and Erickson, D.J. 1992. Application of matchstick geometry to stress dependent permeability in coals. In *SPE rocky mountain regional meeting*. Society of Petroleum Engineers.

Seidle, J.R. and Huitt, L.G. 1995. Experimental measurement of coal matrix shrinkage due to gas desorption and implications for cleat permeability increases. *International Meeting on Petroleum Engineering*. Society of Petroleum Engineers.

Shi, J.Q. and Durucan, S. 2004. Drawdown induced changes in permeability of coalbeds: a new interpretation of the reservoir response to primary recovery. *Transport in porous media*, 56(1), pp. 1-16.

Shi, J.Q. and Durucan, S. 2005. A model for changes in coalbed permeability during primary and enhanced methane recovery. *SPE Reservoir Evaluation & Engineering*, 8(4), pp. 291-299.

Shi, J.Q., Mazumder, S., Wolf, K.H. and Durucan, S. 2008a. Competitive methane desorption by supercritical CO₂ injection in coal. *Transport in porous media*, 75(1), pp. 35-54.

Shi, J.Q., Durucan, S. and Fujioka, M. 2008b. A reservoir simulation study of CO₂ injection and N₂ flooding at the Ishikari coalfield CO₂ storage pilot project, Japan. *International Journal of Greenhouse Gas Control*, 2(1), pp. 47-57.

Siemons, N. and Busch, A. 2007. Measurement and interpretation of supercritical CO₂ sorption on various coals. *International Journal of Coal Geology*, 69(4), pp. 229-242.

Somerton, W.H., Söylemezoğlu, I.M. and Dudley, R.C. 1975. Effect of Stress on Permeability of Coal, *International Journal of Rock Mechanics and Mining Sciences and Geomechanics Abstracts*, 12(5), pp. 129-145. Pergamon.

Span, R. and Wagner, W. 1996. A new equation of state for carbon dioxide covering the fluid region from the triple-point temperature to 1100 K at pressures up to 800 MPa. *Journal of Physical and Chemical Reference Data*, 25(6), pp. 1509-1596.

Speight, J.G. 2005. *Handbook of coal analysis*. Hoboken, New Jersey: John Wiley & Sons, Inc.

Staib, G., Sakurovs, R. and Gray, E.M.A. 2013. A pressure and concentration dependence of CO₂ diffusion in two Australian bituminous coals. *International Journal of Coal Geology*, 116-117, pp. 106-116.

Thomas, L. 2013. *Coal Geology*, 2nd Edition, John Wiley & Sons, Ltd.

Van Bergen, F., Spiers, C., Floor, G. and Bots, P. 2009. Strain development in unconfined coals exposed to CO₂, CH₄ and Ar: effect of moisture. *International Journal of Coal Geology*, 77(1), pp. 43-53.

Vandamme, M., Brochard, L., Lecampion, B. and Coussy, O. 2010. Adsorption and strain: The CO₂-induced swelling of coal. *Journal of the Mechanics and Physics of Solids*, 58(10), pp. 1489-1505.

Viete, D.R. and Ranjith, P.G. 2006. The effect of CO₂ on the geomechanical and permeability behaviour of brown coal: Implications for coal seam CO₂ sequestration. *International Journal of Coal Geology*. 66, pp. 204-216.

- Viete, D.R. and Ranjith, P.G. 2007. The mechanical behaviour of coal with respect to CO₂ sequestration in deep coal seams. *Fuel*, 86(17), pp. 2667-2671.
- Vishal, V., Ranjith, P.G. and Singh, T.N. 2015. An experimental investigation on behaviour of coal under fluid saturation, using acoustic emission. *Journal of Natural Gas Science and Engineering*. 22, pp. 428-436.
- Wang, S., Elsworth, D. and Liu, J. 2011. Permeability evolution in fracture coal: the roles of fracture geometry and water-content. *International Journal of Coal Geology*, 87(1), pp. 13-25.
- Wang, S., Elsworth, D. and Liu, J. 2013a. Permeability evolution during progressive deformation of intact coal and implications for instability in underground coal seams. *International Journal of Rock Mechanics and Mining Sciences*, 58, pp. 34-45.
- Wang, S., Elsworth, D. and Liu, J. 2013b. Mechanical behavior of methane infiltrated coal: the roles of gas desorption, stress level and loading rate. *Rock mechanics and rock engineering*, 46(5), pp. 945-958.
- Wang, C., Wang, C., Wei, M., Gong, B. and Tan, Y. 2014a. Deformation transition of intact coal induced by gas injection. *International Journal of Mining Science and Technology*, 24(6), pp. 833-838.
- Wang, G., Ren, T., Wang, K. and Zhou, A. 2014b. Improved apparent permeability models of gas flow in coal with Klinkenberg effect. *Fuel*, 128, pp. 53-61.
- Wei, X., Massarotto, P., Wang, G., Rudolph, V. and Golding, S.D. 2010. CO₂ sequestration in coals and enhanced coalbed methane recovery: New numerical approach. *Fuel*, 89(5), pp. 1110-1118.
- White, C.M., Smith, D.H., Jones, K.L., Goodman, A.L., Jikich, S.A., Lacount, R.B., Dubose, S.B., Ozdemir, E., Morsi, B., Schroeder, K.T. 2005. Sequestration of Carbon Dioxide in Coal with Enhanced Coalbed Methane Recovery – A Review. *Energy&Fuels*, 19 (3), 659-724.
- Wu, Y-S., Pruess, K. and Persoff, P. (1998). Gas flow in porous media with Klinkenberg effects. *Transport in Porous Media*, 32, pp.117-137.
- Wu, Y., Liu, J., Elsworth, D., Chen, Z., Connell, L. and Pan, Z. 2010. Dual poroelastic response of a coal seam to CO₂ injection. *International Journal of Greenhouse Gas Control*, 4(4), pp. 668-678.
- Zhang, H., Liu, J. and Elsworth, D. 2008. How sorption-induced matrix deformation affects gas flow in coal seams: A new FE model. *International Journal of Rock Mechanics & Mining Sciences*, 45(8), pp. 1226-1236.

3

Theoretical and Numerical Formulation

3.1. Introduction

A theoretical formulation for the coupled chemical and deformation behaviour of fractured rock is described in this chapter. Chemical behaviour represents the gas chemicals forming a gas phase in this work. The main objective of this chapter is to present the developed deformation model, incorporating deformation of fractured rock under the gas sorption induced swelling, coupled with the existing model for the flow of chemicals.

The formulation presented is based on the coupled Thermal, Hydraulic, Chemical and Mechanical model (Thomas, 1988; Thomas and He, 1995; Thomas et al., 1996; Thomas and He, 1998; Cleall, 1998; Sedighi, 2011; Masum; 2012; Thomas et al., 2012; Hosking, 2014). The thermal and hydraulic aspects considered previously fall beyond the scope of the current thesis and, for the sake of conciseness, will not be repeated here. The formulation presented in this chapter considers the behaviour of a non-ideal gas at high pressure which is of relevance to carbon sequestration applications. A numerical formulation is developed based upon the finite element method for spatial discretisation and the finite difference method for temporal discretisation.

General aspects of the theoretical formulation are presented in section 3.2, in addition to the basic assumptions and the primary variables of the formulation.

The governing equations describing the single-component reactive gas transport in a single porosity, single permeability porous medium are shown in section 3.3.

Section 3.4 presents the approach adopted to define the swelling behaviour of coal followed by the governing equation for deformation derived from considerations of stress equilibrium where physico-chemical and mechanical mechanisms of deformation are considered.

The general aspects of numerical formulation are presented in section 3.5. The spatial discretisation of flow and deformation variables is shown in section 3.6, while section 3.7 deals with the temporal discretisation of the variables.

The main conclusions are given in section 3.8.

3.2. Theoretical Formulation – General Aspects

Fractured rocks are heterogeneous porous media, consisting of a natural fracture network that divides the rock into a large number of matrix blocks. In this work, the fractured rock is considered to have a single porosity, single permeability structure represented through fracture network whereas rock matrix is considered only for sorption purposes via the sink/source for geochemical reactions. Fractured rock was assumed as a homogeneous porous medium acknowledging the fact that rocks exhibit some degree of heterogeneity. This may be partly accommodated in this study as the assumption of homogeneity only applies within an individual element. Hence, different rock types may be used within an analysis.

The governing equations of the gas phase were derived using a mass balance approach. The continuum is considered to be a two-phase system, consisting of a solid skeleton and pore gas. Hence, pore water is not considered in this work assuming a completely dry system. The formulation presented here is related to conditions in which high pressure gas flow occurs under isothermal conditions, i.e. in the absence of significant heat sources/sinks. Although temperature fluctuations up to several Kelvin attributed to adiabatic (Joule-Thomson) cooling of injected gas (e.g. Oldenburg, 2007; Jiang et al., 2014) and thermal expansion of the solid skeleton (e.g. Liu et al., 2015) have been reported, such thermal effects are not considered in this work.

The deformation behaviour is governed by a constitutive relationship previously developed using an elastic model for highly swelling porous medium via consideration of stress equilibrium. Details of the developed deformation model will be presented later in the chapter.

The governing equations are expressed in terms of two primary variables, as follows:

- Gas chemical concentration (c_g)
- Displacement (\mathbf{u})

The behaviour of both variables is included within a coupled chemical and deformation formulation. All of the governing equations are then developed in a three-dimensional form.

3.3. Reactive Transport of Single-component Gas

In this formulation pore gas is considered to be composed of a single gas species. Although previously developed thermal, hydraulic, chemical and mechanical model considers pore gas as a mixture of gas species collectively forming the gas phase, formulation for a single gas species is presented here as the aim of this study is to analyse the response of coal subject to a single-component gas injection. The governing equations for a single-component pore gas flow have been derived based on the concept of conservation of mass.

In a single porosity medium, the conservation equation can be expressed mathematically as (Thomas and He, 1998):

$$\frac{\partial(\theta_g c_g \delta V)}{\partial t} = -\delta V \nabla J_g - \delta V R_g \quad (3.1)$$

where t is the time, θ_g is the volumetric gas content, c_g is the gas concentration, δV is the incremental volume, ∇ is the gradient operator, J_g is the total gas flux and R_g represents the sink/source for geochemical reactions.

The volumetric gas content within the fracture network can be expressed in terms of the degree of gas saturation and porosity, given as (Thomas and He, 1995; Thomas et al., 1998a):

$$\theta_g = n S_g \quad (3.2)$$

where n is the porosity and S_g is the degree of gas saturation.

The incremental volume, δV , is a summation of the void volume and solid volume, and can be represented as:

$$\delta V = (1 + e) \delta V_s \quad (3.3)$$

where e is the void ratio and δV_s is the incremental volume of the solids.

Since it is assumed that the majority of gas is stored as an adsorbed gas in the solid phase (coal matrix), the sink/source term R_g can be expressed as (Hosking, 2014):

$$R_g = \rho_s \frac{\partial s_g}{\partial t} \quad (3.4)$$

where ρ_s is the density of the solid phase and s_g is the adsorbed amount in the solid phase.

Substituting equations (3.2), (3.3) and (3.4) into equation (3.1) yields:

$$\frac{\partial(nS_g c_g(1+e)\delta V_s)}{\partial t} = -(1+e)\delta V_s \nabla J_g - (1+e)\delta V_s \rho_s \frac{\partial s_g}{\partial t} \quad (3.5)$$

Since the volume of the solid has been assumed to remain constant, the term δV_s can be eliminated from equation (3.5). Furthermore, the porosity can be related to the void ratio as:

$$n = \frac{e}{(1+e)} \quad (3.6)$$

Assuming a fully gas-saturated porous medium with $S_g = 1$, substituting equation (3.6) into equation (3.5) and then rearranging produces:

$$\frac{\partial(ec_g)}{\partial t} + (1+e)\rho_s \frac{\partial s_g}{\partial t} = -(1+e)\nabla J_g \quad (3.7)$$

Before the terms of equation (3.7) are expanded, brief explanations on gas properties at high pressure, mechanisms of gas transport and sink/source term for adsorption/desorption are provided in the following sections.

3.3.1. Gas Properties at High Pressure

The key gas properties related to the presented formulation are i) real gas bulk compressibility, ii) bulk gas viscosity and iii) gas diffusion coefficients (Hosking, 2014).

In order to consider the real gas compressibility behaviour, a widely used Peng and Robinson (1976) equation of state has been previously implemented within the theoretical framework by Hosking (2014). Through application of such equation of

state, deviations of the behaviour of real gases from an ideal gas behaviour expressed by the compressibility factor (Z) can be obtained.

Gas mixture viscosity has been included in the model by Hosking (2014) using the semi-empirical model proposed by Chung et al. (1988). The presented relationship is based upon the kinetic theory of gases in combination with empirical density-dependent functions to include the behaviour of dense gas mixtures as (Hosking, 2014):

$$\mu_g = 0.1[f(\mu_g^0) + \mu_g^D] \quad (3.8)$$

where μ_g is the absolute gas viscosity, $f(\mu_g^0)$ is a function of the gas mixture viscosity at low pressure and μ_g^D is further adjustment for dense gases.

A single empirical model suggested by Reid et al. (1977) has been adopted in the formulation for the gas diffusion coefficients (Hosking, 2014):

$$D_g = \frac{D_g^0 \rho_g^0}{\rho_g} \quad (3.9)$$

where D_g^0 is a reference value for the diffusion coefficient obtained experimentally at a certain temperature at low gas density of ρ_g^0 , and D_g is the diffusion coefficient at the same temperature but at a higher gas density of ρ_g .

3.3.2. Mechanisms of Gas Transport

The mechanism of single-component flow is a complex physical process and includes two general transport mechanisms, namely advection and diffusion (Bird et al., 1960; Mason et al., 1967). The total gas flux can be presented as:

$$J_g = J_{gAdv} + J_{gDif} \quad (3.10)$$

where J_{gAdv} and J_{gDif} are the advective and diffusive components of flux, respectively. Both of these components will be discussed separately in the following sections.

3.3.2.1. Advection

The advective flow of bulk gases in porous media is driven by the pressure gradient and generally expressed using Darcy's law (Darcy, 1856). According to Darcy's law, the bulk advective flux can be expressed as:

$$J_{gAdv} = c_g \mathbf{v}_g \quad (3.11)$$

where \mathbf{v}_g is the bulk gas velocity.

In this study, the total gas potential is considered as the sum of the potentials due to pressure and gravitational heads (Webb, 2006).

Hence, Darcy's law for bulk gas flow in porous media can be expressed as (Bear and Verruijt, 1987):

$$\mathbf{v}_g = -k_g \left[\nabla \left(\frac{u_g}{\rho_g g} \right) + \nabla z \right] \quad (3.12)$$

where z is the elevation, u_g is the gas pressure, g is the gravitational acceleration and k_g is the gas conductivity given as (Bear and Verruijt, 1987):

$$k_g = \frac{K \rho_g g}{\mu_g} \quad (3.13)$$

where K is the intrinsic permeability.

Application of the real gas law allows the gas pressure to be expressed in terms of gas concentration, giving:

$$u_g = ZRTc_g \quad (3.14)$$

where R is the universal gas constant, Z is the compressibility factor and T is the temperature.

Substituting equation (3.12) and (3.14) into equation (3.11) yields:

$$J_{gAdv} = -\frac{c_g k_g ZRT}{\rho_g g} \nabla c_g - c_g k_g \nabla z \quad (3.15)$$

3.3.2.2. Diffusion

The possible forms of diffusion processes in porous media expressed in equation (3.10) can involve (Bird et al., 1960):

- i) Ordinary diffusion
- ii) Knudsen diffusion
- iii) Configurational diffusion
- iv) Thermal diffusion
- v) Pressure diffusion
- vi) Forced diffusion

Knudsen diffusion becomes important when the mean free path of the gas molecules is comparable to the diameter of the pores (Ho and Webb, 2006). In that case, the interaction between the pore walls and gas molecules becomes predominant which helps in moving the gas molecules in the direction of flow (Klinkenberg, 1941). Similarly, configurational diffusion can become important in very tight pores with dimensions approaching those of a single molecule (Webb, 2006). Since the fracture continuum is considered to be consisted of fractures and pores significantly larger than the mean free path of the gas molecules, both Knudsen diffusion and configurational diffusion are ignored in this study. Thermal diffusion is related to the movement of gas components to diffuse due to thermal gradients (Bird et al., 1960). As this formulation is developed for isothermal conditions, such effect is neglected. Pressure diffusion describes the movement of heavier molecules to high pressure regions and lighter molecules to low pressure regions (Amali and Rolston, 1993). This formulation considers a single component gas flow making pressure diffusion not applicable to this work. Forced diffusion is applicable to systems subject to a local electrical field, and is thus not relevant in this study (Hosking, 2014). In this study, only the ordinary diffusion where the gas species diffuse due to concentration gradients is considered.

A generalised Fick's law of diffusion (Fick, 1855) proposed by Onsager (1945) used to describe the self-diffusion of the gas species can be expressed as:

$$J_{gDif} = -D_g \nabla c_g \quad (3.16)$$

where D_g is the free diffusion coefficient defined in equation (3.9).

Since equation (3.16) is only valid for free fluid diffusion, it can be modified for applications in porous media by replacing the free diffusion coefficient D_g by an effective diffusion coefficient D_{ge} that considers the pore structure of the porous media:

$$D_{ge} = nS_g\tau_g D_g \quad (3.17)$$

where τ_g is the tortuosity factor.

The tortuosity factor can be calculated using Millington and Quirk (1961) model and presented as (Scanlon et al., 1999):

$$\tau_g = \frac{(nS_g)^{10/3}}{n^2} \quad (3.18)$$

Assuming a fully gas-saturated system and substituting equation (3.17) into equation (3.16) yields:

$$J_{gDif} = -n\tau_g D_g \nabla c_g \quad (3.19)$$

3.3.3. Sink/source Term for Adsorption/desorption

Sorption processes can be divided into chemical (chemisorption) and physical (physisorption) sorption, as mentioned in Chapter 2 (White et al., 2005). While the former one considers the sorbate bonding by electron transfer making a direct chemical bond, the latter one occurs via van der Waals forces (Busch and Gensterblum, 2011). The following formulation does not distinguish between these two mechanisms and the sorption process is consistently referred to as a reaction (Hosking, 2014).

Gas stored by sorption in the coal matrix accounts for 95% to 98% of the gas in the coal seam where the remaining gas is stored in the natural fractures either free or dissolved in water (White et al., 2005). Hence, it is reasonable to assume that no sorption occurs within the fracture network and consider sorption only in the solid phase of the system, i.e. coal matrix.

The retention behaviour of gas at the coal surface can be treated as a kinetic or equilibrium reaction (Hosking, 2014). For instance, Hosking (2014) used a kinetic reaction driven by the difference between the equilibrium and actual sorbed amounts

taking place at a rate controlled by the sorption rate. On the other hand, equilibrium sorption can be included using a retardation factor in the storage term of the mass balance equation (Zhang et al., 2008; Hosking, 2014). Such an approach does not explicitly consider the loss/gain of free gas due to adsorption/desorption. Alternately, the effect of sorption retards the advance of the component considered (Bear and Verruijt, 1987; Hosking, 2014). The equilibrium sorption has been used in this study.

In order to model the amount of sorption, a common approach for the equilibrium adsorbed amount using the Langmuir equation (Langmuir, 1918) is used:

$$S_g = S_{max} \frac{u_g}{P_L + u_g} \quad (3.20)$$

where s_{max} and P_L are the Langmuir constants for the maximum sorption capacity and pressure at which half of the maximum sorption is achieved, respectively.

Applying equation (3.14) to equation (3.20) yields:

$$S_g = S_{max} \frac{ZRTc_g}{P_L + ZRTc_g} \quad (3.21)$$

Substituting equation (3.21) into equation (3.4) gives:

$$R_g = \rho_s \frac{\partial S_g}{\partial t} = \rho_s \left[\frac{s_{max} P_L ZRT}{(P_L + ZRTc_g)^2} \right] \frac{\partial c_g}{\partial t} \quad (3.22)$$

3.3.4. Governing Equations for Gas Transport

The transport mechanisms of a single-component gas in a single porosity, single permeability system were described in Section 3.3.2 in terms of advective and diffusive fluxes. Section 3.3.1 briefly explained gas properties at high pressures considered in this study while Section 3.3.3 presented the model for sorption behaviour of gas species on the coal surface. The equation (3.7) of mass conservation for chemical flow can now be expanded in terms of its primary variables.

The first term of the equation (3.7) can be expanded, which leads to the following expression:

$$e \frac{\partial c_g}{\partial t} + c_g \frac{\partial e}{\partial t} + (1 + e) \rho_s \frac{\partial s_g}{\partial t} = -(1 + e) \nabla J_g \quad (3.23)$$

Dividing both sides of the equation (3.23) by $(1 + e)$ and replacing $e(1 + e)$ by n gives:

$$n \frac{\partial c_g}{\partial t} + c_g \frac{1}{1+e} \frac{\partial e}{\partial t} + \rho_s \frac{\partial s_g}{\partial t} = -\nabla J_g \quad (3.24)$$

Considering the second term of equation (3.24), it can be shown that:

$$\frac{1}{1+e} \frac{\partial e}{\partial t} = (1 + e) \frac{\partial n}{\partial t} = \frac{\partial \varepsilon_v}{\partial t} = \mathbf{m}^T \frac{\partial \varepsilon}{\partial t} = \mathbf{m}^T \mathbf{P} \frac{\partial \mathbf{u}}{\partial t} \quad (3.25)$$

where ε_v is the volumetric strain, the rate of change of void ratio with respect to the initial volume. ε is the strain vector and \mathbf{u} is the vector of displacement. The strain matrix \mathbf{P} and the vector \mathbf{m}^T will be defined in section 3.4.2.

Substituting equations (3.15), (3.19), (3.22) and (3.25) into equation (3.24) and grouping similar terms yields:

$$\left[n + \rho_s \left(\frac{s_{max} P_L Z R T}{(P_L + Z R T c_g)^2} \right) \right] \frac{\partial c_g}{\partial t} + c_g \mathbf{m}^T \mathbf{P} \frac{\partial \mathbf{u}}{\partial t} = \nabla \left[\left(n \tau_g D_g + \frac{c_g k_g Z R T}{\rho_g g} \right) \nabla c_g + c_g k_g \nabla Z \right] \quad (3.26)$$

Finally, the governing equation for single-component gas transport in a single porosity medium can be represented in a simplified form as:

$$C_{c_g c_g} \frac{\partial c_g}{\partial t} + C_{c_g \mathbf{u}} \frac{\partial \mathbf{u}}{\partial t} = \nabla \left[K_{c_g c_g} \nabla c_g \right] + J_{c_g} \quad (3.27)$$

where:

$$C_{c_g c_g} = n + \rho_s \left(\frac{s_{max} P_L Z R T}{(P_L + Z R T c_g)^2} \right) \quad (3.28)$$

$$C_{c_g \mathbf{u}} = c_g \mathbf{m}^T \mathbf{P} \quad (3.29)$$

$$K_{c_g c_g} = n \tau_g D_g + \frac{c_g k_g Z R T}{\rho_g g} \quad (3.30)$$

$$J_{c_g} = \nabla (c_g k_g \nabla Z) \quad (3.31)$$

3.4. Deformation Behaviour

This section presents the theoretical background of deformation behaviour in the model. A description of the model and the governing equation will be presented in Sections 3.4.2 to 3.4.6. Prior to this, Section 3.4.1 will present the background and assumptions of the deformation model proposed here.

3.4.1. Background and Assumptions of the Deformation Model

The theoretical model presented in this study is based on the framework for deformation of soils previously presented by Thomas and He (1995; 1997; 1998) and Thomas and Cleall (1999). It is assumed that deformation (hence volume changes) are a result of applied stress and sorption induced swelling. Deformations due to suction and temperature are not dealt within this work.

In order to extend the existing deformation model to consider coal swelling induced by gas sorption, a conceptual model based on expansive soils presented by Alonso et al., (1990), Gens and Alonso (1992), Alonso et al. (1999) and Mašín (2013) is used in this work. A similar approach has been used by Thomas and Cleall (1999) for modelling of expansive clays. The key feature of their model is to define satisfactorily the effects of particle-level phenomena on the overall behaviour of the material (Thomas and Cleall, 1999). This is achieved by considering the behaviour of a porous material at two levels, which are defined as the microstructure and the macrostructure (Alonso et al., 1999). In expansive soils subjected to hydromechanical loading, microstructural changes manifest in aggregate swelling upon wetting, but the overall soil volumetric behaviour depends on the amount of occlusion of macropores by aggregates and on the stability of the macrostructure (Mašín, 2013). Although the abovementioned authors consider reversible strains in the microstructure and irreversible strains at macrostructure, this work considers only elastic behaviour at both structural levels.

Based on the previous works, the following assumptions were adopted:

- Coal is a homogeneous, isotropic and elastic continuum.
- Coal is saturated by gas

- Conditions are isothermal
- Strains are much smaller than the length scale.
- Structure of coal seams commonly includes coal matrix representing the main reservoir for the gas and the macro-porous cleat/fracture network serving as the main flow pathways (Zhang et al., 2008). The behaviour of coal in this work is therefore considered at two levels; 1) gas flow occurs only through the fracture network (macrostructure) of the coal, 2) sorption of gases occurs in the coal matrix (microstructure).
- Swelling phenomenon occurring at the microstructural level is reversible with no preferential orientation; hence the microstructural strains induced by gas sorption are elastic and volumetric.
- Within the macrostructure, the effective stress principle is valid suggesting that for an assumption of null change in total stress only the change in pore pressure dictates the coal deformation.
- Chemical equilibrium exists between microstructure and macrostructure meaning that any amount of sorption induced swelling within the microstructure is based on the chemical concentration within the macropores.
- Microstructural swelling affects the structural arrangement of the macrostructure inducing a change of the macroporosity.

Understanding the changes induced by CO₂ injection into the coal seam is crucial before presenting the developed model. As mentioned, the coal matrix represents the main reservoir for gas and the fractures (voids) the main flow pathways. When the CO₂ is injected into the coal, an increase in gas pressure widens the fractures and increases the total porosity available for flow. At the same time, the gas adsorbs onto the coal matrix and consequently, induces the swelling of the coal matrix which reduces the fracture width and decreases the total porosity available for flow. Hence, the net effect of porosity and consequently, permeability loss or gain, is controlled competitively by the influence in pore pressure increase within fractures and the matrix swelling induced by CO₂ sorption (Zhang et al., 2008).

As mentioned in Chapter 2, the numerical models discussed assume that the volume entirely taken up by coal matrix upon sorption is proportional to the reduction of the fracture volume available for flow. Such an assumption is valid for constant volume conditions where no change in the bulk volume of the coal is observed. However, constant volume condition is difficult to achieve in laboratory through triaxial testing. Hence, swelling of coal samples in triaxial tests results both in the internal and the external (global) swelling (e.g. Liu et al., 2011). This behaviour will be further investigated in Chapter 7.

The development of the proposed model and inclusion in the existing framework will be presented in the following sections.

3.4.2. Stress Equilibrium Equation

Following Alonso et al. (1990), the net stress σ'' can be defined as:

$$\sigma'' = \sigma - u_g \quad (3.32)$$

where σ is the total stress. The current formulation considers a positive sign convention for tensile stresses, but the gas pressure is defined as positive in compression (Vardon, 2009; Masum, 2012).

The net-mean stress, p , and deviatoric stress, q , can be defined as:

$$p = \frac{\sigma_1'' + \sigma_2'' + \sigma_3''}{3} \quad (3.33)$$

$$q = \sqrt{\frac{1}{2}[(\sigma_1 - \sigma_2)^2 + (\sigma_2 - \sigma_3)^2 + (\sigma_3 - \sigma_1)^2]} \quad (3.34)$$

A three-dimensional element of porous medium with unit length and a cross sectional area of $dx dy dz$ under a system of stresses and body forces is shown in Figure 3.1. Surface forces are acting on a boundary surface of a body whilst body forces act through the centroid of the element.

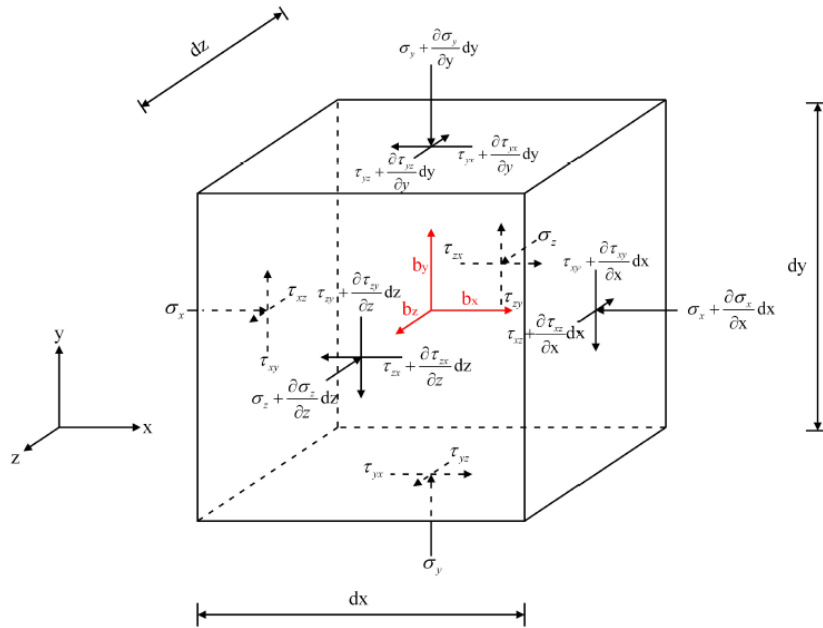


Fig. 3.1. Stresses and forces on a soil/rock element of infinitesimal dimensions (after Fredlund and Rahardjo, 1993).

Following the Newton's first law which dictates that equilibrium is achieved when the resultant of the forces in any direction is zero, summing all of the forces in the x direction yields:

$$\left(\sigma_x + \frac{\partial \sigma_x}{\partial x} dx\right) dydz + \left(\tau_{zx} + \frac{\partial \tau_{zx}}{\partial z} dz\right) dydx + \left(\tau_{yx} + \frac{\partial \tau_{yx}}{\partial y} dy\right) dx dz - \sigma_x dydz - \tau_{zx} dx dy - \tau_{yx} dx dz + b_x dx dy dz = 0 \quad (3.35)$$

Substituting in the total stress equation (3.32) and rearranging yields:

$$\left(\frac{\partial \sigma_x''}{\partial x} + \frac{\partial u_g}{\partial x} + \frac{\partial \tau_{zx}}{\partial z} + \frac{\partial \tau_{yx}}{\partial y} + b_x\right) dx dy dz = 0 \quad (3.36)$$

Since $dx dy dz$ is not equal to zero, equation (3.36) reduces to:

$$\frac{\partial \sigma_x''}{\partial x} + \frac{\partial u_g}{\partial x} + \frac{\partial \tau_{zx}}{\partial z} + \frac{\partial \tau_{yx}}{\partial y} + b_x = 0 \quad (3.37)$$

Similarly, for the y and z directions:

$$\frac{\partial \sigma_y''}{\partial y} + \frac{\partial u_g}{\partial y} + \frac{\partial \tau_{xy}}{\partial x} + \frac{\partial \tau_{zy}}{\partial z} + b_y = 0 \quad (3.38)$$

$$\frac{\partial \sigma_z''}{\partial z} + \frac{\partial u_g}{\partial z} + \frac{\partial \tau_{yz}}{\partial y} + \frac{\partial \tau_{xz}}{\partial x} + b_z = 0 \quad (3.39)$$

Using the principle of superposition for equations (3.37), (3.38) and (3.39), an incremental form as suggested by Thomas and He (1998) follows:

$$\mathbf{P}d\sigma'' + \mathbf{P}mdu_g + d\mathbf{b} = 0 \quad (3.40)$$

where \mathbf{b} is the vector of body forces, \mathbf{P} represents the strain matrix as:

$$\mathbf{P} = \begin{bmatrix} \frac{\partial}{\partial x} & 0 & 0 & \frac{\partial}{\partial z} & 0 & \frac{\partial}{\partial y} \\ 0 & \frac{\partial}{\partial z} & 0 & \frac{\partial}{\partial x} & \frac{\partial}{\partial y} & 0 \\ 0 & 0 & \frac{\partial}{\partial y} & 0 & \frac{\partial}{\partial z} & \frac{\partial}{\partial x} \end{bmatrix} \quad (3.41)$$

For a three dimensional analysis, vector \mathbf{m} can be defined as:

$$\mathbf{m}^T = [1 \quad 1 \quad 1 \quad 0 \quad 0 \quad 0] \quad (3.42)$$

3.4.3. Constitutive Elastic Relationship

Following the assumption that coal can be considered as an elastic porous material, during the increment of stress, it produces only recoverable (elastic) strains. Hence, the increment of total strain $d\varepsilon$ may be defined as:

$$d\varepsilon = d\varepsilon^e \quad (3.43)$$

where $d\varepsilon^e$ is the incremental elastic component of strain.

As described previously, the incremental elastic volumetric strain is the sum of elastic components due to changes in net stress in macrostructure and gas induced swelling in microstructure (coal matrix).

This can be expressed to describe contributions from the microstructural and macrostructural components as (Thomas and Cleall, 1999):

$$d\varepsilon^e = d\varepsilon_{p,M}^e + d\varepsilon_{sw,m}^e \quad (3.44)$$

where the subscripts p and sw represent the components due to change in mean stress and swelling, respectively. Subscript M stands for macro contributions and m for micro contributions.

In order to link the responses of macrostructure and microstructure, i.e. to control the amount of sorption-induced volumetric strain of the microstructure (matrix) responsible for the volume loss of macroporosity, an interaction function f_m is introduced in this work following the approach presented by Mašín (2013). The distinct micro-macrostructure interaction mechanism proposed and its representation is summarised in Figure 3.2.

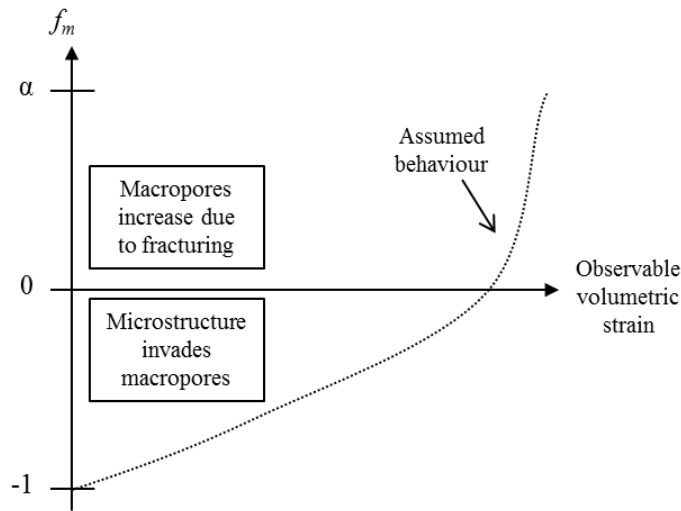


Fig. 3.2. Summary of micro-macrostructure interaction mechanisms (adopted and modified after Alonso and Gens, 1999; Mašín, 2013).

Based on Figure 3.2, for a condition representing ($f_m = -1$), there is a free penetration of microstructure into macrostructure inducing a decrease in macroporosity. In other words, the increase in the volume of the coal matrix is, in fact, the decrease in the volume of the fractures available for flow. At this point, the swelling of the coal matrix is completely internal while inducing no external (observable) sample deformation. This corresponds to a rigid coal macrostructure with existing coal connections between the

coal matrix blocks. As the porosity available for flow and permeability of the sample to gases are interlinked (e.g. Somerton et al., 1975), such decrease in macroporosity leads to a decrease in permeability.

When the internal swelling slowly starts to approach its maximum, further swelling of the coal sample upon sorption translates to global swelling resulting in an observable volumetric strain. Hence, at this point, both the internal and the external swelling occur simultaneously. This particular transition phase corresponds to $(-1 < f_m < 0)$.

When $(f_m = 0)$, there is no more invasion of microstructure expansion in the macrostructure and consequently, the macroporosity is not affected by the internal swelling. This would correspond to the situation where the macrostructure of the coal becomes less rigid allowing free expansion of the sample. It should be noted that at this point, swelling of the coal matrix continues with further increase in gas pressure and completely translates to global swelling. Hence, since there is no more inclusion of microstructure into the macroporosity when $f_m = 0$, the only change in permeability is then controlled by the change in gas pressure within the fractures.

The proposed modelling framework valid for a range of $(-1 \leq f_m \leq 0)$ is analogous with the one presented by Mašín (2013) for expansive soils. However, as previously mentioned in Chapter 2, gas sorption at high pressures can induce micro-fractures and increase the macroporosity of the coal sample. Hence, values of $f_m > 0$ would theoretically correspond to a case where the microstructure would “collapse” connecting the existing fracture network with the gas sorption induced fractures and increase the total porosity of the system available for flow which would potentially lead to increase in permeability. Since such response would fall in the domain of elasto-plastic behaviour, it will not be investigated further as a part of this work.

It should be noted that the proposed model is in line with the experimental observations which will be presented in Chapter 7.

Hence, to allow the coal matrix to occlude into the fracture system, equation (3.44) is modified using the interaction function f_m :

$$d\varepsilon^e = d\varepsilon_{p,M}^e + f_m d\varepsilon_{sw,m}^e \quad (3.45)$$

The elastic stress-strain relationship can be expressed through a generalised Hooke's law:

$$d\sigma'' = \mathbf{D}(d\varepsilon^e - f_m d\varepsilon_{sw,m}^e) \quad (3.46)$$

where \mathbf{D} is the classical elasticity matrix that can be defined in terms of elastic modulus, E , and Poisson's ratio, ν .

The elastic deformation due to changes in the net stress can be defined as (Alonso et al., 1999, Sanchez, 2005; Thomas and Cleall, 1999):

$$d\varepsilon_{p,M}^e = \frac{1}{K_M} dp = A_p dp \quad (3.47)$$

where K_M is the macrostructural bulk modulus and A_p is the volumetric deformation coefficient related to volumetric strain.

The increment of total volumetric strain can be expressed in terms of displacement as (Owen and Hinton, 1980):

$$d\varepsilon = \mathbf{P}^T d\mathbf{u} \quad (3.48)$$

3.4.4. Swelling Behaviour

Swelling of coal is commonly modelled using a Langmuir equation (Langmuir, 1918), as mentioned in Chapter 2. Hence, in order to calculate the volumetric swelling strain, ε_{sw} , the Langmuir equation can be presented as (Zhang et al., 2008):

$$\varepsilon_{sw} = \varepsilon_{max} \frac{u_g}{P_L + u_g} \quad (3.49)$$

where ε_{max} is the maximum volumetric strain and P_L is the gas pressure at which $\varepsilon_{sw} = 0.5 \cdot \varepsilon_{max}$.

Applying equation (3.14) to equation (3.49) and then differentiating it with respect to chemical concentration yields the elastic volumetric component of strain due to gas sorption induced swelling.

This can be written as:

$$d\varepsilon_{sw,m}^e = \left[\frac{\varepsilon_{max} P_L Z R T}{(P_L + Z R T c_g)^2} \right] d c_g = A_{sw} d c_g \quad (3.50)$$

where A_{sw} is a volumetric deformation coefficient related to volumetric strain.

3.4.5. Permeability-porosity Relationship

The volumetric strain is also defined as (Thomas et al., 1996):

$$d\varepsilon = \frac{de}{v} \quad (3.51)$$

where v is the specific volume.

Hence, by knowing the change in void ratio as a result of change in volumetric strain, a widely used approach where permeability varies with porosity is used (Somerton et al., 1975):

$$\frac{K}{K_0} = \left(\frac{n}{n_0} \right)^3 \quad (3.52)$$

Where K_0 is the initial intrinsic permeability at a reference porosity n_0 .

3.4.6. Governing Equation for Deformation

The background and assumptions of the developed deformation model were described in section 3.4.1. The stress equilibrium equation and the elastic stress-strain relationships were presented in sections 3.4.2 and 3.4.3, respectively. The component of the elastic strain induced by swelling under gas sorption was developed in section 3.4.4, while section 3.4.5 presented the relationship used to couple the permeability and porosity.

Substituting equation (3.50) into equation (3.46) yields:

$$d\sigma'' = \mathbf{D}(d\varepsilon - f_m A_{sw} d c_g) \quad (3.53)$$

Rewriting the stress equilibrium equation (3.40) with substitution from equations (3.48) and (3.53) gives:

$$\mathbf{PD}(\mathbf{P}^T d\mathbf{u} - f_m A_{sw} dc_g) + \mathbf{Pm}du_g + d\mathbf{b} = 0 \quad (3.54)$$

Substituting equation (3.14) for the term “ u_g ” and rearranging the similar terms, the governing equation can be written in concise form as:

$$C_{uc_g} dc_g + C_{uu} d\mathbf{u} + d\mathbf{b} = 0 \quad (3.55)$$

where:

$$C_{uc_g} = \mathbf{Pm}ZRT - \mathbf{PD}f_m A_{sw} \quad (3.56)$$

$$C_{uu} = \mathbf{PDP}^T \quad (3.57)$$

3.5. Numerical Formulation – General Aspects

The governing equations for the flow of chemicals representing the gas phase in a deformable material were presented in the previous sections. Due to level of complexity, a direct analytical solution is prevented; therefore, a numerical solution is required. The finite-element method (FEM) is employed to spatially discretise the system of equations, whereas the finite difference method (FDM) is applied to achieve temporal discretisation. The numerical formulation of the coupled heat, moisture, chemicals and deformation has already been presented previously by Thomas et al. (1998a, 1998b), Cleall (1998), Vardon (2009), Sedighi (2011) and Masum (2012). As the main objective of this chapter was to develop the coupled chemical and deformation model which was implemented within the existing numerical framework, the following numerical formulations have been included in this chapter for the sake of completeness.

3.6. Spatial Discretisation

The Galerkin weighted residual finite-element approach is undertaken in this work to obtain the finite element solutions of the theoretical formulation. This method is widely accepted tool for spatial discretisation and has been well documented in the literature

(e.g. Zienkiewicz and Taylor, 1989). Also, it has been previously shown to be suitable for coupled flow and deformation equations (e.g. Thomas and He, 1995; Seetharam et al., 2007; Thomas et al., 1998b; Thomas et al., 2012).

Since the development of the finite element equations using the Galerkin weighted residual method has been described in detail in the literature (e.g. Thomas and He, 1995; Thomas et al., 1998a), a spatial discretisation of the governing equations is presented in this chapter in an abbreviated form. First, a spatial discretisation of the flow variables is presented followed by a spatial discretisation of the deformation variables.

The primary variables (unknowns) and their spatial derivatives can be approximated using shape functions as:

$$\omega \approx \hat{\omega} = \sum_{s=1}^{n_{node}} N_s \omega_s \quad (3.58)$$

and

$$\nabla \hat{\omega} = \sum_{s=1}^{n_{node}} (\nabla N_s) \omega_s \quad (3.59)$$

Where ω represents any of the primary variables (c_g and \mathbf{u}), N_s is the shape function. The subscript s represent the nodal points, the symbol $\hat{}$ indicates an approximated form and n is the number of nodes in an element.

The approximated form ($\hat{\omega}$) is not the exact solution of equation (3.58), hence it contains a residual error, R_Ω , which can be expressed as:

$$R_\Omega = \omega - \hat{\omega} \quad (3.60)$$

where Ω represents the domain.

3.6.1. Spatial Discretisation of the Governing Equations for Flow Variables

The governing equation for gas transport, with substitution for the primary variables from equations (3.58) and (3.59), can be expressed in a general form as:

$$-C_{c_g c_g} \frac{\partial \hat{c}_g}{\partial t} - C_{c_g \mathbf{u}} \frac{\partial \hat{\mathbf{u}}}{\partial t} + \nabla \left[K_{c_g c_g} \nabla \hat{c}_g \right] + J_{c_g} = R_\Omega \quad (3.61)$$

The Galerkin's approach requires that the integral of the weighted errors over the element domain, Ω^e , must be zero, with the shape functions, i.e. N_r , being used as the weighting functions (Thomas, 1988):

$$\int_{\Omega^e} N_r R_{\Omega} d\Omega^e = 0 \quad (3.62)$$

Substitution of equation (3.61) into equation (3.62) gives the weak form of equation (3.61):

$$\int_{\Omega^e} N_r \left[-C_{c_g c_g} \frac{\partial \hat{c}_g}{\partial t} - C_{c_g \mathbf{u}} \frac{\partial \hat{\mathbf{u}}}{\partial t} + \nabla \left(K_{c_g c_g} \nabla \hat{c}_g \right) + J_{c_g} \right] d\Omega^e = 0 \quad (3.63)$$

On expansion, the third term in equation (3.63) can be expressed as:

$$\begin{aligned} \int_{\Omega^e} N_r \left[\nabla \left(K_{c_g c_g} \nabla \hat{c}_g \right) \right] d\Omega^e = \\ \int_{\Omega^e} \nabla \left(N_r K_{c_g c_g} \nabla \hat{c}_g \right) d\Omega^e - \int_{\Omega^e} K_{c_g c_g} \nabla \hat{c}_g \nabla N_r d\Omega^e \end{aligned} \quad (3.64)$$

Also the fourth term, J_{c_g} , can be expressed, with an appropriate substitution from equation (3.31), as:

$$\begin{aligned} \int_{\Omega^e} N_r J_{c_g} d\Omega^e = \int_{\Omega^e} N_r \nabla (c_g k_g \nabla z) d\Omega^e = \int_{\Omega^e} \nabla (N_r c_g k_g \nabla z) d\Omega^e - \\ \int_{\Omega^e} c_g k_g \nabla z \nabla N_r d\Omega^e \end{aligned} \quad (3.65)$$

Substituting equations (3.64) and (3.65) into equation (3.63) yields:

$$\begin{aligned} \int_{\Omega^e} \left[\nabla \left(N_r K_{c_g c_g} \nabla \hat{c}_g \right) - K_{c_g c_g} \nabla \hat{c}_g \nabla N_r + \nabla \left(N_r c_g k_g \nabla z \right) - c_g k_g \nabla z \nabla N_r + \right. \\ \left. N_r \left(-C_{c_g c_g} \frac{\partial \hat{c}_g}{\partial t} - C_{c_g \mathbf{u}} \frac{\partial \hat{\mathbf{u}}}{\partial t} \right) \right] d\Omega^e = 0 \end{aligned} \quad (3.66)$$

Employing the Gauss-Green divergence theorem (e.g. Zienkiewicz and Morgan, 1982), the second order differential terms in equation (3.66) are reduced to first order and surface integrals are introduced. These surface integrals cancel each other and leave only contributions from the boundary surfaces of the domain that are non-zero.

This yields:

$$\begin{aligned} \int_{\Omega^e} \left[-K_{c_g c_g} \nabla \hat{c}_g \nabla N_r - c_g k_g \nabla z \nabla N_r + N_r \left(-C_{c_g c_g} \frac{\partial \hat{c}_g}{\partial t} - C_{c_g \mathbf{u}} \frac{\partial \hat{\mathbf{u}}}{\partial t} \right) \right] d\Omega^e + \\ \int_{\Gamma^e} N_r \left[K_{c_g c_g} \nabla \hat{c}_g + c_g k_g \nabla z \right] \underline{\underline{n}} d\Gamma^e = 0 \end{aligned} \quad (3.67)$$

In equation (3.67), Γ^e is the element boundary surface and \underline{n} represents the direction cosine normal to the surface.

Introducing the expressions for the primary variables and their derivatives, as presented in equations (3.58) and (3.59), and expressing in vector forms, and using the assumption of the Galerkin's method to employ the shape functions as the weighting functions yields:

$$\int_{\Omega^e} \left[K_{c_g c_g} \nabla \mathbf{N}^T \nabla \mathbf{N} \right] d\Omega^e c_{gs} + \int_{\Omega^e} \left[C_{c_g c_g} \mathbf{N}^T \mathbf{N} \right] d\Omega^e \frac{\partial c_{gs}}{\partial t} + \int_{\Omega^e} \left[C_{c_g \mathbf{u}} \mathbf{N}^T \mathbf{N} \right] d\Omega^e \frac{\partial \mathbf{u}_s}{\partial t} + \int_{\Omega^e} [c_g k_g \nabla \mathbf{N}^T \nabla z] d\Omega^e - \int_{\Gamma^e} \mathbf{N}^T [f_{c_g}] \underline{n} d\Gamma^e = 0 \quad (3.68)$$

where f_{c_g} is the approximate pore gas flux normal to the boundary surface, \mathbf{N} is the shape function matrix and the terms c_{gs} and \mathbf{u}_s are the vectors of the gas concentrations and displacements at nodes, respectively.

Equation (3.68) can be expressed in a concise matrix form as:

$$\mathbf{C}_{c_g c_g} \frac{\partial c_{gs}}{\partial t} + \mathbf{C}_{c_g \mathbf{u}} \frac{\partial \mathbf{u}_s}{\partial t} + \mathbf{K}_{c_g c_g} c_{gs} = \mathbf{f}_{c_g} \quad (3.69)$$

where for a domain with elements:

$$\mathbf{C}_{c_g c_g} = \sum_{e=1}^m \int_{\Omega^e} \left[C_{c_g c_g} \mathbf{N}^T \mathbf{N} \right] d\Omega^e \quad (3.70)$$

$$\mathbf{C}_{c_g \mathbf{u}} = \sum_{e=1}^m \int_{\Omega^e} \left[C_{c_g \mathbf{u}} \mathbf{N}^T \mathbf{N} \right] d\Omega^e \quad (3.71)$$

$$\mathbf{K}_{c_g c_g} = \sum_{e=1}^m \int_{\Omega^e} \left[K_{c_g c_g} \nabla \mathbf{N}^T \nabla \mathbf{N} \right] d\Omega^e \quad (3.72)$$

$$\mathbf{f}_{c_g} = - \sum_{e=1}^m \int_{\Omega^e} [c_g k_g \nabla \mathbf{N}^T \nabla z] d\Omega^e + \sum_{e=1}^m \int_{\Gamma^e} \mathbf{N}^T [f_{c_g}] \underline{n} d\Gamma^e \quad (3.73)$$

3.6.2. Spatial Discretisation of the Governing Equations for Displacement Variables

The development of the governing equations of deformation follows the same method described above for the flow variable. Hence, the governing equation for displacement, with substitution from equations (3.58), (3.59) and (3.60) can be presented using the shape function approach as:

$$C_{\mathbf{u}c_g} d\hat{c}_g + C_{\mathbf{u}\mathbf{u}} d\hat{\mathbf{u}} + d\mathbf{b} = R_\Omega \quad (3.74)$$

Using the Galerkin residual method to minimise error over the elemental volume yields:

$$\int_{\Omega^e} N_r [C_{\mathbf{u}c_g} d\hat{c}_g + C_{\mathbf{u}\mathbf{u}} d\hat{\mathbf{u}} + d\mathbf{b}] d\Omega^e = 0 \quad (3.75)$$

Integrating by parts with substitution from section 3.4., yields the weak form and by example of the first term:

$$\begin{aligned} \int_{\Omega^e} N_r C_{\mathbf{u}c_g} d\hat{c}_g d\Omega^e &= \int_{\Omega^e} N_r [\mathbf{P}\mathbf{m}ZRT - \mathbf{P}\mathbf{D}f_m A_{sw}] d\hat{c}_g d\Omega^e = \\ &- \int_{\Omega^e} [\mathbf{P}N_r (\mathbf{m}ZRT - \mathbf{D}f_m A_{sw}) d\hat{c}_g] d\Omega^e + \int_{\Omega^e} \mathbf{P} [N_r (\mathbf{m}ZRT - \\ &\quad \mathbf{D}f_m A_{sw}) d\hat{c}_g] d\Omega^e \end{aligned} \quad (3.76)$$

Using the integration by parts to also expand the second term of equation (3.75) with substitution from equation (3.57) and then expressing equation (3.75) in the weak form gives:

$$\begin{aligned} &- \int_{\Omega^e} [\mathbf{P}N_r (\mathbf{m}ZRT - \mathbf{D}f_m A_{sw}) d\hat{c}_g] d\Omega^e + \int_{\Omega^e} \mathbf{P} [N_r (\mathbf{m}ZRT - \\ &\quad \mathbf{D}f_m A_{sw}) d\hat{c}_g] d\Omega^e - \int_{\Omega^e} [\mathbf{P}N_r \mathbf{D}\mathbf{P}^T d\hat{\mathbf{u}}] d\Omega^e + \int_{\Omega^e} \mathbf{P} [N_r \mathbf{D}\mathbf{P}^T d\hat{\mathbf{u}}] d\Omega^e + \\ &\quad \int_{\Omega^e} N_r d\mathbf{b} d\Omega^e = 0 \end{aligned} \quad (3.77)$$

When the Gauss Green divergence theorem is applied to equation (3.77), it produces surface integrals yielding:

$$\begin{aligned} &- \int_{\Omega^e} [\mathbf{P}N_r (\mathbf{m}ZRT - \mathbf{D}f_m A_{sw}) d\hat{c}_g] d\Omega^e + \\ &\quad \int_{\Gamma^e} [N_r (\mathbf{m}ZRT - \mathbf{D}f_m A_{sw}) d\hat{c}_g] \underline{n} d\Gamma^e - \int_{\Omega^e} [\mathbf{P}N_r \mathbf{D}\mathbf{P}^T d\hat{\mathbf{u}}] d\Omega^e + \\ &\quad \int_{\Gamma^e} [N_r \mathbf{D}\mathbf{P}^T d\hat{\mathbf{u}}] \underline{n} d\Gamma^e + \int_{\Omega^e} N_r d\mathbf{b} d\Omega^e = 0 \end{aligned} \quad (3.78)$$

The surface integral in equation (3.78) may be simplified to:

$$\begin{aligned} \int_{\Gamma^e} [N_r(\mathbf{mZRT} - \mathbf{D}f_m A_{sw}) d\hat{c}_g] \underline{n} d\Gamma^e + \int_{\Gamma^e} [N_r \mathbf{D}\mathbf{P}^T d\hat{\mathbf{u}}] \underline{n} d\Gamma^e = \\ \int_{\Gamma^e} N_r [(\mathbf{mZRT} - \mathbf{D}f_m A_{sw}) d\hat{c}_g + \mathbf{D}\mathbf{P}^T d\hat{\mathbf{u}}] \underline{n} d\Gamma^e = \int_{\Gamma^e} N_r \hat{\underline{T}}_r d\Gamma^e \end{aligned} \quad (3.79)$$

where $\hat{\underline{T}}_r$ is the approximate traction.

Introducing the shape function derivatives into equation (3.78) yields:

$$\begin{aligned} - \int_{\Omega^e} [\mathbf{P}N_r(\mathbf{mZRT} - \mathbf{D}f_m A_{sw})\mathbf{N}] d\Omega^e dc_{gs} - \int_{\Omega^e} [\mathbf{P}N_r \mathbf{D}\mathbf{P}^T \mathbf{N}] d\Omega^e d\mathbf{u}_s + \\ \int_{\Omega^e} \mathbf{N}^T d\mathbf{b} d\Omega^e + \int_{\Gamma^e} N_r \hat{\underline{T}}_r d\Gamma^e = 0 \end{aligned} \quad (3.80)$$

Equation (3.80) must be used in incremental form for transient analysis, found by multiplying the constants by the gradient of time. Doing this and expressing in concise matrix form yields:

$$\mathbf{C}_{uc_g} \frac{\partial c_{gs}}{\partial t} + \mathbf{C}_{uu} \frac{\partial \mathbf{u}_s}{\partial t} = \mathbf{f}_u \quad (3.81)$$

where:

$$\mathbf{C}_{uc_g} = \sum_{e=1}^m \int_{\Omega^e} [\mathbf{P}N_r [\mathbf{mZRT} - \mathbf{D}f_m A_{sw}] \mathbf{N}] \nabla t d\Omega^e \quad (3.82)$$

$$\mathbf{C}_{uu} = \sum_{e=1}^m \int_{\Omega^e} \mathbf{P}N_r \mathbf{D}\mathbf{P}^T \mathbf{N} \nabla t d\Omega^e \quad (3.83)$$

$$\mathbf{f}_u = \sum_{e=1}^m \left[\int_{\Omega^e} (\mathbf{N}^T d\mathbf{b}) d\Omega^e + \int_{\Gamma^e} N_r \hat{\underline{T}}_r d\Gamma^e \right] \quad (3.84)$$

3.7. Temporal Discretisation

Temporally discrete numerical formulation was used in this work to determine the values of the primary variables over time. For this case, a fully implicit mid-interval backward-difference time-stepping algorithm is employed. Such approach was found to produce good results for non-linear equations similar to those shown in the present work (Cook, 1981; Thomas et al., 1998a).

The spatially discretised governing equations presented in section 3.6 can be expressed in matrix form as:

$$\begin{bmatrix} \mathbf{K}_{c_g c_g} & \mathbf{0} \\ \mathbf{0} & \mathbf{0} \end{bmatrix} \times \begin{bmatrix} c_{gs} \\ \mathbf{u}_s \end{bmatrix} + \begin{bmatrix} \mathbf{C}_{c_g c_g} & \mathbf{C}_{c_g \mathbf{u}} \\ \mathbf{C}_{\mathbf{u} c_g} & \mathbf{C}_{\mathbf{u} \mathbf{u}} \end{bmatrix} \times \begin{bmatrix} \dot{c}_{gs} \\ \dot{\mathbf{u}}_s \end{bmatrix} + \begin{bmatrix} f_{cg} \\ f_{\mathbf{u}} \end{bmatrix} = \mathbf{0} \quad (3.85)$$

where $[\dot{c}_{gs}, \dot{\mathbf{u}}_s]$ are time differentials of the primary variable vectors.

Equation (3.85) can be expressed as:

$$\mathbf{A}\phi + \mathbf{B} \frac{\partial \phi}{\partial t} + \mathbf{C} = \{\mathbf{0}\} \quad (3.86)$$

where \mathbf{A} , \mathbf{B} and \mathbf{C} are the matrices of coefficients and ϕ is the vector of variables.

The general form of the fully-implicit mid-interval backward-difference time-stepping algorithm can be expressed as (Thomas et al., 1998a):

$$\mathbf{A}^{\phi_l} [(1 - \Theta)\phi^n + \Theta\phi^{n+1}] + \mathbf{B}^{\phi_l} \left[\frac{\phi^{n+1} - \phi^n}{\Delta t} \right] + \mathbf{C}^{\phi_l} = \{\mathbf{0}\} \quad (3.87)$$

where Θ represents a constant controlling the integration scheme which is equal to 1 for an implicit time integration scheme, 0.5 for a Crank-Nicholson scheme and 0 for an explicit scheme. The superscript ϕ_l represents the level at which the matrices of coefficients are evaluated, and can be expressed in general as:

$$\phi_l = \vartheta(n + 1) + (1 - \vartheta)n \quad (3.88)$$

where ϑ is a constant, which controls the interval for which the matrices \mathbf{A} , \mathbf{B} and \mathbf{C} are evaluated. For the fully implicit mid-interval algorithm in this work, values of 1 and 0.5 were used for constants Θ and ϑ , respectively.

With substitution of these constants into equation (3.87) yields:

$$\mathbf{A}^{n+1/2} \phi^{n+1} + \mathbf{B}^{n+1/2} \left[\frac{\phi^{n+1} - \phi^n}{\Delta t} \right] + \mathbf{C}^{n+1/2} = \{\mathbf{0}\} \quad (3.89)$$

This can be rearranged giving:

$$\phi^{n+1} = \left[\mathbf{A}^{n+1/2} + \frac{\mathbf{B}^{n+1/2}}{\Delta t} \right]^{-1} \left[\frac{\mathbf{B}^{n+1/2} \phi^n}{\Delta t} - \mathbf{C}^{n+1/2} \right] \quad (3.90)$$

On inspection of equation (3.90), it can be seen that the solution vector ϕ^{n+1} can be obtained if the matrices **A**, **B** and **C** are evaluated at the mid-interval. To achieve this, a predictor-corrector algorithm is used, which has the following steps:

- i. Evaluating **A**, **B** and **C** at time n , to produce a first estimate termed the predictor.
- ii. Using the predictor and the previous time step values to evaluate **A**, **B** and **C** at time $n + 1/2$ producing an estimate termed the corrector.
- iii. Checking the convergence of successive correctors using one of the following conditions:

$$|\phi_{iC}^{n+1} - \phi_{(i-1)C}^{n+1}| < \mathbf{TL}_{abs} \quad (3.91)$$

$$\left| \frac{\phi_{iC}^{n+1} - \phi_{(i-1)C}^{n+1}}{\phi_{(i-1)C}^{n+1}} \right| < \mathbf{TL}_{rel} \quad (3.92)$$

where i is the iteration level, C indicates that the corrector has been used and \mathbf{TL}_{abs} and \mathbf{TL}_{rel} are the matrices of absolute and relative tolerances, respectively. To ensure the residual force is within a tolerance limit, the stress equilibrium condition is checked and therefore, the residual force, ζ , can be obtained as (Owen and Hinton, 1980):

$$\int_{\Omega} \mathbf{P}^T \Delta \sigma d\Omega - \Delta F = \zeta \quad (3.93)$$

where ΔF is the increment of applied force.

- iv. If the convergence criterion has not been satisfied, or the residual stress is too great, the analysis returns to point ii. where the corrector becomes the new predictor. If, however, convergence has been achieved and the residual force is below the set tolerance the analysis moves to the next time step and process is repeated.

The number of corrector iterations required for convergence is related to the size of the time step used, the variable gradients, the assigned material parameters and the simulation conditions. Hence, a variable time stepping scheme is used to improve the efficiency of the solution procedure. If the number of iterations exceeds a specified

value, the time step is reduced by a factor. Likewise, if the number of iterations falls below a specified value, the time step size is increased by a factor.

This model has been incorporated in a computer code COMPASS, the **CO**de for **MO**delling **PA**rtially **S**aturated **SO**ils, which has been incrementally developed at the Geoenvironmental Research Centre (GRC), Cardiff University (e.g. Thomas et al., 1998b).

3.8. Conclusions

A theoretical and numerical framework of the transient solution for the coupled chemical and deformation behaviour of a single porosity medium under isothermal conditions was presented. The governing equations were presented in terms of gas chemical concentration and displacement. Many of the fundamental aspects of these equations have been described in detail elsewhere for unsaturated porous medium (e.g. Thomas et al., 1996; Thomas and He, 1998; Thomas and Cleall, 1999). In this work, formulations of deformation were further developed and coupled with the existing gas transport model.

The structure of fractured rock was considered as a single porosity, single permeability framework. It was assumed that coal matrix serves as a sink for geochemical reactions where sorption takes place inducing the swelling of the coal matrix whereas fracture network conduits the flow of gas. Sorption and consequently, swelling of the coal was modelled using an equilibrium approach where the gas pressure within the fracture network dictates the sorption process.

The presented framework provides additional capabilities to study high pressure reactive transport in fractured porous materials such as coal which is used in carbon dioxide sequestration and enhanced coalbed methane recovery.

3.9. References

Alonso, E.E., Gens, A. and Josa, A. 1990. A constitutive model for partially saturated soils. *Géotechnique*, 40(3), pp. 405-430.

- Alonso, E.E., Vaunat, J. and Gens, A. 1999. Modelling the mechanical behaviour of expansive clays. *Engineering Geology*, 54(1-2), pp. 173-183.
- Amali, S. and Rolston, D.E. 1993. Theoretical investigation of multicomponent volatile organic vapour diffusion: Steady-state fluxes. *Journal of Environmental Quality*, 22, pp. 825-831.
- Bear, J. and Verruijt, A. 1987. *Modeling groundwater flow and pollution*. D. Reidel Publishing Company, Dordrecht, The Netherlands.
- Bird, R.B., Stewart, W.E. and Lightfoot, E.N. 1960. *Transport phenomena*. John Wiley and Sons, New York.
- Busch, A. and Gensterblum, Y. 2011. CBM and CO₂-ECBM related sorption processes in coal: A review. *International Journal of Coal Geology*, 87(2), pp. 49-71.
- Cleall, P.J. 1998. *An investigation of the thermo/hydraulic/mechanical behaviour of unsaturated soils, including expansive clays*. Ph.D. Thesis, Cardiff University, Wales, UK.
- Chung, T.-H., Ajlan, M., Lee, L.L. and Starling, K.E. 1988. Generalized multiparameter correlation for nonpolar and polar fluid transport properties. *Industrial and Engineering Chemistry Research*, 27, pp. 671-679.
- Cook, R.D. 1981. *Concepts and applications of finite element analysis*. John Wiley and Sons, New York.
- Darcy, H. 1856. *Les Fontaines Publiques de la Ville de Dijon*. Dalmont, Paris.
- Fick, A. 1855. Ueber diffusion. *Poggendorff's Annalen der Physik und Chemie*, 94, pp. 59-86.
- Fredlund, D.G. and Rahardjo, H. 1993. *Soil Mechanics for Unsaturated Soils*. John Wiley, New York.
- Gens, A. and Alonso, E.E. 1992. A framework for the behaviour of unsaturated expansive clays. *Canadian Geotechnical Journal*, 29, pp. 1013-1032.
- Ho, C. and Webb, S. (2006). *Gas transport in Porous Media*, Springer, Dordrecht, The Netherlands.
- Hosking, L.J. 2014. *Reactive transport modelling of high pressure gas flow in coal*. Ph.D. Thesis, Cardiff University, Wales, UK.
- Jiang, P., Li, X., Xu, R., Wang, Y., Chen, M., Wang, H. and Ruan, B. 2014. Thermal modeling of CO₂ in the injection well and reservoir at the Ordos CCS demonstration project, China. *International Journal of Greenhouse Gas Control*, 23, pp. 135-146.
- Klinkenberg, L.J. 1941. The permeability of porous media to liquids and gases. In: *Drilling and Production Practice*, API, pp. 200-213.
- Langmuir, I. 1918. The adsorption of gases on plane surfaces of glass, mica and platinum. *Journal of the American Chemical Society*, 40(9), pp. 1361-1403.

- Liu, J., Wang, J., Chen, Z., Wang, S., Elsworth, D. and Jiang, Y. 2011. Impact of transition from local swelling to macro swelling on the evolution of coal permeability. *International Journal of Coal Geology*, 88(1), pp. 31-40.
- Liu, Z., Feng, Z., Zhang, Q., Zhao, D. and Guo, H. 2015. Heat and deformation effects on coal during adsorption and desorption of carbon dioxide. *Journal of Natural Gas Science and Engineering*, 25, pp. 242-252.
- Mason, E.A., Malinauskas, A.P. and Evans, R.B. 1967. Flow and diffusion of gases in porous media. *The Journal of Chemical Physics*, 46(8), pp. 3199-3217.
- Masum, S.A. 2012. *Modelling of reactive gas transport in unsaturated soil – a coupled thermo-hydro-chemical-mechanical approach*. Ph.D. Thesis, Cardiff University, Wales, UK.
- Mašin, D. 2013. Double structure hydromechanical coupling formalism and a model for unsaturated expansive clays. *Engineering Geology*, 165, pp. 73-88.
- Millington, R.J. and Quirk, J.M. 1961. Permeability of porous solids. *Transactions of the Faraday Society*, 57, pp. 1200-1207.
- Oldenburg, C.M. 2007. Joule-Thomson cooling due to CO₂ injection into natural gas reservoirs. *Energy Conversion and Management*, 48(6), pp. 1808-1815.
- Onsager, L. 1945. Theories and problems of liquid diffusion. *Annals of the New York Academy of Sciences*, 46, pp. 241-265.
- Owen, D.R.J. and Hinton, E. 1980. *Finite elements in plasticity: theory and practice*, Pineridge Press, Swansea.
- Peng, D.Y. and Robinson, D.B. 1976. A new two-constant equation of state. *Industrial and Engineering Chemistry Fundamentals*, 15(1), pp. 59-64.
- Reid, R.C., Prausnitz, J.M. and Sherwood, T.K. 1977. *The properties of gases and liquids*. 3rd Edition. McGraw-Hill, New York.
- Sanchez, M., Gens, A., do Nascimento Guimarães, L. and Olivella, S. 2005. A double structure generalized plasticity model for expansive materials. *International Journal for Numerical and Analytical Methods in Geomechanics*, 29(8), pp. 751-787.
- Scanlon, B.R., Nicot, J.P. and Massmann, J.M. 1999. Soil gas movement in unsaturated systems. In: Summer, M.E. ed. *Handbook of soil science*, CRC Press, Boca Raton, Florida.
- Sedighi, M. 2011. *An investigation of hydro-geochemical processes in coupled thermal, hydraulic, chemical and mechanical behaviour of unsaturated soils*. Ph.D. Thesis, Cardiff University, Wales, UK.
- Seetharam, S.C., Thomas, H.R. and Cleall, P.J. 2007. Coupled thermo-hydro-chemical-mechanical model for unsaturated soils – Numerical algorithm. *International Journal of Numerical Methods in Engineering*, 70, pp. 1480-1511.
- Somerton, W.H., Söylemezoğlu, I.M. and Dudley, R.C. 1975. Effect of Stress on Permeability of Coal, *International Journal of Rock Mechanics and Mining Sciences and Geomechanics Abstracts*, 12(5), pp. 129-145. Pergamon.

Thomas, H.R. 1988. A nonlinear analysis of two-dimensional heat and moisture transfer in partly saturated soil. *International Journal for Numerical and Analytical Methods in Geomechanics*, 12, pp. 31-44.

Thomas, H.R. and He, Y. 1995. Analysis of coupled heat, moisture and air transfer in a deformable unsaturated soil. *Géotechnique*, 45(4), pp. 677-689.

Thomas, H.R., He, Y., Sansom, M.R. and Li, C.L.W. 1996. On the development of a model of the thermo-mechanical-hydraulic behaviour of unsaturated soils. *Engineering Geology*, 41, pp. 197-218.

Thomas, H.R. and He, Y. 1997. A coupled heat-moisture transfer theory for deformable unsaturated soil and its algorithmic implementation. *International Journal for Numerical Methods in Engineering*, 40, pp. 3421-3441.

Thomas, H.R. and He, Y. 1998. Modelling the behaviour of unsaturated soil using an elasto-plastic constitutive relationship. *Géotechnique*, 48, pp. 589-603.

Thomas, H.R., Rees, S.W. and Sloper, N.J. 1998a. Three-dimensional heat, moisture and air transfer in unsaturated soils. *International Journal of Numerical and Analytical Methods in Geomechanics*, 22(2), pp. 75-95.

Thomas, H.R., He, Y. and Onofrei, C. 1998b. An examination of the validation of a model of the hydro/thermo/mechanical behaviour of engineered clay barriers. *International Journal for Numerical and Analytical Methods in Geomechanics*, 22, pp. 49-71.

Thomas, H.R. and Cleall, P.J. 1999. Inclusion of expansive clay behaviour in coupled thermo hydraulic mechanical models. *Engineering Geology*, 54, pp. 93-108.

Thomas, H.R., Sedighi, M. and Vardon, P.J. 2012. Diffusive reactive transport of multicomponent chemical under coupled thermal, hydraulic, chemical and mechanical conditions. *Geotechnical and Geological Engineering*, 30(4), pp. 841-857.

Vardon, P.J. 2009. *A three-dimensional numerical investigation of the thermo-hydro-mechanical behaviour of a large-scale prototype repository*. Ph.D. Thesis, Cardiff University, Wales, UK.

Webb, S.W. 2006. Gas transport mechanisms. In: Ho, C.K. and Webb, S.W. eds. *Gas transport in porous media*, Springer, Dordrecht, The Netherlands.

White, C.M., Smith, D.H., Jones, K.L., Goodman, A.L., Jikich, S.A., Lacount, R.B., Dubose, S.B., Ozdemir, E., Morsi, B., Schroeder, K.T. 2005. Sequestration of Carbon Dioxide in Coal with Enhanced Coalbed Methane Recovery – A Review. *Energy&Fuels*, 19 (3), pp. 659-724

Zhang, H., Liu, J. and Elsworth, D. 2008. How sorption-induced matrix deformation affects gas flow in coal seams: A new FE model. *International Journal of Rock Mechanics & Mining Sciences*, 45(8), pp. 1226-1236.

Zienkiewicz, O.C. and Morgan, K. 1982. *Finite elements and approximation*. John Wiley and Sons, New York.

Zienkiewicz, O.C. and Taylor, R.L. 1989. *The finite element method*. 4th Edition. McGraw Hill, New York.

4

Materials and Methods

4.1. Introduction

In this chapter, a detailed description of experimental facilities used in this study is presented. As a part of the existing equipment, further upgrades are introduced and discussed. The material properties, experimental procedures and measurement methods employed in this investigation are reported.

Section 4.2 presents the description of the coals used in this study. Preparation of the powdered coal samples is presented followed by a sampling procedure of coal cores for gas sorption measurements, uniaxial compressive testing and core flooding tests.

In Section 4.3, results obtained from characterization tests carried out according to standard procedures on coal samples of this study are presented. In particular, physical properties such as density and porosity as well as data from Proximate, Ultimate, Petrographic and Calorimetric analyses of coals are shown.

A detailed description of the experimental setup used in this work is provided in Section 4.4. In particular, a previously developed (existing) experimental facility consisting of manometric sorption apparatus, triaxial core flooding system and auxiliary units is shown where further developments in the area of the gas supply and backpressure system are presented. Details of the uniaxial compressive testing machine used in this study are presented, as well. As a part of the experimental setup, detailed overview of the experimental procedures related to sorption measurements, gas flow measurements and unconfined compressive tests is presented. In addition, details of the granulometric analysis performed on post-failure sample particles are provided.

The concluding remarks of the chapter are presented in Section 4.5.

4.2. Coal Description and Sample Preparation Methodology

Field specimens were gathered from two different coal mines, namely East Pit East Opencast Coal Site (51°47'57.7''N 3°51'49.4''W) operated by Celtic Energy Ltd. and Aberpergwm coal mine (51°44'28.8''N 3°38'36.0''W) operated by Energybuild and owned by Walter Energy. Both coal mines are located in Wales, UK as a part of the South Wales Coalfield which is approximately 90 km in length along its east-west axis

and 27 km in width along its north-south axis covering an area of 2000 km² (Jones et al., 2004). Figure 4.1 shows the locations of the mines.

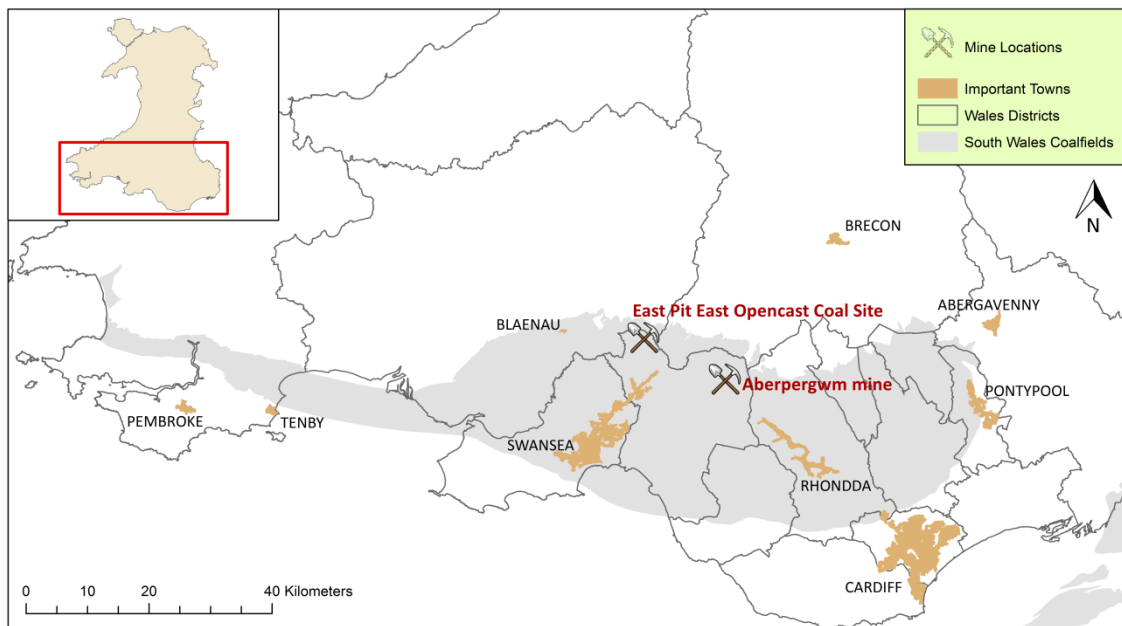


Fig. 4.1. South Wales Coalfield and locations of the East Pit East Opencast Coal Site and the Aberpergwm mine.

Six blocks of coal at the East Pit East Opencast Coal Site were extracted from 150 m depth with dimensions of approximately 0.5 m × 0.5 m × 0.5 m. Five coal blocks obtained from the Aberpergwm mine were a part of the 9ft coal seam located at a depth of 550 m. Extraction of coal blocks from both locations was conducted by staff members of the companies operating the respective mines. Due to the limitations of the equipment used for coal extraction in the Aberpergwm mine, maximum dimensions of the coal blocks obtained were approximately 0.3 m × 0.2 m × 0.1 m. It should be noted that due to its high-quality characteristics, coal obtained at the East Pit East Opencast Coal Site is locally known as Black Diamond. Adopting this terminology, coals obtained from the East Pit East Opencast Coal Site and Aberpergwm mine will be referenced as Black Diamond and 9ft Aberpergwm coals, respectively. For future reference in this thesis, Black Diamond coal will also be referred as BD and 9ft Aberpergwm coal will be referred as AB, where appropriate.

The coal blocks obtained on site were wrapped in cling film and put in plastic bags to minimize the oxidation of the coal surfaces and preserve chemical and physical

properties. Upon arrival in the laboratory, the sealed blocks were labelled and stored in the constant room temperature environment.

4.2.1. Preparation of Powdered Samples for the Gas Sorption Measurements and Characterisation Tests

Preparation of coal samples was conducted following the ASTM D2013/D2013M (2012) standard of practice. Drying of coal at temperatures higher than 70°C creates new cracks and small fissures altering the physical structure of the coal (Gathitu et al., 2009). Hence, to overcome this, an air-drying method following the ASTM D3302/D3302M (2015) was applied to all the samples of this study. Using this approach, moisture within the samples was brought near to equilibrium with the atmosphere in the room. Samples were considered to be air-dried when the loss of the sample mass was not more than 0.1 %/h between two consecutive measurements.

Crushed BD and AB coal samples were divided and sieved using a series of sieves ranging from 0.212 mm to 4 mm. For the purpose of the sorption experiments, obtained fractions were divided into two different grain sizes, i.e. 0.25-0.85 mm and 2.36-4 mm each with a mass of 50 g to be used in the experiment (Figure 4.2). Crushed samples passed through a sieve size of 0.212 mm were used for the Proximate analysis following BS 1016-104.3 (1998), BS 1016-104.4 (1998) and BS 1016-104.1 (1999), and the Ultimate analysis following BS 1016-106.1.1 (1996) and BS 1016-106.4.2 (1996). Obtained coal fractions were sealed and labelled in plastic bags and air-tight containers, and kept in the refrigerator to be used in the experiments.

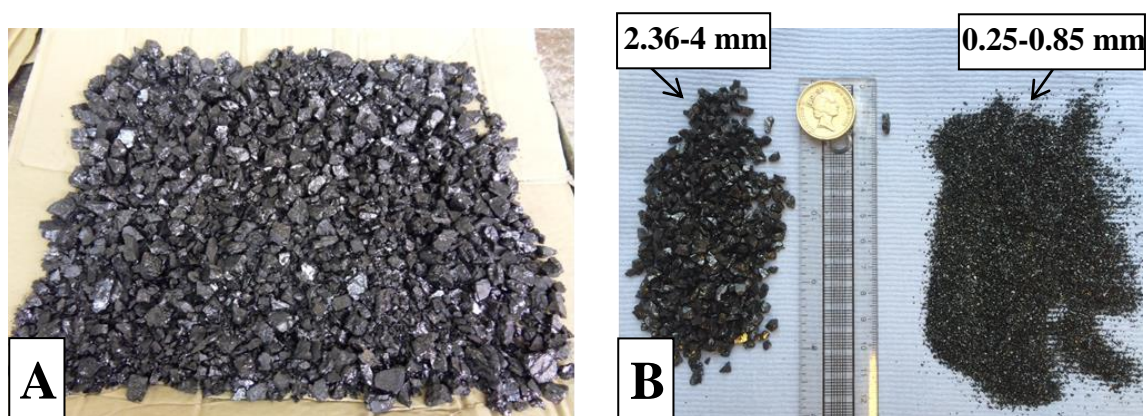


Fig. 4.2. Powdered coal preparation for the sorption experiments; A) Crushed coal before sieving, B) 0.25-0.85 mm and 2.36-4 mm coal fractions after sieving.

4.2.2. Preparation of Core Samples

Coal cores were drilled out of the coal blocks using a coring machine (Figure 4.3). Water was used as a cooling agent while drilling. Three diamond core drilling bits with different internal diameters, i.e. 3.6 cm, 4.4 cm and 7 cm were used to obtain the coal cores. Upon extraction, cores were cut to their required lengths using a diamond circular saw. Fine sand paper was used to produce parallel and smooth ended surfaces, ensuring uniform stress across the face of each specimen during the experiments. The coal samples were then air-dried, wrapped in a cling film and stored in a refrigerator to be used in the experiments.

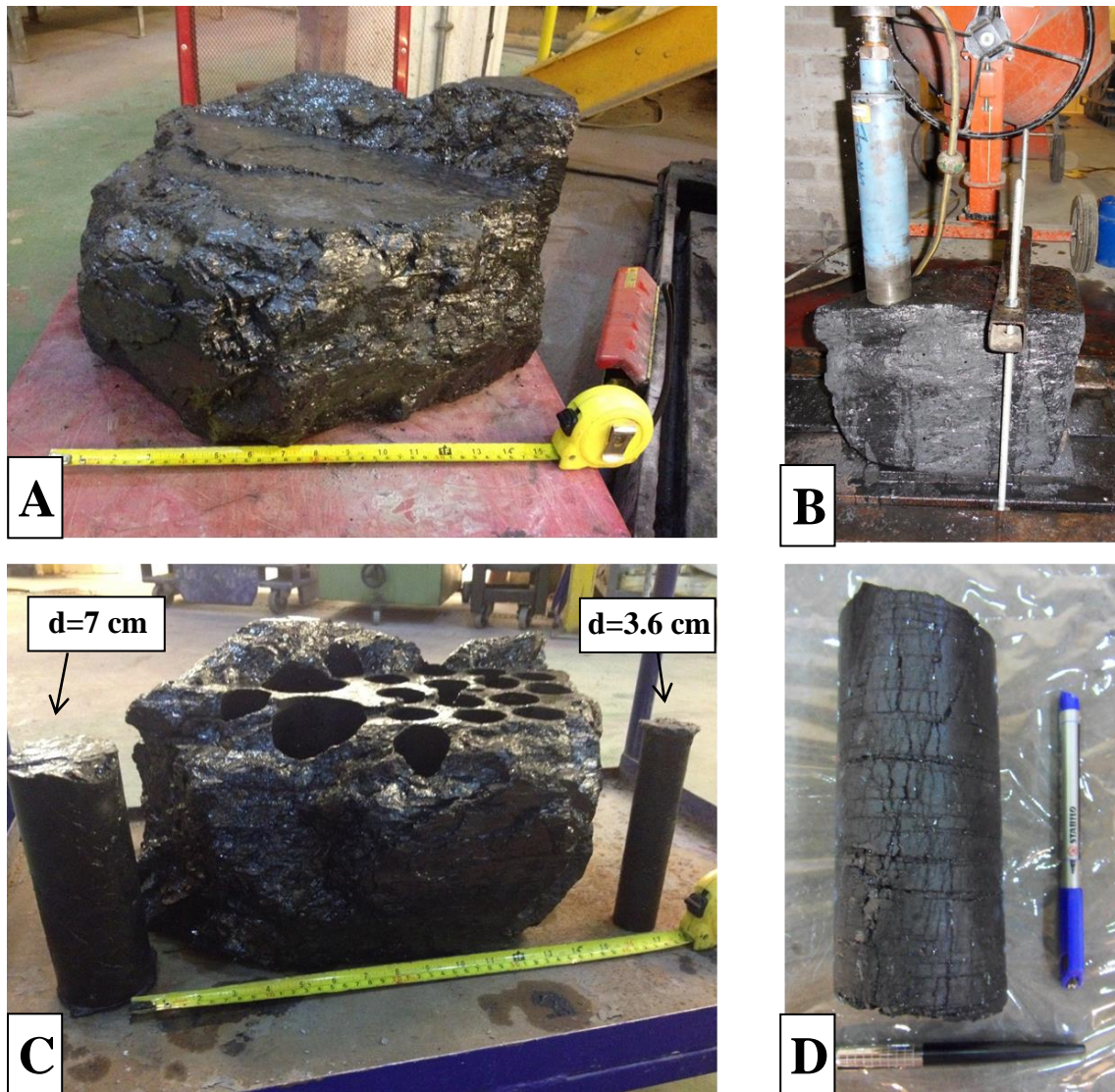


Fig. 4.3. Preparation of the core samples; A) Coal block, B) Drilling process, C) Drilled block, D) Coal core after the coring process.

4.2.2.1. Cores for the Gas Sorption Measurements

Coal cores for the gas sorption measurements were obtained both from BD and AB coal blocks. Measured physical properties and photos of the coal cores used in the gas sorption experiments are presented in Table 4.1 and Figure 4.4, respectively. Although dimensions of the samples differ, similar volumes and masses of the samples ensure comparison of obtained data from the experiments. Results of the experimental measurements conducted on cores described here and powdered samples described in Section 4.2.1, will be presented in Chapter 5.

Table 4.1. Dimensions and physical properties of coal cores used in the gas sorption measurements.

Sample	Diameter (cm)	Length (cm)	Volume (cm ³)	Mass (g)	Density (g/cm ³)
BD core	4.4	3.8	~58	79.3	1.362
AB core	3.6	5.3	~55	74.2	1.368

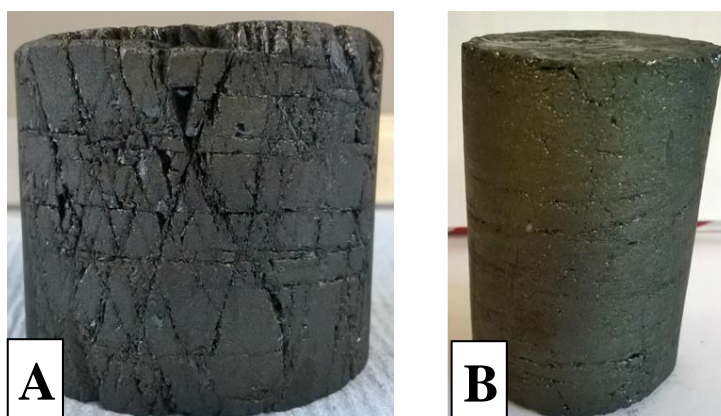


Fig. 4.4. Coal cores used in the gas sorption measurements; A) Black Diamond, B) 9ft Aberpergwm.

4.2.2.2. Cores for the Uniaxial Compressive Tests

A total of twenty coal cores were selected for the uniaxial compressive testing. Although a larger number of coal cores has been extracted, only the ones with minimum fractures or large inconsistencies were chosen. The dimensions of the selected samples are shown in Table 4.2 together with the measured values of mass and density for each coal. While the dimensions and masses of the samples differ slightly, the average density of both BD and AB samples is the same, i.e. 1376 kg/m³.

Table 4.2. Dimensions and physical properties of core samples used in the uniaxial compressive tests.

Sample	Diameter (cm)	Length (cm)	L/D ratio	Mass (g)	Density (g/cm ³)
<i>Black Diamond</i>					
BD1	3.6	7.6	2.1	107.4	1.376
BD2	3.6	7.6	2.1	107.5	1.376
BD3	3.6	7.7	2.1	108.4	1.373
BD4	3.6	7.6	2.1	108.3	1.378
BD5	3.6	7.5	2.1	106.5	1.377
BD6	3.6	7.5	2.1	106.2	1.377
BD7	3.6	7.3	2.0	103.1	1.374
BD8	3.6	7.1	2.0	101.0	1.378
BD9	3.6	7.4	2.1	104.6	1.370
BD10	3.6	7.2	2.0	101.7	1.380
Average	3.6	7.5	2.1	105.4	1.376±0.003
<i>9ft Aberpergwm</i>					
AB1	3.6	7.5	2.1	108.3	1.391
AB2	3.6	6.9	1.9	98.5	1.376
AB3	3.6	6.8	1.9	96.5	1.376
AB4	3.6	7.9	2.2	113.3	1.389
AB5	3.6	5.6	1.6	78.9	1.367
AB6	3.6	5.6	1.6	80.2	1.392
AB7	3.6	6.0	1.7	83.9	1.364
AB8	3.6	6.4	1.8	89.4	1.365
AB9	3.6	5.3	1.5	74.7	1.365
AB10	3.6	7.5	2.1	106.7	1.379
Average	3.6	6.6	1.8	93.0	1.376±0.011

According to the ASTM D4543 (2008), the diameter of the cylindrical weak rock specimens for compressive strength and elastic moduli testing should not be less than 47 mm with a length-to-diameter (L/D) ratio of 2-2.5. However, to make results comparable with the values reported in literature for coals of lower rank (e.g. Perera et al., 2011; Ranjith and Perera, 2012; Perera et al., 2013; Ranathunga et al., 2016) where coals with a diameter of 38 mm were used, it was decided to drill cores of similar diameter in this study, i.e. 36 mm.

Due to the natural variability among the coal blocks provided from the Aberpergwm mine, it was very difficult to drill and cut samples with a fixed length. Consequently, it can be inferred from Table 4.2 that L/D ratio among the AB samples varies more than among the BD samples. However, slight inconsistency in L/D ratio was believed not to

affect the experimental results. Such statement is based on the work of Viète and Ranjith (2006) who have conducted uniaxial compressive tests on samples of equal diameter but different lengths and obtained highly comparable results. A picture of representative coal cores used for uniaxial compressive tests in this study is presented in Figure 4.5. Results of the experimental measurements conducted on cores described here will be presented in Chapter 6.

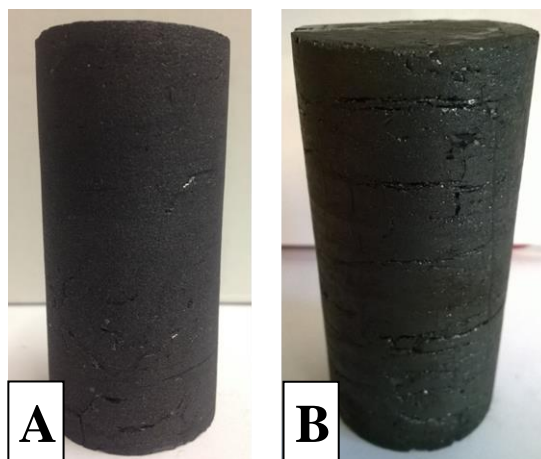


Fig. 4.5. Examples of coal cores used in the unconfined compressive tests; A) Black Diamond, B) 9ft Aberpergwm.

4.2.2.3. Cores for the Triaxial Flooding Tests

Four coal cores were drilled out of the Black Diamond coal blocks to be used in the triaxial core flooding tests. Table 4.3 provides dimensions, masses and calculated density values of the coal cores used in the triaxial flooding experiments. Data shows that calculated density values are in close agreement to the ones obtained on samples for uniaxial compressive testing (see Table 4.2) showing that there is no significant change in bulk density despite the difference in the size of the samples.

Table 4.3. Dimensions and physical properties of core samples used in the triaxial core flooding tests.

Sample	Diameter (cm)	Height (cm)	L/D ratio	Mass (g)	Density (g/cm ³)
Sample A	7	11.5	1.6	598.3	1.372
Sample B	7	11.5	1.6	603.4	1.374
Sample C	7	11.1	1.6	578.8	1.373
Sample D	7	9.2	1.3	484.2	1.382

Photos of the four specimens, samples A, B, C and D are given in Figure 4.6. The distinct fracture network for each particular coal sample can be observed. Samples B and C show highly developed cleat systems. Samples A and D show fracture network without significantly pronounced fracture interconnectivity. The reader's attention is drawn to this observation because of its potential importance in relation to flow characteristics. Results of the experimental measurements conducted on cores described in this section will be presented in Chapter 7.

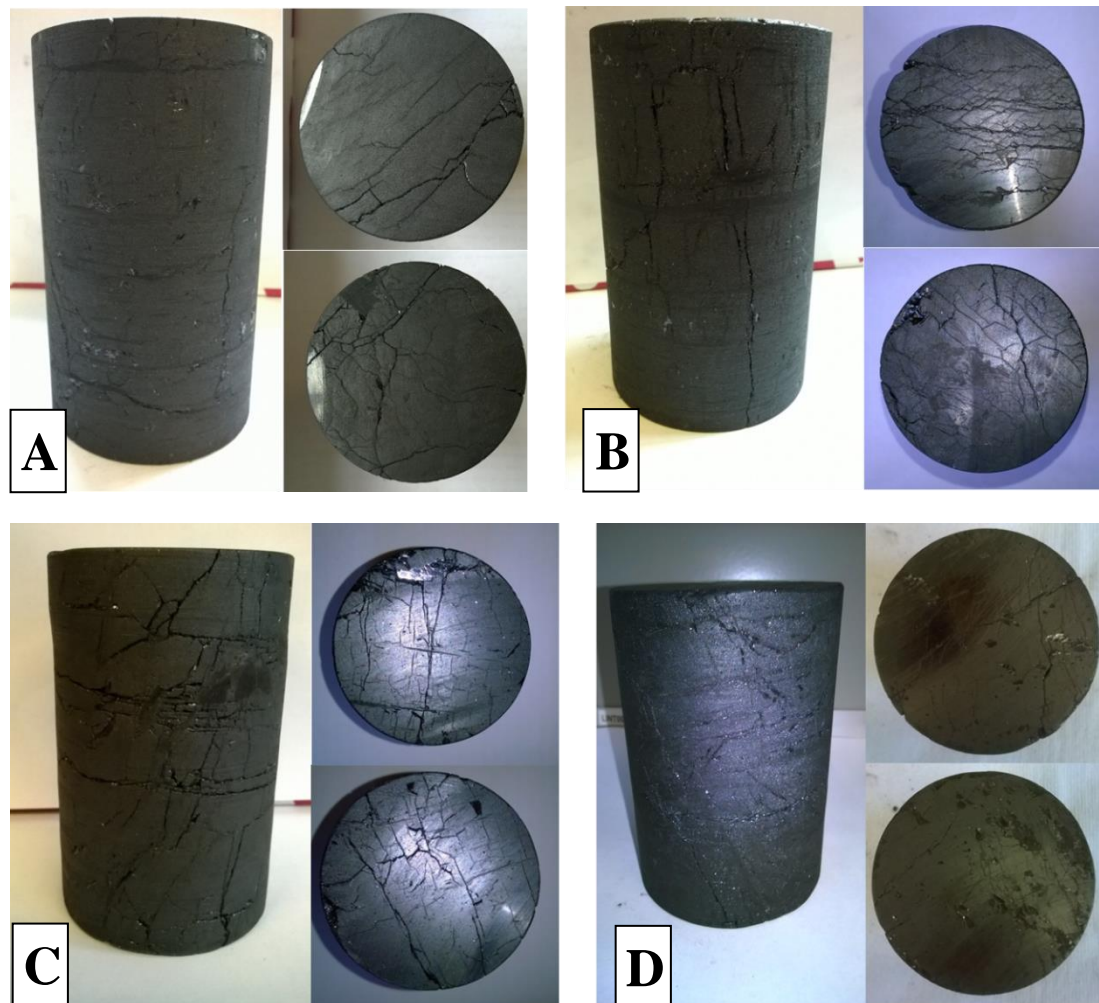


Fig. 4.6. Coal cores used in the triaxial core flooding tests; A) sample A, B) sample B, C) sample C, D) sample D.

4.3. Characterisation Tests

The chemical, petrographic and combustion properties of the coal samples used in this study were obtained by conducting a series of characterization analyses. While

Proximate and Ultimate Analyses on Black Diamond coal were conducted at the School of Engineering, Cardiff University, the results of Proximate, Ultimate, Petrographic and Calorimetric analyses of 9ft Aberpergwm coal samples were provided by Główny Instytut Górnictwa (GIG) Katowice, Poland as a part of the international collaboration. The porosity of the coal samples was estimated based on the relationship between carbon content and porosity given by Rodrigues and Lemos de Sousa (2002).

4.3.1. Proximate, Ultimate, Petrographic and Calorimetric Analyses

A summary of the characterization tests and results obtained in this study are provided in Table 4.4.

Table 4.4. Summary of the characterization tests conducted and the results obtained on coal samples of this study.

Characterization test	Black Diamond		9ft Aberpergwm	
	Value	Method	Value	Method
<i>Proximate analysis</i>				
Moisture content, %	1.65±0.12	BS 1016-104.1 (1999)	0.91±0.3	GIG
Ash content, %	1.65±0.38	BS 1016-104.3 (1998)	4.62±0.3	GIG
Volatile matter, %	5.82±0.21	BS 1016-104.4 (1998)	5.73±0.08	GIG
Fixed carbon content, %	90.88	-	88.73	GIG
<i>Ultimate analysis</i>				
Total carbon content, %	90.12±0.11	BS 1016-106.1.1 (1996)	89.5±0.66	GIG
Total sulphur content, %	0.95±0.02	BS 1016-106.4.2 (1996)	0.87±0.04	GIG
Sulphur after full combustion content, %	-	-	0.25±0.05	GIG
Combustible sulphur content, %	-	-	0.62	GIG
Total hydrogen content, %	-	-	3.16±0.28	GIG
Nitrogen content, %	-	-	1.31±0.12	GIG
Oxygen content, %	-	-	0.33	GIG
<i>Petrography</i>				
Vitrinite reflectance, %	-	-	2.84±0.05	GIG
Vitrinite content, %	-	-	86±7	GIG
Liptinite content, %	-	-	0±1	GIG
Inertinite content, %	-	-	14±1	GIG
Mineral matter content, %	-	-	0±1	GIG
<i>Calorimetry</i>				
Higher calorific value, MJ/kg	-	-	33.6±0.22	GIG
Lower calorific value, MJ/kg	-	-	32.9	GIG

In the Proximate analysis, moisture content represents the mass loss of coal when heated to 105°C, volatile matter is a coal component liberated at high temperature and ash content is the remaining inorganic residue after the combustion (Thomas, 2013). Fixed carbon content is not determined directly but calculated as the difference of the three abovementioned parameters summed and subtracted from 100 (Thomas, 2013).

It can be seen from Table 4.4 that both BD and AB contain high percentage of fixed carbon content, i.e. 90.9% and 88.7%, respectively. Moisture contents, ash contents and volatile matter contents for both samples are relatively low, i.e. 1.65%, 1.65%, 5.82% for BD coal and 0.91%, 4.62%, 5.73% for AB coal, respectively.

Ultimate analysis presents the chemical elements in coal, i.e. carbon, hydrogen, oxygen and sulphur. Due to the limitations of the existing equipment at the School of Engineering, Cardiff University used for conducting the Ultimate analysis, only sulphur and carbon contents are presented for Black Diamond coal. Data for all abovementioned elements is available for 9ft Aberpergwm provided by the Główny Instytut Górnictwa. It should be noted that the results of characterisation tests conducted by GIG were obtained following Polish national standards and International standards.

Calorific value of a coal represents the amount of heat per unit mass of coal when combusted (Thomas, 2013). Petrographic analysis identifies the organic units, i.e. macerals that comprise the coal mass (Thomas, 2013). Three main groups of macerals are vitrinite (woody materials), liptinite (spores, resins and cuticles) and inertinite (oxidized plant material). The mineral content of coal is the non-combustible inorganic fraction (Thomas, 2013).

Data obtained from the coal characterization tests of this study was compared with results of various ranks of coal reported by Speight (2005) and ASTM D388 (2015) in Table 4.5. Based on the results provided in Table 4.5, it can be confirmed that both coal samples of this study can be classified as anthracites.

Table 4.5. Comparison between coal characterisation results for coal samples in this study and those of various ranks of coals reported by Speight (2005) and ASTM D388 (2015) classification of coal rank.

	BD	AB	Anthracite (Speight, 2005)	Anthracitic coals (ASTM D388, 2015)
Moisture content, %	1.65	0.91	3-6	-
Volatile matter, %	1.65	5.73	2-12	<2-14
Fixed carbon, %	90.88	88.73	75-85	>86
Ash, %	1.65	4.62	4-15	-
Sulphur, %	0.95	0.87	0.5-2.5	-
Hydrogen, %	-	3.16	1.5-3.5	-
Carbon, %	90.12	89.5	75-85	-
Nitrogen, %	-	1.31	0.5-1	-
Oxygen, %	-	0.33	5.5-9	-
MJ/kg	-	32.9-33.6	27.912-31.401	>32.6
Density, kg/m ³	1376	1376	1350-1700	-

4.3.2. The Porosity of Coal

The total porosity of the coal is the fraction of the volume of voids over the total volume (Thomas, 2013). Rodrigues and Lemos the Sousa (2002) have presented an empirical relationship between coal porosity and coal rank which was used in this work to estimate the average coal porosity, as shown in Figure 4.7.

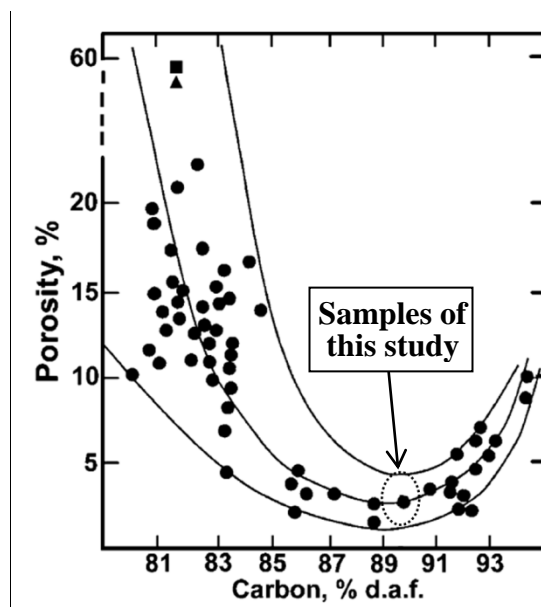


Fig. 4.7. Relationship between coal porosity and coal rank as reported by Rodrigues and Lemos de Sousa (2002).

As both BD and AB coal samples are of the same coal rank with similar carbon content, i.e. BD with 90.12% and AB with 89.5%, the coal porosity was estimated to be $3\pm 2\%$ in both coal samples based on the relationship given in Figure 4.7. Such porosity value is in agreement with the work of Liu et al. (2010) who have obtained porosity of 3.26% on an anthracite coal sample 4-8 mm in diameter. Similarly, Liu et al. (2015) have recently experimentally determined a porosity value of 3.45% for a cylindrical anthracite coal sample 100 mm in diameter and 130 mm in length.

4.4. Experimental Setup and Measurement Methods

The experimental system used in the current study consists of four main sections:

- A manometric sorption apparatus.
- A triaxial core flooding system.
- A high pressure gas supply unit.
- Auxiliary units.

A schematic diagram of the laboratory facility is presented in Figure 4.8. It should be noted that the manometric, triaxial core flooding and auxiliary systems have been constructed and commissioned by Hadi Mosleh (2014). The existing laboratory facility was further enhanced as a part of this study. In particular, a new gas pressure supply unit was added allowing injection of gases under high pressures with precise temperature control. Moreover, a capability to control backpressure of the system was added. The reader's attention is drawn to the red-dashed line region in Figure 4.8 in which the abovementioned modifications to the existing laboratory facility as a part of this work can be observed.

In order to determine the deformation parameters of coals under unconfined conditions, a standard uniaxial compressive machine was used in this study (ASTM D7012, 2014).

Specifications of the experimental facility and measurement methods used in this study are provided in the following sections.

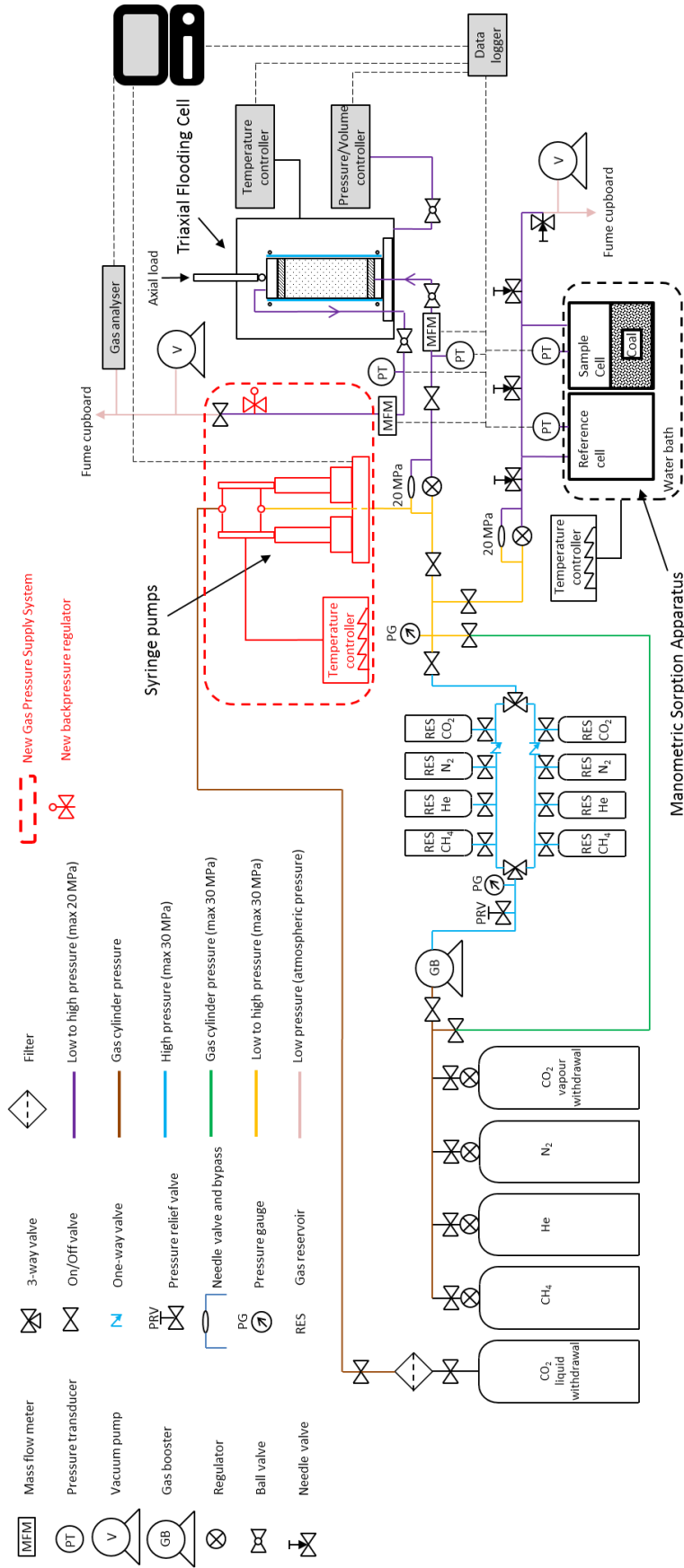


Fig. 4.8. A schematic diagram of the laboratory facility (adopted and modified after Hadi Mosleh, 2014).

4.4.1. Experimental Temperature and Pressure

Critical temperature and critical pressure of carbon dioxide are approximately 304K (31°C) and 7.4 MPa (Span and Wagner, 1996). Above such values, carbon dioxide becomes a supercritical fluid which behaves like a gas but with a density like that of a liquid. At critical pressure, its compressibility is maximized and small changes to thermal parameters can lead to large changes in its local density (Busch and Gensterblum, 2011).

Due to the fact that transition from subcritical to supercritical CO₂, as previously mentioned in Chapter 2, causes changes in the sorptive potential of CO₂ affecting coal's behaviour, it was decided to maintain the temperature throughout all the experiments above the critical temperature for CO₂ enabling carbon dioxide to achieve its supercritical state at high pressures. Furthermore, unmineable coal seams with potential for CO₂ sequestration generally occur at greater depths where pressure and temperature may exceed the critical values of CO₂ (Perera et al., 2013).

During all sorption measurements, temperature of the manometric sorption system was maintained constant at 313±0.01K (40±0.01°C). Similarly, all samples used for uniaxial compressive testing were saturated with CO₂ at 313±0.01K (40±0.01°C). Using the temperature controller, temperature of the triaxial core flooding system was initially set to 310.5±1K (37.5±1°C). However, as mentioned in Chapter 1, thermal effects induced by the gas flow were measured and the methodology of measurements will be shown later in the chapter.

As will be shown in the following sections, injection gas pressures were up to approximately 8.6 MPa and 8.5 MPa in manometric sorption experiments and uniaxial compressive tests, respectively. In triaxial core flooding experiments, maximum injection gas pressures were up to 8.1 MPa. By achieving such pressures, both subcritical and supercritical carbon dioxide were injected. It should be noted that pressure values mentioned in this study are absolute pressure values calculated assuming an atmospheric pressure of 101 325 Pa.

If an average hydrostatic gradient of 0.01 MPa/m is assumed (e.g. Gensterblum, 2013) and based on the injection pressures used in this study, it can be calculated that experimental results presented in the following chapters represent conditions at depths

up to 800-850 m. Likewise, if an average thermal gradient of 0.03 K/m ($^{\circ}\text{C}/\text{m}$) with an average surface temperature of 285K (12°C) is assumed (e.g. Gensterblum, 2013), results of this study represent conditions present at 833-933 m of depth. Hence, it can be inferred that the experimental results obtained in this study are applicable to conditions existing up to approximately 900 m of depth.

4.4.2. Manometric Sorption Apparatus

The manometric sorption apparatus is the most widely used apparatus for determining gas sorption capacities of coal (Buch and Gensterblum, 2011). Figure 4.9 presents components of the manometric sorption system used in this study.

The current setup consists of four main units:

- A manometric unit consisting of reference and sample cells.
- Pressure transducers and needle valves.
- A water bath with temperature controller.
- A calibration cell used for the helium pycnometry test.

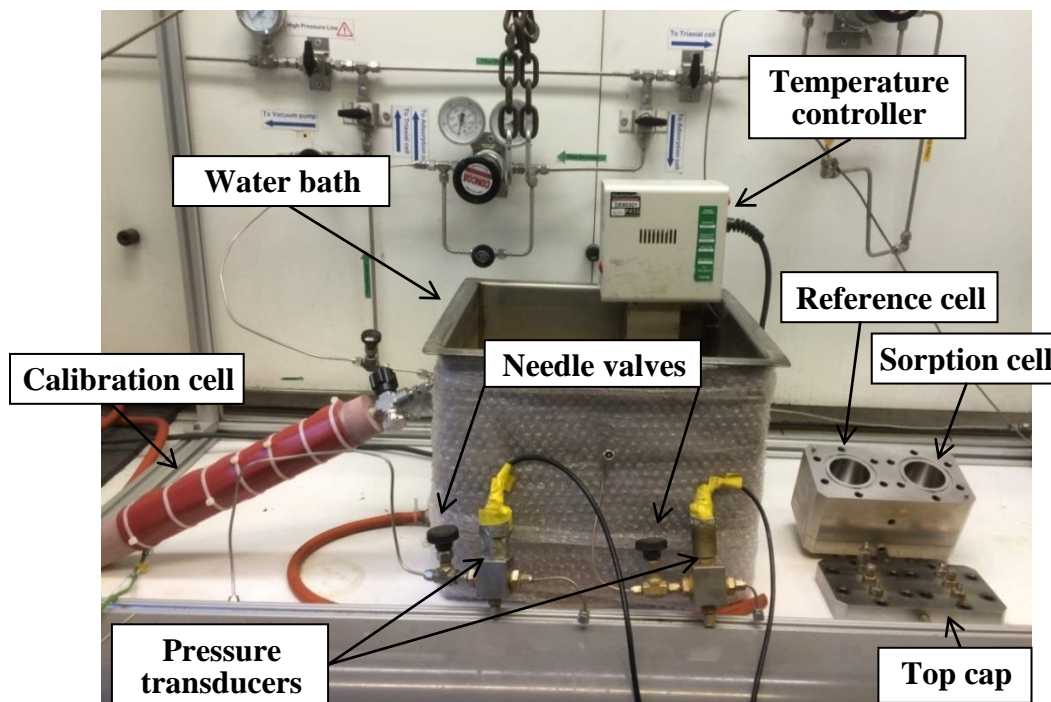


Fig. 4.9. Components of the manometric sorption system (designed and commissioned by Hadi Mosleh, 2014).

The entire system has been designed to tolerate pressures up to 20 MPa and temperatures up to 338K (65°C). Details of the development of the apparatus are provided in Hadi Mosleh (2014).

The manometric sorption method is based on a mass balance principle which employs precise measurements of pressures, volumes and temperatures (Sudibandriyo et al., 2003). The experimental procedure consists of three steps. The first is the determination of the void volume of the reference and sample cells. The second is the calculation of the sorption amount, known as the Gibbs or excess sorption, based on measured values of the pressure, temperature and volumes. The third is the calculation of absolute sorption values using the excess sorption and assuming the density of the adsorbed phase. Details of the three steps are provided in the following sections.

4.4.2.1. The Helium Pycnometry Method

Prior to the sorption experiment, the void volume of the sample cell containing a certain amount of coal is determined by expansion of a non-sorbing gas such as helium. Such a test is known as the helium pycnometry method. In the test, it is assumed that the same pore volume is accessed by He as by CO₂ and that He does not adsorb on the coal surface (Ozdemir et al., 2003; Mohammad et al., 2009). The test consists of three steps. In the first step, a certain amount of gas under isothermal conditions is transferred in the calibration cell (cylinder) of a known volume. The volume of the calibration cell, V_C , designed and commissioned by Hadi Hosleh (2014), used in this study was 489.176 cm³. The injected amount of gas can be calculated as (Pan et al., 2010):

$$n_{inj} = \frac{PV}{ZRT} \quad (4.1)$$

where n_{inj} is the amount of gas (mol), P is the gas pressure (Pa), V is the volume of the cell (m³), Z is the gas compressibility factor, R is the universal gas constant (J.K⁻¹.mol⁻¹) and T is the temperature (K).

In the second and the third step, the calibration cylinder is connected to the reference and sample cells, respectively. At the end of each step when the pressure stabilised, pressure readings are taken.

Taking into account that the amount of gas in the system and temperature are constant, both the volume of the reference cell and the unoccupied volume of the sample cell can be calculated using the following relationship:

$$\left(\frac{PV}{ZR}\right)_C = \left(\frac{PV}{ZR}\right)_{C+R} = \left(\frac{PV}{ZR}\right)_{C+R+S} \quad (4.2)$$

where subscripts C , R and S stand for calibration, reference and sample cells, respectively.

The compressibility factor of helium was derived as a function of temperature and pressure as (Sudibandriyo, 2004):

$$Z_{He} = 1 + \frac{(0.001471 - 0.000004779T + 0.00000000492T^2)}{P} \quad (4.3)$$

where T is temperature (K) and P is pressure (atm).

Three measurements have been conducted for each tested sample where the average values of the calculated volumes for each cell have been used in sorption calculations. It should be noted that prior to the helium pycnometry method, all samples have been vacuumed for 24 hours. Such procedure removes the debris from the pores that would hinder the access of gas and also shrinks the pre-swollen coal matrix (Gathitu et al., 2009).

Results of the volume measurements are presented in Table 4.6 where the void volume of the sample cell represents both the empty volume of the cell and the void volume of the sample.

Table 4.6. The results of the helium pycnometry performed for coal samples of different sizes.

Sample size	Reference Cell Void Volume, V_R (m ³)	Sample Cell Void Volume, V_S (m ³)
<i>Black Diamond</i>		
0.25-0.85 mm	0.00016994	0.00013368
2.36-4 mm	0.00017005	0.00013447
Core	0.00016759	0.00010795
<i>9ft Aberpergwm</i>		
0.25-0.85 mm	0.00016962	0.00013338
2.36-4 mm	0.00016715	0.00013173
Core	0.00017054	0.00011470

4.4.2.2. Sorption Measurements

In the manometric sorption measurement, defined amounts of gas are successively transferred from the reference cell into the sample cell containing the coal mass. Before the sorption process, coal samples were vacuumed for 2 hours to remove any residual helium. The schematic setup for manometric sorption measurement is presented in Figure 4.10.

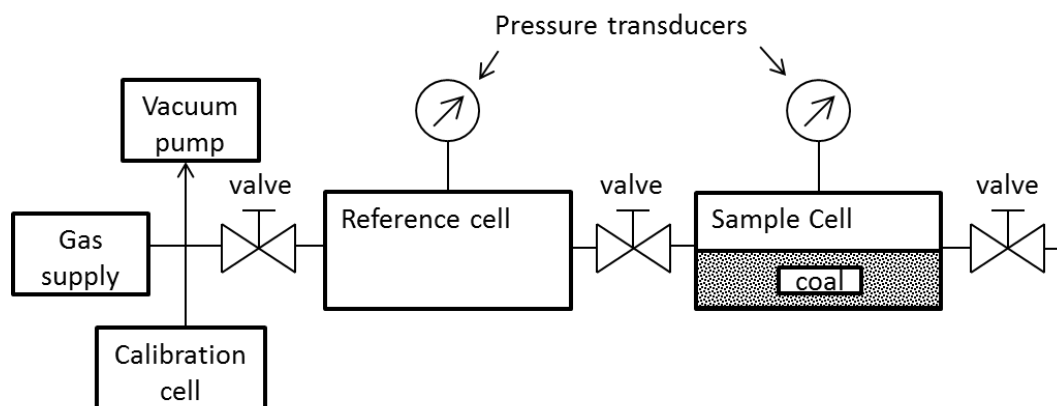


Fig. 4.10. Schematic setup for the manometric sorption measurement.

When the pressure in the reference cell stabilized, the valve connecting it to the sample cell was opened. Immediately after the cells were connected, a substantial pressure drop occurred due to the system volume increase and then slowly continued to decrease due to sorption. At higher pressures, slight fluctuations also occurred as a result of Joule-Thomson cooling effect upon gas expansion (Oldenburg et al., 2007). The sorption equilibrium was reached when the pressure within the manometric sorption cell stabilized. The above steps were repeated until the final pressure level was achieved.

Experimental injection steps used in this study for coal samples of different size are presented in Table 4.7. It can be seen that seven injection steps were applied for each coal sample. However, due to the technical problems, the last injection step both on the BD and AB 2.36-4 mm fractions could not have been conducted.

The amount of gas transferred to the reference cell (n_{inj}) is calculated using a relationship analogous to equation (4.1) taking into account volume of the reference cell V_R . The compressibility factors for CO₂ at different pressures were calculated applying an appropriate equation of state such as Span and Wagner (1996).

Table 4.7. Injection pressures used in the gas sorption measurements on coal samples of different sizes.

Sample size	Injection pressures injected into the reference cell (MPa)						
	1 st step -0.6 MPa	2 nd step -1.1 MPa	3 rd step -2.6 MPa	4 th step -4.1 MPa	5 th step -5.6 MPa	6 th step -7.1 MPa	7 th step -8.6 MPa
<i>Black Diamond</i>							
0.25-0.85 mm	0.610	1.117	2.647	4.102	5.732	7.046	8.514
2.36-4 mm	0.629	1.100	2.650	4.107	5.700	7.149	-
Core	0.616	1.108	2.610	4.084	5.593	7.145	8.604
<i>9ft Aberpergwm</i>							
0.25-0.85 mm	0.620	1.140	2.595	4.121	5.482	7.244	8.718
2.36-4 mm	0.622	1.133	2.602	4.002	5.562	7.132	-
Core	0.633	1.136	2.595	4.136	5.597	7.105	8.588

The excess sorption (n_{ads}^{ex}) can be calculated directly from experimental quantities. It is the difference between the amount of gas injected into the system up to a given pressure step and the gas amount at the free phase (Busch and Gensterblum, 2011):

$$n_{ads}^{ex} = n_{inj} - n_{unads}^{ex} \quad (4.4)$$

To measure the amount of gas sorption, first the amount of unadsorbed gas (n_{unads}^{ex}) in the free gas phase in the system at equilibrium was calculated (Busch and Gensterblum, 2011):

$$n_{unads}^{ex} = \frac{P_{eq}V_{R+S}}{Z_{R+S}RT} = c_g V_{R+S} \quad (4.5)$$

where P_{eq} is the pressure of free gas at equilibrium (Pa) and c_g is the molar density (mol.m^{-3}).

The above steps are repeated at sequentially higher pressures shown in Table 4.7 to obtain a complete sorption isotherm. Hence, the total amount of excess sorbed gas ($n_{ads}^{ex(total)}$) during the N successive pressure steps is given as:

$$n_{ads}^{ex(total)} = \sum_{i=1}^N n_i^{ex} \quad (4.6)$$

The adsorbed amount is usually presented by dividing the n_{ads}^{ex} by the mass of coal in the cell (Sudibandriyo et al., 2003).

For a sorbing gas such as carbon dioxide with high density at high pressures, the excess sorption is the amount of gas sorbed on the coal surface without occupying a specific volume for the sorbed phase (Arri et al., 1992; Ozdemir et al., 2003; Sudibandriyo et al., 2003; Mohammad et al., 2009; Busch and Gensterblum, 2011). Sorption will, however, result in non-uniform concentrations in the vicinity of the coal surface and the formation of the sorbed phase (Krooss et al., 2002). In order to calculate the absolute adsorption, the volume of space occupied by the adsorbed molecules has to be taken into account (Mohammad et al., 2009).

The void volume calculated using a non-adsorbing gas, i.e. helium, relates the various volume elements inside a manometric sorption system (Sudibandriyo et al., 2003):

$$V_{R+S} = V_{gas} + V_{ads} \quad (4.7)$$

where V_{gas} and V_{ads} are volumes taken up by the bulk gas phase and the adsorbed phase, respectively.

Since the volume of the adsorbed phase is negligible at low pressures compared to the volume of the unadsorbed phase, the unadsorbed volume, V_{gas} , approaches that of the volume measured by helium, V_{R+S} (Ozdemir et al., 2003; Mohammad et al., 2009). Therefore, the absolute amount of sorption can be considered to be analogous to the excess sorption in the low pressure region (Mohammad et al., 2009).

However, in the high pressure region above supercritical point where the volume of the adsorbed phase becomes more significant, the volume actually available to the bulk gas phase should be considered. Therefore, the absolute sorbed amount (n^{abs}) is calculated accounting for the reduction of the volume accessible to the gas as a result of the volume occupied by the adsorbed phase as (Sudibandriyo et al., 2003):

$$n^{abs} = n_{inj} - c_g V_{gas} \quad (4.8)$$

Combining equations (4.4) and (4.8) to eliminate n_{inj} and taking into account equations (4.5) and (4.7), the following relation between the excess and the absolute adsorptions is obtained (Sudibandriyo et al., 2003):

$$n_{ads}^{ex} = n^{abs} - c_g V_{ads} \quad (4.9)$$

The volume of the adsorbed phase can be expressed in terms of the amount adsorbed and the molar density of the adsorbed phase, c_{ads} , as (Sudibandriyo et al., 2003):

$$V_{ads} = \frac{n^{abs}}{c_{ads}} \quad (4.10)$$

Substituting equation (4.10) into equation (4.9) yields the relationship connecting the calculated excess sorption and the absolute sorption:

$$n_{ads}^{ex} = V_{ads}(c_{ads} - c_g) \quad (4.11)$$

Equation (4.11) illustrates the physical interpretation of the excess adsorption which is the amount adsorbed in excess of that which would be present if the adsorbed-phase volume were filled with bulk gas (Sudibandriyo et al., 2003; Mohammad et al., 2009).

Rearranging equation (4.11) yields the relationship connecting calculated excess sorption and the absolute sorption:

$$n^{abs} = \frac{n_{ads}^{ex}}{\left(1 - \frac{c_g}{c_{ads}}\right)} \quad (4.12)$$

Molar density of the adsorbed phase cannot be determined directly and certain assumptions have to be made (Busch and Gensterblum, 2011). The choice of adsorbed phase density will be discussed in Chapter 5.

The methodology described above is used to analyse the experimental results presented in Chapter 5.

4.4.3. Uniaxial Compressive Tests

In total, twenty coal specimens were tested via an unconfined uniaxial compressive test. Table 4.8 summarizes the number of specimens and saturation conditions. As presented in the table, four natural (non-saturated) specimens from each coal (BD and AB) were analysed without CO₂ saturation. Six specimens from each coal were saturated with CO₂ at designed pressures before uniaxial compression.

Table 4.8. Saturation pressures applied to the coal samples used in the uniaxial compressive tests.

Samples	Saturation pressures (MPa)		
	1 st step ~2.1 MPa	2 nd step ~4.3 MPa	3 rd step ~8.5 MPa
<i>Black Diamond</i>			
BD1, BD2, BD3, BD4		No saturation	
BD5	2.12	-	-
BD6	2.12	-	-
BD7	-	4.32	-
BD8	-	4.35	-
BD9	-	-	8.56
BD10	-	-	8.55
<i>9ft Aberpergwm</i>			
AB1, AB2, AB3, AB4		No saturation	
AB5	2.05	-	-
AB6	2.05	-	-
AB7	-	4.25	-
AB8	-	4.25	-
AB9	-	-	8.46
AB10	-	-	8.46

Results obtained on natural (non-saturated) specimens created a base reading for all other tests carried out on samples saturated with CO₂ under different saturation conditions. Saturation of samples with CO₂ at 2.1 MPa, 4.3 MPa and 8.5 MPa was conducted to investigate the effect of increasing CO₂ pressure on strength parameters of coal.

Saturation of samples with carbon dioxide was performed in the manometric sorption cell which has been used as a saturation chamber for this purpose. Before injecting CO₂, samples had been vacuumed for one hour to remove any trapped air. After that, CO₂

was injected at a certain pressure and kept constant for two weeks. Time required to prepare, saturate and test all the samples was 17 weeks.

Upon the completion of saturation, chambers were slowly depressurized to avoid any sudden change in pressure which could damage the specimens. After removing the specimens from the saturation chamber, they were wrapped in a plastic cling film and tested within a maximum time of one hour.

Uniaxial compressive tests were performed using a Shimadzu Autograph Load Cell AG-I (Shimadzu Universal Testing Instruments, 2016) with maximum load capacity of 20 kN, shown in Figure 4.11.

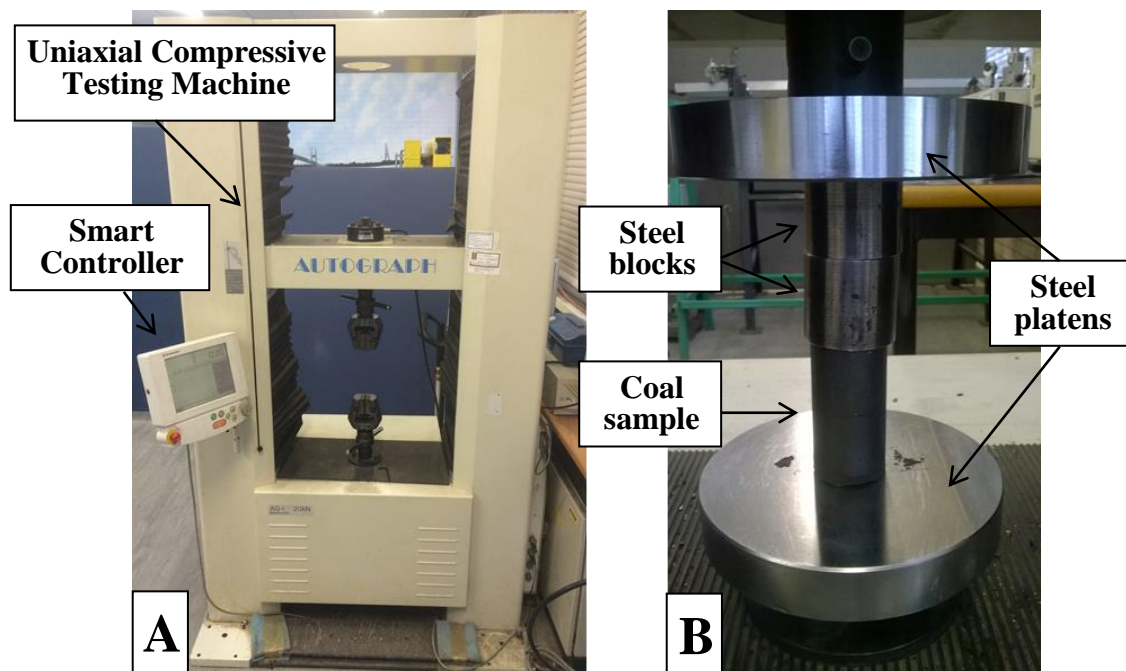


Fig. 4.11. Components of the Uniaxial Compressive Testing Machine; A) Shimadzu Load Cell, B) Position of coal specimen during the uniaxial compressive testing.

Specimens were placed between top and bottom steel platens. To minimize the impact of potential unevenness of the sample surface on measured results, two steel blocks were placed between the sample and the top platen. Blocks were able to move with respect to each other when facing uneven surface allowing equal distribution of stress on the coal specimen. Upon sample placement, the axial load on the specimen was then increased and measured continuously.

An attached smart controller showed test force and displacement in real-time, allowing fine position adjustment. Specimens were subjected to a constant loading rate of 0.1 mm/min where the axial displacement of the specimens was recorded simultaneously using the built-in displacement transducer of the loading machine. Both uniaxial compressive strength (UCS) and the value of elastic modulus (E) were calculated following the ASTM D7012 (2014). It should be noted that a common approach of calculating elastic modulus was adopted in this study where an average slope of the straight-line portion of the stress-strain curve was calculated by dividing the change in stress by the change in strain.

Results obtained using the methodology stated above are presented in Chapter 6.

4.4.3.1. Sieve Analysis

In order to get further insight into the post-failure particle size distribution, Black Diamond specimens were analysed immediately after the failure, i.e. four non-saturated specimens and six CO₂ saturated specimens. Sieves with openings of 6.3 mm, 4 mm, 2 mm, 1.18 mm, 0.6 mm and 0.425 mm were used, as shown in Figure 4.12. Calculation of the mass passing through a certain sieve followed a procedure stated in BS 1337-2 (1990). Results of the sieve analysis are presented in Chapter 6.

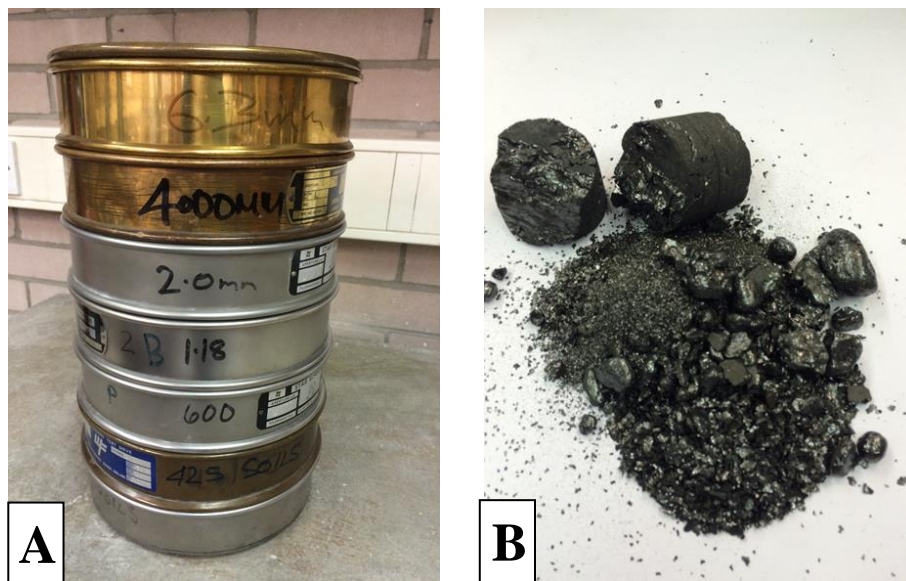


Fig. 4.12. Sieve analysis of Black Diamond coal specimens; A) Sieves, B) Example of size-distributed particles after sieving.

4.4.4. Triaxial Core Flooding System

The triaxial core flooding system was designed to investigate the deformation behaviour and gas flow properties of rocks, up to 0.1 m in diameter and 0.2 m in length (Hadi Mosleh, 2014). The setup allows continuous monitoring of confining stresses, radial and axial displacements of the sample, inlet and outlet flow rates, inlet and outlet gas pressures as well as the temperature. The system has been designed to produce high resolution data for injection pressures up to 20 MPa and temperature values up to 338K (Hadi Mosleh, 2014).

There are three main parts in the setup: 1) the triaxial cell, 2) the gas supply system 3) the auxiliary system which includes the measurement units as well as the temperature control system and confining system. Details of the system development and commissioning have been presented in Hadi Mosleh (2014). However, brief descriptions of the system and measurement procedures are introduced in the following sections.

The triaxial cell is presented in figure 4.13.

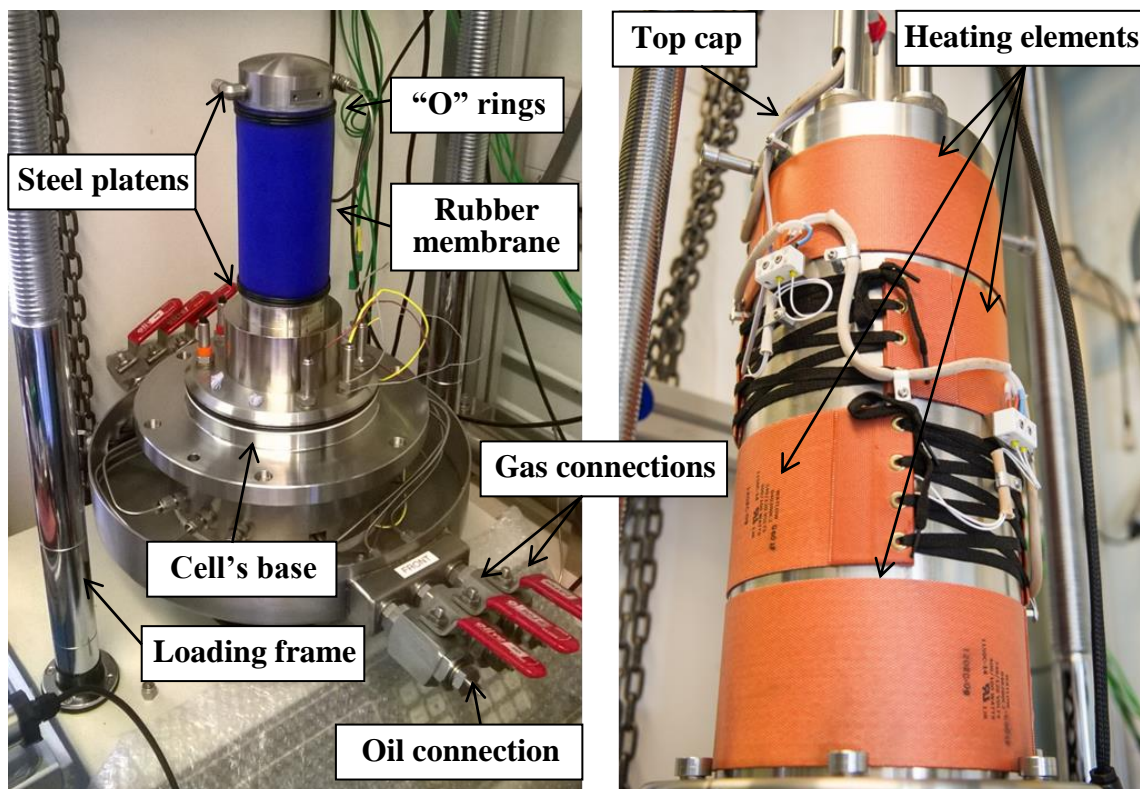


Fig. 4.13. The triaxial cell and its components (designed and commissioned by Hadi Mosleh, 2014).

The core sample is placed between a 70 mm diameter stainless steel top and bottom platens. Two 6 mm thick porous disks are placed between the sample and the platens. The sample and porous disks are placed in an approximately 1.5 mm thick silicone rubber membrane. In order to minimize gas diffusion through the membrane and slippage between the gas samples and the membrane, coal samples were wrapped in PTFE tape. For confining pressures up to approximately 5 MPa, “O” rings were sufficient to secure both ends of the membrane to the base and the top of the cell while for confining pressure larger than 5 MPa, stainless steel hose clips had to be used instead to prevent oil leakage into the sample.

Approximately 6 liters of silicone oil 350 Polydimethylsiloxane was used to fill the triaxial cell after the top cap had been placed. Upon filling completion, confining pressure of 3.1 MPa was applied for samples A, C and D while confining pressure of 5.1 MPa was applied to sample B. Such confinement filled the surface irregularities and provided an effective seal against gas bypass. Vacuuming of each sample was applied for 24 hours before the experiment in order to remove the debris and entrapped air from the pores.

4.4.4.1. Gas Flow and Permeability Measurements

In order to replicate conditions in situ, controlling and monitoring inlet and outlet gas pressures are critical. Table 4.9 presents the list of injection sequences conducted as a part of experimental studies performed and discussed in chapter 7.

Table 4.9. List of injection sequences performed during the gas flow measurement tests.

Injection sequences	Sample A	Sample B	Sample C	Sample D
1 st Helium injection	✓	✓	✓	✓
Carbon dioxide injection	✓	✓	✓	✓
2 nd Helium injection	✓	✓	✓	✓
Nitrogen saturation	-	✓	-	✓
3 rd Helium injection	-	✓	-	✓

All four samples (A, B, C and D) were first tested by sequential injection of helium, carbon dioxide and again, helium. Additionally, two samples (B and D) were saturated with nitrogen (N₂) for 48 hours after which the third helium injection followed. First

helium flow experiments were done to establish a baseline of flow rate and deformation observations without the influence of any sorption related effects. Second and third helium injections were conducted to investigate the influence of CO₂ induced swelling on gas flow and impact of N₂ on swelling reversal, respectively. As mentioned in Chapter 1, nitrogen injection was found to partially reverse the coal swelling induced by CO₂ sorption and increase permeability.

Test conditions applied during the experiments on all four samples are presented in Table 4.10.

Table 4.10. Test conditions for Black diamond coal samples during the gas flow measurement tests.

	Test conditions				
	Low pressure case		High pressure case		
	Sample A	Sample B	Sample C	Sample D	
<i>He and CO₂ Injection</i>					
Confining Pressure, MPa	5.1	5.1	10.1	10.1	
	1 st step	3.8	3.6	7.1	7.1
Injection pressure, MPa	2 nd step	4.2	4.1	7.6	7.6
	3 rd step	4.6	4.6	8.1	8.1
Backpressure, MPa	0.1	1.1	2.6	0.6	
<i>N₂ saturation</i>					
Injection pressure, MPa		3.4		5.5	
Backpressure, MPa		2.7		4.1	

It should be noted that when the experiment started, confining pressures, injection pressures and backpressures were gradually increased to the designed values. The designed values for injection pressures represent values of the 1st step shown in Table 4.10. Likewise, for confining pressures and backpressures, the values presented in Table 4.10 represent the designed values. In particular, injection pressures and backpressures were increased from the atmospheric pressure conditions and confining pressures were increased from the initial level applied during the vacuum process. Such method was applied to reduce the overall injection time since the application of high confining pressures closes the flow pathways and increases the overall experimental time.

Upon reaching the designed values, confining stresses and backpressures were kept constant in all experiments while the injection pressures were further increased in a stepwise manner. At the same time, gas flow rates at the outlet of the sample, temperature of the samples as well as axial and radial strains of the samples were measured. Based on the measured confining and gas pressures, effective stress can be calculated as the difference between the confining pressure and mean pore (gas) pressure (Harpalani and Chen, 1997). The latter one represents the average of injection pressure and backpressure (Gensterblum et al., 2014).

Steady-state method is a routine permeability measurement method used to estimate the permeability of the coal samples to helium and carbon dioxide in this study. In this approach, both inlet and outlet gas pressures are kept constant while the gas flow rate flowing out of the sample is monitored (Tanikawa and Shimamoto, 2006). Taking into account that the mass flux is constant along the sample, the permeability of gases is evaluated using Darcy's equation for compressible gases (Durucan and Edwards, 1986; Tanikawa and Shimamoto, 2006; Gensterblum et al., 2014):

$$K_g = \frac{2P_0 Q_g L \mu_g}{A(P_1^2 - P_2^2)} \quad (4.13)$$

where K_g is the measured permeability to gas (m^2), Q_g is the volumetric flow rate monitored at the outlet of the sample (m^3/s), μ_g is the gas viscosity ($\text{Pa}\cdot\text{s}$), L is the sample length (m), A is the cross-sectional area of the sample (m^2), P_1 and P_2 are the inlet and outlet gas pressures (Pa), respectively. P_0 represents the gas pressure at which the flow rate is measured (Durucan and Edwards, 1986).

The viscosity of gases was calculated at the mean gas pressure using the National Institute of Standards and Technology webbook (Linstrom and Mallard, 2016). The methodology described in this section is used to calculate permeability values based on the experimental data which will be presented in Chapter 7.

4.4.4.2. Deformation Measurements

Radial and axial strains were measured by taking local strain measurements, achieved through placement of two axial and one radial high pressure Linear Variable Differential Transformer (LVDT) local strain transducers on to the sample, as shown in Figure 4.14. Each axial transducer is fixed to the silicone membrane via two mounting blocks which displace relative to one another as the sample deforms. The local radial strain is measured by securing the calliper via two mounting pads 180° apart making the calliper a set of jaws that opens as the sample expands laterally, or closes during lateral contraction of the coal (Rees, 2013). This results in a displacement measurement twice that of the change in sample diameter when undergoing deformation. All displacement transducers can measure the change in sample deformation up to 0.0001 mm.

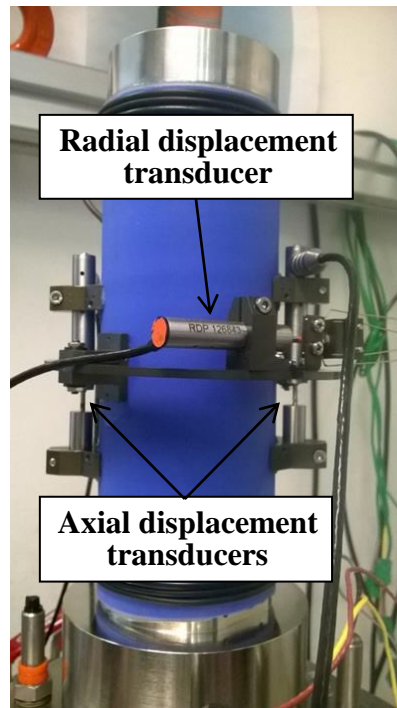


Fig. 4.14. Measurement of axial and radial deformation (designed and commissioned by Hadi Mosleh, 2014).

A convention that tensile strain is measured positive was adopted in this work as a common approach used in the literature investigating the swelling of coal induced by gas sorption (e.g. Day et al., 2008; Majewska et al., 2009; Espinoza et al., 2014). Based on the measurement of displacements both in radial and axial direction, volumetric

strain was calculated by adding two radial strains to the axial strain as (Pan et al., 2010; Lin and Kovscek, 2014):

$$\varepsilon_V = 2 \cdot \varepsilon_R + \varepsilon_A \quad (4.14)$$

where ε_V , ε_R and ε_A stand for volumetric, radial and axial strains, respectively.

It should be noted that after every gas injection sequence, confining pressures were decreased back to the initial condition, i.e. 3.1 MPa for samples A, C and D, and 5.1 MPa for sample B. Likewise, injection pressures and backpressures were decreased back to the atmospheric conditions after which a vacuum was applied for 48 hours to remove gas injected at the previous injection sequence. Since the reversibility of the volumetric strain was not the focal point of this study, measured strain at the end of every gas injection sequence, when the confining stress was restored back to its initial value, was taken as a reference (zero) strain for the following injection sequence.

Deformation of the silicone sleeve and the PTFE tape might slightly influence the measured strains during the initial increase in pressures. However, under the conditions of constant confining pressure and backpressure where only the injection pressure changed, it was assumed that such deformation is negligible in comparison to the coal deformation. This is supported by the fact that standard rubber jackets used in core flooding experiments are slightly deformable changing its thickness for 0.001 mm when exposed to the change in pressure for 6.2 MPa (e.g. Wang et al., 2015).

The triaxial core flooding apparatus has also been developed to measure the volumetric strain of the samples by using the volume of the displaced silicone oil in the oil pressure controller (Hadi Mosleh, 2014). However, it is believed in this work that such measurements could provide inaccurate results due to the fact that the pressure controller does not work under isothermal conditions, i.e. does not have a temperature controlling unit. Hence, any change in the room temperature could affect the volumetric measurements using such approach.

4.4.4.3. Temperature Measurements

Temperatures both at the inlet and the outlet of the samples were measured. The position of the thermocouples is shown in Figure 4.15.

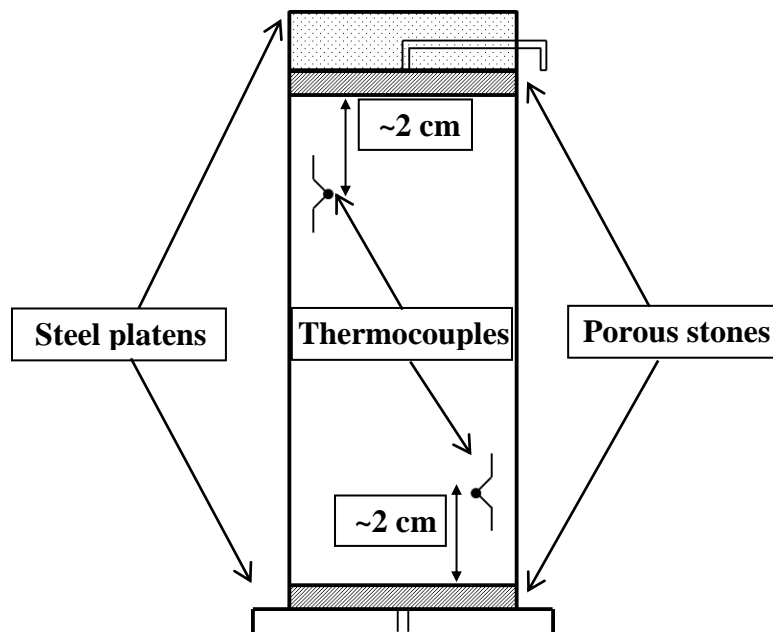


Fig. 4.15. Schematic of the position of thermocouples during the temperature measurement.

The thermocouples were fixed directly on the silicone sleeve. It can be seen from Figure 4.15 that the thermocouples were placed at the opposite sides of the sample, approximately 2 cm from the porous disks, to better represent the temperature across the sample due to coal's heterogeneity.

The purpose of temperature measurements was to register any potential changes in temperature across the sample during gas injection. Results of temperature measurements both for helium and carbon dioxide injection will be presented in Chapter 7.

4.4.5. Gas Supply System

The gas supply unit has been designed by Hadi Mosleh (2014) to deliver different gases at controlled pressures and temperatures to both the manometric apparatus and the triaxial core flooding system.

The designed system consists of (Hadi Mosleh, 2014):

- Four gas cylinders (CO₂, N₂, CH₄, He).
- An air driven gas booster.
- Four pairs of high pressure gas reservoirs.
- Auxiliary units including regulators, valves, pipelines and hoses.

The basic idea, as explained by Hadi Mosleh (2014), was that for low pressure flow experiments, the experimental gas would be supplied directly from the gas cylinders. For high pressure flow experiments, the gas booster would pressurize the gas taken from the gas cylinders and store it in a pressurized form in pairs of high pressure gas reservoirs where it would be subsequently extracted during the experiment (see Fig. 4.8).

Hence, using the same equipment, the high pressure injection of helium and nitrogen was easily performed directly from cylinders pressurized up to 23 MPa while injection of supercritical carbon dioxide was more difficult to achieve. One of the reasons is that CO₂ is stored in cylinders only at pressures up to 5 MPa and at room temperature. Secondly, stable high-flow CO₂ was difficult to maintain with the existing equipment due to the high sensitivity of gas density to the temperature and the oscillatory performance of the gas booster with limited capacity and speed. For that purpose, a new gas supply unit consisting of a dual syringe pump system was added to the existing system which allowed continuous injection of CO₂ under controlled temperature.

Moreover, the existing setup offered injection of gases under atmospheric conditions where the gas leaving the core was allowed to flow directly to the atmosphere. As the purpose of this work was to assess the response of coal by applying different backpressures and injection pressures, the existing system was modified to allow backpressure control.

More details on the existing gas supply unit can be found in Hadi Mosleh (2014). In the following sections, details of the new gas supply system as well as the backpressure controlling unit are provided.

4.4.5.1. High Pressure Gas Supply Units

A high pressure injection system was employed to pressurize gases to the required experimental pressures (Figure 4.16). The system includes:

- A pair of high pressure pumps working in a dual mode.
- A single pump working in an independent mode.
- A temperature controller.
- A valve package.

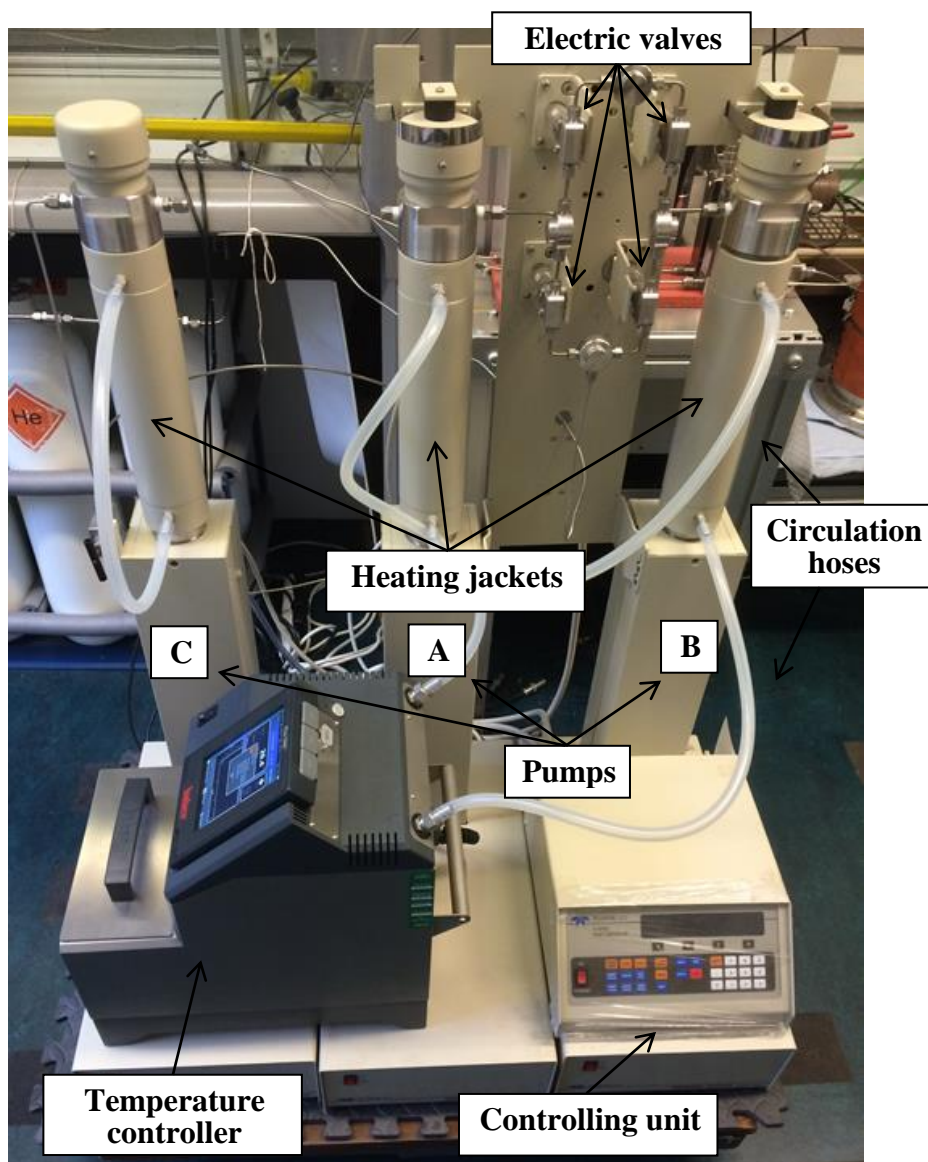


Fig. 4.16. High pressure gas supply system consisting of Teledyne Isco pumps, controlling unit and temperature controller.

In total, three high pressure Teledyne Isco 500D pumps (Teledyne Isco Syringe Pumps, 2016) were employed to ensure constant and pulseless flow of high pressure gas. All pumps can be run either in “constant pressure mode” or “constant flow mode”. The system has been designed in a way that two pumps, i.e. pumps A and B are run in a dual mode providing constant pressure to the system. In dual mode, pumps run simultaneously, i.e. while one pump is providing gas the other one is being refilled, ensuring smooth and uninterrupted flow of gas.

Pumps are connected to a liquid withdrawal carbon dioxide cylinder with 99.99% purity in which the tube runs down the centre of the pressurized cylinder and draws the liquid up through the valve. Due to possible contaminants within the cylinder, a filter was fitted at the top of the cylinder. The continuous flow system contains an electric valve package which provides the best positive valve closure and controls both the filling and the injection processes.

The capabilities and characteristics of the Teledyne Isco 500D pumps are given in Table 4.11. It should be noted that the syringe pump system can be run through LabView software or manually through a controlling unit.

Table 4.11. Specifications of Teledyne Isco 500D pumps (Teledyne Isco, 2016).

Specifications	Value
Capacity	507.38 mL
Flow range	0.001-204 mL/min
Flow accuracy	± 0.5%
Pressure range	0.7 – 258.6 bar
Standard pressure accuracy	0.5% FS
Operating temperature	278 – 313K

Constant temperature in the pumps was achieved using a Huber Pilot One Ministat 125 temperature controller which circulates deionized water contained in the 2.75 dm³ water tank through the heating jackets. The jackets are rated from -35 to 100°C; however, the operational temperature of the temperature controller is 5-35°C. In the experiment, the temperature of carbon dioxide was increased above its critical temperature within the pumps and then further increased to the desired value in the pipeline through glass-fibre heating tapes placed around the pipes connecting the high pressure injection unit and the triaxial cell.

4.4.5.2. Backpressure Units

Multiple pumps, i.e. pumps A and B can also be run in a constant pressure receive mode serving as a backpressure regulator. In that case, pump C can be used as an injection pump providing gas to the system. However, such a setup is applicable to experiments with low flow due to the limited volume of pump C.

During gas injection using multiple pumps (A and B), control of the backpressure in the system can be also achieved through a Swagelok medium- to high-pressure piston-sensing backpressure regulator (Figure 4.17). The regulator is made of stainless steel and can work with pressures up to 140 bar and temperatures between 10-60°C.



Fig. 4.17. Swagelok backpressure regulator.

4.4.6. Auxiliary Units

A list of the auxiliary units and their specifications is given in Table 4.12. All of the listed units are part of the existing laboratory facility designed by Hadi Mosleh (2014).

Table 4.12. List and specifications of auxiliary units (Hadi Mosleh, 2014).

Auxiliary units	Range	Accuracy	Provided by
Pressure transducers	up to 32 MPa	0.15%	GDS Instruments
Pressure/Volume controller	up to 32 MPa	0.1%	GDS Instruments
Flow meters	$3 \times 10^{-7} - 23 \times 10^{-7} \text{ m}^3/\text{s}$	0.5% RD	Bronkhorst
Vacuum pump	-0.09 MPa	-	Buchi
Triaxial cell temp. controller	up to 338K (65°C)	-	GDS Instruments

Each component is used as follows:

- Four pressure transducers are used within the system. Two are placed at the top of the manometric sorption apparatus measuring gas pressures at the reference and sample cells, while two in-line pore pressure transducers measure the inlet and outlet gas pressures of the core flooding system.
- The Pressure/Volume controller, connected directly to the triaxial cell, with a $2 \times 10^{-4} \text{ m}^3$ oil reservoir is employed to pressurize the hydraulic oil in the triaxial cell.
- Two digital mass flow meters measure the inlet and outlet gas flow rates.
- The vacuum pump is used to evacuate both the manometric sorption system and the core flooding system including the pipeline and the valves to avoid any contamination of injected gases with residual moisture or gases from the atmosphere of previous experiments.
- The triaxial cell temperature controller is used to maintain isothermal conditions inside the cell during the experiment by controlling four heating elements (see Fig. 4.13)

The laboratory facility also contains a digital three-zone temperature controller with glass-fiber heater tapes to control the temperature of the pipeline and the calibration cylinder used in helium pycnometry method. Additional capabilities of the system have been provided in Hadi Mosleh (2014).

All measured pressures, temperatures, flow rates and displacements can be continuously monitored and recorded using the GDSLab software. It should be noted that during the core flooding measurements and sorption measurements, high-resolution data was collected every one second and every ten seconds, respectively.

4.5. Conclusions

Details of the sampling methods both for powdered coal samples and core samples of both coals used in this study were presented this chapter. In addition, physical characteristics and dimensions of all coal samples were provided. Powdered coal

samples with grain sizes of 0.25-0.85 mm and 2.36-4 mm and coal cores 3.6 cm and 4.4 cm in diameter were used for the gas sorption measurements. Twenty coal cores 3.6 cm in diameter and the average length-to-diameter ratio of 1.8-2.1 were used for uniaxial compressive tests. Four coal cores 7 cm in diameter and 9.2-11.5 cm in length were used for gas flow experiments using the triaxial core flooding system. In total, thirty coal samples were tested in this study.

The chemical, petrographic and combustion properties of the coal samples used in this study were investigated. The results showed that the coals of this study are high rank coals with approximately 90% of carbon content. The average bulk density of both coals was calculated to be 1376 kg/m³.

The experimental facility, previously designed and commissioned by Hadi Mosleh, (2014) was briefly explained. This included a description of the manometric sorption apparatus, the triaxial core flooding system and the auxiliary units consisting of measurement units, temperature and pressure controllers. As a part of this work, new high pressure gas supply equipment was added and the existing laboratory facility was modified to allow the control of backpressures within the core flooding system. Specifications and capabilities of the new system were explained.

Experimental procedures for sorption measurements, including the helium pycnometry method for the void volume measurements, were presented. Furthermore, methodology of deformation analysis performed on core samples was shown. As a part of the triaxial core flooding tests, measurement practices related to coal permeability, deformation and temperature of the system were provided.

4.6. References

Arri, L.E. , Yee, D., Morgan, W.D. and Jeansonne, M.W. 1992. Modeling coalbed methane production with binary gas sorption. In *SPE Rocky Mountain Regional Meeting*, Society of Petroleum Engineers.

ASTM Standards, 2008. *ASTM D4543. Standard Practices for Preparing Rock Core as Cylindrical Test Specimens and Verifying Conformance to Dimensional and Shape Tolerances. Vol. 04.08*. West Conshohocken, PA: ASTM International.

ASTM Standards, 2012. *ASTM D2013. Standard practice of preparing coal samples for analysis. Vol. 05.06*. West Conshohocken, PA: ASTM International.

ASTM Standards, 2014. *ASTM D7012. Standard Test Methods for Compressive Strength and Elastic Moduli of Intact Rock Core Specimens under Varying States of Stress and Temperatures. Vol. 04.09.* West Conshohocken, PA: ASTM International.

ASTM Standards, 2015. *ASTM D388. Standard Classification of Coals by Rank. Vol. 05.06.* West Conshohocken, PA: ASTM International.

ASTM Standards, 2015. *ASTM D3302/D3302M. Standard Test Method for Total Moisture in Coal. Vol. 05.06.* West Conshohocken, PA: ASTM International.

British Standards Institution, 1990. *BS 1377-2:1990. Methods of test for soils for civil engineering purposes. Classification tests.* Milton Keynes: BSI.

British Standards Institution, 1996. *BS 1016-106.1.1:1996. Methods for analysis and testing of coal and coke. Ultimate analysis of coal and coke. Determination of carbon and hydrogen content, high temperature combustion method.* Milton Keynes: BSI.

British Standards Institution, 1996. *BS 1016-106.4.2:1996. Methods for analysis and testing of coal and coke. Ultimate analysis of coal and coke. Determination of total sulfur content, high temperature combustion method.* Milton Keynes: BSI.

British Standards Institution, 1998. *BS 1016-104.3:1998. Methods for analysis and testing of coal and coke. Proximate analysis, determination of volatile matter content.* Milton Keynes: BSI.

British Standards Institution, 1998. *BS 1016-104.4:1998. Methods for analysis and testing of coal and coke. Proximate analysis, determination of ash.* Milton Keynes: BSI.

British Standards Institution, 1999. *BS 1016-104.1:1999. Methods for analysis and testing of coal and coke. Proximate analysis, determination of moisture content of the general analysis test sample.* Milton Keynes: BSI.

Busch, A. and Gensterblum, Y. 2011. CBM and CO₂-ECBM related sorption processes in coal: A review. *International Journal of Coal Geology*, 87(2), pp. 49-71.

Day, S., Fry, R. and Sakurovs, R. 2008. Swelling of Australian coals in supercritical CO₂. *International Journal of Coal Geology*, 74, pp. 41-52.

Durucan, S. and Edwards, J.S. 1986. The effects of stress and fracturing on permeability of coal. *Mining Science and Technology*, 3, pp. 205-216.

Espinoza, D.N., Vandamme, M., Pereira, J.-M., Dangla, P. and Vidal-Gilbert, S. 2014. Measurement and modeling of adsorptive-poromechanical properties of bituminous coal cores exposed to CO₂: Adsorption, swelling strains, swelling stresses and impact on fracture permeability. *International Journal of Coal Geology*, 134-135, pp. 80-95.

Gathitu, B.B., Chen, W.Y. and McClure, M. 2009. Effects of Coal Interaction with Supercritical CO₂: Physical Structure. *Industrial & Engineering Chemistry Research*, 48(10), pp. 5024-5034.

Gensterblum, Y. 2013. *CBM and CO₂-ECBM related sorption processes in coal.* Ph.D. Thesis, RWTH Aachen University, Germany.

Gensterblum, Y., Ghanizadeh, A. and Krooss, B.M. 2014. Gas permeability measurements on Australian subbituminous coals: Fluid dynamic and poroelastic aspects. *Journal of Natural Gas Science and Engineering*, 19, pp. 202-214.

Hadi Mosleh, M. 2014. *An experimental Investigation of Flow and Reaction Processes during Gas Storage and Displacement in Coal*. Ph.D. Thesis, Cardiff University, Wales, UK.

Harpalani, S. and Chen, G. 1997. Influence of gas production induced volumetric strain on permeability of coal. *Geotechnical and Geological Engineering*, 15, 303-325.

Jones, N.S., Holloway, S., Smith, N.J.P., Browne, M.A.E., Creedy, D.P., Garner, K. and Durucan, S. 2004. *UK Coal Resource for New Exploitation Technologies*. DTI Report No. COAL R271, DTI/Pub URN 04/1879. DTI Cleaner Coal Technology Transfer Programme, Harwell.

Krooss, B.M., van Bergen, F., Gensterblum, Y., Siemons, N., Pagnier, H.J.M. and David, P. 2002. High-pressure methane and carbon dioxide adsorption on dry and moisture-equilibrated Pennsylvanian coals. *International Journal of Coal Geology*, 51 (2), pp. 69-92.

Lin, W. and Kavscek, A.R. 2014. Gas Sorption and the Consequent Volumetric and Permeability Change of Coal I: Experimental. *Transport in Porous Media*, 105(2), pp. 371-389.

Linstrom, P.J. and Mallard, W.G., Eds. NIST Chemistry WebBook, NIST Standard Reference Database Number 69, National Institute of Standards and Technology, Gaithersburg MD, 20899, <http://webbook.nist.gov>, (retrieved October 20, 2016).

Liu, C.J., Wang, G.X., Sang, S.X. and Rudolph, V. 2010. Changes in pore structure of anthracite coal associated with CO₂ sequestration process. *Fuel*, 89(10), pp. 2665-2672.

Liu, Z., Feng, Z., Zhang, Q., Zhao, D. and Guo, H. 2015. Heat and deformation effects on coal during adsorption and desorption of carbon dioxide. *Journal of Natural Gas Science and Engineering*, 25, pp. 242-252.

Majewska, Z., Ceglarska-Stefańska, G., Majewski, S. and Ziętek, J. 2009. Binary gas sorption/desorption experiments on a bituminous coal: Simultaneous measurements on sorption kinetics, volumetric strain and acoustic emission. *International Journal of Coal Geology*, 77 (1-2), pp. 90-102.

Mohammad, S., Fitzgerald, J., Robinson Jr., R.L. and Gasem, K.A.M. 2009. Experimental Uncertainties in Volumetric Methods for Measuring Equilibrium Adsorption. *Energy & Fuels*, 23, pp. 2810-2820.

Oldenburg, C.M. 2007. Joule-Thomson cooling due to CO₂ injection into natural gas reservoirs. *Energy Conversion and Management*, 48(6), pp. 1808-1815.

Ozdemir, E., Morsi, B.I. and Schroeder, K. 2003. Importance of Volume Effects to Adsorption Isotherms of Carbon Dioxide on Coals. *Langmuir*, 19, pp. 9764-9773.

Pan, Z., Connell, L.D. and Camilleri, M. 2010. Laboratory characteristics of coal reservoir permeability for primary and enhanced coalbed methane recovery. *International Journal of Coal Geology*, 82(3), pp. 252-261.

Perera, M.S.A., Ranjith, P.G. and Peter, M. 2011. Effects of saturation medium and pressure on strength parameters of Latrobe Valley brown coal: Carbon dioxide, water and nitrogen saturations. *Energy*, 36(12), pp. 6941-6947.

Perera, M.S.A., Ranjith, P.G. and Viète, D.R. 2013. Effects of gaseous and super-critical carbon dioxide saturation on the mechanical properties of bituminous coal from the Southern Sydney Basin. *Applied Energy*, 110, pp. 73-81.

Ranathunga, A.S., Perera, M.S.A., Ranjith, P.G. and Bui, H. 2016. Super-critical CO₂ saturation-induced property alterations in low rank coal: An experimental study. *The Journal of Supercritical Fluids*, 109, pp. 134-140.

Ranjith, P.G. and Perera, M.S.A. 2012. Effects of cleat performance on strength reduction of coal in CO₂ sequestration. *Energy*, 45(1), pp. 1069-1075.

Rees, S. 2013. GDS Advanced Triaxial Testing: Part 2. <http://www.gdsinstruments.com/> (retrieved November 14, 2016).

Rodrigues, C.F. and Lemos de Sousa, M.J. 2002. The measurement of coal porosity with different gases. *International Journal of Coal Geology*, 48(3-4), pp. 245-251.

Shimadzu Universal Testing Instruments, Autograph AG-IS Series. <http://www.ssi.shimadzu.com/products/literature/testing/agis.pdf>, (retrieved November 14, 2016).

Span, R. and Wagner, W. 1996. A new equation of state for carbon dioxide covering the fluid region from the triple-point temperature to 1100 K at pressures up to 800 MPa. *Journal of Physical and Chemical Reference Data*, 25(6), pp. 1509-1596.

Speight, J.G. 2005. *Handbook of coal analysis*. Hoboken, New Jersey: John Wiley & Sons, Inc.

Sudibandriyo, M. 2004. Measurement of methane, nitrogen and carbon dioxide adsorption on wet selected coals. *Proceedings of Seminar Nasional Teknologi Proses Kimia VI*. Jakarta, March 31, 2004, pp. 1-9.

Sudibandriyo, M., Pan, Z., Fitzgerald, J.E., Robinson Jr., R.L. and Gasem, K.A.M. 2003. Adsorption of Methane, Nitrogen, Carbon dioxide, and Their Binary Mixtures on Dry Activated Carbon at 318.2 K and Pressures up to 13.6 MPa. *Langmuir*, 19, pp. 5323-5331.

Tanikawa, W. and Shimamoto, T. 2006. Klinkenberg effect for gas permeability and its comparison to water permeability for porous sedimentary rocks. *Hydrology and Earth System Sciences*, 3, pp. 1315-1338.

Teledyne Isco Syringe Pumps, 500D Syringe Pump Data Sheet. <http://www.isco.com> (retrieved November 15, 2016)

Thomas, L. 2013. *Coal Geology*, 2nd Edition, John Wiley & Sons, Ltd.

Viète, D.R. and Ranjith, P.G. 2006. The effect of CO₂ on the geomechanical and permeability behaviour of brown coal: Implications for coal seam CO₂ sequestration. *International Journal of Coal Geology*. 66 (3), pp. 204-216.

Wang, Y., Liu, S. and Elsworth, D. 2015. Laboratory investigations of gas flow behaviors in tight anthracite and evaluation of different pulse-decay methods on permeability estimation. *International Journal of Coal Geology*, 149, pp. 118-128.

5

CO₂ Sorption and Kinetics Behaviour

5.1. Introduction

This chapter presents the results of a series of carbon dioxide sorption measurements using the manometric sorption apparatus. The methodology of the measurements as well as the description of the samples used is provided in Chapter 4. The main aims of the study presented in this chapter are: i) to understand the sorption behaviour of CO₂ in samples of different sizes under equilibrium conditions, ii) to investigate the kinetics of the sorption behaviour of CO₂ in samples of different sizes, iii) to assess and compare the response of coals of the same rank, but from different locations and depths, to CO₂ injection, iv) to obtain sorption parameters required for the validation of the numerical model presented in Chapter 3.

Pressure decay curves for all samples from both coals measured at different gas injection pressures are presented in Section 5.2. The time for the gas pressures to reach equilibrium is discussed and compared, for samples of different sizes.

Based on the values of gas pressures injected into the system during each injection step and pressure decay experimental results, the excess sorption values as a function of equilibrium pressure on all samples are presented and analysed in Section 5.3.

Following a discussion in Section 5.3, absolute sorption amounts are calculated and compared for each sample in Section 5.4. The Langmuir adsorption model is fitted to the calculated absolute adsorption amounts. As a result, sorption parameters related to the sorption of carbon dioxide on coal are derived for all samples of both BD and AB coals. A discussion of the results is also provided.

Section 5.5 presents the results of the sorption kinetics of CO₂ on samples from both coals. The kinetic aspects of CO₂ sorption on samples of different sizes are explored using first-order and second-order rate functions. Using these functions, fitting parameters related to the kinetics of CO₂ sorption are obtained and analysed.

The overall conclusions of the chapter are presented in Section 5.6.

5.2. Experimental Pressure Decay Results

The literature review presented in Chapter 2 showed that most of the experimental investigations on gas sorption in coal have mainly focused on gas sorption capacity and kinetics measurements of powdered coals, while experimental investigation on sorption behaviour of larger coal samples has received less attention. In this section, experimental data related to the pressure drop, associated with gas sorption, measured over time after connecting the reference cell to the sample cell is presented for three samples of different sizes of both coals of this study. The results obtained will be used in the following sections to assess the sorption capacity and kinetics behaviour of coals. The manometric sorption apparatus and measurement methodology described in Chapter 4 was used to perform the gas sorption measurements.

Experimental results of the manometric sorption measurements are presented in Figures 5.1–5.14. Every figure shows the pressure measured as a function of time for three samples of different sizes, i.e. powdered coal samples with grain sizes of 0.25-0.85 mm and 2.36-4 mm, and coal cores. The exceptions are Figures 5.13 and 5.14 which show pressure decay curves for samples with grain size of 0.25-0.85 mm and cores.

Figures 5.1 and 5.2 show pressure decay curves during the first injection step for BD and AB samples, respectively. Using the same approach, the following two figures (Fig. 5.3 and 5.4) contain pressure decay curves during the second injection step for BD and AB samples, respectively. In a similar manner, pressure decay results for samples of both coals (BD and AB) for third, fourth, fifth, sixth and seventh injection steps are presented in Figures 5.5 and 5.6, Figures 5.7 and 5.8, Figures 5.9 and 5.10, Figures 5.11 and 5.12, and Figures 5.13 and 5.14, respectively.

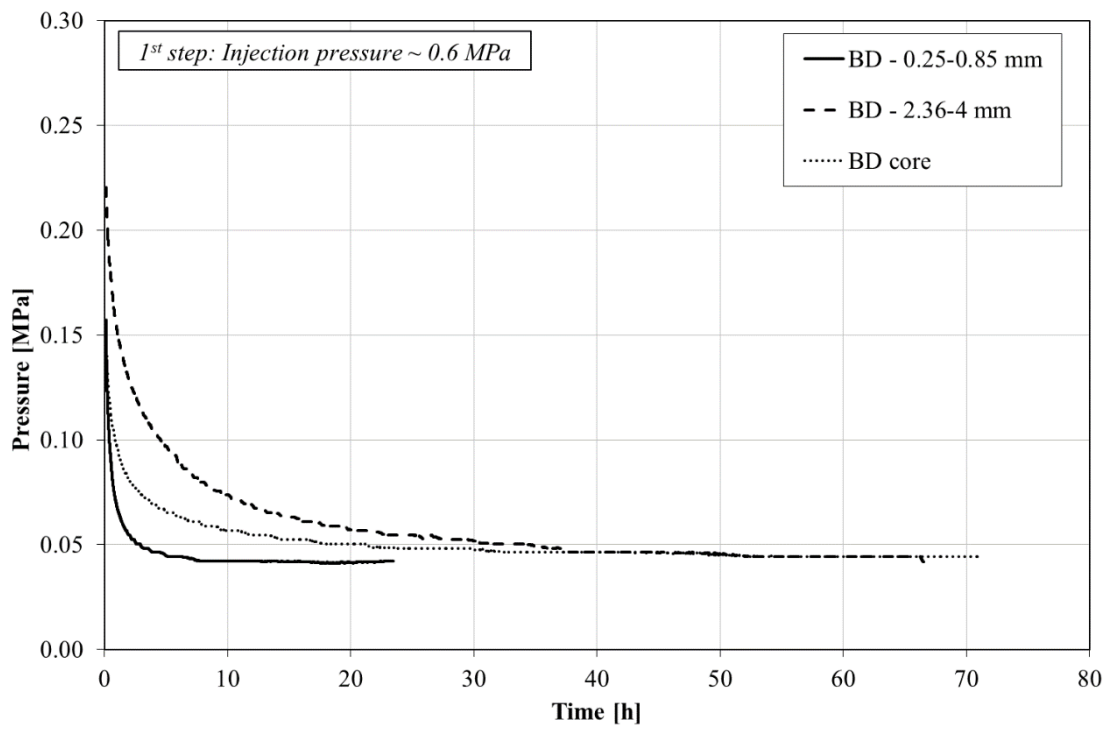


Fig. 5.1. Pressure decay curves for three Black Diamond samples of different sizes - The 1st injection step.

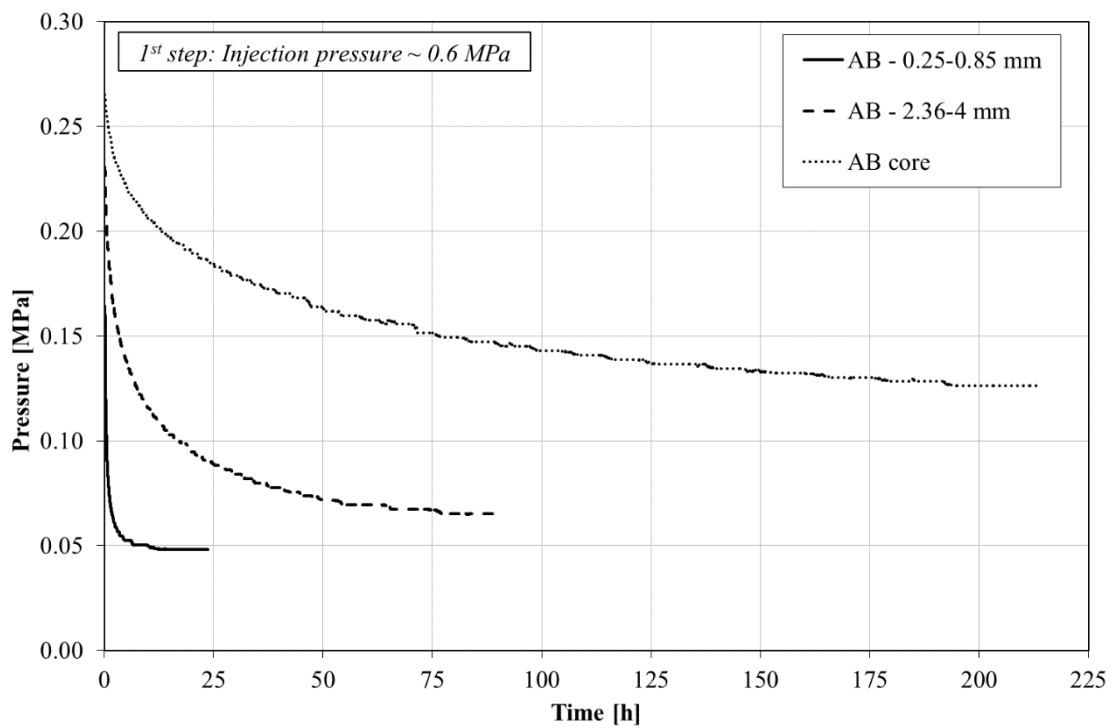


Fig. 5.2. Pressure decay curves for three 9ft Aberpergwm samples of different sizes - The 1st injection step.

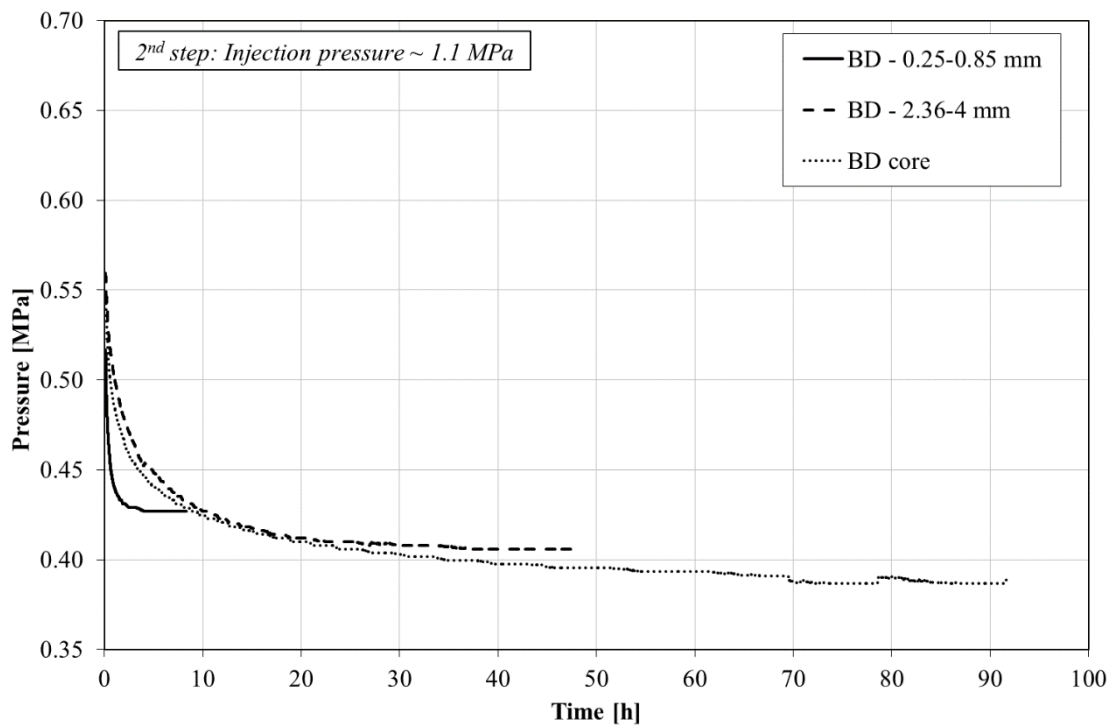


Fig. 5.3. Pressure decay curves for three Black Diamond samples of different sizes - The 2nd injection step.

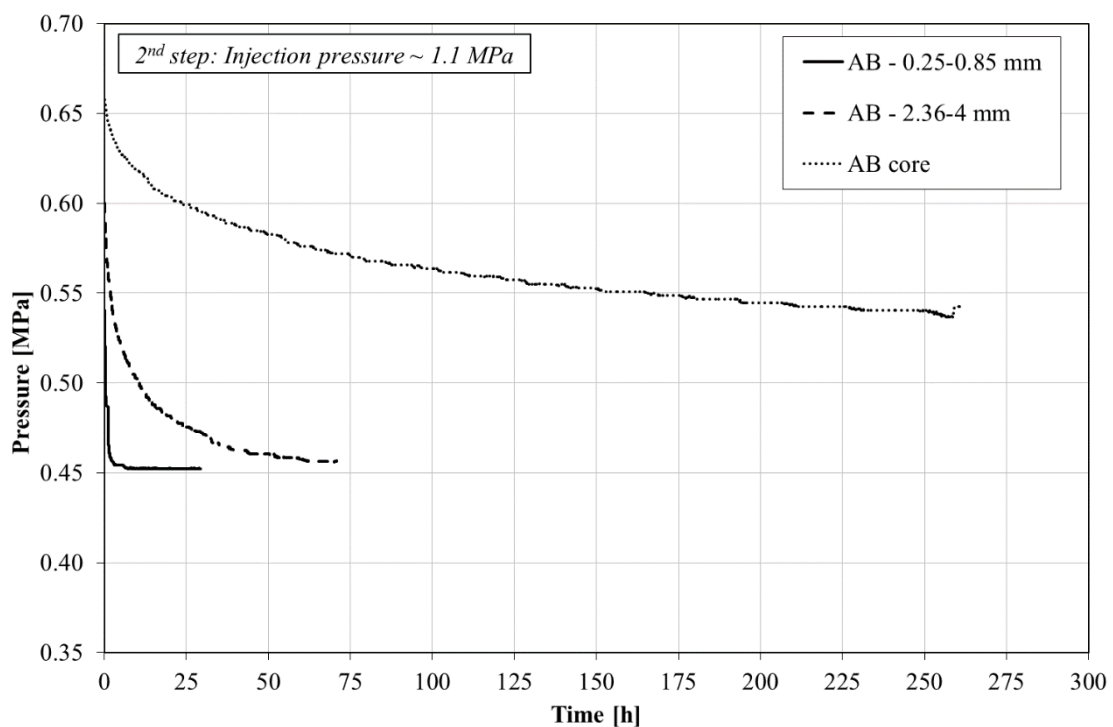


Fig. 5.4. Pressure decay curves for three 9ft Aberpergwm samples of different sizes - The 2nd injection step.

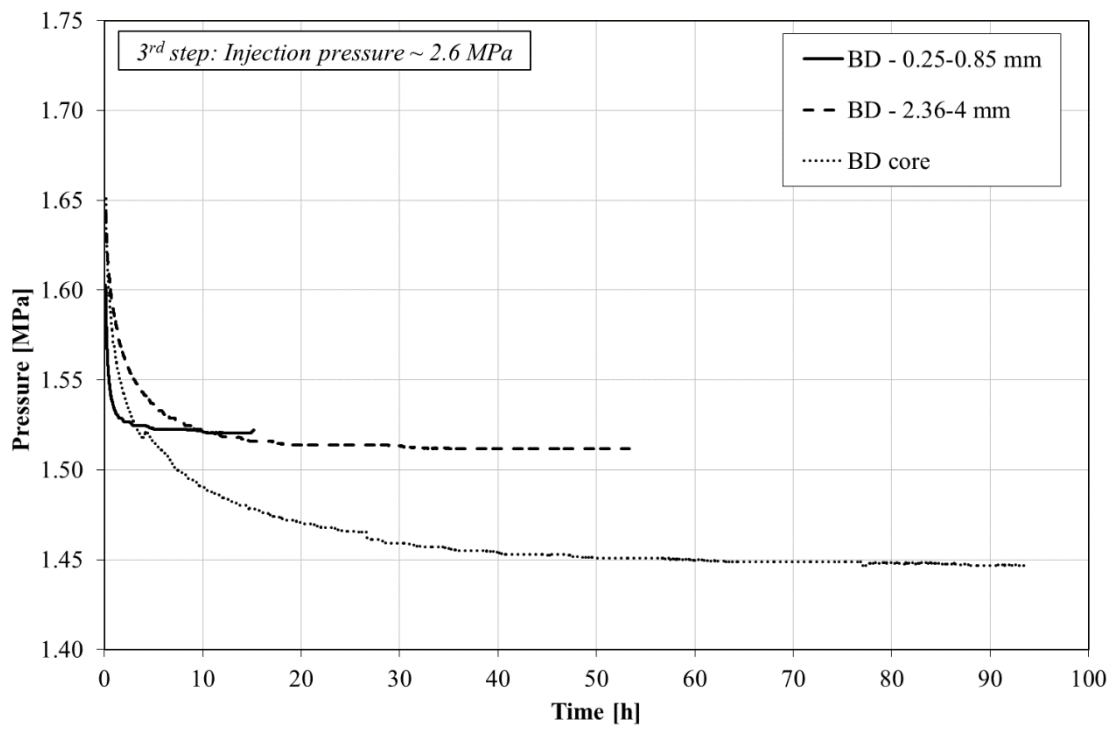


Fig. 5.5. Pressure decay curves for three Black Diamond samples of different sizes - The 3rd injection step.

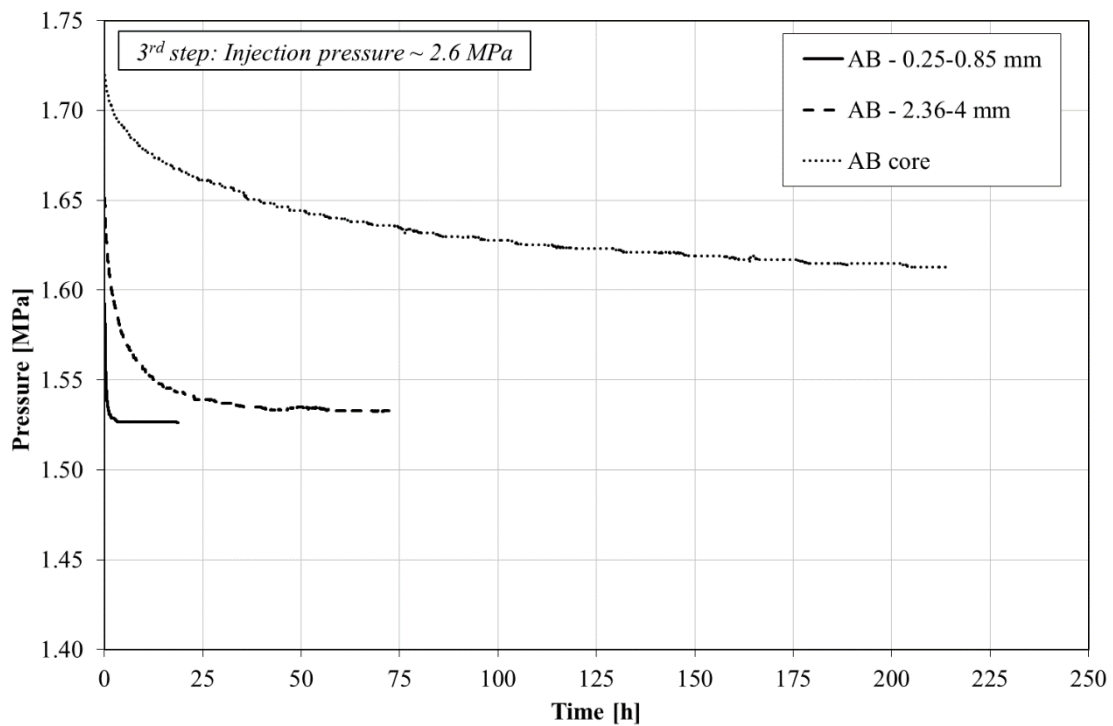


Fig. 5.6. Pressure decay curves for three 9ft Aberpergwm samples of different sizes - The 3rd injection step.

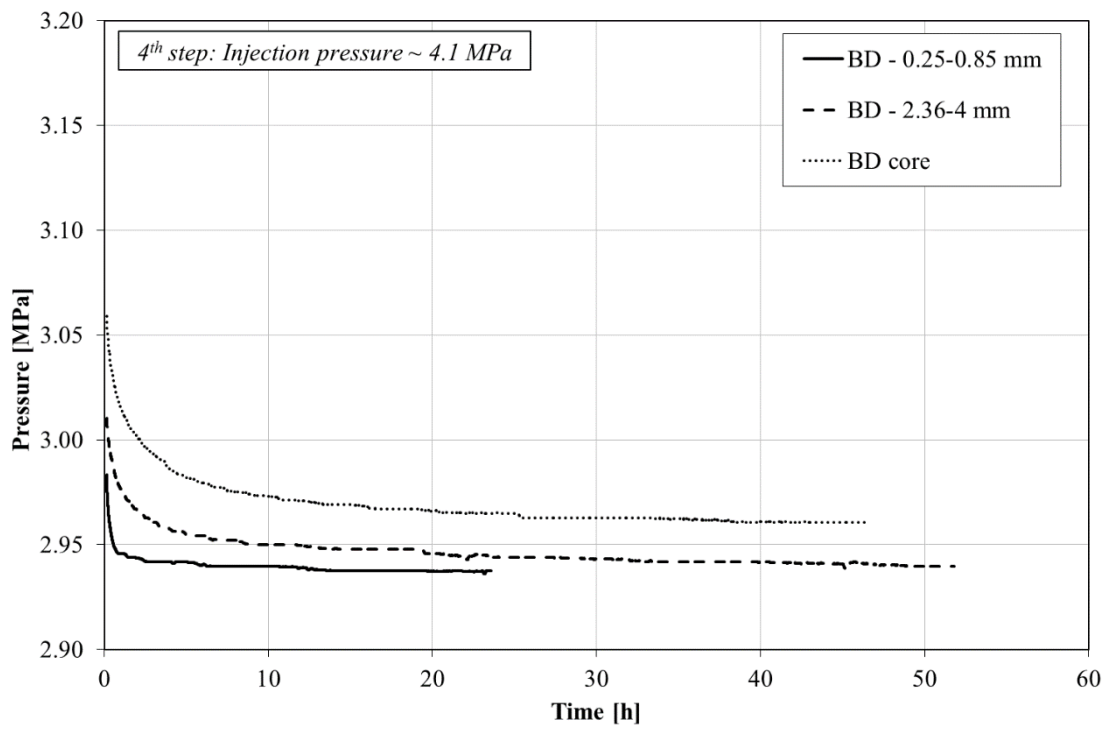


Fig. 5.7. Pressure decay curves for three Black Diamond samples of different sizes - The 4th injection step.

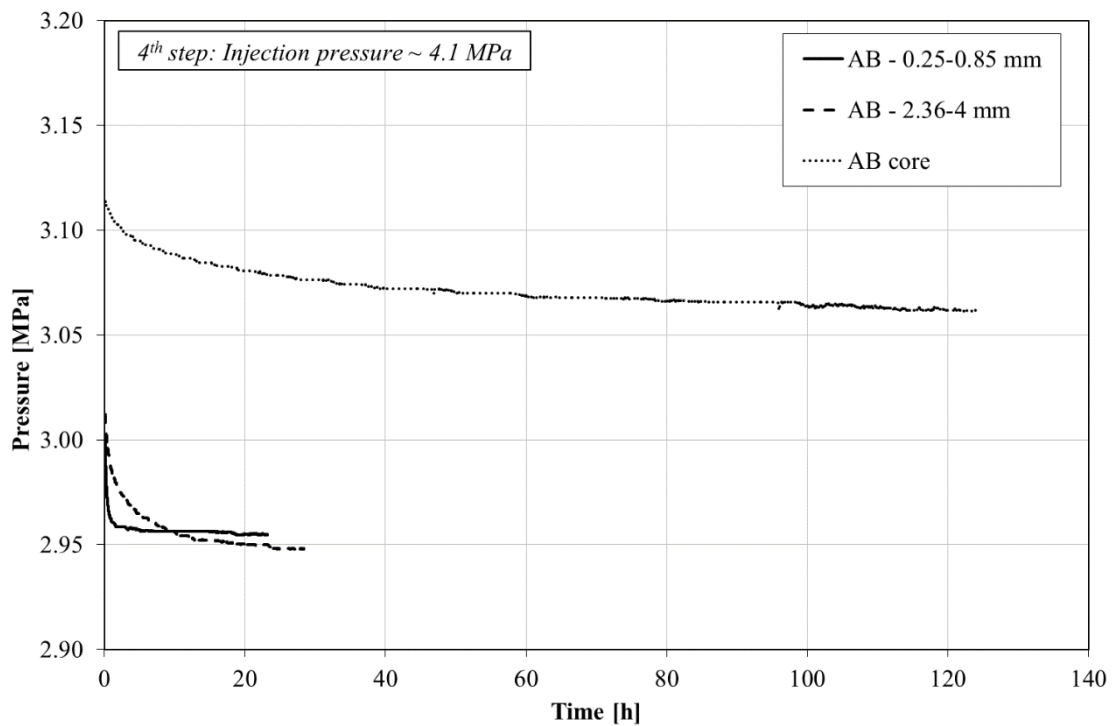


Fig. 5.8. Pressure decay curves for three 9ft Aberpergwm samples of different sizes - The 4th injection step.

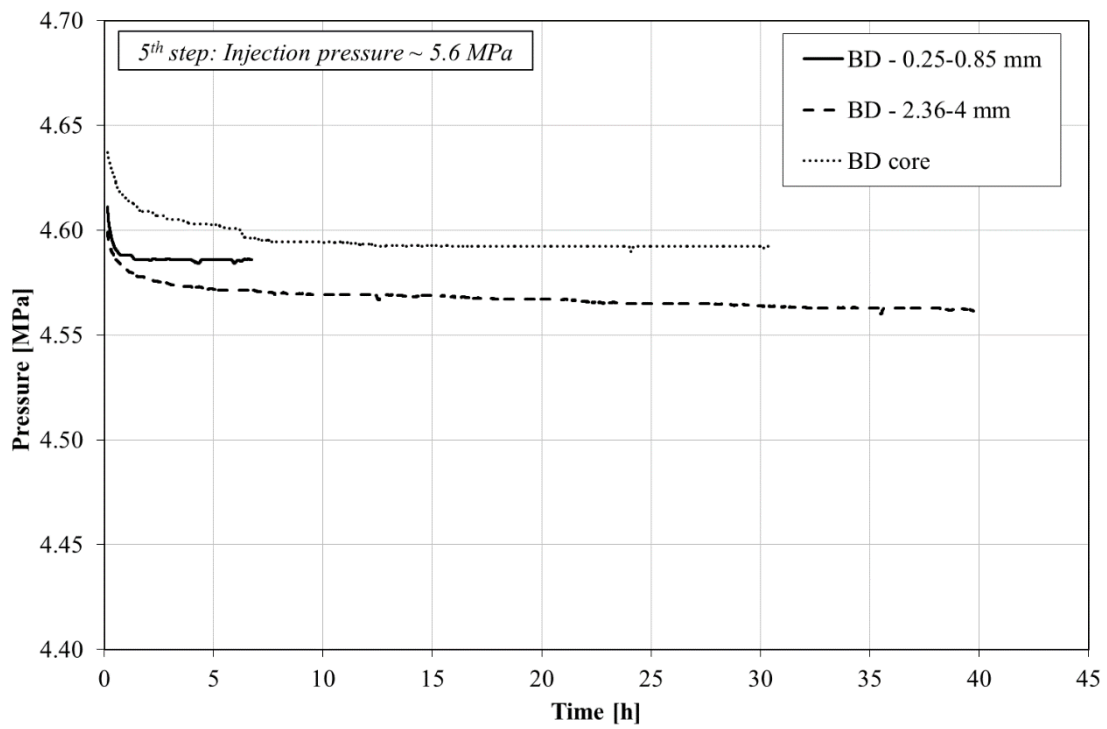


Fig. 5.9. Pressure decay curves for three Black Diamond samples of different sizes - The 5th injection step.

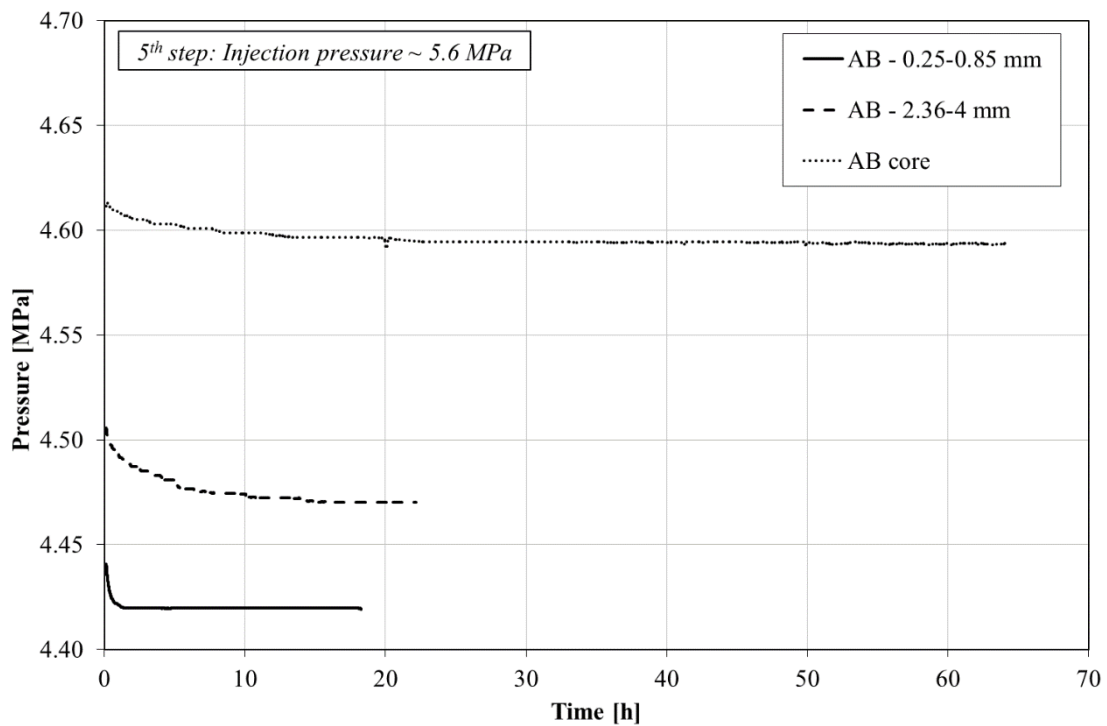


Fig. 5.10. Pressure decay curves for three 9ft Aberpergwm samples of different sizes - The 5th injection step.

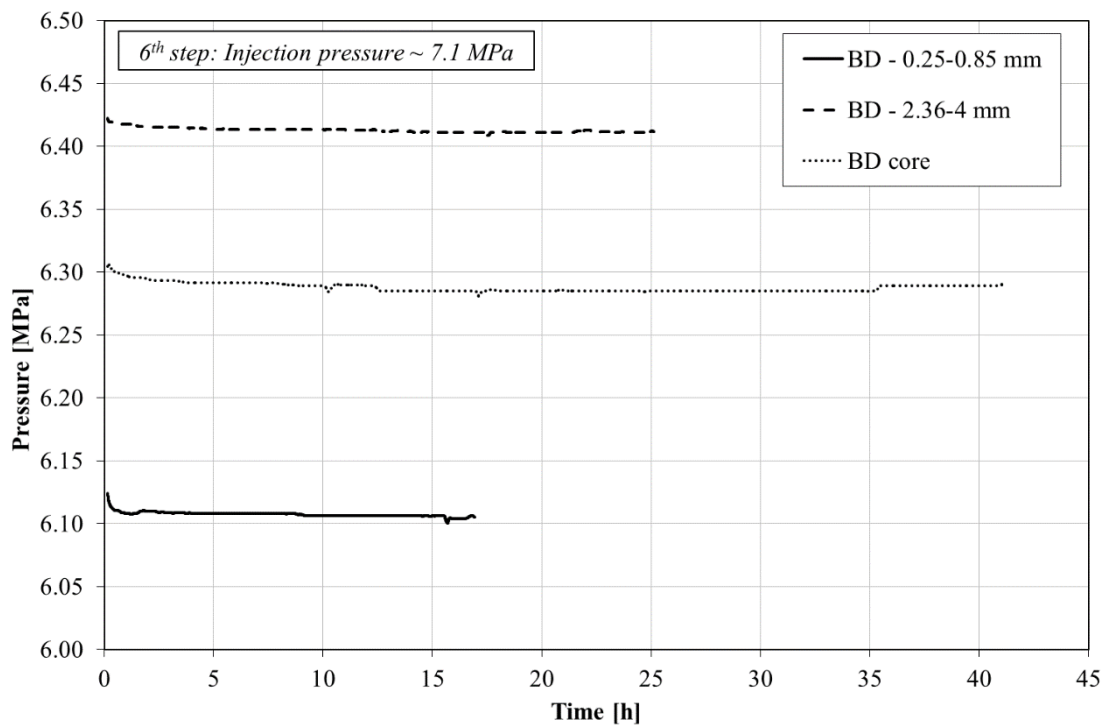


Fig. 5.11. Pressure decay curves for three Black Diamond samples of different sizes - The 6th injection step.

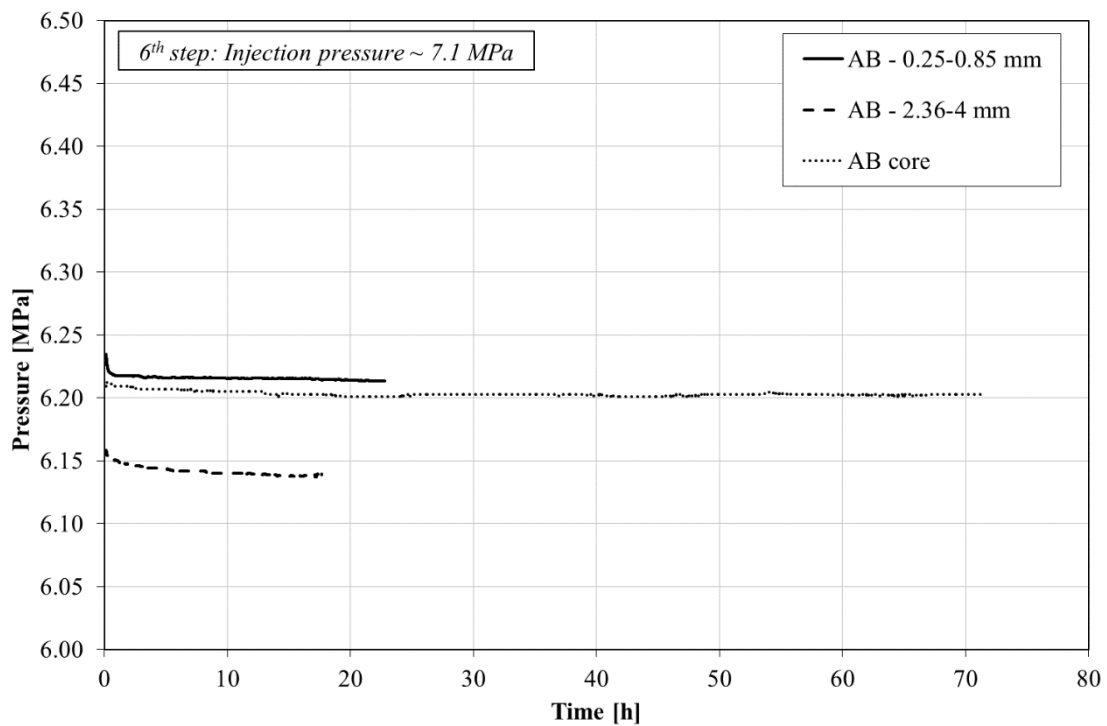


Fig. 5.12. Pressure decay curves for three 9ft Aberpergwm samples of different sizes - The 6th injection step.

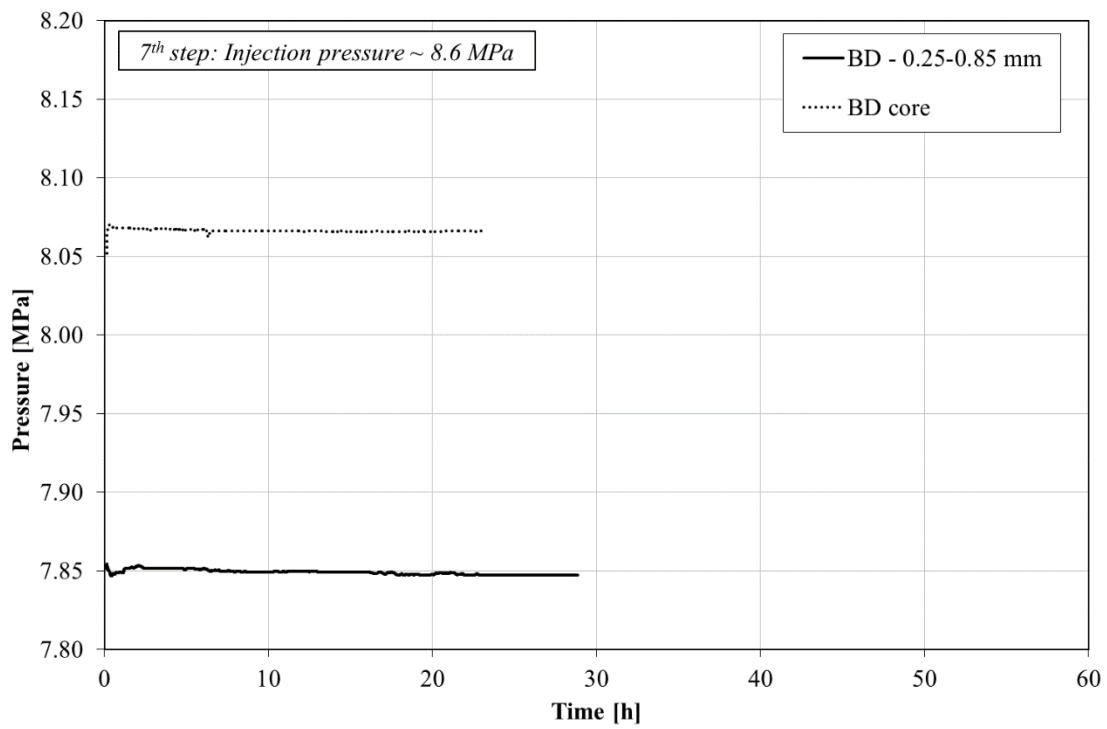


Fig. 5.13. Pressure decay curves for two Black Diamond samples of different sizes - The 7th injection step.

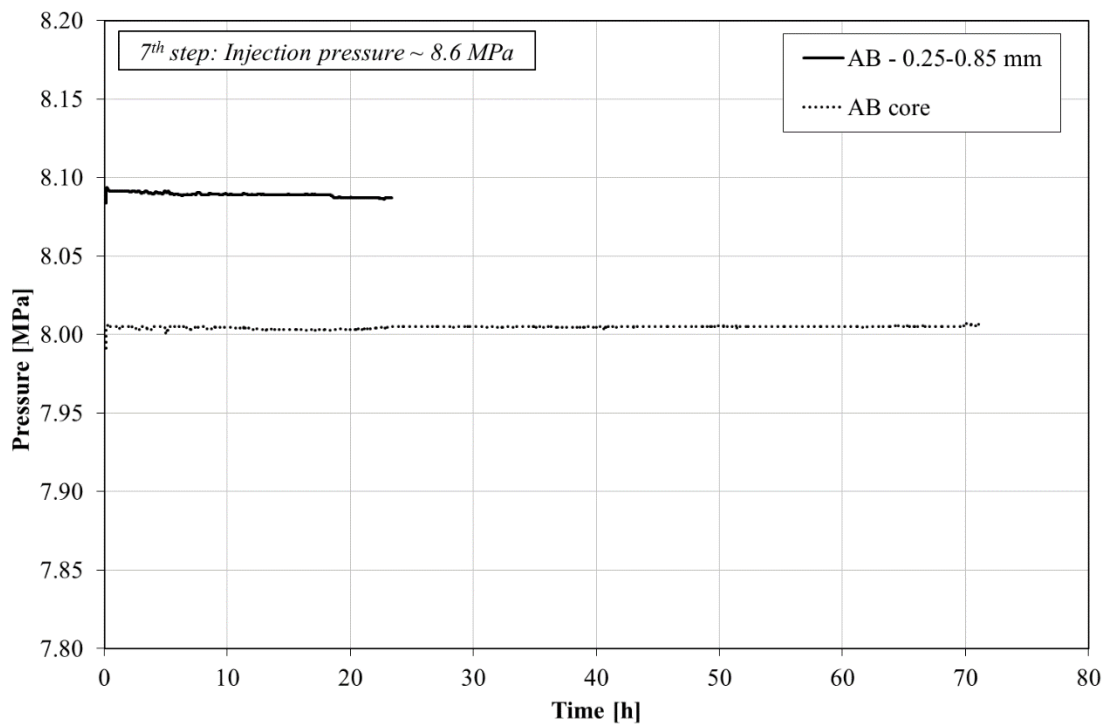


Fig. 5.14. Pressure decay curves for two 9ft Aberpergwm samples of different sizes - The 7th injection step.

It can be seen from the results that the average equilibrium time for samples with grain size of 0.25-0.85 mm from both coals was approximately 8 hours and that shapes of the pressure decay curves for each pressure step of both coals are comparable. In addition, 95% of the sorption was achieved in the first 2 hours of each time step. Samples with grain size of 2.36-4 mm show slightly different behaviour. The BD sample required up to 45 hours to reach equilibrium, while the AB sample required longer time, i.e. up to 60 hours. The difference in the equilibration time is even more pronounced between the core samples. Experimental data for the BD core reveal the equilibration time up to 80 hours while the AB core took 3 times longer to complete the sorption process at each injection step, i.e. up to 250 hours.

Overall, the total carbon dioxide sorption on the smallest coal grains (0.25-0.85 mm) from both BD and AB coals was completed within one week, while experiments on the 2.36-4 mm grains lasted up to two weeks each. Cores from BD and AB coals took the longest time to finish the sorption process, two and a half weeks and six weeks, respectively. Hence, taking into account the preparation and vacuuming time as well as the time required for conducting helium pycnometry method on each specimen, the total duration of gas sorption experiments on all samples took 18 weeks to complete.

It should be noted that a threshold of maximum twelve days for the equilibration time for each step was taken. Although sorption of gases in coal is a slow process which can last up to two weeks for carbon dioxide (e.g. Lutynski et al. 2011), a threshold was chosen to minimize the risk of leakage and associated errors. It can be seen from all the figures that the shapes of the pressure decay curves clearly suggested the end of the sorption process at each step by showing negligible change in measured pressure for a particular period of time. For powdered coal samples with 0.25-0.85 mm and 2.36-4 mm grain sizes, a minimum time period of 5 hours and 10 hours of constant pressure was considered to mark the end of the sorption process, respectively. For core samples, a minimum time period of 20 hours of constant pressure was considered.

As previously mentioned, the pressure drop over time is related to the sorption of CO₂ on coal. Hence, the experimental data presented above is analysed in the following sections in order to obtain further insights into the sorption capacity and kinetics of the coal samples.

5.3. The Excess Sorption Isotherms

The excess sorption of each coal sample was calculated using the measured values of pressure under isothermal conditions presented in the previous section and known void volumes of the manometric sorption system containing coal samples, as described in Chapter 4. The excess sorption values were determined based on measured gas pressures in the reference cell and equilibrium pressures in the sample cell at each injection step using equation (4.1) and equations (4.4-4.6). Summing up the calculated values of excess sorption for each injection step, an excess sorption isotherm was produced for each sample showing the amount of CO₂ on the coal as a function of pressure.

Excess sorption isotherms for all three samples of different sizes from both BD and AB coals are presented in Figures 5.15 to 5.20. In particular, Figures 5.15 and 5.16 contain results on samples with a grain size ranging from 0.25 to 0.85 mm for BD and AB coal samples, respectively. Similarly, excess sorption data for samples with a particle size ranging from 2.36 to 4 mm are presented in Figures 5.17 and 5.18, while the calculated excess sorption values for cores are presented in Figures 5.19 and 5.20, respectively for BD and AB coals.

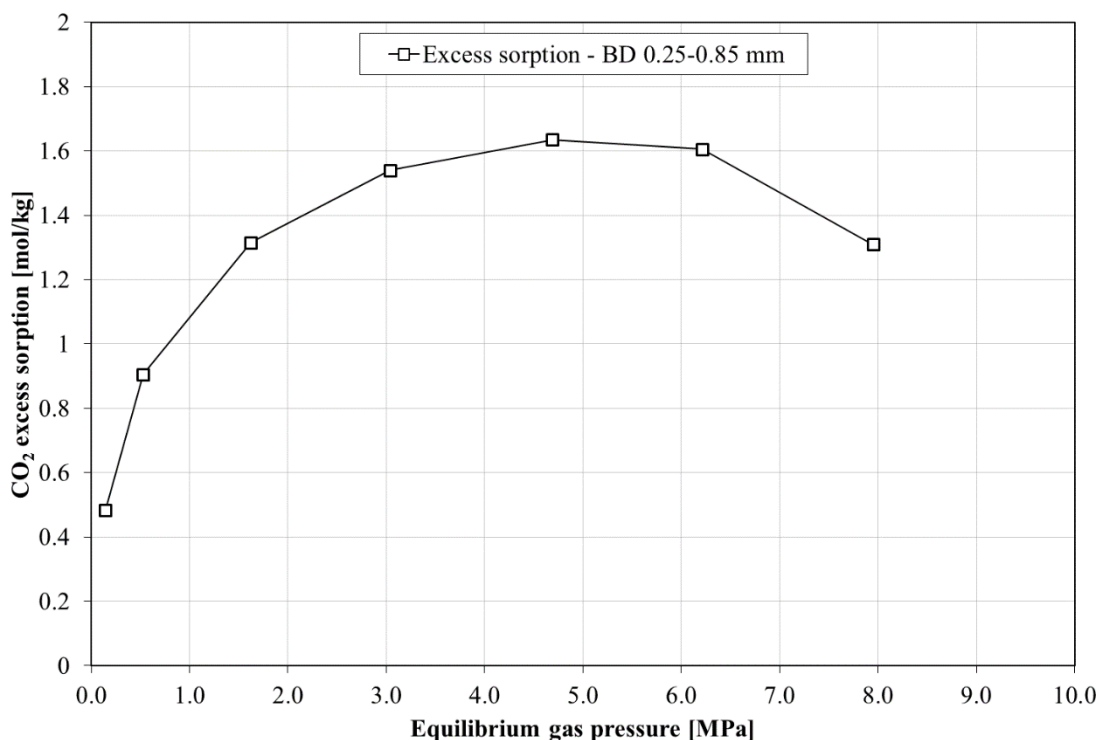


Fig. 5.15. Excess sorption of CO₂ on the Black Diamond coal – grain size 0.25-0.85 mm.

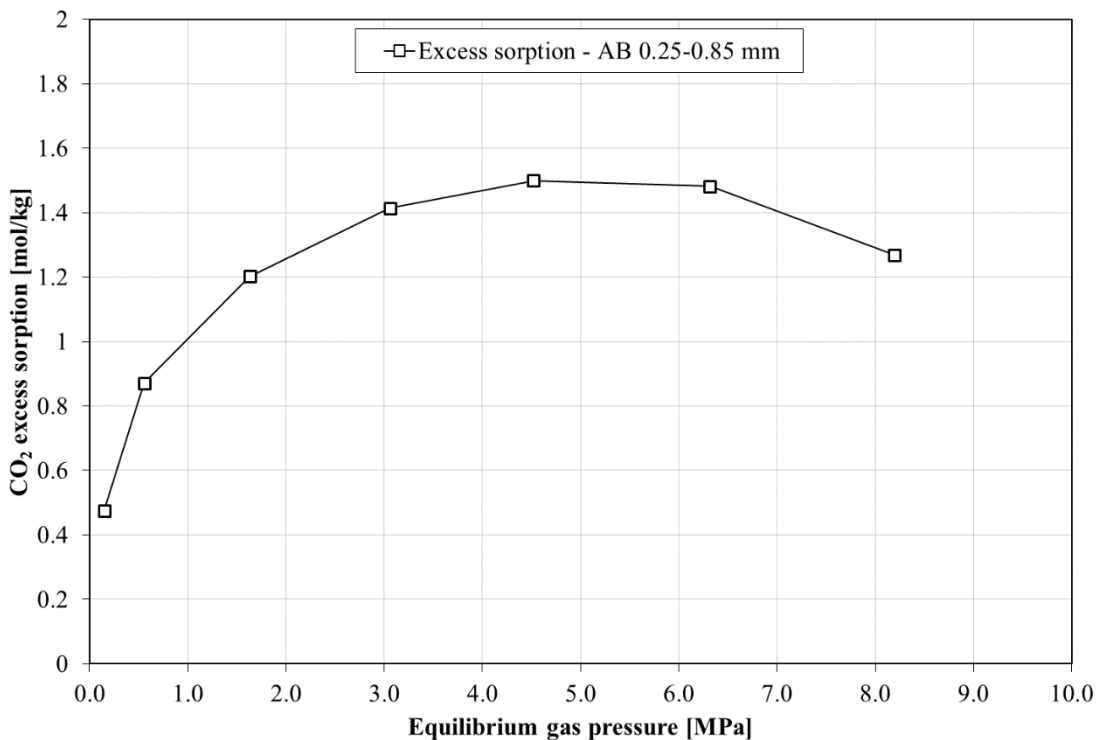


Fig. 5.16. Excess sorption of CO₂ on the 9ft Aberpergwm coal – grain size 0.25-0.85 mm.

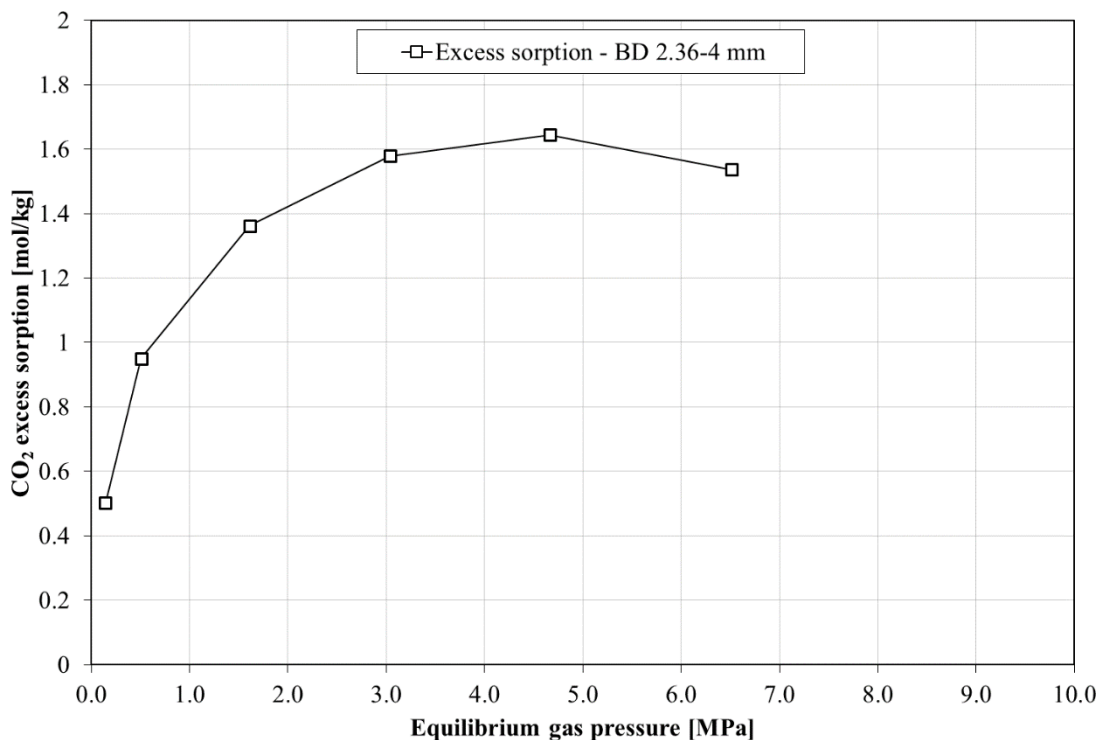


Fig. 5.17. Excess sorption of CO₂ on the Black Diamond coal – grain size 2.36-4 mm.

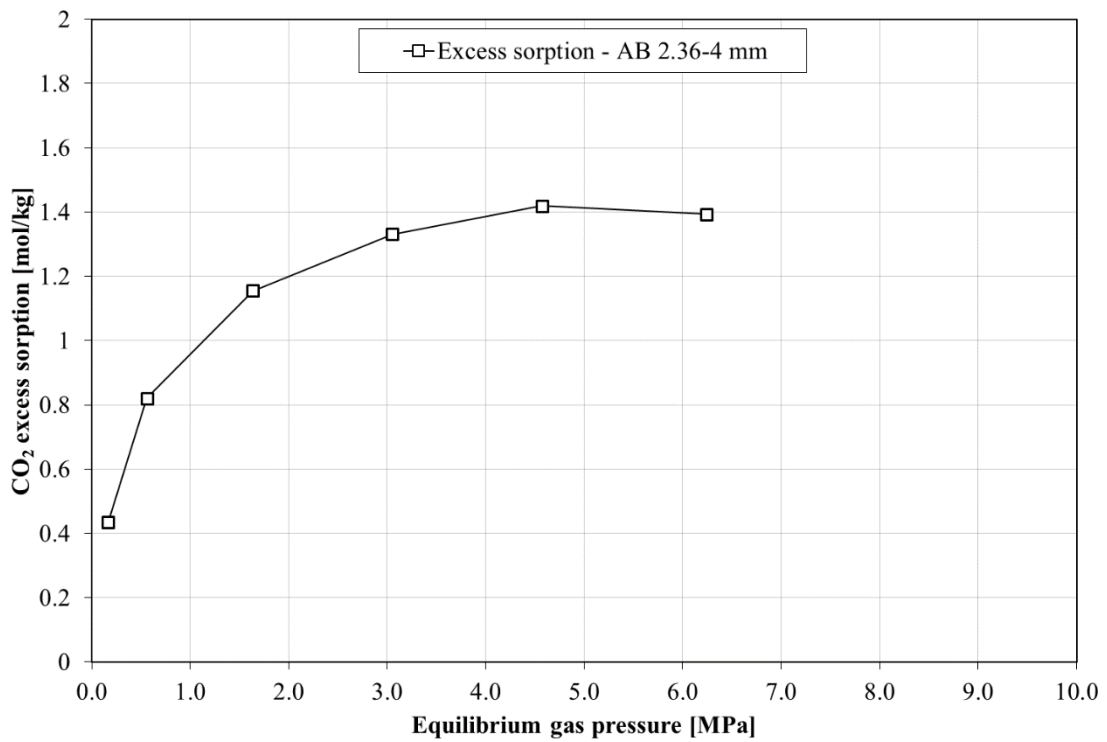


Fig. 5.18. Excess sorption of CO₂ on the 9ft Aberpergwm coal – grain size 2.36-4 mm.

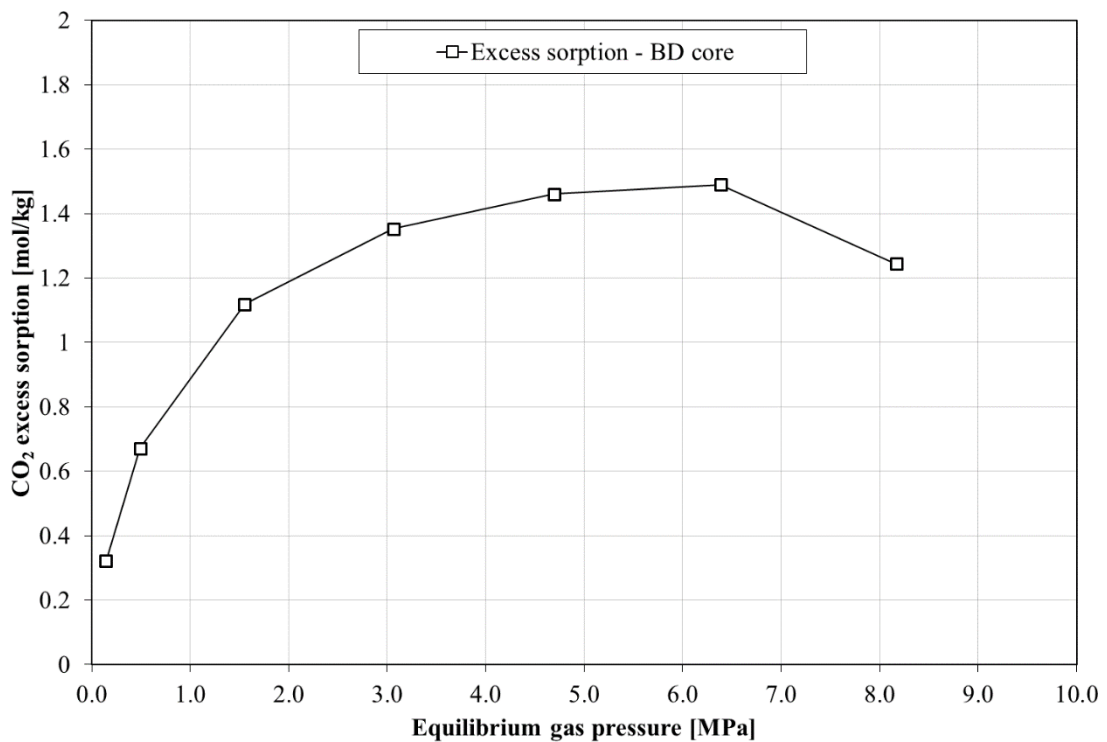


Fig. 5.19. Excess sorption of CO₂ on the Black Diamond coal core.

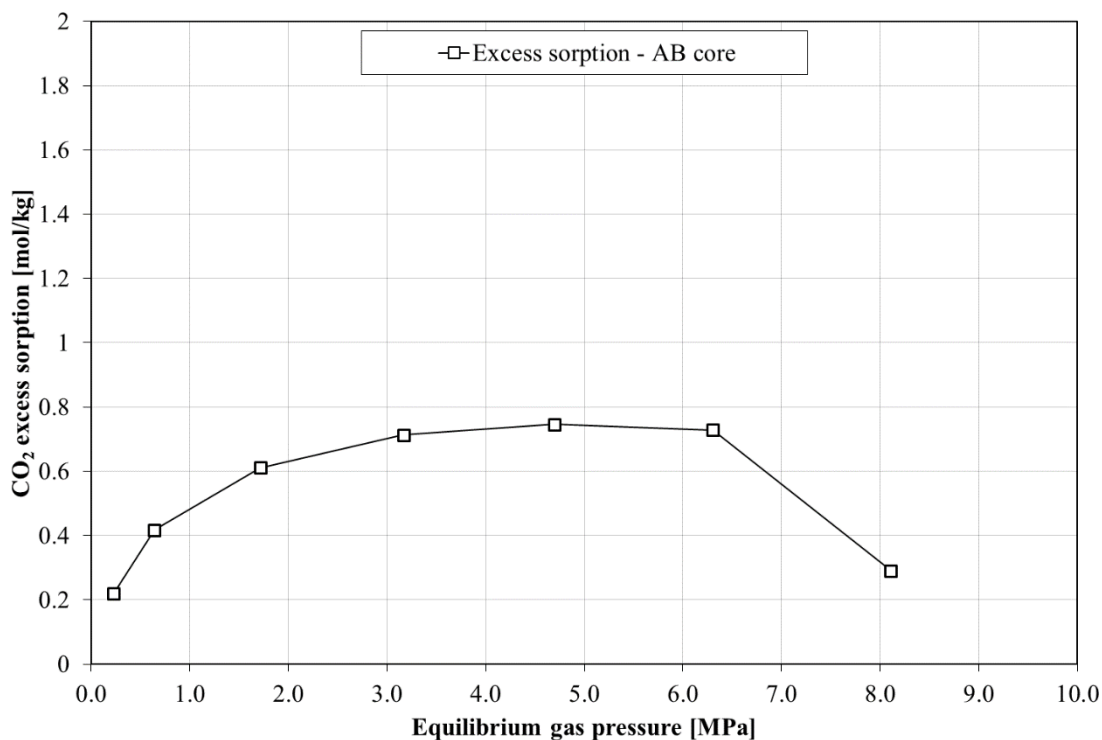


Fig. 5.20. Excess sorption of CO₂ on the 9ft Aberpergwm coal core.

As shown in Figures 5.15 to 5.20 for both BD and AB coal samples, the amount of excess sorption has increased gradually with an increase in gas pressure up to 5 MPa and then decreased with further increase in gas pressure. Such behaviour is attributed to the experimental determination of the excess sorption where the volume of the adsorbed phase is neglected (Mohammad, 2009). Hence, such amount does not represent the absolute sorbed amount, as previously explained in Chapter 4.

As can be seen from Figures 5.15 and 5.16, for the 0.25-0.85 mm grains, the maximum excess sorption amounts calculated at 4.7 MPa and 4.5 MPa of BD and AB coals are 1.63 mol/kg and 1.5 mol/kg, respectively. This suggests that the maximum excess sorption capacity of the AB coal is 8% less than of the BD coal. Results presented in Figures 5.17 and 5.18 for the 2.36-4 mm grains calculated at 4.6 MPa show that the maximum sorbed amount of 1.42 mol/kg for the AB coal is 13% lower than the maximum excess sorption of 1.64 mol/kg for the BD coal.

Figures 5.19 and 5.20 show that the maximum excess sorption values of BD and AB cores calculated at 6.4 MPa and 6.3 MPa are 1.49 mol/kg and 0.75 mol/kg, respectively. This suggests that AB coal core has 50% lower excess sorption capacity compared to

the BD core. As previously shown in Figure 4.4, BD and AB cores exhibit different fracture networks. Although both samples are of the same rank and almost identical carbon content, it could be visually observed that BD coal has a well-developed cleat system in comparison to the AB coal. As a consequence, it can be inferred that total fracture porosity of the BD coal is higher than that of the AB coal allowing higher access of the CO₂ molecules.

5.4. The Absolute Sorption Isotherms

As previously mentioned in Chapter 4, the absolute sorption takes account of the volume occupied by the sorbed phase. The absolute adsorption is not experimentally attainable in a straightforward manner and it has to be calculated from the excess sorption values assuming the density of the adsorbed phase (Fitzgerald et al., 2005). The relationship between the excess sorption (n_{ads}^{ex}) and the absolute sorption (n^{abs}) has been presented in equation (4.12) and it will be presented here for the sake of completeness as:

$$n^{abs} = \frac{n_{ads}^{ex}}{\left(1 - \frac{c_g}{c_{ads}}\right)} \quad (5.1)$$

where c_g and c_{ads} are the densities of the gas phase and the adsorbed phase, respectively.

In order to calculate the absolute sorbed amount using equation (5.1), the density of the adsorbed phase must be known. Since this is not an experimental variable, it is estimated using an extrapolation method (Fitzgerald et al., 2005; Gensterblum et al., 2010). A common approach is to extrapolate the linear portion of the excess sorption curve, presented as a function of gas pressure, after passing through its maximum to an x-axis intercept, where density of the gas phase becomes equal to the density of the adsorbed phase (Gensterblum et al., 2010).

However, the use of this technique requires sufficient data in the linear (high-pressure) range beyond the maximum value of the excess sorption (Gensterblum et al., 2010). Since there are insufficient data in the linear range obtained on the samples of this study (see Figures 5.15-5.20), a commonly used value of 26.81 mmol/cm³ (1180 kg/m³) for

the adsorbed phase density of CO₂ is selected from the literature (e.g. Arri et al., 1992; Fitzgerald et al., 2005; Goodman et al., 2007; Dutta et al., 2008; Gensterblum et al., 2010;). This value represents the saturated liquid density at the triple point (Span and Wagner, 1996). It should be noted that the adsorbed phase density represents a value averaged over the adsorbed phase volume and it is assumed to be constant over the range of pressures used (Mohammad et al., 2009).

Further confidence on the choice of the adsorbed phase density is based on the work of Gensterblum et al. (2010) who have presented the results on the sorption behaviour of powdered Selar Cornish semi-anthracite from the South Wales Coalfield (UK) with grain size up to 2 mm. The experimental study was conducted by three independent European research laboratories using CO₂ pressures up to 16 MPa (Gensterblum et al., 2010). Using the fitting procedure, Gensterblum et al. (2010) have estimated that the adsorbed phase density of CO₂ obtained on the Selar Cornish coal sample is 26.68±3.07 mmol/cm³ (1174±135 kg/m³).

A common approach to fit the absolute sorption calculated using equation (5.1) is to use the Langmuir equation (Langmuir, 1918), as indicated in Chapter 2. The absolute sorbed amount n_L^{abs} (mol/kg) calculated via a Langmuir equation is expressed as:

$$n_L^{abs} = n_L \frac{P_{eq}}{P_L + P_{eq}} \quad (5.2)$$

where P_{eq} is the equilibrium pressure (Pa), n_L and P_L are the Langmuir parameters for the maximum sorption capacity (mol/kg) and the Langmuir pressure (Pa) at which coal achieves half of its maximum sorption, respectively.

In order to fit the Langmuir equation (5.2) to the absolute sorption amount (eq. 5.1), the initial values were considered for the Langmuir parameters and the Langmuir absolute sorption was determined. Based on the calculated values of the absolute sorption using equations (5.1) and (5.2), determination of the sum of the squared differences with a target function F_T was conducted to minimize the residuals (e.g. Bae and Bhatia, 2006; Siemons and Busch, 2007).

The target function,

$$F_T = \sum_i (n_i^{abs} - n_{Li}^{abs})^2 \quad (5.3)$$

was minimized with respect to the Langmuir parameters n_L and P_L . Variable i stands for the number of injection steps.

The optimization procedure was conducted using the Excel solver function by which the automatic adjustment, based on an iterative approach, of the Langmuir parameters to obtain the minimum value of the squared differences is performed.

Figures 5.21 and 5.22 present the absolute sorption isotherms fitted to the calculated absolute adsorption values obtained on 0.25-0.85 mm grains from BD and AB, respectively. Similarly, Figures 5.23 (BD) and 5.24 (AB) show fitted and calculated absolute sorption values for samples with grain size of 2.36-4 mm, while Figures 5.25 (BD) and 5.26 (AB) contain absolute sorption data for cores.

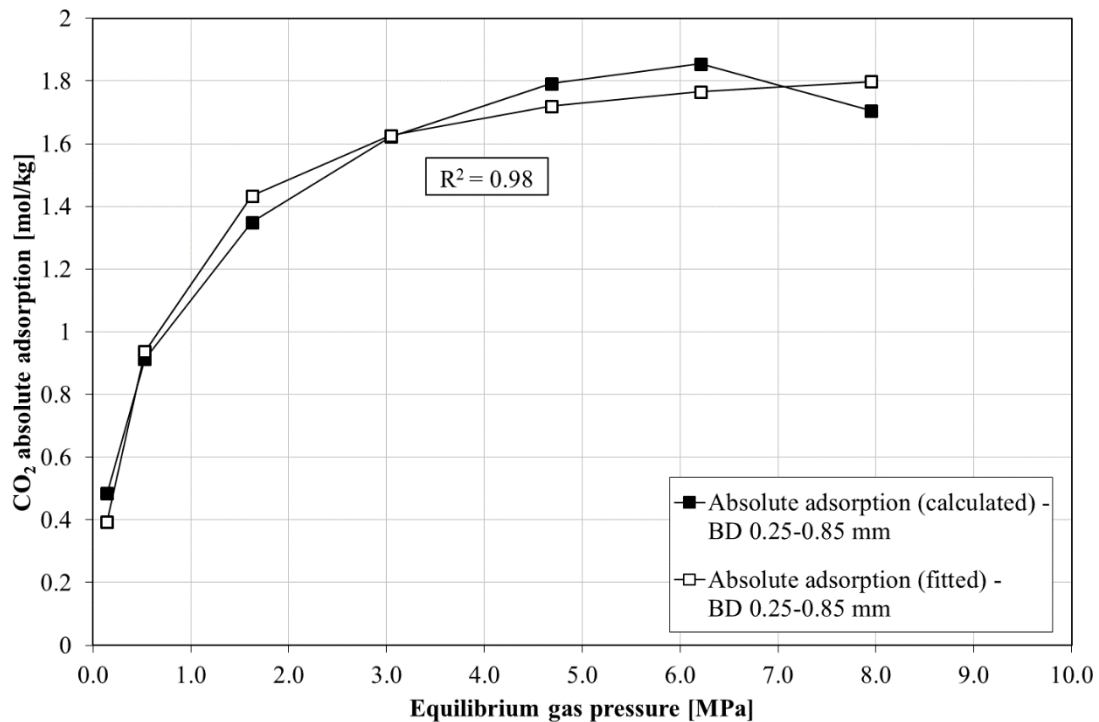


Fig. 5.21. The CO₂ absolute sorption isotherms fitted to the calculated absolute adsorption values on Black Diamond coal – grain size 0.25-0.85 mm.

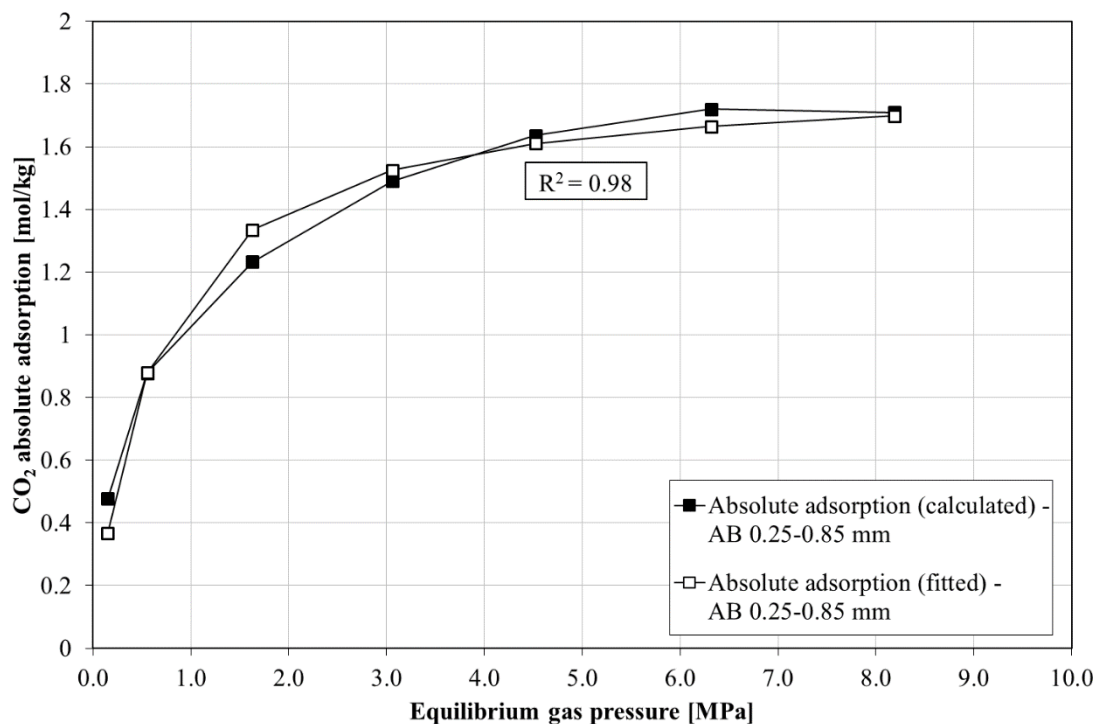


Fig. 5.22. The CO₂ absolute sorption isotherms fitted to the calculated absolute adsorption values on 9ft Aberpergwm coal – grain size 0.25-0.85 mm.

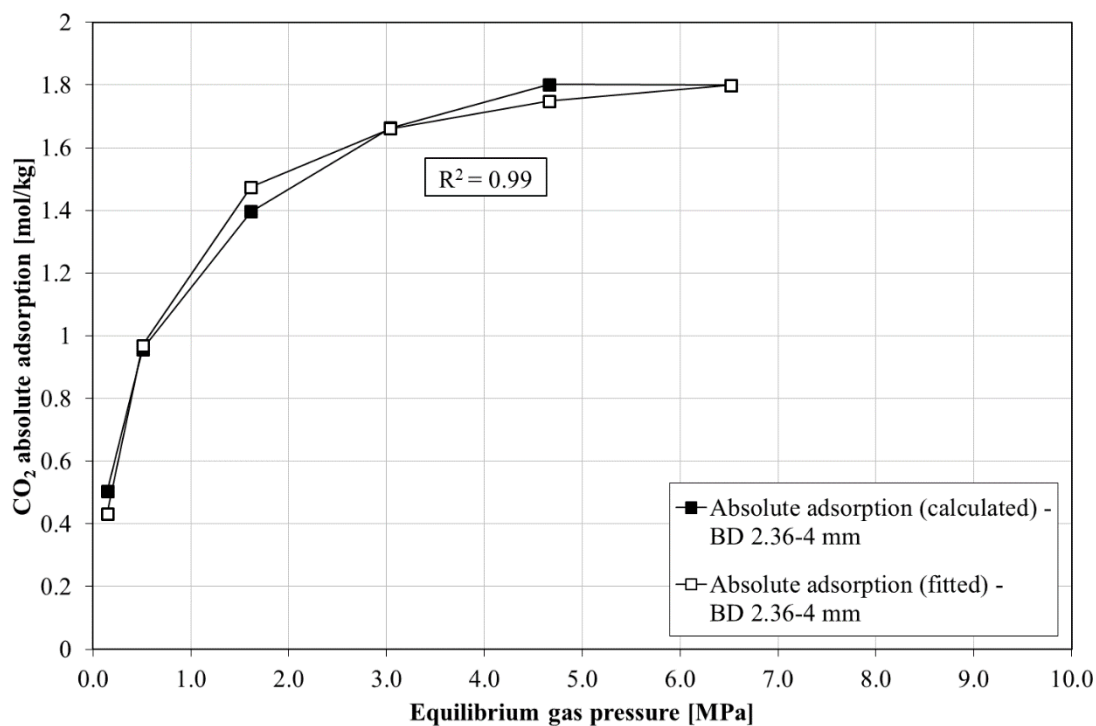


Fig. 5.23. The CO₂ absolute sorption isotherms fitted to the calculated absolute adsorption values on Black Diamond coal – grain size 2.36-4 mm.

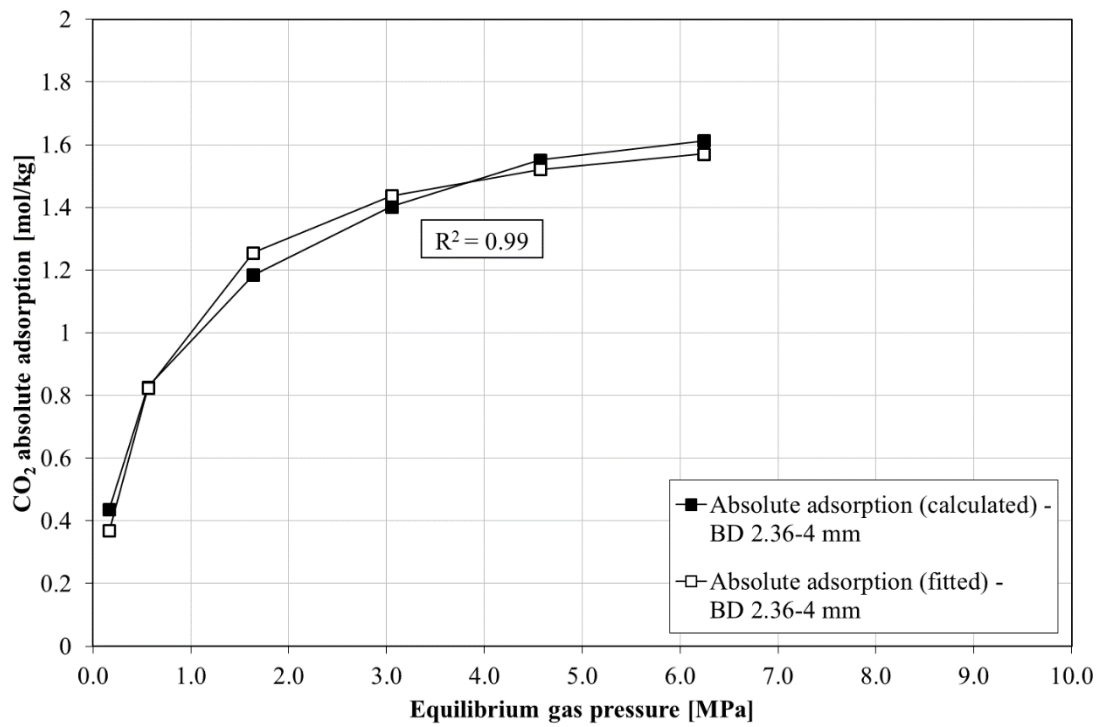


Fig. 5.24. The CO₂ absolute sorption isotherms fitted to the calculated absolute adsorption values on 9ft Aberpergwm coal – grain size 2.36-4 mm.

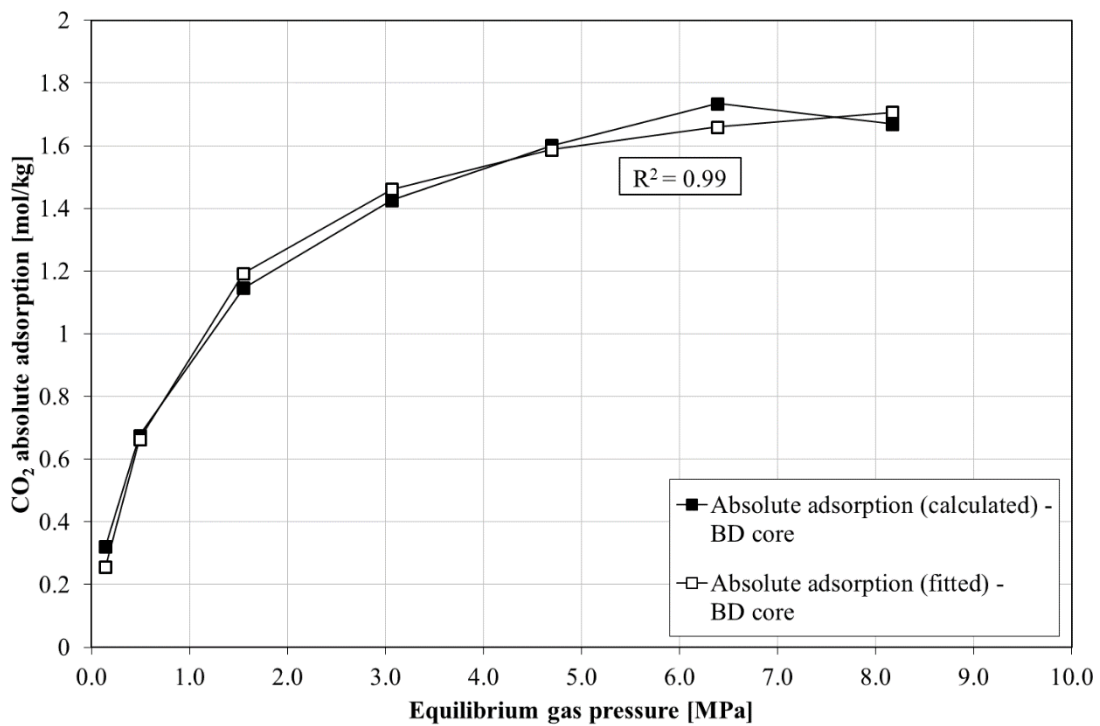


Fig. 5.25. The CO₂ absolute sorption isotherms fitted to the calculated absolute adsorption values on Black Diamond coal core.

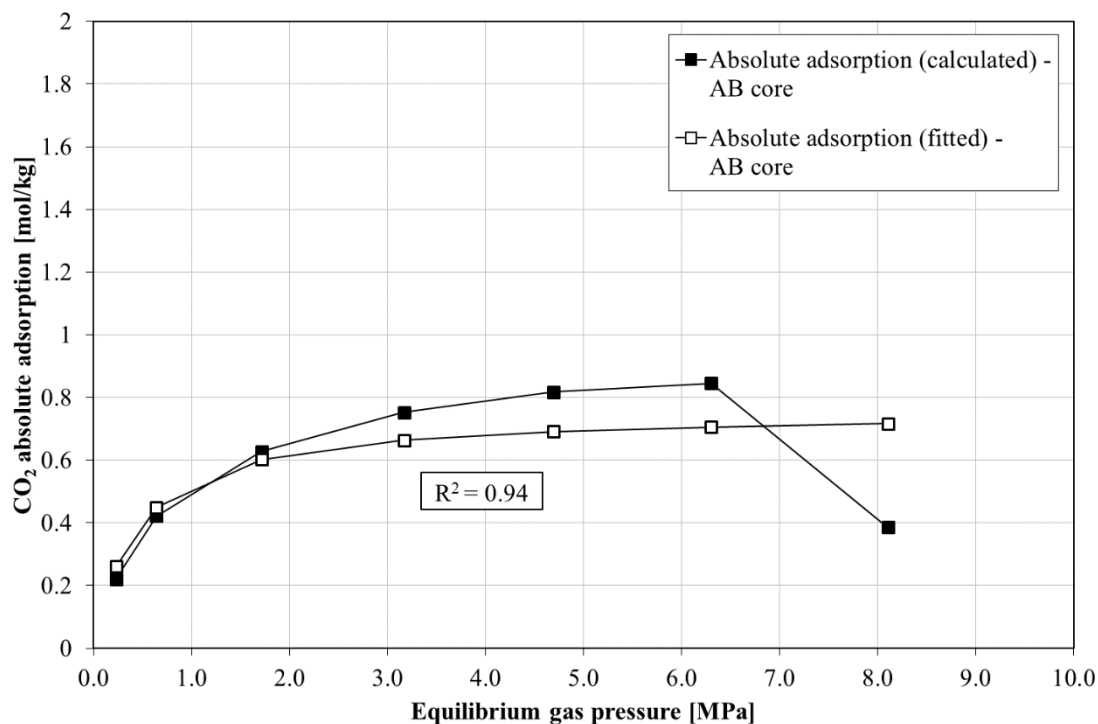


Fig. 5.26. The CO₂ absolute sorption isotherms fitted to the calculated absolute adsorption values on 9ft Aberpergwm coal core.

By observing Figures 5.21-5.26, it can be seen that fitting the Langmuir curve (eq. 5.2) to the absolute adsorption capacity values calculated using equation (5.1) shows good agreement with coefficient of determination (R^2) between 0.94 and 0.99. However, a small difference between the calculated and fitted values at CO₂ pressure of 8.1 MPa in Figure 5.26 could be related to the loss of the void volume due to coal swelling. As mentioned in Chapter 2, volumetric effects induced by sorption of CO₂ could have a detrimental effect on calculated sorption capacity.

It can be observed from all the figures that the amount of absolute sorption, obtained by following the procedure stated above, continuously increases with gas pressure. If the absolute sorption isotherms of three samples of different sizes between the BD and AB coals are compared, it can be noticed that BD samples show higher sorption capacity over the tested pressure range than AB samples.

In particular, if the fitted data presented for 0.25-0.85 mm grains in Figure 5.21 (BD) and Figure 5.22 (AB) are compared, it can be observed that the absolute sorption capacity values of the BD and AB samples at 8 MPa are 1.8 and 1.7 mol/kg, respectively. This suggests that the sorption capacity of the BD is 6% higher than that of

the AB coal. For grains with size of 2.36-4 mm, the absolute sorption capacity values at 6.5 MPa are 1.81 mol/kg (BD) and 1.57 mol/kg (AB) showing a difference of 13% as shown in Figures 5.23 and 5.24, respectively. The presented data for the cores in Figures 5.25 and 5.26 reveal significant difference in absolute sorption capacity values among the coals with 2.4 times higher sorption for BD in comparison to AB coal at 8 MPa. In particular, BD and AB show absolute sorption capacities of 1.71 mol/kg and 0.72 mol/kg, respectively.

Table 5.1 presents the fitted parameters for the absolute gas sorption on all the samples of both coals.

Table 5.1. Fitted (Langmuir) parameters for the absolute CO₂ sorption of all the measured samples in this study.

Grain size	Fitted (Langmuir) parameters for adsorption isotherms	
	P _L (MPa)	n _L (mol/kg)
Black Diamond		
0.25-0.85 mm	0.56	1.92
2.36-4.0 mm	0.51	1.94
Core sample	0.91	1.90
9ft Aberpergwm		
0.25-0.85 mm	0.59	1.82
2.36-4.0 mm	0.61	1.73
Core sample	0.44	0.75

According to the results, maximum absolute sorption capacity values of the BD samples with grain sizes of 0.25-0.85 mm, 2.36-4 mm and core are 1.92 mol/kg, 1.94 mol/kg, and 1.9 mol/kg, respectively. Similarly, results for the AB coal show maximum absolute sorption capacity values of 1.82 mol/kg, 1.73 mol/kg, and 0.75 mol/kg for 0.25-0.85 mm grains, 2.36-4 mm grains and core, respectively. Moreover, as shown in Table 5.1, the pressures at which half of the maximum sorption has been achieved for all samples of both coals vary between 0.44 MPa and 0.91 MPa. This suggests that half of the CO₂ sorption on anthracite samples occurs at low pressures, i.e. <1.0 MPa.

In order to assess the dependence of the maximum absolute sorption capacity on the sample size, values presented in Table 5.1 have been plotted with respect to the average sample volume, as shown in Figure 5.27. It should be noted that the average volume of crushed samples was calculated with an assumption that grains have spherical shape.

Hence, calculated average volumes of 0.09 mm³ and 16.3 mm³ represent samples with grain sizes of 0.25-0.85 mm and 2.36-4 mm, respectively. Volumes of the BD and AB coal cores have been presented in Chapter 4.

It is shown in Figure 5.27 that the change of maximum sorption capacity with an increase in BD sample volume is negligible. It can be inferred that such behaviour is attributed to the interconnectivity of the fracture network and the distance between the fractures in the BD core as can be observed in Figure 4.4. In particular, well-developed cleat system and short distance between the main flow paths allow easy access to the coal matrix for the CO₂ molecules which results in high sorption capacity. As the change in sorption capacity is negligible with an increase in BD sample volume, it can be inferred that the inter-cleat distance in the BD core was small allowing good access to the sorption sites for the CO₂ molecules.

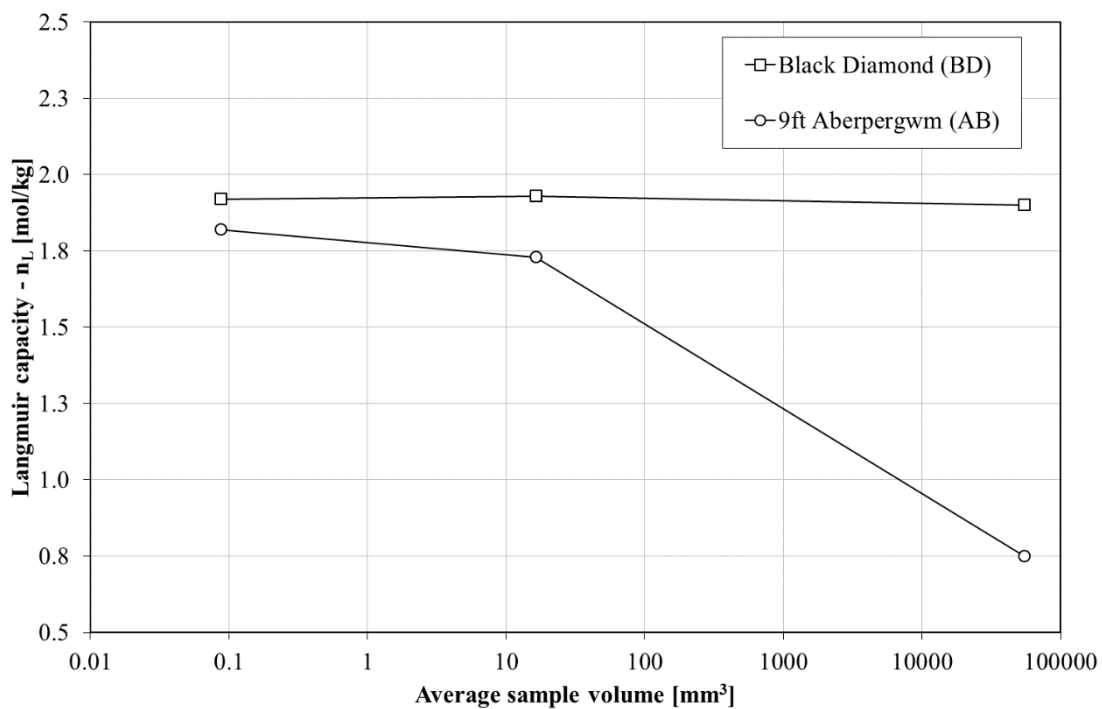


Fig. 5.27. Langmuir (absolute) sorption capacity of both samples versus the average sample volume.

The sorption capacity for the AB coal shows different behaviour. As shown in Figure 5.27, the sorption capacity for AB coal shows a decrease with an increase in the sample volume. Staib et al. (2015) have shown that crushing of the coal increased the total porosity of the sample accessible to helium. Hence, the newly accessible pores as a

result of finer grinding offered more sorption sites and consequently, increased the sorption capacity in crushed samples compared to the core. Interestingly, with an increase in sample size, the difference in absolute sorption capacities between BD and AB coals increases.

Variation in sorption capacity caused by different fracture interconnectivity of the two coals may lie in the depths of the coal seams, i.e. BD obtained from 150 m and AB from 550 m depth. As mentioned in Chapter 1, deeper coal seams may have less developed fracture network as a result of geological effects.

5.5. Adsorption Kinetics

To quantitatively present the pressure drop as a function of time recorded during every injection step, the pressure equilibration curves were normalized using an approach suggested by Busch et al. (2004). In this approach the curves are expressed in terms of the residual or unoccupied sorption capacity, $Q_{residual}(t)$, calculated for each time interval as (Busch et al., 2004):

$$Q_{residual}(t) = \frac{n_t - n_{eq}}{n_{t(0)} - n_{eq}} \quad (5.4)$$

where, n_t , $n_{t(0)}$ and n_{eq} are the gas sorption amount at time t (h), the initial gas sorption at the beginning of each pressure step and the total gas sorption at equilibrium, respectively. Values representing $n_{t(0)}$ and n_{eq} were calculated using equation (4.1) based on the initial and final pressures in the manometric system after connecting the reference cell to the sample cell, respectively (Busch et al., 2004).

Various approaches have been used by different authors to describe the kinetics of gas sorption on coal, as described in Chapter 2. In this work, calculated residual sorption capacity values were analysed based on the first-order rate function, second-order rate function and semi-empirical equation proposed by Busch et al. (2004). Sorption rate models do not necessitate any assumptions regarding the coal pore structure, opposite to the unipore and bidisperse models, while the obtained values can be more generally linked to distinct stages in the adsorption process, as previously described (Busch et al., 2004; Hosking, 2014).

The integrated representation of the first rate-order function can be expressed as (Petrucci, 2002):

$$Q_{residual}(t) = Q_{residual(0)} \cdot e^{-k t} \quad (5.5)$$

where, $Q_{residual(0)}$ is the initial residual sorption at the start of the time step and k is the first-order reaction rate (s^{-1}).

The second-order rate function, in its integrated form, can be presented as (Petrucci, 2002):

$$\frac{1}{Q_{residual}(t)} = \frac{1}{Q_{residual(0)}} + k' t \quad (5.6)$$

where k' is the second-order reaction rate (s^{-1}).

Busch et al. (2004) expressed the amount of the residual capacity by the combined first-order rate function as:

$$Q_{residual}(t) = Q_1 \cdot e^{-k'' t} + Q_2 \cdot e^{-k''' t} \quad (5.7)$$

where Q_1 and Q_2 are the residual sorption capacities with $Q_1 = 1 - Q_2$, where $0 \leq Q_1 \leq 1$, and k'' and k''' are the two first-order reaction rates (s^{-1}).

Figures 5.28 to 5.33 present the results of residual gas sorption capacity with respect to time calculated using the equation (5.4) for all samples. However, in order to study the kinetic effect of the CO₂ sorption process in coal, the last two injection steps were disregarded. Reasons for that are the short time of equilibration and the high Joule-Thomson effect causing temperature changes in the cell and affecting the measured results at the start of the sorption. Figures 5.28 and 5.29 show data for the smallest samples (0.25-0.85 mm), Figures 5.30 and 5.31 for the medium-sized samples (2.36-4 mm) and Figures 5.32 and 5.32 for the cores of BD and AB coals, respectively.

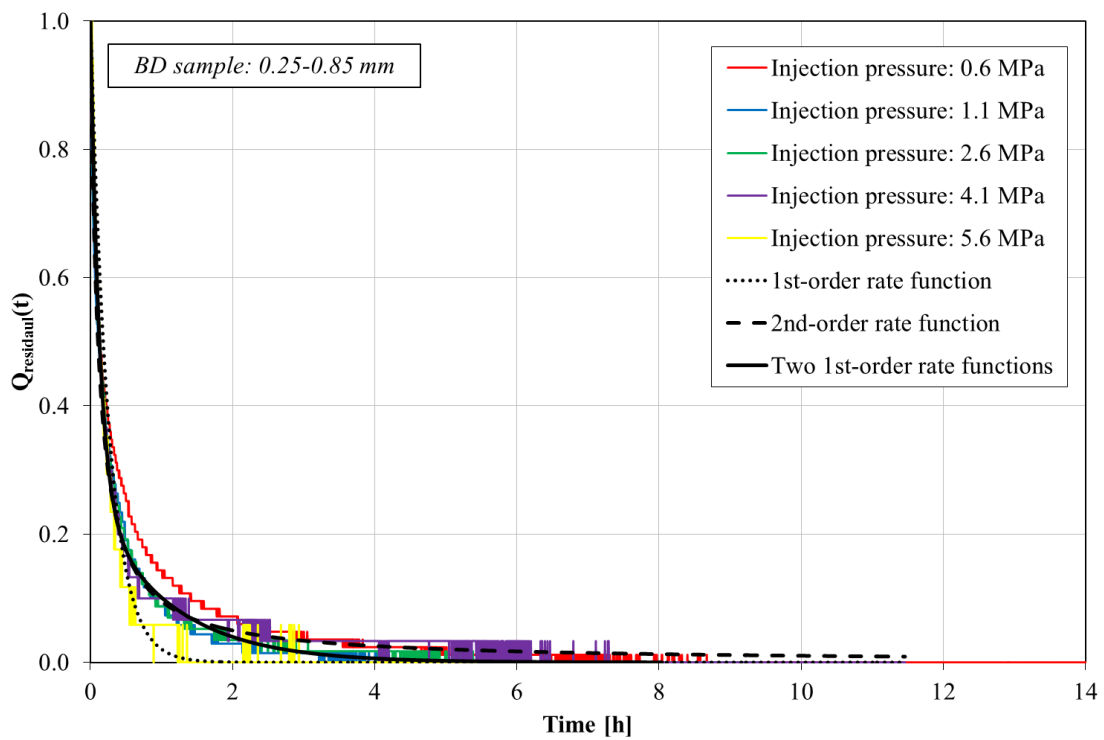


Fig. 5.28. The fits of the experimental residual sorption capacity decline for Black Diamond coal – grain size 0.25-0.85 mm.

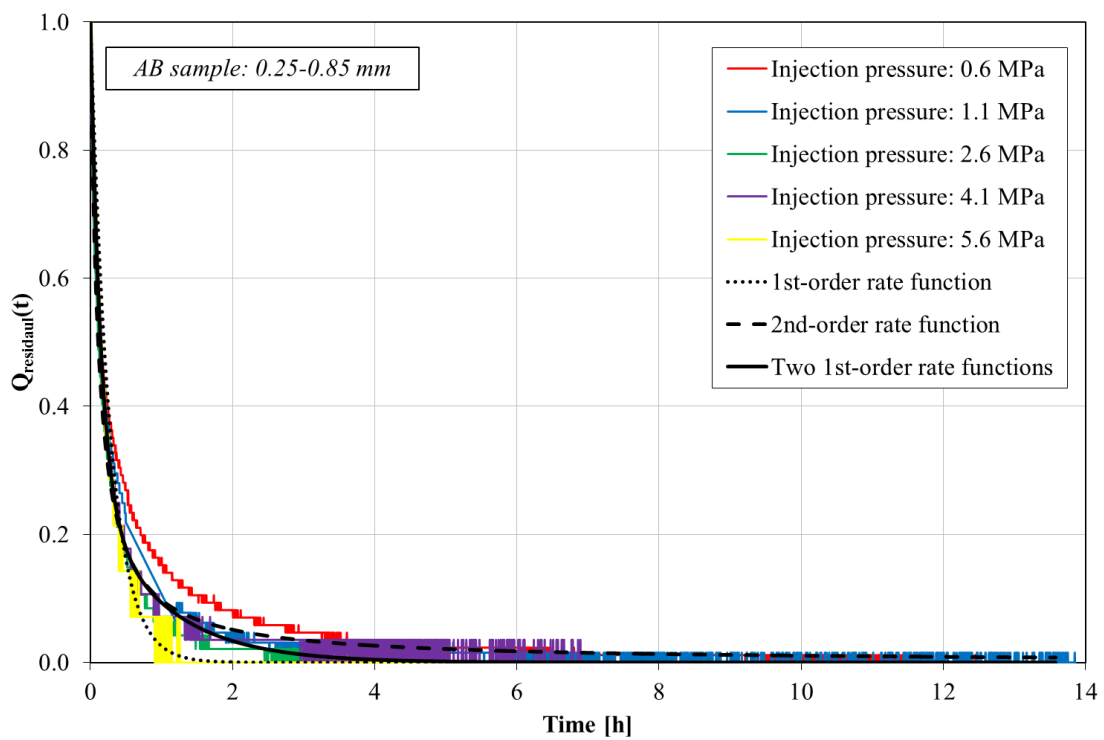


Fig. 5.29. The fits of the experimental residual sorption capacity decline for 9ft Aberpergwm coal – grain size 0.25-0.85 mm.

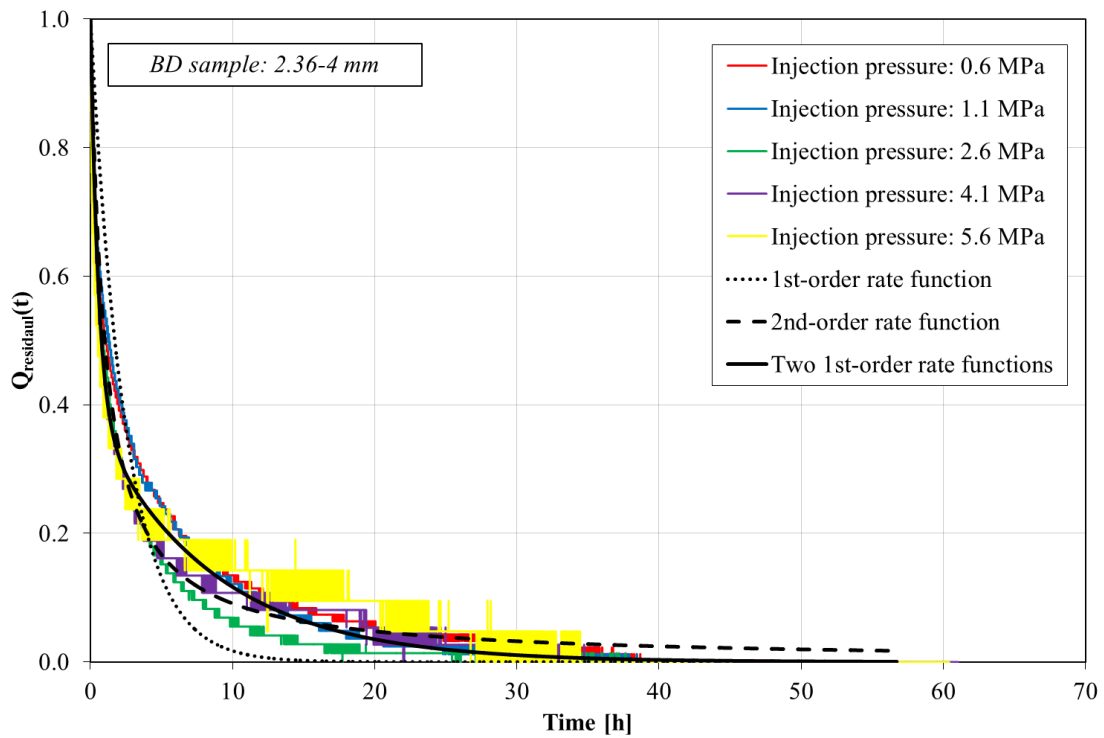


Fig. 5.30. The fits of the experimental residual sorption capacity decline for Black Diamond coal – grain size 2.36-4 mm.

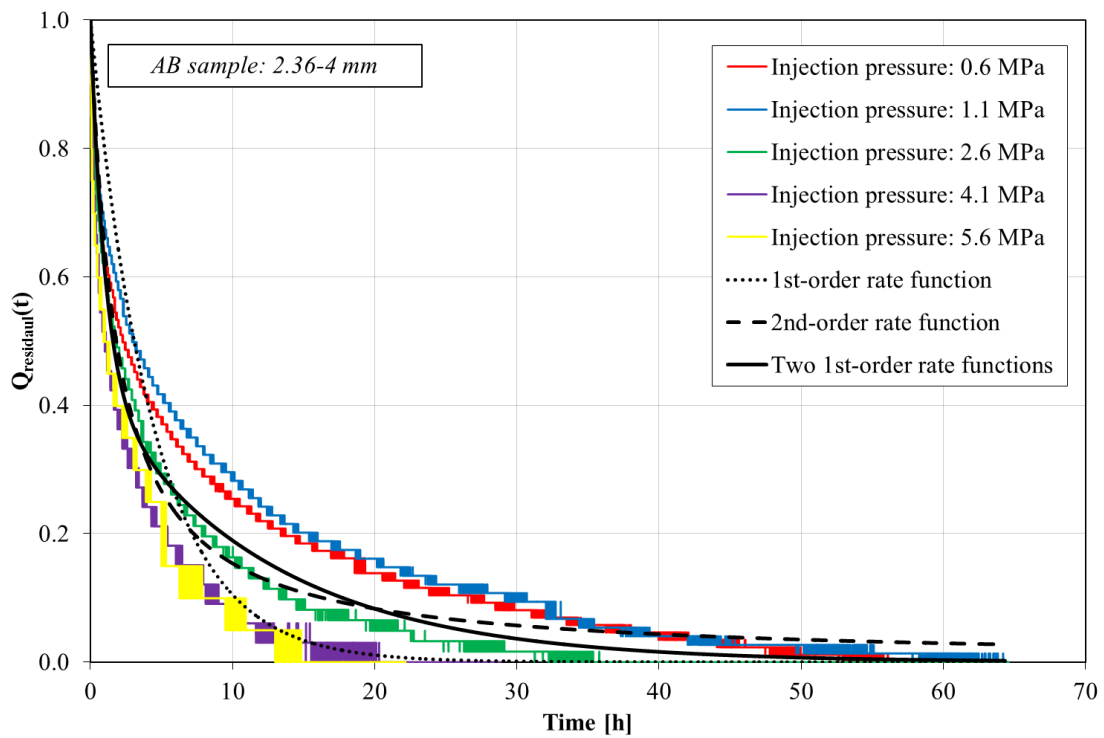


Fig. 5.31. The fits of the experimental residual sorption capacity decline for 9ft Aberpergwm coal – grain size 2.36-4 mm.

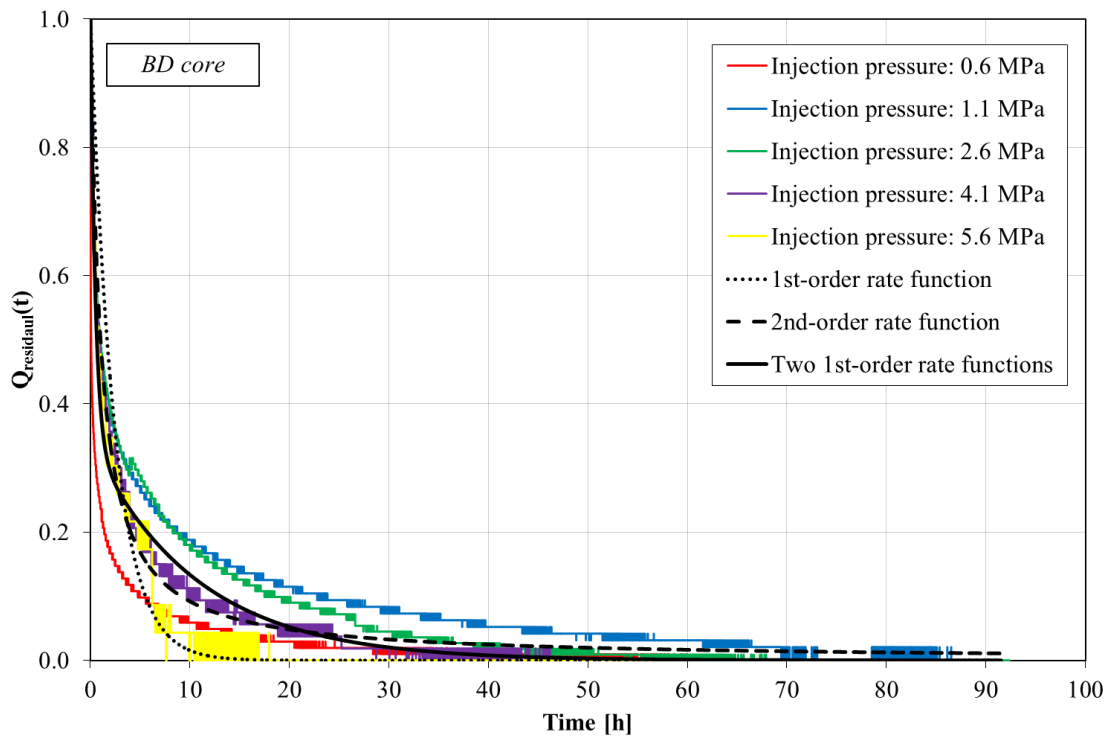


Fig. 5.32. The fits of the experimental residual sorption capacity decline for Black Diamond coal core.

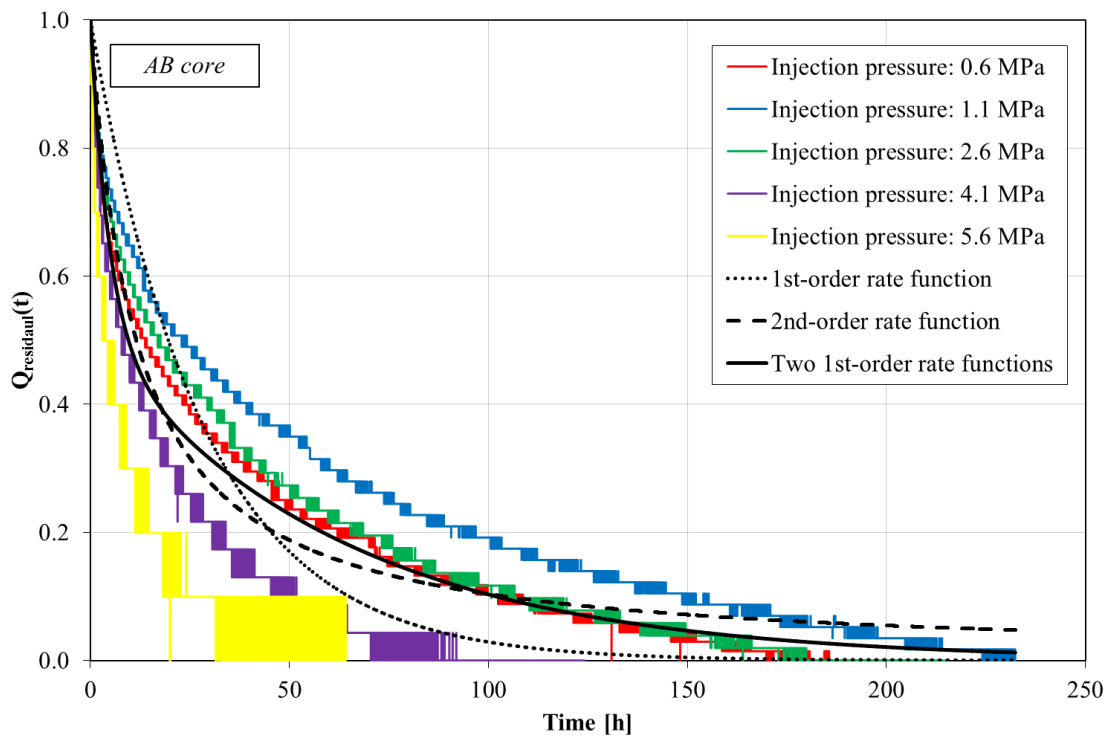


Fig. 5.33. The fits of the experimental residual sorption capacity decline for 9ft Aberpergwm coal core.

In addition, each figure contains three approaches to match experimental pressure decay curves calculated using equations (5.5) to (5.7). Injection pressures stated in the figures refer to the gas pressure in the reference cell before connecting it to the sample cell at the start of each pressure step in the experiment. By inspecting the shape of the pressure decay curves presented in all the figures, it can be seen that as the coal sample size increases, the time for the pressure to reach equilibrium increases as well.

It can be inferred from Figures 5.28 to 5.33 that the first-order kinetics model provides good fit to the data in the early stage of the sorption process while it cannot match the data at later stages of the sorption. The second-order kinetics model fits better to the experimental data, especially at the start of the pressure step, while it slightly overestimates the sorption time at the end of the sorption process.

The comparison of the three approaches suggests that the sorption kinetics is most accurately modelled using the two combined first-order rate function. The reason for that is because such fitting divides the sorption process into two fractions of sorption capacity, i.e. Q_1 and Q_2 associated with the fast and the slow sorption process, respectively (Busch et al., 2004). In particular, the first stage is specified to model the initially rapid sorption, whilst the other is specified to model the more gradual stage that follows (Hosking, 2014).

Although adsorption is a phenomenon occurring at a surface of the coal, the time taken to reach equilibrium in a pressure step is dependent on two major factors. Both the time taken for the molecules to arrive at the adsorption sites within the coal grains and the time required for molecules to physically or chemically interact with the coal surface upon contact must be considered (Hosking, 2014). Hence, the explanation of the behaviour observed in this study might be related to the contributions of the pores of various sizes to the overall sorption process.

It is reasonable to expect that powdered samples with a grain size of 0.25-0.85 mm and 2.36-4 mm have lost most of their macropores (> 50 nm) and the fracture network during the crushing process (Staib et al., 2015). However, for the grain size of 0.25-0.85 mm, it can also be expected that due to the powdering process and the very small grain size as a result, previously restricted and dead-end pores might be opened leading to

easier accessibility of the sorption sites. In particular, this would have resulted in faster sorption in 0.25-0.85 mm grains compared to the samples with grain size of 2.36-4 mm.

In addition, due to the high exposure of sorption sites to CO₂, it can be observed from Figures 5.28-5.32 that more than 80% of the total sorption occurs in the early stage of each pressure step, with the remainder of the sorption occurring at the subsequent slower stage. In contrast, sorption of CO₂ in AB core showed different behaviour with sorption occurring more gradually in each pressure step. This could be caused by the fact that the coal matrix has a heterogeneous structure highly constricted by ultra micropores (< 0.6 nm) in which the sorption is marked by the slow rates (Cui et al., 2004; Katyal et al., 2007). Hence, longer sorption process can be expected in larger samples.

Furthermore, the difference in sorption times for cores of both coals is attributed to the interconnectivity of the fracture network. In the BD core, the complexity and extent of the cleats facilitated faster penetration of gas into the coal and easier access to the coal matrix as explained earlier. In large particles with well-developed fracture network, transport along the cleats is a controlling factor while the inter-cleat diffusion distances remain essentially constant (Busch et al., 2004). Moreover, the maceral composition and the effect of CO₂ sorption on coal structure, by decreasing the macropore volume and increasing the micropore volume in turn, might also play a significant role, as mentioned in Chapter 2. Consequently, the above processes could be responsible for the observed behaviour of increased sorption time for AB coal.

Constants related to the first-order, second-order and two combined first-order rate equations (5.5 to 5.7) were obtained by fitting the models to the experimental results. A summary of the parameters obtained is given in Table 5.2.

Based on the fitting parameters obtained, i.e. sorption rate constants, it can be observed that values of constants decrease with an increase in sample size up to 2.46-4 mm for both coals. However, the reduction of the fitting parameters with further increase in sample size is only observable for the AB coal. Taking this into account as well as the results presented in Figure 5.27 regarding the dependence of maximum sorption capacity on grain volume, it can be inferred that for well-cleated coals, such as BD, increase in size of the bulk specimens should have negligible impact on gas sorption.

Table 5.2. Summary of the sorption rate constants obtained from the first-order, second-order and two combined first-order sorption kinetics models.

Grain size	First-order k (h ⁻¹)	Second-order k' (h ⁻¹)	Two first-order			
			k'' (h ⁻¹)	k''' (h ⁻¹)	Q_1	Q_2
Black Diamond						
0.25-0.85 mm	3.88	9.52	7.89	0.93	0.75	0.25
2.36-4.00 mm	0.41	1.00	1.82	0.12	0.61	0.39
Coal core	0.42	0.99	2.04	0.094	0.66	0.34
9ft Aberpergwm						
0.25-0.85 mm	3.66	9.25	6.85	1.01	0.74	0.26
2.36-4.00 mm	0.23	0.55	0.082	0.98	0.43	0.57
Coal core	0.035	0.086	0.016	0.21	0.51	0.49

Since the two-combined first-order rate function fits the experimental data most accurately, the fast (Q_1) and slow sorption capacities (Q_2), presented as a percentage of the total sorption capacity for both coals with respect to the sample volume, are compared in Figure 5.34.

It can be inferred from Figure 5.34 that for BD coal, the overall contribution to the sorption capacity is dominated by the fast process. In particular, it can be seen that the sample with the smallest volume representing sample with grain size of 0.25-0.85 mm has a 75% percent of the sorption capacity associated with the fast process which decreases to a minimum of 61% with an increase in the sample volume.

Results for the sample with the smallest volume of the AB coal are similar to the results of the BD coal suggesting that when the sorption sites are easily accessible, sorption kinetics of two equally-sized samples of the same rank is the same. As the sample volume increases, AB coal shows similar trend as the BD coal. The percentage of total capacity associated with fast sorption decreases and consequently, the percentage associated with slow sorption increases, yielding a value of 50% both for fast and slow sorption processes in sample with the largest volume, i.e. core.

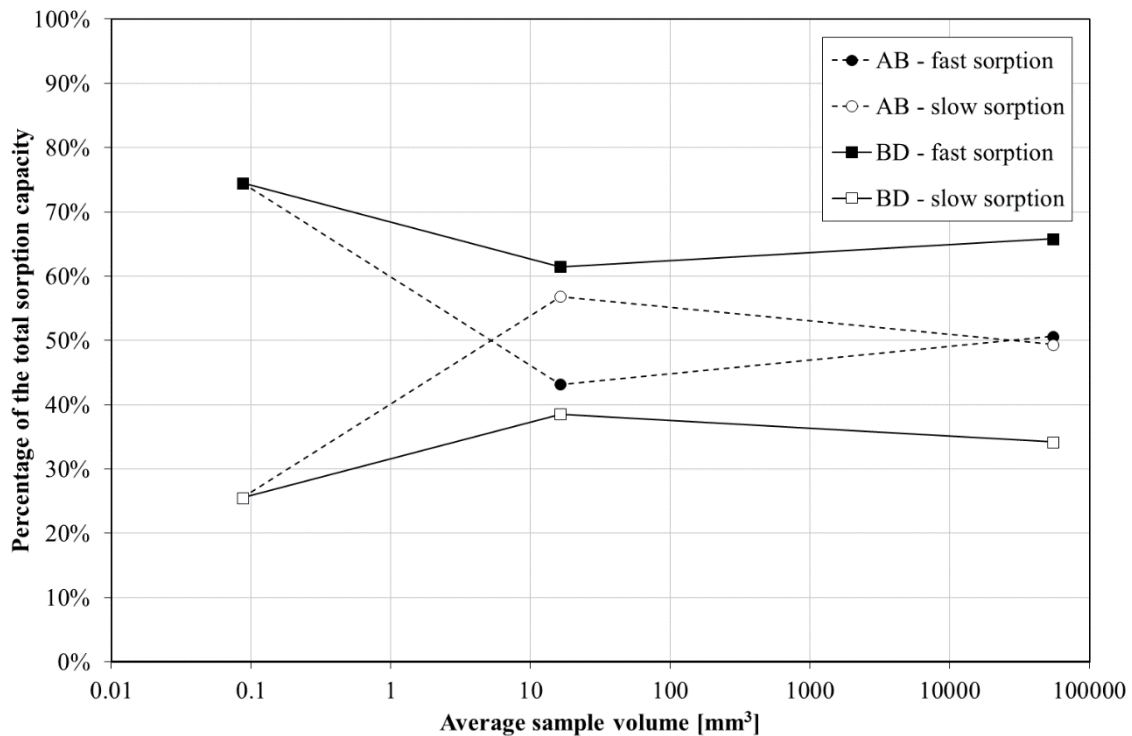


Fig. 5.34. Percentage of total sorption capacities associated with fast and slow sorption versus the average sample volume of both AB and BD coals.

Overall, results of this work on crushed coals, i.e. samples with grain sizes of 0.25-0.85 mm and 2.36-4 mm, are in general comparison with the work by other authors. As mentioned in Chapter 2, few authors have reported that CO₂ kinetics in crushed samples with larger grain sizes is much slower than in finely crushed coal. However, this work suggests that the response of larger samples, i.e. cores, is related to the structure of the coal. Based on the results, it can be inferred that the sorption on the well-fractured core with high accessibility to the sorption sites occurs faster than in coals with less developed pore network.

5.6. Conclusions

In this chapter, experimental results of the sorption measurements of CO₂ on Black Diamond and 9ft Aberpergwm coal samples of different sizes have been presented and discussed. In particular, the response of samples of the same rank, but from different depths with grain sizes of 0.25-0.85 mm and 2.36-4 mm, and coal cores to CO₂ injection was explored. Based on the pressure decay curves obtained, both the excess and

absolute sorption amounts and the kinetic aspects of CO₂ sorption were assessed and presented.

In relation to the maximum excess sorption values, results obtained on powdered samples suggest slightly higher sorption capacity for BD coal than for AB coal. The largest difference in the maximum excess sorption of 13% was calculated. However, investigation of carbon dioxide sorption on cores revealed more significant decrease in excess sorption capacity of maximum 50% for AB with respect to BD coal.

The absolute amounts of CO₂ sorbed on both coals were calculated using the excess sorption values and taking into account the volume of the adsorbed phase. Fitting the Langmuir equation to the obtained experimental absolute sorption amounts was then conducted. Based on the calculated maximum absolute sorption values, the maximum difference in storage capacities between BD and AB crushed samples was 13%. On the other hand, the maximum sorption capacity of the AB core was 58% lower than of the BD core. In addition, while BD coal showed negligible change in maximum sorption capacity with an increase in sample size, AB coal showed the opposite behaviour reaching a maximum difference of 59% in sorption capacity between the core and the powdered samples.

The decrease in absolute sorption capacity with an increase in sample size for the AB coal was attributed to the lack of cleats and fracture interconnectivity as a result of combined geological effects dominant on different depths. In particular, shallower coals, even of the same rank, can have better developed fracture network allowing easier accessibility of sorption sites to the gas molecules. In addition, grinding of coals increases the total porosity accessible to gases and hence, crushed samples showed higher sorption capacity than the cores.

By investigating the pressure decay over time of all samples, it was shown that gas sorption fitted by a two-stage model, splitting gas sorption into a fast and slow process, fits the experimental data more satisfactorily than one-stage models. The sorption time on the smallest sample (0.25-0.85 mm) for both coals yielded identical results where almost 95% of sorption occurred in the first 2 hours of each injection step. Larger samples showed an increase in time required for sorption to finish. While samples with grain size of 2.36-4 mm from both coals and BD core required between 40 and 80 hours

to achieve equilibration, AB core required up to 250 hours to complete the sorption process at each injection step.

Based on the abovementioned observations, the time required for the gas injected in coal samples to reach equilibrium is analogous to the coal's behaviour in relation to the sorption capacity. In other words, coals that had the fastest sorption resulted in the highest sorption capacity. An explanation to such behaviour was offered through the structure of the high-rank coals. Where the fracture network is sufficiently developed and distance between the cleats is small enough, accessibility to the sorption sites is high.

Overall, the measured adsorbed amount and time associated with the sorption on the smallest samples could be attributed to the pore filling and CO₂ dissolution in the coal structure due to the high exposure of pores to the gas. Larger samples would additionally include transport mechanisms within the cleat system, mass exchange between the fractures and the matrix as well as the diffusion of the gas molecules within the microporous system to the sorption sites. This would serve as a possible explanation for the slower sorption process in larger samples. Hence, through this work, distribution and inter-connectivity of the pores and cleats have proven to have a significant effect on the sorption behaviour of CO₂ on coal.

More discussion on the effect of CO₂ sorption on the coal structure and gas transport in coal will be provided in Chapters 6 and 7, respectively.

5.7. References

Arri, L.E. , Yee, D., Morgan, W.D. and Jeansonne, M.W. 1992. Modeling coalbed methane production with binary gas sorption. In *SPE Rocky Mountain Regional Meeting*, Society of Petroleum Engineers.

Bae, J.-S. and Bhatia, S.K. 2006. High-pressure Adsorption of Methane and Carbon Dioxide on Coal. *Energy & Fuels*, 20, pp. 2599-2607.

Busch, A., Gensterblum, Y., Krooss, B.M. and Littke, R. 2004. Methane and carbon dioxide adsorption-diffusion experiments on coal: upscaling and modeling. *International Journal of Coal Geology*, 60(2-4), pp. 151-168.

Cui, X., Bustin, R.M. and Dipple, G. 2004. Selective transport of CO₂, CH₄ and N₂ in coals: insights from modeling of experimental gas adsorption data. *Fuel*, 83(3), pp. 293-303.

- Dutta, P., Harpalani, S. and Prusty, B. 2008. Modeling of CO₂ sorption on coal. *Fuel*, 87(10-11), pp. 2023-2036.
- Fitzgerald, J.E., Pan, Z., Sudibandriyo, M., Robinson, J.R.L., Gasem, K.A.M. and Reeves, S. 2005. Adsorption of methane, nitrogen, carbon dioxide and their mixtures on wet Tiffany coal. *Fuel*, 84(18), pp. 2351-2363.
- Gensterblum, Y., van Hemert, P., Billemont, P., Battistutta, E., Busch, A., Krooss, B.M., De Weireld, G. and Wolf, K.H.A.A. 2010. European inter-laboratory comparison of high pressure CO₂ sorption isotherms II: Natural coals. *International Journal of Coal Geology*, 84(2), pp. 115-124.
- Goodman, A.L., Busch, A., Bustin, R.M., Chikatamarla, L., Day, S., Duffy, G.J., Fitzgerald, J.E., Gasem, K.A.M., Gensterblum, Y., Hartman, C., Jing, C., Krooss, B.M., Mohammed, S., Pratt, T., Robinson Jr., R.L., Romanov, V., Sakurovs, R., Schroeder, K. and White, C.M. 2007. Inter-laboratory comparison II: CO₂ isotherms measured on moisture-equilibrated Argonne premium coals at 55°C and up to 15 MPa. *International Journal of Coal Geology*, 72(3-4), pp. 153-164.
- He, J., Shi, Y., Ahn, S., Kang, J.W. and Lee, C. 2010. Adsorption and desorption of CO₂ on Korean coal under subcritical to supercritical conditions. *The Journal of Physical Chemistry*, 114(14), pp. 4854-4861.
- Hosking, L.J. 2014. *Reactive transport modelling of high pressure gas flow in coal*. Ph.D. Thesis, Cardiff University, Wales, UK.
- Katyal, S., Valix, M. and Thambimuthu, K. 2007. Study of Parameters Affecting Enhanced Coal Bed Methane Recovery. *Energy Sources, Part A*, 29(3), pp. 193-205.
- Langmuir, I. 1918. The adsorption of gases on plane surfaces of glass, mica and platinum. *Journal of the American Chemical Society*, 40(9), pp. 1361-1403.
- Lutynski, M.A., Battistutta, E., Bruining, H. and Wolf, K.H.A.A. 2011. Discrepancies in the assessment of CO₂ storage capacity and methane recovery from coal with selected equations of state. Part I. Experimental isotherm calculation. *Physicochemical Problems of Mineral Processing*, 47, pp. 159-168.
- Mohammad, S., Fitzgerald, J., Robinson Jr., R.L. and Gasem, K.A.M. 2009. Experimental Uncertainties in Volumetric Methods for Measuring Equilibrium Adsorption. *Energy & Fuels*, 23, pp. 2810-2820.
- Petrucci, R.H., Harwood, W.S. and Herring, F.G. 2002. *General Chemistry: Principles and Modern Applications*, vol 1, Prentice Hall.
- Siemons, N. and Busch, A. 2007. Measurement and interpretation of supercritical CO₂ sorption on various coals. *International Journal of Coal Geology*, 69(4), pp. 229-242.
- Span, R. and Wagner, W. 1996. A new equation of state for carbon dioxide covering the fluid region from the triple-point temperature to 1100 K at pressures up to 800 MPa. *Journal of Physical and Chemical Reference Data*, 25(6), pp. 1509-1596.

Staib, G., Sakurovs, R. and Gray, E.M.A. 2015. Dispersive diffusion of gases in coals. Part II: An assessment of previously proposed physical mechanisms of diffusion in coal. *Fuel*, 143, pp. 620-629.

6

Effects of CO₂ Sorption on the Deformation Properties

6.1. Introduction

The results of the unconfined compressive tests conducted on twenty anthracite coal specimens are presented in this chapter. Both BD and AB coals were employed for this study. Eight samples were tested in natural (non-saturated) air-dried state. Twelve specimens were exposed to CO₂ for two weeks at 313K and at three different pressures, i.e. 2.1 MPa, 4.3 MPa and 8.5 MPa, before testing.

The aim of this chapter is to provide a better understanding of the coal-CO₂ interaction and its impact on coal structure and deformation properties through experimental investigation. To achieve this, the main objectives of the experimental results presented here are: i) to determine the unconfined compressive strengths and elastic moduli of the intact coal specimens both non-saturated and saturated with CO₂, ii) to assess the dependence of the deformation parameters obtained on CO₂ pressure, iii) to analyse the effect of CO₂ saturation on the failure patterns of samples tested, iv) to determine the distribution of particle sizes after the failure of the samples.

Stress-strain behaviour of non-saturated specimens and specimens saturated both with subcritical CO₂ and supercritical CO₂ is presented in Section 6.2. Based on stress-strain data, values of unconfined compressive strength and elastic modulus are calculated and presented. In addition, the change in deformation parameters with an increase in gas saturation pressure is shown and discussed. Observed reductions in elastic modulus and unconfined compressive strength are then quantified by applying a fitting curve to the experimentally determined values and obtaining the parameters related to the reduction of deformation properties as a function of gas pressure.

Failure patterns of non-saturated and CO₂ saturated specimens of both coals are analysed and discussed in Section 6.3, based on the photographs taken before and after the coal failure.

Following the observations in Section 6.3, results of the post-failure sieve analysis are presented in Section 6.4 for non-saturated and CO₂ saturated specimens. The effect of CO₂ saturation under different pressures on particle distribution of samples after failure is analysed and discussed.

Finally, the concluding remarks of the chapter are presented in Section 6.5.

6.2. CO₂ Saturation Effect on Deformation Parameters

Experimental results of unconfined compressive tests carried out on non-saturated and CO₂ saturated specimens of Black Diamond and 9ft Aberpergwm coals are presented in this section. The preparation of samples for uniaxial compression, assembling on the testing cell and the procedure for the determination of deformation parameters have been presented in Chapter 4. As previously mentioned, a total of twenty specimens have been tested under uniaxial load. Using the measured loading force and displacement on each sample of known dimensions, stress and strain values were determined.

Axial stress versus strain curves for non-saturated and CO₂ saturated specimens from both coals are presented in Figures 6.1-6.8. In particular, the figure for AB specimens follows the figure for BD specimens, i.e. experimental data for non-saturated BD and AB specimens are presented in Figures 6.1 and 6.2, respectively. Those figures are then followed by figures containing data obtained on 2.1 MPa, 4.3 MPa and 8.5 MPa saturated specimens for BD and AB in a similar manner.

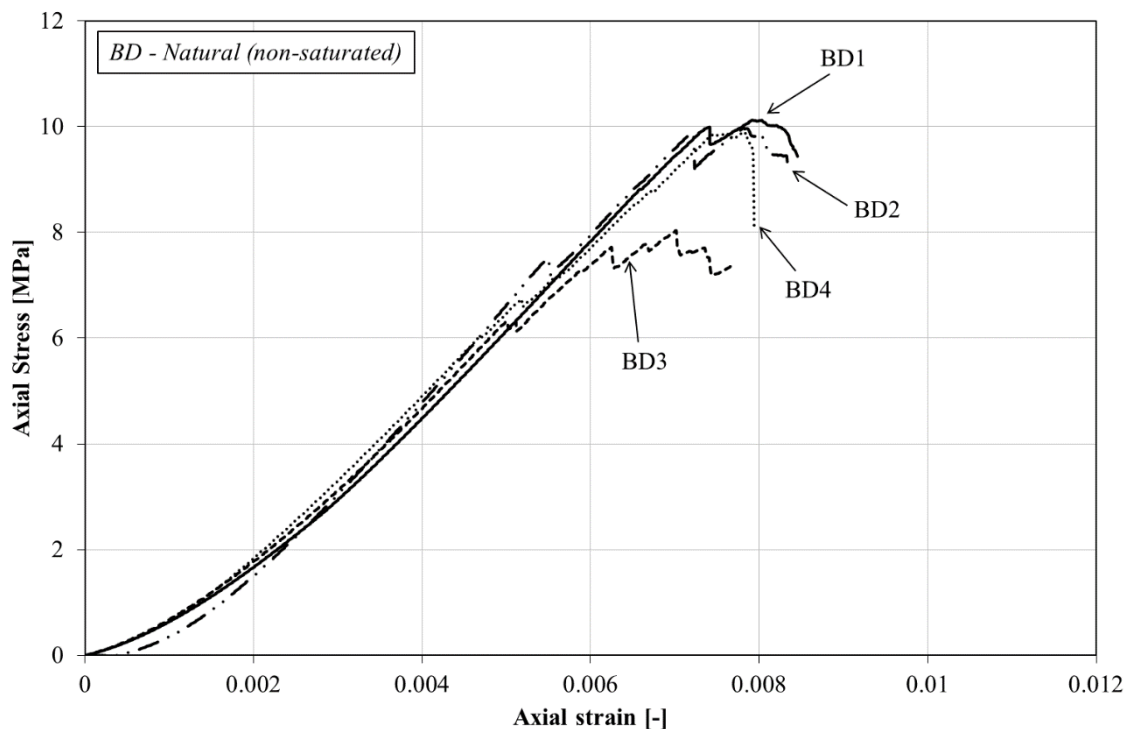


Fig. 6.1. Axial stress versus strain curves of natural (non-saturated) Black Diamond specimens.

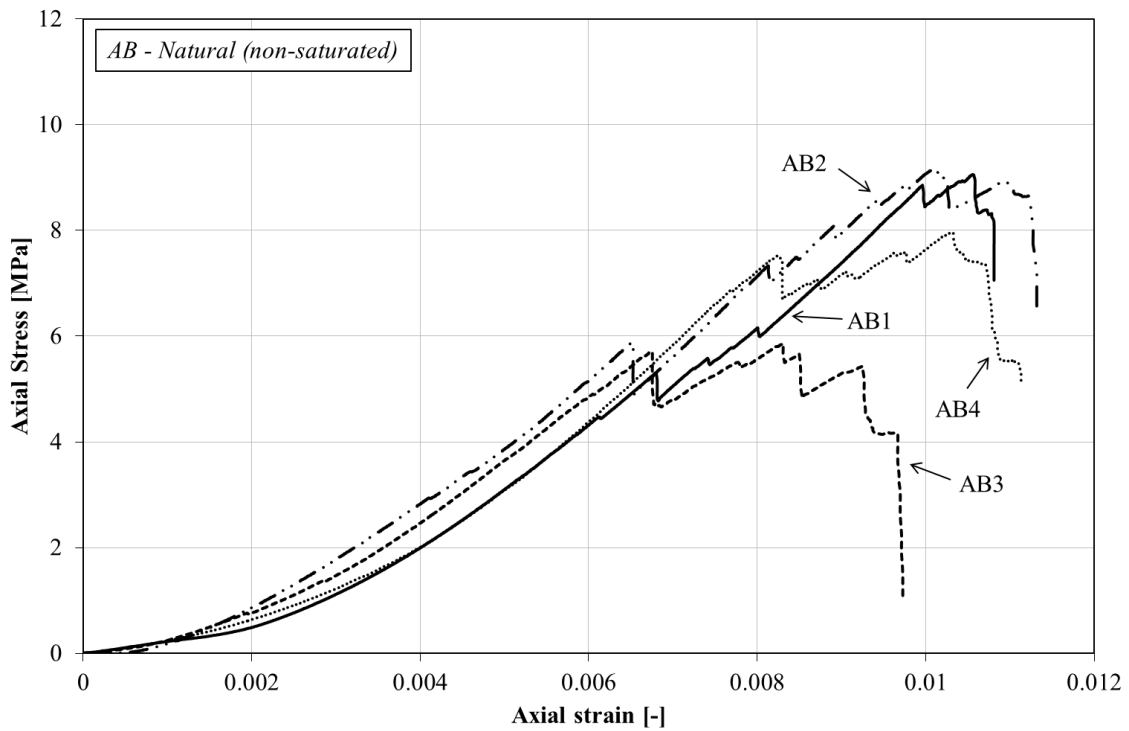


Fig. 6.2. Axial stress versus strain curves of natural (non-saturated) 9ft Aberpergwm specimens.

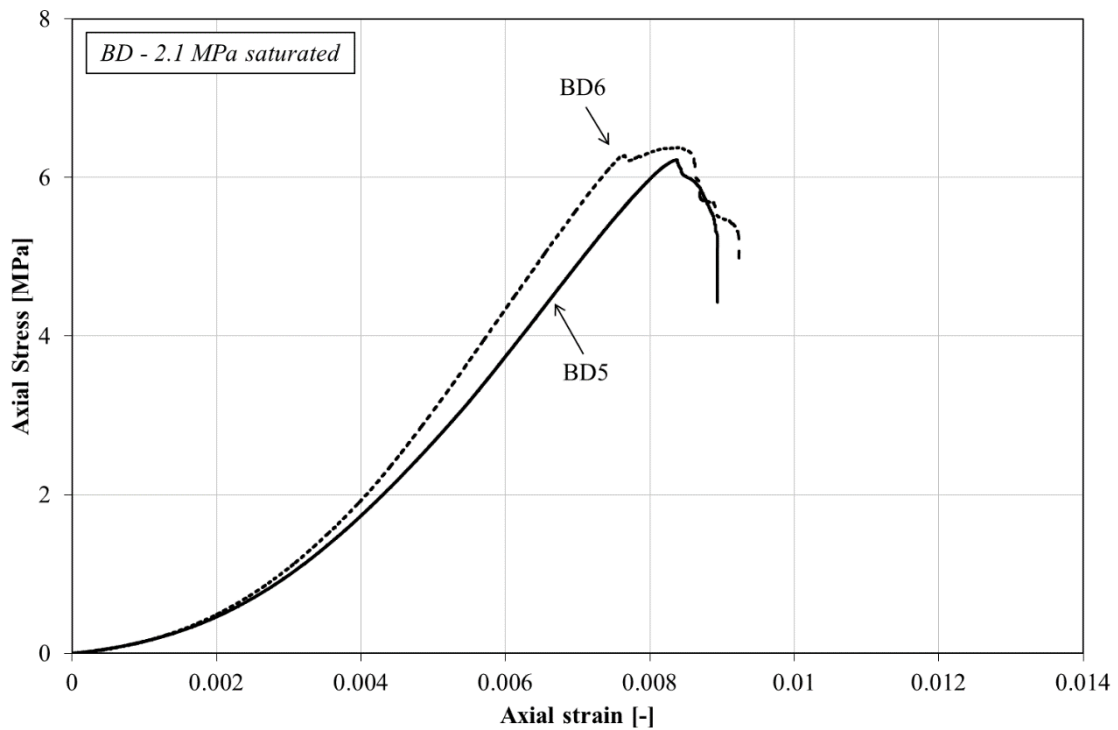


Fig. 6.3. Axial stress versus strain curves of Black Diamond specimens saturated with CO₂ at 2.1 MPa.

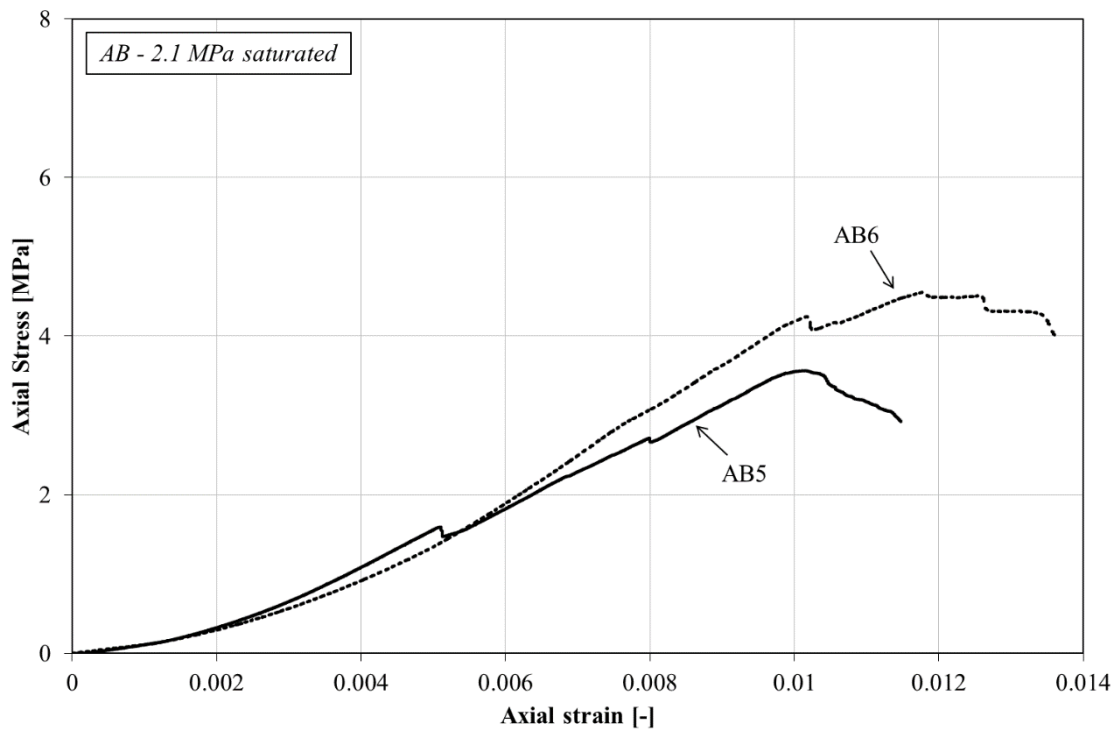


Fig. 6.4. Axial stress versus strain curves of 9ft Aberpergwm specimens saturated with CO₂ at 2.1 MPa.

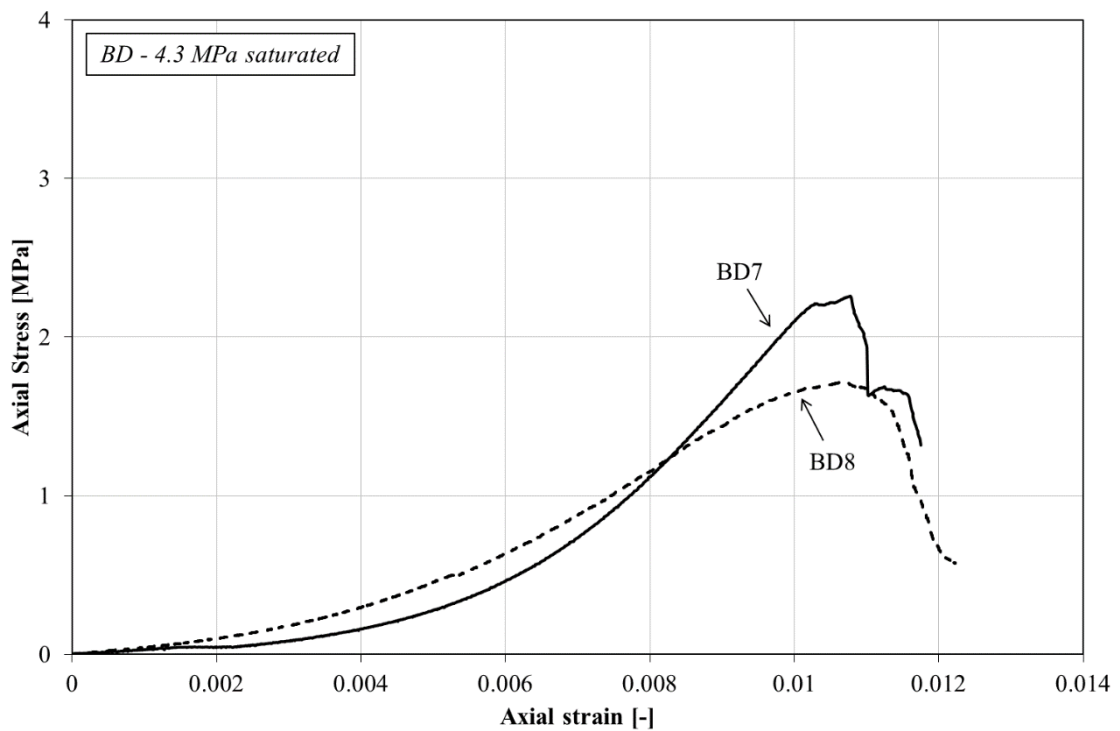


Fig. 6.5. Axial stress versus strain curves of Black Diamond specimens saturated with CO₂ at 4.3 MPa.

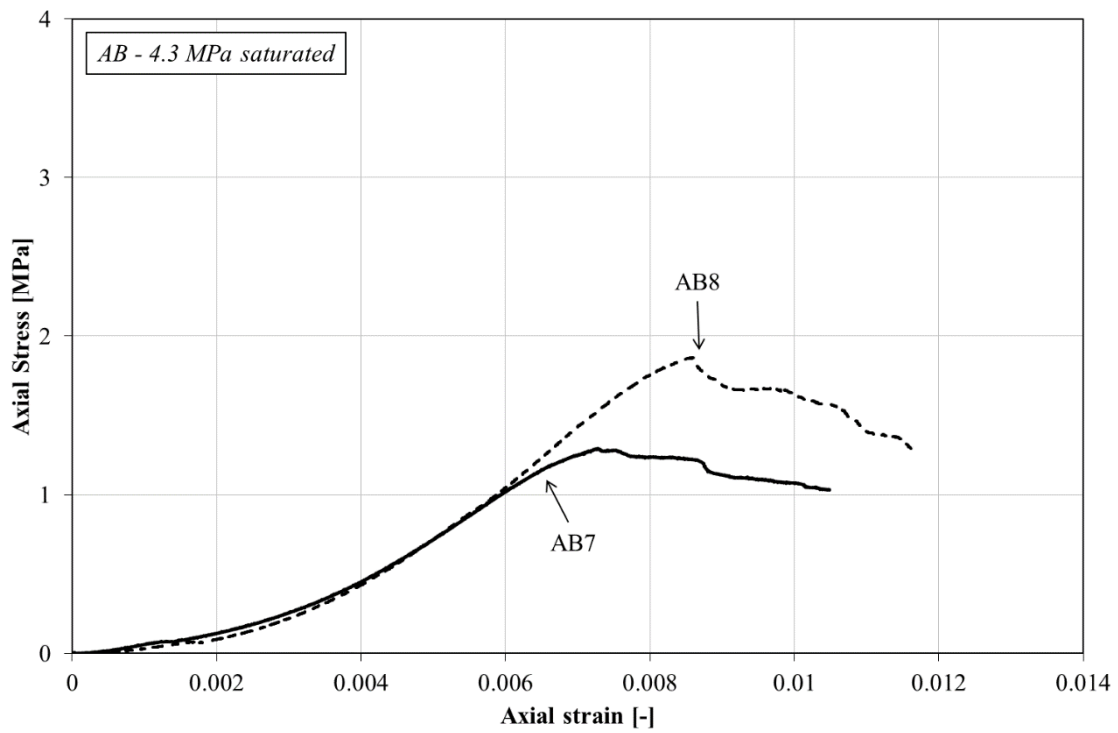


Fig. 6.6. Axial stress versus strain curves of 9ft Aberpergwm specimens saturated with CO₂ at 4.3 MPa.

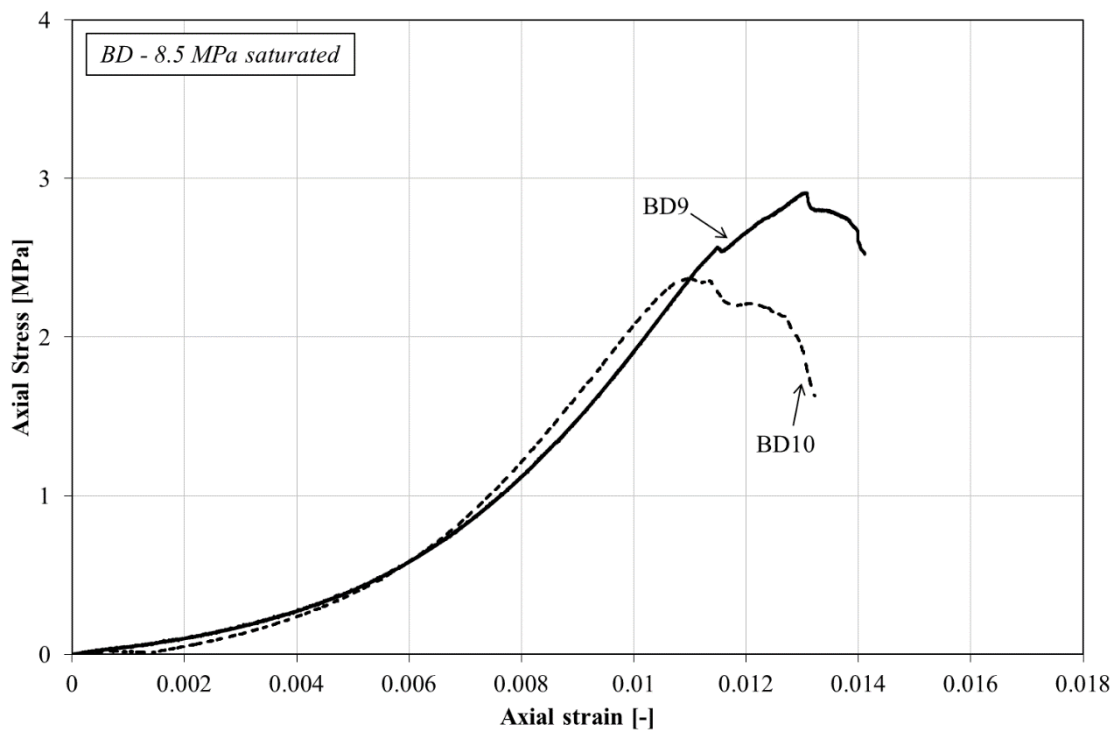


Fig. 6.7. Axial stress versus strain curves of Black Diamond specimens saturated with CO₂ at 8.5 MPa.

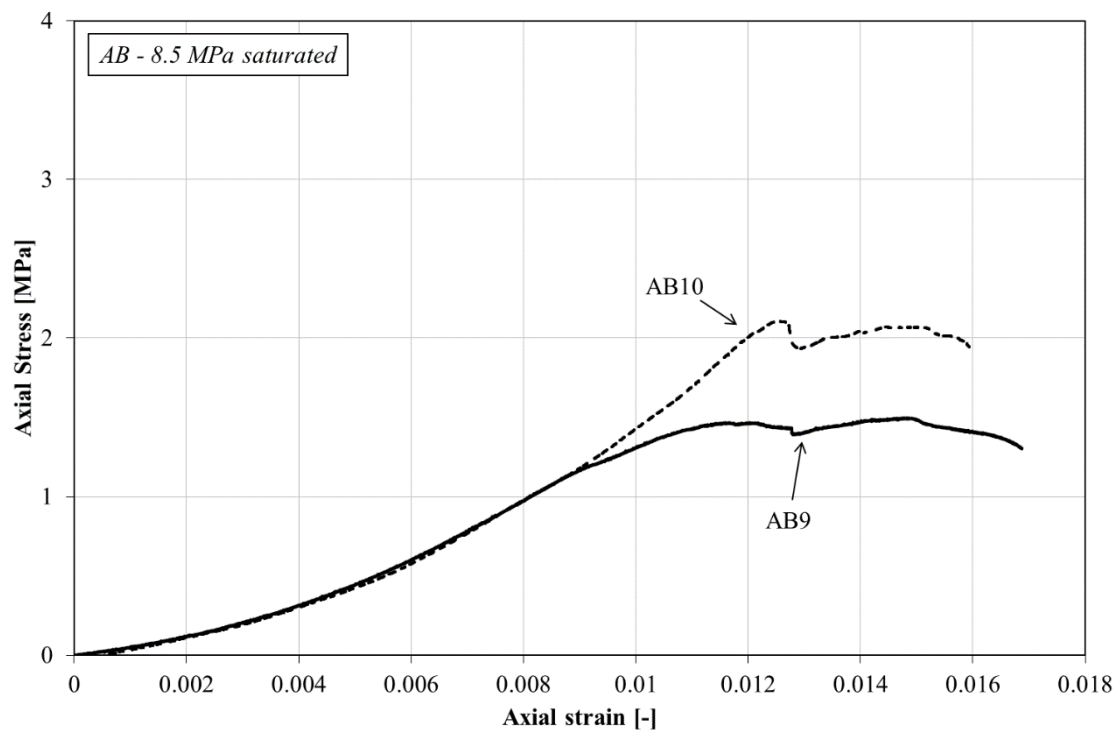


Fig. 6.8. Axial stress versus strain curves of 9ft Aberpergwm specimens saturated with CO₂ at 8.5 MPa.

Slopes of the curves and maximum recorded stress values of 10 MPa obtained on three non-saturated BD specimens are comparable, as shown in Figure 6.1. The exception is sample BD3 which experienced failure at a lower value of applied stress, i.e. 8 MPa. Figure 6.2 shows that the slopes of the curves of non-saturated AB specimens are also comparable, however; maximum recorded stress values range between 6 MPa and 9.1 MPa.

Experimental results of the two BD specimens saturated with CO₂ at 2.1 MPa show comparable behaviour with maximum recorded stress values of 6.3 MPa. Although both AB specimens saturated at 2.1 MPa show similar slopes of the curves, maximum stress values are 3.6 MPa and 4.6 MPa.

Stress-strain results of specimens saturated at 4.3 MPa and 8.5 MPa of both coals are shown in Figures 6.5-6.8. Slopes of the curves of the two specimens in each figure are similar. However, maximum stress values show a deviation between the two samples presented in each figure. In particular, two BD specimens saturated at 4.3 MPa and two saturated at 8.5 MPa show peak stress values of 2.3 MPa and 1.7 MPa, and 2.9 MPa and 2.4 MPa, respectively. Similarly, AB samples saturated at 4.3 MPa show maximum

stress values of 1.3 MPa and 1.9 MPa, while samples saturated at 8.5 MPa show maximum stresses of 1.5 MPa and 2.1 MPa.

A discrepancy among the results reported above could be related to the small inconsistency in length-to-diameter ratio (see Table 4.2). However, pre-existing fractures, orientation of the newly created cracks and connectivity with the pre-existing ones as well as the inhomogeneity within the coal samples could affect the response of the samples under uniaxial compression (Viète and Ranjith, 2006; Masoudian et al., 2014).

By comparing the Figures (6.1 to 6.8), it can be observed that the stress-strain behaviour of samples saturated with CO₂ is different than of non-saturated samples. In particular, samples exposed to CO₂ can be compressed more for the same value of applied stress than the non-saturated samples.

Furthermore, non-saturated samples show sudden drop in measured stress after the failure while CO₂ saturated specimens show more gradual drop in stress. This is especially notable for the supercritical CO₂ saturated samples. Such observation suggests that besides lowering the deformation parameters, CO₂ saturation also affects the failure mode. It should be noted that during the testing procedure, non-saturated samples showed brittle behaviour with fast crack propagation and high outburst of the material. In contrast, CO₂ saturated samples showed ductile behaviour with extensive deformation characterized by slow crack growth before the final failure, with negligible material outburst. Further analysis of such behaviour will be presented later in the chapter.

Calculated values of elastic modulus and unconfined compressive strength of BD and AB samples are presented in Table 6.1 where a general reduction in values with an increase in saturation pressure can be observed. Based on the deformation parameters of four non-saturated specimens and two samples saturated at different pressures of each coal, average values of unconfined compressive strength and elastic modulus are also calculated and presented in Table 6.1. In addition, reduction of average values of CO₂ saturated samples was calculated with respect to the average values of non-saturated samples and presented in Table 6.1.

Table 6.1. Unconfined compressive strength (UCS) and elastic modulus (E) values of natural (non-saturated) and CO₂ saturated Black Diamond (BD) and 9ft Aberpergwm (AB) coal samples.

Specimen	L/D ratio	UCS (MPa)	Average UCS (MPa)	ΔUCS (%)	E (GPa)	Average E (GPa)	ΔE (%)
Black Diamond							
<i>Natural (non-saturated)</i>							
BD1	2.1	10.12			1.51		
BD2	2.1	9.97	9.51	-	1.72	1.59	-
BD3	2.1	8.03	±0.86		1.53	±0.08	
BD4	2.1	9.90			1.57		
<i>2.1 MPa saturated</i>							
BD5	2.1	6.23	6.31	-33.7	1.04	1.13	-29.0
BD6	2.1	6.38	±0.08		1.21	±0.08	
<i>4.3 MPa saturated</i>							
BD7	2.0	2.26	1.99	-79.1	0.48	0.37	-76.8
BD8	2.0	1.72	±0.27		0.26	±0.11	
<i>8.5 MPa saturated</i>							
BD9	2.1	2.91	2.65	-72.2	0.39	0.40	-74.8
BD10	2.0	2.38	±0.27		0.42	±0.02	
9ft Aberpergwm							
<i>Natural (non-saturated)</i>							
AB1	2.1	9.06			1.15		
AB2	1.9	9.15	8.01	-	1.06	1.13	-
AB3	1.9	5.86	±1.33		1.15	±0.04	
AB4	2.2	7.97			1.16		
<i>2.1 MPa saturated</i>							
AB5	1.6	3.57	4.06	-49.3	0.41	0.49	-56.3
AB6	1.6	4.56	±0.49		0.58	±0.08	
<i>4.3 MPa saturated</i>							
AB7	1.6	1.29	1.58	-80.3	0.28	0.29	-74.5
AB8	1.8	1.87	±0.29		0.30	±0.01	
<i>8.5 MPa saturated</i>							
AB9	1.5	1.50	1.80	-77.5	0.18	0.19	-82.9
AB10	2.1	2.11	±0.31		0.21	±0.02	

The relationship between the average elastic modulus of non-saturated samples and CO₂ saturated samples used to calculate the reductions presented in Table 6.1 is:

$$\Delta E = \left(1 - \frac{E_{CO_2}}{E_{natural}}\right) \times 100 \quad (6.1)$$

where ΔE is the reduction in elastic modulus, $E_{natural}$ (GPa) and E_{CO_2} (GPa) are the elastic modulus of natural (non-saturated) and CO₂ saturated coal, respectively.

Similarly, reduction in unconfined compressive strength (ΔUCS) is expressed as:

$$\Delta UCS = \left(1 - \frac{UCS_{CO_2}}{UCS_{natural}}\right) \times 100 \quad (6.2)$$

where $UCS_{natural}$ (MPa) and UCS_{CO_2} (MPa) are the unconfined compressive strength of natural (non-saturated) and CO₂ saturated coal, respectively.

It can be seen from Table 6.1 that the average elastic moduli of non-saturated BD and AB specimens are 1.59 GPa and 1.13 GPa, respectively. The average unconfined compressive strength of BD specimens is 9.51 MPa while AB specimens show 8.01 MPa. BD specimens saturated with CO₂ at 2.1 MPa, 4.3 MPa and 8.5 MPa exhibit the average elastic modulus values of 1.13 GPa, 0.37 GPa and 0.4 GPa and the average unconfined compressive strengths of 6.31 MPa, 1.99 MPa and 2.65 MPa, respectively. The average elastic moduli and unconfined compressive strengths of AB specimens saturated with CO₂ at the same pressures are 0.49 GPa, 0.29 GPa, 0.19 GPa and 4.06 MPa, 1.58 MPa, 1.8 MPa, respectively.

As mentioned in Chapter 2, there is no information about the effect of subcritical and supercritical CO₂ saturation on elastic deformation and failure of high-rank anthracitic coals as well as the coals from the South Wales coalfield reported in the literature, according to the author's knowledge.

If the average deformation values of BD and AB samples are compared, a difference can be observed. Non-saturated AB coal shows lower average values of unconfined compressive strength and elastic modulus than the non-saturated BD coal, i.e. 16% and 29%, respectively. Similarly, CO₂ saturated AB coals show lower values of deformation parameters than BD coals. In particular, AB samples saturated at 2.1 MPa, 4.3 MPa and 8.5 MPa exhibit 36%, 21% and 32% reduction of unconfined compressive strength and 57%, 22% and 53% reduction of elastic modulus in comparison to BD samples, respectively. Since the intention was to choose the specimens from both coals with minimum amount of visible cleats in order to minimize the impact of fracture system on measured values, such differences between the samples could be attributed to the orientation and interconnectivity of the internal cleat system. However, it can be inferred that despite the difference, obtained values are in the same order of magnitude and hence comparable.

In order to establish a relationship between the deformation parameters of all samples, unconfined compressive strength versus elastic modulus values of all tested specimens are plotted in Figure 6.9. As can be observed, elastic modulus and unconfined compressive strength show linear relationship, i.e. samples with higher strength show higher values of elastic modulus. In addition, it can be seen that the regression line fits closely to the presented experimental results resulting in coefficient of regression of 0.9.

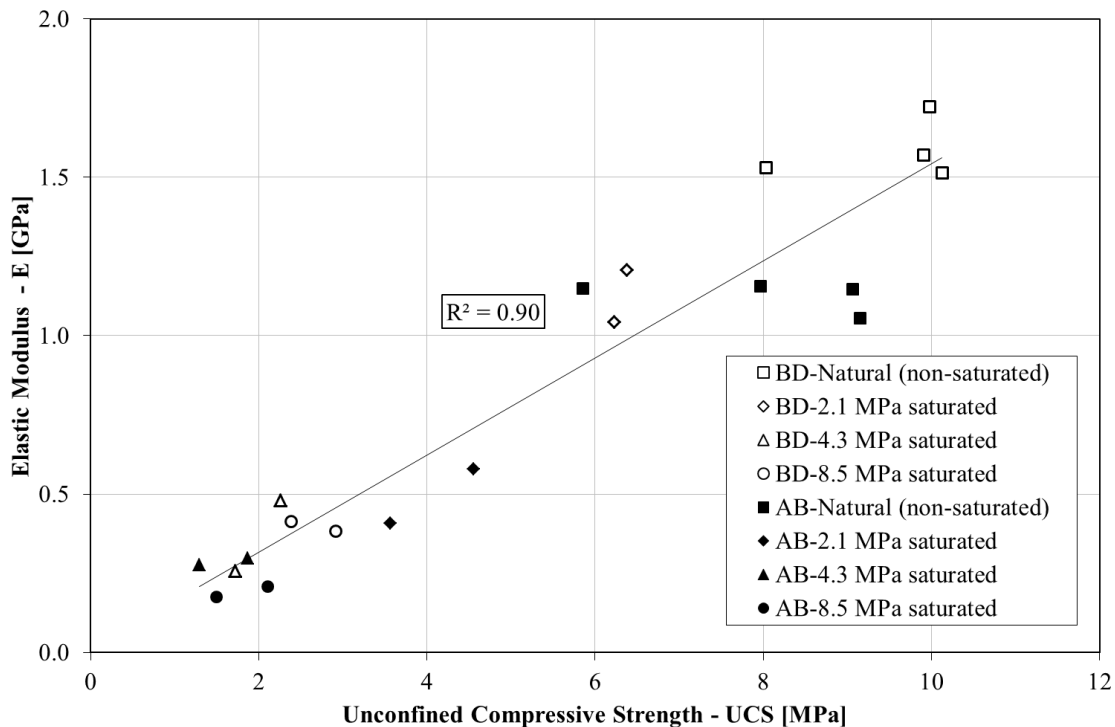


Fig. 6.9. Uniaxial compressive strength versus elastic modulus of natural (non-saturated) and CO₂ saturated coal specimens.

Based on the deformation values presented in Table 6.1, changes of unconfined compressive strength and elastic modulus values with an increase in saturation pressure are presented in Figures 6.10 and 6.11, respectively. It can be seen in Figure 6.10 that both samples show similar behaviour where a steep decrease in the unconfined compressive strength occurs from the initial values of 8-10 MPa up to approximately 2.1 MPa at 4.3 MPa CO₂ pressure and then show negligible decrease in values with an increase in gas pressure.

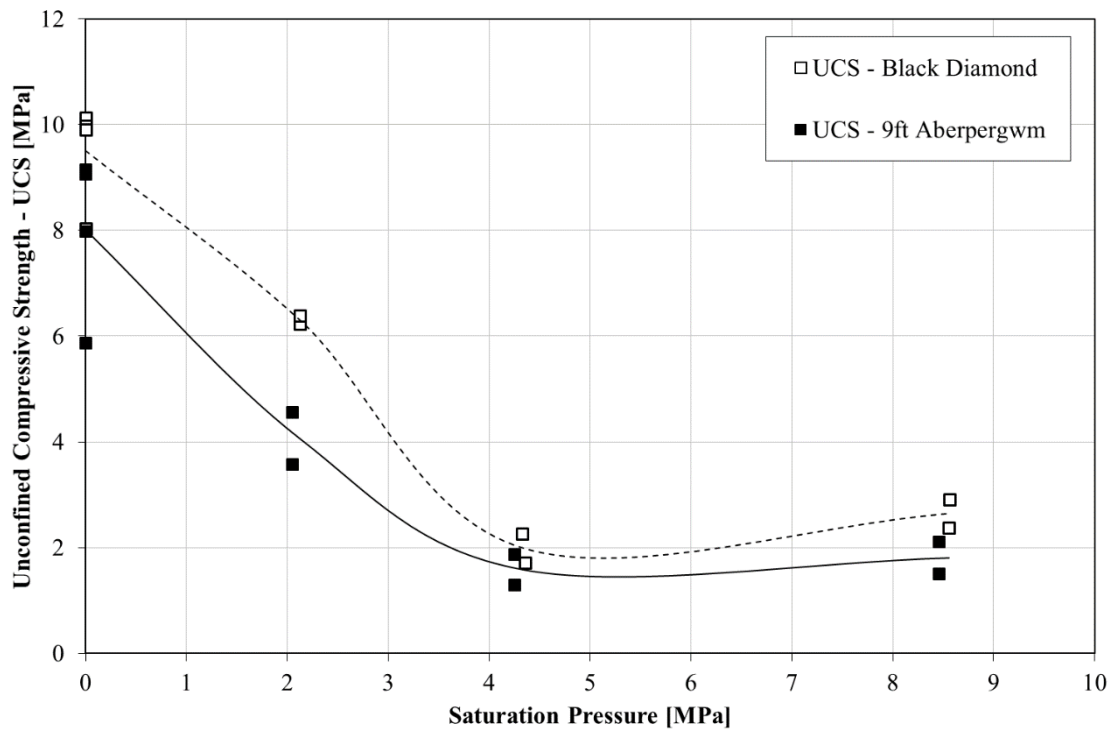


Fig. 6.10. Carbon dioxide-induced unconfined compressive strength decrease versus the saturation pressure of BD and AB specimens.

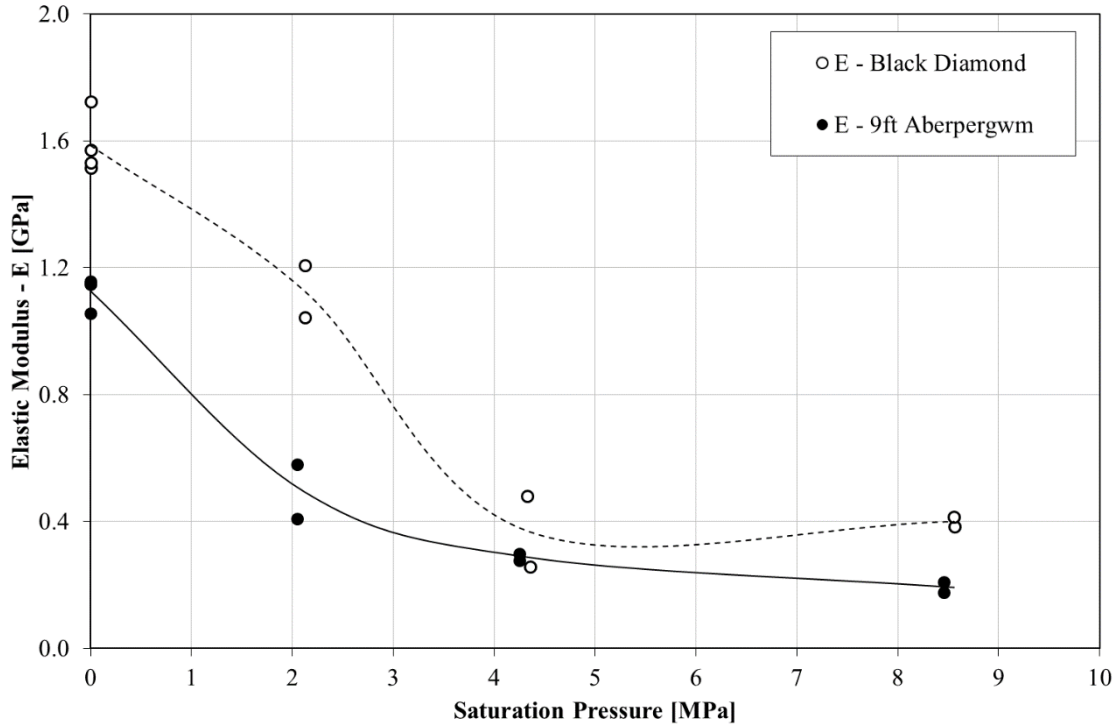


Fig. 6.11. Carbon dioxide-induced elastic modulus decrease versus the saturation pressure of BD and AB specimens.

Similarly, values of elastic modulus in Figure 6.11 of both coals show a decrease from initial values ranging between 1.2-1.6 GPa to 0.3-0.4 GPa at 4.3 MPa gas pressure with negligible further decrease with an increase in CO₂ pressure.

Hence, it can be observed that increasing the gas pressure from subcritical region at 4.3 MPa to supercritical region at 8.5 MPa does not have a significant effect on the calculated values of strength parameters of both BD and AB coals. Such observation can be expected due to the fact that when sorption reaches close to maximum at higher pressures, decrease in deformation parameters should also be minimal (Masoudian et al., 2014). In particular, as discussed and shown in Chapter 5, BD and AB cores exhibit half of their maximum sorption at 0.91 MPa and 0.44 MPa, respectively. Consequently, it can be expected that majority of structural re-arrangement and its effect on coal strength and elastic modulus occurred in the subcritical region, up to 4.3 MPa in this case, whereas no significant change has been observed with further increase in gas pressure.

However, this is not completely consistent with the work of Perera et al. (2013) and Ranathunga et al. (2016) who have performed an experimental study of supercritical CO₂ saturation-induced mechanical property alterations in low rank coals. Perera et al. (2013) and Ranathunga et al. (2016) have concluded that during the increase of the CO₂ saturation pressure from the subcritical to supercritical zone, both deformation parameter reductions were subjected to a sudden increment which was related to the greater sorptive capacity of supercritical CO₂ compared to subcritical CO₂. This might be related to the difference in sorption behaviour of low ranks coals compared to high ranks coals. Siemons and Busch (2007) and Gensterblum et al. (2010) have shown that low rank coals exhibit half of their sorption at higher pressures (e.g. 3.77 MPa) while high rank coals show the opposite behaviour, i.e. half of the sorption is reached at lower pressures (e.g. 0.96 MPa).

In order to improve the ability to interpret the data presented in Figures 6.10 and 6.11, average values of reduction of deformation parameters of both samples versus the gas pressure are plotted in Figure 6.12.

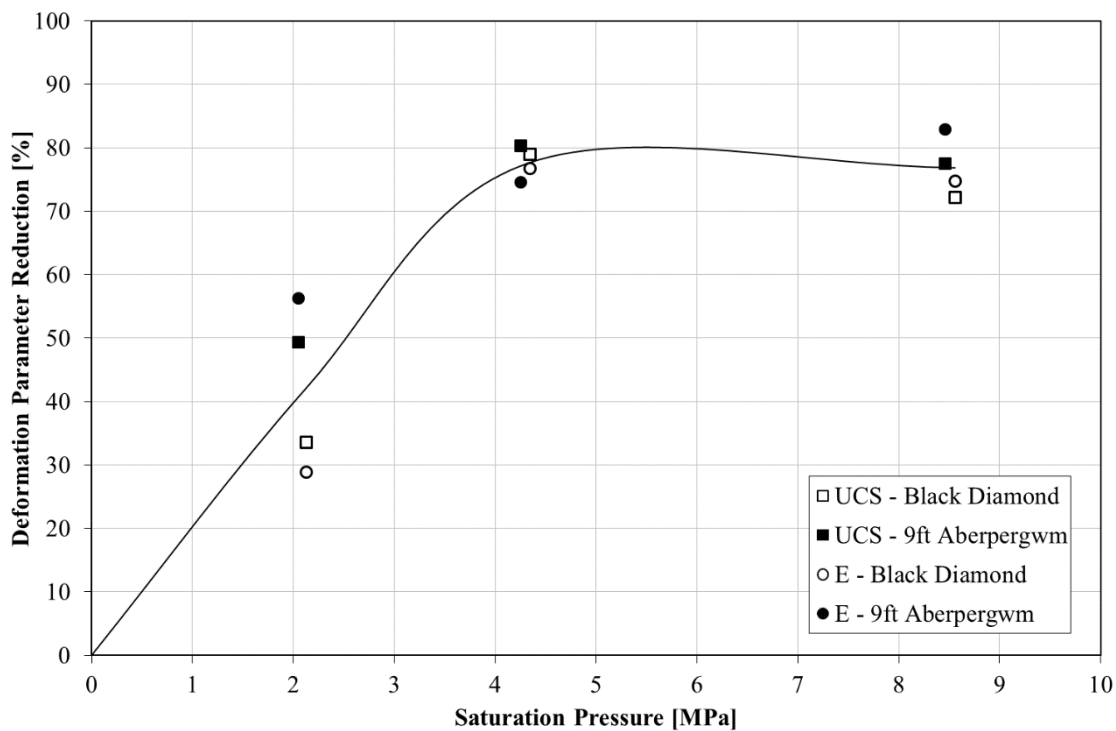


Fig. 6.12. Reduction of deformation parameters with an increase in saturation pressure.

Although BD coal shows higher values of unconfined compressive strength and elastic modulus than the AB coal (see Table 6.1), it can be observed in Figure 6.12 that the reduction percentage of deformation parameters of both samples is similar, especially at 4.3 MPa and 8.5 MPa saturation pressures showing a maximum decrease of approximately 80%. In other words, by observing the shape of the curve presented in Figure 6.12, it can be inferred that the calculated reductions in deformation parameters increase gradually up to 4.3 MPa and then reach a plateau. However, a deviation of parameters between the coals saturated at 2.1 MPa can be observed. In particular, BD and AB samples showed 29-34% and 49-56% of reduction in deformation parameters, respectively.

Interestingly, despite the 60% lower maximum sorption capacity of the AB core compared to the BD core, as shown in Chapter 5, the maximum reduction of deformation parameters of both coals at 4.3 MPa and 8.5 MPa is comparable. Such observation suggests that the area most affected and weakened by CO₂ sorption is the region adjacent to the main fractures highly accessible to the CO₂ molecules. This supports the conclusion of Perera et al. (2013) and Vishal et al. (2015) that carbon

dioxide saturation causes reduction of coal strength predominantly along its major fractures by enhancing their propagation.

As mentioned previously, reduction of deformation parameters of low rank coal samples saturated with CO₂ in comparison to non-saturated samples has been reported. To restate, Perera et al. (2011) have conducted deformation analysis on brown coal saturated with CO₂ at 2.1 MPa pressure finding a reduction in unconfined compressive strength and elastic modulus of 7% and 19%, respectively. More recently, Ranathunga et al. (2016) have reported for lignite saturated with CO₂ at 2 MPa compared to non-saturated lignite, a 6% and 16% decrease in unconfined compressive strength and elastic modulus, respectively.

Hence, by comparing the reduction values of samples saturated with CO₂ at 2.1 MPa in this study (i.e. reductions between 29% and 56%) to the values reported in the literature mentioned above, it can be observed that saturation of anthracite coal with CO₂ has a more detrimental effect on deformation parameters than of lignite coal subjected to CO₂ at the same pressure. As the sorption capacity of coals increases with rank due to the well-developed cleat system resulting from an increase in degree of coalification providing easier access for CO₂ molecules, deformation properties of high rank coals are expected to be more affected than of low rank coals (Ranjith and Perera, 2012).

6.2.1. Parametrisation of Changes in Unconfined Compressive Strength and Elastic Modulus

It has been shown that reductions in elastic modulus and unconfined compressive strength of CO₂ saturated samples compared to non-saturated samples become larger at higher saturation pressures. Hence, the observed reductions are quantified by fitting a simple model to the experimental results and obtaining the fitting parameters in this section. Since the change in measured deformation parameters is caused by gas sorption, such change can be mathematically related to gas pressure (Masoudian et al., 2014).

Following the approach that the elastic modulus reduction is modelled using a Langmuir (1918) equation, ΔE can be written as (Masoudian et al., 2014):

$$\Delta E = \Delta E_{max} \frac{P}{P_E + P} \quad (6.3)$$

where ΔE_{max} is the maximum reduction in elastic modulus (Langmuir parameter), P is the gas pressure (MPa) and P_E is the Langmuir pressure (MPa) of elastic modulus reduction.

Similarly, ΔUCS can be written as (Masoudian et al., 2014):

$$\Delta UCS = \Delta UCS_{max} \frac{P}{P_{UCS} + P} \quad (6.4)$$

where ΔUCS_{max} is the maximum reduction in strength (Langmuir parameter) and P_{UCS} is the Langmuir pressure (MPa) of unconfined compressive strength reduction.

The fitting of the Langmuir curve to the experimental data followed the same procedure as in Chapter 5 for absolute sorption where determination of the sum of the squared differences with a target function was minimized with respect to the Langmuir parameters using the Excel solver function.

Figures 6.13 and 6.14 present the curves fitted to the experimental data of unconfined compressive strength reduction and elastic modulus reduction of both samples as a function of CO₂ pressure, respectively.

It can be observed from both figures that fitted curves show good agreement with the experimental data. Elastic modulus of the AB coal shows the best agreement over the entire range of pressures used, whereas other fittings are not as successful in the subcritical region. Nevertheless, taking into account the natural variability of the fracture network in the coal samples, the number of experimentally determined points as well as the simplicity of the approach, such fitting provides a reasonable estimate to the reduction of strength parameters related to the CO₂ saturation for the range of pressures used in this study.

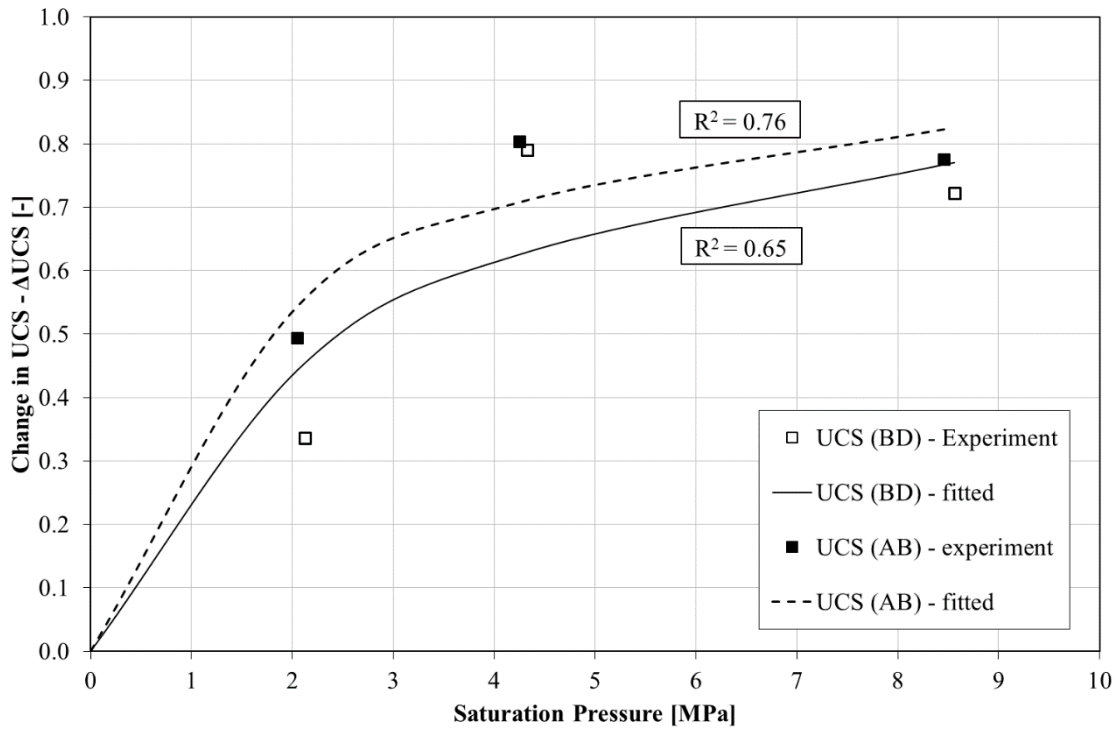


Fig. 6.13. The unconfined compressive strength reduction isotherms fitted to the calculated unconfined compressive strength reduction values of BD and AB coals.

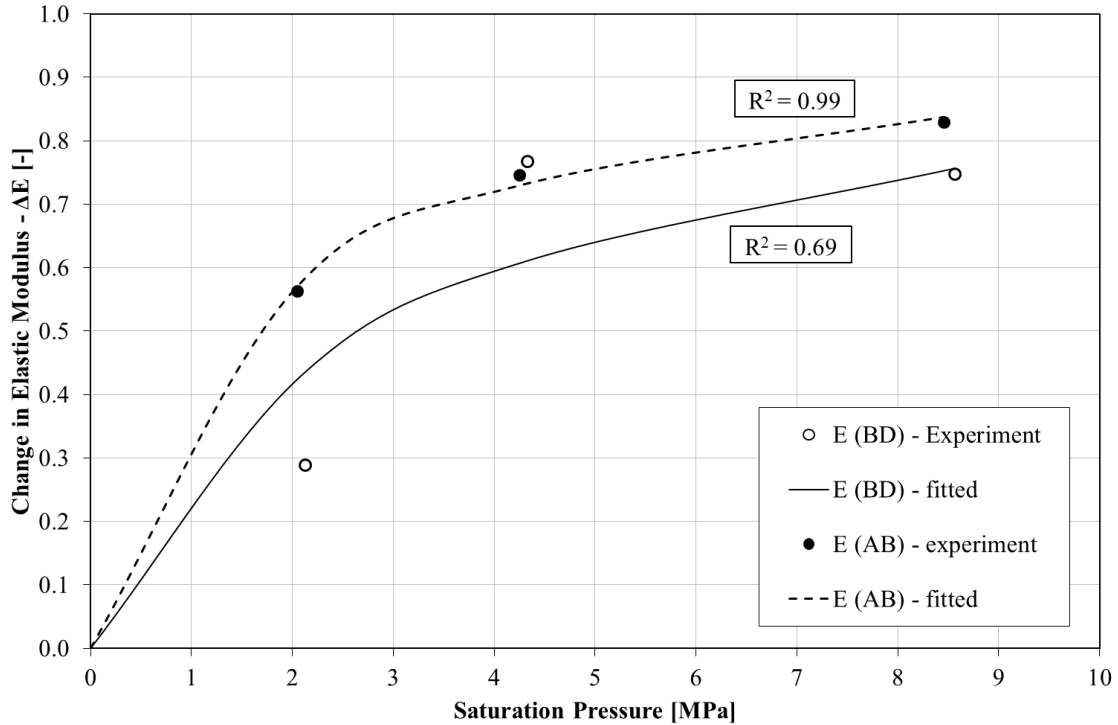


Fig. 6.14. The elastic modulus reduction isotherms fitted to the calculated elastic modulus reduction values of BD and AB coals.

Table 6.2 presents the parameters obtained using the fitting approach related to the reduction of deformation parameters of both samples. It can be observed that the unconfined compressive strength and elastic modulus of CO₂ saturated AB coal experience half of their maximum reduction values at 1.69 MPa and 1.53 MPa gas pressures, respectively. In comparison, BD experienced half of the maximum reduction of unconfined compressive strength and elastic modulus at 2.53 MPa and 2.74 MPa, respectively. Such observation is in agreement with the findings on the sorption capacity of both core samples presented in Chapter 5 where AB coal sample experienced half of its sorption at lower pressure than the BD coal.

Table 6.2. Fitted parameters of the proposed model for reduction of unconfined compressive strength and elastic modulus of BD and AB coals.

Deformation parameter	Fitted (Langmuir) parameters	
	P _{UCS} (MPa), P _E (MPa)	UCS _{max} (-), E _{max} (-)
<i>Black Diamond</i>		
Unconfined compressive strength	2.53	1.0
Elastic modulus	2.74	1.0
<i>9ft Aberpergwm</i>		
Unconfined compressive strength	1.69	0.98
Elastic modulus	1.53	0.99

6.3. Failure Patterns

To visualize the effect of CO₂ saturation on failure mechanism of the coals of this study, photographs were taken before and after the failure of both natural and CO₂ saturated specimens. The photographs containing natural (non-saturated) samples and samples saturated at 2.1 MPa, 4.3 MPa and 8.5 MPa are shown in Figures 6.15, 6.16, 6.17 and 6.18, respectively.

It can be observed that non-saturated coals (Figure 6.15) fail predominantly through axial splitting where a number of axial cracks propagated along the entire length of the specimens. Such splitting occurred with rapid and unstable crack initiation and propagation, common for brittle materials, outbursting the samples into pieces.

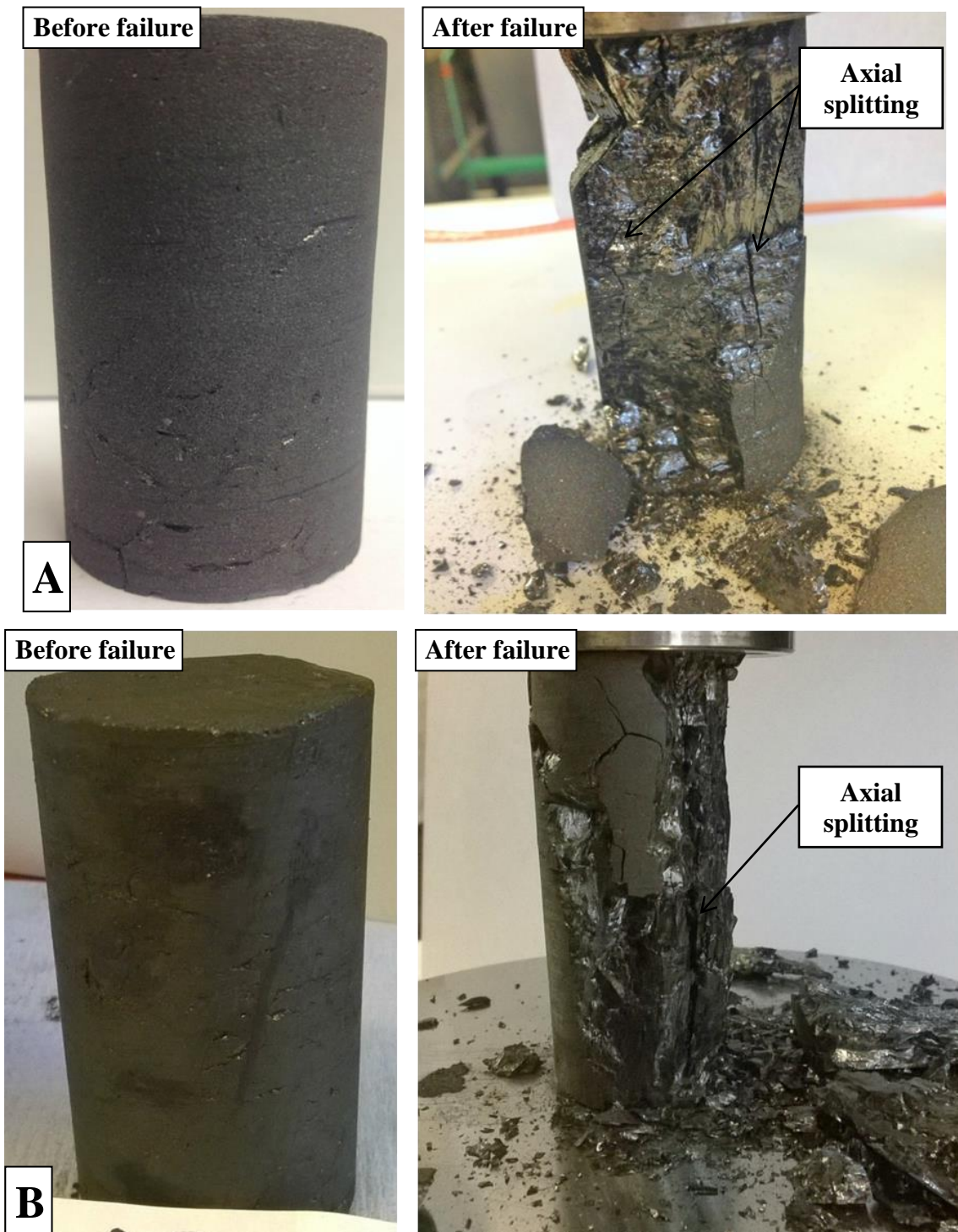


Fig. 6.15. Failure patterns of non-saturated coal samples; A) Black Diamond, B) 9ft Aberpergwm.

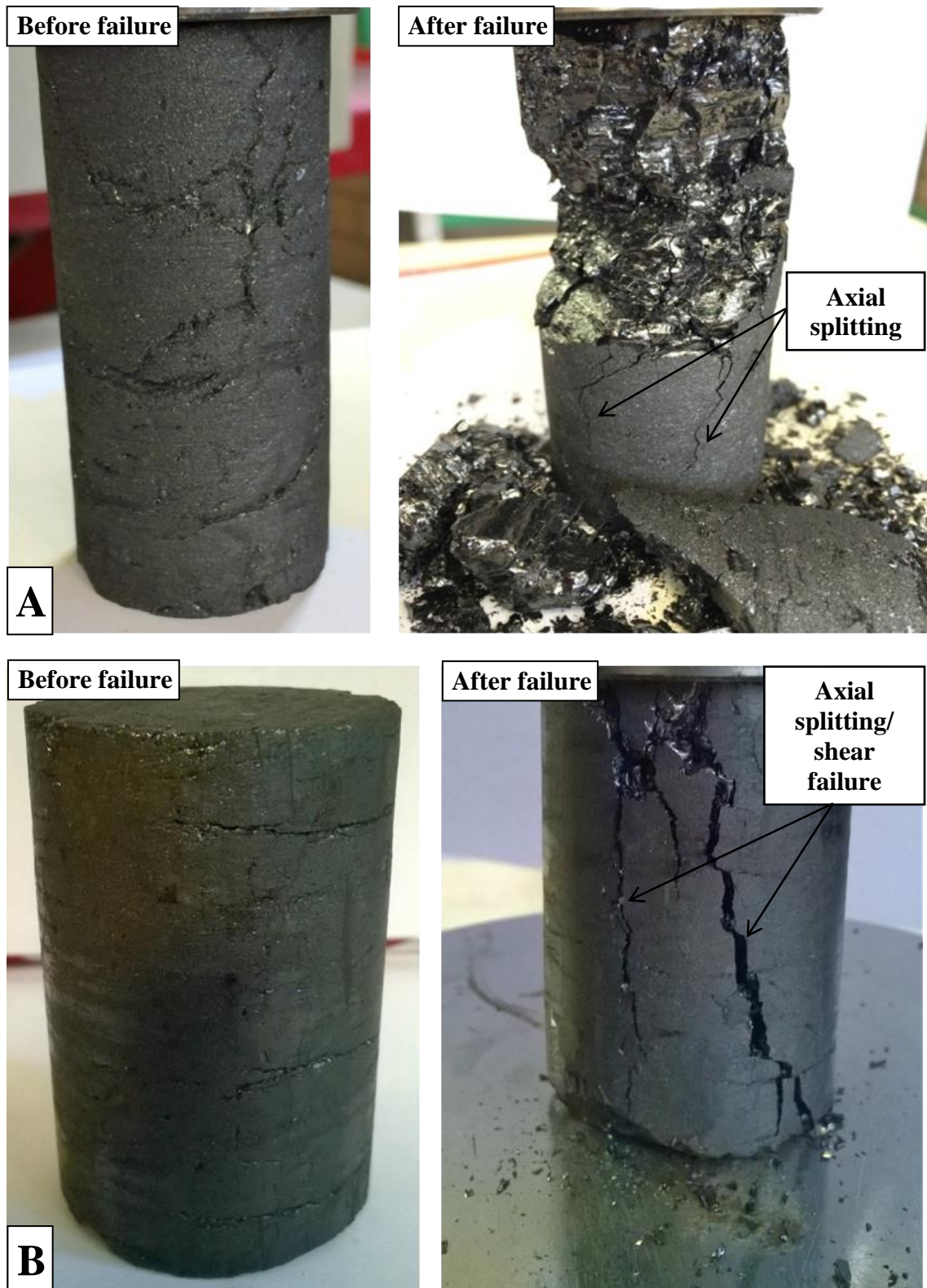


Fig. 6.16. Failure patterns of samples saturated with CO₂ at 2.1 MPa; A) Black Diamond, B) 9ft Aberpergwm.

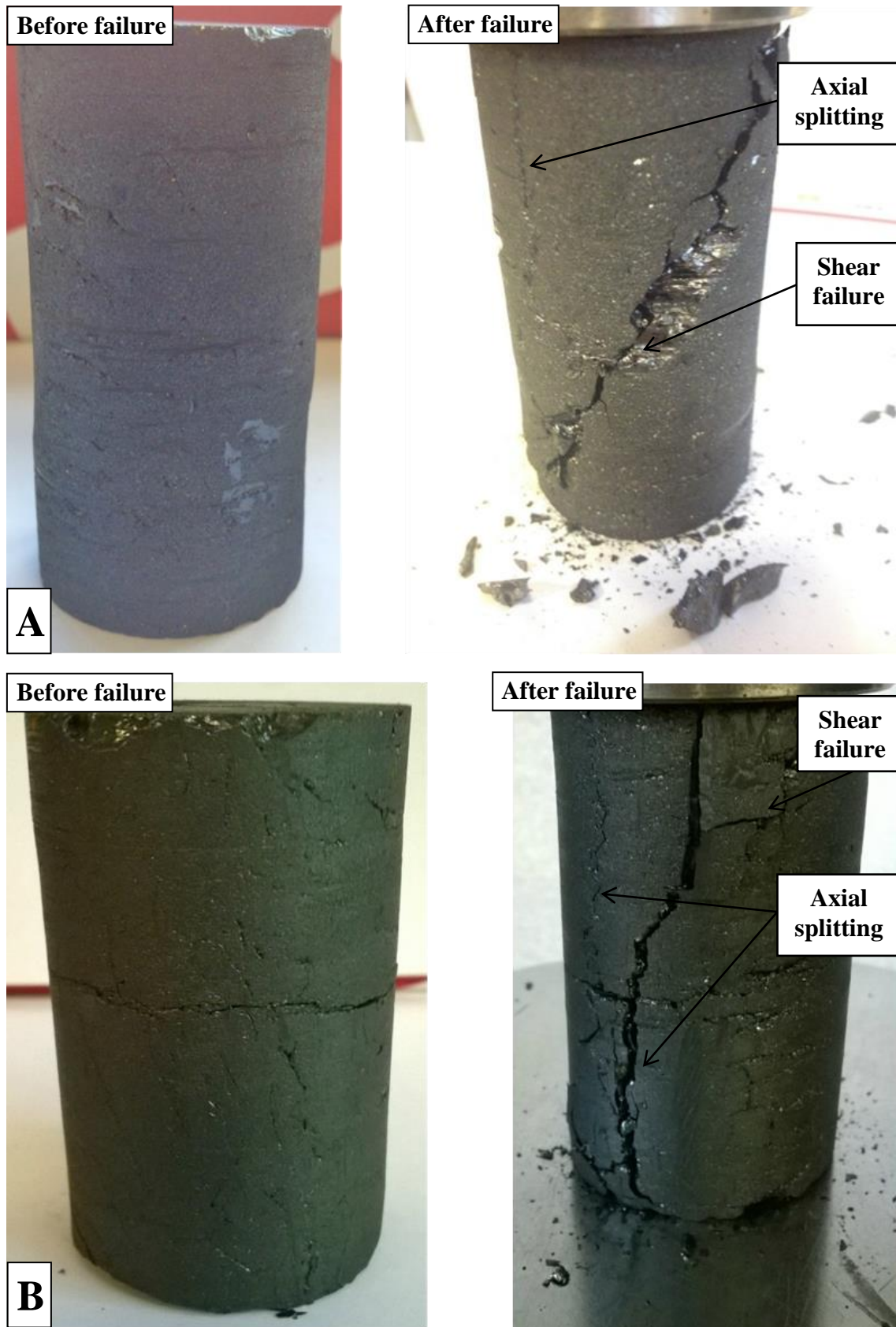


Fig. 6.17. Failure patterns of samples saturated with CO₂ at 4.3 MPa; A) Black Diamond, B) 9ft Aberpergwm.

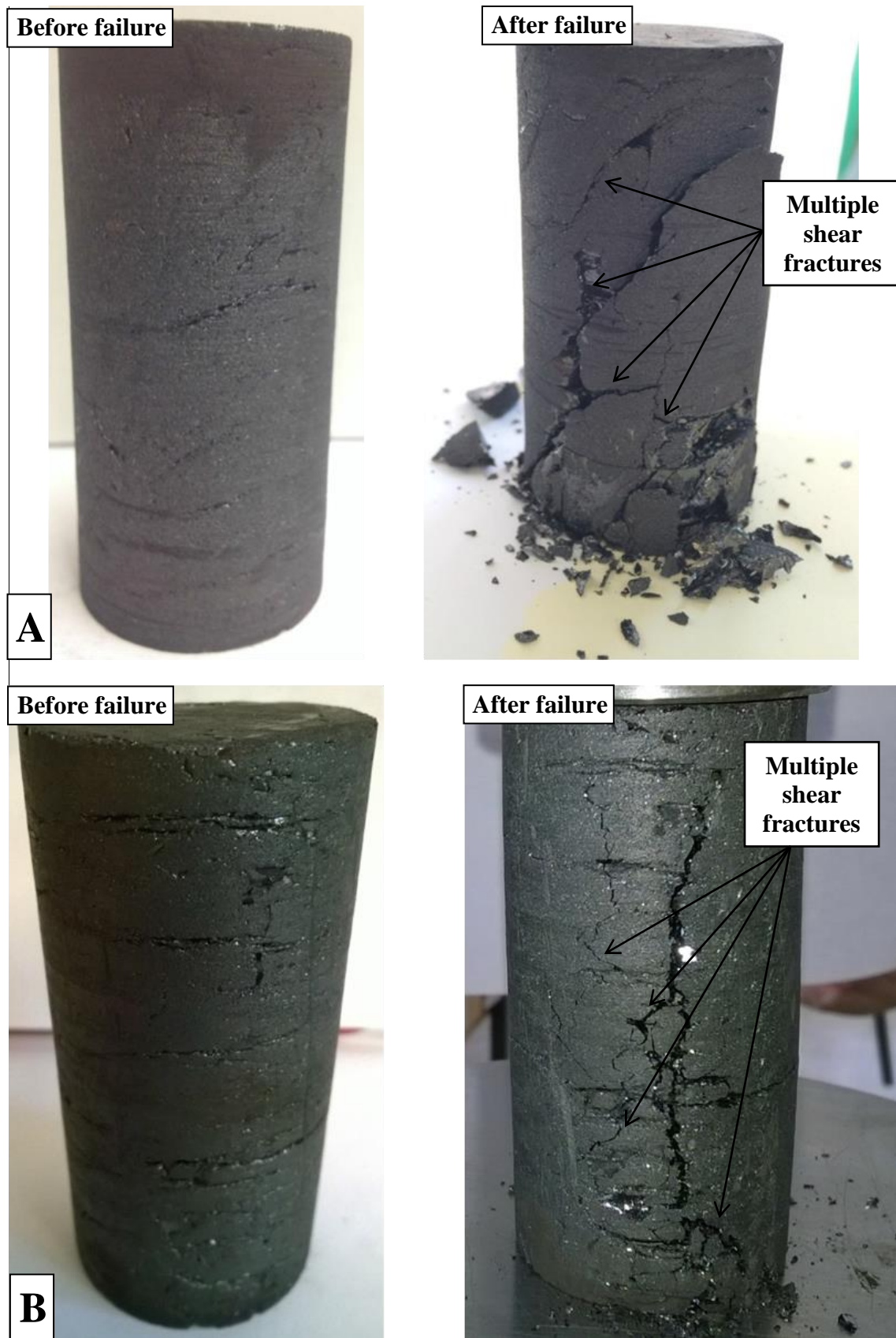


Fig. 6.18. Failure patterns of samples saturated with CO₂ at 8.5 MPa; A) Black Diamond, B) 9ft Aberpergwm.

Samples saturated with CO₂ at 2.1 MPa showed similar behaviour to those of non-saturated samples (Figure 6.16). However, a set of non-longitudinal fractures was also visible, especially on the AB sample. Predominant shear failure occurred in samples saturated at 4.3 MPa of CO₂ (Figure 6.17). In addition, a set of axial fractures was visible for both samples suggesting that the overall failure could be a combination of fracture propagation in axial and non-axial directions. For coals saturated in supercritical CO₂, i.e. at 8.5 MPa, multiple shear fractures orientated in different directions can be observed (Figure 6.18).

Interestingly, both BD and AB samples exhibited comparable behaviour in terms of failure patterns. The only distinction is for specimens saturated at 2.1 MPa where BD shows higher outburst of the material than the AB coal suggesting predominantly axial splitting within the BD coal. This is in accordance with the strength parameter reduction (Figure 6.12) where it has been shown that AB samples saturated at 2.1 MPa lost more than half of their original strength while BD samples lost a third of their original strength. Consequently, higher residual strength of BD coal resulted in a behaviour more similar to the natural coal, i.e. brittle behaviour while AB showed more ductile behaviour.

Overall, by comparing failure types of non-saturated and CO₂ saturated specimens, a distinction can be observed. While former ones show predominantly axial splitting, the latter ones fail through a visible shear plane and existing fractures weakened by the CO₂ sorption.

As mentioned in Chapter 2, natural coals result in brittle manner with irregular longitudinal splitting to increasing stress, while a network of shear fractures will develop in ductile rocks (Jaeger et al., 2007; Thomas, 2013). Furthermore, CO₂ sorption induced swelling causes crack initiation and enhancement of the existing fracture lines along the coal (Gathitu et al., 2009; Hol et al., 2012; Vishal et al., 2015).

Hence, based on the observations presented above, it can be concluded that CO₂ saturation affects the response of coal subjected to axial stress. In particular, it can be inferred that coals treated with CO₂ show more ductile behaviour than non-saturated coals as a result of changes within the coal structure.

6.4. Post-failure Sieve Analysis

As previously stated in Chapter 2, it has been suggested that a combination of the change in cleat surface roughness and micro-fracturing of the coal due to CO₂ dissolution within the structure is responsible for reduction of coal's deformation properties. Wang et al. (2011) have suggested that the results of post-failure sieve analysis could confirm the weakening effect of CO₂ sorption on coal structure where coals saturated with CO₂ result in smaller average particle sizes after the failure compared to non-saturated coals. Hence, in order to assess the impact of CO₂ sorption on coal structure over the range of pressures used in this study, a post-failure sieve analysis of BD coal specimens was conducted. The methodology of the sieving process has been presented in Chapter 4.

Figure 6.19 shows coal particles as a result of a failure of both non-saturated and CO₂ saturated BD samples under axial compression. By inspecting the figure, it can be seen that failure of the non-saturated sample resulted in a large coal lump accompanied by a number of smaller particles. Conversely, CO₂ saturated samples showed more gradual distribution of the coal particles. Experimental results of post-failure sieve analyses are presented in Tables 6.3 to 6.12.

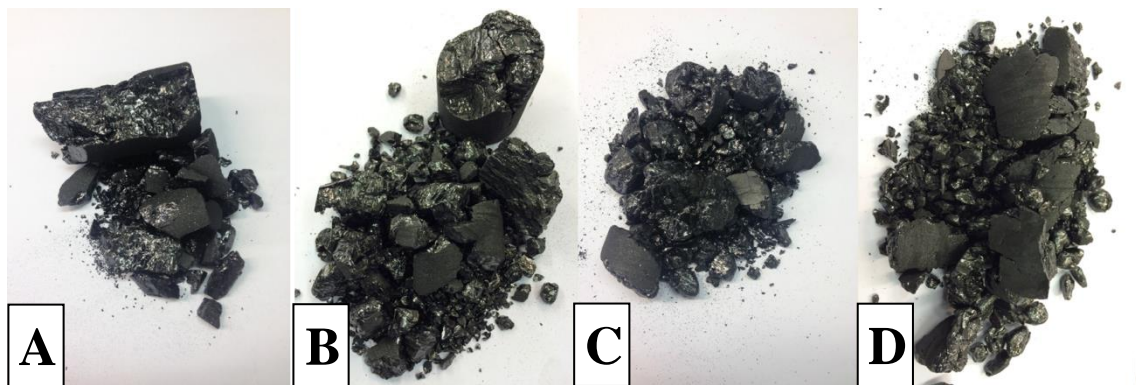


Fig. 6.19. Black Diamond coal post-failure particles; A) natural (non-saturated) sample, B) 2.1 MPa saturated sample; C) 4.3 MPa saturated sample, D) 8.5 MPa saturated sample.

Table 6.3. Results of post-failure sieve analysis on natural (non-saturated) BD1 specimen.

BD1					
Sieve Diameter (mm)	Mass of empty sieve (g)	Mass of sieve + coal (g)	Coal retained (g)	Percent retained (%)	Percent passing (%)
6.3	732.99	832.08	99.09	93.41	6.59
4.0	442.90	445.67	2.77	2.61	3.98
2.0	393.06	395.41	2.35	2.22	1.76
1.18	352.64	353.52	0.88	0.83	0.93
0.6	314.99	315.55	0.56	0.53	0.41
0.425	294.08	294.21	0.13	0.12	0.28
0 (Pan)	244.16	244.46	0.30	0.28	0

Table 6.4. Results of post-failure sieve analysis on natural (non-saturated) BD2 specimen.

BD2					
Sieve Diameter (mm)	Mass of empty sieve (g)	Mass of sieve + coal (g)	Coal retained (g)	Percent retained (%)	Percent passing (%)
6.3	732.99	832.34	99.35	92.92	7.08
4.0	442.90	446.35	3.45	3.23	3.85
2.0	393.06	395.18	2.12	1.98	1.87
1.18	352.64	353.55	0.91	0.85	1.02
0.6	314.99	315.59	0.60	0.56	0.46
0.425	294.08	294.23	0.15	0.14	0.32
0 (Pan)	244.16	244.5	0.34	0.32	0

Table 6.5. Results of post-failure sieve analysis on natural (non-saturated) BD3 specimen.

BD3					
Sieve Diameter (mm)	Mass of empty sieve (g)	Mass of sieve + coal (g)	Coal retained (g)	Percent retained (%)	Percent passing (%)
6.3	732.99	834.85	101.86	94.84	5.16
4.0	442.90	445.86	2.96	2.76	2.40
2.0	393.06	394.58	1.52	1.42	0.99
1.18	352.64	353.09	0.45	0.42	0.57
0.6	314.99	315.33	0.34	0.32	0.25
0.425	294.08	294.15	0.07	0.07	0.19
0 (Pan)	244.16	244.36	0.2	0.19	0

Table 6.6. Results of post-failure sieve analysis on natural (non-saturated) BD4 specimen.

BD4					
Sieve Diameter (mm)	Mass of empty sieve (g)	Mass of sieve + coal (g)	Coal retained (g)	Percent retained (%)	Percent passing (%)
6.3	732.99	831.63	98.64	91.86	8.14
4.0	442.90	447.07	4.17	3.88	4.26
2.0	393.06	395.71	2.65	2.47	1.79
1.18	352.64	353.53	0.89	0.83	0.96
0.6	314.99	315.55	0.56	0.52	0.44
0.425	294.08	294.21	0.13	0.12	0.32
0 (Pan)	244.16	244.5	0.34	0.32	0

Table 6.7. Results of post-failure sieve analysis on BD5 specimen saturated with CO₂ at 2.1 MPa.

BD5					
Sieve Diameter (mm)	Mass of empty sieve (g)	Mass of sieve + coal (g)	Coal retained (g)	Percent retained (%)	Percent passing (%)
6.3	732.99	827.99	95	88.85	11.15
4.0	442.89	447.25	4.36	4.08	7.07
2.0	429.44	433.78	4.34	4.06	3.01
1.18	352.63	354.12	1.49	1.39	1.62
0.6	314.99	316.06	1.07	1.00	0.62
0.425	294.05	294.29	0.24	0.22	0.39
0 (Pan)	244.15	244.57	0.42	0.39	0

Table 6.8. Results of post-failure sieve analysis on BD6 specimen saturated with CO₂ at 2.1 MPa.

BD6					
Sieve Diameter (mm)	Mass of empty sieve (g)	Mass of sieve + coal (g)	Coal retained (g)	Percent retained (%)	Percent passing (%)
6.3	732.99	820.57	87.58	81.35	18.65
4.0	442.89	451.15	8.26	7.67	10.98
2.0	429.44	435.92	6.48	6.02	4.96
1.18	352.63	355.27	2.64	2.45	2.51
0.6	314.99	316.75	1.76	1.63	0.87
0.425	294.05	294.39	0.34	0.32	0.56
0 (Pan)	244.15	244.75	0.60	0.56	0

Table 6.9. Results of post-failure sieve analysis on BD7 specimen saturated with CO₂ at 4.3 MPa.

BD7					
Sieve Diameter (mm)	Mass of empty sieve (g)	Mass of sieve + coal (g)	Coal retained (g)	Percent retained (%)	Percent passing (%)
6.3	732.99	815.38	82.39	78.93	21.07
4.0	442.90	452.08	9.18	8.79	12.27
2.0	393.06	399.44	6.38	6.11	6.16
1.18	352.64	355.33	2.69	2.58	3.58
0.6	314.99	317.23	2.24	2.15	1.44
0.425	294.08	294.59	0.51	0.49	0.95
0 (Pan)	244.16	245.15	0.99	0.95	0

Table 6.10. Results of post-failure sieve analysis on BD8 specimen saturated with CO₂ at 4.3 MPa.

BD8					
Sieve Diameter (mm)	Mass of empty sieve (g)	Mass of sieve + coal (g)	Coal retained (g)	Percent retained (%)	Percent passing (%)
6.3	733.00	799.33	66.33	64.48	35.52
4.0	547.63	563.03	15.4	14.97	20.55
2.0	420.67	432.22	11.55	11.23	9.32
1.18	351.47	356.01	4.54	4.41	4.91
0.6	318.73	321.81	3.08	2.99	1.92
0.425	289.37	290.11	0.74	0.72	1.19
0 (Pan)	243.4	244.63	1.23	1.19	0

Table 6.11. Results of post-failure sieve analysis on BD9 specimen saturated with CO₂ at 8.5 MPa.

BD9					
Sieve Diameter (mm)	Mass of empty sieve (g)	Mass of sieve + coal (g)	Coal retained (g)	Percent retained (%)	Percent passing (%)
6.3	732.99	806.3	73.31	69.73	30.27
4.0	547.67	560.54	12.87	12.24	18.03
2.0	429.45	439.2	9.75	9.27	8.76
1.18	352.64	356.72	4.08	3.88	4.88
0.6	315.00	318.15	3.15	2.99	1.88
0.425	294.07	294.76	0.69	0.66	1.23
0 (Pan)	244.16	245.45	1.29	1.23	0

Table 6.12. Results of post-failure sieve analysis on BD10 specimen saturated with CO₂ at 8.5 MPa.

BD10					
Sieve Diameter (mm)	Mass of empty sieve (g)	Mass of sieve + coal (g)	Coal retained (g)	Percent retained (%)	Percent passing (%)
6.3	732.97	805	72.03	70.22	29.78
4.0	547.63	559.64	12.01	11.71	18.07
2.0	420.67	430.37	9.70	9.46	8.62
1.18	351.48	355.24	3.76	3.67	4.95
0.6	318.73	321.73	3.00	2.92	2.03
0.425	289.4	290.18	0.78	0.76	1.27
0 (Pan)	237.56	238.86	1.3	1.27	0

Based on experimental data presented in Tables 6.3 to 6.6, it can be seen that four non-saturated specimens show comparable results. In particular, 5.19-8.14% of non-saturated particles passed through the 6.3 mm sieve opening. For samples saturated at 2.1 MPa (Tables 6.7 and 6.8), 4.3 MPa (Tables 6.9 and 6.10) and 8.5 MPa (Tables 6.11 and 6.12), the percentage of particles passing through the largest sieve is 11.15-18.65%, 21.07-35.52% and 29.78-30.27%, respectively.

Based on the presented values, the average percentage of particles passing through a certain sieve for natural and CO₂ saturated specimens was calculated. Comparison of the obtained average values with respect to sieve size is presented in Figure 6.20.

It can be inferred from the figure that specimens saturated with CO₂ show higher percentage of particles passing through sieves than non-saturated specimens. In particular, approximately 7%, 15%, 28% and 30% of the total coal mass of non-saturated, 2.1 MPa saturated, 4.3 MPa saturated and 8.5 MPa saturated coal specimens passed through the largest sieve size of 6.3 mm, respectively. Such results confirm the previous assumption that CO₂ saturated coals result in smaller particles after the failure than the non-saturated specimens indirectly proving the micro-fracturing of the coal caused by CO₂ sorption. Additionally, it can be inferred from Figure 6.20 that the percentage of particles passing through sieves depends on saturation pressure.

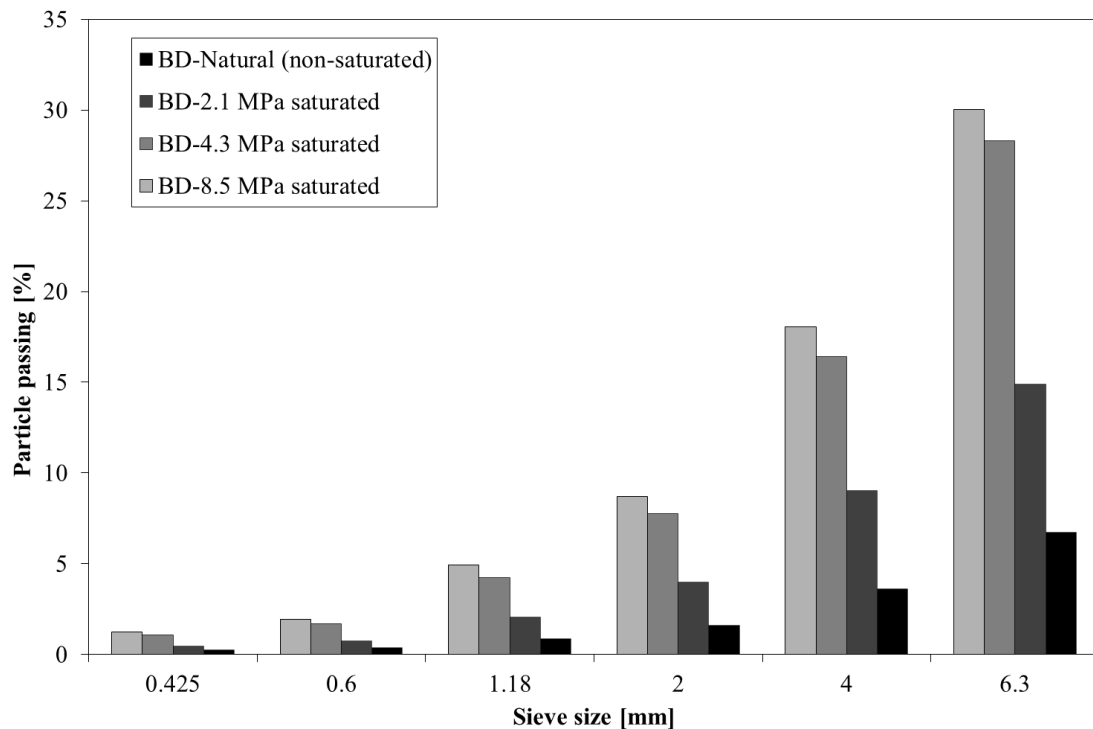


Fig. 6.20. Comparison of the post-failure particle size distribution of natural (non-saturated) and CO₂ saturated Black Diamond samples.

In order to assess the difference in percentages of particles passing through each sieve between the non-saturated and CO₂ saturated samples, Figure 6.21 shows the passing ratio versus the gas saturation pressure for each sieve. Passing ratio is calculated as the average percentage of particles passing through a certain sieve for CO₂ saturated samples divided by the average percentage of particles passing for natural (non-saturated) coal specimens.

Figure 6.21 shows that for specimens saturated at 2.1 MPa, there are 1.7 to 2.5 more particles passing through the sieves compared to non-saturated specimens. For specimens saturated at 4.3 MPa and 8.5 MPa, the amount of particles passing through all the sieves compared to non-saturated specimens is 3.9-4.9 and 4.5-5.6 times higher, respectively. Hence, it can be seen that as the saturation pressure increases, the passing ratio steeply increases up to 4.3 MPa and then shows a more gradual further increase with gas pressure.

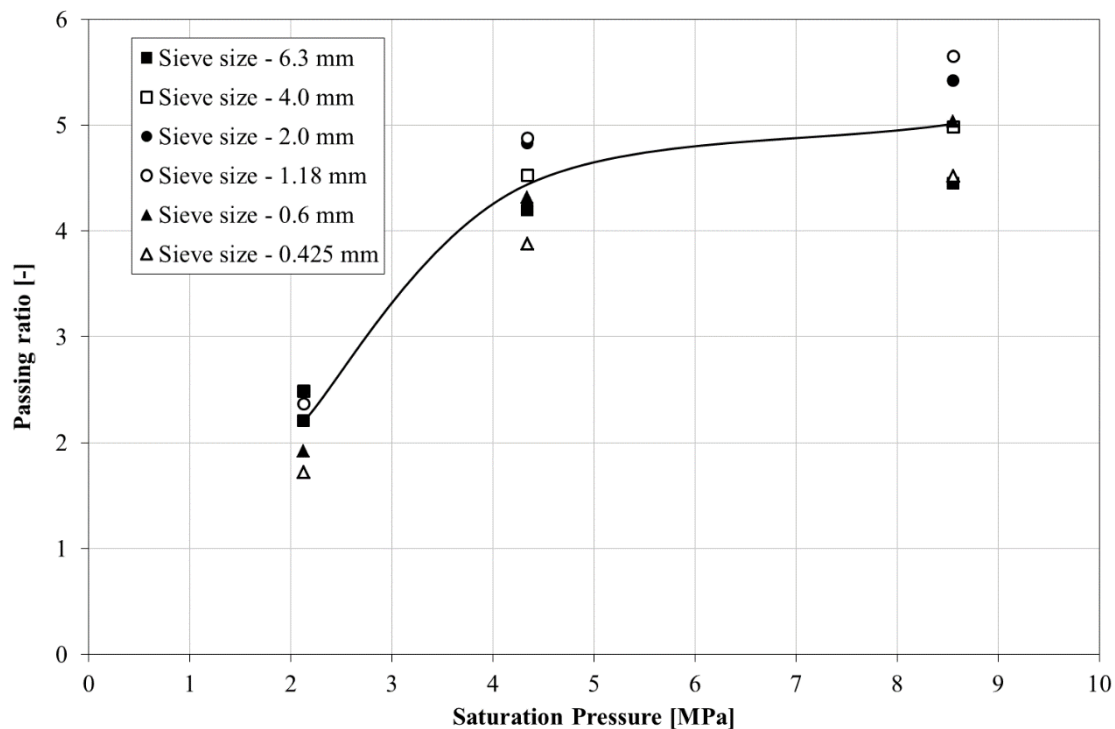


Fig. 6.21. Passing ratio versus the saturation pressure for particles passing through sieves of different sizes.

6.5. Conclusions

The influence of CO₂ sorption on elastic deformation and failure under axial load of twenty unconfined coal specimens was investigated in this chapter. According to the author's knowledge, this is the first experimental analysis of anthracite coal's behaviour as well as the behaviour of South Wales coals dealing with the change in deformation properties with an increase in CO₂ pressure up to 8.5 MPa.

Axial stress versus strain curves for all specimens suggested a distinctive behaviour of natural (non-saturated) and CO₂ saturated coals. Natural coals showed relatively high average unconfined compressive strengths (8-9.5 MPa) and elastic moduli (1.1-1.6 GPa) resulting in a brittle behaviour with sudden drop in measured stress after failure. Oppositely, CO₂ saturated samples showed a decreasing trend of deformation parameters with an increase in gas pressure exhibiting a ductile behaviour.

The relationship between the unconfined compressive strength and elastic modulus values of all samples was found to be linear suggesting that coal samples more difficult

to compress have higher maximum strength. Although BD coal showed slightly higher values than the AB coal, the obtained values were in the same order of magnitude and comparable. The difference in results was attributed to the heterogeneous structure of the coal samples.

Saturation of coal specimens at different CO₂ pressures showed to have a detrimental effect on coal's structure lowering the measured strength and elastic modulus values up to approximately 80% at 4.3 MPa and 8.5 MPa in comparison to the values obtained on specimens not treated with CO₂. Through comparison with the data from the literature for the same gas pressure conditions, it was shown that CO₂ saturation causes more detrimental effect on the structure of high rank coals than of low rank coals.

Parametrization of the reduction of deformation parameters was achieved using a Langmuir curve. The Langmuir pressure values obtained for unconfined compressive strength and elastic modulus are higher than those obtained for sorption capacity in Chapter 5 for the same coals suggesting that sorption capacity and reduction in deformation parameters do not necessarily follow a pure linear relationship.

Visual inspection of the failure patterns revealed that non-saturated specimens failed predominantly through axial splitting while the failure of the cores saturated with CO₂ occurred through a combination of shear fractures oriented in different directions. Results of the post-failure sieve analysis showed that on average, only 7% of non-saturated particles passed through 6.3 mm sieve, while 2.1 MPa saturated, 4.3 MPa and 8.5 MPa saturated coals showed 15%, 28% and 30% of particles passing through the same sieve, respectively. Under those circumstances, post-failure sieve analysis of the Black Diamond coal specimens demonstrated that CO₂ treated samples disintegrated on smaller particles than specimens without any CO₂ saturation after failure.

Overall, this chapter showed the weakening effect of CO₂ on anthracite coals making them more ductile and less resistive to deformation under applied stress. Presented observations imply that the reduction of the coal deformation properties due to CO₂ sorption could contribute to the overall performance of a coal seam subject to CO₂ sequestration. A sensitivity analysis dealing with the change in elastic modulus of the coal and its impact on coal's transport properties will be conducted and presented in Chapter 9.

6.6. References

- Gathitu, B.B., Chen, W.Y. and McClure, M. 2009. Effects of Coal Interaction with Supercritical CO₂: Physical Structure. *Industrial & Engineering Chemistry Research*, 48(10), pp. 5024-5034.
- Gensterblum, Y., van Hemert, P., Billemont, P., Battistutta, E., Busch, A., Krooss, B.M., De Weireld, G. and Wolf, K.H.A.A. 2010. European inter-laboratory comparison of high pressure CO₂ sorption isotherms II: Natural coals. *International Journal of Coal Geology*. 84(2), pp. 115-124.
- Hol, S., Spiers, C.J. and Peach, C.J. 2012. Microfracturing of coal due to interaction with CO₂ under unconfined conditions. *Fuel*, 97, pp. 569-584.
- Jaeger, J.C., Cook, N.G.W. and Zimmerman, R.W. 2007. *Fundamentals of Rock Mechanics*, 4th Edition, Blackwell Publishing.
- Langmuir, I. 1918. The adsorption of gases on plane surfaces of glass, mica and platinum. *Journal of the American Chemical Society*, 40(9), pp. 1361-1403.
- Masoudian, M.S., Airey, D.W. and El-Zein, A. 2014. Experimental investigations on the effect of CO₂ on mechanics of coal. *International Journal of Coal Geology*, 128-129, pp. 12-23.
- Perera, M.S.A., Ranjith, P.G. and Peter, M. 2011. Effects of saturation medium and pressure on strength parameters of Latrobe Valley brown coal: Carbon dioxide, water and nitrogen saturations. *Energy*, 36(12), pp. 6941-6947.
- Perera, M.S.A., Ranjith, P.G. and Viete, D.R. 2013. Effects of gaseous and super-critical carbon dioxide saturation on the mechanical properties of bituminous coal from the Southern Sydney Basin. *Applied Energy*, 110, pp. 73-81.
- Ranathunga, A.S., Perera, M.S.A., Ranjith, P.G. and Bui, H. 2016. Super-critical CO₂ saturation-induced property alterations in low rank coal: An experimental study. *The Journal of Supercritical Fluids*, 109, pp. 134-140.
- Ranjith, P.G. and Perera, M.S.A. 2012. Effects of cleat performance on strength reduction of coal in CO₂ sequestration. *Energy*, 45(1), pp. 1069-1075.
- Siemons, N. and Busch, A. 2007. Measurement and interpretation of supercritical CO₂ sorption on various coals. *International Journal of Coal Geology*, 69(4), pp. 229-242.
- Thomas, L. 2013. *Coal Geology*, 2nd Edition, John Wiley & Sons, Ltd.
- Viete, D.R. and Ranjith, P.G. 2006. The effect of CO₂ on the geomechanical and permeability behaviour of brown coal: Implications for coal seam CO₂ sequestration. *International Journal of Coal Geology*. 66, pp. 204-216.
- Vishal, V., Ranjith, P.G. and Singh, T.N. 2015. An experimental investigation on behaviour of coal under fluid saturation, using acoustic emission. *Journal of Natural Gas Science and Engineering*. 22, pp. 428-436.
- Wang, S., Elsworth, D. and Liu, J. 2011. Permeability evolution in fractured coal: The roles of fracture geometry and water-content. *International Journal of Coal Geology*, 87(1), pp. 13-25.

7

Gas Transport and Reaction Behaviour

7.1. Introduction

The results of the investigation of gas transport and reactions in intact Black Diamond coal samples under confined conditions are presented in this chapter. The response of four core specimens is explored by injecting different gases at low and high pressures.

A sequential injection of helium (He), carbon dioxide (CO₂) and again, He is conducted for all samples whereas two samples are additionally saturated with nitrogen (N₂) followed by re-injection of He. First He injection is used to set the base values of flow rates and volumetric response of samples compared with the results of subsequent injections. Injection of CO₂ is conducted to investigate the effect of CO₂ sorption on the response of coal samples. Saturation of two cores with N₂ is performed to analyse the effect of N₂ saturation on reversibility of CO₂ sorption induced effects. Second and third He injections are used to measure the flow rates and coal volumetric response after CO₂ injection and N₂ saturation, respectively.

Two samples (A and B) are tested under low injection pressure conditions (3.6-4.6 MPa) while two samples (C and D) are investigated under high injection pressure conditions (7.1-8.1 MPa). Confining stresses, injection pressures and backpressures, flow rates at the sample outlet, temperature and radial and axial strains are constantly measured throughout all experiments which provide a high-resolution data on gas flow through coal cores under different stress conditions. The methodology of gas flow measurements, test conditions and the description of the samples used were provided in Chapter 4.

The main objectives of the study presented in this chapter are i) to investigate the flow and deformation behaviour of coal during low and high pressure injection of non-sorptive (He) and sorptive (CO₂) gases, ii) to provide insights on coal swelling and its effects on measured flow rate and resulting permeability, iii) to study the reversibility of CO₂ sorption in relation to permeability measured by non-sorbing gas (He), iv) to assess the impact of N₂ sorption on reversibility of CO₂ sorption and v) to assess the thermal changes in coal induced by flow of He and CO₂ and their impact on coal behaviour.

Section 7.2 presents the results during He and CO₂ injection both at low and high pressures into core samples. Observed flow rates and deformation of coal samples throughout the experiments are presented. Based on measured parameters, the

permeability values of four coal samples tested in this study to He and CO₂ with respect to effective stress are evaluated.

In Section 7.3, temperature measurements for all samples are presented. The observed changes in temperature during CO₂ injection are further elaborated.

Based on the radial and axial strains measured throughout the duration of the experiments, volumetric swelling of the coal samples due to CO₂ injection is analysed and its connection to the observed flow rate is discussed in Section 7.4.

Flow behaviour of all samples during He injection after CO₂ induced swelling is then evaluated in Section 7.5. In addition, the effect of N₂ injection on reversal of CO₂ sorption in two samples is assessed.

The conclusions of this chapter are presented in Section 7.6.

7.2. Injection of He and CO₂ in Coal under Confined Conditions

This section presents the experimental results during both He and CO₂ injections under low and high gas pressures in four coal samples under confined conditions. The preparation of the coal samples, assembling on the triaxial cell, experimental procedures and test conditions have been provided in Chapter 4. By continuously measuring axial and radial strains and flow rates throughout the duration of the experiments, results presented in this section provide insights into coal's dynamic response to constant flow of gases through samples. As discussed in Chapter 2, previous work has mostly focused on the calculation of permeability values and volumetric strains at steady state conditions.

Firstly, results of flow rate and deformation with an increase in injection pressure during He injection, where the impact of sorption induced strain is negligible, are presented. Such results provide insights into the coal's behaviour as a result of non-sorptive gas injection whereas any change in flow rate and displacement is attributed purely to the mechanical expansion of flow paths as a result of increase in gas pressure.

Secondly, experimental results measured during subcritical and supercritical CO₂ injections are presented. In order to make comparisons, all experimental conditions for CO₂ injection were identical to the He injection experiments (see Table 4.10). The

results of coal deformation induced by CO₂ sorption and flow rate evolution with an increase in injection pressure are presented and discussed.

Based on measured values of the gas pressures and flow rates achieved at steady state condition, permeability values of each coal sample to He and CO₂ are calculated following the procedure presented in Chapter 4. It should be noted that minimum average gas pressures, calculated based on the injection pressures and backpressures presented in Table 4.10, used within samples A, B, C and D are 1.95 MPa, 2.35 MPa, 4.85 MPa and 3.85 MPa, respectively. As discussed and explained in Chapter 2, the Klinkenberg (slip flow) effect is relatively small for gas pressures above 1.7 MPa. Hence, the Klinkenberg effect is disregarded in this study.

7.2.1. Low Pressure He Injection

Figures 7.1 and 7.2 show flow rates recorded at the sample outlet, confining pressures, injection pressures and backpressures measured during He injection in coal samples A and B, respectively. Both figures suggest that confining pressures, injection pressures and backpressures were stable during the experiment ensuring reliable measurement of the flow rates. In addition, it can be seen that the maximum time for achieving steady-state condition after each increase in injection pressure is up to one hour.

It can be observed from both figures that there is an increase in measured flow rate with an increase in injection pressure. Due to the fact that He can be considered as a non-sorbing gas, only the change in gas pressure within the sample is expected to dictate the change in observed flow rate. Further inspection of the figures reveals that sample A shows a lower flow rate than sample B. In particular, at injection pressures of 3.8 MPa, 4.2 MPa and 4.6 MPa, coal A shows flow rates of 1 g/h, 2 g/h and 4 g/h, respectively. Coal B shows higher values where injection pressures of 3.6 MPa, 4.1 MPa and 4.6 MPa resulted in flow rates of 6 g/h, 15 g/h and 40 g/h, respectively. Hence, the flow rate in sample B is ten times higher than the flow rate in sample A, for the same injection pressure of 4.6 MPa at the end of the experiment.

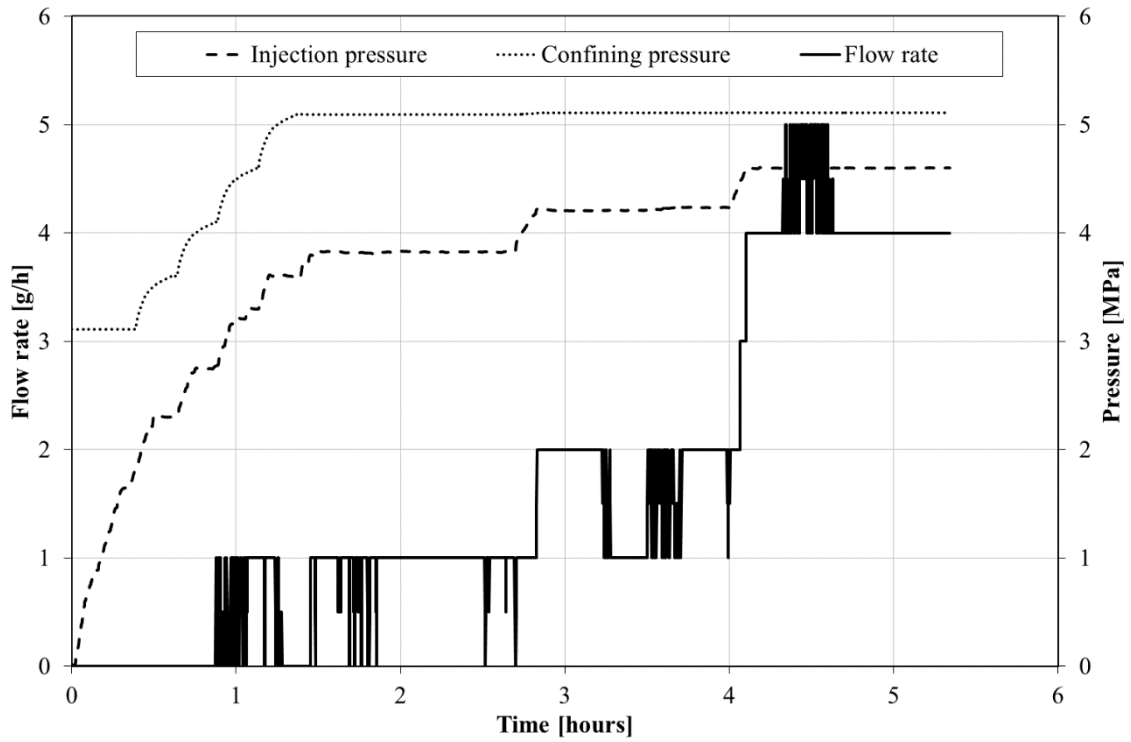


Fig. 7.1. Experimental results of low pressure helium injection measurements for sample A.

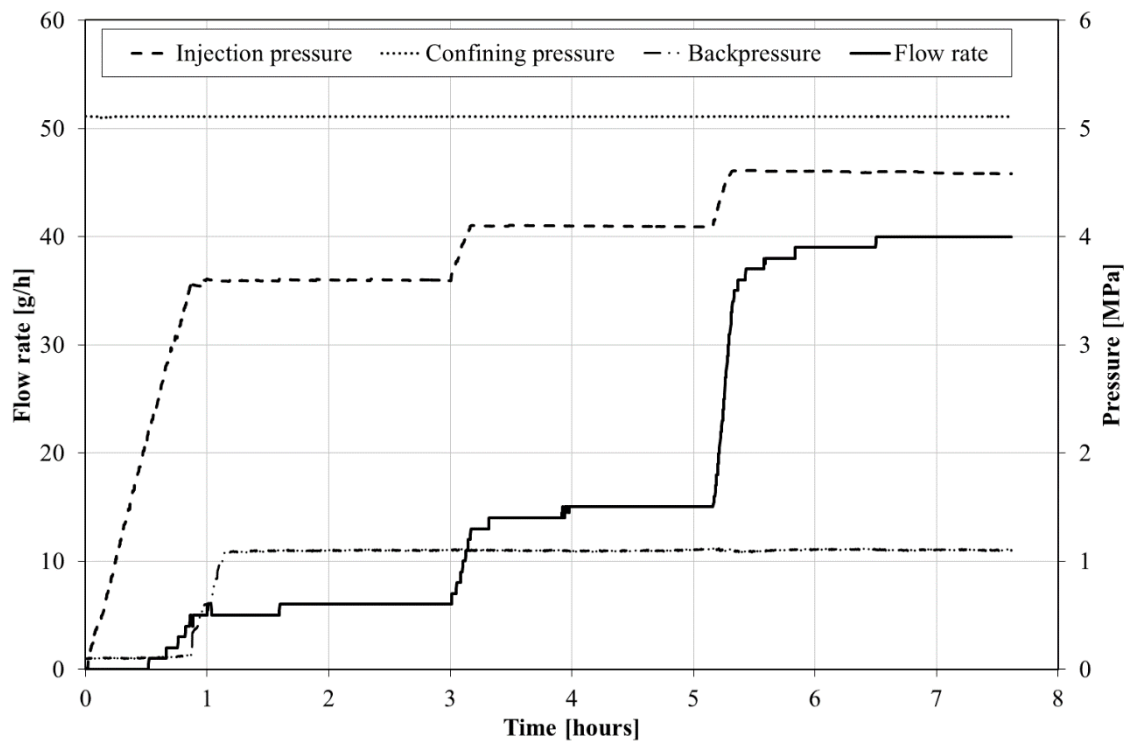


Fig. 7.2. Experimental results of low pressure helium injection measurements for sample B.

Such an observation could be attributed to the differences in the structure of each sample and different backpressures used within the samples. As shown in Chapter 4, sample B has a more developed fracture network than sample A (see Figure 4.6). In addition, sample B had a constant backpressure of 1.1 MPa throughout the experiment, while the gas injected into sample A was allowed to flow directly to the atmosphere. Hence, for the same injection pressure of 4.6 MPa in both samples confined by constant pressure of 5.1 MPa, higher applied backpressure resulted in a higher mean gas pressure across sample B compared to sample A.

Furthermore, for the increase in injection pressure of 0.8 MPa (from 3.8 MPa to 4.6 MPa) in sample A, the increase in flow rate is fourfold while sample B shows sevenfold increase in flow rate with the increase of 1 MPa in injection pressure. Hence, it can be inferred that sample B is more compressible resulting in a higher increase in flow rate with an increase in injection pressure. Such a statement can also be supported by the results for axial and radial strains presented in Figures 7.3 and 7.4 for samples A and B, respectively.

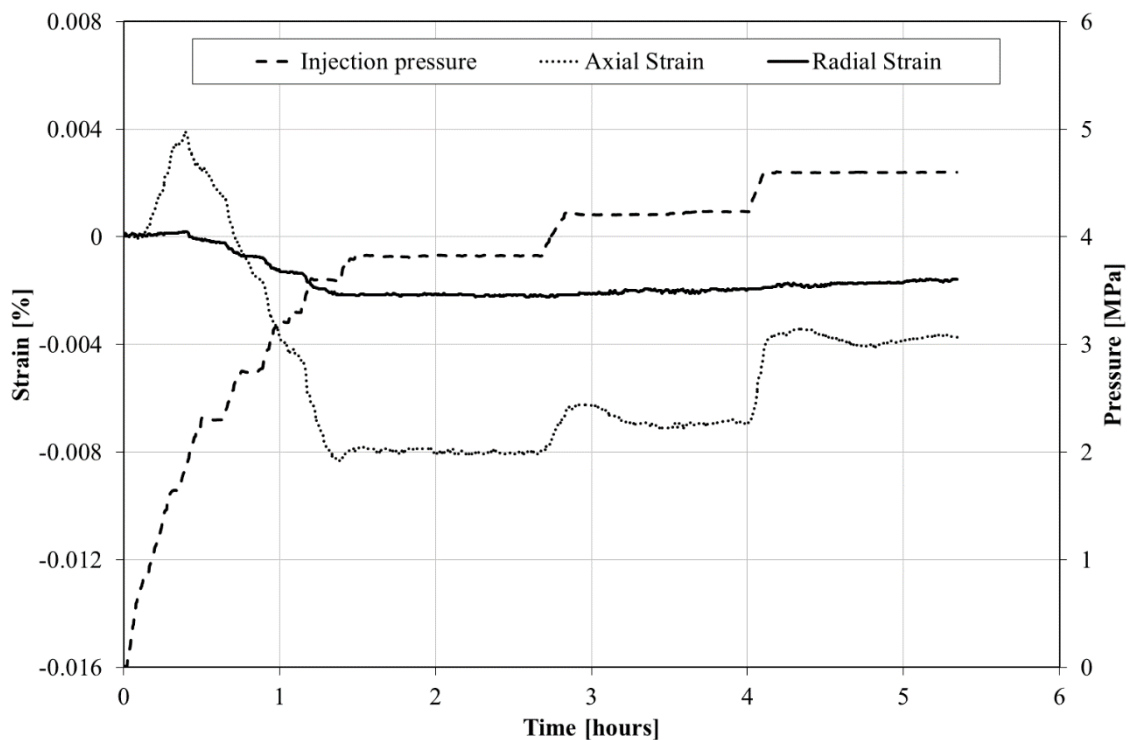


Fig. 7.3. Experimental results of axial and radial strain measurements during low pressure helium injection for sample A.

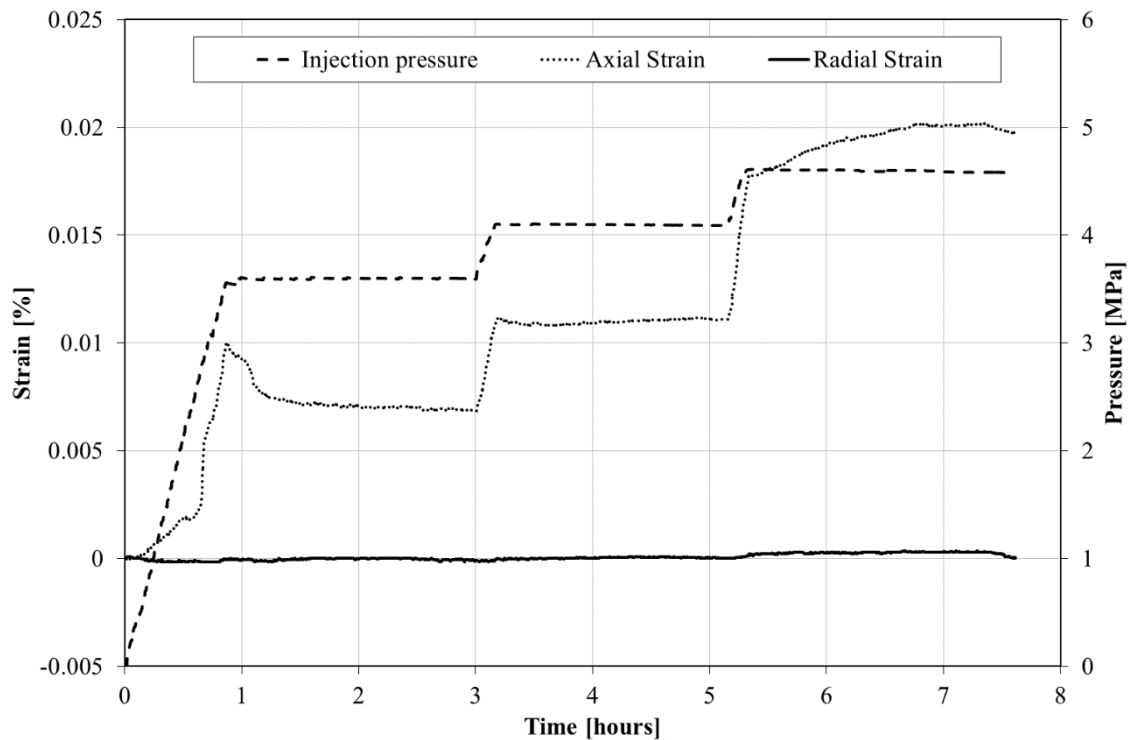


Fig. 7.4. Experimental results of axial and radial strain measurements during low pressure helium injection for sample B.

Results presented in Figure 7.3 show that the initial axial compression, due to the initial increase in confining stress and injection pressure to the desired values (see Section 4.4.4.1), was 0.008% which was taken as a reference state for the first injection step. By further increasing the injection pressure by 0.8 MPa and keeping the confining stress constant, sample A expanded in the axial direction by 0.004%. On the other hand, for a change of injection pressure of 1 MPa, sample B expanded by 0.013%, i.e. from 0.007% to 0.02% (Figure 7.4). Hence, samples A and B experienced a change in axial strain of 0.005 %/MPa and 0.013 %/MPa, respectively. Based on the axial strain results, sample B is 2.6 times more compressible than sample A. As the increase or decrease in compaction of the sample can be attributed to the response of major cleats and preferential flow paths, it is reasonable to expect that any change in the aperture of the fractures will affect the flow behaviour (Hol et al., 2014).

Interestingly, deformation in axial direction of both samples appears to be more significant than in radial direction during the increase in injection pressure while keeping the confining pressure constant. However, negligible radial expansion could be related to the compressibility of the silicone sleeve which was not taken into account

but could have partially accommodated radial expansion of the sample during helium injection.

Furthermore, it can be observed from flow rates and strains presented for both samples that as the injection pressure increases, coal samples appear to become more compressible. For instance, sample B shows that for a change in injection pressure from 3.6 MPa to 4.1 MPa and then from 4.1 MPa to 4.6 MPa, changes in axial strain are 0.004% and 0.009%, respectively. Under those circumstances, for the same change in injection pressures, flow rates increased for 9 g/h and 25 g/h, respectively.

7.2.2. High Pressure He Injection

The results of flow rates and pressures measured during high pressure He injection in samples C and D are presented in Figures 7.5 and 7.6, respectively. Time duration of the experiments reveals that for both specimens the steady state condition was achieved very quickly, within a maximum of half an hour after each increase in injection pressure.

Sample C exhibited flow rates of 24 g/h, 32 g/h and 43 g/h for injection pressures of 7.1 MPa, 7.6 MPa and 8.1 MPa, respectively showing eight times higher flow rates than sample D for the same injection pressures. Similar to the observations for low pressure helium injection presented earlier, differences in measured flow rates between the two samples could be attributed to the variations in the structure of the respective samples as well as the mean gas pressures used within the samples. As can be seen in Figure 4.6, samples C and D exhibit different fracture network. In addition, test conditions presented in Table 4.10 show that the same injection pressures and confining pressures were applied to both samples. However, the applied backpressure of 2.6 MPa was higher in sample C than the backpressure of 0.6 MPa applied in sample D increasing the mean gas pressure within the sample C compared to sample D.

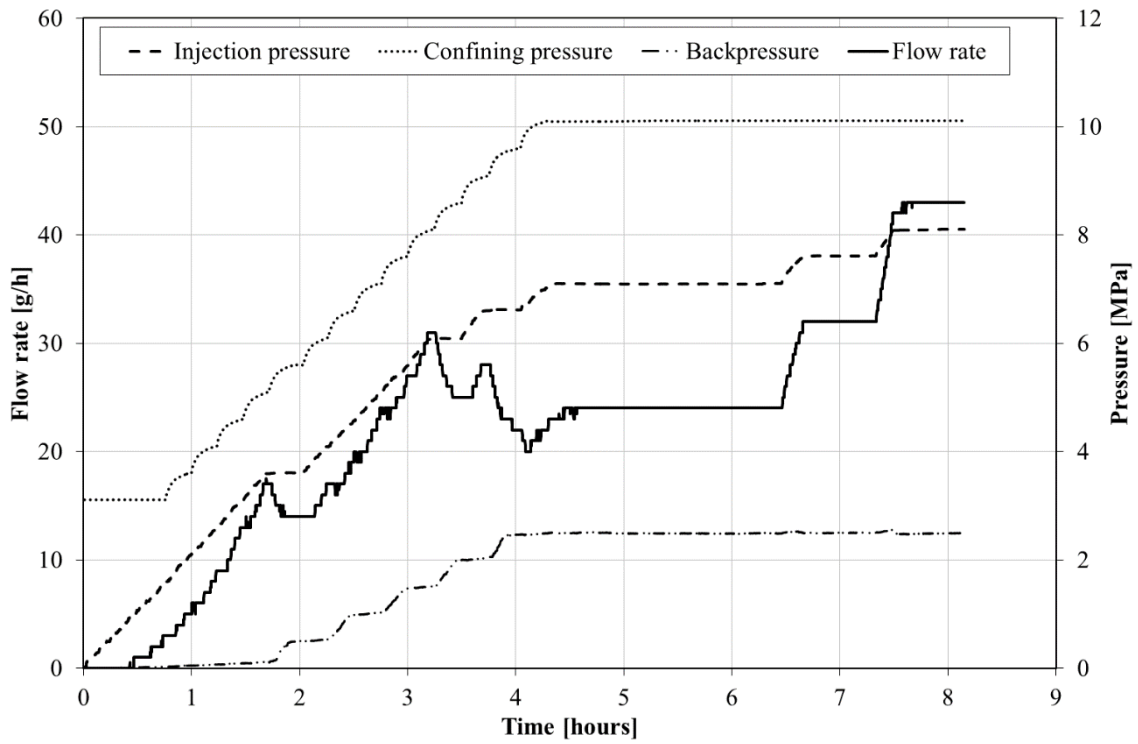


Fig. 7.5. Experimental results of high pressure helium injection measurements for sample C.

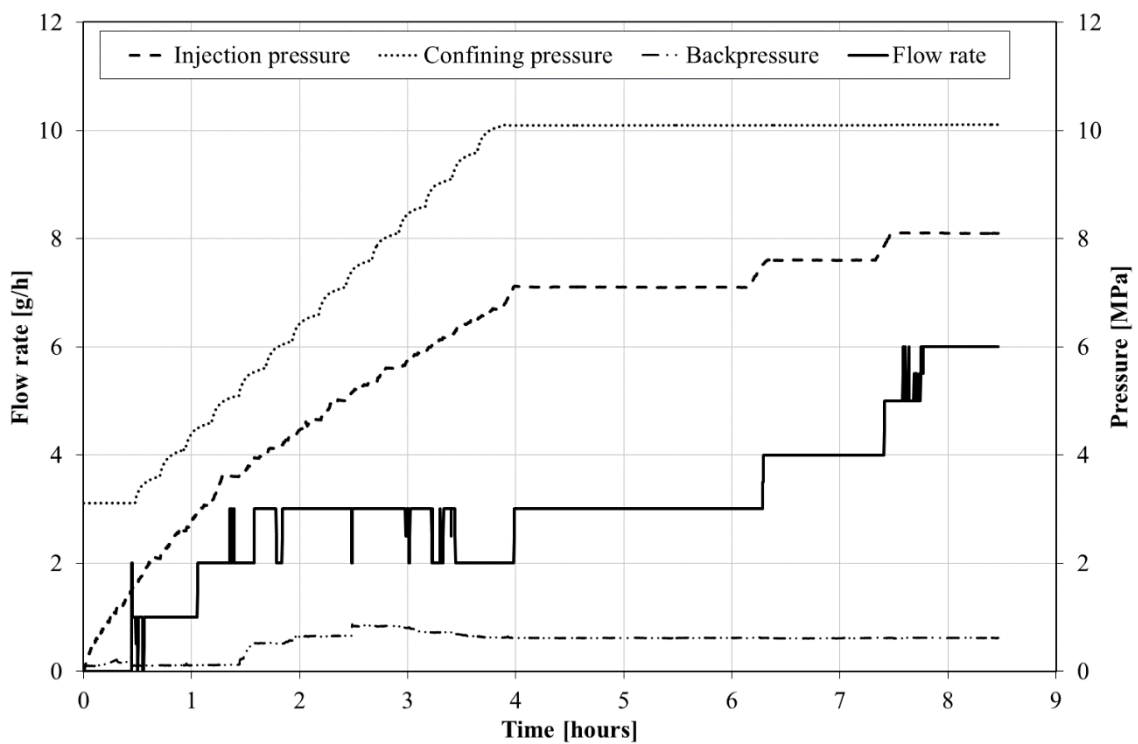


Fig. 7.6. Experimental results of high pressure helium injection measurements for sample D.

Despite the higher flow rates observed in sample C in comparison to sample D, by inspecting the change in flow rates with an increase in injection pressures, it can be seen that sample D appears to be more compressible than sample C. In particular, sample C and sample D experienced 1.8 times and 3 times increase in flow rates for 1 MPa increase in injection pressure, respectively.

Measured strains of samples C and D are presented in Figures 7.7 and 7.8, respectively. During the initial compression, due to the increase in confining stress to the desired value, samples C and D experienced compressive axial strain of 0.0225% and 0.015%, respectively. Taking those values as a baseline, an increase of 1 MPa of injection pressure resulted in an expansion of 0.005% in sample C and an expansion of 0.019% in sample D. Both samples experienced negligible expansion in radial direction with an increase in injection pressure.

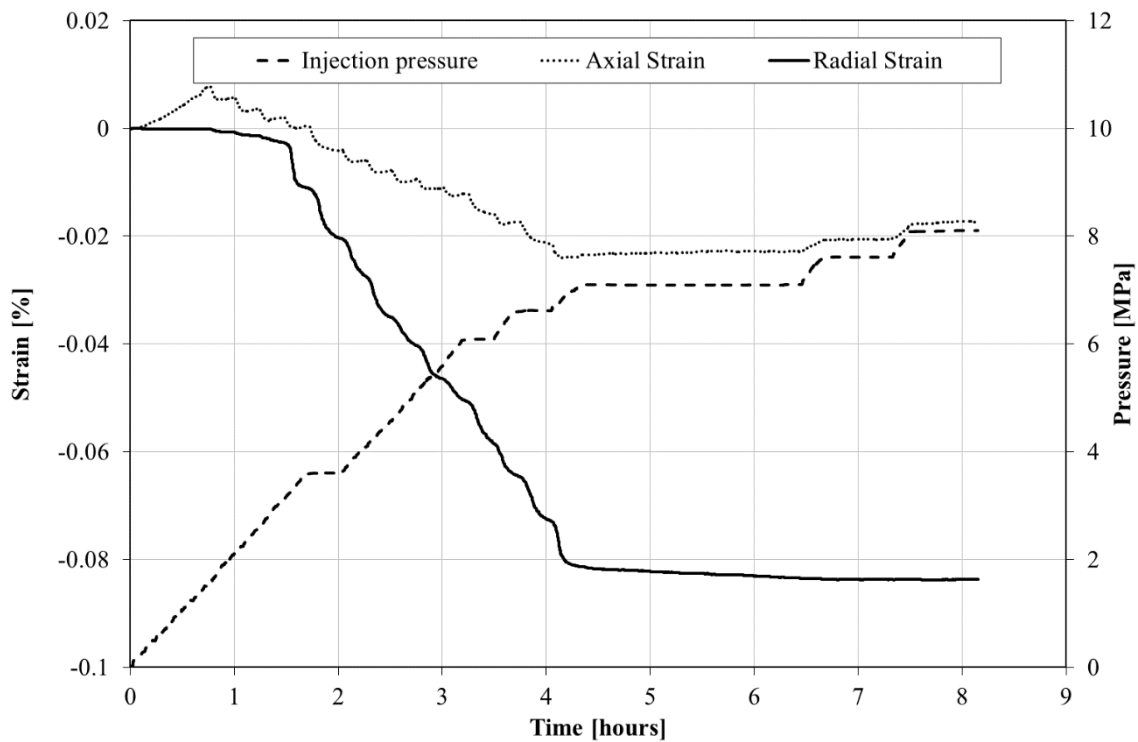


Fig. 7.7. Experimental results of axial and radial strain measurements during high pressure helium injection for sample C.

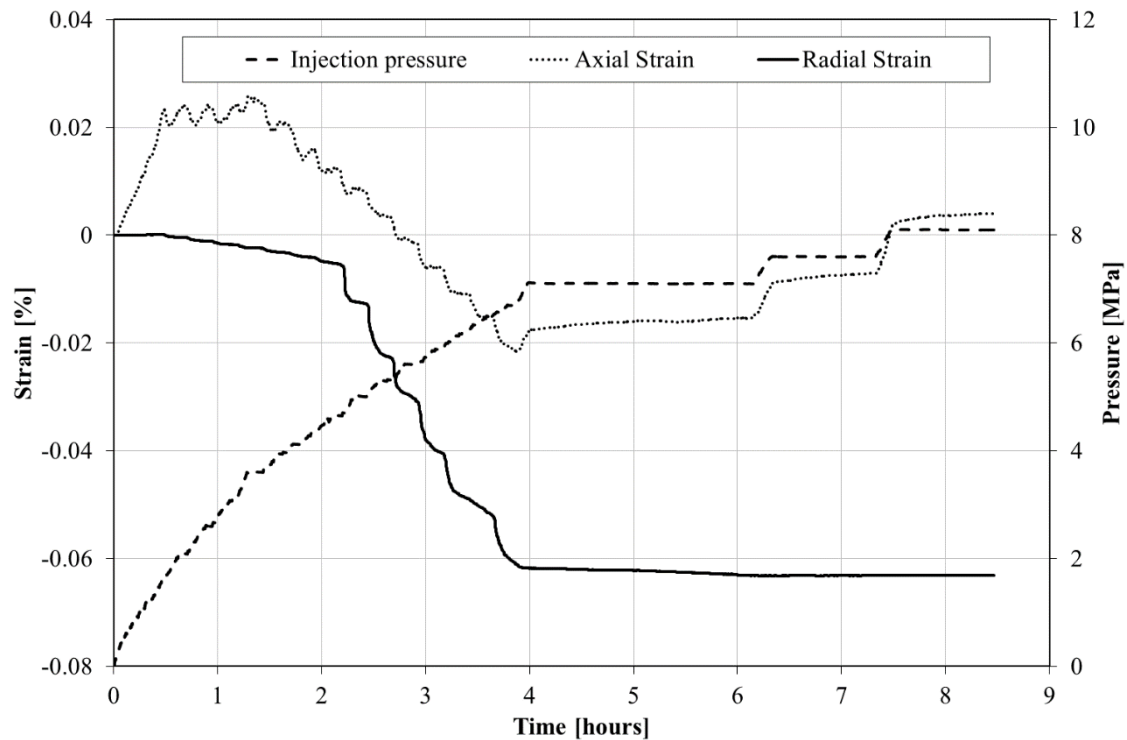


Fig. 7.8. Experimental results of axial and radial strain measurements during high pressure helium injection for sample D.

7.2.3. Permeability to He

In this work, the permeability of coal to gases was evaluated using a steady-state method, as described previously in Chapter 4. Using Darcy's law (eq. 4.13), permeability to He was evaluated when both the flow rates and the measured axial and radial strains have reached equilibrium at the end of each injection step, i.e. when there were no further changes in recorded values with time. Based on calculated values at each of the three injection steps, a set of three permeability values for each sample was obtained.

It should be noted that during the three injections steps in each sample, confining stresses and backpressures were kept constant, as mentioned earlier. Hence, the only change in calculated permeability was caused by an increase in injection pressure. However, to make the calculated values comparable with the literature, permeability values are presented as a function of effective stress. The effective stress is calculated based on the measured confining pressures and mean pressures used within the samples

at each injection step, as said in Chapter 4. Furthermore, as already mentioned, mean gas pressure represents the average of injection pressure and backpressure.

Such a procedure was conducted to assess the change in calculated permeability to He with the change in effective stress. As shown in Chapter 2, permeability is considered to be a function of porosity of the coal sample (e.g. Somerton et al. 1975). The change in porosity could not be measured in this experiment during the gas injection. However, as the porosity available for flow decreases as a result of fracture closure induced by redistribution of stresses, it is reasonable to expect that permeability depends on the changes in effective stress (e.g. Durucan and Edwards, 1986; Liu et al., 1999; Meng et al., 2015).

Permeability values of all four samples to He were plotted versus the effective stress and are presented in Figure 7.9. From the results presented for each sample, a general trend of permeability reduction as a result of increase in effective stress can be observed. An exponential function (equation 2.2) shown as solid line, reported by many researchers as mentioned in Chapter 2, is fitted to the permeability values obtained for each sample.

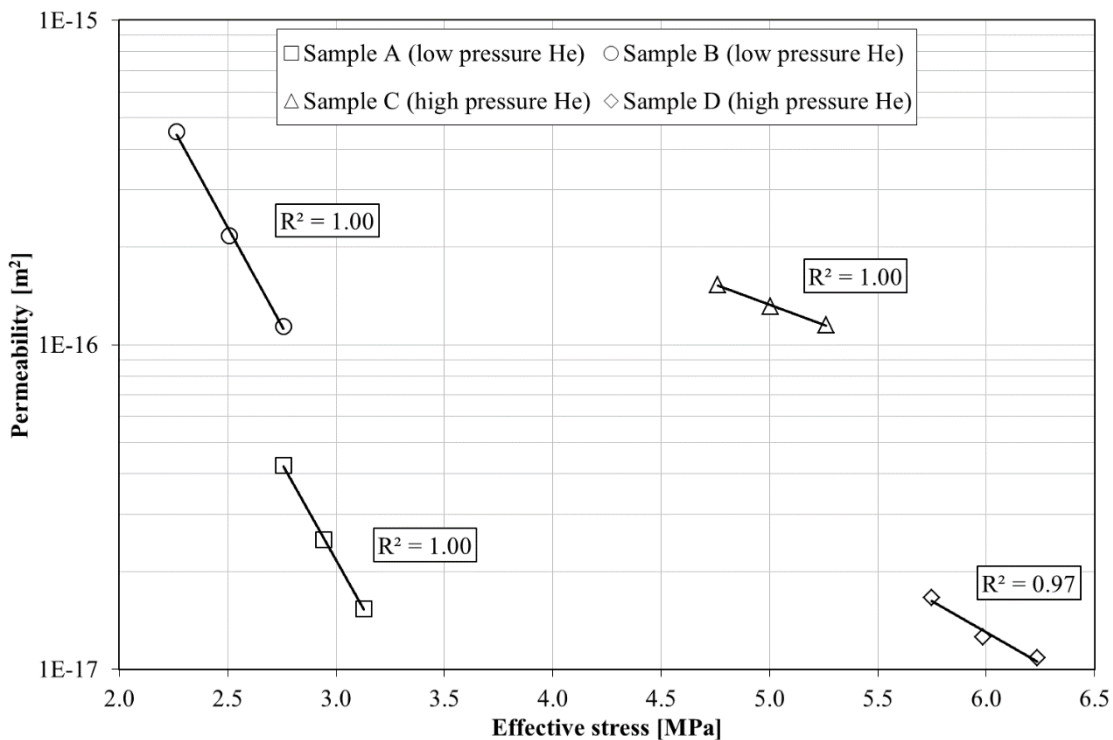


Fig. 7.9. The relationship between permeability to helium and effective stress.

The overall agreement between the calculated permeability values and fitted curves is very good with the values of coefficient of determination ranging between 0.97 and 1. It can be seen that experimental data for all four samples show that Black Diamond coal exhibits He permeability values between $5 \times 10^{-16} \text{ m}^2$ to $1 \times 10^{-17} \text{ m}^2$ for effective stress conditions ranging from 2.25-6.25 MPa. However, each coal sample exhibits a different permeability trend. Based on the exponential fitting to the experimental results, empirical relations between the coal permeability to helium and effective stress were developed for all samples and are presented in Table 7.1 where k and σ'' stand for permeability and effective stress, respectively.

Table 7.1. Helium permeability and effective stress relationships.

Sample	Relationship
<i>Low pressure injection</i>	
Sample A	$K_g = 8.06 \times 10^{-14} \exp(-2.739\sigma'')$
Sample B	$K_g = 2.51 \times 10^{-13} \exp(-2.798\sigma'')$
<i>High pressure injection</i>	
Sample C	$K_g = 2.29 \times 10^{-15} \exp(-0.570\sigma'')$
Sample D	$K_g = 2.58 \times 10^{-15} \exp(-0.882\sigma'')$

By comparing the relationships presented, it can be seen that values of the exponents between samples A and B, and between samples C and D are comparable. The value of the exponent in the exponential function indicates the rate at which permeability changes with respect to effective stress (Harpalani and McPherson, 1985). Hence, the results obtained suggest that samples A and B will experience higher change in permeability with an increase in effective stress compared to samples C and D. Such observation is in agreement with the literature where it was reported that under low effective stress, the change in deformation and permeability exhibits a steep gradient attributed to the immediate opening or closure of existing fractures (Durucan and Edwards, 1986, Meng et al., 2015). In other words, when the effective stress is low (<3.15 MPa in this case), coals have high sensitivity to effective stress.

7.2.4. Subcritical CO₂ Injection

Figures 7.10 and 7.11 show measured flow rates and pressures for samples A and B, respectively, subject to subcritical CO₂ injection.

At the first injection step, where the injection pressure was 3.8 MPa for sample A and 3.6 MPa for sample B, it can be observed that both samples showed initial increase in flow rates and then a gradual decrease. As mentioned in Chapter 2 and will be shown later in the current section, CO₂ sorption induces swelling of the coal matrix. Hence, the observed reduction in flow rates could be attributed to the swelling of the coal matrix upon sorption of CO₂ and closure of the dominant flow paths. Increasing the injection pressure to 4.2 MPa (Sample A) and 4.1 MPa (Sample B), flow rates in both samples recovered. By further increasing the injection pressure to 4.6 MPa, both samples showed sudden increase in flow rate. This increase could be related to the fracture widening caused by an increase in injection pressure. Sample A showed maximum flow rate of 2 g/h in the last injection step while sample B showed 70 times higher flow rate at the same injection pressure of 4.6 MPa.

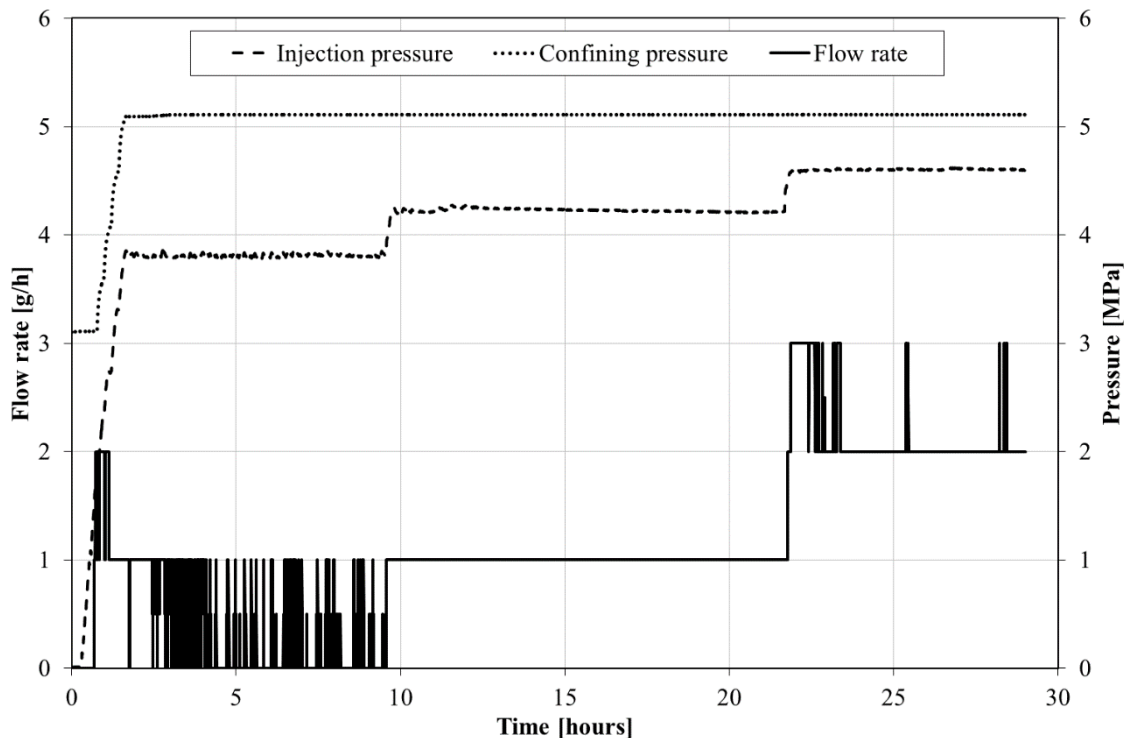


Fig. 7.10. Experimental results of subcritical carbon dioxide injection measurements for sample A.

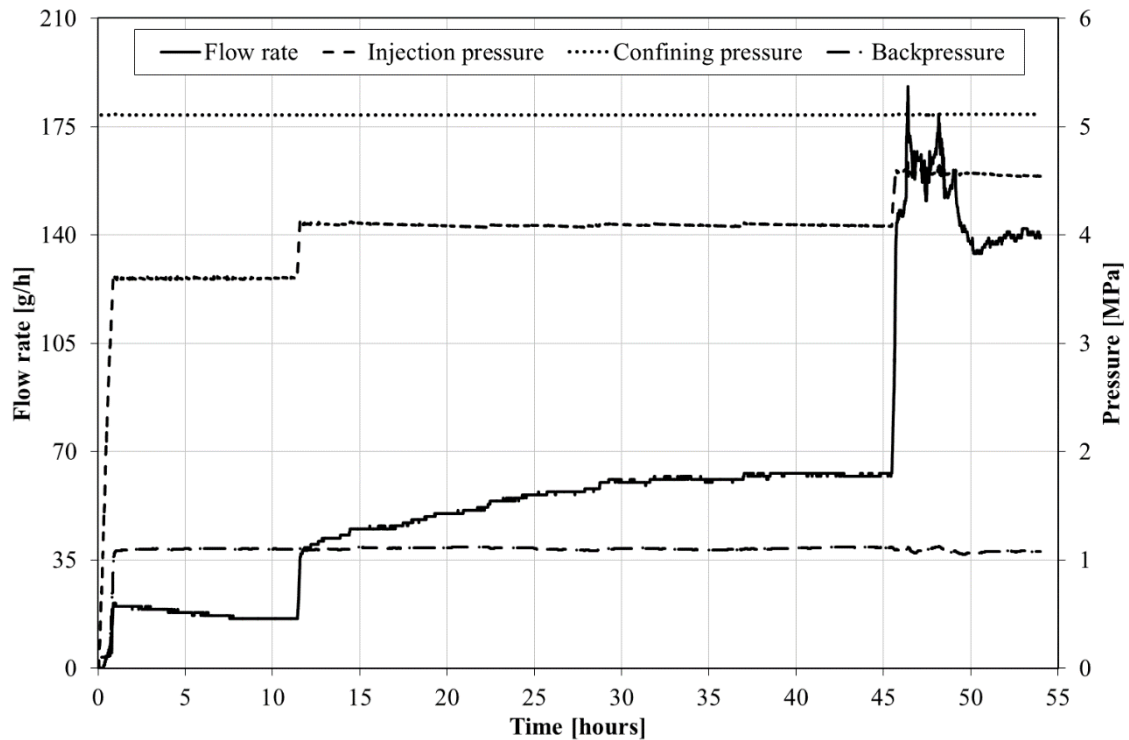


Fig. 7.11. Experimental results of subcritical carbon dioxide injection measurements for sample B.

CO₂ sorption shows slightly different behaviour at each injection step for both samples, but in general it requires a minimum of seven hours to reach equilibrium at each injection step. The only exception was the second injection step of sample B which took more than 15 hours to reach steady state. If the results measured during He injection presented earlier and the results measured during CO₂ injection in samples A and B are compared, the overall time for CO₂ experiments was minimum four times higher than for He experiments.

Measured strains of samples A and B are presented in Figures 7.12 and 7.13, respectively. Results reveal that sample A experienced minimal increase in both axial and radial strains during the first two injection steps. In the third injection step, maximum recorded axial and radial strains for sample A at injection pressure of 4.6 MPa were 0.05% and 0.11%, respectively. On the contrary, sample B at the end of the second step expanded axially and radially by 0.06% and 0.09%, respectively. Interestingly, in the third injection step a sudden increase in sample B swelling occurred leading to maximum axial and radial strains of 0.2% and 0.44%, respectively.

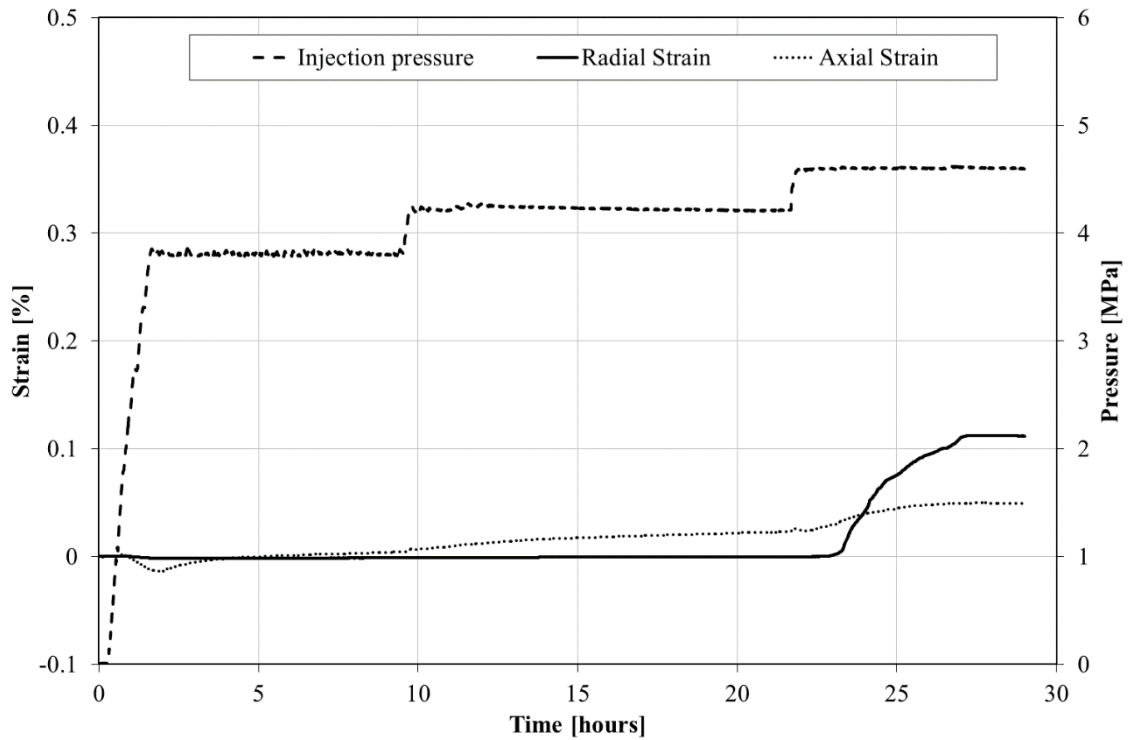


Fig. 7.12. Experimental results of axial and radial strain measurements during subcritical carbon dioxide injection for sample A.

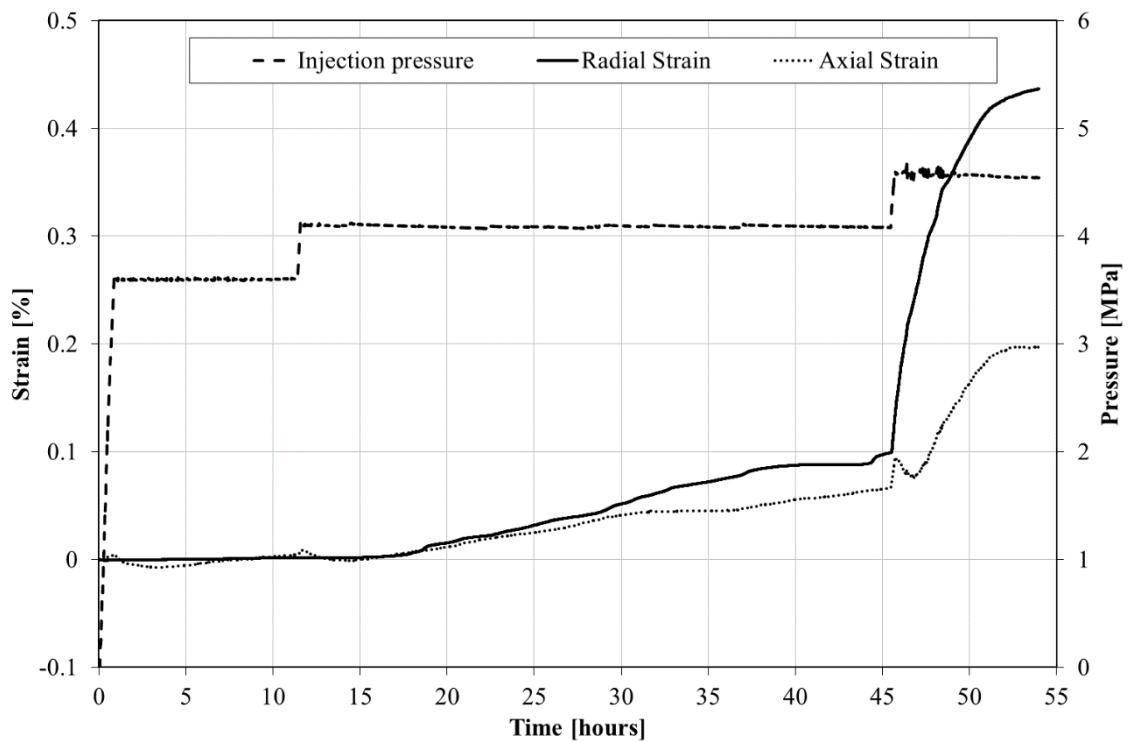


Fig. 7.13. Experimental results of axial and radial strain measurements during subcritical carbon dioxide injection for sample B.

Based on the experimental results presented both for He and CO₂ injections, it can be observed that strains measured during CO₂ injection are a minimum one order of magnitude higher than strains measured during He injection. To restate, samples A and B expanded in axial direction, during the three He injection steps, by 0.004% and 0.013%, respectively. During the three CO₂ injection steps, sample A expanded axially by 0.05% and sample B by 0.2%. In addition, while there was a negligible radial expansion of both samples during He injection, samples A and B swelled during CO₂ injection by 0.11% and 0.44%, respectively. Hence, CO₂ swelling induced deformations dominate over the effective stress generated ones.

7.2.5. Supercritical CO₂ Injection

The results of flow rates and pressures measured during supercritical CO₂ injection in samples C and D are presented in Figures 7.14 and 7.15, respectively. Although during the first injection step CO₂ is still in the subcritical region (7.1 MPa), the focal point of this investigation was to assess the flow and deformation behaviour of coal when the CO₂ pressure is increased from subcritical to supercritical region (7.6 and 8.1 MPa).

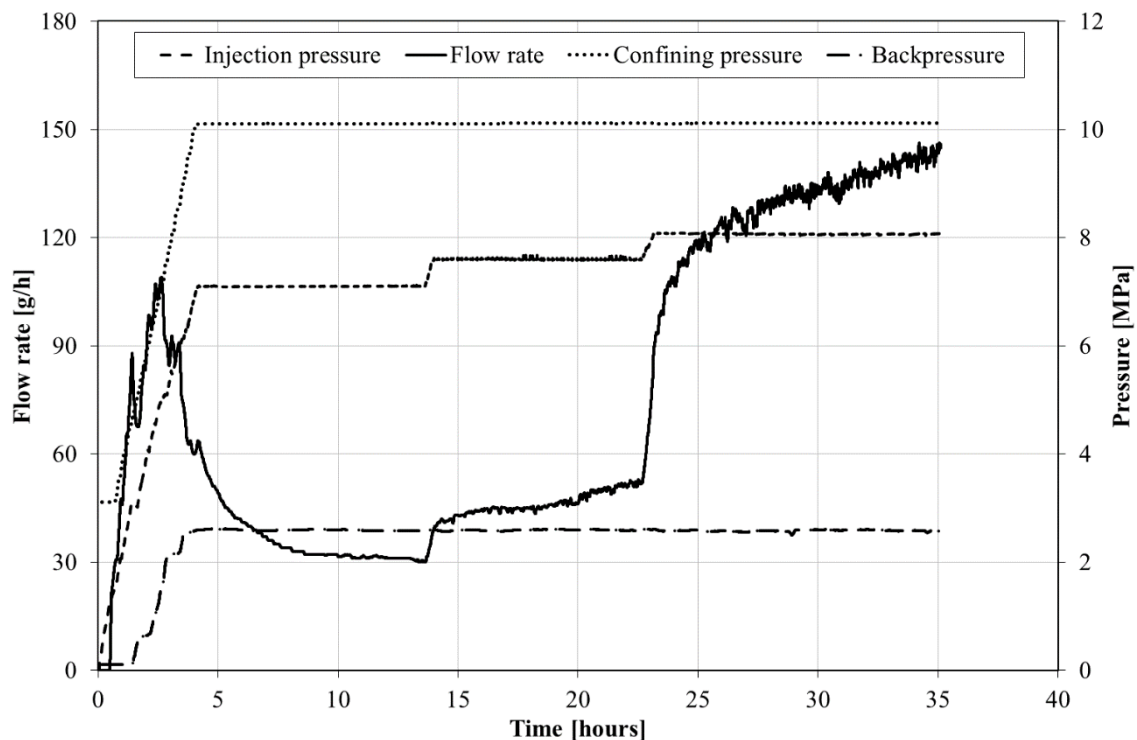


Fig. 7.14. Experimental results of supercritical carbon dioxide injection measurements for sample C.

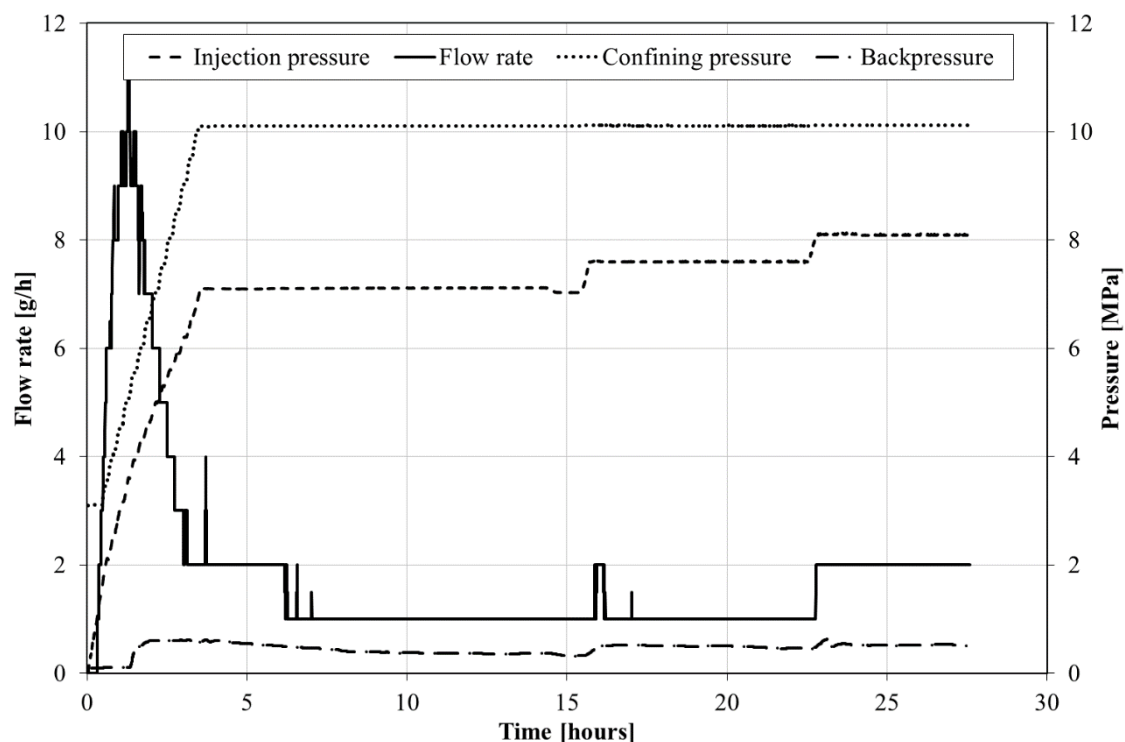


Fig. 7.15. Experimental results of supercritical carbon dioxide injection measurements for sample D.

By inspecting the time duration of the CO₂ injection in both Figures 7.14 and 7.15, it can be observed that both samples required a minimum period of five hours to reach steady-state condition during each injection step. It should be noted that the experiment on sample C had to be stopped due to technical issues with the oil pressure controller after 35 hours of injection at which point both the flow rate and the expansion of the sample had not reached steady state.

It can be seen from Figures 7.14 and 7.15 that increasing the injection pressure up to 7.1 MPa resulted in a continuous increase in flow rates. Once the pressure stabilized at 7.1 MPa, a substantial reduction in flow rates for both samples occurred. Minimum recorded flow rates at the end of the first injection step (7.1 MPa) for samples C and D are 31 g/h and 1 g/h, respectively. As the pressure increased to 7.6 MPa, increase in flow rate is visible only for sample C. At the end of the third injection step, maximum recorded flow rates for samples C and D are 142 g/h and 2 g/h, respectively. These values show that up to 70 times higher flow rates were recorded in sample C than in sample D for the same injection pressures.

Expansions in axial and radial directions of both samples during CO₂ injection are presented in Figure 7.16 (sample C) and Figure 7.17 (sample D).

Sample C accommodated the swelling induced by CO₂ sorption in the first injection step (7.1 MPa) by expanding externally reaching a radial strain of 0.18%. Further increase in injection pressure to 7.6 MPa and 8.1 MPa resulted in radial expansion of 0.3% and 0.78%, respectively. Interestingly, sample C only showed significant axial expansion in the last injection step (8.1 MPa) with the strain value of 0.19% suggesting that expansion in the radial direction was four times higher than in the axial direction.

Expansion of sample D was primarily in the radial direction with significant axial strain of 0.17% only in the last two injection steps. For the injection pressure of 7.1 MPa, 7.6 MPa and 8.1 MPa, sample D experienced radial strains of 0.42%, 0.6% and 0.85%, respectively. Consequently, the radial strain in the last injection step was five times larger than the axial strain. However, radial expansion of sample D followed different pattern than of sample C. Results reveal that during the first two injection steps, sample D experienced two times higher radial strain compared to sample C. Moreover, in the last injection step, sample D achieved steady-state condition more quickly than sample C.

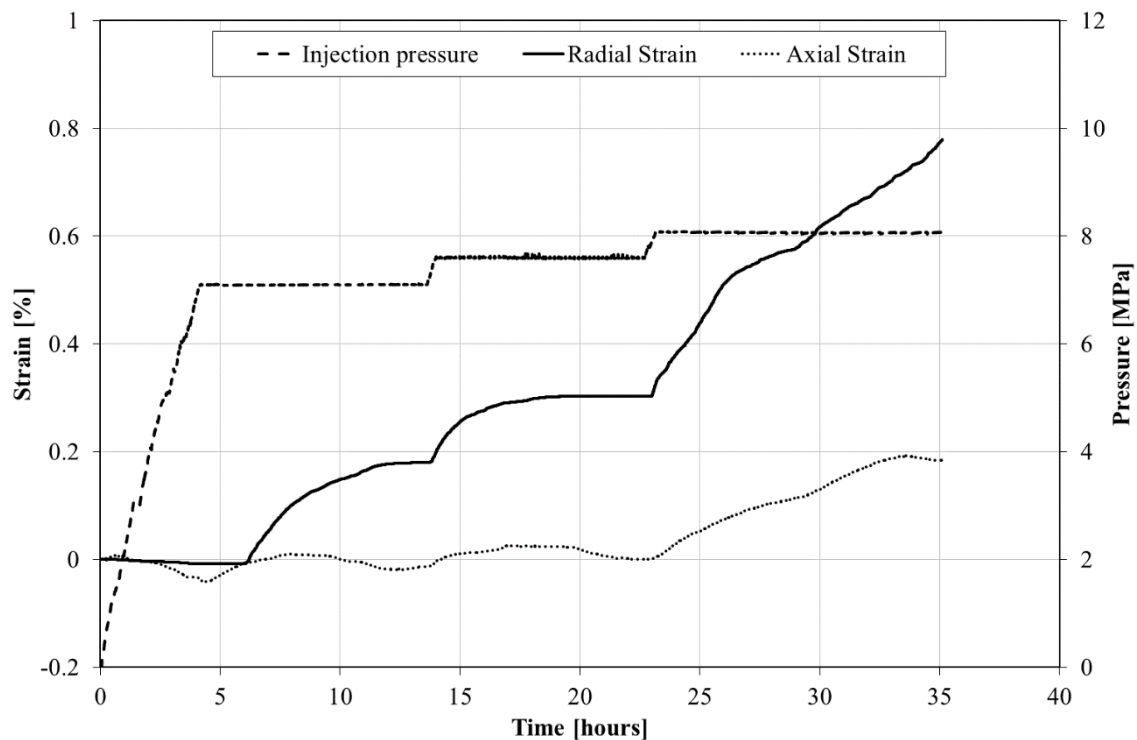


Fig. 7.16. Experimental results of axial and radial strain measurements due to supercritical carbon dioxide injection for sample C.

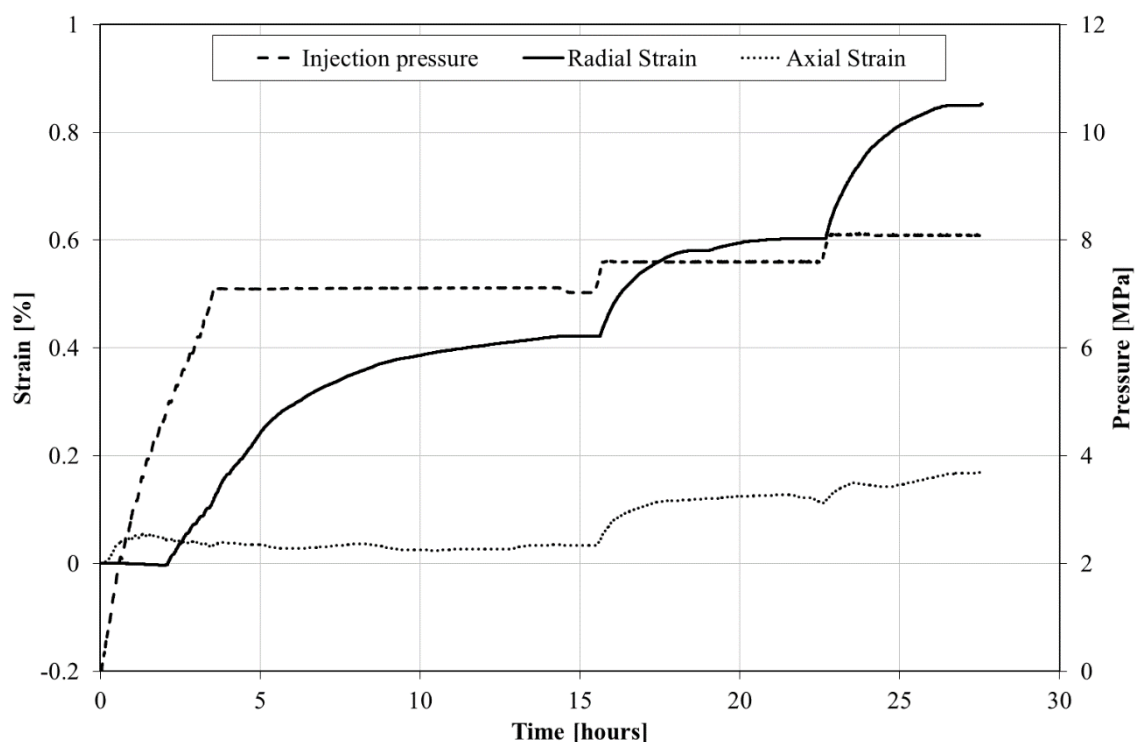


Fig. 7.17. Experimental results of axial and radial strain measurements due to supercritical carbon dioxide injection for sample D.

Bearing in mind that the confining pressure was increased in a parallel manner with the injection pressure and the backpressure up to the desired values during the first four hours of the experiment, the external expansion induced by CO₂ sorption appeared to be largely unaffected by an increase in confining stress. This suggests that confining stress was offering minimal constraint to the coal allowing it to swell freely. Such findings support the work of Espinoza et al. (2014) who have experimentally shown that near constant volume conditions for injection pressure of 2 MPa can only be achieved by applying high confining stresses, i.e. between 23 MPa and 32 MPa. In addition, Espinoza et al. (2014) have shown that if CO₂ injection pressure of 10 MPa is to be used, at least 60 MPa of confining stress should be applied to achieve near constant volume conditions which is six times higher than in this study.

7.2.6. Permeability to CO₂

The permeability coefficients of all four coal samples subjected to both subcritical CO₂ and supercritical CO₂ injection were calculated based on equation (4.13). Following the

same approach mentioned earlier for He injection, calculated permeability values to CO₂ are presented in Figure 7.18 versus the effective stress. In addition, an exponential function was fitted to the calculated permeability values.

Permeability values of all four samples show reduction with an increase in effective stress. Based on the presented data, it can be seen that CO₂ permeability values range from 1×10^{-16} m² to 2×10^{-19} m² for effective stress conditions of 2.25-6.4 MPa. Compared to values of permeability to He presented earlier, obtained CO₂ permeability values are a minimum one order of magnitude lower. The exponential regression between the permeability and effective stress for samples A, B and C is very good with coefficient of determination ranging between 0.95-1. However, fitting of the exponential function to the calculated permeability values of sample D to CO₂ shows poorer agreement, i.e. coefficient of determination is 0.49.

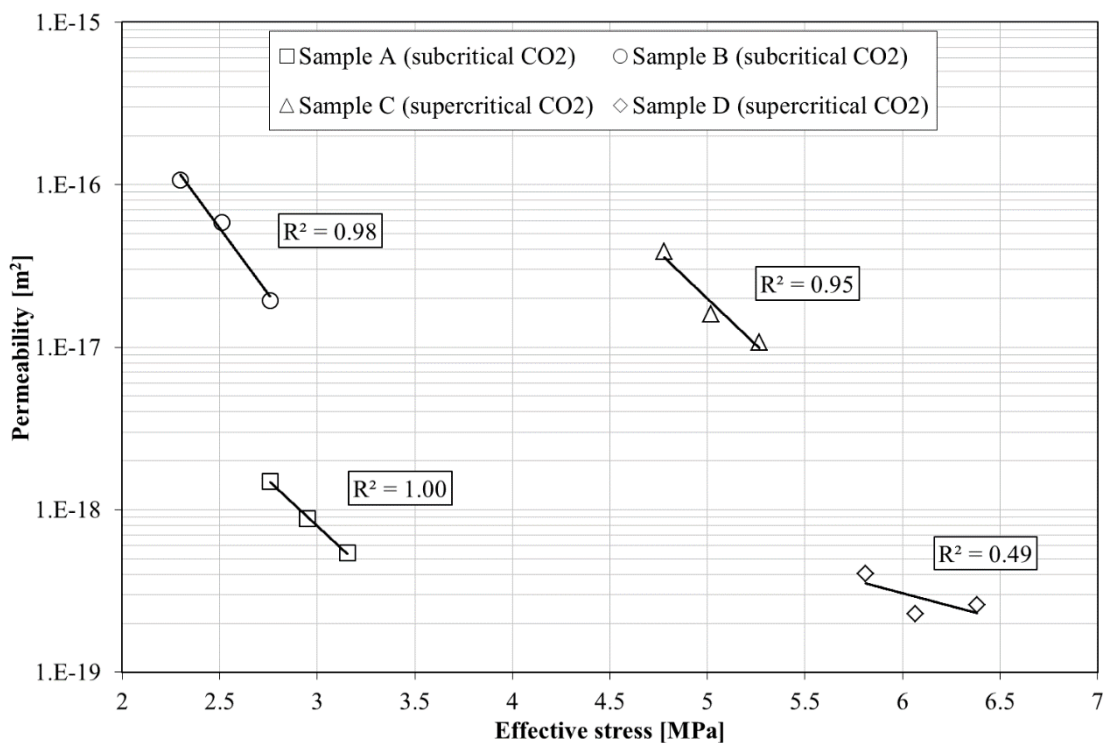


Fig. 7.18. The relationship between permeability to carbon dioxide and effective stress.

Exponential relationships between the permeability to CO₂ and effective stress for all samples are presented in Table 7.2. If the relationships are compared, it can be observed that samples A, B and C will experience higher reduction in permeability to CO₂ than sample D for the same change in effective stress.

Table 7.2. Carbon dioxide permeability and effective stress relationships.

Sample	Relationship
<i>Low pressure injection</i>	
Sample A	$K_g = 6.47 \times 10^{-13} \exp(-3.760\sigma'')$
Sample B	$K_g = 1.78 \times 10^{-15} \exp(-2.571\sigma'')$
<i>High pressure injection</i>	
Sample C	$K_g = 1.04 \times 10^{-11} \exp(-2.634\sigma'')$
Sample D	$K_g = 2.54 \times 10^{-17} \exp(-0.736\sigma'')$

7.3. Temperature Changes due to Gas Injection

In this section, the results of temperature measurements continuously taken during both He and CO₂ injection in all samples are presented. As explained in Chapter 4, thermocouples were placed close to the inlet and the outlet of all samples. This was done to assess any potential temperature changes induced by high flow of gases under the established pressure gradient across the samples. Temperature results during He injection for samples A, B, C and D are presented in Figures 7.19, 7.20, 7.21 and 7.22 respectively. In the same figures, a difference between the injection pressures and backpressures was plotted. Since the pressure drop across the sample causes the gas to expand and cools down or heats up, as mentioned in Chapter 2, parallel plot of pressure differences across the samples and temperatures will help to assess the effect of pressure drop on measured temperatures.

Based on the temperature data recorded at the inlet and the outlet of all samples, it can be observed that the average temperature throughout the injection of He was stable. In particular, the average temperature in all samples was kept at $37.5 \pm 1^\circ\text{C}$.

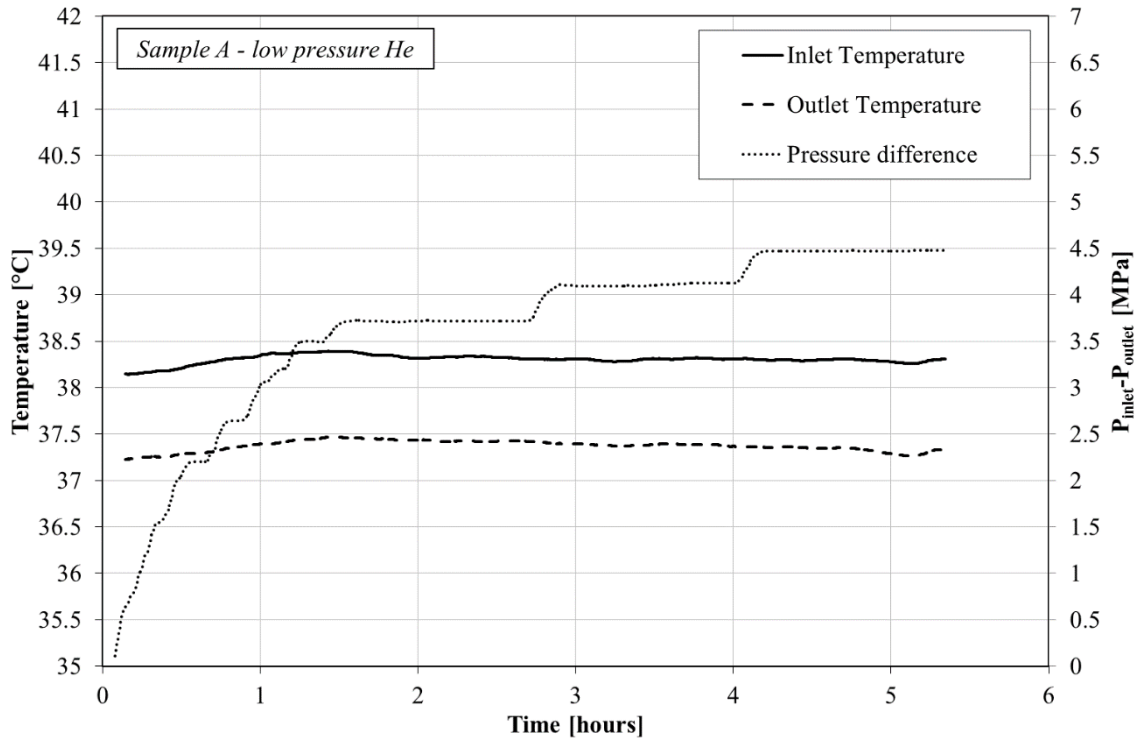


Fig. 7.19. Experimental temperature measured on sample A during low pressure helium injection.

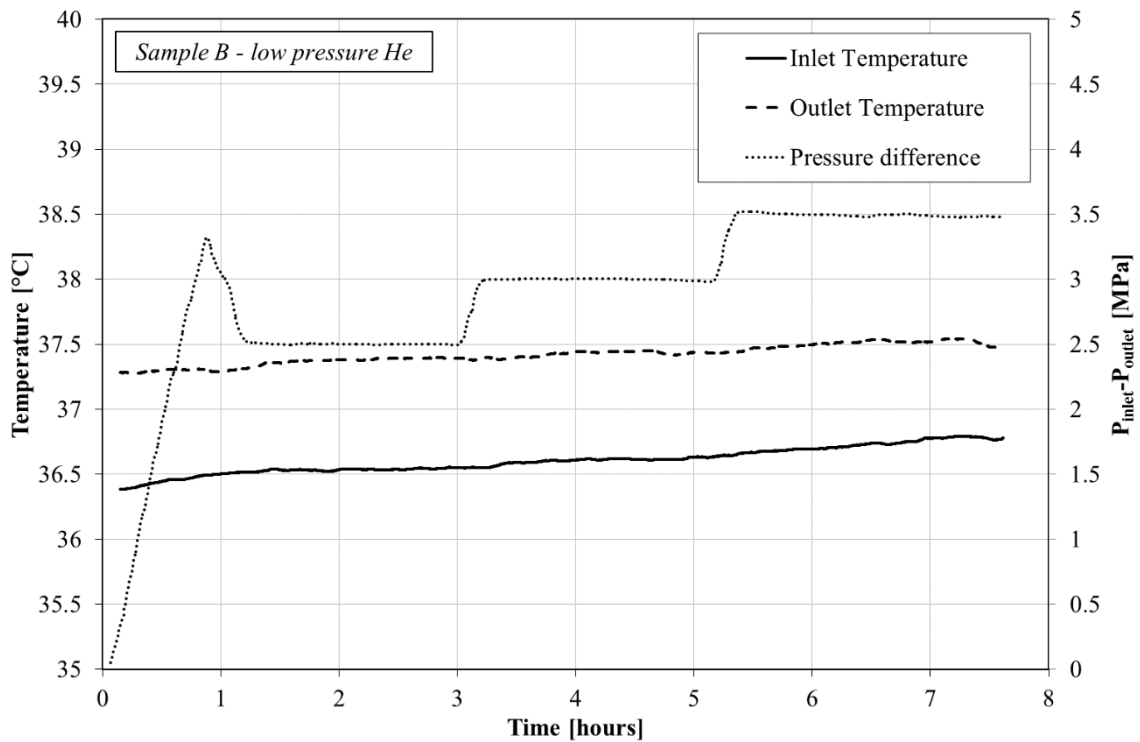


Fig. 7.20. Experimental temperature measured on sample B during low pressure helium injection.

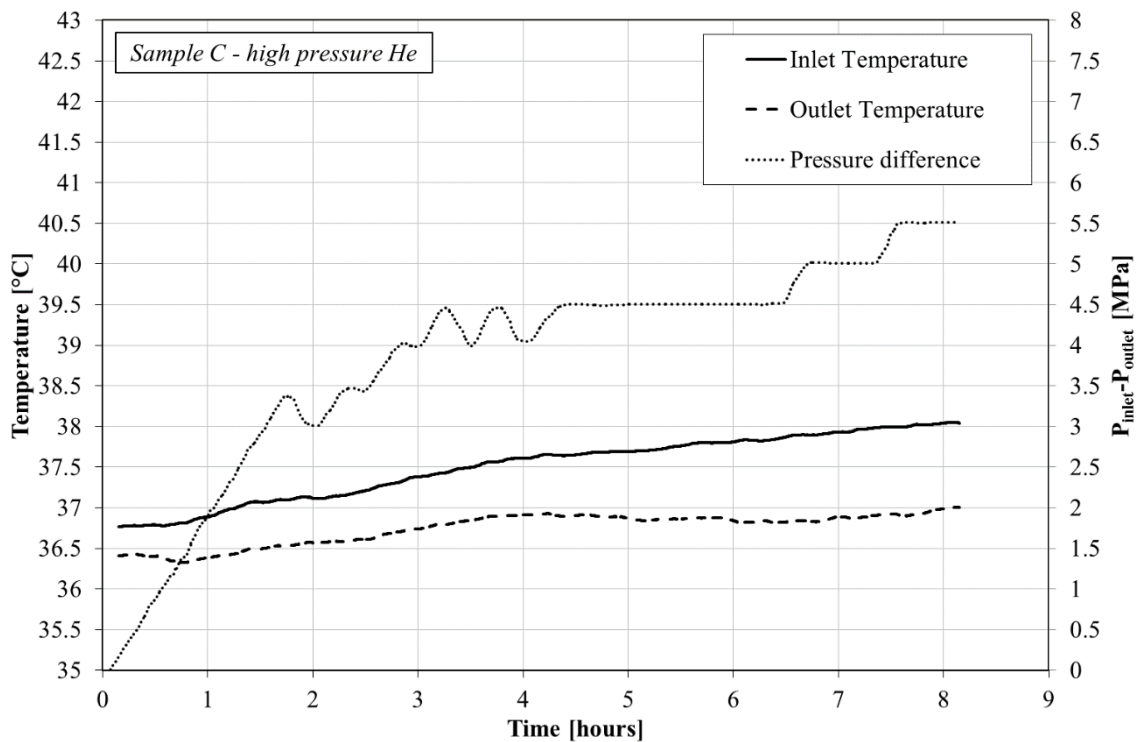


Fig. 7.21. Experimental temperature measured on sample C during high pressure helium injection.

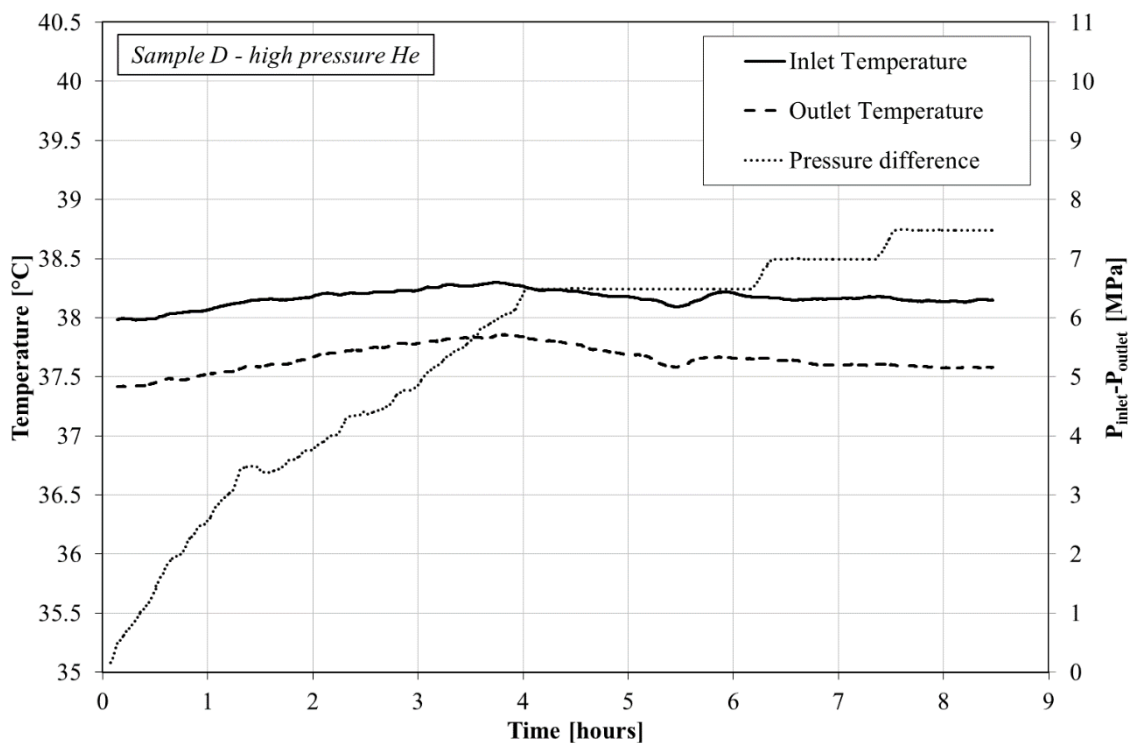


Fig. 7.22. Experimental temperature measured on sample D during high pressure helium injection.

However, it can be seen that a small temperature difference of approximately 0.8°C exists between the inlet and the outlet of the samples. The reason for that lies in the way the triaxial cell was insulated. During all the experiments, two fume cupboards had to be turned on at all times to minimize the potential gas leakage hazard causing a constant draft across the laboratory. Such a phenomenon affected the temperature control of the cell. Moreover, as the duration of the He experiments was between 6 hours and 9 hours, changes in the room temperature during the day could have had a slight effect on the measured temperature.

In relation to the Joule-Thomson effect, as mentioned previously in chapter 2, helium experiences slight warming effect upon expansion which is expected to have negligible impact on the overall experimental system. This is confirmed from the figures. Carbon dioxide, however, experiences significant cooling effect upon expansion which could potentially affect the temperature conditions during the CO_2 injection. Results of temperature measurements during CO_2 injection for samples A, B, C and D are presented in Figures 7.23, 7.24, 7.25 and 7.26, respectively.

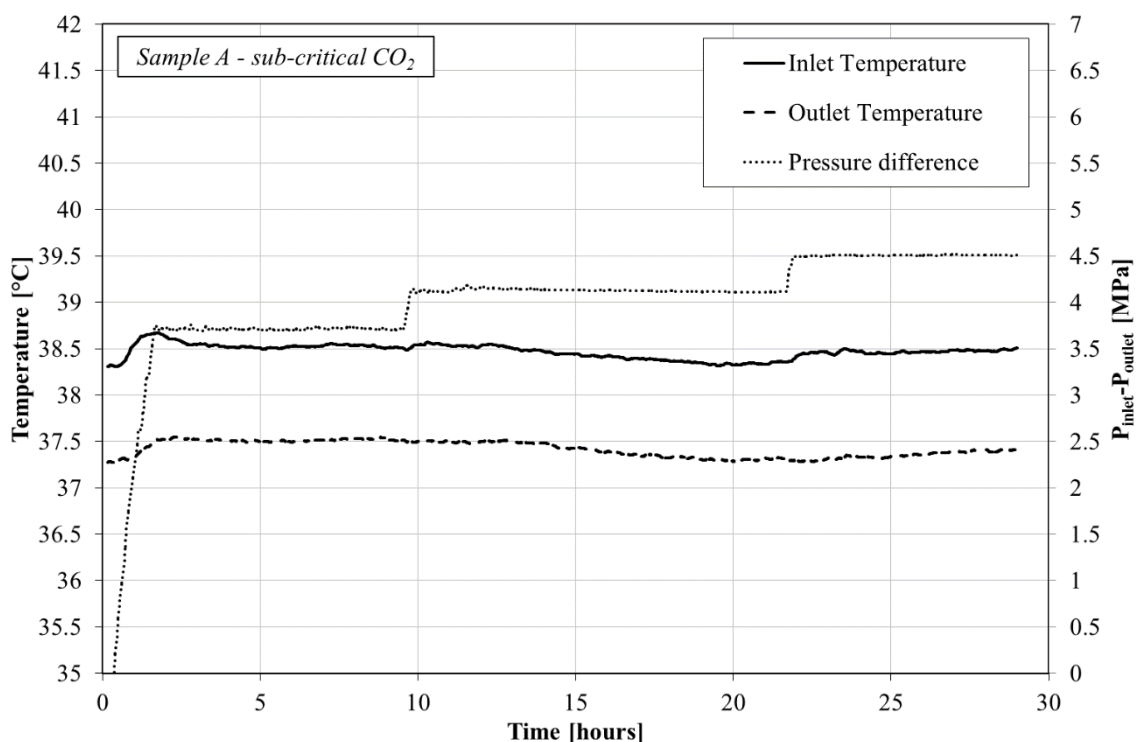


Fig. 7.23. Experimental temperature measured on sample A during subcritical carbon dioxide injection.

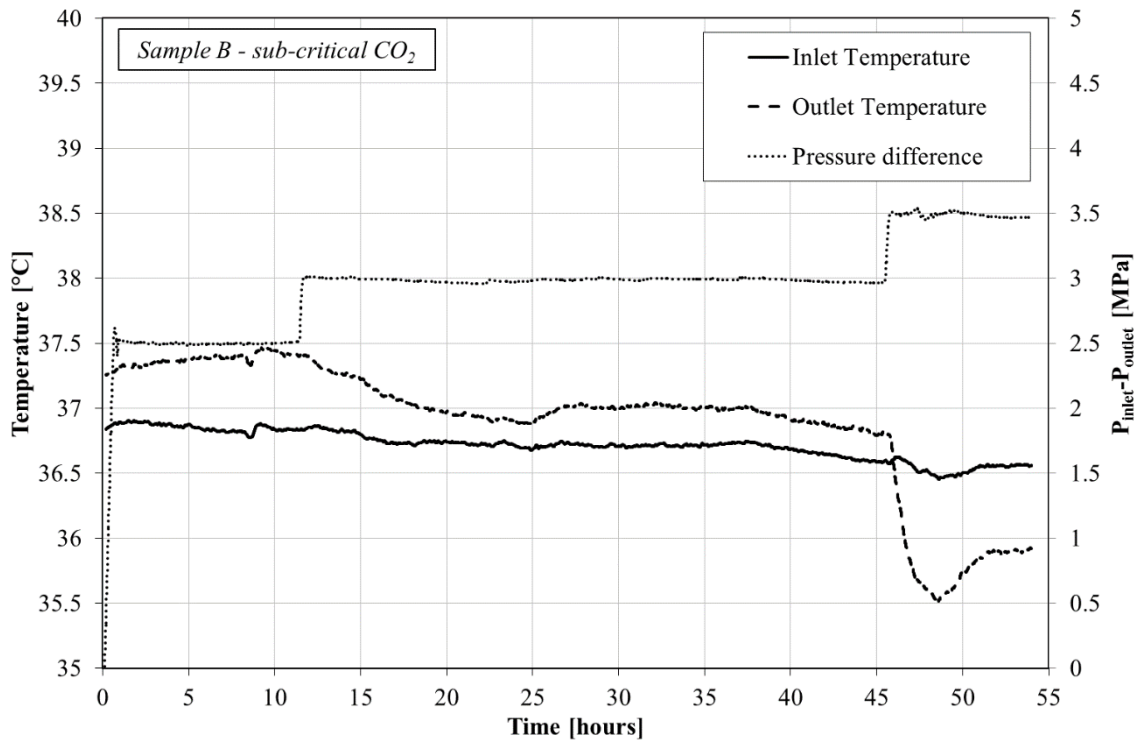


Fig. 7.24. Experimental temperature measured on sample B during subcritical carbon dioxide injection.

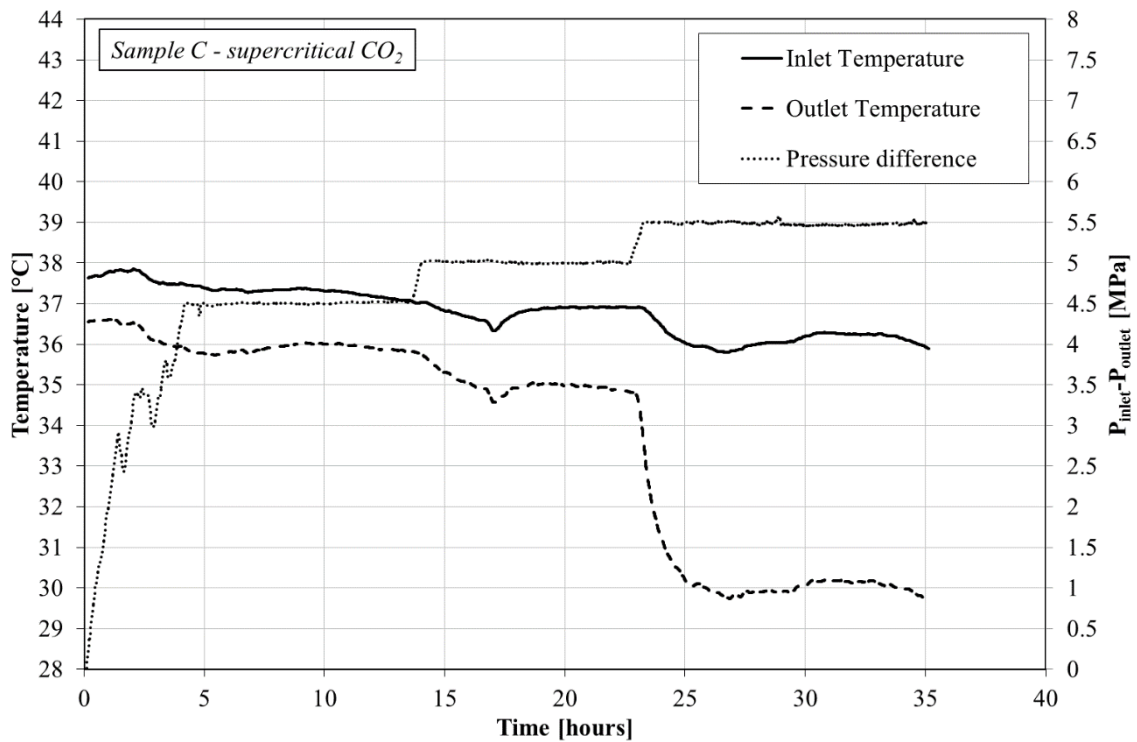


Fig. 7.25. Experimental temperature measured on sample C during supercritical carbon dioxide injection.

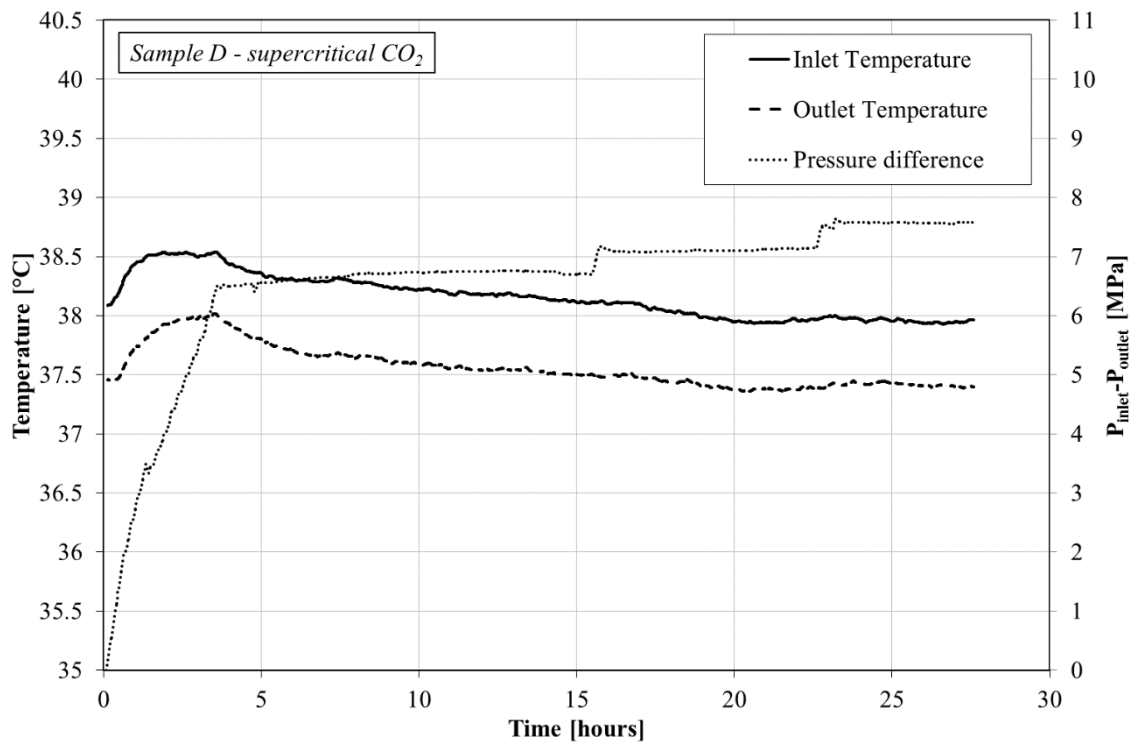


Fig. 7.26. Experimental temperature measured on sample D during supercritical carbon dioxide injection.

Constant inlet and outlet temperatures over the duration of the experiment on sample A were recorded. On the contrary, for a maximum pressure difference of 3.5 MPa, temperature drops of approximately 0.5°C and 1.5°C at the inlet and the outlet of the sample B were measured, respectively. When supercritical CO₂ was injected into sample C, observed temperature drops caused by pressure difference of 5.5 MPa were 1.8°C and 6.8°C at the inlet and outlet of the sample, respectively. However, for even higher pressure difference of 7.6 MPa, temperature drop of only 0.5°C both at the inlet and the outlet of the sample D was recorded.

There are two reasons for such distinctive behaviour between the samples. The first one is the established pressure gradient across the sample and the second one is the amount of gas flowing through the sample. As shown earlier, both samples A and D exhibited maximum flow rates of 2 g/h (Figures 7.10 and 7.15). Such small rates suggest that the porosity of the sample involved in flow for the given experimental conditions is relatively small. As a result, small porosity corresponds to high volumetric capacity of the system resulting in less cooling (Oldenburg, 2007; Singh et al., 2011). In other words, where there is a small amount of gas involved in flow, residual heat from the

reservoir (in this case confining oil and heating system) is enough to eliminate the effect of temperature drop induced by gas expansion.

In contrast to samples A and D, samples B and C experienced a measurable drop in temperature caused by CO₂ injection. Inspection of flow rates (Figures 7.11 and 7.14) reveals maximum values of approximately 140 g/h. Such high flow rates, under an established pressure gradient across the samples, induced temperature changes. As mentioned in the literature review, near-critical CO₂ was shown to undergo a cooling of between 5-10°C for a pressure difference of 1 MPa (e.g. Kazemifar and Kyritsis, 2014; Linstrom and Mallard, 2016). However, in this work, a maximum temperature drop of 6.8°C close to the outlet of the sample C was registered under a pressure difference of 5.5 MPa.

The difference between the temperature that would be expected based on Joule-Thomson coefficients reported in the literature and the temperature recorded in this work could be related to the position of the thermocouples which have been placed on the silicon sleeve, as shown in Chapter 4. This implies that temperature drop within the samples itself could be even higher which could not be registered due to the difference in thermal properties of the sleeve, PTFE tape and the coal. In particular, thermal conductivity of anthracite coal was found to be low, i.e. 0.2-0.4 W.m⁻¹.K⁻¹ (Zhu et al., 2011; Liu et al., 2015). Moreover, residual heat provided by the coal grains and the confining oil serves to diminish the cooling effect as time goes on (Oldenburg, 2007).

The connection between sorption related aspects such as permeability change induced by swelling and temperature has been previously extensively studied, as already presented in Chapter 2. To restate, sorption capacity of high rank coals increases with a decrease in temperature (e.g. Krooss et al., 2002; Sakurovs et al., 2008; Battistutta et al., 2010; Li et al., 2010, Pini et al., 2010). As a result, the magnitude of a sorption-induced matrix swelling at lower temperatures is larger than at higher temperatures (Baran et al., 2015). In addition, the coefficient of thermal expansion of coal of 1.87x10⁻⁵K⁻¹, determined within the temperature range from 293K (20°C) to 313 K (40°C), suggests that coal matrix shrinks upon cooling (Liu et al., 2015).

Hence, combined effects of thermal contraction and increased sorption upon temperature drop could contribute to the deformation and transport properties of coal. In

particular, while the former would enhance the flow rate by contracting the coal matrix and widening the flow paths in turn, the latter would further increase the recorded radial and axial strain through enhanced swelling due to increased CO₂ sorption. Meng et al. (2015) have shown that coal permeability to He decreases with the increase in temperature due to thermal expansion of coal matrix.

In relation to the increased sorption during temperature reduction, elastic modulus of coals could be reduced even further allowing easier deformation of coal under applied stresses. In addition, thermal stresses induced by rapid cooling could induce new fractures and connect the existing ones increasing the void volume responsible for gas flow. Such coupled phenomenon could explain observations made particularly for samples B and C where in the last injection step, both flow rates and expansion of the sample experienced sudden increase. Further assessment on the impact of swelling on flow behaviour of coal will be conducted in the following section.

Through analyses based on numerical modelling and analytical solutions, Oldenburg (2007) and Mathias et al. (2010) have concluded that Joule-Thomson cooling occurs in constant rate injection scenarios where the initial permeability of the system is low. In that case, low permeability would increase the pressure gradient in the reservoir enhancing the effect of Joule-Thomson cooling. This is in agreement with the observations made in this work where coals B and C having almost identical flow rates at the end of the experiment (140 g/h) but different pressure gradients across the samples yielded different downstream temperature drops, i.e. 1.5°C and 6.8°C, respectively.

On the other hand, where less CO₂ mass enters the less permeable layer within a real field reservoir, negligible temperature drop can be expected associated with stronger thermal supplement from the reservoir (Li et al., 2014). In accordance with such statement, samples A and D having small flow rates (2 g/h) exhibited almost negligible change in temperature despite experiencing a substantial pressure drop across the length of the samples.

The results reported above are of importance for future research on carbon dioxide storage in coals. Temperature discrepancy between the injected fluid and the coal seams can change the physical, chemical and thermal state of the subsurface formation and

break the pre-existing equilibrium conditions (Qu et al., 2012). Hence, further understanding of the processes related to the Joule-Thomson cooling which include increased sorption of CO₂, formation of CO₂ and CH₄ hydrates, freezing of residual water in the rock system and generation of thermal stresses that could fracture the formation is required. It can be expected that all these effects would affect the injectivity and the stability of the system.

7.4. Flow of CO₂ and the Induced Volumetric Swelling of Coal

All four samples by the end of the experiments have shown both radial and axial expansion induced by CO₂ sorption. To further understand how swelling affects the behaviour of samples, the evolution of volumetric strains and flow rates over the time duration of the experiments is further analysed. The procedure used for calculation of volumetric strains based on measured values of radial and axial strains shown earlier was presented in Chapter 4. Both the results of flow rates and volumetric strains obtained for samples A, B, C and D are presented as a function of time in Figures 7.27, 7.28, 7.29 and 7.30, respectively.

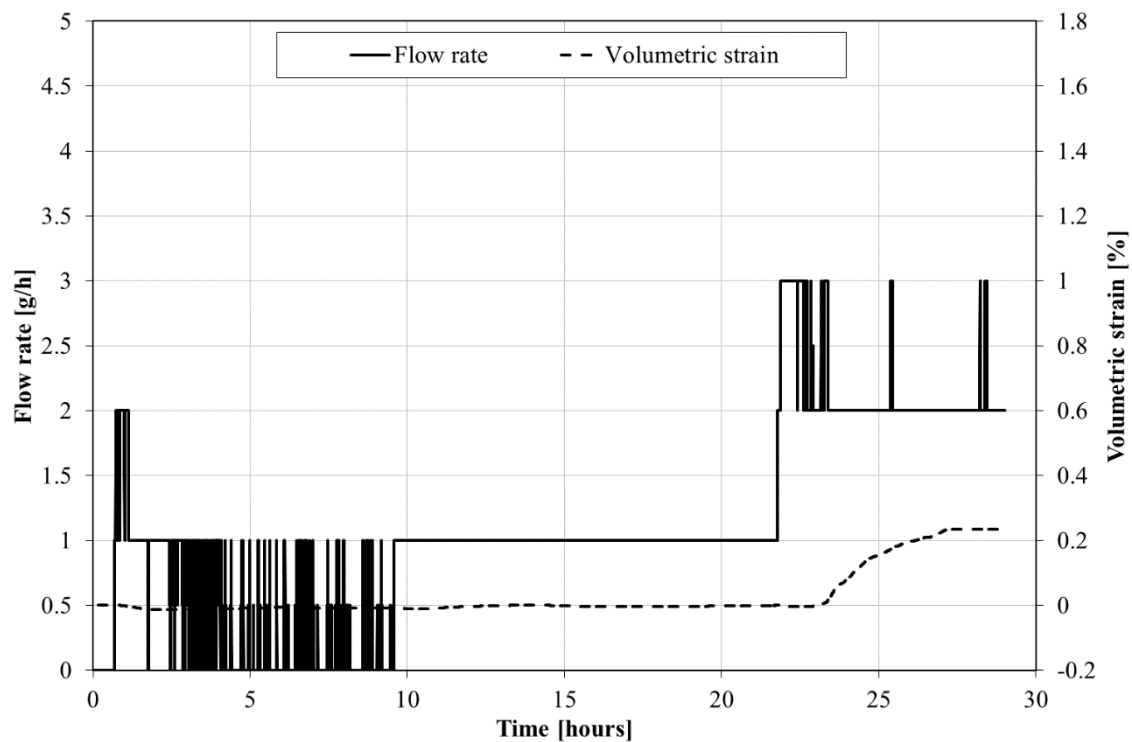


Fig. 7.27. Flow rate and volumetric strain time series for subcritical CO₂ injection in sample A.

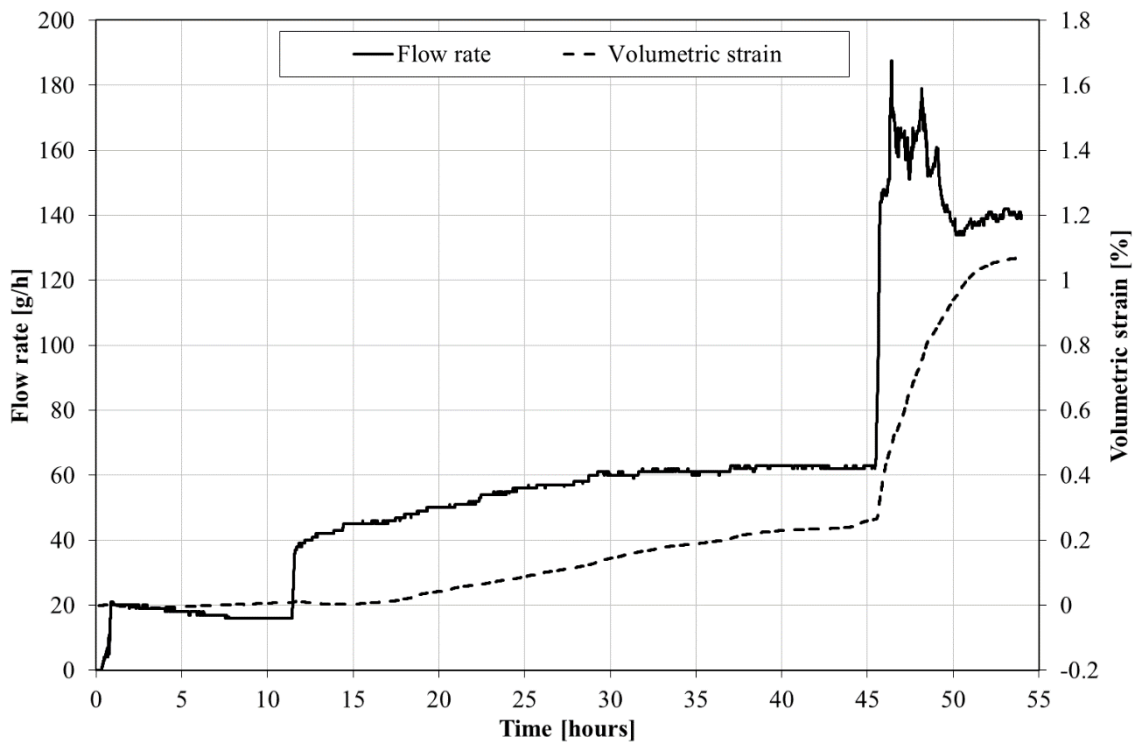


Fig. 7.28. Flow rate and volumetric strain time series for subcritical CO₂ injection in sample B.

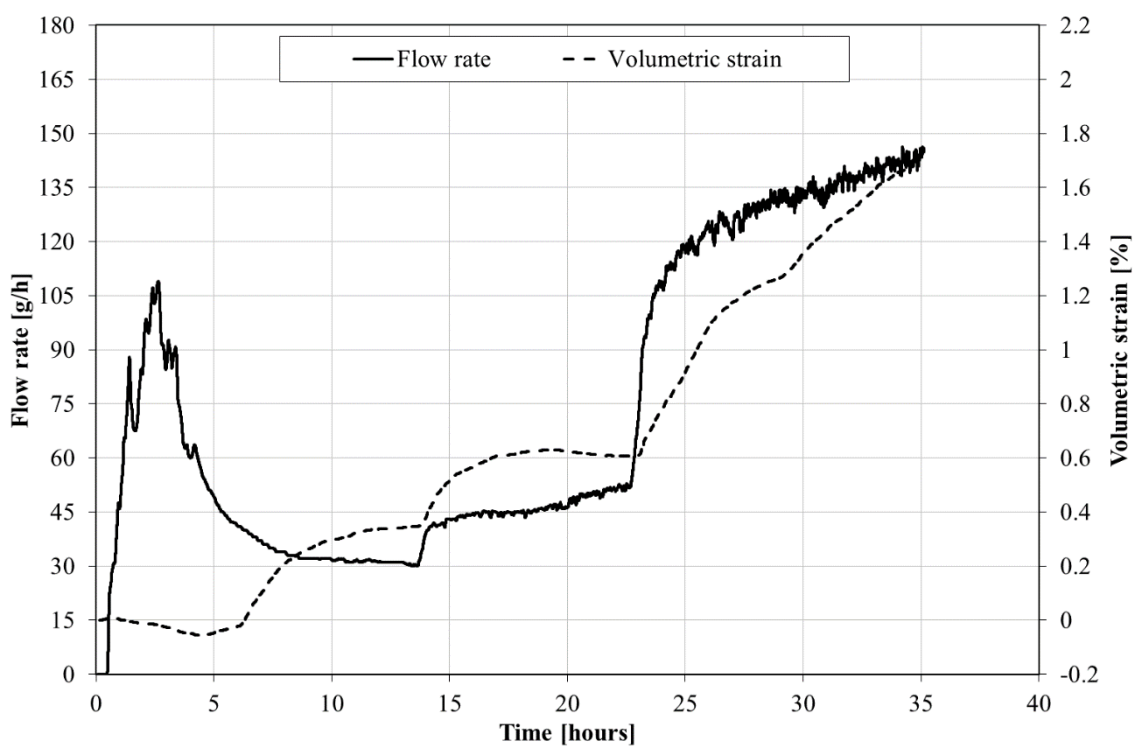


Fig. 7.29. Flow rate and volumetric strain time series for supercritical CO₂ injection in sample C.

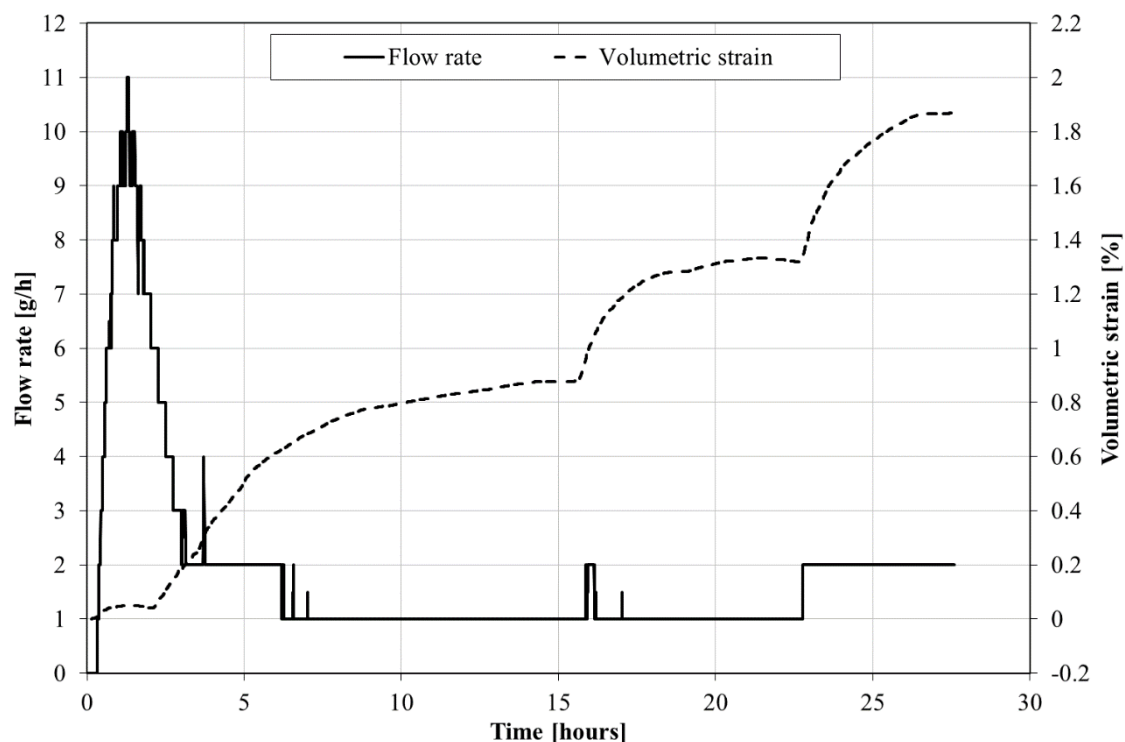


Fig. 7.30. Flow rate and volumetric strain time series for supercritical CO_2 injection in sample D.

All coals show an initial increase followed by a decrease in flow rates in the first injection step and then recovery in the subsequent steps, as mentioned earlier. However, the recovery in flow rates in Samples B and C was more significant than in Samples A and D which was clearly observable during the last injection step when the injection pressure was increased to 4.6 MPa and 8.1 MPa, respectively. If the results of temperature changes induced by CO_2 flow presented in previous section are recalled (see Fig. 7.24 and 7.25), it can be inferred that the sudden recovery in flow rates occurred simultaneously with the temperature drop.

Moreover, if the flow rates are compared with the evolution of volumetric strains, an interesting observation can be made. During the reduction in flow rates in the first injection step for all samples, there was a negligible change in the measured external volumetric strain. This would suggest that the reduction of the flow rates was induced by closure of existing flow paths due to the internal swelling of the coal matrix.

Furthermore, time evolutions of volumetric strain of samples A and B are different than samples C and B. While samples tested with low pressure CO_2 show substantial

expansion only by the end of the experiment, samples tested with high pressure CO₂ show expansion at very early stages of the experiment.

If maximum volumetric strain values between the samples are compared, it can be seen that samples A, B, C and D swelled by 0.22%, 1.07%, 1.73% and 1.88%, respectively. Bearing in mind that maximum mean CO₂ pressures in the respective samples by the end of third injection step were 2.35 MPa, 2.85 MPa, 5.35 MPa and 4.35 MPa (see Table 4.10), it can be inferred that there is a non-linear connection between maximum recorded volumetric strains and maximum mean CO₂ pressure. While volumetric strains registered at high pressures of samples C and D are comparable, volumetric strain of sample A is five times lower than of sample B.

Because the time duration of the experiments and maximum calculated volumetric strain values were different for each sample, both experimental times and volumetric strains were normalized with respect to the maximum recorded values for all samples. The calculated values are presented as a percentage in Figure 7.31 to further assess the swelling pattern among the samples.

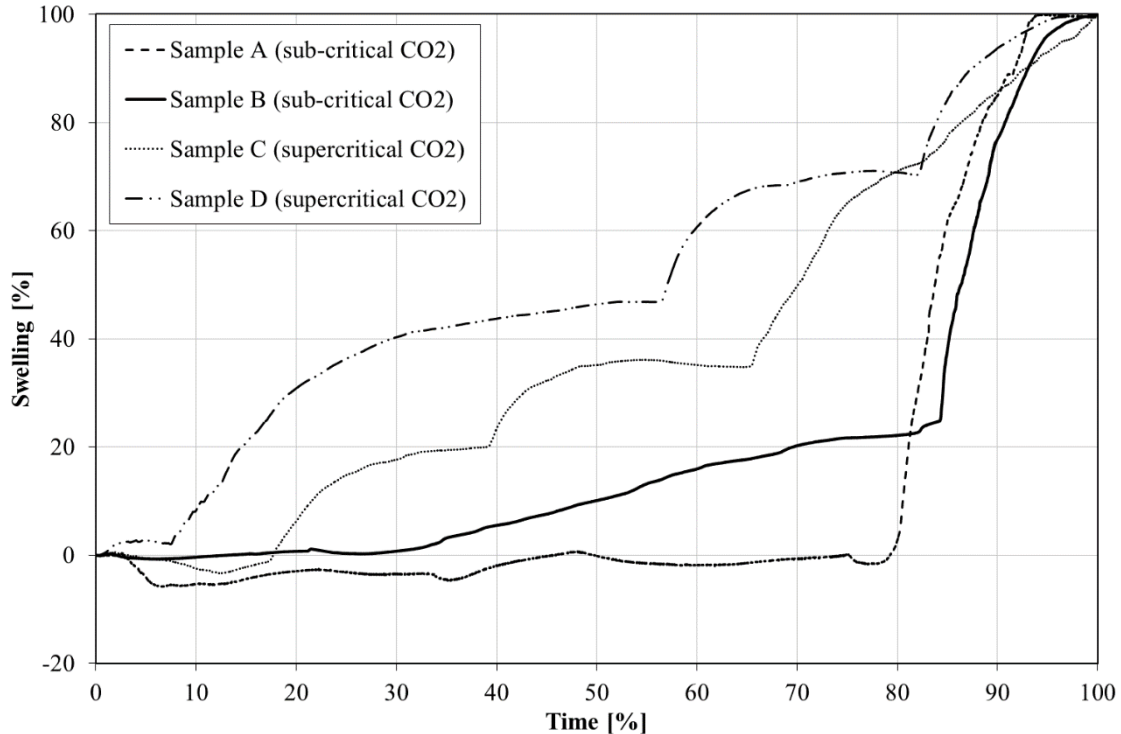


Fig. 7.31. Normalized volumetric strains versus the normalized experimental times for all specimens during carbon dioxide injections.

For injection of subcritical carbon dioxide, both samples (A and B) show that up to 80% of the experimental time, recorded swelling was relatively low. In particular, sample B exhibited approximately 22% of its maximum swelling strain while sample A showed negligible expansion. Since maximum mean gas pressure used within that time for sample A was 2.15 MPa and for sample B was 2.6 MPa, it can be concluded that for such values of CO₂ pressure, swelling predominantly occurs locally, i.e. internally. After that, in the remaining 20% of the experimental time, both samples experienced significant global volumetric swelling.

Coal samples flooded with supercritical CO₂ showed different behaviour. Negligible global expansion was recorded within 18% and 8% of the total experimental time for samples C and D, respectively. During the remaining time of the experiment, both samples showed significant swelling as the injection pressure increased. Interestingly, by the end of the second step, sample C exhibited 37% of its maximum swelling strain while sample D exhibited 70%. This means that sample C experienced almost two thirds of its maximum swelling in the third injection step.

Results suggesting that at low mean gas pressures used in this study, i.e. up to 2.65 MPa, the internal swelling is a dominant process while at higher pressure global expansion of the samples occurs are in agreement with previous findings. Hol and Spiers (2012) reported a non-linear relationship between absolute sorption and global swelling strain at low values of sorption (0.5 mol/kg) attributing it to the internal accommodation of sorption-induced swelling at low pressures.

Reasons for the behaviour with regards to flow rate recovery and volumetric expansion described above could be related to the temperature drop induced by Joule-Thomson effect. As mentioned in the previous section and Chapter 2, temperature reduction increases the sorption capacity which could have enhanced the swelling for samples B and C.

Moreover, it can be inferred that higher mean gas pressure within sample C could have had a more detrimental effect on the structure of sample C than sample D. This is supported by the fact that sample C had a constant backpressure of 2.6 MPa while sample D had 0.6 MPa. This would then mean that over the length of the sample, assuming a linear pressure gradient at the end of the third injection step with 8.1 MPa of

injection pressure, there was more of CO_2 in supercritical state in sample C than in sample D. Supercritical CO_2 , due to its greater sorptive capacity compared to subcritical corresponds to greater matrix swelling contributing to coal mass strength reduction as previously mentioned.

The response of coal samples to CO_2 injection described above can be presented through a schematic concept presented in Figure 7.32.

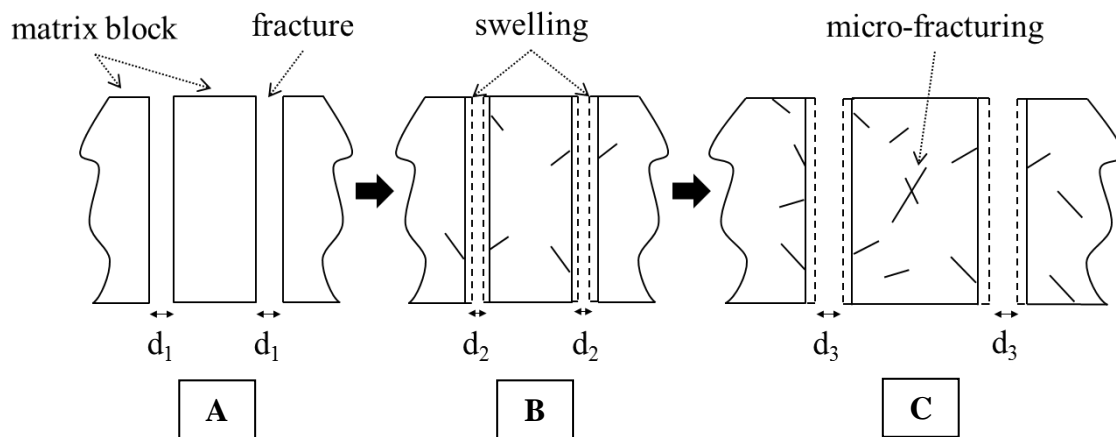


Fig. 7.32. Schematic concept of swelling behaviour; A) before CO_2 injection, B) during local swelling, C) during both local and global swelling.

Before CO_2 injection, fracture aperture is d_1 . As the CO_2 is being injected into the coal, sorption induced coal matrix swelling affects the flow rate by reducing the aperture of the fractures. In this process, small micro-fractures in the near-cleat region might appear. At the same time, increase in gas pressure within the system increases the fracture width. As a net result of these two competitive effects, fracture aperture changes to d_2 . During this process the coal structure is rigid enough, which is sufficient not to allow global expansion of the sample.

As the pressure in the system is further increased, internal swelling is approaching its maximum. During this process, coal structure becomes less rigid resulting in global expansion of the sample upon CO_2 sorption. Such global expansion can be further enhanced by a temperature drop in the system under high flow rates and established pressure gradient inducing increased sorption and swelling. During the global expansion of the sample, flow rate increases as a result of two combined effects. On one hand, the increase in injection pressure enhances the fracture dilatation. On the other hand,

potential micro-fracturing induced by matrix swelling could weaken the coal structure allowing easier compression of coal matrix blocks with an increase in gas pressure. It can be expected that if the coal matrix is more compressible, the loss in porosity and permeability upon swelling is less pronounced (Nikoosokhan et al., 2012). Additionally, if the sufficiently high flow of gas induces temperature drop within the coal sample, thermal contraction of the coal matrix and thermally induced stresses can also be expected. Hence, these combined effects yield a recovery and further enhancement of flow rate by changing the fracture aperture to d_3 . It should be noted that findings presented here support the theory for the swelling model developed in Chapter 3.

7.5. Reversibility of CO₂ Sorption and the Effect on Gas Flow

In order to assess the effect of CO₂ sorption and induced structural changes on absolute permeability measured by first He injection, all samples were tested by re-injecting He after the CO₂ injection under the same experimental conditions. Although the results on swelling reversal of coals are contradictory reporting both complete reversal and non-reversal, structurally induced changes are suggested to be permanent, as mentioned in Chapter 2. However, N₂ injection was found to partially reverse the swelling and enhances permeability (e.g. Fujioka et al, 2010).

Hence, the main objective of the experiments reported here is to examine the extent of which the CO₂ sorption affects the structural rearrangement and impacts the absolute permeability measured by He. As mentioned in Chapter 4, samples B and D were saturated with N₂ each for two days to investigate whether the flow rates measured during second injection of He can be enhanced and CO₂ induced swelling reversed. It should be noted that before third He injection, samples have been left to desorb from N₂ for at least 48 hours aided by applying the vacuum of -20 kPa.

The results of flow rates and volumetric strains obtained by first and second He injection in samples A, B, C and D are presented in Figures 7.33, 7.34, 7.35 and 7.36, respectively. In addition, Figures 7.34 and 7.36 contain experimental results obtained by third injection of He after N₂ saturation in samples B and D, respectively.

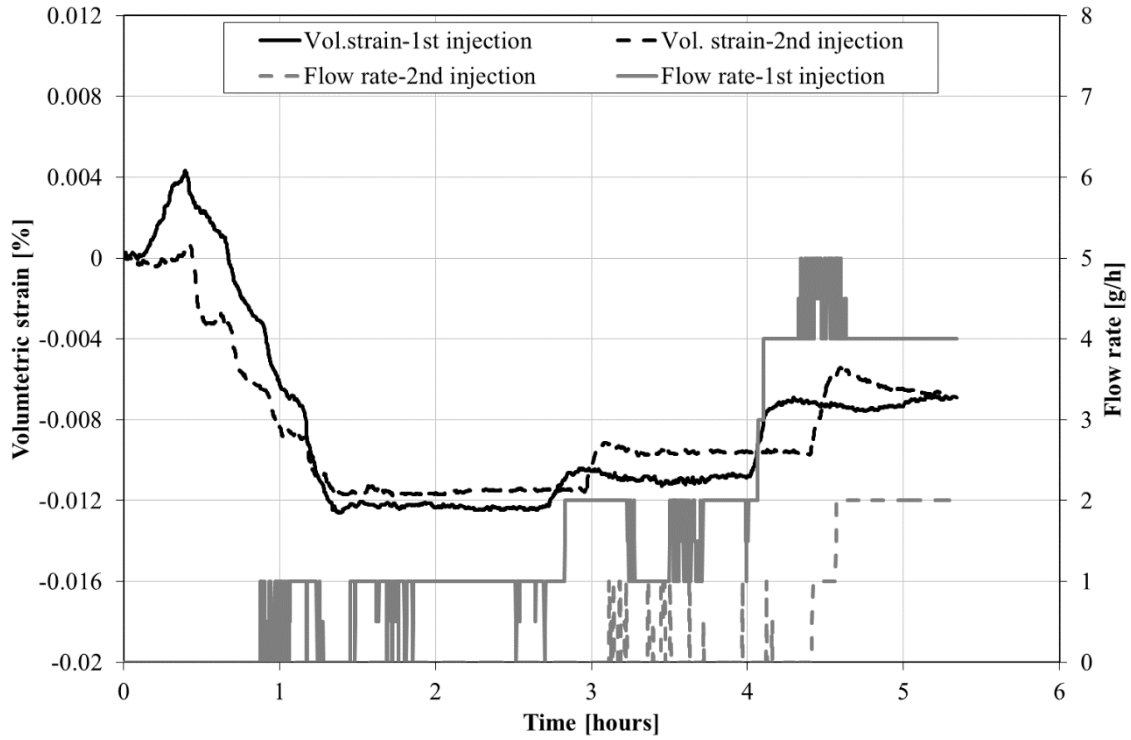


Fig. 7.33. Volumetric strain and flow rates measured during low pressure helium injections before (1st injection) and after (2nd injection) CO₂ saturation for sample A.

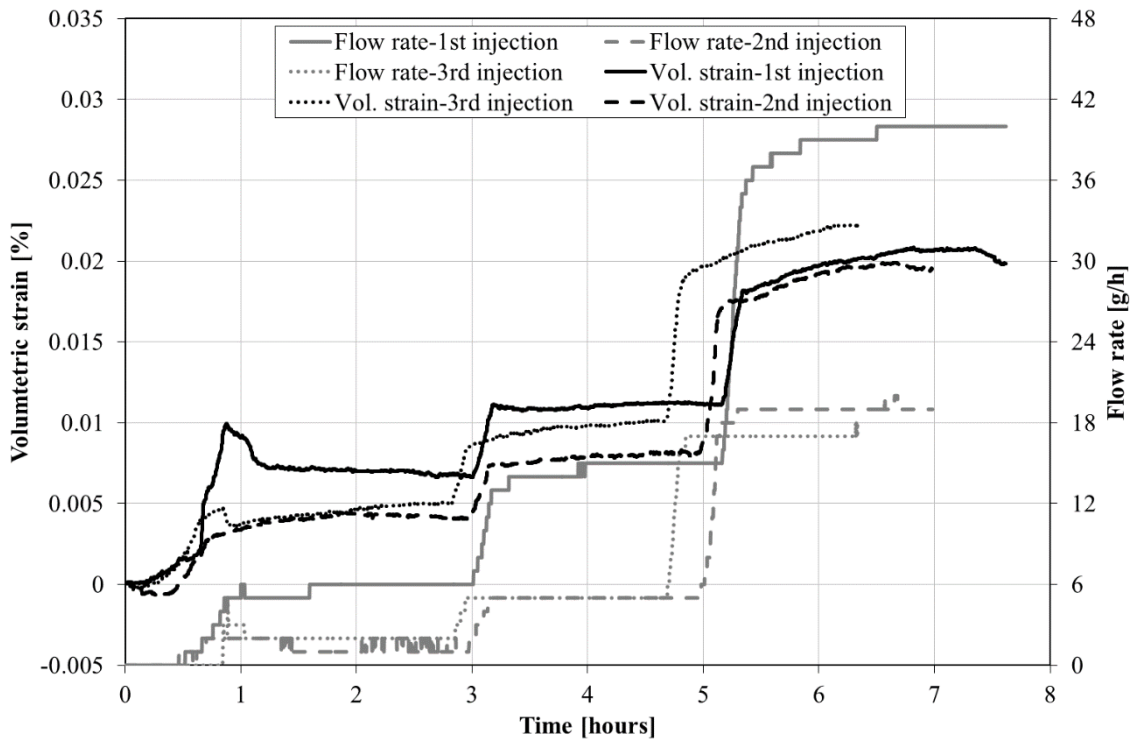


Fig. 7.34. Volumetric strain and flow rates measured during low pressure helium injections before (1st injection) and after (2nd injection) CO₂ saturation, and after N₂ saturation (3rd injection) for sample B.

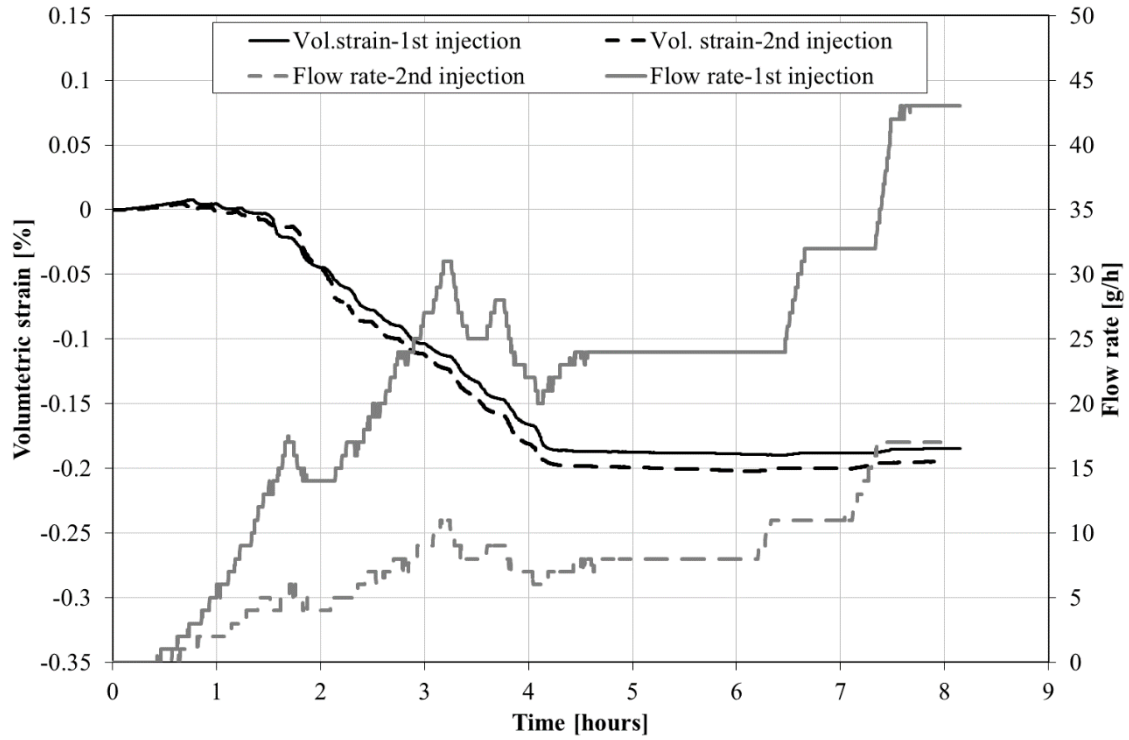


Fig. 7.35. Volumetric strain and flow rates measured during high pressure helium injections before (1st injection) and after (2nd injection) CO₂ saturation for sample C.

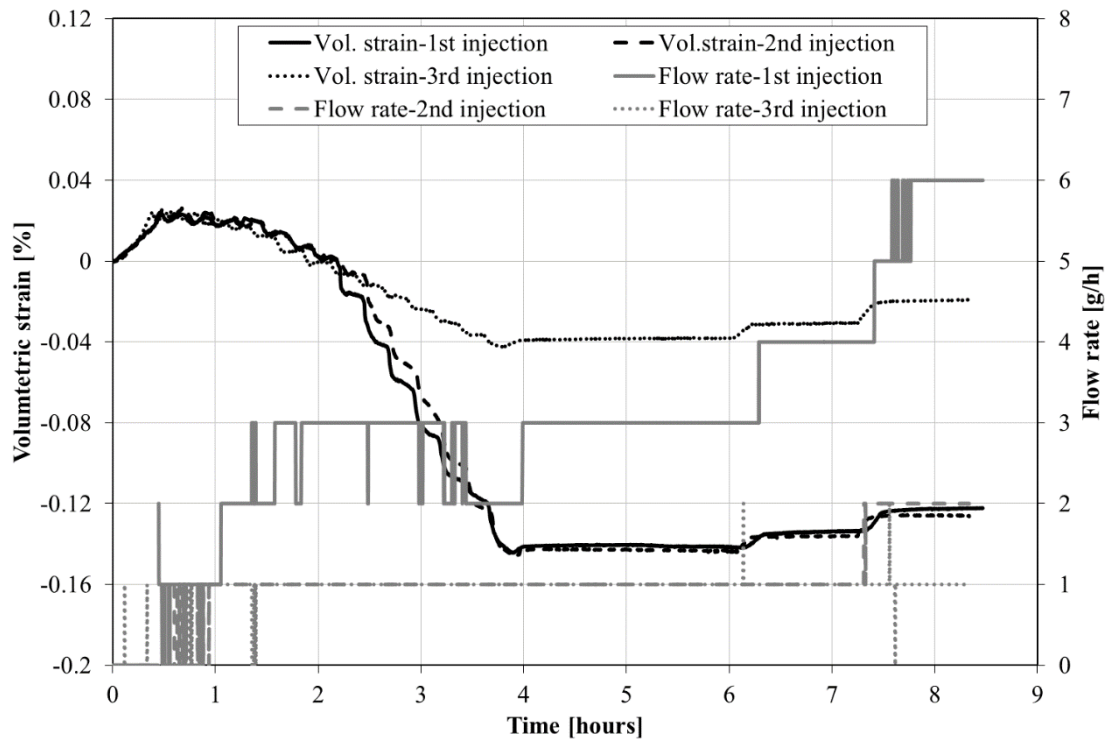


Fig. 7.36. Volumetric strain and flow rates measured during high pressure helium injections before (1st injection) and after (2nd injection) CO₂ saturation, and after N₂ saturation (3rd injection) for sample D.

Experimental results on flow rates measured at the second He injection of all samples show a decrease compared to the flow rates measured during the first He injection. In particular, flow rates of 2 g/h, 19 g/h, 17 g/h and 2 g/h were recorded at the end of second He injection for samples A, B, C and D, respectively. Consequently, for samples A and B, measured flow rates at the second He injection were 50 and 52% lower than in the first He injection, respectively. Reduction of up to 60% and 66% in flow rates was observed for samples C and D, respectively.

It should be mentioned that permeability evolution can be stress-history dependent producing different values of permeability with each successive cycle in highly fissured coals (Durucan and Edwards, 1986; Alexis et al., 2015). However, permeability response is mainly controlled by the magnitude of the applied stress rather than the number of applied load cycles (Wang et al., 2013). This suggests that for the same experimental conditions during sequential injection of gases in this study, repeated injections were not the primary cause for the difference in measured flow rates.

Parallel to flow rates, volumetric behaviour of coals during the first He injection and subsequent He re-injection have been recorded, as shown in Figures 7.33-7.36. Since CO₂ injection was found to reduce deformation parameters of coal, as shown in Chapter 6, it is reasonable to expect that lower values of elastic modulus would result in higher expansion of coal with second He injection. However, opposite to the expectation, results for all samples show that volumetric behaviour during the first and the second He injection followed a similar trend.

Based on the experimental results from the third He injection, i.e. after N₂ saturation (Figures 7.34 and 7.36), it can be observed that saturation of samples with N₂ did not cause any recovery in flow rates. Within the first two injection steps, the second and the third He flow rates were identical. A potential explanation for that could be because N₂ has a relatively larger kinetic diameter than CO₂ making it more difficult to permeate meso- and micro-pores easily accessible to CO₂ (Cui et al., 2004). Moreover, CO₂ is also preferentially adsorbed due to its higher sorption affinity into smaller pores than N₂ (Cui et al., 2004).

Regarding the volumetric expansion measured during the third He injection sequence, volumetric response of sample B showed good agreement with previous He injections

while sample D experienced less global expansion in comparison to the first two He injection sequences. Surprisingly, this reduction in observed expansion did not have any effect on measured flow rates which are in close agreement with the flow rates obtained in the second helium injection.

7.6. Conclusions

This chapter presented experimental results obtained during injection of He and CO₂ in four Black Diamond coal samples under confined conditions. Firstly, experimental data for low and high pressure He injections were presented and discussed. It was shown that all recorded pressure values were stable throughout the duration of experiments providing reliable data for permeability calculations and analyses. Results showed that He flow rates increase with a positive change in injection pressure under constant confining pressure for all samples with sample expansion predominantly in axial direction. Based on measured experimental data, permeability values were calculated using Darcy's law and presented as a function of effective stress. It was found that absolute permeability to He measured on all samples range between $5 \times 10^{-16} \text{ m}^2$ to $1 \times 10^{-17} \text{ m}^2$ for effective stress conditions ranging from 2.25-6.25 MPa. The presented values were then fitted with an exponential function. Relationships obtained suggested that samples tested under low stress conditions are more compressible than samples tested under high stress conditions.

Following the He injection results, data obtained during subcritical and supercritical CO₂ injection were shown. Measured flow rates in all samples showed an increase followed by a decline during the initial injection of CO₂. This was attributed to the coal matrix swelling and its effect on the reduction of porosity available for gas flow. As the pressure further increased, flow rates recovered showing an ascending trend with an increase in injection pressure.

Coal deformation was found to be more than one order of magnitude higher in case of CO₂ injection than in case of He injection. During CO₂ injection, coal samples were expanding both in radial and axial directions. In particular, radial strain was found to be 2.2 times and more than 4 times larger than the axial strain during subcritical and

supercritical CO₂ injections, respectively. Calculated permeability values of all samples vary between $1 \times 10^{-16} \text{ m}^2$ and $2 \times 10^{-19} \text{ m}^2$ for effective stress conditions of 2.25-6.4 MPa.

Temperatures at the inlet and the outlet of the samples both for He and CO₂ injections were then presented and discussed. He injection for all samples occurred at constant temperature conditions, while CO₂ injection in two samples showed different behaviour. Presented data show that, when there is an established pressure gradient in the sample with a sufficiently high flow rate of CO₂, temperature drop associated with Joule-Thomson cooling effect is observed. Taking into account coal's sorption dependence on temperature, possibility of thermally induced stresses within the coal as well as its thermal expansion/shrinkage, it was suggested that such temperature drop could contribute to the response of coal seams during carbon dioxide injection and should be taken into account in further research in relation to carbon dioxide sequestration in coals. To the author's knowledge, this is the first time that the temperature drop associated with the Joule-Thomson cooling effect during CO₂ injection was experimentally measured across the coal sample.

Volumetric expansion of the coal associated with CO₂ sorption and its impact on measured flow rates was investigated. Results revealed that the majority of swelling under low gas pressures (< 2.65 MPa in this case) occurred locally with a sudden global expansion of coal samples upon approaching maximum internal swelling, i.e. at high pressure injection. Such transition in swelling behaviour was explained through a schematic concept taking into account the role of fracture network and changes in injection pressure accompanied by coal weakening induced by CO₂ sorption. Measured flow rates were found to decrease during the internal swelling induced by fracture closure and then rebound with a positive change in injection pressure. Such recovery was found to be more pronounced in coals experiencing temperature reduction induced by CO₂ expansion and related adiabatic cooling effect.

Changes induced by volumetric swelling of coal due to CO₂ sorption were found to be irreversible and detrimental on absolute permeability of coal measured by He. Re-injection of He, after treating the samples with CO₂, resulted in approximately 50-66% lower flow rates compared to the injection of He before CO₂ injection. Despite reported findings in the literature of N₂ effect on swelling reversal, it was found in this work that

saturation of anthracite samples with N₂ did not induce flow rate recovery, i.e. He flow rates before and after N₂ saturation were comparable.

The results obtained from this experimental programme provide a detailed insight into the behaviour of coal under injection of non-sorbing (He) and sorbing (CO₂) gases. In addition, the high resolution data obtained provide a unique benchmark to validate numerical models in this field. The validation of the numerical model, presented in Chapter 3, will be conducted in Chapter 8 using the experimental data shown here for sample A.

7.7. References

- Baran, P., Zarębska, K. and Bukowska, M. 2015. Expansion of Hard Coal Accompanying the Sorption of Methane and Carbon Dioxide in Isothermal and Non-isothermal Processes. *Energy & Fuels*, 29(3), pp. 1899-1904.
- Battistutta, E., van Hemert, P., Lutynski, M., Bruining, H. and Wolf, K.H. 2010. Swelling and sorption experiments on methane, nitrogen and carbon dioxide on dry Selar Cornish coal. *International Journal of Coal Geology*, 84(1), pp. 39-48.
- Cui, X., Bustin, R.M. and Dipple, G. 2004. Selective transport of CO₂, CH₄, and N₂ in coals: insights from modeling of experimental gas adsorption data. *Fuel*, 83, pp. 293-303.
- Durucan, S. and Edwards, J.S. 1986. The effects of stress and fracturing on permeability of coal. *Mining Science and Technology*, 3, pp. 205-216.
- Espinoza, D.N., Vandamme, M., Pereira, J.-M., Dangla, P. and Vidal-Gilbert, S. 2014. Measurement and modeling of adsorptive-poromechanical properties of bituminous coal cores exposed to CO₂: Adsorption, swelling strains, swelling stresses and impact on fracture permeability. *International Journal of Coal Geology*, 134-135, pp. 80-95.
- Fujioka, M., Yamaguchi, S. and Nako, M. 2010. CO₂-ECBM field tests in the Ishikari Coal Basin of Japan. *International Journal of Coal Geology*, 82(3-4), pp. 287-298.
- Harpalani, S. and McPherson, M.J. 1985. Effect of stress on permeability of coal. *Quarterly Review of Methane from Coal Seams Technology*, 3, pp. 23-28.
- Hol, S. and Spiers, C.J. 2012. Competition between adsorption-induced swelling and elastic compression of coal at CO₂ pressures up to 100 MPa. *Journal of the Mechanics and Physics of Solids*, 60(11), pp. 1862-1882.
- Hol, S., Gensterblum, Y. and Massarotto, P. 2014. Sorption and changes in bulk modulus of coal – experimental evidence and governing mechanisms for CBM and ECBM applications. *International Journal of Coal Geology*, 128-129, pp. 119-133.

- Kazemifar, F. and Kyritsis, D. 2014. Experimental investigation of near-critical CO₂ tube-flow and Joule-Thomson throttling for carbon capture and sequestration. *Experimental Thermal and Fluid Science*, 53, pp. 161-170.
- Krooss, B.M., van Bergen, F., Gensterblum, Y., Siemons, N., Pagnier, H.J.M. and David, P. 2002. High-pressure methane and carbon dioxide adsorption on dry and moisture-equilibrated Pennsylvanian coals. *International Journal of Coal Geology*, 51(2), pp. 69-92.
- Li, D., Liu, Q., Weniger, P., Gensterblum, Y., Busch, A. and Krooss, B.M. 2010. High-pressure sorption isotherms and sorption kinetics of CH₄ and CO₂ on coals. *Fuel*, 89(3), pp. 569-580.
- Li, X., Xu, R. and Jiang, P. 2014. Modelling and Interpretation of a Temperature Drop in the Wellbore in Ordos CO₂ Storage Project, China. *Energy Procedia*, 63, pp. 6413-6419.
- Liu, J., Elsworth, D. and Brady, B.H. 1999. Linking stress-dependent effective porosity and hydraulic conductivity fields to RMR. *International Journal of Rock Mechanics and Mining Sciences*, 36, pp. 581-596.
- Liu, Z., Feng, Z., Zhang, Q., Zhao, D. and Guo, H. 2015. Heat and deformation effects on coal during adsorption and desorption of carbon dioxide. *Journal of Natural Gas Science and Engineering*, 25, pp. 242-252.
- Mathias, S.A., Gluyas, J.G., Oldenburg, C.M. and Tsang, C.-F. 2010. Analytical solution for Joule-Thomson cooling during CO₂ geo-sequestration in depleted oil and gas reservoirs. *International Journal of Greenhouse Gas Control*, 4(5), pp. 806-810.
- Meng, Y., Li, Y. and Lai, F. 2015. Experimental study on porosity and permeability of anthracite coal under different stresses. *Journal of Petroleum Science and Engineering*, 133, pp. 810-817.
- Nikoosokhan, S., Vandamme, M. and Dangla, P. 2012. A Poromechanical Model for Coal Seams Injected with Carbon Dioxide: From an Isotherm of Adsorption to a Swelling of the Reservoir. *Oil & Gas Science and Technology*, 67(5), pp. 777-786.
- Oldenburg, C.M. 2007. Joule-Thomson cooling due to CO₂ injection into natural gas reservoirs. *Energy Conversion and Management*, 48(6), pp. 1808-1815.
- Pini, R., Ottiger, S., Burlini, L., Storti, G. and Mazzotti, M. 2010. Sorption of carbon dioxide, methane and nitrogen in dry coals at high pressures and moderate temperatures. *International Journal of Greenhouse Gas Control*, 4, pp. 90-101.
- Qu, H., Liu, J., Chen, Z., Wang, J., Pan, Z., Connell, L. and Elsworth, D. 2012. Complex evolution of coal permeability during CO₂ injection under variable temperatures. *International Journal of Greenhouse Gas Control*, 9, pp. 281-293.
- Sakurovs, R., Day, S., Weir, S. and Duffy, G. 2008. Temperature dependence of sorption of gases by coals and charcoals. *International Journal of Coal Geology*, 73(3-4), pp. 250-258.
- Singh, A.K., Goerke, U.-J. and Kolditz, O. 2011. Numerical simulation of non-isothermal compositional gas flow: Application to carbon dioxide injection into gas reservoirs. *Energy*, 36(5), pp. 3446-3458.

Somerton, W.H., Söylemezoglu, I.M. and Dudley, R.C. 1975. Effect of Stress on Permeability of Coal, *International Journal of Rock Mechanics and Mining Sciences and Geomechanics Abstracts*, 12(5), pp. 129-145. Pergamon.

Wang, S., Elsworth, D., Liu, J. 2013. Permeability evolution during progressive deformation of intact coal and implications for instability in underground coal seams. *International Journal of Rock Mechanics & Mining Sciences*, 58, pp. 34-45.

Zhu, W.C., Wei, C.H, Liu, J., Qu, H.Y. and Elsworth, D. 2011. A model of coal-gas interaction under variable temperatures. *International Journal of Coal Geology*, 86(2-3), pp. 213-221.

8

Model Verification and Validation

8.1. Introduction

This chapter describes the verification and validation of the model. The aim of the verification exercises is to ensure that the governing differential equations are correctly solved by the numerical model. The validation tests are applied to confirm the ability of the proposed model to correctly reflect the material behaviour and various physical mechanisms involved.

Based upon the availability of required information, the model is compared against analytical solutions and in case of unavailability of information about analytical solutions, simple verification methods involving well-known models developed for certain conditions are used to verify the developed model. Validation of the developed model includes comparisons of numerical results with experimental data, previously presented in Chapter 7, related to helium and carbon dioxide injection in coal core. Such exercises present a crucial step before application of the model for predictive purposes.

The work presented in Section 8.2 deals with the verification tests. Section 8.2.1 describes the steady state gas concentration profile induced by gas injection and abstraction in a single porosity medium. The subset of the numerical formulation dealing with the elastic deformation behaviour of a single porosity medium subject to the compressive stress, the injection of a non-sorbing gas and the injection of a sorbing gas is addressed in Sections 8.2.2, 8.2.3 and 8.2.4, respectively. In addition, Sections 8.2.3 and 8.2.4 evaluate the implementation of the permeability-porosity relationship. Conclusions reached on the completion of the verification exercises are discussed in Section 8.2.5.

The validation exercises, which include comparison of the results obtained using the numerical model and during the experiment, are presented in Section 8.3. To achieve this, experimental results shown in Chapter 7 for sample A are presented in Section 8.3.1 in terms of permeability change with time, both for helium and carbon dioxide injections. Material parameters and simulation conditions are presented in Section 8.3.2. Two injection scenarios are considered for dry, gas-saturated system. Firstly, non-sorbing gas (He) injection is conducted to analyse the permeability change purely due to the mechanical deformation of the sample induced by the change in gas pressure. Secondly, sorbing gas (CO₂) injection is performed to predict the permeability evolution

taking into account swelling phenomena of coal due to gas sorption, too. In Section 8.3.3, prediction of the permeability evolution by the numerical model is conducted and compared with the experimental data for an intact coal core. A discussion related to various physical and chemical mechanisms considered in the model is included. Conclusion to the validation exercises is presented in Section 8.3.4.

Overall conclusions to the complete verification and validation programme are presented in Section 8.4.

8.2. Verification Exercises

This section deals with the verification of the numerical model. At this point it should be noted that since the theoretical and numerical formulations for the coupled chemical and deformation behaviour of fractured rock presented in Chapter 3 have been implemented within an existing framework, major components of the model were previously examined, verified and validated for a number of tests. For the cases involving coupled moisture, air, heat and deformation, the numerical model was verified by King (1994) and Sansom (1995). Substantial development of the COMPASS model presented by Thomas and He (1995, 1997, 1998), Thomas et al. (1998) and Thomas and Cleall (1999) was further examined and verified by Mitchell (2002).

More recently, in relation to high pressure gas transport, the multicomponent gas module for ideal gases was verified by Masum (2012). Hosking (2014) conducted a series of exercises focused on verifying that particular components related to the real gas transport and sorption behaviour were correctly implemented in the model. This included comparisons against analytical solutions for pure diffusive and advective-diffusive gas transport as well as the comparison of simulation results with those presented in the literature for an alternative numerical model.

However, the author made changes to the numerical model, both in terms of structure and additional theoretical relationships. Therefore, it was considered necessary to repeat some exercises to check that the original structure of the numerical model was not affected and to present additional exercises to verify the validity of the new developments of the model.

The verification of the numerical model is conducted here by dividing the complete numerical model down into a number of subsets which are compared directly to either an analytical solution or an alternative model. Initial verification of the single phase flow of gas chemicals is addressed through comparison with an analytical solution. The elastic deformation is then verified both against an analytical solution and alternative models.

8.2.1. Steady State Advection-diffusion of Single-component Gas (Test I)

Gas is known to be a highly compressible fluid where its bulk density can vary greatly with pressure. This section presents an exercise related to the gas compressibility predicted by the numerical model during steady state advection and diffusion. Results of the numerical analysis are compared with the analytical solution presented by Wu et al. (1998) for the steady state, one dimensional mass balance equation for gas transport in a homogeneous single porosity medium.

8.2.1.1. Analytical Solution

The mass balance equation (3.26) presented in Chapter 3 is reduced to a non-deformable single porosity form in this exercise. In addition, the effects of geochemical reactions and gravity are neglected. Hence, the simplified mass balance based on equation (3.26) can then be expressed as:

$$\frac{\partial(nc_g)}{\partial t} = \nabla \left[\left(n\tau_g D_g + \frac{c_g K Z R T}{\mu_g} \right) \nabla c_g \right] \quad (8.1)$$

All symbols were previously defined in Chapter 3.

For a steady state gas flow, the left hand side of equation (8.1) becomes zero, producing:

$$\nabla \left[\left(n\tau_g D_g + \frac{c_g K Z R T}{\mu_g} \right) \nabla c_g \right] = 0 \quad (8.2)$$

Wu et al. (1998) presented an analytical steady state solution for one dimensional, linear and horizontal flow. The solution is adopted here, only expressed in terms of gas

concentrations instead of bulk gas pressure used in the original solution. The boundary conditions used by Wu et al. (1998), for an equation similar to the equation (8.2), are: at the inlet ($x=0$), a constant gas flux is imposed, and at the outlet ($x=L$), the gas pressure is kept constant. The analytical solution is then given as (Wu et al., 1998):

$$c_g(x) = \frac{1}{RT} \sqrt{u_{gL}^2 + \frac{2Q_g RT \mu_g (L_x - x)}{K}} \quad (8.3)$$

where u_{gL} is the pressure at the outlet boundary, Q_g is the total gas flux at the inlet boundary and L_x is the length of the domain.

Equation (8.3) is used to calculate the gas concentration profile at steady state and the results obtained will be compared with the results predicted by the numerical model.

8.2.1.2. Simulation Conditions

The system considered is a 1 m long domain with a 0.1 m height, discretised into 20 equally-sized 4-noded quadrilateral elements. A summary of the initial and boundary conditions used is presented in Figure 8.1.

Inlet boundary conditions	Initial conditions	Outlet boundary conditions
$Q_g = 1 \times 10^{-3} \text{ mol m}^{-2} \text{ s}^{-1}$	$c_g = 39.31 \text{ mol m}^{-3}$	$RTc_g = 101325 \text{ Pa}$

Fig. 8.1. Schematic of the initial and boundary conditions used in Test I.

The domain is initially saturated with CO_2 at atmospheric conditions. At the inlet and the outlet boundaries, a constant CO_2 flux equal to $1 \times 10^{-3} \text{ mol m}^{-2} \text{ s}^{-1}$ and a fixed atmospheric pressure of 101 325 Pa are prescribed, respectively.

In this exercise, it was assumed that the gas behaves as an ideal gas, i.e. the compressibility factor was set to 1.0. The simulation was conducted under isothermal conditions with a constant temperature of 310K. A summary of material parameters used in this verification exercise is given in Table 8.1.

Table 8.1. Input material and initial parameters used in Test I.

Material and initial parameters	Value
Temperature, T (K)	310
Porosity, n (-)	0.1
Permeability, K (m^2)	1.0×10^{-15}
Gas dynamic viscosity, μ (Pa s)	1.84×10^{-5}
Free diffusion coefficient, D_g ($\text{m}^2 \text{s}^{-1}$)	5.0×10^{-5}
Tortuosity (Millington and Quirk, 1961), τ_g (m^2)	$n^{10/3}/n^2$

8.2.1.3. Results

The concentration of CO_2 in the domain when CO_2 reaches the steady state condition is presented in Figure 8.2. Non-linear steady state profiles, as a result of both the numerical model and the analytical solution, can be observed. Such non-linear behaviour is related to the dependence of gas density on gas concentration, i.e. gas pressure. Results of the numerical simulation and the analytical solution show excellent agreement. It may therefore be concluded that the advective-diffusive flow mechanism produces the expected behaviour for a single component gas transport.

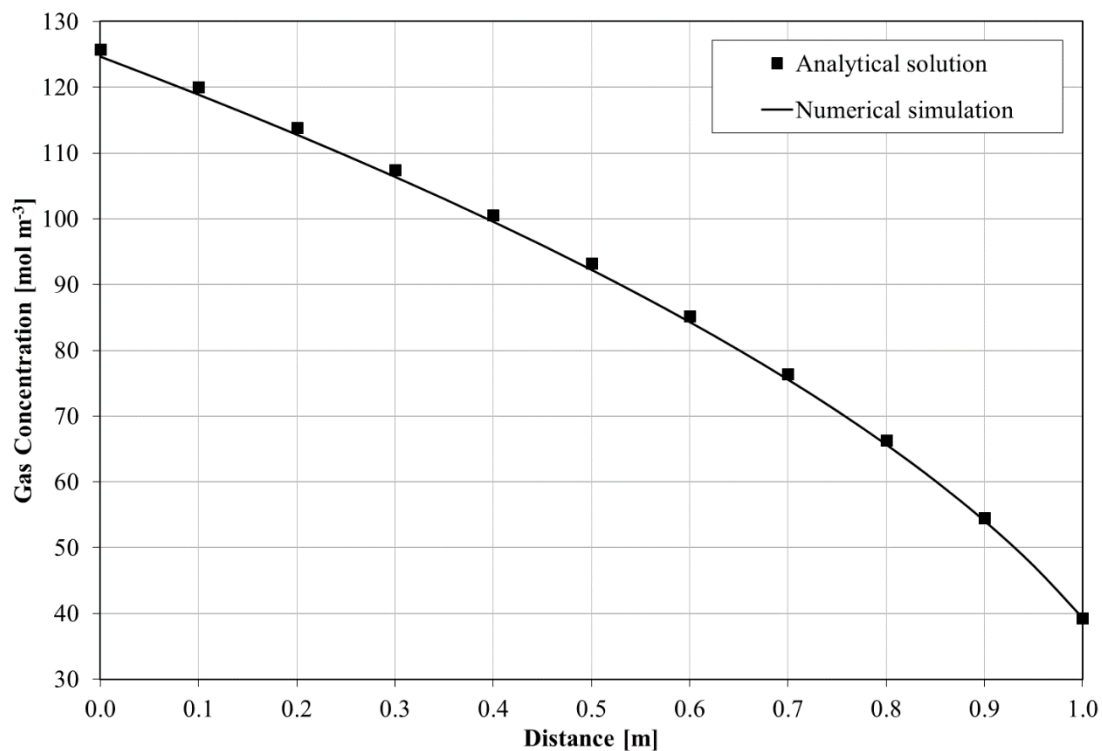


Fig. 8.2. Steady state profile of CO_2 in the domain obtained using the numerical model and the analytical solution.

8.2.2. Elastic Deformation Behaviour under the Applied Load (Test II)

The aim of this section is to verify that the numerical model is able to solve the stress equilibrium equation for an elastic problem. An analytical solution for the deflection of a horizontal column under the action of a distributed load is utilised for this exercises.

8.2.2.1. Analytical Solution

For this exercise, the stress-strain relationship presented previously in Chapter 3, can be expressed in one-dimensional case for an elastic medium as:

$$\sigma_x = \frac{E}{(1-2\nu)(1+\nu)} [(1-\nu)\varepsilon_x + \nu(\varepsilon_y + \varepsilon_z)] \quad (8.4)$$

All symbols were previously defined in Chapter 3.

For a case where deformation is prevented in both the z and y directions, the strains in respective directions are zero. Introducing this restriction to equation (8.4) yields:

$$\varepsilon_x = \frac{(1-2\nu)(1+\nu)}{E(1-\nu)} \sigma_x \quad (8.5)$$

Redefining the strain presented in equation (3.48) for one-dimensional case in terms of displacement, u , yields:

$$\frac{\partial u}{\partial x} = \frac{(1-2\nu)(1+\nu)}{E(1-\nu)} \sigma_x \quad (8.6)$$

The general solution for equation (8.6), represented as the horizontal displacement of the horizontal column at a distance x from its fixed end, can be found as (Cleall, 1998):

$$u = \frac{(1-2\nu)(1+\nu)}{E(1-\nu)} \sigma_x x \quad (8.7)$$

8.2.2.2. Simulation Conditions

The problem analysed is a horizontal column of length 1 m and width 0.1 m. The domain was discretised into 20 equally-sized 4-noded quadrilateral elements. A distributed stress of 10^5 Pa is applied to the right (inlet boundary) surface of the column with the left (outlet boundary) hand end of the sample being fully restrained. Also, all

boundaries of the column are restrained for deforming vertically. The schematic of the initial and boundary conditions used is shown in Figure 8.3, while the material parameters assigned are presented in Table 8.2.

Inlet boundary conditions	Initial conditions	Outlet boundary conditions
$Stress=10^5 Pa$ $dy=0$	$Stress: 0 Pa$	$dx=0$ $dy=0$

Fig. 8.3. Schematic of the initial and boundary conditions used in Test II.

Table 8.2. Input material parameters used in Test II.

Material and initial parameters	Value
Elastic modulus, E (GPa)	0.1
Poisson's ratio, ν (-)	0.4

8.2.2.3. Results

Figure 8.4 shows the displacements throughout the column.

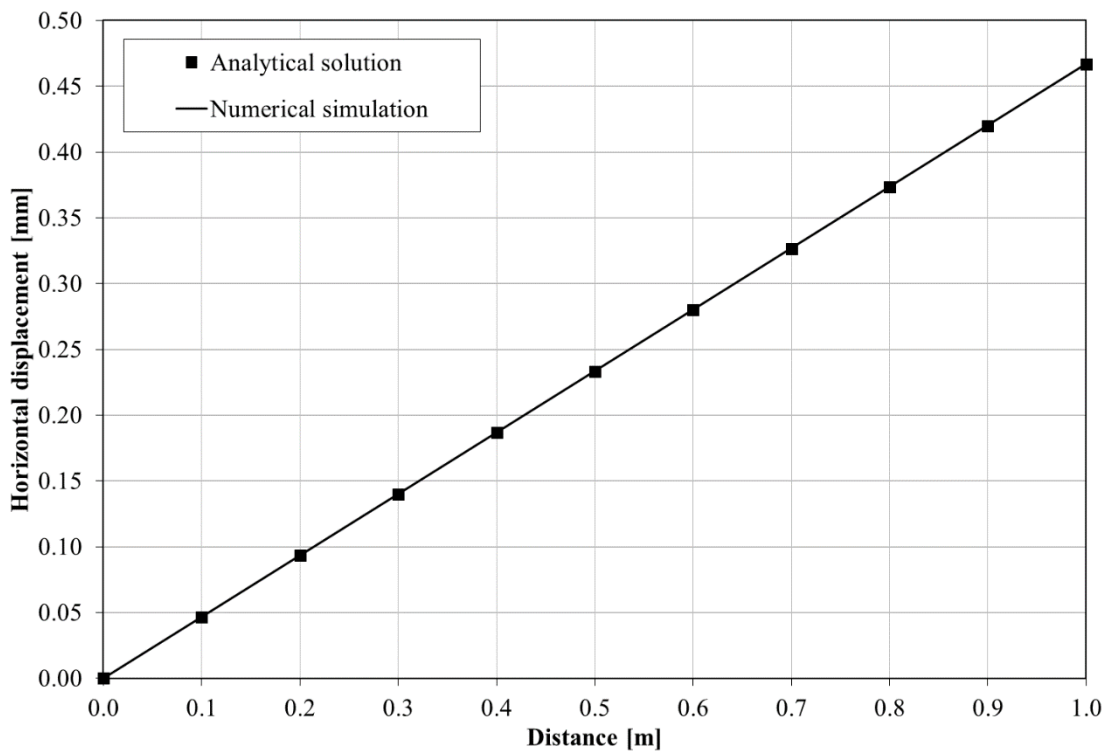


Fig. 8.4. Horizontal displacements obtained using the numerical model and the analytical solution.

An excellent correlation can be seen between the curve from the proposed model and the analytical values. These results verify that the numerical model is able to correctly represent the elastic deformation of a porous material when subjected to a compressive load.

8.2.3. Elastic Deformation Behaviour with Permeability-porosity Relationship under the Non-sorbing Gas Injection (Test III)

Verification of the numerical model's ability to represent the elastic behaviour of a porous medium under gas injection and changes in permeability of the system described by the theoretical model is addressed in this section. As described in Chapter 3, the elastic stress-strain relationship was expressed through a generalised Hooke's law where the elastic deformation was presented through changes in net stress and gas sorption induced swelling (eq. 3.54). If the swelling of the porous medium is neglected, for a condition of null change in total stress, gas pressure changes drive the elastic deformation of the porous medium (Palmer and Mansoori, 1998). Based on the volumetric strain expressed in terms of displacement and its relation to the void ratio of the porous medium, the ratio of calculated permeability and initial permeability can then be calculated using equation (3.52).

Palmer and Mansoori (1998) used the same approach, based on the equation of linear elasticity for strain changes in porous rock, to develop an analytical solution for the changes in permeability calculated as a function of elastic modulus, initial porosity and pressure under uniaxial strain conditions. The model for changes in permeability developed by Palmer and Mansoori (1998) can be expressed in terms of gas chemicals:

$$\frac{K}{K_0} = \left[1 + \frac{1}{n_0} \frac{(1-2\nu)(1+\nu)}{E(1-\nu)} (ZRTc_g - ZRTc_{g0}) \right]^3 \quad (8.8)$$

where subscript "0" denotes the initial value of the respective parameter. All other symbols were previously described in Chapter 3.

Hence, the permeability ratio can be defined as:

$$K_R = \frac{K}{K_0} \quad (8.9)$$

The results of the numerical analysis, neglecting the swelling of the porous medium induced by gas sorption, are compared with the theoretical model presented by Palmer and Mansoori (1998) for calculating permeability in coals as a function of gas pressure.

8.2.3.1. Simulation Conditions

A two dimensional domain with 1 m length and 0.1 m width was spatially discretised into 20 equally-sized 4-noded quadrilateral elements. Figure 8.5 provides a summary of the initial and boundary conditions prescribed in the simulation.

Inlet boundary conditions	Initial conditions	Outlet boundary conditions
$ZRTc_g = \text{prescribed}$ $dy=0$	$\text{Stress: } 0 \text{ Pa}$ $c_{g0} = 39.31 \text{ mol m}^{-3}$	$dx=0, dy=0$ $ZRTc_g = 101325 \text{ Pa}$

Fig. 8.5. Schematic of the initial and boundary conditions used in Test III.

The domain was initially saturated with an ideal gas at atmospheric conditions. A fixed pressure of 101325 Pa is applied at the outlet boundary (left hand end of the sample), while at the inlet boundary (right hand end of the sample) a time-dependant gas concentration is imposed. In particular, gas pressure is increased monotonously from atmospheric conditions (101325 Pa) to 5 MPa over the duration of 4000 seconds and then remains constant until the end of the simulation.

Based on the basic assumption of the Palmer and Mansoori (1998) model which was developed only to be valid under uniaxial strain conditions, all boundaries were restrained for deforming vertically. In addition, the outlet boundary was fully restrained. The simulation was conducted under isothermal conditions with a constant temperature of 310K.

Material parameters used for this exercise are shown in Table 8.3.

Table 8.3. Input material and initial parameters used in Test III.

Material and initial parameters	Value
Temperature, T (K)	310
Initial permeability, K_0 (m ²)	1.0×10^{-15}
Initial porosity, n_0 (-)	0.01
Elastic modulus, E (GPa)	1.0
Poisson's ratio, ν (-)	0.4

8.2.3.2. Results

Figure 8.6 shows the results obtained at the inlet boundary using the numerical model. In particular, it can be observed that the permeability to gas increases with an increase in gas pressure. Based on Figure 8.6, it can be seen that a close agreement of the results of the numerical model with the benchmark obtained based on the model developed by Palmer and Mansoori (1998) is achieved. This confirms a valid calculation of permeability evolution based on the deformation model.

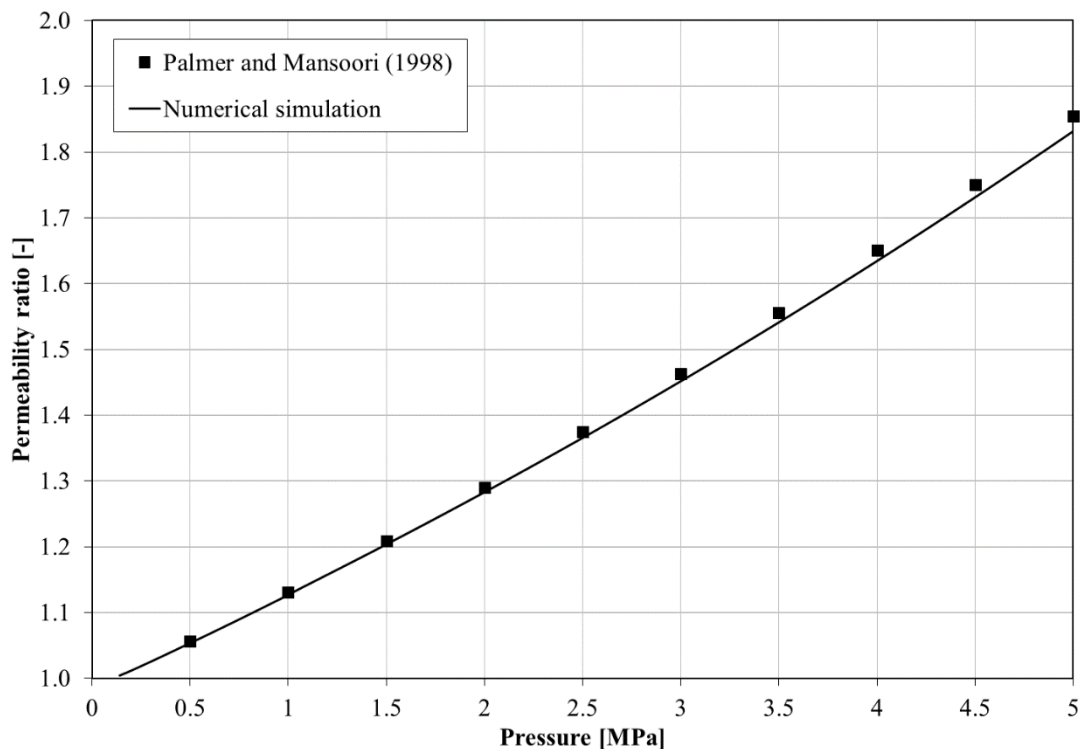


Fig. 8.6. Permeability ratio as a function of non-sorbing gas pressure obtained using the numerical model and the Palmer and Mansoori (1998) model.

8.2.4. Elastic Deformation Behaviour with Permeability-porosity Relationship under the Sorbing Gas Injection (Test IV)

The verification exercise presented in this section is conducted to examine the correctness of the numerical model to predict the swelling of the porous medium induced by gas sorption and its effect on calculated permeability. As previously discussed, coal matrix swells by adsorption of gases such as CO₂ and CH₄, reducing the permeability of coal. It was shown in Chapter 3 that the volumetric strain related to sorption-induced swelling is described employing a commonly used Langmuir (1918) isotherm (eq. 3.50).

The same isotherm was used by Seidle and Huitt (1995) to calculate the permeability increase/decrease due to matrix shrinkage/swelling by assuming that coal sorption-induced strain is proportional to the gas pressure within the system.

Using the same cubic relationship between porosity and permeability as presented in equation (3.52), the model developed by Seidle and Huitt (1995) is expressed in terms of gas concentration as:

$$\frac{K}{K_0} = \left[1 + \frac{\varepsilon_{max}}{3} \left(1 + \frac{2}{n_0} \right) \left(\frac{ZRTc_{g0}}{P_L + ZRTc_{g0}} - \frac{ZRTc_g}{P_L + ZRTc_g} \right) \right]^3 \quad (8.10)$$

All symbols were previously defined in Chapter 3.

It should be noted that the model developed by Seidle and Huitt (1995) considers the effect of coal matrix swelling/shrinkage only, ignoring the impact of coal compressibility. Therefore, Seidle and Huitt (1995) model is limited to specific conditions in which sorption-induced strain dwarfs pressure-induced, elastic changes in coal permeability. In order to achieve that, a high value of elastic modulus was chosen to be used in the numerical model to minimize the effect of coal elastic expansion due to gas pressure increase. As a result, only the swelling strain had a dominant effect on the permeability evolution.

8.2.4.1. Simulation Conditions

For this exercise a two dimensional domain of size 1 m by 0.1 m was spatially discretised into 100 equally-sized 4-noded quadrilateral elements. Figure 8.7 provides a summary of the initial and boundary conditions used in the simulation. The specified gas pressures were expressed in terms of the primary variables of gas concentrations via the Peng and Robinson (1976) equation of state.

Inlet boundary conditions	Initial conditions	Outlet boundary conditions
$ZRTc_g = \text{prescribed}$ $dy=0$	$\text{Stress: } 0 \text{ Pa}$ $c_{g0} = 39.51 \text{ mol m}^{-3}$	$dx=0, dy=0$ $ZRTc_g = 101325 \text{ Pa}$

Fig. 8.7. Schematic of the initial and boundary conditions used in Test IV.

The sample was considered to be initially saturated with CO₂ at atmospheric pressure. A fixed CO₂ pressure of 101325 Pa was applied at the outlet boundary, while at the inlet boundary a time-dependant CO₂ concentration was imposed. In particular, CO₂ pressure was increased continuously from atmospheric conditions (101325 Pa) to 5 MPa over the duration of 1300 seconds and then remained constant until the end of the simulation. The total time of the simulation was 5000 seconds. Seidle and Huitt (1995) model was developed to represent the behaviour of in situ coal deposits. Hence, it can be considered to be applicable to uniaxial strain conditions (Liu et al., 2011). Therefore, all boundaries were restrained for deforming vertically, while the outlet boundary was fully restrained. The system remained isothermal at 310K throughout the simulation period.

The major parameters related to the Peng and Robinson (1976) equation of state, viscosity model and material parameters used in the simulation are presented in Table 8.4. Gas properties required by the equation of state and gas mixture viscosity model were selected from Cussler (1997) and Poling et al. (2001).

Table 8.4. Input material and initial parameters used in Test IV.

Material and initial parameters	Value
Temperature, T (K)	310
Initial permeability, K_0 (m ²)	1×10^{-15}
Initial porosity, n_0 (-)	0.01
Elastic modulus, E (GPa)	1×10^6
Poisson's ratio, ν (-)	0.4
Langmuir pressure (sorption), P_L (MPa)	2.0
Langmuir capacity, s_{max} (mol kg ⁻¹)	1.9
Langmuir volumetric strain constant, ε_{max} (-)	0.015
Langmuir pressure (swelling), P_L (MPa)	2.0
Free diffusion coefficient, D_g (m ² s ⁻¹)	1.48×10^{-5}
Critical pressure, u_{gc} (MPa)	7.38
Critical temperature, T_c (K)	304.21
Critical volume, V_c (m ³ mol ⁻¹)	9.4×10^{-5}
Acentricity factor, ω_A (-)	0.224
Collision diameter, σ_c (Å)	3.941
Collision integral, Ω (-)	195.2
Molecular mass, M_g (kg mol ⁻¹)	0.04401

8.2.4.2. Results

The permeability ratio as a function of CO₂ pressure evaluated at the inlet boundary is presented in Figure 8.8. It can be seen that there is a sharp decrease in permeability with an increase in CO₂ pressure during the initial stage, followed by a more gradual decrease in permeability with further increase in CO₂ pressure. There is a close agreement between the results obtained using the numerical model and those presented using the model developed by Seidle and Huitt (1995). Hence, the exercise has illustrated the capability of the model to simulate the influence of volumetric strain induced by gas sorption, i.e. pressure increase in the system, on permeability evolution.

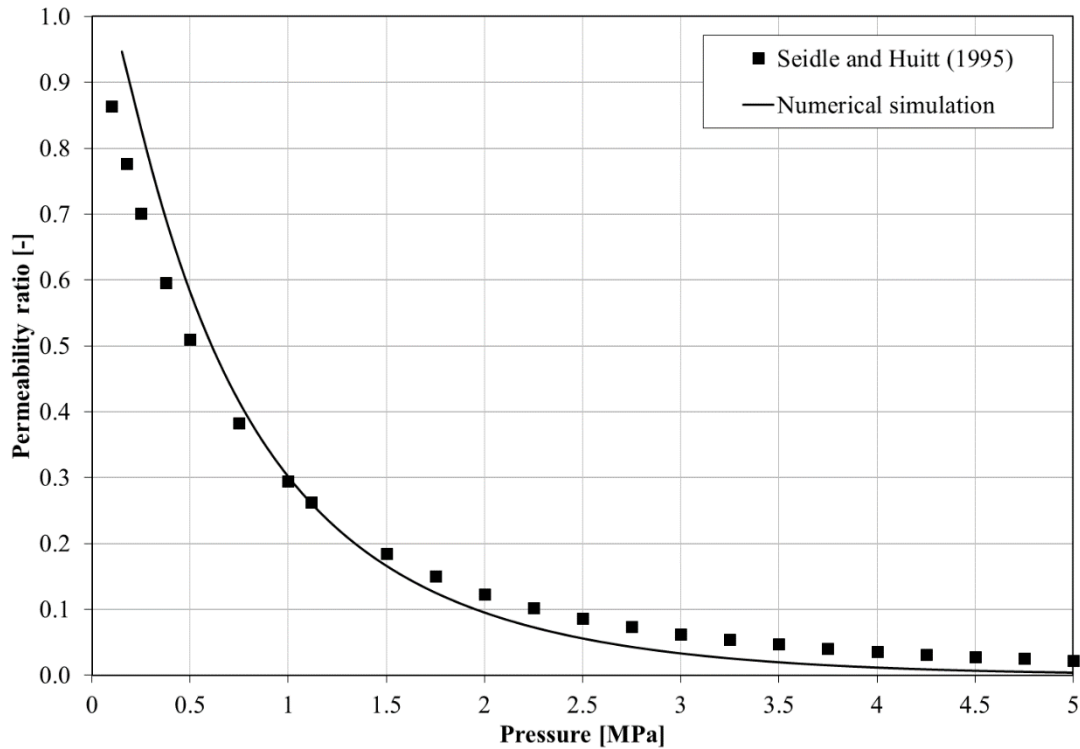


Fig. 8.8. Permeability ratio as a function of CO_2 gas pressure obtained using the numerical model and the Seidle and Huitt (1995) model.

8.2.5. Conclusion to Verification Exercises

The aim of verification exercises presented above was to test the accuracy of the numerical model. The results presented showed very good correlation with both the analytical and the alternative solutions giving confidence in the overall mathematical correctness of the numerical model.

8.3. Validation Exercises

The permeability of coal to gases is stress dependent, decreasing as the level of stress increases (Durucan and Edwards, 1986; Pan et al., 2010). In addition, shrinkage/swelling of the coal matrix when saturated with sorbing gases such as methane and carbon dioxide leads to an increase/decrease in the size of the fracture aperture, thus increasing/decreasing the porosity and consequently, permeability (Harpalani and Chen, 1992). Hence, for sorbing gases, the flow through the fractures is

influenced by two opposite changes. Where coal swelling due to gas sorption is larger than the effect of fracture dilation under gas pressure increase, the permeability may decrease. For this reason, swelling of the coal matrix induced by sorption can have a significant impact on the permeability of coal (Harpalani and Chen, 1992).

The aim of the validation exercises presented below is to gain confidence in the numerical model to represent the mechanisms of behaviour exhibited by coal subject to both non-sorbing and sorbing gas injection. The experimental data, which will be used in this section to validate the numerical model, is based on the measurements obtained on sample A previously presented in Chapter 7. The predicted changes in permeability of coal are compared with the experimental data for helium injection scenario where no sorption takes place and the only variation in permeability is related to the change in gas pressure within the fracture network (macrostructure). In addition, the experimental data obtained during subcritical CO₂ injection and the results of the numerical simulation for carbon dioxide injection scenario, where sorption within the coal matrix affects the porosity of the coal, are compared. As a part of the validation exercise, an effect of various material parameters on the overall behaviour will be discussed.

8.3.1. Experimental Data

The experimental results presented in Chapter 7 for sample A are analysed here and are presented in terms of permeability change over time. The results obtained will be used in the following sections to validate the numerical model. It should be noted that experimental data related to both He and CO₂ injection in sample A were selected for this validation exercise due to the isothermal conditions maintained during the injection of both gases in sample A. As shown in Chapter 7, the temperature of the sample A was constant throughout the injection of He and CO₂ with no Joule-Thomson effect due to the relatively low flow of gases through the sample.

As previously mentioned, gas pressures both at the inlet and outlet of the sample as well as flow rates at the outlet of the sample were constantly monitored throughout the experiments. Using such data and applying it to Darcy's law for compressible fluids presented in equation (4.13), permeability of coal sample both to He and CO₂ was calculated.

Although the calculation of permeability using equation (4.13) is commonly conducted at steady state conditions, i.e. when the gas flow rate, gas pressures and the deformation of the coal sample had stabilised, it can be assumed that applying Darcy's equation to the initial period (first 1.5 hours of the experiment) when the injection pressure is being increased to the designed value offers a good approximation of the permeability in the system. Such statement is supported by the fact that all measurements were done under isothermal conditions and the obtained data are stable and of high-resolution, as shown in Chapter 7.

Figures 8.9 and 8.10 show the time evolution of permeability to He and CO₂, respectively. Results for He injection (Figure 8.9) show that during the initial period of increasing the injection pressure up to the desired value of 3.8 MPa, there was no recorded flow during the first hour and hence no permeability value could be calculated. This is attributed to the “threshold phenomenon” where a certain non-zero pressure gradient is required to initiate the flow (Chen et al., 2006). As the injection pressure approached 2.6 MPa, a low flow rate was observed yielding a sudden increase in calculated permeability. Further increase in injection pressures to 4.2 MPa and 4.6 MPa increased the flow rate and consequently, permeability.

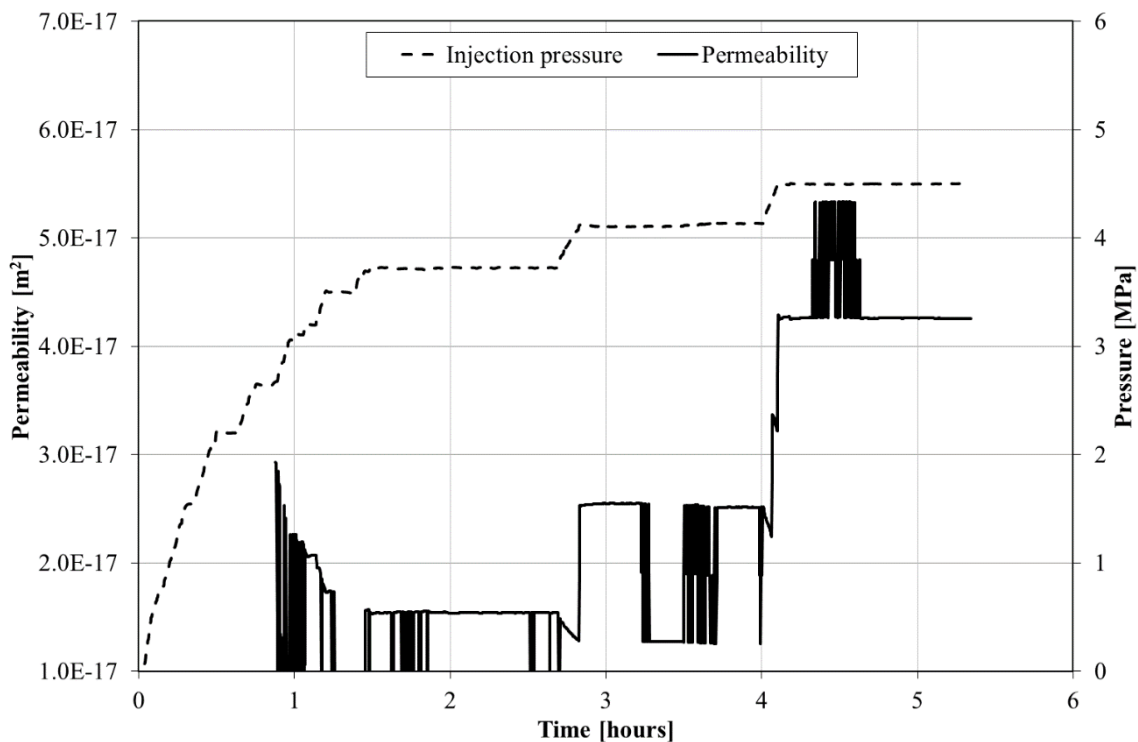


Fig. 8.9. Experimental results of permeability to helium with respect to time for sample A.

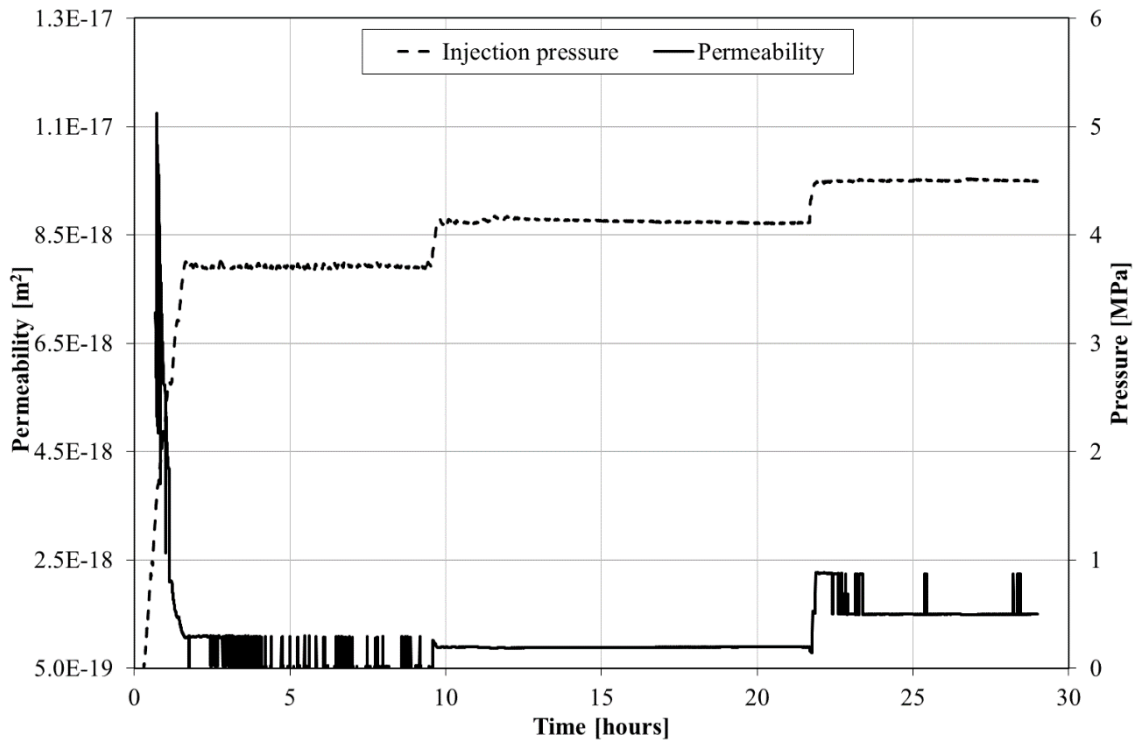


Fig. 8.10. Experimental results of permeability to carbon dioxide with respect to time for sample A.

During the initial increase in injection pressure to the desired value (3.8 MPa) for CO₂ case (Fig. 8.10), there was a sharp increase in permeability followed by a sudden drop. As the injection pressure increased further, there was a slight recovery in permeability. Presented experimental data for permeability change with time will be used to compare with the results of numerical analysis later in the chapter.

8.3.2. Simulation Conditions

As mentioned in Chapter 4, coal core (sample A) used for gas flow measurements was of 0.115 m length and 0.07 m diameter. Those values were used as dimensions of the domain for numerical analysis. Gas was injected at the inlet of the sample (bottom of the core) and the flow rate was monitored at the outlet of the sample (top of the core). As the inlet and outlet pressures were uniformly applied over the surfaces using porous stones, the system was treated as a two-dimensional problem.

The domain was discretised into 100 equally sized 4-noded quadrilateral elements. Using a variable time step, the size of the time step was allowed to vary depending on

the state of convergence. The initial and maximum time steps adopted were 0.01 second and 10 seconds, respectively. In the case of He injection, the simulation was run for the entire duration of the experiment, i.e. 19 000 seconds. In relation to CO₂ scenario, the simulation was run until the end of the second injection step where the injection pressure was raised to 4.1 MPa and remained constant. Hence, the duration of the simulation is 78000 seconds. This corresponds to 80% of the total experimental time and the reason for choosing such value lies in the assumptions used for developing the deformation model.

As explained in Chapter 3, microstructural (matrix) swelling affects the macrostructure by decreasing its porosity, i.e. any increase in matrix volume due to sorption is proportional to decrease in macropore volume. In order to completely satisfy such assumption, the value of interaction function f_m must be equal to -1 which means free penetration of microstructure into macrostructure. Since the interaction function depends on the observable volumetric strain (see Fig. 3.2), experimental results showing the volumetric strain throughout the duration of the experiment (see Fig. 7.27 and Fig. 7.31) suggest that the observable global volumetric strain was negligible up to 80% of experimental time. Hence, it was assumed that the sorption-induced swelling was predominantly internal, narrowing the cleats and decreasing the measured flow rate.

In order to be able to simulate the remaining 20% of experimental time, when the sample experienced global volumetric swelling due to gas sorption, values of function f_m in that case would be larger than -1. However, since the measured volumetric strain is commonly expressed as a function of pressure (e.g. Mitra et al., 2012), it can be assumed that function f_m would also depend on pressure. As this lies beyond the scope of this work, the values of interaction function during the global swelling of the sample are not known. Hence, the behaviour of coal's permeability to CO₂ during its global swelling cannot be determined at this point suggesting further research and development in this area.

Since both He and CO₂ injections were conducted using identical experimental procedure, where the injection pressure was increased to the desired value and the backpressure at the outlet of the sample was kept atmospheric, simulation conditions presented in Figure 8.11 apply to both injection cases. Pressures at the inlet of the

sample for both injection scenarios were prescribed based on the injection pressures measured during the experiments. The prescribed pressure-time curves used in the simulation for the He and CO₂ injections were based on the experimental pressure evolution with time presented in Figures 8.9 and 8.10, respectively. At the start of both simulations, the initial gas pressure in the core was uniform at 101 325 Pa.

Inlet boundary conditions	Initial conditions	Outlet boundary conditions
<u>Fixed gas pressure:</u> $ZRTc_g = \text{prescribed as experimentally recorded}$	<u>Free gas:</u> Helium Injection: $c_g = 39.19 \text{ mol m}^{-3}$ Carbon dioxide injection: $c_g = 39.38 \text{ mol m}^{-3}$ <u>Stress:</u> 0 MPa	<u>Fixed gas pressure:</u> Helium Injection: $RTc_g = 101325 \text{ Pa}$ Carbon dioxide injection: $ZRTc_g = 101325 \text{ Pa}$ <u>Deformation:</u> $dx = 0, dy = 0$

Fig. 8.11. Schematic of the initial and boundary conditions used in the simulations for helium and carbon dioxide injection.

Most of the material parameters, both physical and chemical, were based on the work presented in Chapters 4 to 7. Where required, a combination of literature review and history matching of the experimental data was conducted to obtain necessary data for numerical analysis, not possible to collect through this research. For obtaining such data, the intention of the author was to assess the literature sources which dealt with coals from South Wales Coalfield or alternatively, coals of the same rank (anthracite) from different locations. It is believed by the author that such approach would allow more accuracy when predicting the permeability evolution of the coal used in this study. Temperature of the system was constant throughout the simulation and the reference value of 311K was taken as an average experimental temperature between the inlet and the outlet of the sample as presented in Chapter 7.

A summary of the material parameters and constitutive relationships is provided in Table 8.5.

Table 8.5. Input material and initial parameters for the prediction of permeability changes.

Material and initial parameters	Value	Reference
Temperature, T (K)	311	Chapter 7
Initial porosity, n_0 (-)	0.01	See section 8.3.2
Coal density, ρ (kg m^{-3})	1376	Chapter 4
Poisson's ratio, ν (-)	0.4	Durucan et al. (2009)
Elastic modulus, E (GPa)	1.6	Chapter 6
Initial permeability, K_0 (m^2)	1.65×10^{-17}	Chapter 7
Additional parameters required for helium injection scenario		
Compressibility factor, Z (-)	1	Sudibandriyo (2004)
Free diffusion coefficient, D_g ($\text{m}^2 \text{s}^{-1}$)	6.58×10^{-5}	Cussler (1997)
Critical pressure, u_{gc} (MPa)	0.23	Poling et al. (2001)
Critical temperature, T_c (K)	5.19	Poling et al. (2001)
Critical volume, V_c ($\text{m}^3 \text{mol}^{-1}$)	5.73×10^{-5}	Poling et al. (2001)
Acentricity factor, ω_A (-)	-0.39	Poling et al. (2001)
Collision diameter, σ_c (Å)	2.55	Cussler (1997)
Collision integral, Ω (-)	10.2	Cussler (1997)
Molecular mass, M_g (kg mol^{-1})	0.004003	Zhu et al. (2002)
Additional parameters required for carbon dioxide injection scenario		
Langmuir pressure (sorption), P_L (MPa)	0.91	Chapter 5
Langmuir capacity, s_{max} (mol kg^{-1})	1.90	Chapter 5
Langmuir volumetric strain constant, ε_{max} (-)	1.42	Battistutta et al. (2010)
Langmuir pressure (swelling), P_L (MPa)	1.38	Battistutta et al. (2010)
Compressibility factor, Z (-)		Peng and Robinson (1976)
Free diffusion coefficient, D_g ($\text{m}^2 \text{s}^{-1}$)	1.48×10^{-5}	Cussler (1997)
Critical pressure, u_{gc} (MPa)	7.38	Poling et al. (2001)
Critical temperature, T_c (K)	304.21	Poling et al. (2001)
Critical volume, V_c ($\text{m}^3 \text{mol}^{-1}$)	9.4×10^{-5}	Poling et al. (2001)
Acentricity factor, ω_A (-)	0.224	Poling et al. (2001)
Collision diameter, σ_c (Å)	3.941	Cussler (1997)
Collision integral, Ω (-)	195.2	Cussler (1997)
Molecular mass, M_g (kg mol^{-1})	0.04401	Zhu et al. (2002)

One of the material parameters that had to be assumed based on the literature review is the initial fracture porosity. As mentioned in chapter 4, the total porosity of the Black Diamond coal is estimated to be 3% on average. To revoke the previously mentioned fact, coal is a dual porosity rock with the coal matrix consisting primarily of micropores accounting for most of the total porosity, and the fractures for the permeability of coal to fluid (Harpalani and Chen, 1992). Despite the large porosity of the microporous matrix system, the flow in such pores can be neglected due to the fact that the matrix permeability is about 8-9 orders of magnitude less than the fracture permeability (Seidle, 2011). Hence, only fracture porosity is considered to contribute to gas flow.

It can be seen from Table 8.6 that the range of reported values of fracture porosity in the literature generally varies between 0.1% and 3%. Hence, a commonly used, arbitrary value of 1% (e.g. Chen et al., 2012; Masoudian et al., 2013) for fracture porosity was chosen to be used in this work which fits in to the range of reported values.

Table 8.6. Range of fracture porosity values as reported in the literature.

Fracture porosity value (%)	Reference
0.5-2.5	Laubach et al. (1998)
0.1-0.5	Palmer and Mansoori (1998)
0.4	Shi et al. (2008)
0.37-3	Balan and Gumrah (2009)
1	Chen et al. (2012)
1	Masoudian et al. (2013)
0.46-1.1	Connell et al. (2016)

Values of coal density and elastic modulus were taken from experimental data for Black Diamond coal presented in Chapter 4 and Chapter 6, respectively. However, the value of Poisson's ratio of the coal was selected based on the literature survey. As Masoudian (2016) reported in his review paper, coal has a greater Poisson's ratio compared to other sedimentary rocks which can vary between 0.15 and 0.49. In this work, value of the Poisson's ratio of 0.4 reported for the 9ft seam from the Selar open cast site in South Wales, UK by Durucan et al. (2009) was selected. Since the reported coal is also anthracite with 89.9% of fixed carbon from the same coalfield, it is reasonable to believe that the chosen value provides a good approximation for the coal of this study.

Initial permeability of the studied coal sample was selected based on the He permeability data presented in Chapter 7. As shown, exponential relationship which relates permeability (k) and effective stress (σ'') was fitted to the experimentally determined permeability values for the He injection case. To restate, the relationship obtained is $k = 8.06 \times 10^{-14} \exp(-2.74\sigma'')$. It was mentioned in Chapter 4 that before injection of gases, confining pressure was increased to 3.1 MPa. Hence at that point, it can be inferred that the total stress applied on the sample was equal to the effective stress. Using the value of 3.1 MPa as an effective stress and substituting it into the relationship presented above, the value of permeability to He of $1.65 \times 10^{-17} \text{ m}^2$ at effective stress of 3.1 MPa was obtained representing an initial value at the start of the experiment. It should be noted that the He permeability relationship was chosen due to the fact that He is a non-sorbing gas whereas its injection causes purely mechanical expansion of coal sample compared to CO_2 . Hence, the permeability value determined using He represents an intrinsic value.

Additional parameters both for He and CO_2 injection scenarios provided in Table 8.5 represent widely reported thermodynamic gas property values used for calculation of compressibility factors and viscosity. However, due to the sorptive behaviour of CO_2 in comparison to He, parameters related to the sorption of CO_2 and induced swelling are also reported.

As presented in Chapter 3, both the sorption capacity and the sorption-induced strain are calculated using a Langmuir isotherm. Values of Langmuir capacity and Langmuir pressure (sorption) are based on experimental results for Black Diamond coal core presented in Chapter 5 while the value of Langmuir volumetric strain is obtained based on the literature survey. The volumetric increase of coal due to swelling was reported to be up to 4.2% at pressures higher than 15 MPa (Siemons and Busch, 2007; Hol and Spiers, 2012). However, Reucroft and Sethuraman (1987) reported that swelling usually decreases with increasing coal rank. In order to obtain value representative to the coal from this study, Langmuir volumetric strain of 1.42% and Langmuir pressure constant of 1.38 MPa reported by Battistutta et al. (2010) for unconfined dry Selar Cornish coal from South Wales Coalfield were adopted.

It should be noted that a maximum volumetric strain of 1.88% was recorded for Black Diamond coal (sample D) at mean gas pressure of 4.35 MPa, as shown in Chapter 7. However, as the CO₂ expansion and related cooling effect could have increased the sorption capacity of coal and affected the swelling behaviour of coal, value presented by Battistutta et al. (2010) measured under isothermal conditions was taken into account.

8.3.3. Results

Before the permeability values obtained by the numerical model are compared with experimental data, time evolutions of gas pressure at the inlet boundary obtained from simulations were plotted against experimental pressure data. Results of both experimentally measured and simulated inlet pressures for the helium injection and the carbon dioxide injection cases are presented in Figures 8.12 and 8.13, respectively. There is a close agreement between the results obtained using the numerical model and those measured throughout the experiment both for helium and carbon dioxide injection scenarios.

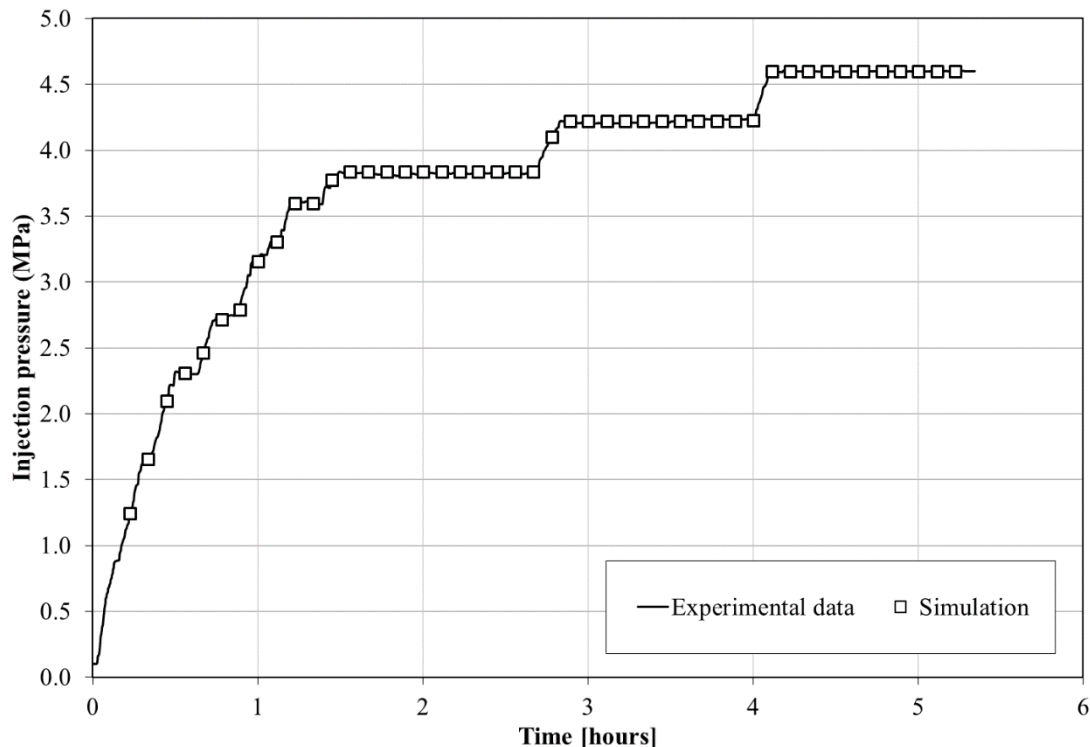


Fig. 8.12. Pressure evolution at the inlet of the sample for helium injection, obtained using the numerical model and during the experiment.

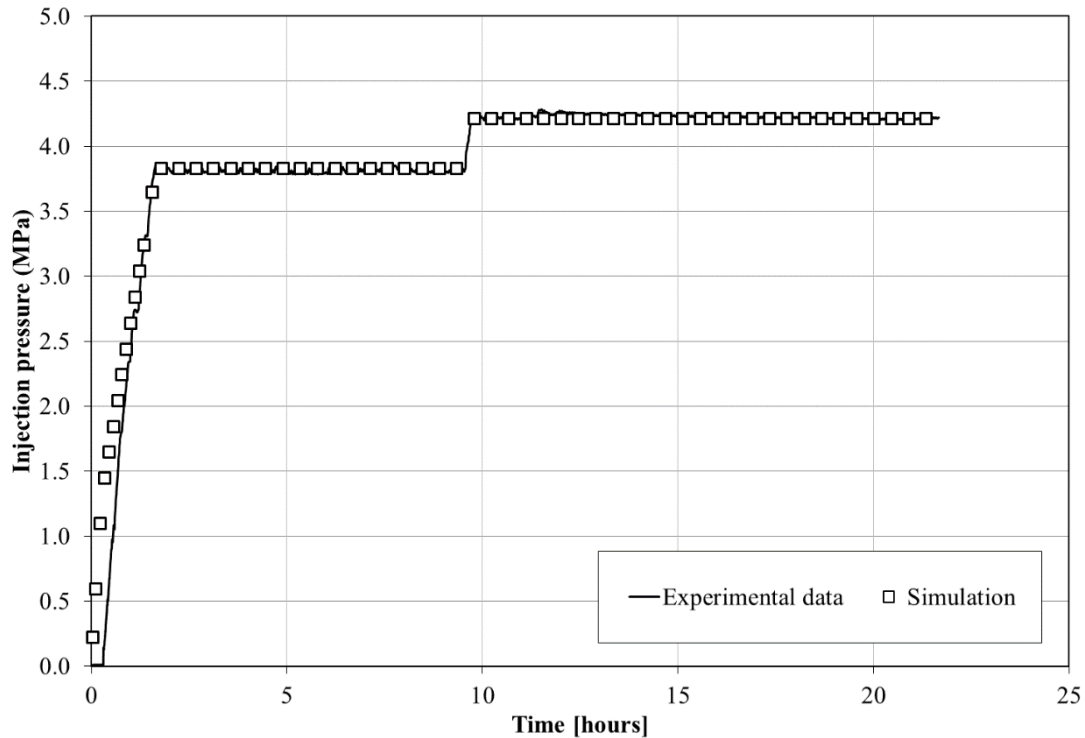


Fig. 8.13. Pressure evolution at the inlet of the sample for carbon dioxide injection, obtained using the numerical model and during the experiment.

During the analysis of the permeability evolution within the sample, it is important to appreciate the level of uncertainty in approximating the average permeability across the sample. As shown in Chapter 4, permeability data is calculated using Darcy's law which takes into account the length of the sample, the area of the cross-section of the sample perpendicular to the flow of gas, gas pressures measured at the inlet and the outlet of the sample, the volumetric flow rate measured at a reference gas pressure at the outlet of the sample and the viscosity of the gas evaluated at the mean gas pressure. Hence, it can be inferred that experimentally determined permeability values represent an average value over the sample domain.

However, the variation in permeability in reality exists over the sample domain due to the pore pressure distribution across the core. Therefore, the results of permeability obtained using the numerical simulation were presented at the inlet boundary, at the centre of the domain and at the location 0.1 m away from the inlet boundary. This was done in order to assess the permeability evolution at different locations within the sample domain.

Figure 8.14 presents the variation in permeability to He with respect to time observed in the experiment and predicted by the numerical model. Experimentally determined permeability after 2.5 hours of the experiment is 7% lower than the initial permeability of $1.65 \times 10^{-17} \text{ m}^2$. As shown earlier, there was no stress applied on the sample in the simulation. However, such assumption is partially true for experimental conditions. As described in Chapter 7, during the first 1.5 hour of the experiment, both confining and injection pressures were simultaneously increased upon reaching the designed values. After reaching the designed values of 5.1 MPa of confining pressure and 3.8 MPa of injection pressure, the resulting effective stress at this point was 3.15 MPa. Since this value is slightly higher than the effective stress at which the initial permeability was evaluated, i.e. 3.1 MPa, it is reasonable that the lower value of permeability occurs at higher effective stress.

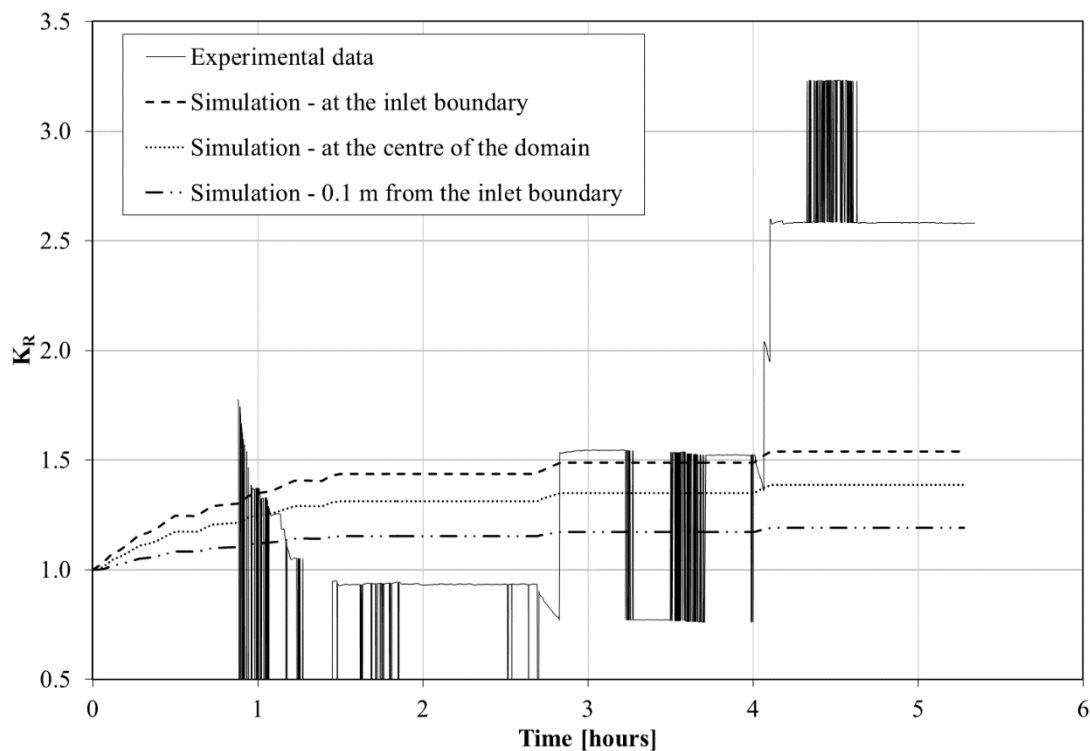


Fig. 8.14. The variation in permeability to helium with respect to time observed in the experiment and predicted by the numerical model

It was shown in Chapter 7 that confining stress applied in this study provided negligible confinement to the sample, i.e. it did not prevent the sample from external (volumetric) expansion. Hence, it should be noted that the simplification of the boundary conditions (no applied stress on the boundaries) in the numerical simulation was introduced due to

the fact that the main focus of this study, i.e. observation of coal behaviour when increasing the injection pressure in three injection steps from 3.8 MPa to 4.6 MPa, was conducted under null change of total stress. This was achieved by keeping the confining pressure of 5.1 MPa constant after 1.5 hour of the experiment. Hence, from this point onward, only the change in injection pressure dictated the change in coal response. The first 1.5 hours of the experiment were attributed to the increase in pressures to the designed values, as described earlier.

From the curves in Figure 8.14, it can be seen that the permeability to He predicted by the numerical model continually increases during the first 1.5 hours of the simulation at any point within the domain. Based on the pressure data previously presented in Figure 8.12, it can be observed that such response of coal is related to the increase in gas pressure within the domain. When the injection pressure was increased to 3.8 MPa and remained constant for one hour allowing the flow of He through the sample to reach steady state, it can be seen that the predicted permeability at any point is higher than the experimentally determined permeability.

The simulated permeability values, after 2.5 hours when the injection pressure stabilised at 3.8 MPa, determined at the inlet boundary, at the centre of the domain and 0.1 m away from the inlet boundary are 44%, 31% and 15% higher than the initial permeability, respectively. Hence, it can be seen that permeability over the domain changes. This difference is related to the distribution of the gas pressure within the domain. As shown in Figure 8.12, inlet pressure was defined through a time curve based on experimental results while the backpressure was fixed at atmospheric pressure. Therefore, due to the pressure gradient established within the domain, lower values of permeability correspond to the regions with lower gas pressure. If experimental results are compared to the simulated permeability values at the inlet boundary after 2.5 hours of the experiment, it can be seen that there is a 35% difference between the results.

As the injection pressure increased further to 4.2 MPa and 4.6 MPa, the experimental permeability increased up to 1.55 times and 2.58 times compared to the initial permeability, respectively. For the same increase in injection pressures, simulated permeability values at the inlet boundary increased 1.49 times and 1.54 times compared to the initial permeability, respectively. Hence, the permeability values obtained at the

inlet boundary after 3.8 hours and 5 hours by the numerical model were 4% and 40% lower than the experimentally determined permeability values, respectively. Such difference could be related to several aspects.

First, the response of coal to a non-sorbing gas injection is in reality related to two different physico-mechanical phenomena, i.e. dilatation of the fractures and compressibility of the coal matrix. When the gas pressure in fractures increases, the fractures are being dilated. At the same time, the hydrostatic load of the pore gas pressure in the fractures compresses the matrix blocks. These combined effects then increase the fracture permeability (Hosking, 2014). Since the behaviour of the coal system, containing both fractures and coal matrix, is represented through a single value of elastic modulus in the numerical model, such simplification might result in differences between the experimental data and the results of the simulation. In other words, the value of elastic modulus obtained through uniaxial compressive loading of the sample might not reflect the elastic response of coal subject to injection of high-pressure gas.

Second, as previously discussed in Chapter 7, coal becomes more compressible with an increase in injection pressure. This is predominantly attributed to the response of fractures subject to gas pressure change and the compressibility of the solid phase, i.e. coal matrix (Hol et al., 2014). Although the compressibility of the coal is often assumed to be constant, the compressibility of the fractures is both porosity and stress dependent (Pan and Connell, 2012). Hence, assuming a constant compressibility of the coal over the range of pressures used in the numerical model might under-predict the permeability evolution.

Third, the choice of elastic modulus value to be used in the simulation was based on experimental results presented in Chapter 6, obtained on core samples 36 mm in diameter. As shown in Chapter 4, only the samples with negligible amount of visible fractures were chosen for uniaxial tests. Hence, it can be assumed that obtained values would represent elastic modulus of coal matrix, rather than well-fractured larger specimens. This is in accordance with previous work where it was shown that elastic modulus and compressive strength of coal decrease with an increase in sample size related to the presence of fracture planes in the larger specimens (e.g. Bieniawski, 1968;

Medhurst and Brown, 1998; Speight, 2005). Since core samples used in the triaxial tests were twice in size than the samples used for uniaxial compressive tests, it can be inferred that such difference in size could result in lower elastic modulus for sample A. Consequently, lower value of elastic modulus would lead to higher deformation of coal sample subject to gas pressure resulting in higher permeability and better agreement with experimental data.

Fourth, the choice of initial fracture porosity is expected to affect the permeability evolution since fracture porosity drives the change in permeability with pressure depletion (Harpalani and Chen, 1997). In this work, porosity value of 1% based on the literature survey was chosen which serves as an approximation since the measurement of cleat porosity was not a part of this study. Hence, a different value of initial cleat porosity would affect the permeability evolution.

The time-evolution of permeability to CO₂ observed in the experiment and predicted by the numerical model is presented in Figure 8.15. After 1.5 hours and 20 hours, the experimentally determined permeability decreased by a minimum of 93% and 95% compared to the initial permeability, respectively.

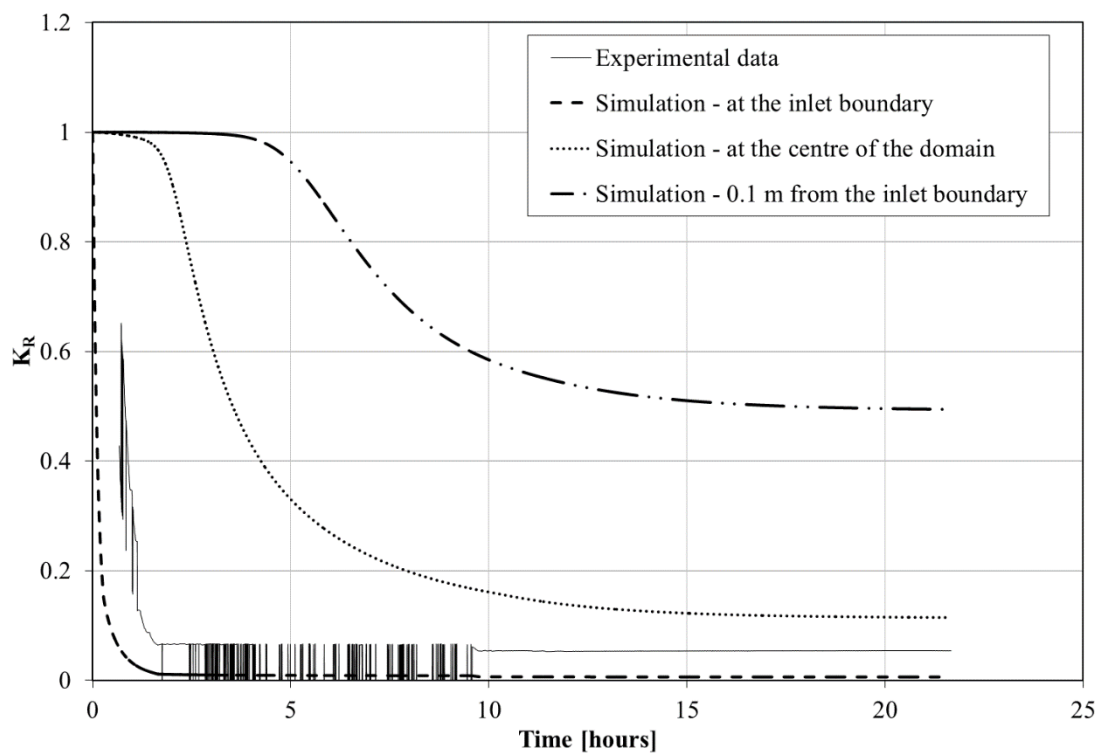


Fig. 8.15. The variation in permeability to carbon dioxide with respect to time observed in the experiment and predicted by the numerical model

It can be seen that the predicted permeability curve determined at the inlet boundary follows a similar trend as the experimentally determined permeability curve. However, permeability reduction in the simulation occurs much faster than in the experiment and reduces by 99% compared to the initial permeability after 1.5 hours of simulation. If the pressure evolution at the inlet boundary presented in Figure 8.13 is taken into account, it can be inferred that the permeability reduction is proportional to the pressure increase at the inlet boundary. At the end of the simulation when the inlet pressure reached 4.2 MPa, the permeability loss remained 99%.

By observing the permeability curves determined at the centre of the domain and 0.1 m away from the inlet boundary, it can be seen that permeability reduces by 89% and 51% at the end of simulation, respectively. As explained previously for He injection simulation, this is related to the distribution of the gas pressure within the domain, i.e. higher gas pressure closer to the inlet of the sample compared to the outlet. However, shapes of the curves suggest that permeability reduction depends on the gas breakthrough. In particular, there were 1.5 hours and 5 hours required for permeability change to occur at the centre of the domain and 0.1 m from the inlet boundary, respectively.

Differences between the variation in permeability observed in the experiment and predicted by the numerical model described above are related to the approach used to model the coal swelling behaviour. As presented in Chapter 3, the sorption strain of the coal matrix was assumed to be in equilibrium with the free gas concentrations in the pores. This means that applying a fixed concentration boundary would have caused an instantaneous sorption strain at the boundary. In particular, at the injection boundary, the permeability would instantaneously reduce as a result of large adsorption induced strain choking the flow of gas due to a significant loss in the permeability. Hence, the reduced flow rate would restrict both the injection of CO₂ and its arrival at the abstraction boundary.

However, gas adsorption and coal swelling are known to be a kinetic reaction, as shown in Chapters 5 and 7, respectively. Hence, the equilibrium behaviour could not be completely realistic and the sorption strain should be calculated using the kinetic adsorbed amounts. Implementing this would require a good understanding of the

relationship between the adsorbed amount and the sorption strain at non-equilibrium conditions which is beyond the scope of the present work. Nevertheless, an equilibrium approach gives good results completely capturing the permeability trend with the change in CO₂ pressure.

It should be also noted that the approach to model the swelling strain presented in Chapter 3 assumed an isotropic swelling of the porous material. As it was previously mentioned that coals are heterogeneous and sample dependent materials, difficult to describe with a simple structural models which show strong anisotropic swelling behaviour, assuming isotropy may lead to erroneous predictions of permeability behaviour (e.g. Pan and Connell, 2011).

8.3.4. Conclusion to Validation Exercises

The purpose of the validation exercises presented above was to gain confidence in the proposed theoretical model to represent the mechanisms of behaviour exhibited by coal. The exercises focused on two important aspects, i.e. the impact of coal deformation subject to both non-sorbing (He) gas and sorbing (CO₂) gas on permeability evolution.

It can be concluded that the validation of all the aspects of coal behaviour was addressed. However, it is recognised by the author that certain discrepancies between the simulated and the experimental results exist. In relation to that, assumptions of the deformation model and uncertainties related to the choice of initial parameters were identified to be the cause of the abovementioned discrepancies. Nonetheless, good level of correlation between the experimental and predicted results gives confidence in the model. In particular, it was shown that the predicted behaviour follows the experimentally observed response of coal subject both to He and CO₂ injection.

8.4. Conclusions

The aim of this chapter was to achieve the verification and the validation of the proposed model and its numerical solution. Initial work was carried out to verify that the numerical model can predict the steady state gas concentration profile that would be expected for a highly compressible fluid. The ability of the numerical model to predict

the elastic response of the sample subject to both compressive stress and injection of a non-sorbing gas was then verified. In addition, prediction of the permeability evolution as a function of porosity change was verified. This was then followed by the verification of the numerical model to predict the change in permeability due to the swelling of coal induced by injection of a sorbing gas. The results presented showed, in all cases, excellent correlation with the analytical solutions and alternative models producing confidence in to ability of the numerical model to correctly solve the governing equations.

The validation of the proposed model was addressed through comparison of the simulation results with the permeability data calculated based on experimental measurements presented in Chapter 7 for Sample A. The developed numerical model was applied to simulate two scenarios for gas injection in coal, namely, helium injection and carbon dioxide injection. The results obtained gave confidence that the numerical model represented the mechanisms involved correctly. However, some limitations of the deformation model were identified. Primarily, assumptions introduced during the development of the model and the uncertainties related to the choice of material parameters were stressed out to be the main reasons of the discrepancies between the experimental data and the results predicted by the numerical model. The effect of physical and chemical parameters on the response of coal subject to CO₂ injection will be investigated in a further application in Chapter 9.

8.5. References

- Balan, H.O. and Gumrah, F. 2009. Assessment of shrinkage-swelling influences in coal seams using rank-dependent physical properties. *International Journal of Coal Geology*, 77(1-2), pp. 203-213.
- Battistutta, E., van Hemert, P., Lutynski, M., Bruining, H. and Wolf, K.H. 2010. Swelling and sorption experiments on methane, nitrogen and carbon dioxide on dry Selar Cornish coal. *International Journal of Coal Geology*, 84(1), pp. 39-48.
- Bieniawski, Z.T., 1968. The effect of specimen size on compressive strength of coal. *International Journal of Rock Mechanics and Mining Sciences*, 5, pp. 325-335.
- Chen, Z., Huan, G. and Ma, Y. 2006. *Computational Methods for multiphase flows in porous media (Computational Science and Engineering)*. Philadelphia: Society for Industrial and Applied Mathematics (SIAM).

- Chen, D., Pan, Z., Liu, J. and Connell, L.D. 2012. Characteristic of anisotropic coal permeability and its impact on optimal design of multi-lateral well for coalbed methane production. *Journal of Petroleum Science and Engineering*, 88-89, pp. 13-28.
- Cleall, P.J. 1998. *An investigation of the thermo/hydraulic/mechanical behaviour of unsaturated soils, including expansive clays*. Ph.D. Thesis, Cardiff University, Wales, UK.
- Connell, L.D., Mazumder, S., Sander, R., Camilleri, M., Pan, Z. and Heryanto, D. 2016. Laboratory characterisation of coal matrix shrinkage, cleat compressibility and the geomechanical properties determining reservoir permeability. *Fuel*, 165, pp. 499-512.
- Cussler, E.L. 1997. *Diffusion: mass transfer in fluid systems*. 2nd Edition. Cambridge University Press, Cambridge.
- Durucan, S. and Edwards, J.S. 1986. The effects of stress and fracturing on permeability of coal. *Mining Science and Technology*, 3, pp. 205-216.
- Durucan, S., Ahsan, M. and Shi, J.Q. 2009. Matrix shrinkage and swelling characteristics of European coals. *Energy Procedia*, 1(1), pp. 3055-3062.
- Harpalani, S. and Chen, G. 1992. Effect of gas production on porosity and permeability of coal. In: *Proceedings of the Symposium of Coalbed Methane R and D in Australia*, pp. 67-73.
- Harpalani, S. and Chen, G. 1997. Influence of gas production induced volumetric strain on permeability of coal. *Geotechnical and Geological Engineering*, 15, 303-325.
- Hol, S. and Spiers, C.J. 2012. Competition between adsorption-induced swelling and elastic compression of coal at CO₂ pressures up to 100 MPa. *Journal of the Mechanics and Physics of Solids*, 60(11), pp. 1862-1882.
- Hol, S., Gensterblum, Y. and Massarotto, P. 2014. Sorption and changes in bulk modulus of coal – experimental evidence and governing mechanisms for CBM and ECBM applications. *International Journal of Coal Geology*, 128-129, pp. 119-133.
- Hosking, L.J. 2014. *Reactive transport modelling of high pressure gas flow in coal*. Ph.D. Thesis, Cardiff University, Wales, UK.
- King, S.D. 1991. *A potential based model of coupled heat and moisture transfer in unsaturated soil*. Ph.D. Thesis, University of Wales, Cardiff, UK.
- Langmuir, I. 1918. The adsorption of gases on plane surfaces of glass, mica and platinum. *Journal of the American Chemical Society*, 40(9), pp. 1361-1403.
- Laubach, S.E., Marrett, R.A., Olson, J.E. and Scott, A.R. 1998. Characteristics and origins of coal cleat: A review. *International Journal of Coal Geology*, 35(1-4), pp. 175-207.
- Liu, J., Chen, Z., Elsworth, D., Qu, H. and Chen, D. 2011. Interactions of multiple processes during CBM extraction: A critical review. *International Journal of Coal Geology*, 87(3-4), pp. 175-189.
- Masoudian, M.S., Airey, D.W. and El-Zein, A. 2013. A chemo-poro-mechanical model for sequestration of carbon dioxide in coalbeds. *Géotechnique*, 63(3), pp. 235-243.

Masoudian, M.S. 2016. Multiphysics of carbon dioxide sequestration in coalbeds: A review with a focus on geomechanical characteristics of coal. *Journal of Rock Mechanics and Geotechnical Engineering*, 8(1), pp. 93-112.

Masum, S.A. 2012. *Modelling of reactive gas transport in unsaturated soil – a coupled thermo-hydro-chemical-mechanical approach*. Ph.D. Thesis, Cardiff University, Wales, UK.

Medhurst, T.P. and Brown, E.T. 1998. A study of the Mechanical Behaviour of Coal for Pillar Design. *International Journal of Rock Mechanics and Mining Sciences*. 35(8), pp. 1087-1105.

Millington, R.J. and Quirk, J.M. 1961. Permeability of porous solids. *Transactions of the Faraday Society*, 57, pp. 1200-1207.

Mitchell, H.P. 2002. *An investigation into the thermo/hydro/mechanical interactions involved in high level nuclear waste disposal*. Ph.D. Thesis, University of Wales, Cardiff, UK.

Mitra, A., Harpalani, S. and Liu, S. 2012. Laboratory measurement and modeling of coal permeability with continued methane production: Part 1 – Laboratory results. *Fuel*, 94, pp. 110-116.

Palmer, I. and Mansoori, J. 1998. How Permeability Depends on Stress and Pore Pressure in Coalbeds: A New Model. *Society of Petroleum Engineers Reservoir Evaluation and Engineering*, 1(6), pp. 539-544.

Pan, Z., Connell, L.D. and Camilleri, M. 2010. Laboratory characterisation of coal reservoir permeability for primary and enhanced coalbed methane recovery. *International Journal of Coal Geology*, 82(3-4), pp. 252-261.

Pan, Z. and Connell, L.D. 2011. Modelling of anisotropic coal swelling and its impact on permeability behaviour for primary and enhanced coalbed methane recovery. *International Journal of Coal Geology*, 85(3-4), pp. 257-267.

Pan, Z. and Connell, L.D. 2012. Modelling permeability for coal reservoirs: A review of analytical methods and testing data. *International Journal of Coal Geology*, 92, pp. 1-44.

Peng, D.Y. and Robinson, D.B. 1976. A new two-constant equation of state. *Industrial and Engineering Chemistry Fundamentals*, 15(1), pp. 59-64.

Poling, B.E., Prausnitz, J.M. and O'Connell, J.P. 2001. *The properties of gases and liquids*. Vol 5, New York, McGraw-Hill.

Reucroft, P.J. and Sethuraman, A.R. 1987. Effect of Pressure on Carbon Dioxide Induced Coal Swelling. *Energy & Fuels*, 1, pp. 72-75.

Sansom, M.R. 1995. *A fully coupled numerical analysis of mass, air, and heat transfer in unsaturated soil*. Ph.D. Thesis, University of Wales, Cardiff, UK.

Seidle, J. 2011. *Fundamentals of coalbed methane reservoir engineering*. PennWell Corporation, Tulsa, Oklahoma, USA.

Seidle, J.R. and Huitt, L.G. 1995. Experimental measurement of coal matrix shrinkage due to gas desorption and implications for cleat permeability increases. *International Meeting on Petroleum Engineering*. Society of Petroleum Engineers.

Shi, J-Q., Durucan, S. and Fujioka, M. 2008. A reservoir simulation study of CO₂ injection and N₂ flooding at the Ishikari coalfield CO₂ storage pilot project, Japan. *International Journal of Greenhouse Gas Control*, 2(1), pp. 47-57.

Siemons, N. and Busch, A. 2007. Measurement and interpretation of supercritical CO₂ sorption on various coals. *International Journal of Coal Geology*, 69(4), pp. 229-242.

Speight, J.G. 2005. *Handbook of coal analysis*. Hoboken, New Jersey: John Wiley & Sons, Inc.

Sudibandriyo, M. 2004. Measurement of methane, nitrogen and carbon dioxide adsorption on wet selected coals. *Proceedings of Seminar Nasional Teknologi Proses Kimia VI*. Jakarta, March 31, 2004, pp. 1-9.

Thomas, H.R. and He, Y. 1995. Analysis of coupled heat, moisture and air transfer in a deformable unsaturated soil. *Géotechnique*, 45(4), pp. 677-689.

Thomas, H.R. and He, Y. 1997. A coupled heat-moisture transfer theory for deformable unsaturated soil and its algorithmic implementation. *International Journal for Numerical Methods in Engineering*, 40, pp. 3421-3441.

Thomas, H.R. and He, Y. 1998. Modelling the behaviour of unsaturated soil using an elastoplastic constitutive relationship. *Géotechnique*, 48, pp. 589-603.

Thomas, H.R., Rees, S.W. and Sloper, N.J. 1998. Three-dimensional heat, moisture and air transfer in unsaturated soils. *International Journal of Numerical and Analytical Methods in Geomechanics*, 22(2), pp. 75-95.

Thomas, H.R. and Cleall, P.J. 1999. Inclusion of expansive clay behaviour in coupled thermo hydraulic mechanical models. *Engineering Geology*, 54, pp. 93-108.

Wu, Y-S., Pruess, K. and Persoff, P. (1998). Gas flow in porous media with Klinkenberg effects. *Transport in Porous Media*, 32, pp.117-137.

Zhu, Y., Lu, X., Zhou, J., Wang, Y. and Shi, J. 2002. Prediction of diffusion coefficients for gas, liquid and supercritical fluid: application to pure real fluids and infinite dilute binary solutions based on the simulation of Lennard-Jones fluid. *Fluid Phase Equilibria*, 194-197, pp. 1141-1159.

9

Numerical Simulations – Coal Response and Gas Transport During Supercritical CO₂ Injection

9.1. Introduction

In Chapter 8, the verification and validation of the model were presented. Laboratory scale data, presented previously in Chapter 7, both for helium and subcritical carbon dioxide injection up to 4.6 MPa were used to validate the model. The simulations in this chapter deal with the response of a larger coal sample subject to supercritical carbon dioxide injection. The outcome of these simulations is to better understand the major mechanisms which control the reactive transport of CO₂ in coal. In particular, the main objective of the discussion provided is to assess the role of the elastic modulus and the parameter defining the coal swelling on the permeability evolution and the gas breakthrough. This is of practical importance to enhance the knowledge related to the impact of major coal properties on the gas transport in coal potentially used for the carbon dioxide sequestration purposes.

The description of the simulation scenarios is presented in Section 9.2. In addition, details related to the model domain, material parameters, initial and boundary conditions as well as the time scheme used in the simulations are provided. A larger domain, i.e. 1 m long and 0.5 m wide, was used for the simulations, compared to the 0.115 m long and 0.07 m wide domain used in the previous chapter for the validation exercise. Such a decision was made based on the discussion provided in Chapter 8 that the difference in material properties between samples of different sizes affect the coal response subject to gas injection. Hence, the simulations were developed to investigate the effect of elastic modulus and swelling related parameters on the overall behaviour of a larger coal sample. In this chapter, four scenarios are considered which include a combination of elastic modulus and Langmuir pressure values. In particular, a value of elastic modulus of 3 GPa and a value of Langmuir pressure of 5 MPa are initially considered. In addition to that, the response of coal to CO₂ injection was assessed when both of the above mentioned values are reduced by 80%.

The results of the above simulations are presented in Section 9.3. The simulated results are presented in terms of the temporal evolution of the permeability to CO₂. Based on the results presented, residual porosity values available for flow at the end of the each simulation are determined. In addition, profiles of the gas pressure across the sample domain at various times during the simulation are presented. A discussion focusing on

the gas transport for the simulation scenarios considered is provided. The concluding remarks are given in Section 9.4.

9.2. Simulation Conditions and Material Parameters

The simulation scenarios developed to investigate the effect of elastic modulus and parameters defining the sorption-induced swelling on the gas flow in coal, 1 m long with a 0.5 m width, are covered in this section. Similar as in the previous chapter, the system was treated as a two-dimensional problem in which the pressures are applied uniformly over the inlet and the outlet boundaries of the sample. The domain was discretised into 100 equally sized 4-noded quadrilateral elements. A variable time step was used which allowed the size of the time step to vary depending on the state of convergence. The initial and maximum time steps adopted were 0.01 second and 100 seconds, respectively. Using a variable time step, if the convergence criterion was not met within a specified maximum number of iterations, the time step was decreased by a factor. Conversely, the time step was increased by a factor when the convergence criterion was met within a specified number of iterations.

The total duration of each simulation was six hours (21600 seconds). Following the observations based on the experimental measurements presented in previous chapters, one might expect that the transport of CO₂ within the coal matrix and its sorption on the sample of such size are transient processes which could take more than six hours. Such transient processes would involve gas exchange between the fractures and the matrix, diffusion through the matrix and sorption of the gas molecules on the sorption sites. However, as described in Chapter 3 and further explained in Chapter 8, an equilibrium approach was used in this study to model both the sorption and the sorption induced swelling meaning that any change in gas concentration within the fractures would have caused an instantaneous change in sorption strain. Therefore, the time duration of six hours was sufficient to study the behaviour of coal subject to supercritical CO₂ injection in this work.

A summary of the supercritical CO₂ injection scenarios considered in the simulations is provided in Table 9.1.

Table 9.1. Summary of the scenarios considered in this chapter for the simulation of supercritical CO₂ injection.

Test ID	Elastic Modulus	Swelling (Langmuir) pressure
Test I	High (initial) value	High (initial) value
Test II	High (initial) value	Low (reduced) value
Test III	Low (reduced) value	High (initial) value
Test IV	Low (reduced) value	Low (reduced) value

Test I represents the scenario with high (initial) values of both the elastic modulus and the swelling (Langmuir) pressure. In Tests II and III, values of the swelling (Langmuir) pressure and the elastic modulus reduced by 80% from the high values are considered, respectively. A case where both the elastic modulus and the swelling pressure are reduced by 80% from the high values is dealt with in Test IV.

A summary of elastic modulus and swelling pressure values used in each scenario are provided in Table 9.2 along with other material and input parameters required for the numerical simulation.

All simulations were conducted under isothermal conditions with a constant temperature of 308K. Such temperature was chosen due to the previously mentioned fact that CO₂ achieves its supercritical state at temperatures and pressures higher than 304K and 7.4 MPa, respectively. In addition, a value of 308K represents approximate temperature at 750 m below the ground level (Gensterblum, 2013). Such depth falls within the favourable depth range for CO₂-ECBM application (White et al., 2005).

As shown previously in Table 8.6, the range of fracture porosity values for coal samples varies between 0.1% and 3%. Hence, the initial porosity of the system was arbitrarily set to 2%, as larger coal samples are expected to have more pronounced and interconnected cleat system than the smaller samples (Bieniawski, 1968; Medhurst and Brown, 1998). As it is expected that coal samples with higher porosity exhibit higher permeability, the initial permeability of the coal sample investigated in this simulation was chosen to be $1 \times 10^{-16} \text{ m}^2$. Such value fits into the range of experimentally determined absolute (helium) permeability values between $5 \times 10^{-16} \text{ m}^2$ and $1 \times 10^{-17} \text{ m}^2$, as presented in Chapter 7. Coal density was 1376 kg m^{-3} , as experimentally determined and reported in Chapter 4 for both coals of this study.

Table 9.2. Input material and initial parameters used in this chapter for the simulation of supercritical CO₂ injection.

Material and initial parameters	Value			
Temperature, T (K)	308			
Initial porosity, n_0 (-)	0.02			
Initial permeability, K_0 (m ²)	1.0×10^{-16}			
Poisson's ratio, ν (-)	0.35			
Coal density, ρ (kg m ⁻³)	1376			
Langmuir capacity, s_{max} (mol kg ⁻¹)	0.75			
Langmuir volumetric strain constant, ε_{max} (-)	2.4			
Free diffusion coefficient, D_g (m ² s ⁻¹)	1.48×10^{-5}			
Tortuosity (Millington and Quirk, 1961), τ_g (m ²)	$n^{10/3}/n^2$			
Critical pressure, u_{gc} (MPa)	7.38			
Critical temperature, T_c (K)	304.21			
Critical volume, V_c (m ³ mol ⁻¹)	9.4×10^{-5}			
Acentricity factor, ω_A (-)	0.224			
Collision diameter, σ_c (Å)	3.941			
Collision integral, Ω (-)	195.2			
Molecular mass, M_g (kg mol ⁻¹)	0.04401			
Compressibility factor, Z (-)	Peng and Robinson (1976)			
	Test I	Test II	Test III	Test IV
Elastic modulus, E (GPa)	3.0	3.0	0.6	0.6
Langmuir pressure, P_L (MPa)	5.0	1.0	5.0	1.0

The maximum (Langmuir) capacity of 0.75 mol kg⁻¹ of the sample investigated in this study was chosen based on the experimentally determined sorption capacity for the 9ft Aberpergwm coal core, as reported in Chapter 5. Values of the maximum (Langmuir) volumetric strain and the Poisson's ratio of coal were chosen based on the literature survey. Durucan et al. (2009) have reported the abovementioned values for coals of different rank, i.e. high volatile bituminous, semi-anthracite and anthracite. The reported values for the Poisson's ratio range between 0.26 and 0.42, and for the Langmuir volumetric strain up 4% (Durucan et al., 2009). Hence, arbitrarily chosen values of 0.35 and 2.4% for Poisson's ratio and Langmuir volumetric strain were chosen, respectively.

Gas properties required by the Peng and Robinson (1976) equation of state and the gas viscosity model presented by Chung et al. (1988) are the same as reported in Table 8.5 for carbon dioxide and are reported here for the sake of completeness.

Material parameters mentioned above were identical for each of the simulations. As described previously, only the values of the elastic modulus and the Langmuir pressure were different in each simulation scenario. In particular, the highest values of the elastic modulus and the Langmuir pressure were set in Test I, i.e. 3 GPa and 5 MPa, respectively. In Test II, the value of the Langmuir pressure was reduced by 80%, i.e. to 1 MPa, while the value of the elastic modulus was kept at 3 GPa. Conversely for Test III, the value of the Langmuir pressure was kept at 5 MPa while the value of the elastic modulus was decreased by 80%, i.e. to 0.6 GPa. In Test IV, both values reduced by 80% compared to the values shown in Test I were used.

It should be noted that all values of the elastic modulus and the Langmuir pressure used in the simulations presented in this chapter are within the range of reported values for the respective parameters. As shown in Chapter 5 and also reported in the literature, the value of the Langmuir pressure is commonly up to 5 MPa (e.g. Connell et al., 2016). However, values of the Langmuir pressure up to 16 MPa were also reported (e.g. Pan et al., 2010). In terms of the elastic modulus, the values obtained on non-saturated (natural) coal samples presented in Chapter 6 were 1.6 GPa for the Black Diamond coal and 1.13 GPa for the 9ft Aberpergwm coal. However, as the elastic modulus is dependent on the size and fracture network of each sample as well as the maturity of the coal, values of elastic modulus can generally range between 0.04 GPa to 3.9 GPa (e.g. Viete and Ranjith, 2006; Durucan et al, 2009; Ranathunga et al., 2016).

The reason why the reduction of 80% was taken for both parameters is based on the findings presented in Chapters 5 and 6. To restate, it was shown in Chapter 5 that samples of the same rank, but from different locations showed different values of the Langmuir pressure. In addition, it was shown in Chapter 6 that saturation of coal samples with supercritical CO₂ can decrease the deformation parameters up to 80%. Therefore, the intention in this chapter was to investigate the response of coal samples when the major parameters affecting the behaviour of coal differ by a certain amount.

In each simulation, the inlet and the outlet boundaries are the right- and left-hand faces of the model, respectively. A schematic of the initial and boundary conditions used in all simulation scenarios are provided in Figure 9.1.

Inlet boundary conditions	Initial conditions	Outlet boundary conditions
<u>Fixed gas pressure:</u> $ZRTc_g = \text{prescribed}$	<u>Free gas:</u> $c_g = 39.38 \text{ mol m}^{-3}$	<u>Fixed gas pressure:</u> $ZRTc_g = 101325 \text{ Pa}$
<u>Deformation:</u> $dy = 0$	<u>Stress:</u> 0 MPa	<u>Deformation:</u> $dx = 0, dy = 0$

Fig. 9.1. Schematic of the initial and boundary conditions used in the simulation of supercritical carbon dioxide injection.

The usual condition in a reservoir is the uniaxial strain condition where the overburden stress remains constant and the lateral boundaries of a reservoir are fixed (Palmer and Mansoori, 1998; Palmer, 2009). However, as shown in Chapter 7, laboratory experiments are conducted under the condition of free swelling which might not completely represent the real condition. Hence, in order to simulate the conditions difficult to achieve in the experiment, which are at the same time expected to represent the real reservoir conditions, all boundaries of the domain were restrained for deforming vertically. In addition, the outlet boundary was restrained for deforming horizontally.

The domain was initially saturated with CO₂ at atmospheric conditions. A fixed pressure of 101325 Pa was applied at the outlet boundary, while at the inlet boundary a time-dependant gas concentration was imposed. In particular, gas pressure was increased monotonously from atmospheric conditions (101325 Pa) to 7.5 MPa over the duration of 3600 seconds and then remained constant until the end of the simulation. As mentioned earlier, CO₂ is at its supercritical state at pressures above 7.4 MPa. In addition, such a value represents approximate pressure at 750 m below the ground level (Gensterblum, 2013). In order to prescribe the boundary conditions, gas pressures were converted to equivalent gas concentrations, c_g , using the real gas law as:

$$c_g = \frac{u_g}{ZRT} \quad (9.1)$$

All symbols were described previously in Chapter 3.

9.3. Simulation Results

The results of the numerical simulations for Tests I to IV, described in Section 9.2, are shown in Sections 9.3.1 to 9.3.3. In particular, ratios of the calculated permeability with respect to the initial permeability evaluated at the inlet boundary over the duration of each simulation are discussed in Section 9.3.1. Based on the permeability ratios obtained at the end of each simulation, the resulting permeability and porosity values are evaluated in Section 9.3.2. Pressure breakthroughs at various times during the simulation for each test are presented in Section 9.3.3.

The ratio of the calculated permeability with respect to the initial permeability, K_R , was evaluated using the equation (8.9) presented previously in Chapter 8. Such relationship was used to calculate the permeability at the end of each test.

As shown in Chapter 3, there is a cubic relationship between porosity and permeability of the coal system. In order to determine the corresponding porosity, n , available for flow from the permeability ratio obtained, equation (3.52) was rearranged and used here as:

$$n = n_0 \sqrt[3]{K_R} \quad (9.2)$$

where n_0 is the initial porosity.

9.3.1. Permeability Evolution

The main purpose of the numerical results presented in this section is to assess the influence of different values of the elastic modulus and the Langmuir pressure on the temporal evolution of permeability during the supercritical CO₂ injection. As the pressure within the system is the highest at the injection point, the permeability calculated in each simulation is evaluated at the inlet boundary.

Figure 9.2 presents the evolution of the ratio of permeability calculated at any point of the Tests I to IV with respect to the initial permeability of the system, i.e. $1 \times 10^{-16} \text{ m}^2$. In addition, the time evolution of the injection pressure is presented. Due to the fact that the deformation model was developed based on the equilibrium approach, where any

change in swelling strain follows the change in pressure, the time evolution of the injection pressure will allow easier evaluation of the observed changes in permeability.

Based on the permeability ratios presented for Test I, it can be seen that the permeability approximately continually reduces with an increase in the injection pressure reaching a reduction of 91% with respect to the initial permeability at the end of the simulation. Similarly, permeability reduces with an increase in gas pressure in Test II, however, achieving a maximum reduction of 97% at the end of the simulation.

By comparing the results obtained in Test I and Test II, it can be observed that the shapes of the curves are different. While the rate of permeability reduction is approximately constant during the increase in injection pressure in Test I, the resulting curve for Test II can be divided in two portions. There is a sharp decline in permeability during the first 400 seconds achieving majority of the total reduction, whereas for the next 3200 seconds, the permeability is reducing at a lower rate until it reaches a constant value.

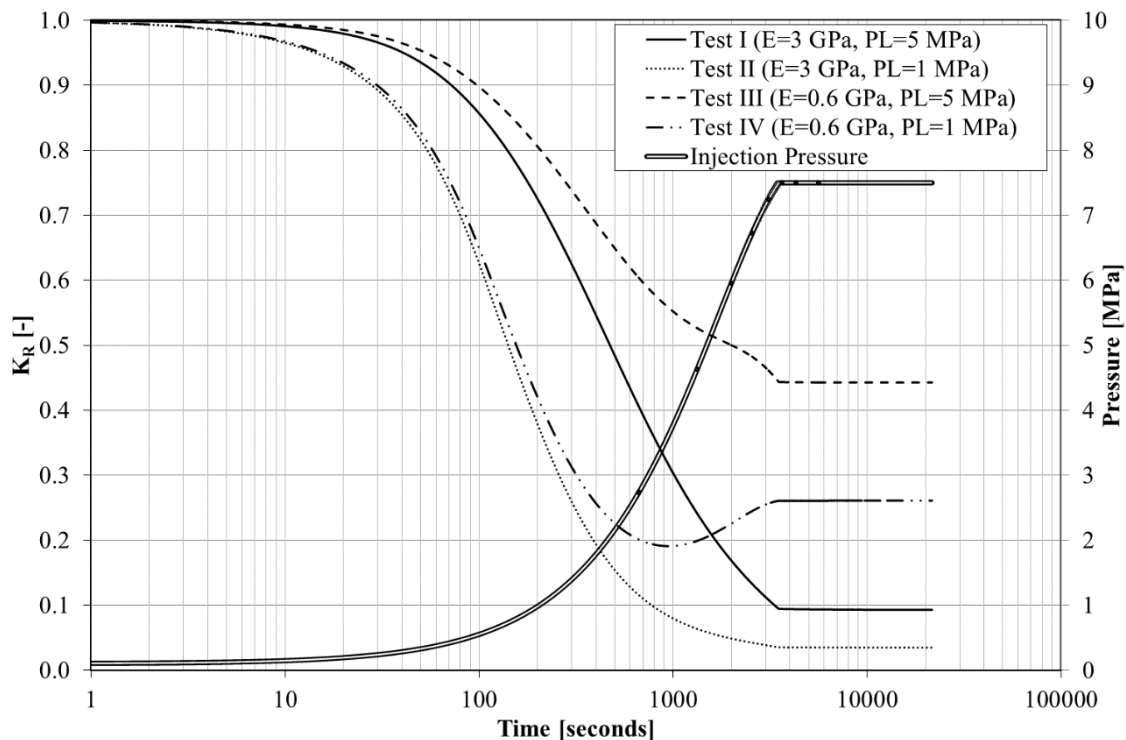


Fig. 9.2. Evolution of the ratio of permeability predicted by the numerical model at any point during the simulation with respect to the initial permeability ($k_0=1 \times 10^{-16} \text{ m}^2$), and the evolution of the injection pressure for Tests I to IV.

As in both Tests I and II the value of elastic modulus was the same, i.e. 3 GPa, the reason for such distinct behaviour lies in the choice of the Langmuir pressure values. It was discussed previously that the value of the Langmuir pressure represents the pressure at which half of the sorption and the corresponding swelling has been completed. In other words, its value determines the shape of the curve. Taking this into account, coal has swelled by 50% of its maximum capacity when the injection pressure was increased to 1 MPa after 200 seconds in Test II. Hence, any further increase in injection pressure resulted in a reduced rate of permeability reduction. Conversely, coal in Test I achieved half of its maximum swelling after 1500 seconds when the injection pressure reached 5 MPa causing almost a continuous decrease in permeability with an increase in pressure up to 7.5 MPa.

Numerical results obtained from Test III and Test IV reveal that CO₂ injection reduced the permeability of the sample by maximum of 56% and 81%, respectively. Since the value of the elastic modulus was equal in both Tests III and IV, the difference in the observed reductions is caused by the choice of the Langmuir pressure values, similarly as explained for Tests I and II.

However, when the higher portion of swelling was completed at lower pressure in Test IV compared to Test III, it can be observed that the value of low elastic modulus allowed coal in Test IV to recover part of its permeability, i.e. by 7%, upon reaching higher pressures. In other words, when the swelling approached close to its maximum after 900 seconds upon reaching the injection pressure of 3.4 MPa, the effect of coal mechanical expansion due to increase in injection pressure started to dominate over the coal swelling allowing the rebound in permeability with further increase in injection pressure.

Moreover, inspecting the shape of the curves from Tests III and IV suggests that lower value of the elastic modulus affects the permeability evolution in a different way compared to the high elastic modulus scenarios (Tests I and II). As the lower value of elastic modulus allows higher deformation of the coal, while the higher value of Langmuir pressure leads to less CO₂ induced swelling at lower pressures, it can be observed that a combination of such values allowed coals in Tests III and IV to achieve less reduction in permeability by the end of the simulation than in Tests I and II.

Hence, by comparing the results of all four tests, it can be concluded that coal samples with high elastic modulus (Tests I and II) appeared to be highly affected by the swelling strain dominating over the mechanical expansion of coal subject to pressure increase. Conversely, coal samples with lower value of elastic modulus (Tests III and IV) were less affected by the swelling strain.

In addition, it can be observed that Tests I and III, for samples with high value of Langmuir pressure, show that the significant portion of permeability reduction appears at later stages than in Tests II and IV for samples with low value of Langmuir pressure. In particular, the reduction of permeability after 200 seconds of simulation, when the injection pressure reached 1 MPa, was 27% and 20% for Tests I and III and 62% and 58% for Tests II and IV, respectively. This shows that cases with higher value of Langmuir pressure achieved less swelling at lower pressures.

9.3.2. Porosity Determination

In order to quantify the simulated results presented above, the permeability ratios are used to determine the resulting values of the permeability and the residual porosity available for flow at the end of the each simulation using equations (8.11) and (9.2), respectively. Calculated values of permeability as a function of porosity for Tests I to IV are presented in Figure 9.3.

It can be observed from Figure 9.3 that lower values of permeability predicted by the numerical model correspond to lower values of porosity. In addition, it can be seen that when porosity is reduced by 50%, i.e. from 2% to 1%, there is a decrease in permeability of approximately one order of magnitude with respect to the initial value of $1 \times 10^{-16} \text{ m}^2$.

If the porosity results of Tests I and II are compared, where high value of elastic modulus was used (i.e. 3 GPa), it can be seen that the residual porosity available for flow at the end of both simulations is 0.91% and 0.65%, respectively. This means that the reduction of the Langmuir pressure by 80% resulted in 28% difference in residual porosity values.

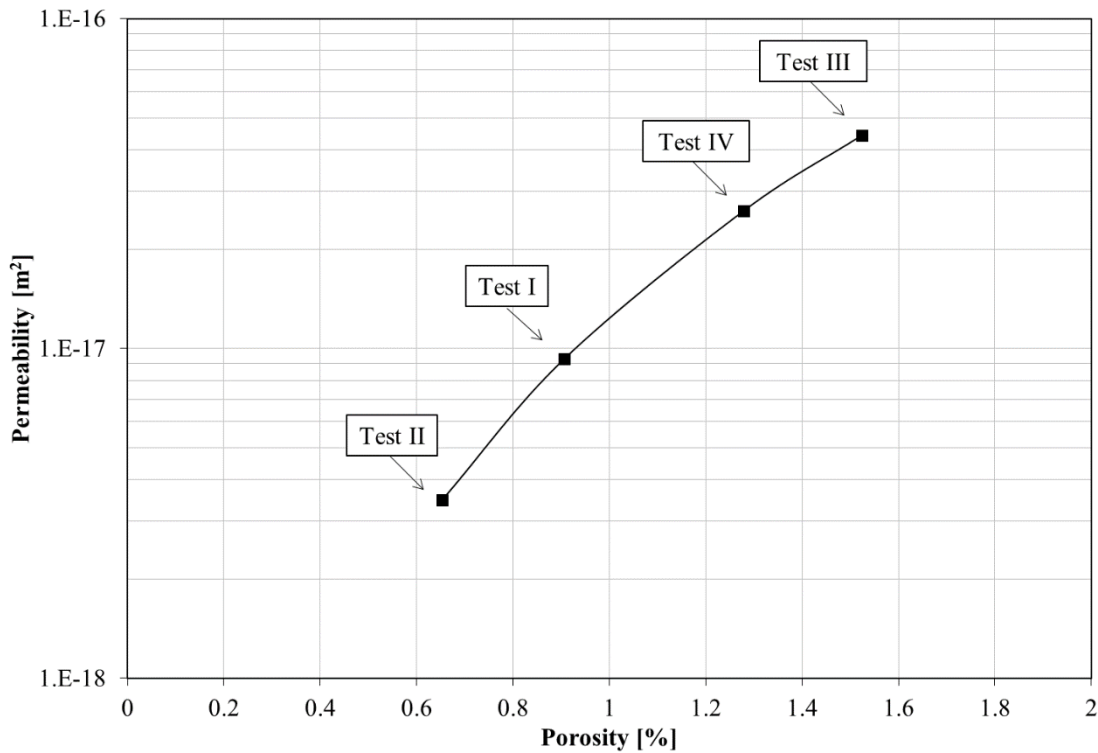


Fig. 9.3. Permeability and porosity values predicted by the numerical model at the end of Tests I to IV.

The residual porosity values for Tests III and IV, where low value of elastic modulus was used (i.e. 0.6 GPa), are 1.52% and 1.28%, respectively. Hence, the reduction of the Langmuir pressure by 80% in those cases led to 16% difference in porosity values. By comparing the abovementioned results of Tests I and II with Tests III and IV, it can be seen that more deformable coal samples are less affected by the value of the Langmuir pressure.

Cases where the Langmuir pressure values were kept constant and only the elastic modulus values were different, i.e. Test I versus Test III and Test II versus Test IV (see Tables 9.1 and 9.2), can also be compared to assess the role of the reduced elastic modulus on the difference in residual porosity values.

In particular, decreasing the elastic modulus value by 80% and keeping the Langmuir pressure high (i.e. 5 MPa), the difference in residual porosity values between Tests I and III is 41%. For the cases where the Langmuir pressure is low (i.e. 1 MPa), such difference in porosity values between Tests II and IV is 49%.

Based on the abovementioned, it can be concluded that the reduction of the elastic modulus value of 80% has a more significant impact on the residual porosity values determined at the end of the simulation than the same reduction of the Langmuir pressure value.

9.3.3. Gas Breakthrough

In order to assess the influence of permeability change with an increase in the injection pressure on the gas transport through the coal sample, pressure profiles across the domain at different times of each test are presented and discussed in this section. Pressure profiles are evaluated at different times of each simulation. In particular, pressure across the domain is analysed after 200 seconds, 1500 seconds and 3600 seconds (1 hour) for all tests which represent the time when the injection pressure was raised to 1 MPa, 5 MPa and 7.5 MPa, respectively. In addition, results obtained at the end of each simulation are presented. Where possible, pressure profiles evaluated at the end of the every hour are also included. However, in cases where the steady state was achieved quickly, i.e. before the end of the simulation, the results for later stages were not presented. This was done in order to keep the results presented in the figures concise and easy to interpret.

The profiles of CO₂ in the domain evaluated at different times for Tests I to IV are presented in Figures 9.4 to 9.7, respectively.

The results for Test I (Fig. 9.4), where high values of both the elastic modulus and the Langmuir pressure were prescribed, illustrate that the CO₂ within the domain advanced by 0.06 m, 0.33 m and 0.67 m after 200 seconds, 1500 seconds and 1 hour, respectively. After 2 hours, the gas has already reached the outlet boundary but the steady state was achieved after 3 hours.

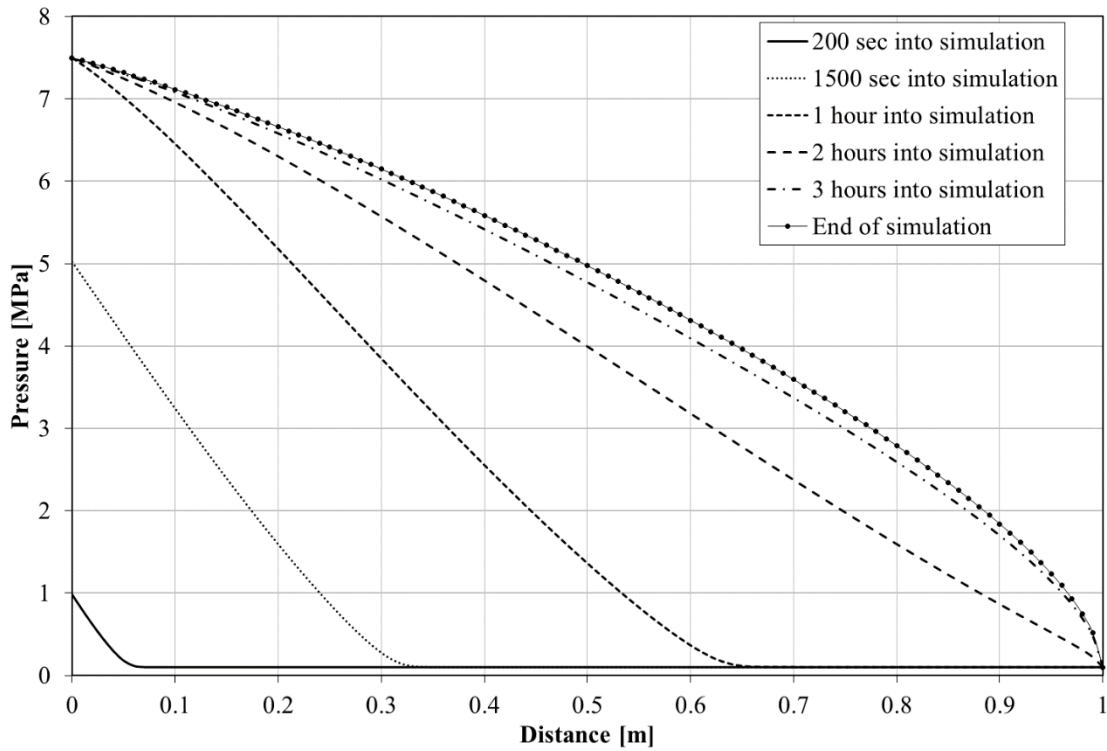


Fig. 9.4. Profiles of CO₂ in the domain at different times predicted by the numerical model for Test I ($E=3$ GPa, $P_L=5$ MPa).

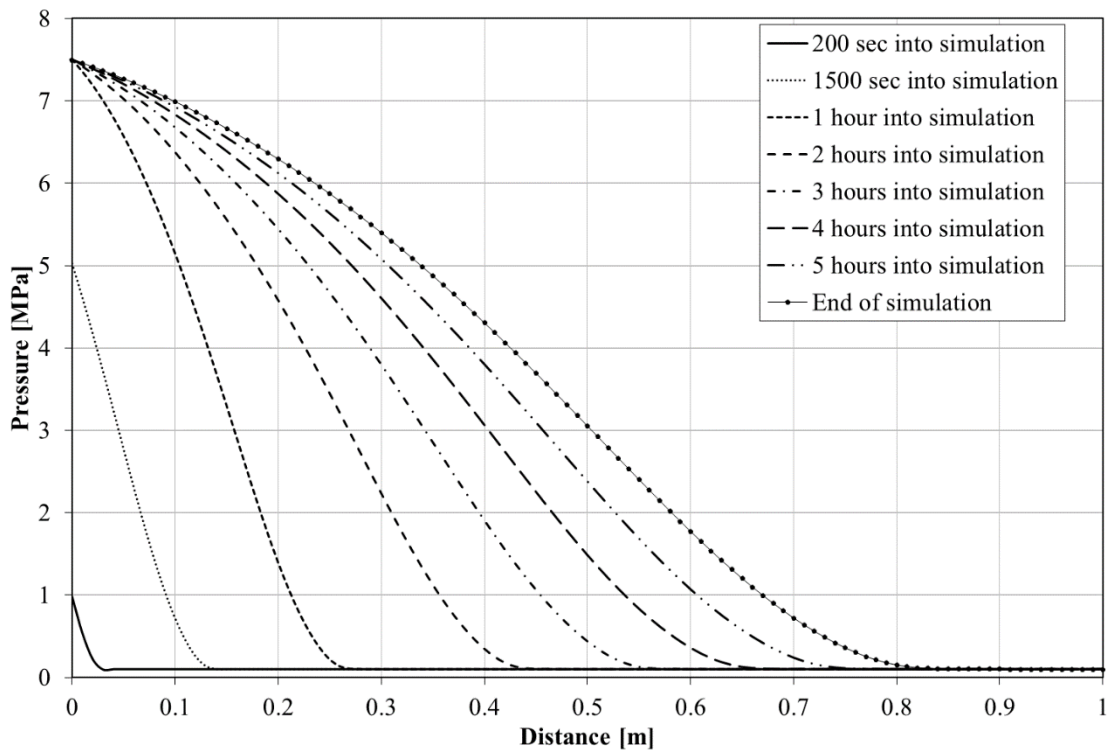


Fig. 9.5. Profiles of CO₂ in the domain at different times predicted by the numerical model for Test II ($E=3$ GPa, $P_L=1$ MPa).

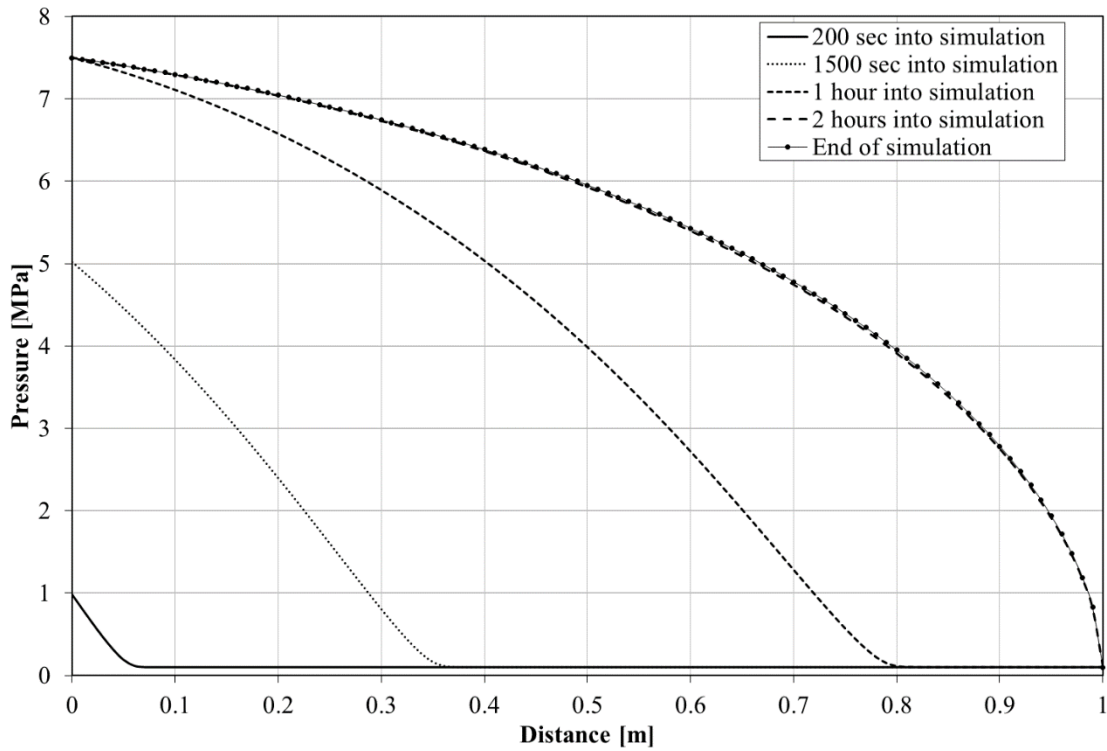


Fig. 9.6. Profiles of CO₂ in the domain at different times predicted by the numerical model for Test III ($E=0.6$ GPa, $P_L=5$ MPa).

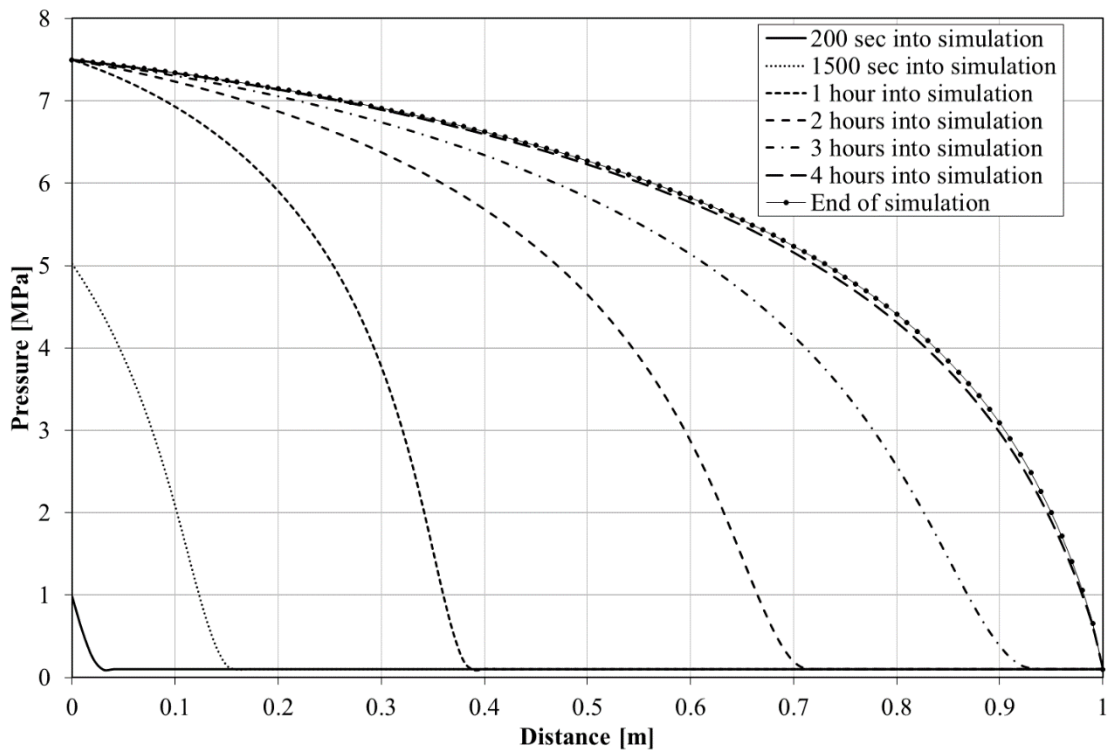


Fig. 9.7. Profiles of CO₂ in the domain at different times predicted by the numerical model for Test IV ($E=0.6$ GPa, $P_L=1$ MPa).

In Test II (Fig. 9.5), where the reduced value of the Langmuir pressure was prescribed, the rate of advance of CO₂ was slower compared to Test I. In particular, after 200 seconds, 1500 seconds and 1 hour CO₂ progressed up to 0.03 m, 0.13 m and 0.27 m in the domain, respectively. After 4 hours, the gas reached 0.67 m in the domain which is 4 times longer compared to Test I for the same distance. In addition, the steady state was not achieved by the end of the simulation.

The difference in the results between Tests I and II is caused by the value of the Langmuir pressure. Prescribing a reduced value of the Langmuir pressure in Test II led to a more significant swelling of the coal at an early stage of the simulation compared to Test I. This caused a rapid reduction in permeability in Test II (see Fig. 9.2) which restricted the flow of gas within the domain. Since in both cases the value of the elastic modulus was high, the mechanical deformation of the coal was dwarfed by the CO₂ induced swelling.

Figure 9.6 illustrates the pressure profiles at various times in the domain for Test III, where only the value of the elastic modulus was reduced. It can be observed that CO₂ in the domain reached 0.06 m, 0.36 m and 0.8 m after 200 seconds, 1500 seconds and 1 hour, respectively. After 2 hours, the steady state within the domain was achieved. If compared to Test I, it can be seen that the results at 200 seconds are similar. This is related to the permeability evolution for both cases, as observed in Figure 9.2, where the curves for Tests I and III were closely matched up to 200 seconds when the injection pressure reached 1 MPa. With further increase in time, i.e. pressure, both curves showed distinct behaviour (see Fig. 9.2) leading to different gas breakthroughs between the tests. Based on such observation it can be concluded that the effect of the reduced elastic modulus in Test III compared to Test I allowed larger mechanical deformation of the sample. Consequently, less reduction in porosity due to CO₂ induced swelling led to easier breakthrough of the gas across the domain.

The results presented for Test IV (Fig. 9.7), where both the reduced values of elastic modulus and Langmuir pressure were prescribed, show that after 200 seconds, 1500 seconds and 1 hour CO₂ advanced by 0.03 m, 0.16 m and 0.39 m, respectively. The steady state was achieved after 4 hours of constant gas injection which is 2 times longer than in Test III. It can be noticed that the results evaluated at 200 seconds are

comparable to the results for Test II which is related to almost identical permeability evolution for both cases at early stages of the simulation. Further increase in pressure allowed the CO₂ to advance faster through the domain in Test IV due the permeability rebound related to the reduced value of elastic modulus (see Fig. 9.2).

9.4. Conclusions

In this chapter, a series of numerical simulations was conducted to investigate the response of coal samples under high-pressure gas injection. The main purpose was to assess the effect of the elastic modulus and the parameter defining the swelling of the coal with respect to pressure, on coal response subject to supercritical CO₂ injection. By presenting four scenarios, defined by different combinations of the elastic modulus and the Langmuir pressure values, the assessment of the permeability evolutions, the residual porosity values at the end of each simulation and the pressure profiles across the domain was conducted.

It was demonstrated that the permeability response of coal samples with high value of elastic modulus is highly affected by the CO₂ sorption induced strain. In such cases, swelling strain dwarfs the elastic deformation of coal subject to pressure injection leading to continual decrease in permeability with an increase in gas pressure. Such effect is more pronounced in coal samples that exhibit large swelling strain at low pressures reducing the available porosity for flow. On the other hand, the results of numerical simulation also suggested that coal samples that are less resistant to deformation under the applied stress are less affected by the coal swelling and can restore part of its permeability after the initial decrease caused by the sorption induced swelling.

Based on the permeability results obtained, residual porosity values at the end of each simulation scenario were calculated to assess and quantify the impact of permeability reduction due to sorption induced swelling on the porosity. For the simulation conditions considered, it was found that the reduction in porosity of 50% led to a decrease in predicted permeability by approximately one order of magnitude.

By presenting the gas pressure profiles at different times of each simulation, an effect of the permeability reduction on the gas transport in coal samples was investigated. It was generally shown that the permeability predictions and the gas progress through the sample are highly dependent on the value of the elastic modulus and the Langmuir pressure. In particular, coals with low elastic modulus would be less influenced by the swelling strain and would exhibit elastic response under gas injection allowing good access of the gas molecules into the porous system of the coal. Moreover, coals that swell gradually over the range of pressures would only lose a smaller portion of its injectivity at early stages of CO₂ injection, compared to coals that swell significantly at low pressures, allowing quick breakthrough of gas through the sample.

Hence, based on the work presented it can be concluded that coals that are easily deformed during gas injection and at the same time exhibit gradual swelling with an increase in gas pressure, are favourable for sequestration purposes. Therefore, it is suggested that it would be important to take into account the damaging effect of carbon dioxide adsorption on the coal structure which makes coals easier to deform as well as to understand the swelling pattern of the coal in order to assess the carbon dioxide sequestration potential in coal seams.

The numerical simulations presented are unlike any others previously undertaken, according to the author's knowledge. Therefore, it can be said that the findings have increased the available knowledge base. In particular, this study demonstrated that the interactions between the coal and the carbon dioxide are complex. As a result of this study, it can be concluded that coupling between the gas flow, its reaction with the coal and the deformation of the coal is required to understand the process of carbon dioxide sequestration in coal.

9.5. References

Bieniawski, Z.T., 1968. The effect of specimen size on compressive strength of coal. *International Journal of Rock Mechanics and Mining Sciences*, 5, pp. 325-335.

Chung, T.-H., Ajlan, M., Lee, L.L. and Starling, K.E. 1988. Generalized multiparameter correlation for nonpolar and polar fluid transport properties. *Industrial and Engineering Chemistry Research*, 27, pp. 671-679.

- Connell, L.D., Mazumder, S., Sander, R., Camilleri, M., Pan, Z. and Heryanto, D. 2016. Laboratory characterisation of coal matrix shrinkage, cleat compressibility and the geomechanical properties determining reservoir permeability. *Fuel*, 165, pp. 499-512.
- Durucan, S., Ahsan, M. and Shi, J.Q. 2009. Matrix shrinkage and swelling characteristics of European coals. *Energy Procedia*, 1(1), pp. 3055-3062.
- Gensterblum, Y. 2013. *CBM and CO₂-ECBM related sorption processes in coal*. Ph.D. Thesis, RWTH Aachen University, Germany.
- Medhurst, T.P. and Brown, E.T. 1998. A study of the Mechanical Behaviour of Coal for Pillar Design. *International Journal of Rock Mechanics and Mining Sciences*. 35(8), pp. 1087-1105.
- Millington, R.J. and Quirk, J.M. 1961. Permeability of porous solids. *Transactions of the Faraday Society*, 57, pp. 1200-1207.
- Palmer, I. 2009. Permeability changes in coal: Analytical modeling. *International Journal of Coal Geology*, 77(1-2), pp. 119-126.
- Palmer, I. and Mansoori, J. 1998. How Permeability Depends on Stress and Pore Pressure in Coalbeds: A New Model. *Society of Petroleum Engineers Reservoir Evaluation and Engineering*, 1(6), pp. 539-544.
- Pan, Z., Connell, L.D. and Camilleri, M. 2010. Laboratory characterisation of coal reservoir permeability for primary and enhanced coalbed methane recovery. *International Journal of Coal Geology*, 82(3-4), pp. 252-261.
- Peng, D.Y. and Robinson, D.B. 1976. A new two-constant equation of state. *Industrial and Engineering Chemistry Fundamentals*, 15(1), pp. 59-64.
- Ranathunga, A.S., Perera, M.S.A., Ranjith, P.G. and Bui, H. 2016. Super-critical CO₂ saturation-induced property alterations in low rank coal: An experimental study. *The Journal of Supercritical Fluids*, 109, pp. 134-140.
- Viete, D.R. and Ranjith, P.G. 2006. The effect of CO₂ on the geomechanical and permeability behaviour of brown coal: Implications for coal seam CO₂ sequestration. *International Journal of Coal Geology*. 66, pp. 204-216.
- White, C.M., Smith, D.H., Jones, K.L., Goodman, A.L., Jikich, S.A., Lacount, R.B., Dubose, S.B., Ozdemir, E., Morsi, B., Schroeder, K.T. 2005. Sequestration of Carbon Dioxide in Coal with Enhanced Coalbed Methane Recovery – A Review. *Energy&Fuels*, 19 (3), 659-724.

10

Conclusions and Suggestions for Further Research

10.1. Introduction

The work presented in this thesis aimed in general to provide an improved understanding of the coal response and processes related to gas injection with regards to carbon sequestration process through both experimental and numerical investigations. Specifically the tasks as stated in the introduction were to:

- Study the sorption behaviour of both subcritical and supercritical carbon dioxide in unconfined coal samples of different sizes including powdered and intact coal specimens.
- Investigate the effect of subcritical and supercritical carbon dioxide sorption on the deformation behaviour and failure of coals using uniaxial compressive tests.
- Study the coal response under isotropic confining conditions to continuous injection of subcritical and supercritical gases.
- Analyse the effect of carbon dioxide sorption induced swelling on the ability of coal to allow gas flow.
- Assess the effect of nitrogen injection on the reversibility of CO₂ sorption induced changes.
- Advance a coupled thermo-hydro-chemo-mechanical (THCM) model to include the appropriate constitutive relationship for single porosity coal deformation induced by physical and chemical coal-gas interactions.
- Apply and validate the numerical model using experimental results.
- Perform numerical investigations under a series of conditions of practical importance for carbon dioxide sequestration in coal.

It is claimed that each of these tasks has been completed.

The summary of the developments and the achievements related to the tasks of this thesis will be broadly presented in two sections (10.2 and 10.3) with respect to i) Laboratory-scale experimental study and ii) Numerical study. Following this, conclusions and contributions of both the experimental and numerical studies will be given in Section 10.4. The overall conclusions of the thesis will be discussed in Section 10.5 and suggestions for further work will be made in section 10.6.

10.2. Summary of the Laboratory-scale Experimental Study

A state of the art literature review presented in Chapter 2 highlighted that there was a limited number of studies related to the dynamic response of high-rank anthracitic coals to the injection of supercritical gases. Further to this, majority of the studies focused on investigations related to the behaviour of powdered coal samples as well as neglecting the effect of gas expansion and related thermal effects on the coal behaviour.

An existing experimental facility, presented in Chapter 4, was used to investigate the sorption behaviour and reactive transport of gases under high pressure conditions. The facility comprises of three main sections: i) a manometric sorption apparatus, ii) a triaxial core flooding system and iii) the ancillary system including the gas supply unit and gas analysing unit. However, as one of the main objectives of this thesis was to investigate the response of coal samples subject to supercritical carbon dioxide injection, stable and isothermal flow of CO₂ was difficult to achieve with the existing equipment.

Therefore, a new gas pressure supply unit was implemented within the scope of this thesis allowing the injection of gases up to 25.9 MPa. Furthermore, to allow injection of high gas pressures within the system and to replicate the in situ conditions, the existing system was modified to allow the control of the backpressure. Such advancement of the laboratory facility, presented in Chapter 4, is considered to be an important advantage as it provides a platform for pulseless, controlled, high-flow and temperature-controlled injection of gases under high pressures.

Before the experimental investigation of coal response to gas injection, a detailed characterisation of the coal samples collected from South Wales coalfield was also conducted in Chapter 4. In particular, coal samples from the East Pit East Opencast Coal site (Black Diamond) from 150 m depth and from the Aberpergwm coal mine (9ft seam) from 550 m depth were used in this study. The results showed that both coals of this study were high rank coals with 90% of carbon content and bulk density of 1376 kg/m³. As both coals of this study are of the same rank and from the same coalfield, however from different depths and locations (16.4 km apart), it recognised that data sets obtained on such coals provide new information for the South Wales coal.

Sorption measurements of CO₂ were conducted on powdered and intact samples of both coals of this study for gas equilibrium pressures up to 8.1 MPa. The experimental data

obtained in terms of pressure decay curves, presented in Chapter 5, were used to calculate the excess and absolute sorption amounts of CO₂ sorption. It was found that sorption capacities of both powdered and intact samples from Aberpergwm mine were lower than sorption capacities of Black Diamond samples. This was particularly observable for intact samples where the maximum difference was 58%. It was also observed that there was a negligible difference in sorption capacities among the Black Diamond samples of different sizes, while the 9ft Aberpergwm coal showed a non-linear decrease in sorption capacity with an increase in sample size.

Moreover, using the experimentally measured pressure decay curves, the kinetics of gas sorption was also analysed and presented in Chapter 5. The results revealed that the rate of CO₂ sorption varies with an increase in sample size. For instance, smallest fractions of both coals showed identical behaviour where 95% of the sorption was achieved in the first 2 hours of each injection step. Intact samples of Black Diamond and 9ft Aberpergwm coal required up to 80 hours and 250 hours to complete the sorption process at each injection step, respectively.

The above described behaviour and differences between the two coals of this study were attributed to different fracture interconnectivity of the respective coals resulting from different burial depths where deeper coal seams may have less developed fracture network as a result of geological effects. In addition, grinding of coals is known to increase the total porosity available to gases and hence, crushed samples showed higher capacity and faster sorption than the intact samples. Overall, this study has provided new insights into the sorption behaviour of samples of various sizes from different depths and locations exposed to both subcritical and supercritical CO₂ suggesting that coals that had the fastest sorption resulted in the highest sorption capacity.

In order to assess the effect of both subcritical and supercritical CO₂ sorption on the coal structure and deformation properties, both non-saturated (natural) and CO₂ saturated coal samples from both locations were tested via uniaxial compression to determine the elastic moduli and unconfined compressive strengths of the respective coals in Chapter 6. Investigation indicated that non-saturated samples show brittle behaviour while CO₂ sorption enabled coals to exhibit ductile behaviour. Saturation with supercritical CO₂ at 8.5 MPa resulted in a maximum reduction of uniaxial

compressive strengths and elastic moduli of both coals by 80% compared to the values obtained on non-saturated samples. Through comparison with the literature data on low rank coals, it was shown that both subcritical and supercritical CO₂ sorption causes more detrimental effect on the deformation parameters of high rank coals.

By visually inspecting the failure patterns of tested specimens, as presented in Chapter 6, it was indicated that non-saturated samples fail predominantly through axial splitting while the failure of CO₂ saturated samples occurs through a network of shear fractures. As a result, the post-failure sieve analysis showed that CO₂ saturated samples disintegrated on smaller particles than non-saturated samples. In particular, there were up to five times more particles from subcritical CO₂ saturated samples and up to six times more particles from supercritical CO₂ saturated samples passing through each sieve than particles from non-saturated samples. The above work proved that both subcritical and supercritical CO₂ sorption affects the coal structure and elastic response to uniaxial compression. The presented work on high rank anthracitic coal samples as well as the samples from the South Wales coalfield is the first within the research field.

The results of a sequential injection of helium, carbon dioxide and nitrogen gases in Black Diamond samples under confined conditions were presented in Chapter 7. In those experiments, the coupled effects of variations induced by non-sorbing (helium) and sorbing gas (carbon dioxide) injections on the flow behaviour and deformation response of coal samples were investigated in more detail. Moreover, thermal changes induced by the flow of gases and their impact on the response of coal samples were assessed. The impact of N₂ sorption on the reversibility of the CO₂ sorption induced changes was also studied.

The observations made during helium injection suggested that flow rates, i.e. permeability, increase with a positive change in injection pressure as a result of the mechanical expansions of the pores available for flow. Findings of the carbon dioxide injections highlighted the effect of sorption induced swelling on the flow behaviour. In general, it was found that during the initial period of CO₂ injection, measured flow rates decreased in all samples where the recovery in flow rates was only achieved by increasing the gas injection pressure.

By re-introducing helium after treating samples with CO₂, the effect of CO₂ sorption induced changes on measured flow rates was assessed. It was found that CO₂ swelling decreased the ability of coal to conduct helium by 50-66%. Moreover, introduction of nitrogen for a period of 48 hours appeared to be negligible on the reversal of changes induced by CO₂ sorption which was confirmed by observing that the helium flow rates before and after N₂ injection were the same. This shows that exposure of anthracite samples to N₂ does not reverse the changes induced by CO₂ sorption.

Coal deformation in radial and axial directions was found to be more than one order of magnitude higher during carbon dioxide injection than helium injection. In addition, swelling in the direction perpendicular to the gas flow than in the direction parallel to it was more pronounced during supercritical CO₂ injection than subcritical CO₂ injection. Moreover, by comparing the swelling behaviour of samples subjected to injection of subcritical and supercritical CO₂, the results obtained highlighted that samples under low gas pressures exhibit significantly lower global volumetric swelling. In other words, sorption of CO₂ under subcritical conditions (up to injection pressures of 2.65 MPa in this work) induced predominantly internal swelling reducing the measured flow rates, whereas significant observable volumetric swelling appeared only at the end of the experiments. Conversely, injection of supercritical CO₂ induced significant global volumetric swelling of the samples throughout the lifespan of the experiments. Such observation provided new insights into the coal volumetric behaviour and the response of its internal structure to CO₂ injection under different pressures.

Temperature sensors were positioned close to the inlet and the outlet of the samples to assess the thermal changes induced by the gas flow. Prior to this study no attempts have been made to investigate gas flow induced changes on coal behaviour, despite the fact that it is widely acknowledged that CO₂ cools down upon expansion. Results revealed that helium flow did not cause any thermal changes while carbon dioxide flow induced temperature drop across the samples in which both the pressure gradient and high flow rates were established. In particular, a maximum temperature drop of 6.8°C was observed as a result of the adiabatic gas expansion, i.e. Joule-Thomson effect. However, it was recognised that such temperature drop could be even higher within the sample, as the measurements were affected by the difference in thermal properties of the confining sleeve, PTFE tape and the coal samples.

By conducting analysis of the coal response during the temperature change period, it was observed that samples that experienced thermal changes due to the gas expansion showed more pronounced change in flow rates and measured volumetric expansion than samples not experiencing thermal changes. In other words, there was a substantial recovery in measured flow rates during non-isothermal CO₂ injection compared to isothermal CO₂ flow. To the author's knowledge, these are the first non-isothermal experimental results on gas induced thermal changes within the coal samples.

10.3. Summary of the Numerical Study

A coupled gas chemical-mechanical modelling investigation was undertaken by advancing the coupled numerical tool COMPASS. The model was developed to include the elastic response of coal subject to injection of sorptive gases that induce coal swelling under isothermal conditions. The formulation was implemented in a coupled THCM model.

The developed model, presented in Chapter 3, considers the behaviour of the material at two levels, i.e. microstructure and macrostructure. Using such approach, the effects of physical and chemical interaction of gases with coal and their combined effect on the resulting permeability can be modelled. In particular, when the sorbing gas is injected into the coal, increase in gas pressure increases the porosity available for flow due to mechanical expansion of the sample. However, at the same time, the sorption induced swelling reduces the porosity of the system. Hence, these competitive effects define the loss or gain in porosity and consequently, permeability of the system. As the previous model used analytical expressions to describe the porosity and permeability evolutions in the coal system, coupling the gas module with the mechanical model and extending the latter one to include the swelling of porous material subject to gas injection was regarded as an important extension.

A numerical approximation was adopted to solve the series of governing equations. A finite element solution was employed for spatial discretisation based on the Galerkin weighted residual method, while the temporal discretisation was achieved via a finite difference scheme based on a mid-interval backward-difference time-stepping algorithm.

A number of verification exercises were conducted in Chapter 8 to assess the correctness of the implementation of the theoretical and numerical developments in the model. The benchmarks for the verification tests were provided by analytical or alternative solutions presented in the literature. The ability of the numerical model to predict the steady state gas concentration profile for the flow of a highly compressible fluid was verified considering the benchmark provided by the results of an analytical solution. In addition, the results of an analytical solution were used to assess the capability of the model to predict the elastic response of the sample under compressive stress. The results of two alternative models presented in the literature compared with the results of the model predicting the permeability evolution during both sorbing and non-sorbing gas injections were also shown. The comparisons indicated the mathematical correctness of the approach used in this study. Hence, confidence was built in the theoretical and numerical implementation for further applications and explorations of the developments provided in the model.

Validation of the developed model was also conducted in Chapter 8 using high resolution experimental data obtained on Black Diamond coal as a part of this study. The experimental data presented in Chapter 7 were used to calculate the permeability evolution for two injection scenarios, i.e. helium injection and subcritical carbon dioxide injection. The developed numerical model was then used to simulate both laboratory scale injection scenarios. Comparisons with the experimental results showed that the numerical models represented the mechanisms involved correctly. However, a number of limitations were highlighted.

Firstly, the simplifications introduced into the boundary conditions of the numerical model compared to experimental conditions were recognised to be the cause of the discrepancies at the initial stage of the simulation. In addition, it was noted that the material parameters experimentally determined on samples that do not represent the conditions of the sample used in the simulation and arbitrarily chosen material parameters based on the literature survey could have had an impact on the simulated behaviour.

The simplifications and assumptions introduced into the development of the deformation model were also recognised as factors affecting the simulated response of

coal subject to gas injection. In particular, treating coal as a single porosity medium and not taking into account gas sorption as a kinetic process may lead to differences between the experiments and the model. Moreover, assuming coal as an elastic homogeneous medium with no preferential swelling orientation might not completely represent the real behaviour of the coal under gas injection. It is widely established in the literature that coal is a heterogeneous porous medium with anisotropic response during gas injection. These findings imply that further development and testing of the model is required in the future work. Nonetheless, the predicted trends for the single-component system were largely reasonable giving confidence to the application of the model.

The response of a larger coal sample, compared to the one used in the validation exercise, was investigated applying the validated model in Chapter 9. The coupled chemical gas-mechanical behaviour of the coal subject to supercritical carbon dioxide injection was studied to assess the role of both the elastic modulus and the parameter defining the coal swelling on the coal response. Based on the simulation results, it was demonstrated that coals that are difficult to deform and that swell significantly at low gas pressures exhibit a rapid decrease in porosity and permeability during the gas injection process. Consequently, the gas flow across the domain is restricted minimising the amount of gas that can be injected within the sample.

Hence, the conclusion was made that coals that are less resistive to deformation under applied stress and exhibit gradual swelling over the injection pressure range considered are favourable for carbon sequestration purposes. In such coals, sorption induced swelling is expected not to significantly dominate over the mechanical expansion of the pore network during gas injection, allowing higher and faster injection of CO₂. Hence, following the experimental findings presented in Chapter 6, which clearly suggested the damaging effect of carbon dioxide sorption on coal's deformation parameters, it was concluded that this phenomenon could be beneficial for carbon sequestration purposes.

Overall, the analysis of the results provided valuable insights into the role of the parameters responsible for coal behaviour during supercritical carbon dioxide injection. Equally important, it was demonstrated that the coupling between the gas flow induced

reactions and the deformation of the coal is essential to understand the processes related to carbon sequestration.

10.4. Conclusions of the Experimental and Numerical Studies

The following conclusions based on the experimental and numerical studies performed can be drawn:

- The results of the gas sorption behaviour in samples of different sizes provided important information on the sorption capacity and the kinetics of sorption both for subcritical and supercritical carbon dioxide injection up to 8.5 MPa. The results demonstrated that well-fractured coal samples exhibited higher sorption capacity and require less time to reach equilibrium with the injected gas compared to the less fractured samples.
- In addition, the sorption behaviour of samples from the deeper coal seam was found to be size-dependent. The presented data is considered to be essential for the assessment of the carbon dioxide sequestration potential of the South Wales coal seams.
- The investigation of the uniaxial compression on the non-saturated and carbon dioxide saturated samples has provided a valuable insight into the effect of CO₂ sorption on the coal structure. It was demonstrated that the sorption of CO₂ non-linearly reduces the uniaxial compressive strengths and elastic moduli of both coals of this study with respect to gas pressure, reaching 80% reduction with supercritical CO₂ injection at 8.5 MPa, compared to the value obtained on non-saturated samples. Such data-set is produced for the first time for high-rank coals (anthracites) as well as for the South Wales coals.
- It was found that CO₂ sorption affects the failure mode of the coals and the resulting post-failure grain sizes suggesting that CO₂ saturated coal samples become more ductile through enhancement of the existing fractures and inducement of the new ones.
- The study of gas transport behaviour in coal has provided a notable insight into the coal response during both isothermal and non-isothermal injection of

subcritical and supercritical gases. By continuously monitoring the pressures at the inlet and the outlet of the studied samples, flow rates, temperature across the samples as well as the radial and axial displacements, a more detailed resolution of data has been provided compared to previous examples in the literature.

- It was found that the CO₂ sorption induced swelling is non-reversible, even when using nitrogen as a displacement gas, decreasing the ability of coal to conduct gases by 50-66%.
- It was observed that sorption of CO₂ within the low pressure (subcritical) region induces negligible observable volumetric swelling suggesting that coal predominantly swells internally reducing the porosity available for flow. On the other hand, sorption of CO₂ at high pressures induces significant observable swelling of samples.
- During the high-flow CO₂ injection, it was demonstrated that the expansion of CO₂ induced by pressure gradient reduces the temperature of the system affecting the response of the coal. The non-isothermal flow proved to have a positive effect on the flow rates enhancing the flow of gas with an increase in gas pressure. Such data provided new experimental evidence on the behaviour of coal samples both under subcritical and supercritical CO₂ injection under variable temperature conditions. To the author's knowledge, the thermal effects resulting from the CO₂ injection are the first ones experimentally reported with regards to carbon sequestration in coal.
- Verification and validation of the developed model provided further confidence in the accuracy of the numerical implementation of the governing equations as well as the validity of the model under the conditions of the benchmarks considered.
- A series of laboratory scale simulations for larger coal sample showed that the deformability of the coal and its affinity to CO₂ with respect to gas pressure define its potential for carbon sequestration. Based on the results of the analysis, it can be concluded that the effect of the CO₂ sorption induced swelling on the permeability reduction decreases with an increase in elasticity of the coal suggesting that the reduction of deformation parameters by CO₂ sorption is

beneficial for the permeability evolution of coal samples during CO₂ sequestration process.

10.5. Overall Conclusions of the Thesis

In today's world, where the anthropogenic emissions of greenhouse gases are proved to be significantly contributing to the warming of the climate system, carbon sequestration has been identified as a crucial technology capable of delivering significant emissions reductions. Carbon dioxide storage in coal is an appealing way of addressing the increasing levels of CO₂ in the atmosphere as it simultaneously enhances the recovery of natural gas which can offset the costs for capture, transportation and storage. However, as mentioned in Chapter 1, the reduction of coal permeability with CO₂ injection associated with coal swelling is one of the main technical issues that should be solved before putting a large-scale CO₂ sequestration project into practice.

Experimental and numerical investigations have been performed in this thesis to enhance the understanding of the coal-gas interactions associated with the CO₂ sequestration in coals.

Experimental results of the sorption behaviour of coals from two locations in the South Wales coalfield showed high affinity to CO₂ with a potential to store up to 1.94 moles of CO₂ per kilogram of coal. This is clearly a positive finding from a carbon sequestration perspective as it is proving a high storage potential of anthracite coals.

For the first time, it was experimentally demonstrated for anthracite coals that CO₂ sorption reduces the deformation properties of coals up to 80% making them more ductile and less resistive to deformation under applied stress. In addition, comparisons of the failure patterns as well as the post-failure sieve analysis of non-saturated and CO₂ saturated coals suggested that the CO₂ sorption affects the coal structure by enhancing the propagation of existing fractures and inducing new ones. Both of these findings are beneficial for the carbon sequestration process as the former one allows easier deformation of coals and widening of the flow paths upon CO₂ injection. On the other hand, the latter one provides enhancement of the existing flow paths and creation of

new ones increasing the volume of the voids responsible for conducting the flow of CO₂.

It was experimentally shown in this study that high flow of CO₂ under an established pressure gradient causes thermal changes of the system. Following the previous findings from the literature, this is a favourable condition as it is widely established that the storage capacity of coals to CO₂ is inversely proportional to the temperature of the coal system. Furthermore, the experiments have shown that the recovery in permeability during CO₂ injection, after an initial drop caused by coal swelling, is more pronounced in coals experiencing thermal changes than in samples under isothermal flow. In relation to that, it was suggested that combined effects of thermally induced stresses within the coal, thermal contraction of the coal and coal weakening under increased sorption could have increased the void volume responsible for gas flow and consequently, increased permeability which is advantageous for the CO₂ sequestration.

The capability of the existing numerical THCM model was further advanced to include the coupled behaviour of coal elastic deformation during gas flow and sorption processes. Application of such model provides further insights into the complex interactions between coal and carbon dioxide by delivering answers to questions related to long term behaviour of CO₂ sequestration in a cheaper and less time-consuming way compared to experimental and in situ investigations.

Through such application in this work, it was shown that the elastic modulus of the coal subjected to uniaxial conditions has a significant impact on the coal response to CO₂ injection. Coals less resistive to deformation under gas injection are less likely to experience significant reduction in permeability due to coal swelling. Even in conditions of rapid coal swelling during early stages of CO₂ injection, such coals could experience recovery in the permeability at later stages. This investigation suggested that the reduction of coal's deformation properties with CO₂ sorption could be beneficial to the injectivity of the coal seams.

Overall, it is claimed that a comprehensive experimental and numerical research presented in this work provides new and positive insights and findings in relation to carbon sequestration in coals giving confidence that the storage of CO₂ in deep, unmineable coalbeds could be technically feasible. However, throughout this thesis, an

attention has been drawn to the need for continued experimental and computational research and development as many of the potential environmental and technical problems still remain unanswered.

10.6. Suggestions for Further Research

The research findings presented in thesis have highlighted a number of potential avenues for future research works. The suggestions for further research are described below.

First and foremost, the maximum gas pressure applied in this study was up to 8.5 MPa to study the effect of supercritical CO₂ on coal behaviour. As the new supply system allows pulseless and controlled injection of gas pressures up to 25.9 MPa, it is suggested that the coal-gas interactions can be further studied at higher gas pressures representing injection conditions at higher depths.

Second, injection of mixed gases into coals would provide valuable information of coal-gas interactions which is currently lacking within the research area. It is widely acknowledged that in the real case scenarios, various gases mixed with CO₂ would also be sequestered while enhancing the production of CH₄.

It is also recognised that studying the inclusion of the water content and associated couplings of hydraulic and gas behaviour can be further studied as the current work focused only on the behaviour of a dry system. This could then include the effect of the dissolution of gases within the liquid phase and the changes in the pH of the system on the sorption behaviour of coal samples. In addition, studying the effect of dissolution of minerals present in the coals under lowered pH of the overall system on the transport properties of coals is also suggested to be studied. This would allow further insights into the behaviour of coals under real conditions as it is widely acknowledged that coal seams targeted for sequestration are saturated with water.

Furthermore, sorption behaviour and kinetics should be investigated under confined, triaxial conditions. Under the same conditions, the effect of CO₂ saturation and its duration on the deformation parameters of coals should be also studied. In relation to that, studying the structure of coals exposed to CO₂ would provide further assessment of

the micro-structural changes induced by CO₂ sorption. As the current work related to such phenomena has been predominantly conducted on unconfined samples with arbitrarily chosen saturation times, such research would allow further insights into the coal behaviour under the conditions expected underground and the implications related to the stability of the seams over time.

As experimentally demonstrated for the first time in this thesis, Joule-Thomson effect can be significant during high-flow CO₂ injection inducing temperature changes within the system. Following previous literature findings, changes in temperature might have implications on both the sorption and the flow properties as well as the effect on the overall stability of the coal seams and the state of the water in the coal reservoir. Therefore, further research is suggested to focus on the effect of such thermal changes on the sorption behaviour of coals under dry and saturated conditions.

It is also suggested that confined conditions expected to represent the real underground conditions, such as zero lateral strain and constant volume conditions, should be achieved in the experiments to understand the response of coal during the high-pressure gas injection. Research presented in the scope of this thesis demonstrated that significant coal volumetric swelling is a major restraint to achieve such conditions with the current laboratory facility. Achieving such conditions and studying the behaviour of coal subject to high pressure gas injection would then assist with the validation of the numerical models.

Despite the fact that data sets related to the behaviour of coals of different rank to the injection of various gases are continuously increasing, it is recognised that there is a lack of data related to the response of large coal samples. As larger coal samples exhibit higher degree of heterogeneity than small samples commonly used in the experiments, full-scale or “mock-up” tests would reveal the behaviour of coals in state as expected underground.

The potential of coal seams as reservoirs for storing CO₂ is widely recognised. Despite this and growing environmental concerns, there are still no full-scale CO₂-ECBM projects due the substantial reduction of permeability induced by coal swelling. As it was demonstrated through pilot-tests that fracturing restores permeability, it is suggested that further research both experimentally and numerically investigates the

effect of fracturing on the permeability evolution of the coal as well as the potential implications it might have on the stability of the underground system.

Development of the deformation model presented in Chapter 3 introduced an interaction function which controls the amount of sorption-induced volumetric swelling responsible from the volume loss of porosity available for flow. As in this numerical work only free penetration of microstructure into macrostructure was considered (value of the function was -1), it is suggested that further research is conducted to define the interaction function with respect to volumetric strain, i.e. gas pressure. This is related to the fact that it has been experimentally shown in Chapter 7 that coal under isotropic conditions swells both internally and externally (globally). Furthermore, as one of the main assumptions of the deformation model was to consider coal as an elastic isotropic continuum, further work within the domain of plastic deformations is suggested. This is supported by the observations presented in Chapters 6 and 7 where it has been shown that CO₂ sorption non-reversibly affects the coal structure.

Results of the numerical simulations conducted using the developed model suggest that further developments should be conducted taking into account dual porosity nature of the coal seams and the related interactions between the fractures and the coal matrix. In addition, the kinetics of the sorption and induced swelling as well as the damaging effect of CO₂ sorption on the deformation parameters of coal under non-isothermal conditions should be taken into account which would provide further understanding of the processes occurring in coal seams and increase the likelihood of identifying proper engineering solutions to the existing problems.